

AD-A171 227

AGARD-CP-383

AGARD-CP-383

AGARD

ADVISORY GROUP FOR AEROSPACE RESEARCH & DEVELOPMENT

7 RUE ANCELE 92200 NEUILLY SUR SEINE FRANCE

AGARD CONFERENCE PROCEEDINGS No.383

Guided Optical Structures in the Military Environment

This document has been approved
for public release and sale; its
distribution is unlimited.

DTIC
ELECTE
AUG 26 1986
S A D

DTIC FILE COPY

NORTH ATLANTIC TREATY ORGANIZATION



DISTRIBUTION AND AVAILABILITY
ON BACK COVER

86 8 22 090

DISCLAIMER NOTICE

**THIS DOCUMENT IS BEST QUALITY
PRACTICABLE. THE COPY FURNISHED
TO DTIC CONTAINED A SIGNIFICANT
NUMBER OF PAGES WHICH DO NOT
REPRODUCE LEGIBLY.**

NORTH ATLANTIC TREATY ORGANIZATION
ADVISORY GROUP FOR AEROSPACE RESEARCH AND DEVELOPMENT
(ORGANISATION DU TRAITE DE L'ATLANTIQUE NORD)

AGARD Conference Proceedings No.383
GUIDED OPTICAL STRUCTURES IN THE
MILITARY ENVIRONMENT

Edited by
Dr H.Hodara, US
and
Prof. B.Crosignani, IT

THE MISSION OF AGARD

The mission of AGARD is to bring together the leading personalities of the NATO nations in the fields of science and technology relating to aerospace for the following purposes:

- Exchanging of scientific and technical information;
- Continuously stimulating advances in the aerospace sciences relevant to strengthening the common defence posture;
- Improving the co-operation among member nations in aerospace research and development;
- Providing scientific and technical advice and assistance to the Military Committee in the field of aerospace research and development (with particular regard to its military application);
- Rendering scientific and technical assistance, as requested, to other NATO bodies and to member nations in connection with research and development problems in the aerospace field;
- Providing assistance to member nations for the purpose of increasing their scientific and technical potential;
- Recommending effective ways for the member nations to use their research and development capabilities for the common benefit of the NATO community.

The highest authority within AGARD is the National Delegates Board consisting of officially appointed senior representatives from each member nation. The mission of AGARD is carried out through the Panels which are composed of experts appointed by the National Delegates, the Consultant and Exchange Programme and the Aerospace Applications Studies Programme. The results of AGARD work are reported to the member nations and the NATO Authorities through the AGARD series of publications of which this is one.

Participation in AGARD activities is by invitation only and is normally limited to citizens of the NATO nations.

The content of this publication has been reproduced
directly from material supplied by AGARD or the authors.

Published May 1986
Copyright © AGARD 1986
All Rights Reserved

ISBN 92-835-0391-0



Printed by Specialised Printing Services Limited
40 Chigwell Lane, Loughton, Essex IG10 3TZ

THEME

The last AGARD meeting dealing with related topics was in 1977, jointly with the Avionics Panel: "Optical Fibres, Integrated Optics and their Military Applications". Seven years have elapsed and a whole new technology has arisen: single-mode structures in the form of optical fibres and planar waveguides operating at long wavelength, 1.3 μm and beyond, with minimum attenuation and dispersion. Fibres with attenuation below 0.5 dB/km, and bandwidths in the hundreds of GHz-km have opened up long distance, repeaterless transmission on land and underwater; and addition, the single-mode structure has bred a new class of *passive* devices: sensors capable of detecting sound, magnetic field, motion, temperature, humidity and many other characteristics, all of them approaching the theoretical detection limit. Planar waveguides built out of dimensions less than one micron capable of confining light and creating high-power densities with a few applied volts are responsible for new *active* components: single mode high efficiency, long-life chips operating at room temperature, electro-optic switches, and components capable of generating new frequencies through Raman scattering and other nonlinear phenomena.

The combination of single-mode structures and low loss operation at 1.3 μm and beyond are responsible for far reaching military applications of tactical and strategic import; for instance:

- Rapidly deployable tactical communication.
- Undersea surveillance systems.
- Interferometric and evanescent coupling sensors, in particular fibreoptic gyroscopes, magnetometers, and hydrophones.

The new technology and the resultant military systems and components formed the basis of this meeting. This Specialists' Meeting brought together experts from the military, academia and industry to combine and unify the technology and the military applications.

La dernière réunion AGARD traitant de sujets apparentés fut organisée en 1977 en association avec le Panel Avioniques. Le thème en était "Fibres Optiques, Optique Intégrée et leurs Applications Militaires". Sept années se sont écoulées depuis cette date, et toute une technologie nouvelle a pris naissance: les structures à mode simple sous forme de fibres optiques et de guides d'ondes planaires fonctionnant à de grandes longueurs d'ondes (1,3 μm et au delà) avec une atténuation et une dispersion minimales. Les fibres caractérisées par une atténuation inférieure à 0,5 dB/km, et des bandes passantes de l'ordre de plusieurs centaines de GHz-km ont ouvert la voie aux transmissions longues distances sans répéteurs sur terre et sous l'eau. En outre, la structure à mode simple a donné naissance à une nouvelle classe de dispositifs *passifs*: des senseurs capables de détecter le son, le champ magnétique, le mouvement, la température, l'humidité et bien d'autres caractéristiques approchant toutes de la limite théorique de détection. Des guides d'ondes réalisés dans des dimensions inférieures à un micron, capables de renfermer la lumière et de créer des puissances volumiques élevées avec applications de quelques volts, sont à l'origine de nouveaux composants *actifs*: des "chips" laser à mode simple, de rendement élevé, de grande longévité, fonctionnant à la température ambiante, des commutateurs électro-optiques et des composants capables de produire de nouvelles fréquences par diffusion Raman et autres phénomènes linéaires.

L'association de structures à mode simple et d'un fonctionnement à faible taux de perte, à 1,3 μm et au delà, permet d'envisager des applications militaires de grande envergure, et d'importance tactique et stratégique, comme par exemple:

- Des communications tactiques à déploiement rapide.
- Des systèmes de surveillance sous-marine.
- Des senseurs de couplage interférométriques et évanescents, en particulier des gyroscopes en milieu fibré, des magnétomètres et hydrophones.

Cette technologie nouvelle ainsi que les systèmes de composants militaires qui en ont résulté constituent la base de la réunion qui vous a été présentée. A cette réunion de spécialistes, ont pris part des experts militaires, universitaires et industriels qui se sont efforcés d'associer et d'unifier la technologie et ses applications militaires.

EDITORS' INTRODUCTION

The AGARD meeting on "Guided Optical Structures in the Military Environment", held in Istanbul, Turkey, provided the participants with a broad up-to-date survey of the progresses recently achieved in two very important sectors of civil and military applications: fibre optic communications and fibre optic sensors. Many experts from leading industries in Canada, Europe and the United States, various universities, and government laboratories attended the meeting and contributed to create a particularly lively and productive scientific atmosphere.

To many participants who believed fibre optics technology and development had reached a plateau, this meeting showed that the field is still expanding, especially as far as sensors, devices and new fibre materials are concerned. For example, the exploiting and control of various kinds of nonlinear optical effects allow us to foresee a number of new applications where fast response and low power requirements play a fundamental role. The performance of fibre sensors such as fibre gyros are rapidly approaching theoretical limits; in addition sources, modulators and detector are now capable of furnishing bandwidth beyond 15 GHz. The investigation of new materials for infrared waveguides, with expected losses of 10 dB/km in the 2.55 μm region, also aroused a great deal of interest in the audience for its potential in long repeaterless telecommunication links. Traditional optical fibre communication systems have been shown to have reached a degree of technological maturity and reliability which make them particularly valuable in connection with tactical and military applications.

In conclusion, the meeting was fruitful as it presented a balanced blend between advanced research and applications, and left the attendees with a favourable impression of the relevance and timing of the work they are pursuing.

B.CROSIGNANI and H.HODARA

ELECTROMAGNETIC WAVE PROPAGATION PANEL

Chairman: Dr J.H.Blythe
Communications Research Lab.
Marconi Research Centre
West Hanningfield Road
Great Baddow, Chelmsford
Essex CM2 8HN, UK

Deputy Chairman: Dr H.Solicher
US Army, CECOM
Attn: AMSEL-COM-RN-1
Fort Monmouth, NJ 07703
USA

TECHNICAL PROGRAMME COMMITTEE

Dr H.Hodara (US), Co-Chairman
Dr E.Spliz (FR), Co-Chairman
Dr C.Bolsrobert (FR)
Mr B.Hendrickson (US)
Prof. J.E.Midwinter (UK)
Prof. A.M.Scheggi (IT)
Dr S.Watenabe (US)
Dr M.White (US)
Dr G.Winzer (GE)

HOST NATION COORDINATOR

Mr O.Yargicoglu
TUBITAK-BAE
Ataturk Bulvari 221
Kavaklidere/Ankara
Turkey

PANEL EXECUTIVE

Lt Colonel M.V.Stratton

From Europe
AGARD-NATO
7 rue Ancelle
92200 Neuilly sur Seine

From US and Canada
AGARD-NATO
APO New York 0977



Accession For	
NTIS GRA&I	<input checked="checked" type="checkbox"/>
DTIC TAB	<input type="checkbox"/>
Unannounced	<input type="checkbox"/>
Justification	
By _____	
Distribution/	
Availability Codes	
Dist	Avail and/or Special
A-1	

CONTENTS

	Page
THEME	iii
EDITORS' INTRODUCTION	iv
ELECTROMAGNETIC WAVE PROPAGATION PANEL	v
TECHNICAL EVALUATION REPORT by B.Crosgnani and H.Hodara	ix
 <u>SESSION I – SENSORS</u>	
SUMMARY OF SESSION I by G.Winzer	S1
PROGRESS IN OPTICAL FIBER SENSORS by T.G.Giallorenzi	1
FIBRE OPTIC GYROSCOPES IN INERTIAL NAVIGATION by B.Culshaw and J.D.Nuttall	2
COMPARISON OF RING LASER AND FIBER-OPTIC GYRO TECHNOLOGY by E.Udd, S.F.Watanabe and R.F.Cahill	3
CLOSED LOOP FIBER OPTIC GYRO by D.H.Lewis, B.Bednarz, J.A.Dankowycz, K.Jew, G.Joslin and W.A.Young	4
PROGRESS WITH MULTIPLIED SENSOR ARRAYS BASED ON REFLECTION AT SPLICED JOINTS BETWEEN SENSORS by J.P.Dakin, C.A.Wade and P.B.Withers	5
MAGNETIC AND PRESSURE SENSORS USING THE COMPENSATED POLARIMETRIC SENSOR CONFIGURATION by J.P.Dakin, C.R.Batchellor and J.A.Rex	6
FIBER OPTIC DEVICE FOR TEMPERATURE REMOTE SENSING by A.M.Schegg, M.Brencl, G.Conforti, F.Cosi, R.Falciai and A.G.Mignani	7
OPTICAL FIBER SENSORS FOR THE MEASUREMENT OF PULSED ELECTRIC CURRENTS by G.W.Day, J.D.O.McFadden, L.R.Veaser, G.I.Chandler and R.W.Cernosek	8
NONLINEAR ELLIPSE ROTATION IN A LOW-BIREFRINGENCE OPTICAL FIBER by B.Crosgnani, S.Trillo, P.Di Porto and S.Wabnitz	9
PROGRESS IN OPTICAL FIBER GYROSCOPES USING INTEGRATED OPTICS by H.C.Lefevre, J.P.Bettini, S.Vatoux and M.Papuchon	9A
 <u>SESSION II – DEVICES AND TECHNIQUES</u>	
SUMMARY OF SESSION II by T.G.Giallorenzi	S2
WAVELENGTH DIVISION MULTIPLEXING AT 1.5 μ m FOR HIGH CAPACITY OPTICAL TRANSMISSION by J.Hegarty, N.A.Olsson and R.A.Logan	10
A SPHERICAL WAVEGUIDE MULTIPLEXER-DEMULTIPLEXER by V.Russo, S.Sottini, G.C.Rhigini and S.Trigari	11
A STUDY OF METHODS OF PHASE NOISE REDUCTION OF SEMICONDUCTOR LASERS FOR SENSOR APPLICATIONS by J.P.Dakin and F.B.Withers	12

	Reference
OPTICAL QUADRATURE DEMODULATOR FOR COHERENT DETECTION AND SENSOR APPLICATIONS by S.F.Watanabe, A.A.Joseph, H.B.Turner, S.A.Holmes and J.T.Freidah	13
EFFECTS OF OPTICAL FEEDBACK ON THE PERFORMANCE OF HIGH DATA RATE SINGLE-MODE FIBER SYSTEMS by R.Kell, K.Mathyssek and E.Hörmann	14
PERFORMANCE OF INTEGRATED OPTICAL FREQUENCY SHIFTERS PIGTAILED TO HIGH BIREFRINGENCE FIBRES USING ION MILLED GROOVES by I.Andonovic, W.Johnstone, D.N.McFadyen, A.McDonach, M.S.Ner and S.Beaumont	15
NONLINEAR PLANAR GUIDED WAVE INTERACTIONS AND DEVICES by G.I.Stegeman, C.T.Seaton and H.G.Winful	16
BISTABILITY IN NONLINEAR WAVEGUIDES by M.Bertolotti, C.Sibilia and I.Anselmi	17
INTEGRATED OPTICS OPTICAL LIMITERS by C.T.Seaton, J.D.Valera and G.I.Stegeman	18
PIN-FET PREAMPLIFIER FOR HIGH-SPEED OPTICAL TRANSMISSION SYSTEMS by B.Schwaderer	19
OPTOELECTRONIC BROADBAND SWITCHING FOR COMMUNICATIONS AND SIGNAL PROCESSING by R.I.MacDonald and D.K.W.Lam	20
ACOUSTOOPTIC SPECTRUM ANALYZER USING A PLANAR BRAGG-CELL by M.Stockmann and P.Clemens	21
MODULATORS AND PHOTODETECTORS FOR MICROWAVE/MILLIMETER-WAVE FIBER OPTIC SYSTEMS* by J.J.Pan	22
 <u>SESSION III – GLASS FLUORIDE AND CRYSTALLINE FIBERS</u> 	
SUMMARY OF SESSION III by J.Lucas	S3
PREPARATION AND PROPERTIES OF INFRARED TRANSMITTING HEAVY METAL FLUORIDE GLASS OPTICAL FIBERS by D.C.Tran	23
Paper 24 withdrawn	
GLASS FIBRES FOR TRANSMISSION IN THE 8-12 MICROMETRES WAVEBAND by N.J.Pitt and M.G.Scott	25
SINGLE CRYSTAL FIBERS by R.S.Felgelson	26
VERRES FLUORES POUR GUIDES D'ONDE INFRA ROUGE par J.Lucas	26A
 <u>SESSION IV – COMMUNICATIONS</u> 	
SUMMARY OF SESSION IV by B.Hendrickson	S4
WIDE BANDWIDTH, LONG DISTANCE FIBRE-OPTIC COMMUNICATION SYSTEMS by S.D.Walker, L.C.Blank and L.Bickers	27

	Reference
PERFORMANCE OF RF FIBER OPTIC LINKS by T.R.Joseph and W.E.Stephens	28
FIBER OPTICS: A SURVIVABLE AND COST-EFFECTIVE TRANSMISSION MEDIUM FOR TERRESTRIAL NETWORKS by M.Aslam	29
SINGLE-MODE-FIBERS FOR FIBEROPTIC-GUIDED MISSILES -- A COMPARISON WITH GRADED-INDEX MULTIMODE FIBERS by K.H.Niederhofer and W.D.Schuck	30
LIGHTWAVE TECHNOLOGY IN FUTURE RADAR EQUIPMENT DESIGNS by C.M.Gee, A.E.Popa and H.W.Yen	31
TACTICAL FIBER OPTIC ASSEMBLY REQUIREMENTS by V.E.Kalomiris	32
A HYBRID TRANSMISSION SCHEME ON SINGLE MODE FIBERS FOR TACTICAL COMMUNICATIONS by S.S.Cheng	33
LIST OF PARTICIPANTS	P

TECHNICAL EVALUATION REPORT

by

B. Crosignani
Fondazione "Ugo Bordonini"
ISPT
Viale Europa 160
00153 Roma, Italy

and

H. Hodara
President
Tetra Tech. Inc.
630 North Rosemead Bld
Pasadena, CA 99107, USA

The AGARD meeting on "Guided Optical Structures in the Military Environment" held in Istanbul, Turkey was divided into four sessions: Sensors, Devices and Techniques, Glass Fluoride and Crystalline Fibres, and Communications.

The technical content of each of the sessions was fairly advanced, and the quality of the papers and of their presentation consistently high. Because of the remoteness of the meeting place, the size of the audience was small, about eighty participants. However, this small size coupled with the specialized nature of the talks contributed to create a sense of closeness among the participants which gave rise to a lively scientific atmosphere and allowed for a lot more personal discussions and interactions.

The first session, "Sensors", concentrated on fibre gyros. The French, English and American groups presented a very up-to-date overview of the state-of-the-art and illustrated their specific projects; the audience was introduced to the very core of the current problems and was able to make a comparison with the more conventional mechanical and laser gyros. That session also produced review papers on fibre optical sensors that amply covered other types of sensors (acoustic, magnetic), thus broadening its scope.

The second session reviewed significant engineering progress in devices and techniques. The talks were basically technology oriented, except for theoretical papers on nonlinear optics with applications to a number of new devices. The quality of the speakers was good, and they were able to convey a feel for the technical problems encountered in producing a good device, as for example an R.F. spectrum analyzer. The general impression was that of confidence in the possibility of realizing practical telecommunication applications in the near future.

The third session, although the shortest, was the most exciting one: it was entirely devoted to new materials for infrared waveguide. This new technology will have a significant impact, particularly in transoceanic telecommunication systems, because of the low losses exhibited by some of the new materials; it may also have application in endoscopy, laser machining, remote IR spectroscopy, and so on. In addition, the possibility of new devices appears promising thanks to the development of single crystal fibres that use a technique which transforms high melting oxides in short length single crystal fibres.

The last session dedicated to applications helped the audience to assess present results, and pointed out the potentials of optical fibres in solving a number of practical problems, especially in the military environment: for instance, a fibre optic based radar system and a missile-borne imaging device.

In conclusion, the meeting served the dual purpose of 1) presenting an up-to-date review of the latest developments in fibre optics that impact military applications, and 2) disseminating technical information among the NATO scientific community and providing international synergy to the solution of military problems.

SUMMARY OF SESSION I

SENSORS

by

G. Winzer, Chairman

Sensors based on guided optical structures -- a technology which is increasingly being talked about. After optical communications, this type of sensorics constitutes another important applications area of waveguide optics. In practice of course, optical sensors are always used in conjunction with optical-fiber routes for transmitting measured signals. An example is a section of pressure-sensitive fiber which is spliced into the measuring zone between two sections of pressure-insensitive transmission fiber. It is only fashionable to try to find optical elements responsive to stimuli for all kinds of sensors, or is it the advantages of this new technology that spark intensive activity in this area? Both explanations are right. The benefits include, in many cases, small sensor volume and weight, increased sensitivity to the parameter to be measured, no maintenance, ruggedness, no warmup time and, finally, undisturbed transmission of the measured signal through electromagnetically polluted surroundings. Two classes of optical sensors complement each other: the simple and already widely distributed amplitude-mode sensors, and interferometric sensors. In the former, the intensity of the transmitted light signal is amplitude-modulated by the measured parameter, whereas the latter can detect even extremely small changes in light phase caused by the measured parameter affecting the optical path in the interferometer. T.G. Giallorenzi presented an introduction to optical sensor technology, which is of particular interest to military applications, and also explained the market situation with its strong growth rates and the state-of-the-art at Naval Research Labs.

Session I - Sensors occupied the entire first day of the conference, with ten lectures. In terms of numbers, the contributions on optical gyros predominated. The strong R&D activity as well as the market competition in this sector are clearly reflected by the confusing plethora or acronyms for the various gyro systems: FOG, AFOG, DFOG, MOG, RLG etc..

The conference participants focused their attention particularly on three contributions during this session. In their paper on "Comparison of ring lasers and fiber-optic gyro technology", E. Udd, S.F. Watanabe and R.F. Cahill presented results obtained with both types of optical gyro and explained the requirements of the various product application areas. "Rate grade gyros" are the domain of fiber gyros, "inertial navigation grade gyros" that of ring laser gyros. "Tactical grade gyros" represent the principal field of current competition between these two types of gyro. The fiber gyro's less attractive performance data, such as its zero stability of 0.1-10 deg/h (as against 0.01 deg/h for laser gyros) must be even more strongly countered or overridden by its other strengths such as cost benefits, small dimensions, weight, power requirements and design flexibility. In their paper on "Progress in optical fiber gyroscopes using integrated optics" (ref.9A), H.C. Lefevre, J.P. Bettini, S. Vatoux and M. Papuchon showed that considerable progress had meanwhile been made in the development of fiber gyros.

A device from Thomson CSF's central laboratories with a small housing 35 mm in height and 100 mm in diameter is almost ready for full-scale production. It contains a fiber coil, transmitter, receiver, fiber coupler and an integrated-optical lithium niobate circuit (power divider, polarizer and phase modulator). The gyro has a signal drift of 0.12 deg/h and can be further improved. A special feature is the modulator controlled by an incremental, digitally generated voltage ramp. This allows simpler evaluation of the phase shift generated by the modulator and thus of the gyro's rotational speed. An original contribution was made by J.P. Dakin and C.A. Wade on evaluating the signals of a hydrophonic array by a time multiplexing method with the aid of optical time domain reflectometry (OTDR).

It was presented in their paper entitled "Progress with multiplexed sensor arrays based on reflection at spliced joints between sensors". Optical pulse pairs generated with the aid of a Bragg cell can be coherently detected after reflection at local splices inserted between the sensor's fiber coils specifically for this purpose.

The brief discussion which concluded the ten lectures on sensors seemed to lack enthusiasm. What were the reasons for this? Did the chairman's prompting lack fire or did the participants find the first day of the conference after arrival long enough and the "warmup" time too short, or had the lecturers failed to work out clearly enough the relevance of their subject to the field of military applications? All these factors may have played their part, as well as the fact that the users had been insufficiently insistent in telling the developers exactly what they wanted and needed. And yet, if we regard this meeting as a mirror reflecting the activities covered by the major specialist conferences in the field of optical fiber sensor (OFS) technology, it is well to state that the audience in Istanbul could obtain from it an undistorted picture of the state-of-the-art of this still young and exciting technology.

PROGRESS IN OPTICAL FIBER SENSORS

by

T.G. Giallorenzi
Naval Research Laboratory
Washington, DC 20375-5000

ABSTRACT

A review of the status of Optical Fiber Sensor Technology is presented and the effects of laser noise and demodulation techniques on performance are reviewed. Recent work on the development of fiber telemetry scheme for use with optical fiber sensors is also detailed.

I INTRODUCTION

Based on recent technological progress, Optical Fiber Sensor technology is on the verge of commercialization. Recent market forecasts¹ predict a hundredfold increase in the size of the fiber sensor market by 1993. The basis of these forecasts is the fact that many optical fiber sensors (OFS) have been demonstrated with competitive performance and cost projections. These sensors appear to have found unique applications in laboratory instrumentation where extreme sensitivities, hostile environment operation and/or probe compactness are principal prerequisites to their use. Fiber sensors permit probing of perturbations in inaccessible locations, in the presence of high electrical and magnetic fields, and in corrosive and other hostile environments.

In control systems, fiber sensors are suited for machinery and process monitoring and have been demonstrated to possess adequate sensitivity. Presently several machine manufacturers offer optical fiber sensors as options whereas wide utilization awaits definitive demonstrations of their advantages. This is expected to be realized when fiber sensors are integrated with optical fiber telemetry to provide a "dielectric" control system which can operate in particularly noisy or hostile environments. Power plants and heavy machinery manufacturing facilities appear to be prime candidates for early usage. Optical telemetry also provides unique capabilities to remotely sense hazardous environments. Detection of explosive gas accumulation in inaccessible and/or remote locations is readily accomplished with fiber optics while at the same time eliminating the dangers of sparking from electrical sensor or telemetry shorts.

Medical instrumentation based on fiber sensors has been developed and has begun to find clinical and laboratory use. While no breakthrough in market development is yet predicted in this area, it is generally realized that fiber sensors are ideally suited for invasive probing because of their small size and biochemical inertness. These sensors presently offer competitive capabilities and when further developed should be as common place as endoscopes. Finally, the military is examining the use of fiber sensors and has actively pursued the development of several sensor types. Control systems sensors and monitor sensors (damage control, fuel status, etc.) are being evaluated and are expected to find application.

With the technical progress of the past several years along with the appearance of several important applications, the basis for the use of fiber sensors will gradually grow, first with specialty applications where some unique fiber sensor attribute makes them the device of choice, then eventually with common, widespread functions when the marriage of fiber sensors and telemetry is fully realized.

In the following sections, a brief review of sensor progress and trends will be presented. Discussion will then center on demodulation techniques and injection laser noise. Potential telemetry configurations currently under study for use with OFS will be described.

II SENSOR DEVELOPMENTAL TRENDS

(A) Amplitude Mode Sensors

In this class of sensors, the light intensity transmitted by optical fibers is amplitude modulated by the perturbation under study. This class of sensor has been widely developed and is being evaluated for use in flight controls, industrial process monitoring, medical probes, laboratory instrumentation to name a few applications. Because amplitude modulation sensors are easy and cheap to fabricate, many laboratories have developed devices of this type; however, packaging and tailoring these devices for specific applications has been somewhat more limited. Current research and development has now shifted from simple demonstration of amplitude sensors to perfecting these devices for

incorporation into specific applications. For example, a high temperature microbend pressure sensor has been developed by Babcock and Wilcox² for use in flight control systems. The sensor (Figure 1) was characterized up to ± 690 kPa and temperatures to 540°C. The experimental data showed a linear dependence on the applied pressure and a minimal offset and slope change when the temperature was varied. These variations will be calibrated out before the sensor is used in flight applications. This work illustrates the shift in sensor development to qualify OFS over the full range of requirements for specific applications.

A second trend which will be described in greater detail later is the use of OFS with fiber telemetry. A representative example of fiber sensor telemetry is a remote gas sensor for CH_4 and C_2H_2 which used a 20 km optical fiber for remote sensing³. Adequate sensitivities were demonstrated and the use of the fiber remote sensor permits probing in hostile (corrosive gases, heat, etc.) environments.

(B) Gyroscope

The development of optical fiber gyros has progressed to the point where it now appears certain that they will impact many inertial navigation and control applications. The attractiveness of these devices arises from their potential for low cost, compact size, ruggedness, extremely high sensitivity and reliability. This last feature is based on the fact that fiber gyros possess no moving parts. Research and development efforts to date have concentrated on the demonstration of gyro sensitivity whereas the more recent efforts have not shifted to dynamic range, linearity, scale factor, stability and packaging issues.

Nonreciprocal Generated Noise Sources. A Sagnac interferometer measures nonreciprocal effects, i.e. the sign of the phase shift of the light depends on the direction of propagation in the fiber loop. Non-reciprocal effects occurring in the fiber such as the Faraday effect and the nonlinear Kerr effect, produce nonreciprocal phase shifts that a Sagnac interferometer will measure. These latter effects appear as noise sources and must be minimized.

The Faraday effect, which is a magnetically induced rotation of the optical polarization, is observed if the fiber loop is placed in a field gradient, or if the optical polarization changes its orientation as the light propagates around the loop. Since this effect is indistinguishable from a Sagnac signal, it results in noise and zero shifts in the gyroscope output. Both magnetic shielding and polarization-holding fibers have been used to reduce Faraday effects in fiber gyroscopes to acceptable levels.

The Kerr effect is an optical-intensity-induced nonreciprocity. At high optical intensities, the propagation constants for the counterpropagating beams become intensity dependent. This is a nonlinear optical effect related to four-wave mixing that has found application in nonlinear spectroscopy. In particular, when the counterpropagating beams have unequal intensities, the propagation constants become unequal and cause a nonreciprocal phase shift indistinguishable from the Sagnac effect. This effect has been minimized by the use of a broadband laser or superluminescent diode source with a broad frequency spectrum. When summed over the wavelength components of such a source, the Kerr-induced phase shift averages to zero.

Fiber Based Noise Sources. There are additional difficulties which arise from the input coupler and the nature of single-mode fiber, and result in nonreciprocal operation. For reciprocal gyro operation the counterpropagating beams should possess identical optical polarization states and should travel a common path. This means that the beams should enter and exit the fiber coupler through a common port. The polarization state may be specified by a polarizer placed before the fiber coupler.

The setup with a polarizer provides the output Sagnac signal $2\phi_s$. A mathematical analysis shows that the signal obtained from the unused port of the original Sagnac beamsplitter (or coupler) has an additional phase bias or zero shift ϕ_0 added to the Sagnac signal $2\phi_s$. This additional phase bias depends on the detailed properties of the coupler and is environmentally sensitive leading to large drifts. Therefore only the input port of the interferometer is monitored.

Polarization mode coupling in the fiber is a second source of non-reciprocal noise in the gyro. A single-mode fiber actually supports two polarization modes that have very similar transverse mode structures but that are polarized at 90° to each other. In ordinary single-mode fiber, slight ellipticities in the core of the fiber cause these polarization modes to have slightly different propagation velocities. Coupling between the polarization modes is caused by fiber bends or jacket pressure and is very sensitive to thermal and acoustic fluctuations. Nonreciprocal gyro operation results when one beam travels one path between the polarization modes and the counter-rotating beam travels a different one. Because of the rapid temporal fluctuations of the mode-coupling centers, the nonreciprocal output of the Sagnac interferometer due to this effect appears as noise and is referred to as polarization noise. The most straightforward solution to this problem is achieved by using high-birefringence polarization-maintaining fibers which are now available from several manufacturers.

The final noise source resulting in the fiber is due to Rayleigh back-scattering. Rayleigh backscattering occurs when light is reflected from microscopic density fluctuations in the fiber, and the next backreflected signal is the sum of each component from each segment of the fiber. If a coherent laser is used there is coherent summation of scattered light. The composite phase from all the scattering centers is influenced by thermal and acoustic perturbations along the fiber, resulting in the backscattered signal becoming a rapidly time-fluctuating quantity. In fiber gyroscopes the Rayleigh backscattered components mix with the counterpropagating beam, and after interference are indistinguishable from a Sagnac signal. Since Rayleigh backscattering is a coherent effect, it may readily be reduced if the coherence of the laser is

reduced. This was successfully achieved by the use of superluminescent diodes. The point of using a limited coherence source is that such a source has adequate coherence to measure the very small Sagnac phase shifts due to rotation since the counter-rotating beams travel almost identical pathlengths (within a few microns), but that its limited coherence reduces the magnitude of many noise sources, such as Rayleigh scattering by limiting the amount of scattered noise that can coherently add at the detector.

Sensitivity and dynamic range. The theoretical sensitivity of the fiber gyro is illustrated in Figure 2, along with currently achieved results. The quantum limit of sensitivity in fiberoptic gyroscopes is caused by shot noise in the optical detector. Since shot noise has a white noise spectrum, a random drift coefficient can be derived, which is usually expressed as units of degrees over the square root of time in hours. The theoretical performance of fiber gyros, when determined in this fashion, appears to exceed the equivalent theoretical performance of ring laser gyroscopes.

The current status of high-sensitivity rotation detection is illustrated by a fiber gyroscope recently demonstrated at the Naval Research Laboratory. This device used polarization-holding fiber in the coil and Sagnac coupler. The fiber length was 430 m wound on a 16-cm radius drum and had a sensitivity of 5×10^{-4} °/hr. This and other experiments have shown, at least in a laboratory environment, that the fiber optical gyro can operate at the level required for navigational quality strapdown inertial systems.

One of the most serious current limitations in the use of a passive fiber gyroscope is the limitation on linear dynamic range caused by an output proportional to $\sin 2\phi$. At large rotation rates the sin function is non-linear, and, for 2ϕ values of near 90° , sensitivity to changes in rotation vanishes. Between a noise floor and a linearity limit of ppm the linear dynamic range of about four decades is obtained. For rotation rates exceeded 10^4 times the noise floor gyro output is very non-linear. Since many initial navigation applications require five to six decade of linear dynamic range, this difficulty currently represents one of the major problems to implementation. Two strategies have been developed for solving this problem, signal nulling and signal processing.

In the signal-nulling approach, an output phase shift is artificially generated of equal magnitude but opposite sign to the Sagnac phase shift so that the gyro is always operating about its zero point, where it is linear. The rotation rate signal is derived from the nulling signal required. The dynamic range is only limited by the ability to generate the phase-nulling signal. The most popular implementation of this approach is the use of an acoustic-optic Bragg cell in the fiber loop, which frequency-shifts the light passing through it in one direction relative to the counterpropagating beam. This frequency shift is seen as a phase shift in the output which is used to null the total output signal. A feedback loop from the detector is used to drive the Bragg cell and also provide a frequency output signal, in which frequency is proportional to rotation.

The phase-nulling gyro simulates a ring laser gyroscope, in that a frequency difference between counterpropagating beams is proportional to rotation. This is expressed by the output equation

$$f = \frac{2R}{n\lambda_0} \Omega$$

Unfortunately fiber index of refraction n appears explicitly in this equation whereas previously it did not. Due to the temperature dependence of n , thermal drift problems are introduced and make it more difficult for this type of gyro to operate stably over a broad temperature range.

Another approach to the linear dynamic range problem is to apply some type of signal processing to linearize the sin output. The accuracy and speed with which these processes can be carried out are of great interest because this technique avoids the addition of extra optical components in the gyro.

(C) Mach Zehnder Interferometric Sensors

These sensor types have been widely researched and together with the Sagnac sensor offers the potential for extremely sensitive devices. Table I presents a comparison of the state of the art of conventional sensors and the theoretical sensitivity of the fiber sensors. Based on the potential for major advances in sensor sensitivities, many research laboratories have pursued work on interferometric sensors which can be divided into research on fiber coatings and demodulation schemes. The key to widespread applicability of interferometric sensors is the fact that the shift in optical phase caused by a particular environmental parameter—pressure, temperature, magnetic/electric field, etc., can be effectively controlled by application of appropriate jacketing materials on the optical fiber. The application of these coatings usually involves straightforward procedures, and, more importantly, does not affect the optical performance of the optical fiber waveguide. This "dissociation" of the waveguide itself from the designer's attempt to control its sensitivity is perhaps the most important factor responsible for the rapid pace at which this generic sensor technology has been developed.

For the usual case in which the perturbing field generates fiber strains whose wavelengths are large compared to the fiber diameter, the normalized phase shift is given by:

$$\frac{\Delta\phi}{\phi} = \epsilon_r - \frac{n^2}{2} \left[(P_{11} + P_{12}) \epsilon_r - P_{12} \epsilon_z \right] + \left(\frac{\partial n}{\partial T_0} \right) \Delta T_0$$

where ϵ_z , ϵ_r are the axial and radial strains induced in the fiber core, the P 's are the photoelastic constants and $(\partial n / \partial T)_\epsilon$ is the index variation of the core with temperature at constant strain. Thus, except for the case of temperature, the calculation of the phase response of an optical fiber sensor is reduced to the mechanical problem of calculating the strains communicated by the perturbation to the fiber core, and because these strains depend strongly on the fiber jacket parameters, the sensitivity can be optimized by careful design of the coating.

For example, the application of an appropriate coating to the optical fiber produces a composite structure which can provide substantially increased strain levels in the fiber core. This is accomplished for the acoustic case by elastomeric coatings with high compressibility, for magnetic sensing with magnetostrictive coatings, for the thermal case with large linear expansion coefficient materials and for electric field sensing with piezoelectric materials. Elaborate computer programs now exist with which to perform these designs.

The principles of coating technology are now well understood and materials research is centered on reducing these principles to practice. Further development of coatings and perfection of demodulation technique should permit realization of the performances predicted in Table I while at the current time competitive performance with conventional sensors has already been demonstrated as is illustrated in Figure 3. This figure illustrates sensor performance relative to the theoretically predicted performance for an acoustic sensor.

III DEMODULATION TECHNIQUES

In a Mach-Zehnder sensor, one of the fiber arms of the interferometer serves as the signal arm, the other as the reference arm. The resulting optical phase shift is converted interferometrically to an intensity signal. The design of the demodulation scheme is made non-trivial by the presence of low frequency random temperature and pressure fluctuations which the arms of the interferometer experience. These fluctuations produce differential drifts between the arms of the interferometer. The drift causes changes in the amplitude of the detected signal (signal fading), as well as distortion of the signal.

The purpose of the demodulation scheme in fiber optic interferometers is to transform the optical output of the interferometer into an electrical signal proportional to the amplitude of the relative phase shift. Typical requirements of the detection scheme are: to be able to resolve signals corresponding to 10^{-6} rad phase shift, to have a linear response and to have a large dynamic range ($10^6 \rightarrow 10^7$). Specific requirements such as packaging and low power consumption are also important. In this paper, we will concentrate on two new techniques using laser tuning; passive homodyne techniques and (3×3) directional couplers. Each of these schemes have achieved μ rad performance; however, each scheme has specific advantages and disadvantages which will be briefly described below.

The homodyne scheme (referred to as phase swept) uses a large phase modulation (produced by laser tuning) applied to the interferometer, such that by appropriate beating and filtering, two signals with a $\pi/2$ relative phase shift are produced.

The variation in the light intensity detected at the output of an interferometer may be written as

$$I = A + B \cos \theta(t) \quad (1)$$

where $\theta(t)$ is the phase difference between the arms of the interferometer. The constants A and B are proportional to the input optical power, but B also depends on the mixing efficiency of the interferometer. If a sinusoidal modulation with a frequency ω_0 and amplitude C is imposed on the interferometer, then (1) becomes

$$I = A + B \cos (C \cos \omega_0 t + \phi(t)) \quad (2)$$

where $\phi(t)$ includes not only the signal of interest, but environmental effects as well. Expanding (2) in terms of Bessel functions produces

$$I = A + B \left\{ \left[J_0(C) + 2 \sum_{k=1}^{\infty} (-1)^k J_{2k}(C) \cos 2k\omega_0 t \right] \cos \phi(t) - \left[2 \sum_{k=0}^{\infty} (-1)^k J_{2k+1}(C) \cos (2k+1)\omega_0 t \right] \sin \phi(t) \right\} \quad (3)$$

From this expression it is clear that when $\phi(t) = 0$, only even multiples of ω_0 are present in the output signal, whereas for $\phi(t) = \pi/2$ rad (quadrature condition), only the odd multiples of ω_0 survive.

In a similar fashion the phase angle $\phi(t)$ can be separated into a signal component of frequency ω and the environmental drifts $\psi(t)$, $\phi(t) = D \cos \omega t + \psi(t)$ and expanded

$$\cos \phi(t) = \left[J_0(D) + 2 \sum_{k=1}^{\infty} (-1)^k J_{2k}(D) \cos 2k\omega t \right] \cos \psi(t) - \left[2 \sum_{k=0}^{\infty} (-1)^k J_{2k+1}(D) \cos (2k+1)\omega t \right] \sin \psi(t) \quad (4)$$

$$\sin \phi(t) = \left[2 \sum_{k=0}^{\infty} (-1)^k J_{2k+1}(D) \cos(k+1)\omega t \right] \cos \psi(t) + \left[J_0(D) + \sum_{k=1}^{\infty} (-1)^k J_{2k}(D) \cos 2k\omega t \right] \sin \psi(t) \quad (4)$$

These equations along with (3) show that when $\psi(t) = 0$, even (odd) multiples of ω are present in the output signal centered about the even (odd) multiples of ω_0 . For the case when $\psi(t) = \pi/2$ rad, even (odd) multiples of ω are present about the odd (even) multiples of ω_0 .

The sidebands contain the signal of interest and are either present about the even or the odd multiples of ω_0 . The signal is obtained by mixing the total output signal with the proper multiple of ω_0 and low-pass filtering to remove the terms above the highest frequency of interest.

For the carrier frequencies considered in the experiment, namely 0, ω_0 , and $2\omega_0$, the output signals after mixing and filtering are

$$\begin{aligned} &A + BJ_0(C) \cos \phi(t) \\ &BGJ_1(C) \sin \phi(t) \\ &- BHJ_2(C) \cos \phi(t), \end{aligned} \quad (5)$$

respectively, and where G and H are the amplitude of the mixing signals for ω_0 and $2\omega_0$.

In order to obtain a signal that does not fade as a function of undesired fluctuations, two signals, one containing the sine $\phi(t)$ and the other cosine $\phi(t)$ are utilized. The time derivative of the sine and cosine terms are cross multiplied with the cosine and sine terms, respectively, to yield the desired sine and cosine squared terms. The process will be illustrated by considering the output signals for ω_0 and $2\omega_0$. The time derivative of these are obtained from (5) and are given by

$$\begin{aligned} &BGJ_1(C) \dot{\phi}(t) \cos \phi(t) \\ &BHJ_2(C) \dot{\phi}(t). \end{aligned} \quad (6)$$

Multiplying this by the signal for the other frequency produces $B^2GHJ_1(C)J_2(C) \dot{\phi}(t) \cos^2 \phi(t)$

and

$$-B^2GHJ_1(C)J_2(C) \dot{\phi}(t) \sin^2 \phi(t). \quad (7)$$

Subtracting gives

$$\begin{aligned} &B^2GHJ_1(C)J_2(C) \dot{\phi}(t) (\sin^2 \phi(t) + \cos^2 \phi(t)) \\ &= B^2GHJ_1(C)J_2(C) \dot{\phi}(t). \end{aligned} \quad (8)$$

This output can then be integrated to produce the signal $\phi(t)$ which includes all of the drift information in addition to the actual signal. This scheme has the advantage of having no reset problem. This scheme requires an AGC (owing to polarization fading) and may have a somewhat limited frequency range (two orders of magnitude), however, the tuning range may be varied over a fairly wide frequency range (~ 0.1 Hz \rightarrow 10 kHz).

The (3×3) coupler passive scheme is potentially a true passive scheme, where the required $\pi/2$ phase shift between the two outputs is achieved by replacing the conventional final (2×2) directional coupler, by a (3×3) device. The optical and electronic configuration is shown in Fig. 4.

$$\begin{aligned} P_1 &= -2B_2(1 + \cos \theta), \\ P_{II,III} &= B_1 + B_2 \cos \theta \pm B_3 \sin \theta. \end{aligned} \quad (9)$$

where P_{II}/P_{III} takes the plus (minus) sign and B_i ($i = 1, 2, 3$) are constants dependent on the coupling coefficients of the fiber coupler. To obtain the required $\pi/2$ phase difference required P_{II} and P_{III} were processed to form the sum and difference

$$\begin{aligned} P_{II} &= P_{II} + P_{III} = 2(B_1 + B_2 \cos \theta), \\ P_{III} &= P_{II} - P_{III} = 2B_3 \sin \theta. \end{aligned} \quad (10)$$

After signal processing one obtains

$$\begin{aligned} D &= P_{II} P_{III} - P_{III} P_{II} \\ &= 4B_1 B_3 \theta \cos \theta + 4B_2 B_3 \theta, \end{aligned}$$

$$E = \int D dt = +4B_1B_3\sin\theta + 4B_2B_3\theta. \quad (11)$$

Note that B_1 is the dc output of P_{II} , P_{III} . By introducing offsets in the processing electronics, B_1 can be set to zero. Then

$$D = 4B_2B_3\theta,$$

thus

$$E = \int D dt = 4B_2B_3\theta. \quad (12)$$

which is directly proportional to the interferometer's phase shift. It can be seen from Eq. (11) that unless the electronics is correctly balanced (i.e., $B_1 = 0$) distortions will be present in the output. These equations, although derived for a single polarization system, serve to demonstrate the principle of operation. In practice, small deviations from the $\pi/2$ phase shift (between P_{II} and P_{III}) were observed as different input polarizations were used. Consequently, Eq. (12) should be multiplied by a factor $\cos \Delta$ (where Δ is the angular deviation from $\pi/2$) to allow for this effect.

As before, an AGC is required. In general, the properties of the (3×3) directional coupler determine the stability and fidelity of the detection scheme.

Noise in the Interferometer Noise sources which result in a loss of sensor sensitivity may be split into three basic groups, (1) coherence length, (2) intensity noise, and (3) phase noise frequency jitter. All three parameters⁴ are strongly dependent on light fed back into the laser cavity. The amplitude and phase of the light fed back into the laser cavity as well as the effective external cavity length are all important in determining the laser's properties⁴. The free running laser has a coherence length of only a few meters, requiring the sensing and reference fiber to be balanced to within ± 1 m. The amplitude of the laser's intensity noise is similar to that of gas lasers⁴, but has a $1/f$ characteristic which may limit performance at low frequencies; common mode rejection techniques are therefore desirable. The interferometer is extremely sensitive to low frequency (i.e., in the signal band) jitter of the laser's emission. This quasi-random noise source (also with a $1/f$ characteristic) results in noise in the interferometer which has an amplitude proportional to the path length difference in the interferometer. Typical results are shown in Fig. 5 for a number of different laser structures. The measures were made with an unbalanced Michelson Interferometer (this noise is often termed phase noise). As can be seen from this figure for μ radian performance, path differences of less than \sim mm are required. Different schemes to stabilize the laser output using optical feedback or electronic feedback are being considered; they will be discussed briefly below.

A method to increase the frequency stability of the laser is to take the noise output and form a feedback loop to the laser's constant current supply. The experimental arrangement is shown in Fig. 6. The feedback circuit is adjusted such that when the voltage output of the photodiode is equal to the voltage that corresponds to the maximum slope of the Fabry-Perot response, the error signal applied to the diode laser is zero. However, when the laser's frequency shifts, the feedback circuit imposes a current on the constant bias current of the laser proportional to the laser's frequency deviation. The frequency response of the feedback loop is determined by the overall loop gain of the system and is adjusted to a maximum for stable operation.

The results of the phase noise measurement for the free running laser are shown in Fig. 7a (upper trace). The characteristic $f^{-1/2}$ frequency dependence is observed; it should be noted that the phase noise contribution was ~ 2.5 orders of magnitude larger than the contribution due to amplitude noise, which is shown in Fig. 7b. The lower trace in Fig. 7a shows the phase noise output when the feedback circuit is switched on; a substantial reduction in the phase noise is observed. Below 5 Hz, the noise is reduced by 60 dB (electrical noise power); at 250 Hz a ~ 30 dB reduction was observed. Despite the large reduction in phase noise, no change in the laser's amplitude noise was observed. This is similar to the effect of optical feedback stabilization. Similar results may of course be obtained by using a Mach-Zehnder (bulk or fiber) to provide the stabilization feedback.

It has been shown⁵ that the frequency and intensity instabilities of GaAlAs lasers are partly correlated. However, the correlation is too low to, for example, stabilize the frequency by stabilizing the intensity.⁶ However, the intensity noise emitted by the laser's front facet may be substantially reduced by stabilizing the output of the rear facet.

IV. TELEMETRY

Many of the application areas for sensor technology involve a large number of sensors. These may be in the form of large sensor arrays as are found, for example, in acoustic streamers towed by surface ships engaged in the exploration for oil deposits or involve the distribution of a variety of sensor types for control in engine, power plant, factory, or ship control platforms.

In the design of such sensor systems, optical sensors and fiber telemetry have a clear, intrinsic advantage over conventional electrical technology. The use of optical sensors and fiber optic telemetry make possible all-optical, multi-element sensor systems capable of supporting a very large number of high bandwidth sensor devices with no requirement for electrical power away from the processing platform. This derives from the high transmission bandwidth of the optical fibers, the all optical nature of the sensors, and the ability to remotely modulate the optical signal delivered to the sensor. These principles are illustrated in Fig. 8. As for the case of a ship control system, shown in the upper left, one complete

suite of sensor types — liquid level, temperature, smoke, pressure, and discharge — is excited by an optical fiber carrying light of wavelength, λ_1 . At a second location a second identical sensor suite is excited by an optical fiber carrying wavelength λ_2 , a third suite λ_3 , and so on. A single return fiber carries the light back from all sensor suites, where wavelength division demultiplexing is used to extract the signals from one particular suite. The signals from each individual sensor making up that suite can be separated by pulsing the optical source in a time sufficiently short compared to the optical transit time from adjacent sensors. For each laser source (1 milliwatt) at λ_1 and associated fiber pair, information from approximately ten to fifty sensors can be collected, the exact number depending on the desired sensor threshold detectability. Thus, for a small bundle containing some fifty fibers, a high bandwidth sensor system with as many as several thousand passive sensors can be deployed with no requirement for electric signals or electric power away from the processing platform.

This is only one of the many configurations possible. For example, in place of wavelength multiplexing, frequency division multiplexing can be achieved by straightforward frequency modulation of the laser sources as shown in the upper right of Figure 8.

Research activity at Stanford University⁷ and University College London⁸ on multiplexing several interferometric sensors has led to the demonstration of two techniques potentially capable of the principle of operation. One arm of each sensor loop (I_1 and I_2) carries the sensed information in the form of phase modulation on the optical carrier. I_1 and I_2 are chosen to be much longer than the source coherence length λ_c so that the sensed phase modulation will not be converted into detectable intensity modulation at the sensor output. The phase information can still be retrieved by the receiving loops which match the respective sensor loops to within a fraction λ_c . If $|I_1 - I_2|$ is much larger than λ_c , cross talk is eliminated, and the detector at the output of L_1 reflects only the information imposed on I_1 . Figure 10 illustrates a configuration to multiplex interferometric sensors by utilizing the frequency modulation schemes described by equations 1 through 8. The principal attraction of this scheme is the possibility to perform passive sensing without the use of electrical components in the sensor head.⁸ By frequency modulating the laser and having different path lengths within each sensor, signals from each sensor may be separated. The principle involved is as follows: for a single sensor and a periodic linear ramp modulation of the source frequency, the detector output will contain a component oscillating at a frequency characteristic of the path imbalance of the interferometer. A multiple sensor system may be multiplexed choosing the interferometric sensors to have a different path imbalance so that each interferometer may be identified by a particular frequency component in the detector output. There will, of course, be frequency components associated with paths through two or more interferometers, and these could occur at frequencies associated with other interferometers in the system. The novel contribution made by these authors is the development of design procedures to ensure that there is no ambiguity between cross-term signals and desired signals from the interferometers.⁸ These authors predict that up to a thousand sensors may be multiplexed using their scheme.⁸

Multiplexing interferometric sensors remains in an early stage of development with several issues to be resolved such as increased shot noise arising from serial multiplexing, polarization scrambling degradation of multisensor performance and cross talk.

1. J.Zilber, "Fiber Optic Sensor Market Development," Proceedings of 2nd Optical Fiber Sensor Conference, pp. 177—181, Stuttgart, FRG, 1984.
2. D.Varshneva, W.L.Ghering & J.W.Berthold, "High Temperature Fiber Optic Microbend Pressure Sensor," Proceedings, Optical Fiber Communications Conference, pp. 140—141, San Diego, 1985.
3. H.Inaha, K.Chan & H.Ito, "All Optical Remote Gas Sensor Systems over 20 Kw Range," Proceedings of 2nd Optical Fiber Sensor Conference, pp. 211—214, Stuttgart, FRG, 1984.
4. L.Goldberg, H.F.Taylor, A.Dandridge, J.F.Weller and R.O.Miles, "Spectral Characteristics of Semiconductor Lasers with Optical Feedback," IEEE J.Quant. Elect., 18, 555, 1982.
5. A.Dandridge and H.F.Taylor, "Intensity and Frequency Instabilities and GaAlAs Diode Lasers," IEEE J.Quantum Elect., 18, 1738, 1982.
6. A.Dandridge and A.B.Tveten, "Properties of Diode Lasers with Intensity Noise Control," Appl. Opt., 22, 311, 1983.
7. J.L.Brook, B.Y.Kim, H.J.Shaw, "Coherence Multiplexing of Fiber Optic Interferometric Sensors," Proceedings Third Optical Fiber Sensor Conference, pp. 128-129, 1985.
8. I.Sakai & G.Parry, "Multiplexing Interferometric Fiber Sensor by Frequency Modulation Techniques", Proceedings Third Optical Fiber Sensor Conference, pp. 125—129, 1985.

DETECTION THRESHOLD

DETECTION DEVICE	STATE OF THE ART	FIBER SENSOR THEORETICAL LIMIT
Acoustic Sensor	20 dB re:1 μ Pa Piezoceramics, Human Ear	- 25 dB re:1 μ Pa 1 km Fiber, 150 μ watts
Magnetic Sensor Ambient Temp Cryogenic	10 ⁻⁶ GAUSS 10 ⁻¹¹ GAUSS	10 ⁻¹² GAUSS
Accelerometer	5 \times 10 ⁻⁷ G's	2 \times 10 ⁻⁸ G's
Rate of Rotation	10 ⁻² $\sqrt{\text{HR}}$ Mechanical 7 \times 10 ⁻⁴ $\sqrt{\text{HR}}$ Ring Laser	10 ⁻⁶ $\sqrt{\text{HR}}$
Thermal Sensor	5 \times 10 ⁻⁴ $^{\circ}\text{C}$ 10 ² Hz Bandwidth Semiconductor Thermistors	10 ⁻⁶ degrees/ 1 cm of fiber 10 ³ Hz Bandwidth
Strain	10 ⁻⁶ Semiconductor	10 ⁻¹¹ / 1 cm of fiber

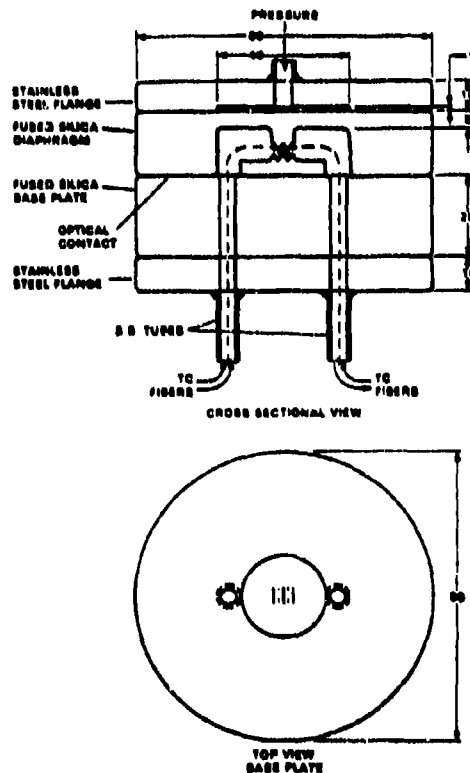


Figure 1 Temperature compensated microbend sensor. All dimensions are in millimeters and fibers are shown as dotted lines.

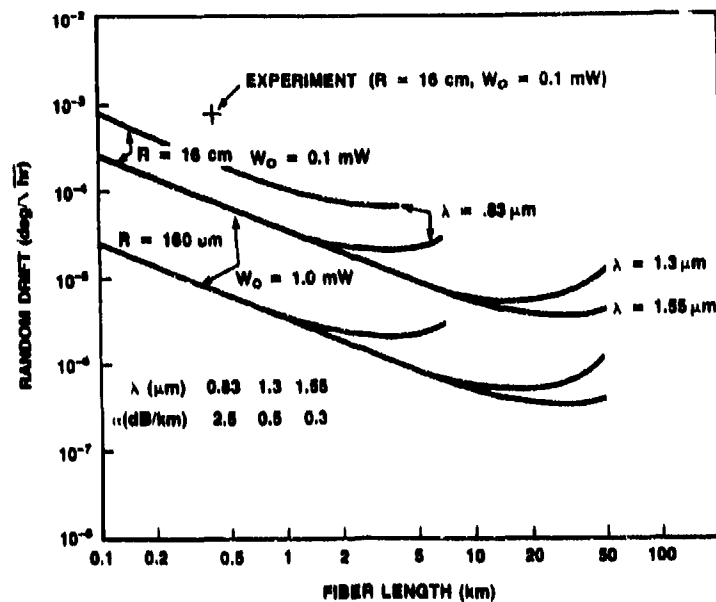


Figure 2 Optical fiber gyro random drift performance.

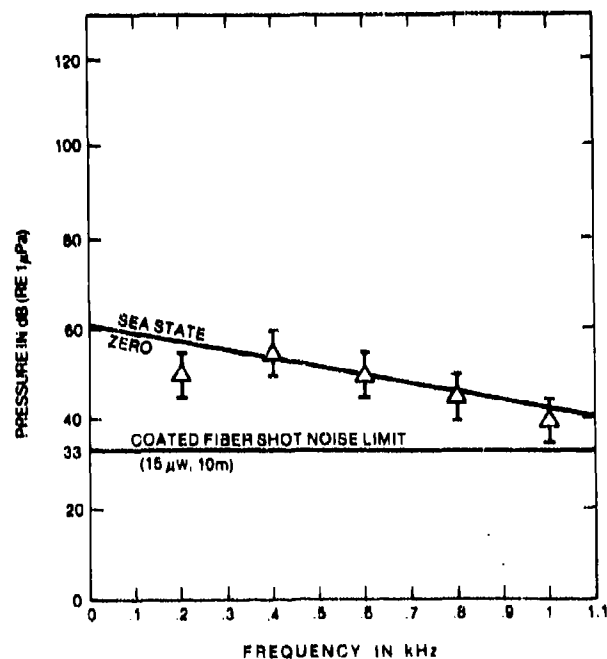


Figure 3 Representative minimum detectable acoustic levels for optical fiber sensor. The sensing element is 10 meter of Hytrel-Silicone jacketed fiber.

PASSIVE HOMODYNE

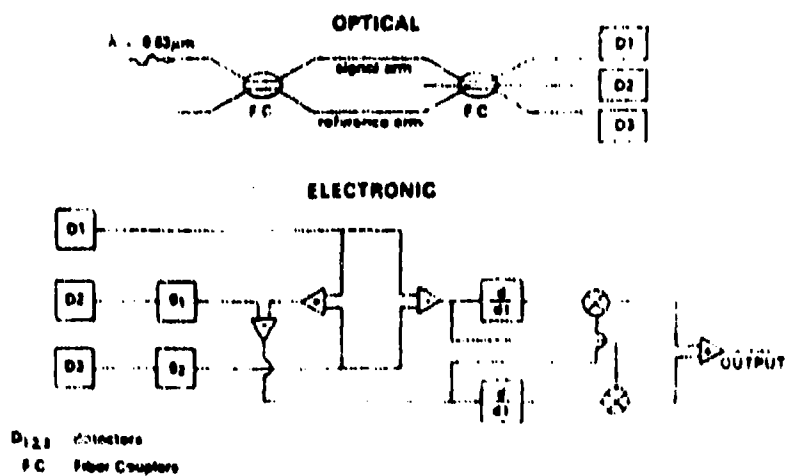


Figure 4 Schematic of the optical and electronic circuitry for a (3×3) passive detection scheme.

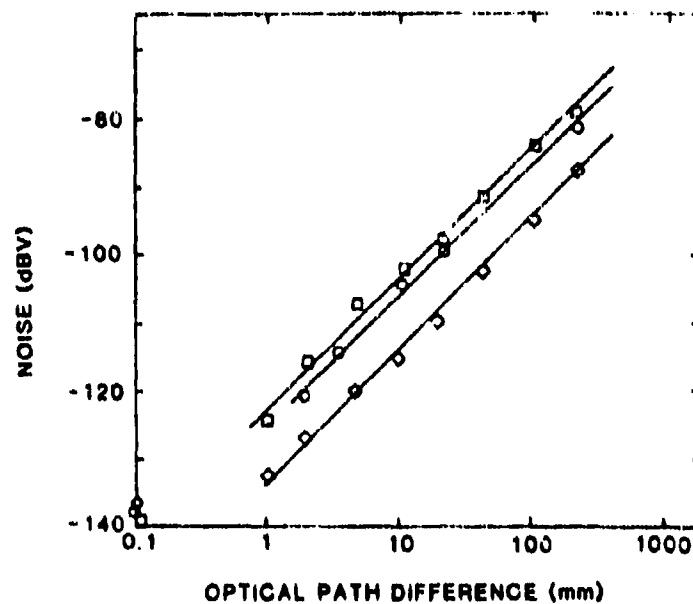


Figure 5 Noise output of a Michelson interferometer as a function of path length difference for three types of GaAlAs laser structures: \circ , TJS; \square , Bh; \diamond , CSP.

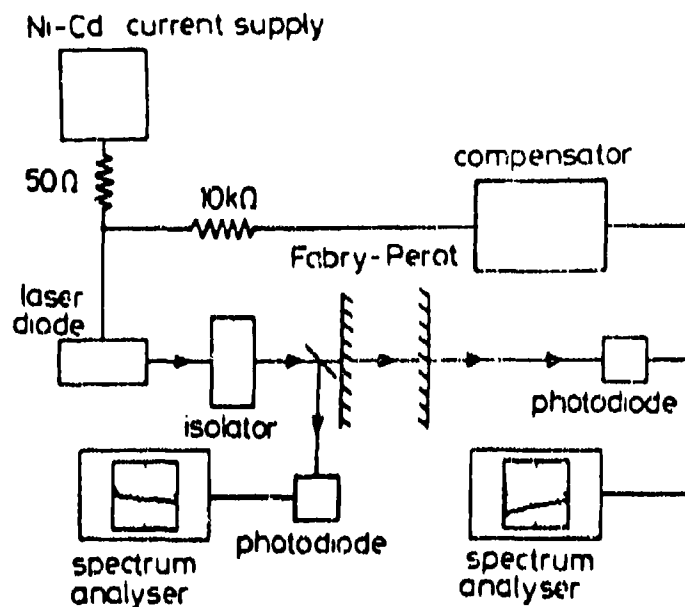


Figure 6 Schematic diagram of an electronic laser stabilization.

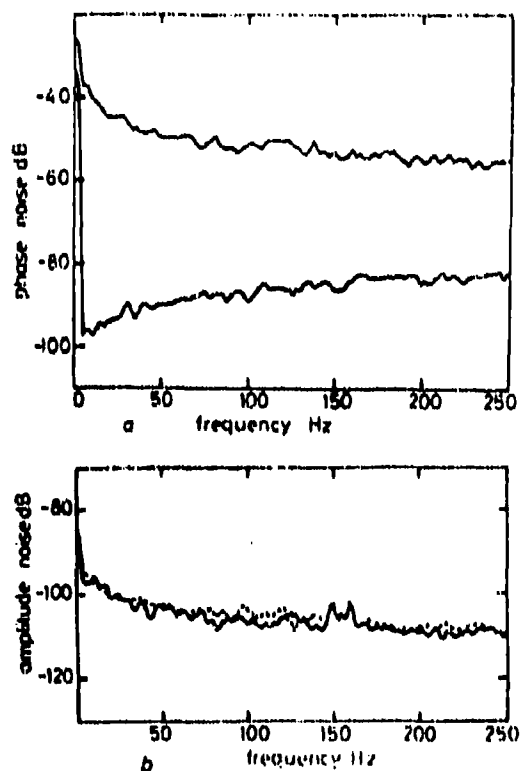


Figure 7 Frequency dependence of the laser diodes phase noise (1 Hz bandwidth) obtained using output of a Fabry-Perot interferometer. Upper trace: free running laser; lower trace; with current feedback stabilization. (b) Frequency dependence of intensity noise (1 Hz bandwidth) with and without frequency stabilization.

ALL-OPTICAL FIBER SENSOR SYSTEM

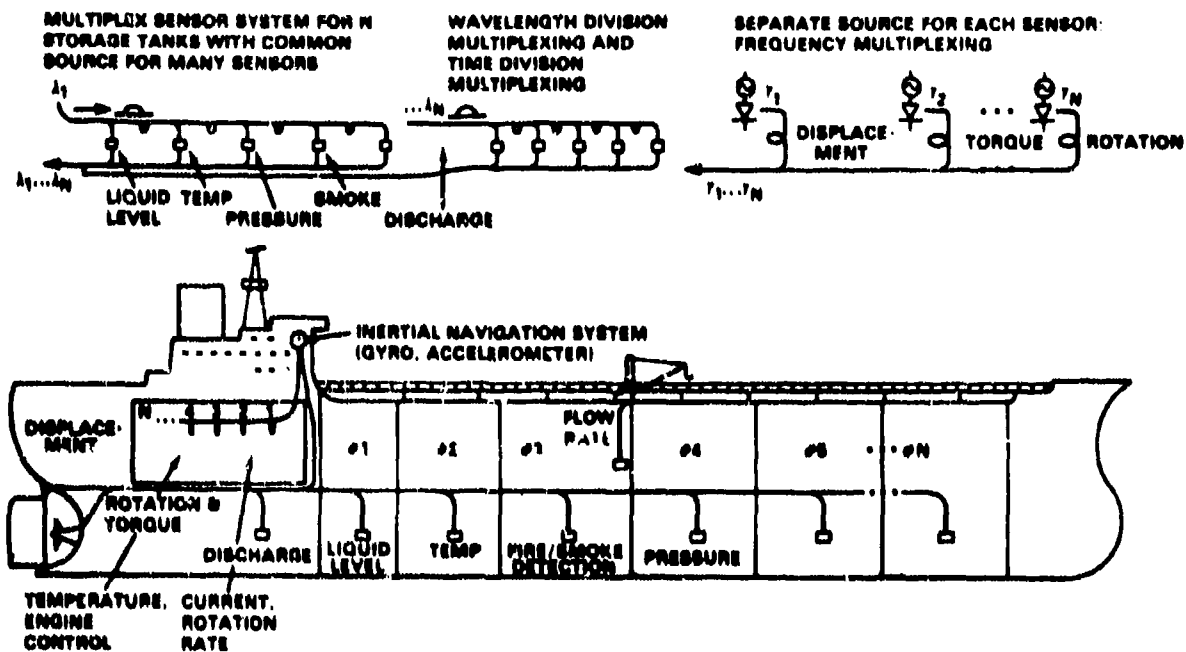


Figure 8 Optical fiber telemetry system for sensor suite.

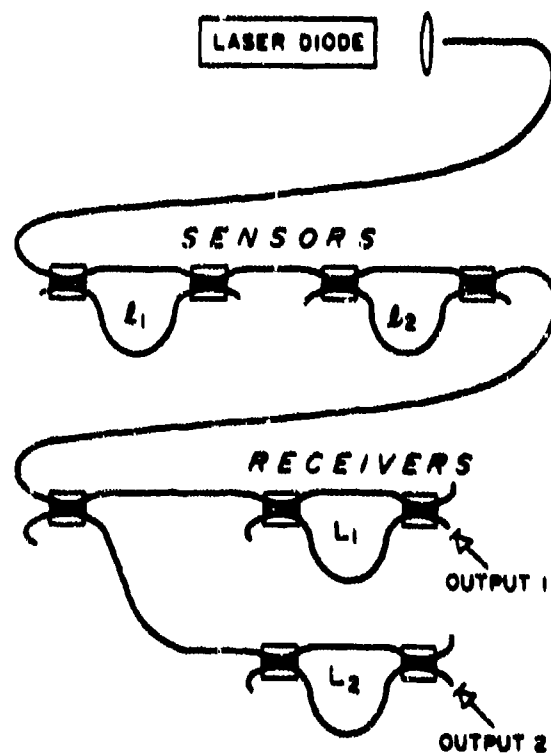


Figure 9 Coherence multiplexed telemetry system and interferometric sensors.

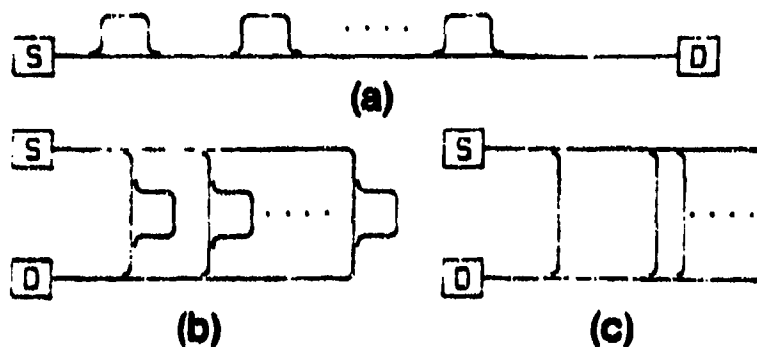


Figure 10 Three fiber telemetry schemes: (a) serial, (b) parallel with separate reference arms, (c) parallel with common reference arms.

DISCUSSION

J. Dakin, UK

In your review lecture you stated that up to a thousand sensors could possibly be multiplexed using the multiple-coupler fibre bus topology with either FMCW or coherence multiplexing techniques. Do you really believe that the loss budgets and the difficulties in frequency and sensors length allocation would permit this number of sensors in practice?

Author's Reply

A practical number of sensors that can be multiplexed from a single source is tens of sensors. The loss budget will limit you to these numbers. The 1000 number is a theoretical number describing the number of distinct channels people believe are possible for the various multiplexing schemes. To date, channel crosstalk problems have not realistically been addressed and may further limit the number of sensors.

J. Lucas, Fr

Is there any interest to shift to the IR domain to increase either the sensitivity of sensors or the domain of applications?

Author's Reply

Going to longer wavelengths normally increases the sensor self-noise and therefore does not favour longer wavelength operation. However, you may want to use long wavelength transmitting fibres to perform IR spectroscopy at remote locations.

Fibre Optic Gyroscopes in Inertial Navigation

Brian Culshaw
Department of Electronic & Electrical Engineering,
University of Strathclyde,
Royal College Building,
204 George Street,
Glasgow, G1 1XW
Scotland

John D. Nuttall
Navigation Systems Department,
Ferranti plc,
Silverknowes,
Edinburgh,
EH4 4AD
Scotland

Abstract

This paper discusses the potential application of fibre optic gyroscopes (FOG) in inertial navigation (IN) systems. The requirements for IN are briefly reviewed and compared to the reported performance of experimental FOG's. This leads to the identification of areas in which further work is necessary, in both physical understanding and technological developments.

Introduction

There has been considerable international effort in the design and testing of laboratory prototypes of the fibre optic gyroscopes in the past few years.^(1,2,3) The emphasis in these programmes has almost invariably been on the realization of a gyroscope with a performance compatible with missile applications. For missile use, the fibre optic gyroscope has the attractions that it can measure high angular rates (perhaps 1000°/sec), and can survive high vibration and acceleration levels. Additionally, instant switch-on, potentially long shelf-life and low weight are attractive features. By contrast, the requirements on sensitivity, drift and scale factor stability are relatively modest, though there are severe cost constraints.

In this paper, we examine the fibre optic gyroscope as a candidate for an alternative application, that of inertial navigation. We show that each element of the required performance has been demonstrated, in a laboratory environment, on one fibre optic gyroscope or another, but not all on the same gyroscope architecture. We then indicate the directions of current research which could lead to an inertial-navigation-quality instrument in the future.

The Inertial Navigation Gyroscope Specification

In inertial navigation, the position of an aircraft, ship or other vehicle is monitored by detecting the accelerations to which the body is subjected, and, by double integration, determining the distance travelled. Three (single-axis) accelerometers are required, and, as it is necessary to know in which directions the accelerometers are pointing, the inertial navigation system also requires three (single-axis) rotation sensors (i.e. gyroscopes).

Traditionally, the six instruments are mounted in a fully-aerobatic gimbal set, and oriented with one accelerometer's sensitive axis vertical, and the other two horizontal. As the vehicle moves, the gimbals are servoed to keep the accelerometers pointing in the same direction, using the gyroscopes as the sensors for the servomechanism.

More recently, it has become fashionable to dispense with the gimbals, and to use the gyros (and much computing power) to keep track of where the accelerometers are pointing. Then the detected accelerations can be resolved back into the appropriate coordinates. This latter system, known as 'strapdown', exchanges some of the mechanical complexities of the gimbaled system for a vast increase in computing requirements. In addition, better quality gyroscopes and accelerometers are needed for a strapdown system. These matters are explained in more detail in reference 4.

In Table 1, we summarise the requirements for a gyroscope for the two inertial navigation systems (i.e. strapdown and gimbaled), and for a typical lower-grade missile (i.e. non-inertial-navigation) gyro. The figures in the table should be used with caution, as they give only a rough idea. The terms in the table need some explanation. By 'maximum scale factor error' we mean that the instrument must be capable of measuring a rotation rate to that accuracy, after the subtraction of any zero-rate error, and after any corrections for non-linearities have been made. This figure must be applicable over the input range 'drift' to 'maximum rate'.

'Drift' is a complex subject⁽⁵⁾. It concerns the gyro output when there is no input. It is usual to subtract the d.c. (zero frequency) component of this output, and to make some correction for the g-sensitive component of this. In the table we refer to the drift figure after these corrections have been made. There is no standardised notation but sometimes 'noise' is used to denote the higher frequency components, and, in fibre optic gyro work, it is often quoted after a one-second filter on the output. 'Drift' is used to denote lower frequency noise. Essentially the phrase 'drift must be less than x°/hr ' means that the instrument, in normal use, should be capable of detecting a change of rotation rate of x°/hr over any time from zero to a reasonable period for the proposed use (e.g. 1 hour for aircraft systems). Mechanical gyroscopes have pronounced mechanical resonances in the noise spectrum, but are well characterised⁽⁶⁾. The FOG is often assumed to exhibit a white noise spectrum, though there is to date insufficient experimental data to confirm this with conviction.

It is generally assumed that the fibre optic gyro will be a strapdown sensor, and therefore must meet the most demanding requirements given in Table 1. This assumption is reasonable, because mechanical gyros in gimbal systems have reached a high degree of maturity, and the emphasis in inertial navigation has switched to strapdown systems. The latter, usually exploiting the Ring Laser Gyro, promise lower overall cost-of-ownership, though they are unlikely to offer high reliability or higher accuracy than a gimbaled system with mechanical gyros and modern electronics.

It is interesting to compare the market situation of the fibre optic gyroscope with that in the better known role of fibre optic systems in communications. Here the prime role of fibre optics is undoubtedly in high capacity, long haul trunk networks - in other words at the very high performance end of the spectrum. Fibre optic systems have achieved only modest success in short range systems, as may be needed in, for instance, industrial plant, buildings, aircraft etc. The principal reason for this low penetration is that the fibre system is expensive relative to its electrical counterpart and so must offer unique advantages in order to be competitive. In some aircraft applications, light weight and immunity to EMI are attractive, so there are some applications niches.

In the fibre optic gyroscope, the same observations are certainly true for the modest performance applications, where the competition is cheap mechanical gyros. At the inertial system level and above, the fibre gyroscope appears to offer one substantial advantage - there are on initial evaluation, very few precision assembly steps in the construction of the final device. In fact the only apparent ones are in the fabrication of fibre optic couplers and modulators. The remaining mechanical assembly features do not require an extremely high degree of mechanical precision, though the final assembly must, of course be mechanically stable. The instrument would require calibration in the usual way.

Demonstrated Performance of Fibre Optic Gyroscope

The fibre-optic gyroscopes which have been demonstrated so far may be divided into two classes. Those of one class, illustrated by figure 1, are designed primarily with the objective of low-noise levels and good sensitivity to low rotation rates, whilst those belonging to the other class, (figure 2) are intended to detect high angular rates with a good scale factor stability.

The low-noise architecture comprises the minimum configuration for a fully reciprocal fibre-optic gyroscope⁽⁷⁾, with a source whose spectrum minimises problems due to the Kerr effect⁽⁸⁾, and uses a simple, phase-modulation detection technique. This configuration has been demonstrated to have the low noise level required for inertial navigation⁽⁸⁾. However, the drift performance of this instrument is erratic, due largely to variation of the fibre birefringence with temperature, and to an imperfect polariser. Thus, for example, the instrument may be used to detect a step change in input rate of 0.01 °/hr, but could not detect a change of this size if it occurred over a period of minutes. For this reason the instrument in this form is unsuitable for inertial navigation. More recently a modification of this design, using birefringent fibre⁽⁹⁾, has been reported. It demonstrated both drift and noise performance near that required for inertial navigation, but all instruments of this type show limited dynamic range and poor scale factor linearity.

The second class of fibre optic gyro architecture is aimed primarily at high dynamic range and good scale factor, with noise and drift being of less importance. The best performance to date has been achieved in frequency-shifted closed-loop systems⁽¹⁰⁾. The original systems used Bragg cell shifters, but for all guided architectures a particular favourite is the acousto-optic frequency shifter^(11,12). This has been demonstrated in integrated optics, and approached in all-fibre components⁽¹³⁾. As integrated optics causes interface losses, these systems transmit relatively low optical power at the detector and hence exhibit relatively high noise levels (perhaps 1°/hr in a one Hertz bandwidth).

In both the basic systems described above, there is an inherent ambiguity in the measured value of rotation rate because the Sagnac induced time difference is measured with reference to the optical period. Thus the gyro output is a sinusoidal function of the rate input, and it is fundamentally impossible to distinguish between time differences which are separated by an integral number of optical periods. Of course, it is possible to avoid going into the second optical period, by using a short length of fibre, but this produces a lower signal and hence causes noise problems. The detection threshold, dictated by shot noise, is typically 10^{-7} radians in one Hertz (or the equivalent time difference is a frequency-nulling system). If a dynamic range exceeding 10^6 is required, the upper end must lie in the second optical period. Thus either an ancillary system is needed to resolve this ambiguity or a direct time-measuring architecture needs to be evolved. To the authors' knowledge, no such architecture has yet been demonstrated. There is also a more fundamental problem with scale factor stability, concerning the relationship between optical phase, wavelength and rotation rate.

The measured phase relationship is

$$\phi = \frac{4\pi LR}{\lambda_0 c} \Omega$$

where ϕ is the optical phase measured
 Ω is the rotation rate
 L is the total fibre
 R is the coil radius (assumed circular)
 λ_0 is the free space optical wavelength

Some error-correction can, in principle at least, be built into the read-out computation. For example, the values of L and R may be thermally modelled and it may also be necessary to model the influence of linear acceleration on the shape of the loop. However, this still leaves a question over the direct relationship between the optical wavelength and the value of the observed phase, and therefore of the perceived rotation rate. If a gyroscope scale factor accuracy of 20 ppm is required, the source wavelength has to be known to an accuracy which is probably an order of magnitude better than this.

There is the same requirement on the ring laser gyro, which also detects rotation using the Sagnac effect. In this device, the length of the resonant cavity is adjusted by a piezo-electric transducer, to lock onto the peak of gain curve. This is relatively straightforward because the gas laser has a well-defined gain curve centred on the photon energy corresponding to the relevant atomic or molecular transition. In solid state lasers, band structure effects remove this well-defined centre.

Semiconductor sources (usually heavily-multimoded lasers or light emitting diodes) are often favoured for the fibre optic gyro because their optical waveform statistics have the correct properties to compensate for Kerr-effect-induced offset drift. Additionally their short coherence length minimises coherent back-scatter. Typically such a source has a centre wavelength of 850nm and a linewidth of a few nm, or 10000 ppm. It is difficult even to define the meaning of the 'mean' wavelength of such a source to ppm precision.

Also the centre wavelength of the source will vary with temperature (because the band gap is temperature dependent) at around 300 ppm °C⁻¹.

One approach to measuring the optical wavelength to correct for these factors is to exploit the fringe ambiguity in a frequency-modulated feedback system⁽¹⁴⁾ and measure the apparent rotation rate on adjacent fringes. There is a slight fibre dispersion effect which causes the two measured rotation rates to differ. By measuring the temperature of the loop and knowing the dispersion characteristics, a fit may be made to determine the effective source wavelength. Scale factor stability of around 100 ppm is claimed for this approach. The technique, which involves measurement of frequency difference in adjacent fringes, involves measurement of frequency differences of less than

100 Hz/nm of optical wavelength change. Measurement of wavelength to ppm implies that this difference should be monitored in millihertz. These are then some practical difficulties implied in measuring this difference in a non-stationary system, simply concerned with tracking this frequency difference over a sufficiently long period to make the measurement. Some well-designed software is essential here, but even so it seems very difficult to extrapolate this technique into ppm measurements.

Implications for fibre optic gyroscope design

In this section we examine the areas in which further work is required for the development of a inertial-navigation quality instrument.

The requirement for scale factor stability implies either stabilisation or measurement of optical wavelength to 10 ppm or better. The implications here are that a source with a line width of less than 10 ppm would be preferred and a high degree of central wavelength stability would also be required. These observations point to the use of lasers. The linewidth considerations also imply the use of either a single-mode semiconductor laser, a solid-state laser, or a gas laser. However, if the use of a super-luminescent diode is abandoned, the advantages of Kerr-effect compensation are lost, and coherent back-scatter becomes a bigger problem. A more thorough understanding of backscatter is therefore an essential stage in the evolution of the inertial-grade system, and initial work on this has been published recently (15,16,17).

The specification of the optical source and its wavelength stability raises a number of questions. It is impossible to rely on the energy gap of a semiconductor source to provide the frequency reference, and the use of a gas laser is unattractive, though not entirely impractical. The inevitable conclusion is that some form of wavelength stabilisation or wavelength measurement is required. The former has been demonstrated to the required 10 ppm accuracy by many workers, (18, 19) though there is then the question concerning the inherent stability of the reference element to which the laser is stabilised, and some careful mechanical design is needed here. The alternative approach, that of measuring the wavelength over the anticipated range of operating characteristics of the source, requires a parts per million measurement over a wavelength range of perhaps 5% - corresponding to about 10,000 resolvable points. Spectrometers with this performance do exist, but compactness is far from one of their features! Indirect measurements, like the dispersion related technique described earlier, often involve monitoring second order phenomena so the measurement is relatively insensitive.

If it is assumed that the optimum architecture for scale factor stability and dynamic range is the frequency-shifted open-loop system - and no better option has been convincingly demonstrated - then an all-guided optical frequency-shifter is essential to minimise noise. It seems likely that the present ones in integrated optics (11) have too high interface losses for inertial navigation work, and an all-fibre one would be better (20). There is currently no general agreement on the technical specification of such a device. The other principal passive components for an all-fibre gyroscope (the couplers and the polarising elements) are, or soon will be, commercially available.

In this context, we should mention a number of ingenious detection schemes which avoid the need for an all-fibre frequency shifter (21, 22). These utilise a phase-modulation approach to derive an electrical phase output, in which the detected signal is independent of the amplitude of the optical signal at the detector. Typical of these schemes are harmonic-feedback concepts (21), heterodyne-detection (22) and phase-gated systems (22).

Environmental Aspects

The fibre optic gyroscope is, of course, sensitive to any effect, which violates the conditions of Lorenz reciprocity. The Sagnac (rotation) effect and the Faraday effect are the only truly non-reciprocal phenomena. However time variations in the fibre loop are also important. Consequently, the fibre optic gyroscope is sensitive to magnetic fields, temperature gradient, pressure gradients and vibration. There is little published data though the rule of thumb that the earth's magnetic field can produce slowly varying offsets of the order of earth rotation rate has emerged.

This magnetic sensitivity may be minimised by the use of polarisation-holding fibre, which inhibits the effects of the non-reciprocal circular birefringence induced by the Faraday effect, but magnetic shielding may prove to be necessary as well.

Temperature gradients can be a serious problem, as pointed out by Shupe (24), though "anti-Shupe" windings of the sensor unit can appreciably reduce the impact of thermal gradients. Pressure and vibration effects are closely related to thermal effects, in that both arise from reciprocity failure in the presence of a time-varying transmission medium. Improved coil winding techniques and overall packaging may substantially reduce the errors from this source.

Conclusions

In this paper we have shown that much of the basic work towards an inertial-navigation quality fibre optic gyro has been completed, though progress is needed in a number of areas. The most important of these seem to be in gaining a full physical understanding of coherent backscatter, in evolving novel FOG architectures and in designing all fibre components, especially frequency modulators. In our judgement, these remaining problems are not insuperable, but clearly a lengthy development phase lies ahead before the full strapdown inertial specification is achieved.

Acknowledgements

The authors wish to thank James Mackintosh, Joan McMillan and Ian Gilles (of Strathclyde University) and Sid Smith (of RAE, Farnborough) for stimulating discussions, and the management of Ferranti for their permission to publish.

References

1. S. Ezekial and H.J. Arditty (eds), "Fibre Optic Rotation Sensors and Related Technologies", Topics in Applied Physics, Vol 32 Springer-Verlag 1982.
2. R.A. Bergh, H.C. Lefevre and H.J. Shaw, "An overview of fibre optic gyroscopes", IEEE J-LT 2 p 91 April 1984.
3. B. Culshaw and I.P. Giles, "Fibre Optic Gyroscopes", J. Phys E., p 3 January 1983.
4. J.D. Nuttall, "Gyroscopes for Inertial Navigation", to be published IEE Proceedings J. 1985.
5. A.D. King, "Measurements of gyro in-run drift", Proceedings 1984 DGON Conference on Gyroscope Technology, Stuttgart 12 September 1984.
6. B. Traynor, "Rate gyroscope applications", to be published IEE Proceedings J. 1985.
7. R.A. Bergh, H.C. Lefevre and H.J. Shaw. "All-single mode fibre optic gyroscope with long term stability", Optics Letters 6 p 502 1981.
8. R.A. Bergh, B. Culshaw, C.C. Cutler, H.C. Lefevre and H.J. Shaw. "Source statistics and the Kerr effect in fibre optic gyroscopes", Optics Letters 7 p 363, 1982.
9. W.K. Burns, R.P. Moeller, C.A. Willarruei and M. Abebe. "All fibre gyroscope with polarization holding fibre", Optics Letters 9 p 570, 1984.
10. J.L. Davis and S. Ezekial. "Closed loop low noise fibre optic rotation sensor", Optics Letters 6 p 505, 1981.
11. C. Kay.
To be published IEE Proceedings J 1985.
12. R.C. Cummings, "The serrodyne frequency translator", Proc. IRE, 45 p 175, 1957.
13. C.A. Wade and J.P. Dakin
To be published IEE Proceedings J 1985.
14. E. Udd, R.J. Michal and R.F. Cahill, "Scale factor correction in the phase nulling optical gyro," Proc. SPIE 478 paper 21. 1984.
15. K. Takada, "Calculation of Rayleigh backscattering noise in fibre optic gyroscopes", J. Optical Soc. America A, 2 p 872 June 1985.
16. H.J. Shaw and C.C. Cutler, Private communication 1985.
17. I.P. Giles, J. Mackintosh and B. Culshaw to be published DGON Gyro Symposium, Stuttgart 1985.
18. W. Auch, private communication 1984.
19. See for example R. Wyatt, "Spectral linewidth of external cavity semiconductor lasers with strong frequency selective feedback" Electronics Letters 21, p 658, 1985. There is continuous reporting of this topic in Electronics Letters, IEEE J.QE and IEE Proceedings J.
20. R.C. Youngquist et al
To be published IEE Proceedings J 1985.
21. J.W. Parker, M.C. Bone and E. Jones. "Integrated optic fibre gyroscope with on-chip modulator and harmonic feedback operation", Proc. 2nd International Conference on Optical Fibre Sensors, Stuttgart 1984 p 301 Proceedings published by VDE-Verlag GmbH.
22. I.P. Giles, "Heterodyne fibre optic gyroscope", to be published, IEE Proceedings J 1985.
23. B Y Kim and H.J. Shaw, "Phase nulling all fibre gyroscope", Optics Letters 9 p 378, 1984.
24. D.M. Shupe, "Thermally induced non reciprocity in the fibre optic interferometer", Applied Optics 18 p 915 1979.

Table 1

	Missile mid-course inertial navigation for 500 m accuracy in 20 km [1]	Inertial Navigation for 1 nautical mile error after 1 hour measurement time [3]	
		Gimballed	Strapdown
Maximum rate [2]	400°/sec	0.3°/sec	400°/sec
Maximum Scale factor error [2]	1000 ppm	200 ppm	10 ppm
Drift [2]	100°/hr	0.01°/hr	0.01°/hr
Dynamic range	1.5×10^4	10^5	1.5×10^8

Notes

- [1] the most demanding missile application quoted by Traynor (reference 6)
 [2] these terms are discussed in the text
 [3] Nuttall (reference 4)

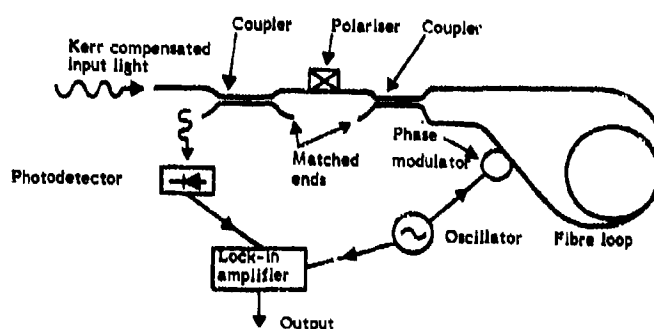


FIGURE 1 THE SIMPLEST LOW NOISE GYROSCOPE SHOWING THE USE OF LOCK-IN AMPLIFIER DETECTION

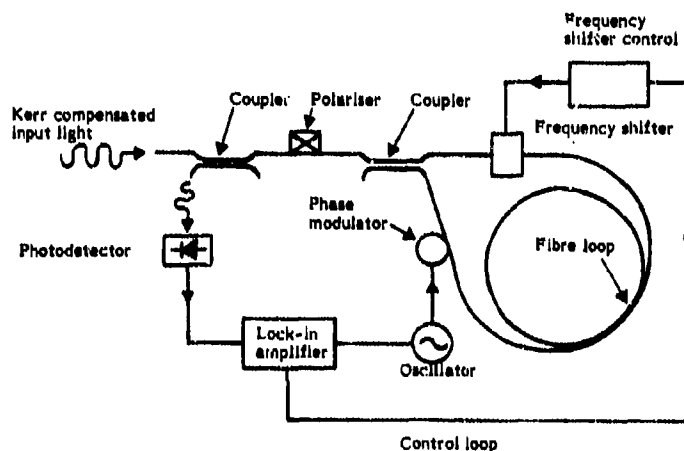


FIGURE 2 CLOSED LOOP ARCHITECTURE FIBRE OPTIC GYROSCOPE. THIS IS A MINIMUM CONFIGURATION LOW NOISE GYROSCOPE INCORPORATING A FREQUENCY SHIFTER TO PROVIDE NULLING ACTION. THE LOCK-IN AMPLIFIER IS USED TO DETECT THE NULL.

DISCUSSION

H. Lefevre, Fr

Does the cancellation of first order backscatter require very low loss fibre in addition to 10^{-50} splitting in the interferometer?

Author's Reply

Yes, the splitting ratio criteria also depends on the symmetry of the loss within the loop.

R. Feigelson, US

Do you see an advantage in using other types of lasers rather than a semiconductor diode laser?

Author's Reply

Maybe, perhaps the ideal source has about 1 GHz bandwidth. A fully filled doppler broadened gas laser line sounds good, or perhaps fibre crystal laser if this proves to have the necessary stability and bandwidth.

B. Schwaderser, Ge

I'm not working in this field of optical gyros, but can you give me the figures of optical typical power, if backscatter is a problem?

Author's Reply

Typical: one mW launched $1/10$ uW detected in the most loss free systems. For integrated optic systems, another 10 dB loss is typical.

COMPARISON OF RING LASER AND FIBER-OPTIC GYRO TECHNOLOGY

E. Udd, S. F. Watanabe, and R. F. Cahill
 McDonnell Douglas Astronautics Company
 5301 Bolsa Avenue
 Huntington Beach, California 92647

ABSTRACT

Substantial progress has been made in recent years toward the development of producible fiber-optic rotation sensors. These devices have the potential of being the solid-state replacement for many applications currently using mechanical gyro technology. Ring laser gyro technology which has been under development for approximately 23 years is now being introduced into commercial and military aircraft for inertial navigation. The fundamentals of the usage of Sagnac interferometry for rotation sensing will be reviewed as well as the differences between fiber-optic gyro and ring laser gyro technology. Examples will be given of applications where fiber-optic gyro or ring laser gyro technology is particularly suitable. Distinctions will be made between analog fiber-optic gyros which offer the lowest possible cost but are limited in performance capability and digital fiber-optic gyros which offer the wide dynamic range and accurate scale factor correction required for more stringent applications.

INTRODUCTION

In order to meet the performance requirements of advanced inertial guidance applications, highly reliable, rapid reaction rotation sensors are needed. Table 1 and Figure 1 provide a summary of the requirements for typical applications. State-of-the-art mechanical gyros are available but high cost, long warm-up time, limited high rate sensing capability, and problems associated with shock and vibration have caused a large number of companies and government agencies to investigate the usage of optical rotation sensor technology. Concepts based on ring laser gyro technology have been under development since 1963 (References 1-3) and have been pursued by such companies as Honeywell, Litton, Singer, Sperry, Rockwell, Raytheon, United Technologies, and Ferranti. These efforts culminated in the delivery by Honeywell in 1981 of the first production prototypes to support the development of the Boeing 757/767 aircraft. Fiber-optic gyro technology is comparatively new with the first laboratory demonstration models being reported in 1976 by Vali and Shorthill (References 4-7). Companies pursuing fiber-optic gyro development have been: McDonnell Douglas, Litton, Standard Electric Lorentz, Martin Marietta, Nippon Electric Company, Sperry, Honeywell, Northrop, Bendix, and Singer. The introduction of fiber-optic gyros into the field has been relatively rapid with the delivery by McDonnell Douglas of production prototypes to Develco, in 1985, to support an oil field borehole survey tool. As these technologies have progressed, it has become increasingly evident that there are applications where both the ring laser and fiber-optic gyro offer the potential of superior performance with respect to existing technology. This paper summarizes the strengths and weaknesses of existing optical gyro technologies and projects where each technology may be used in future applications.

THE SAGNAC EFFECT

Both ring laser and fiber-optic gyro technology are based on the Sagnac effect (Reference 8) which arises due to differences in the propagation time between clockwise and counterclockwise beams of light about a closed optical path. Consider an optical path constrained to lie in a two-dimensional plane perpendicular to the rotational axis as is shown in Figure 2. The more general case of an optical path in three dimensions may be handled by looking at the projection of that path onto three orthogonal planes.

Let the polar coordinates of the optical path be given by $r = r(\phi)$. Also, define the angle between $rd\phi$ and ds , ds being the differential along the optical pathlength, to be

$$\theta = \cos^{-1} \left[\frac{rd\phi}{ds} \right] \quad (1)$$

Associated with ds is a change in the optical perimeter due to rotation which has the differential form, Ω being the rotation rate, of

$$dP = \Omega r dt \cos \theta = \Omega r \left[\frac{rd\phi}{ds} \right] dt \quad (2)$$

but

$dt = ds/c$ so Eq. (2) becomes

$$dP = nr^2 \frac{d\phi}{ds} \frac{ds}{c} = \frac{nr^2}{c} d\phi \quad (3)$$

The total change in optical pathlength due to rotation experienced by light traveling about the ring is given by

$$\Delta P = \pm \oint \frac{nr^2(\phi)}{c} d\phi = \pm \frac{n}{c} \oint r^2(\phi) d\phi \quad (4)$$

To evaluate this last integral note that each differential element is just twice the area of a triangle formed by $r(\phi)$, $r(\phi + d\phi)$ and $rd\phi$ as in Figure 3. Also, notice that the sum of all such triangles is just the area enclosed by the optical path which shall be designated as A . Consequently, Eq.(4) reduces to the form

$$\Delta P = \pm \frac{2An}{c} \quad (5)$$

where the sign depends upon the sense of integration. The measurement of this pathlength difference between the counterpropagating beams along the optical path forms the basis of the ring laser and fiber-optic gyro. The means of accomplishing this pathlength difference measurement are very different and will be discussed in the following sections.

FUNDAMENTAL ASPECTS OF THE RING LASER GYRO

In order for the optical path described above to support lasing, there must be an integral number of optical waves about one complete circuit. Optical beams having wavelengths that do not satisfy this pathlength matching condition interfere with themselves as they make subsequent circuits about the optical path. Thus, in order to compensate for a change in the perimeter of the optical path due to rotation ΔP , the wavelength and frequency must change. In particular, it must follow that

$$\frac{P}{\lambda} = \frac{P + \Delta P}{\lambda + \Delta \lambda} \quad (6)$$

or

$$\frac{\lambda + \Delta \lambda}{\lambda} = \frac{P + \Delta P}{P} \quad (7)$$

which reduces to

$$\frac{\Delta \lambda}{\lambda} = \frac{\Delta P}{P} \quad (8)$$

Using the relationship $v = c/\lambda$ and

$$\Delta \lambda = -\frac{c}{v^2} \Delta v \quad (9)$$

with Eq.(8) results in

$$-\frac{\Delta v}{v} = \frac{\Delta \lambda}{\lambda} = \frac{\Delta P}{P} \quad (10)$$

Eq. (10) is the fundamental equation relating frequency, wavelength and perimeter change in a ring laser. In a conventional ring laser, two modes propagate; one in a clockwise direction, the other, counterclockwise. If the ring laser rotates at n then Eq.(4) indicates that the effective optical pathlength will increase for light traveling in the direction of rotation and decrease for the oppositely traveling light. Thus, if the light from the two counterpropagating beams are beat together, the resulting signal has a frequency

$$f = 2|\Delta v| = 2v\frac{\Delta P}{P} \\ = \frac{4Avn}{cP} = \frac{4An}{\lambda P} \quad (11)$$

This last equation is the fundamental relation for the ring laser gyro. Ideally, the performance of a ring laser gyro would be governed by Eq.(11). In practice, for low rotation rates, the clockwise (cw) and counterclockwise (ccw) beams may couple together in frequency. This phenomenon is known as "lock in" since the two counterpropagating beams are locked together in frequency resulting in a dead zone over which the effective output of the ring laser gyro is zero. The mechanism by which the cw and ccw beams interact is believed to be small amounts of backscatter from the ring laser mirrors and the gain medium itself (Reference 9). Usage of high quality, low scatter mirrors have reduced the problem from several degrees per second in the 1960s - to the "dead band" regions of about 1000 degrees per hour in the 1970s - and for cavity lengths

with mirror separation on the order of 8 cm to a few degrees per hour in the 1980s. Eq.(11) can be modified so that it incorporates this phenomenon by defining a critical rotation rate Ω_c such that lock-in occurs for rotation rates smaller than this value. Eq.(11) then becomes

$$f = \begin{cases} 0, & \Omega^2 < \Omega_c^2 \\ \frac{4A}{\lambda P} \sqrt{\Omega^2 - \Omega_c^2}, & \Omega^2 \geq \Omega_c^2 \end{cases} \quad (12)$$

While Eq.(12) holds in the "lock-in" region and for rotation rates Ω , the observed behavior between these two regions may be very complex depending upon such factors as power level, gain media, mode structure and wavelength (References 10 and 11). Figure 4 illustrates the operating characteristics of a ring laser with lock-in.

In order to circumvent the problems associated with "lock-in" ring laser gyros which operate at low rotation rates incorporate some sort of "biasing" whereby the frequencies of the counterpropagating beams are separated. Figure 5 illustrates many of the problems associated with biasing. By increasing the optical quality of mirrors and optical surfaces the dead band region may be reduced. This also means higher cost in terms of optical components and manufacture. To compensate for the presence of a dead zone periodic switching is often used. That is, the effective optical pathlength of the cw and ccw beams are changed periodically. Switching to a rotation rate Ω outside of the dead zone and then back to $-\Omega$ results in the gyro sensing $\Omega + \Delta\Omega$ and then $-\Omega + \Delta\Omega$. Adding these two rotation rates gives twice the actual rotation. There are a number of problems associated with operating in a periodic bias mode. Since it is desirable to minimize the magnitude of the periodic bias as well as minimize the amount of time spent in the lock-in region, high quality and consequently, high cost optical components must be used. Secondly, while periodic biasing reduces bias instability problems to a minimum, information may be lost during periodic passage through the dead band. Finally, upper rate is limited by the maximum rate at which the ring laser is dithered as one end of the swing may fall into the dead zone region.

Another means of biasing involves the use of a fixed bias where the difference between cw and ccw beams are stabilized to a value corresponding to a rotation rate on the linear portion of Figure 5. Successful implementation of such a technique implies extreme bias stability, as small deviations may cause large errors in rotation rate readings. Examples of such biasing techniques include stabilization with an intracavity quartz crystal or saturable absorber (References 12-14). More complex bias schemes also exist which have multiple bias by taking advantage of polarization effects and usage of intracavity elements (References 14 and 15).

Figure 6 is a block diagram of a typical ring laser gyro that would employ mechanical dithering.

FUNDAMENTALS OF FIBER-OPTIC GYROS

From Eq.(6) the total pathlength difference between the counterpropagating beams along the optical path is

$$\Delta L = \frac{4A}{c} \Omega \quad (13)$$

For simplicity, consider the case of a fiber-optic gyro consisting of a circular coil of N turns. The effective enclosed area of this geometry is NA and the number of turns, N , is equal to the length, L , of the fiber coil divided by its perimeter of $L/2\pi R$. Substituting these results into Eq.(13) renders

$$\Delta L = \frac{2RL}{c} \Omega \quad (14)$$

To determine the fraction of a fringe shift between the two counterpropagating beams when they are mixed, we divide this pathlength difference by the wavelength of light in vacuum, λ , to obtain

$$Z_R = \frac{2RL}{\lambda c} \Omega \quad (15)$$

FIBER-OPTIC INERTIAL SENSOR FUNDAMENTALS

ANALOG FIBER-OPTIC GYROS

The simplest form of passive fiber-optic gyro consists of a light source of wavelength λ and a central beamsplitter that is used to generate counterpropagating light beams in the fiber-optic coil (Reference 4). Its output is given by

$$Z_R = \frac{2RL}{\lambda c} \Omega \quad (16)$$

where R is the radius of the fiber coil, L is the length of the fiber coil, λ is the wavelength of the light source, and c is the speed of light in vacuum. Figure 7 illustrates the layout of an implementation of this fiber-optic gyro concept. A single-mode fiber spatial filter and polarizer are appropriately placed to ensure that both counterpropagating beams transverse the same path in the fiber-optic coil

(Reference 16). The two counterpropagating beams mix and fall onto the detector, which is used to monitor cosinusoidal intensity changes caused by rotation. To pull the signal out of the direct current (DC) band, nonreciprocal phase shifts between the counterpropagating beams are introduced at a rate of ω . As an example, this may be accomplished by injecting an optical phase dither at a rate ω in the absence of rotation. Upon rotation of the system, odd harmonics of the signal at ω fall onto the detector with an amplitude that depends on the magnitude of the rate of rotation and with a phase that depends on the direction of rotation.

This type of fiber-optic gyro, deemed the analog fiber-optic gyro (AFOG), provides a small, low-cost technique suitable for applications with modest dynamic range and scale factor requirements (a dynamic range of 3000 and a 1% scale factor correction would be typical). Examples of applications where this type of gyro would be appropriate include yaw and pitch measuring, attitude stabilization, gyrocompassing from a platform such as a submarine, and antitank missiles.

Recently, work has been performed to attempt to extend the dynamic range of the AFOG (References 17 and 18) by accepting regions of relatively high nonlinearity and low sensitivity. The digital fiber-optic gyro described in the next section provides a fundamental means of overcoming these limitations.

DIGITAL FIBER-OPTIC GYRO

For applications that require high performance and wide dynamic range, such as ejection seats, tactical missiles, and jet fighter heading sensors, a means has been devised to introduce a nonreciprocal phase shift into the system and to null out phase shifts caused by rotation (References 19 and 20). A block diagram of a gyro incorporating this system is shown in Figure 8. Light from the source is spatially filtered and polarized before being split into counterpropagating beams. The clockwise-circulating beam of light passes through the fiber-optic coil at a frequency $F_c + F$. Both counterpropagating beams recombine on the beam splitter at frequency $F_c + F$. The relative fringe shift caused by the frequency difference between the two beams propagating in the fiber-optic coil is given by

$$Z_F = Ft_D = - \frac{F L n}{c} \quad (17)$$

where t_D is the time delay through the fiber coil and n is the index of refraction.

In order for this system to be nulled, the fringe shift caused by rotation must be offset by the fringe shift caused by the frequency difference of the light beams counterpropagating through the fiber-optic coil. That is, the criterion for a nulled condition is expressed by

$$Z_R + Z_F = 0 \text{ (or any integer value, when using an offset frequency)} \quad (18)$$

Combining Eqs.(16) and (17), the output frequency, F , is

$$F = \left[\frac{2R}{\lambda n} \right] \omega \quad (19)$$

It may be noticed from Eq.(17) that a sign change in Eq.(19) occurs if the frequency shift is impressed upon the cw instead of the ccw beam.

To ensure that the nulling condition of Eq.(18) holds, an alternating current (AC) phase-sensitive detection scheme has been devised. Nonreciprocal phase shifts between the counterpropagating beams are introduced by injecting an optical phase dither at a rate ω . When the condition of Eq.(18) holds, only the second and higher-order even harmonics of the ω appear on the detector. Upon rotation of the system, first- and higher-order odd harmonic signals of ω fall onto the detector with an amplitude and phase dependent upon rotation rate. This signal is synchronously demodulated, and the resultant output voltage is applied to an integrator which, in turn, corrects the output frequency of the voltage-controlled oscillator, closing the feedback loop and nulling the system. Figure 9 illustrates analog and digital fiber-optic gyro product areas.

COMPARISON OF RING LASER AND FIBER-OPTIC GYRO

The major difference, with respect to performance, between ring laser and fiber-optic gyro technology is that ring laser gyros utilize lasing characteristics. Fiber-optic gyros, by contrast, are passive cavity devices whose light source is external to the rotationally sensitive medium. For this type of device optimum performance is achieved using a broadband light source dominated by spontaneous rather than stimulated emission. The second major difference is that the type of technologies used for the two optical rotation sensors is vastly different manifesting itself in such areas as power supply consideration, size, weight, packaging flexibility, assembly and ultimately cost.

PERFORMANCE CONSIDERATIONS

Table 2 lists various performance characteristics comparing ring laser, analog and digital fiber optic gyros. Important operational performance parameters that are key to evaluating the quality of any gyro include sensitivity, bias drift, scale factor

errors, linearity, and dynamic range. Strongly coupled to these operational performance characteristics are such issues as environmental performance, especially temperature, shock and vibration characteristics, package size and weight, form factor power requirements and reliability. The output equations for the ring laser and fiber-optic gyros form a basis on which operational performance characteristics may be made.

The analog fiber-optic gyro has a sensitivity that depends upon the length of fiber employed for a given enclosed area. Thus, longer lengths of fiber would be expected to result in higher sensitivity. As lower loss fiber becomes available as well as higher quality light sources the sensitivity of these devices would be expected to continue to improve. Early calculations showed that the sensitivity of the fiber optic gyro could be comparable, or better, than existing ring laser gyro technology (Reference 21). Progress has been made and these predictions have been verified by recent experiments (Reference 22). The sensitivity of the ring laser gyro is limited mainly by operation at low gain levels to avoid nonlinear effects and sensitivity that depends upon a single transit about the lasing cavity.

The differences in rotationally sensitive optical pathlengths also manifest themselves in procedures to reduce bias drift errors. Ring laser gyros rely on such techniques as low expansion coefficient optical cavities, active pathlength control, symmetrical placement of anodes and cathodes, to ensure that both counterpropagating lasing beams in the cavity traverse the same optical path. Fiber-optic gyros rely on external elements to the optical sensing path such as polarizers and spatial filters to ensure the beam traverse reciprocal paths. The packaging of the fiber coil is critical since time dependent environmental changes that occur on the order of the transit time of light through the fiber coil will result in nonreciprocal effects and a net bias drift.

Scale factor issues for the ring laser largely involve limitations of means to overcome lock-in and mode pulling phenomenon. Sufficient progress has, however, been made in this area so that corrections of better than one part per million are possible. In order to achieve a good scale factor for the fiber-optic gyro the most promising approach appears to be the digital fiber-optic gyro. The output of this device has a scale factor equation that is identical to the ring laser gyro. There are, however, important differences in the implementation of these devices. The ring laser gyro typically uses a helium neon laser which has a very stable wavelength and index of refraction that is nearly one. The digital fiber-optic gyro can also use a helium neon laser as a stable source and scale factor correction techniques may be used to monitor the optical pathlength change of the fiber coil (Reference 23). In order to achieve high performance the coherence of the light source should be as short as possible to minimize backscatter. While this is possible to achieve in a gas laser, solid state low coherence length light sources such as superradiant diodes and light emitting diodes are readily available and offer the advantages of solid state technology. These light sources however, do change wavelength with such parameters as time, current and temperature often in a manner that is difficult to model. The wavelength of the light source may be measured (Reference 23) if the optical pathlength is known. This involves careful packaging and modeling of the fiber coil under various environmental conditions, the most important of which is temperature.

The limits of linearity and dynamic range of the ring laser gyro depend upon lock-in and the design of the means to overcome it. For ring laser gyros utilizing mechanical dithering this usually means an upper rate limit constrained by the peak velocity at which the unit is dithered. Generally, for large ring laser gyros with optical pathlengths of 30 cm, this constrains upper rate to a few hundred degrees per second for a typical design. The digital fiber-optic gyro is limited in upper rate by the dynamic range of the frequency shifters, typically a few thousand degrees per second. Both devices may be offset to sense very high rotation rates.

While the operational performance parameters are important, environmental conditions, packaging, power requirements, and reliability often dictate the technology that will be employed for a particular application. Both ring laser gyros and fiber-optic gyros have demonstrated the capacity to operate under hostile environmental conditions that would be difficult, if not impossible, for mechanical gyros to perform under. The major differences between the technologies involves the usage of a gas-filled tube as the active element for the ring laser gyro versus solid-state elements for the fiber-optic gyro.

Ease of packaging is perhaps one of the most important advantages of fiber-optic gyro technology over ring laser gyro technology. The rotationally sensitive fiber coil may be formed into ovals, racetracks, squares and even nonplanar shapes quickly and cheaply. Tradeoffs can readily be made to give optimum sensitivity for constrained geometries. A similar change for a ring laser gyro would involve a major development effort. The fiber-optic gyro also may be arranged so that the rotationally sensitive coil is placed remotely from the rest of the optics minimizing the weight for such applications as seeker heads (Reference 24).

Many advanced applications have severe power and weight constraints placed upon them. Currently the power requirements of the two technologies are comparable. The ring laser gyro requires a power supply capable of delivering several hundred volts, but only a few milliamps of current. The fiber optic gyro utilizes solid state components, and may be operated off a conventional five volt supply but it has relatively large current requirements presently due to such elements as superradiant

diodes. Other considerations involve the weight associated with the solid glass block and dither mechanism associated with the ring laser gyro versus a solid-state light source and detector, a fiber coil, fiber couplers and polarizers as well as modulators. When the components involved in construction of a ring laser gyro are compared to those associated with a fiber-optic gyro, fiber-optic gyros appear to have a clear advantage with respect to the potential to be extremely light weight.

Another issue associated with ring laser gyros involves the trade off between size and weight and reliability. The smallest ring laser gyros that have been made are only a few centimeters in diameter but have operating lifetimes limited to a few hundred hours at best. This is due to the relatively high current required to operate the unit causing the gas medium to be pumped out of the system. A second issue involves low leak rates that would be insignificant for a large ring laser gyro causing shelf life problems for a very small unit. Large ring laser gyros such as those built for commercial aircraft navigation have demonstrated reliability greater than 10,000 hours. Intrinsically, fiber-optic gyros are solid-state devices and lifetimes are not size dependent since the light source is much smaller than any practical package. The element that currently appears to be the main limitation for the fiber-optic gyro is the light source used in many high performance applications, the superradiant diode. The lifetime of these units has been steadily improving and prescreened devices have lifetimes on the order of a few thousand hours. It is expected that further development work will result in lifetimes in the 10,000 to 100,000 hour range. Light emitting diodes with extremely long lifetimes (>100,000 hours) are also usable in many applications where performance requirements are not as high.

TECHNOLOGY COMPARISONS

An important aspect of ring laser and fiber-optic gyros is their relative affordability which is closely tied to the technology associated with each device. Table 3 summarizes some of these considerations. The ring laser gyro is a very specialized instrument and much of the technology associated with its successful introduction has been borne by the companies developing the technology and the defense industry. Fiber-optic gyros, by contrast, have much more synergism with work performed by other commercial efforts such as the telecommunication industry and will benefit from related work being performed in support of compact audio disk players and copiers. Fiber-optic gyro development is also strongly supported by work being done on other fiber-optic sensors in the field of acoustic, magnetic and electric field sensing.

As mass production of key elements and subassemblies for the fiber-optic gyro occurs it is anticipated that this technology will gradually form a significant cost advantage with respect to the ring laser gyro. This situation will be further augmented by the ability to assemble the units under conventional manufacturing conditions as opposed to the more stringent clean-room conditions necessary for the ring laser.

Significant engineering issues remain before fiber-optic gyros with performance characteristics similar to inertial navigation grade ring laser gyros will exist. It is anticipated that in the near future fiber-optic gyros will begin to penetrate the market for devices with bias stability of more than about 1 degree per hour while ring laser gyros will dominate the market for inertial navigation grade devices with performance of 0.01 degrees per hour or less. Performance applications that require units that fall between these two regions could go with either technology. In the long term the critical question will be the ability of the ring laser gyro to be cost competitive with respect to the fiber-optic gyro.

Although much of the initial work on fiber-optic gyros was performed at universities and by industry that traditionally were not participants in the inertial sensor market this situation has shifted dramatically in the last few years. Presently, virtually every major maker of inertial sensors has a fiber-optic gyro program. This may be representative of the relative lack of maturity of this technology when compared to ring laser gyros. The number of firms pursuing ring laser gyros has dropped as these sensors have entered the marketplace. Table 4 is a partial list of companies involved in these areas.

SUMMARY

Ring laser and fiber-optic gyro technology have been compared. For high performance applications of 0.01 degree per hour or better, ring laser technology will dominate in the near future while fiber-optic gyro will start to make inroads in the 1-10 degree per hour regime. In the long term it is expected that fiber-optic gyros will offer a significant challenge to ring laser gyro technology through advantages related to cost, power, size, weight and packaging flexibility.

REFERENCES

1. E. K. Proctor, "On the Minimum Detectable Rotation Rate for a Laser Rotation Sensor", Proc. IEEE (Correspondence) 51, p. 1035, July 1963.
2. P. Walsh and G. Kiminy, "Laser Operation Without Spikes in a Ruby Ring", J. Appl. Phys., 34, p. 956, 1963.

3. W. N. Marek, J. R. Schneider, and R. M. Salamon, "Measurement of Fresnel drag with the Ring Laser", J. Appl. Phys., 35, p. 2556, 1964.
4. V. Vali and R. W. Shorthill, "Fiber Ring Interferometer", Applied Optics, 15, p. 1099, 1976.
5. V. Vali and R. W. Shorthill, "Ring Interferometer 950 m Long", Applied Optics, 16, p. 290, 1977.
6. V. Vali, R. W. Shorthill, and M. F. Berg, "Fresnel-Fizeau Effect in a Rotating Optical Fiber Ring Interferometer", Applied Optics, 16, p. 2605, 1977.
7. V. Vali, R. W. Shorthill, R. Goldstein, and R. S. Krostad, "Laser Gyroscope", U.S. Patent No. 4,013,365, 1977.
8. E. J. Post, "Sagnac Effect", Rev. Mod. Phys., 39, p. 475, 1967.
9. F. Aronowitz and R. J. Collings, "Mode Coupling Due to Backscatter in a He-Ne Traveling-Wave Ring Laser", Applied Physics Letters, 9, p. 55, 1966.
10. F. Aronowitz, J. Killpatrick, and S. P. Callaghan, "Power Dependent Correction to the Scale Factor in the Laser Gyro", IEEE Journal of Quantum Electronics, QE-10, p. 201, 1974.
11. F. Aronowitz and W. H. Lim, "Positive Scale Factor Correction in the Laser Gyro", IEEE Journal of Quantum Electronics, QE-13, p. 338, 1977.
12. H. B. Greenstein, "Method and Apparatus for the Operation of Ring Laser in a Biased Mode", U.S. Patent No. 3,879,130, 1975.
13. R. E. McClure, and Vahrer, "An Improved Ring Laser Bias Element", NAECON '78, Dayton, Ohio, May 16-18, 1978.
14. I. W. Smith and J. A. Dorachner, "Biasing of the Raytheon Four-Frequency Ring Laser Gyroscope", Proc. of SPIE, 157, p. 21, 1978.
15. J. Brisman, H. Cook, and D. Lysoby, "Differential Laser Gyro Developments", Institute of Navigation, Bicentennial National Aerospace Symposium, Warminster, Pa., April 27-28, 1976.
16. R. Ulrich, "Fiber-Optic Rotation Sensing With Low Drift", Optics Letters, 5, p. 173, 1980.
17. K. Bohm, P. Martin, E. Weidel, and K. Pettermann, "Direct Rotation-Rate Detection with a Fiber-Optic Gyro Using Digital Data Processing", Electronic Letters, 19, p. 987, 1983.
18. B. Y. Kim and H. J. Shaw, "Gated Phase-Modulation Approach to Fiber-Optic Gyroscopes with Linearized Scale Factor", Optics Letters, 9, p. 275, 1984.
19. J. L. Davis and S. Ezekiel, "Techniques for Shot-Noise Limited Inertial Rotation Measurement Using a Multiturn Fiber Sagnac Interferometer", Proceedings of SPIE, 157, p. 131, 1978.
20. R. F. Cahill and E. Udd, "Phase-Nulling Fiber-Optic Laser Gyro", Optics Letters, 4, p. 93, 1979.
21. S. Lin, "Sensitivity Limits of an Optical-Fiber Gyroscope", Proceedings of SPIE, 157, p. 149, 1978.
22. W. K. Burns, R. P. Moeller, C. A. Villarruel, and M. Abebe, "All-Fiber Gyroscope with Polarization-Holding Fiber", Optics Letters, 9, p. 570, 1984.
23. E. Udd, R. J. Michal, and R. F. Cahill, "Scale Factor Correction in the Phase-Nulling Optical Gyro", Proceedings of SPIE, 478, p. 136, 1984.
24. E. Udd and R. F. Cahill, "Compact Fiber-Optic Gyro", Fiber-Optic Rotation Sensors, Springer-Verlag, New York, N.Y., p. 302, 1982.

Table 1. Gyro Requirements

Application>	Full Scale (°/sec)	Scale Factor Stability (PPM)	Bias Stability (°/hr)	Warm Up Time (sec)	Cost	Size	Life (Yrs)
Aircraft Navigation	100	25	.01	>300	High	Not Critical	>1
Space Booster	10-30	50	0.1	>300	Medium	Not Critical	>1
Spacecraft	10	~50	.1-.001	>300	High	Med-Small	>1
Torpedo	400	100-500	10-100	-	Low	Med-Small	3-5
Air-to-Ground Tactical Missile (Terminal Aided)	100-200	500	<0.1	60	Very Low	Small	3-5
Radar Guided, Ground-Air Missile	200-500	>1000	10-50	1/4 - 10	Low-Med	Small	5-10
Cannon Launched	>500	-	-	-	Very Low	Small	

Table 2. Performance Comparison

	Ring Laser Gyro	Analog Fiber-Optic Gyro	Digital Fiber-Optic Gyro
Output	$F = \frac{4A}{\lambda L n} \Omega$ $n = 1$ Frequency proportional to rate or counts per turning angle	$\phi = \frac{8\pi NA}{\lambda c} \Omega$ Voltage proportional to rate	$F = \frac{4A}{\lambda L n} \Omega$ $n = 1.6$ Frequency proportional to rate or counts per turning angle
Characteristic Pathlength	Generally 1m <30cm	50m - 5km (longer lengths are possible)	50m - 5km (longer lengths are possible)
Thermal Errors	o Packaging o Electrode placement o Pathlength control	o Packaging o Thermal control and compensation	o Packaging o Thermal control and compensation of active elements
Critical Issue	Lock-in Compensation	Reduction in Scattering Polarization Control	Reduction in Scattering Polarization Control
Dynamic Range	$>10^8$	$10^3 - 10^5$	$>10^8$
Scale Factor Correction	<1 PPM	1000 - 10,000 PPM	<100 PPM

Table 3. Technology Comparisons

	Ring Laser Gyros	Analog Fiber-Optic Gyro	Digital Fiber-Optic Gyro
Lifetime Determinant	Gas-filled Tube	Solid-State Components	Solid-State Components
Precision Machining	Yes	No	No
Precision Alignment	Yes Mirrors	Light Source Pigtail Fiber Coupler Fabrication	Interfacing to Frequency Shifters
Dither Mechanism to Avoid Lock-in	Yes	No	No
Ultra-clean Room Assembly	Yes	No	No
Flexible Geometry	No	Yes	Yes
Closely Related Support Industries	None	o Telecommunications o Audio & Video Compact Disk Players	o Telecommunications o Audio & Video Compact Disk Players

Table 4. Partial Listing of Companies Active in the Area

Ring Laser Gyros	Analog Fiber Optic Gyros	Digital Fiber Optic Gyros
---	AEG-Telefunken	---
British Aerospace	---	British Aerospace
Honeywell	Honeywell	---
Litton	Litton	Litton
---	McDonnell Douglas	McDonnell Douglas
---	---	Nippon Electric Company
---	SEL	SEL
Singer	Singer	---
---	STL	---
Sundstrand	---	---
---	Thomson-CSF	---
---	Sperry	---
---	Bendix	---
---	Lear Siegler	---
Northrop	Northrop	Northrop

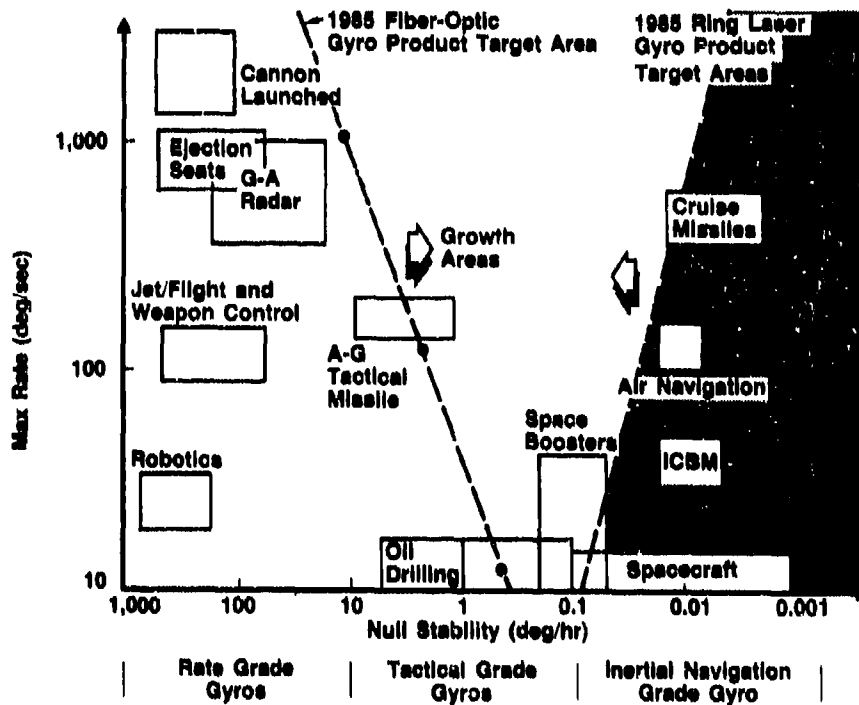


Figure 1. 1985 Ring Laser and Fiber-Optic Gyro Product Target Areas

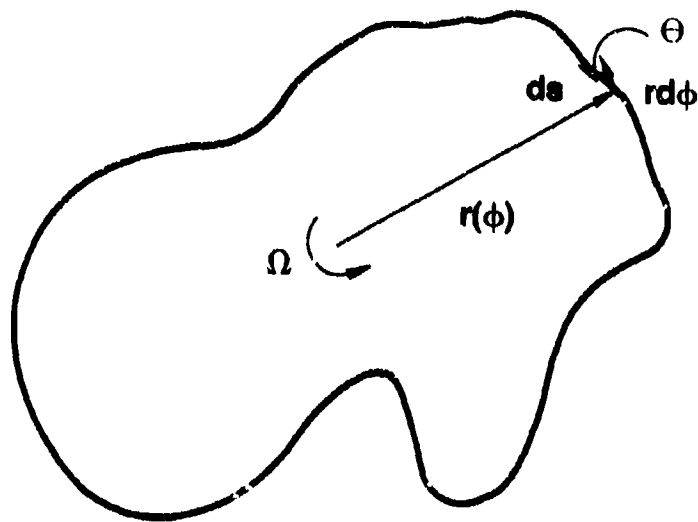


Figure 2. Optical Path with an Arbitrarily Shaped Perimeter

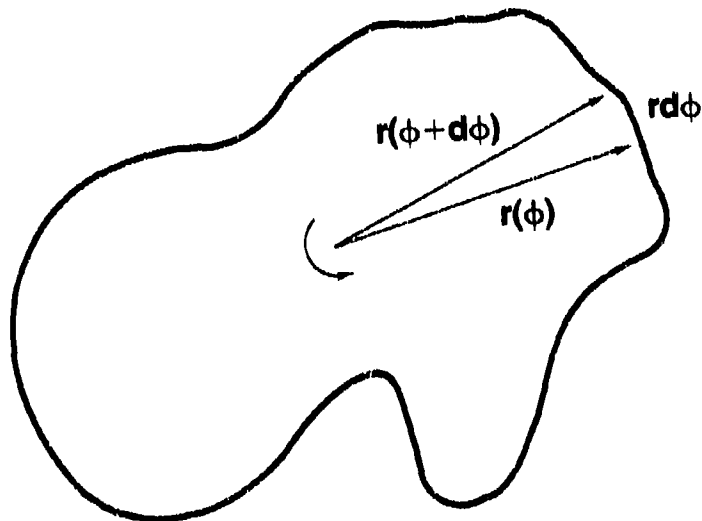


Figure 3. Differential Element for the Integral of Equation Four (4)

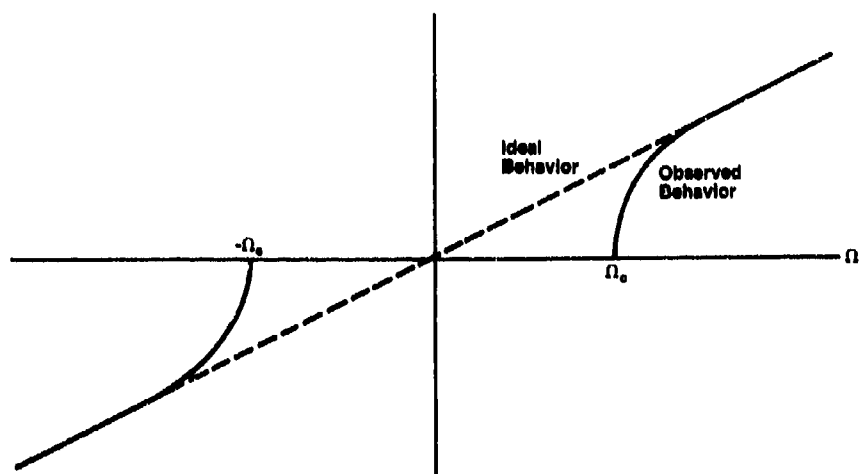


Figure 4. Lock-In Zone

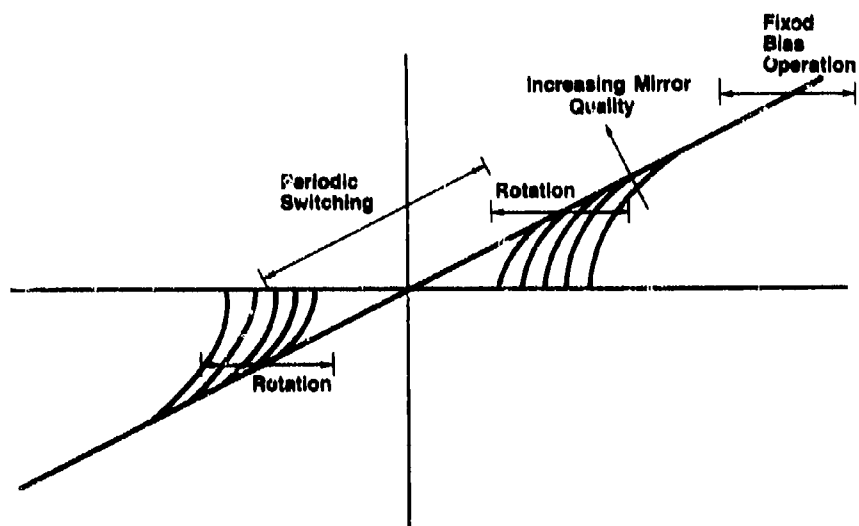


Figure 5. Nonlinear Effects of the Lock-In Zone

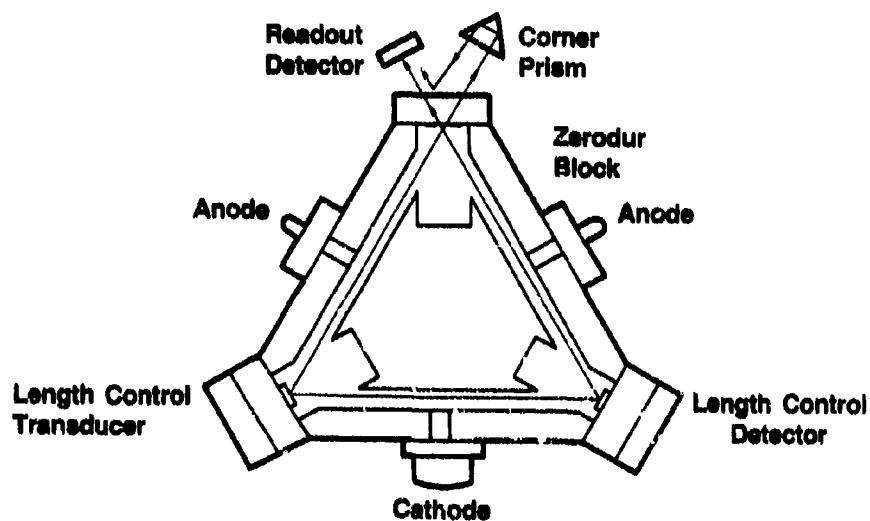


Figure 6. Ring Laser Gyro Block Assembly

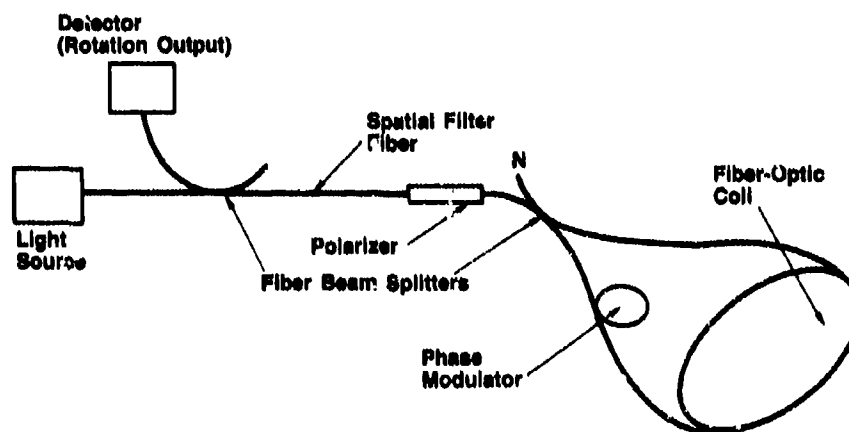


Figure 7. Block Diagram of the Analog Fiber-Optic Gyro

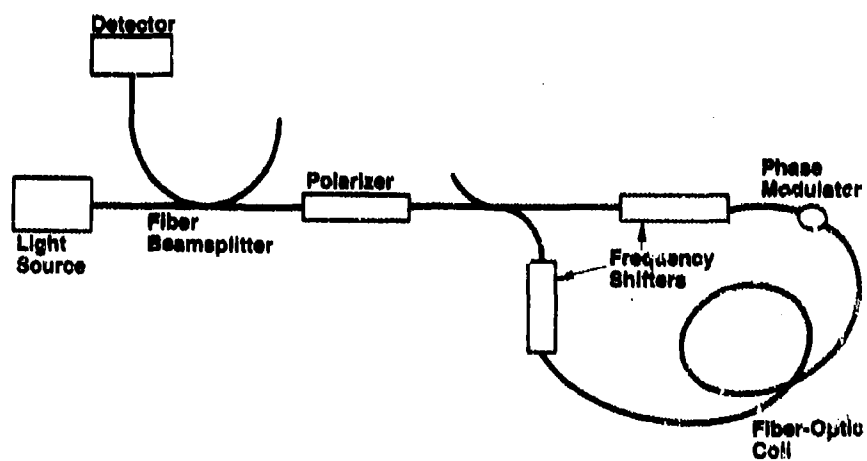


Figure 8. Block Diagram of the Digital Fiber-Optic Gyro

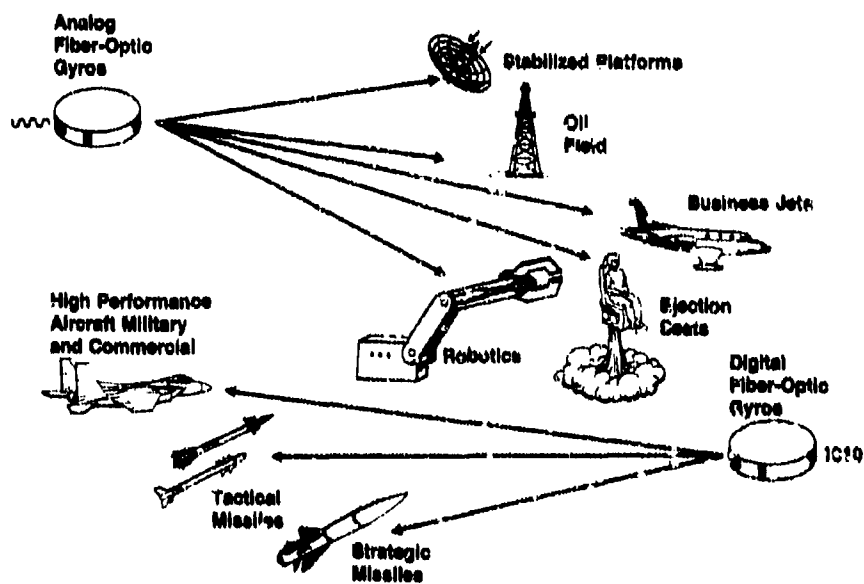


Figure 9. Analog and Digital Fiber-Optic Gyro Product Areas

DISCUSSION

J. Fridman, US

In your system you use a super luminescent edge emitting LED as a source to overcome modal noise, rather than a coherent source as proposed by Dr Culshaw in the previous paper No.2. Please comment on the reasons for taking this well-known approach, and the advantages or disadvantages of your technique over Dr Culshaw's approach.

Author's Reply

Appropriate techniques have been developed to compensate for scale factor shifts due to temperature dependence of superluminescent diode wavelengths. Given that sufficient power is available from these diodes, the use of the broadband source alleviates sensitivity to the backscatter problems that one addressed in Paper No.2.

J. Willson, UK

In the down-well two-axis gyro, how is the rate information transmitted to the surface? Is there any plan to use optical fibres for transmission?

Author's Reply

Strictly conventional telemetry system. No, the customer only requires the sensors at present.

Closed loop fiber optic gyro

D.H.Lewis, B.Bednarsz, J.A.Dankowych, K.Jew, G.Joslin, W.A.Young

Advanced Optical Systems Group, Litton Systems (Canada) Limited
25 Cityview Dr., Rexdale, Ontario, Canada, M9W 5A7

Abstract

This paper describes a breadboard closed loop gyroscope using ordinary single mode fiber and a multi-mode diode laser. Closed loop rotation rate bias stability data are presented for both short term ($\tau = 1$ sec) and long term ($\tau = 100$ sec., $N\tau = 6$ hrs). The performance of the gyro is displayed in the frequency domain as well as in the time domain. The performance achieved was a rotation rate noise of $5^\circ/\text{hr}$ for 1 sec. integration, $0.55^\circ/\text{hr}$ for 100 second integration and an extrapolated drift of $0.09^\circ/\text{hr}$. The long term (6 hours) bias stability was $1^\circ/\text{hr}$.

Introduction

Since the first demonstration of a Sagnac interferometer in a glass fiber in 1976¹, work on fiber optic gyroes has progressed rapidly. It now seems clear that all of the important noise and drift mechanisms are understood. Gyro configurations demonstrating excellent short and long term random drift have been reported^{2,3}. Other gyro configurations exhibiting linear behaviour over a large range have also been described^{4,5,6}. Nothing has been published on gyroes that exhibit both good long term drift ($< 0.1^\circ/\text{hr}$ for more than 10 hours) and high linearity using ordinary single mode fiber. This paper describes a breadboard gyro that is potentially capable of such performance and presents preliminary performance data. The optical components of the gyro are mounted in a relatively compact 2500 cm³ package with an associated electronics module. This arrangement was chosen to allow commercially available components to be used and still have a gyro small enough to undergo a range of performance tests.

System description

The gyro (Figure 1) is a simple Sagnac interferometer in a configuration described first by Ulrich⁷. To this has been added two acousto-optic modulators (AOMs) and integral gain servo electronics to provide a phase nulling closed loop system as described by Davis and Ezekiel⁸. The generator driving one of the AOMs is sinusoidally frequency modulated to provide the phase modulation that is used to measure the net non-reciprocal phase shift. The same generator is frequency modulated to produce a non-reciprocal frequency shift in the fiber coil and a proportional non-reciprocal phase shift. The integral gain servo electronics maintains the net non-reciprocal phase shift at zero. The output of the gyro is the difference between the frequencies of generators 1 and 2.

The principal attractions of this system are the strict linearity of the gyro output and the nominal insensitivity of the output to intensity fluctuations. There are, of course, some disadvantages. The gyro scale factor is a function of the refractive index of the fiber, and so of temperature. There is a bias that results in the optical paths between the primary directional coupler and the AOMs are of unequal lengths. For this gyro a 1 mm difference will produce a bias of $530^\circ/\text{hr}$. Another bias source is caused by frequency dependence of the AOM efficiencies. Because one of the AOMs is frequency modulated, this produces an amplitude modulation of the light which, in general, will have a component at the reference frequency. The bias resulting from this amplitude modulation can be reduced by selecting the reference period to be twice the transit time of the loop⁹. This method requires the modulation coefficients to be independent of the direction of propagation. Unfortunately an important source of amplitude modulation arises from operation of the frequency modulated AOM at other than the Bragg angle. This misalignment will normally be different for the two directions of propagation at the AOM, which will cause the amplitude modulation coefficients to depend upon propagation direction.

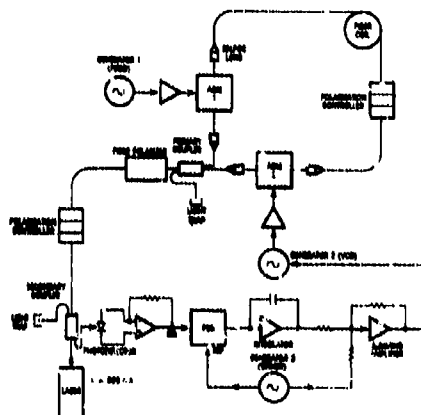


Figure 1. Phase-nulling gyroscope.

The optics module (Figure 2) is divided into two compartments. One contains the fiber sensing coil while the other contains the remaining optical components. The coil compartment is thermally insulated from the rest of the components and is internally mounted in such a way as to minimize the thermal gradients. The coil is also shielded against magnetic fields. The heat generating components are mounted on the top plate to reduce heat transfer to the spool.

The gyro is a nearly all fiber system with two bulk AOMs. The fiber pigtails on the various components are fusion spliced. The directional couplers are biconical fused taper types. The fiber polarizer is a section of coiled birefringent fiber. The laser is a multimode semiconductor unit with a centre wavelength of 825 nm. Its spectrum is shown in Figure 3. Three types of polarization controllers have been used: manual⁸, magnetic squeezer⁹ and piezoelectric squeezer¹⁰.

The sensing coil consists of 500 m of non-polarization-preserving fiber orthocyclically wound with 22 layers at 48 turns per layer on an aluminum spool. The mean diameter of the coil is 15.1 cm. The fiber is Corning XSMF, a single-mode transmission grade type with a 5 μ m core, a cutoff wavelength of 780 nm and a transmission loss of 2.2 dB/km.

As the AOMs and their associated lenses are a potential source of instability, considerable effort went into the design of this portion of the gyro. Graded index (GRIN) lenses were chosen to collimate the light through the AOMs because of their superiority to conventional lenses. Each GRIN lens is mounted in one end of a case 5 mm in diameter and 40 mm in length. The other end of the case accepts a single mode fiber pigtail held in place by UV curing epoxy resin. This assembly produces a collimator with excellent mechanical and thermal stability and negligible phase distortion of the transmitted beam.

For fibers terminated in GRIN lenses, fiber to fiber coupling efficiencies approaching 90 percent were measured. This efficiency can be attributed to the AR coating on the GRIN to air interfaces and the excellent index and modal match between the GRIN lens and the single mode fiber. These properties also greatly reduce the problems of backscatter and reflection that are often experienced when using bulk optic components. The GRIN collimators also exhibited a high degree of collimation. The projected light was found to have a divergence of 3.6 mrad, which is only marginally in excess of the beam divergence that is consistent with the measured beam waist. The beam to casing collinearity was measured to be better than 4 mrad. The overall efficiency of the GRIN - AOM assembly was measured as 53 percent.

Each GRIN - AOM module was assembled as a unit, with each GRIN lens mounted in a vee block whose mounting surfaces were ground to compensate for the lens' measured collinearity errors. The GRIN - AOM block has proven to be a stable arrangement. We expect that improved beam to casing collinearity will simplify the mount construction.

The power budget for the gyro starts with the fact that a minimum of 9 dB of input power is lost at unused coupler arms before reaching the detector. In the breadboard gyro, couplers are not ideal and have an insertion loss of 0.9 dB. The sensing coil is 500 m in length with an attenuation of 2.2 dB/km for a total loss of 1.1 dB. The AOM modules in the sensing coil each contribute 3.0 dB of loss for a total loss of 6.0 dB. The fiber polarizer contributes a 1.0 dB insertion loss to incoming and outgoing light for a total loss of 2.0 dB. These individual components composed of dissimilar fibers are all connected by fusion splices each having a mean loss of 0.4 dB for a total splice loss of 6.0 dB. Finally, all of these components had to be packaged which required bending of the fiber leading to approximately 3 dB of bend loss. This power budget shows a total loss between the multimode laser source and detector of 30.7 dB.

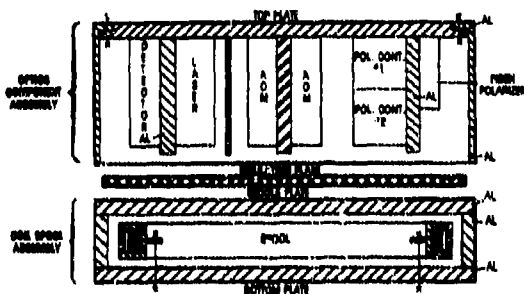


Figure 2. Optics module

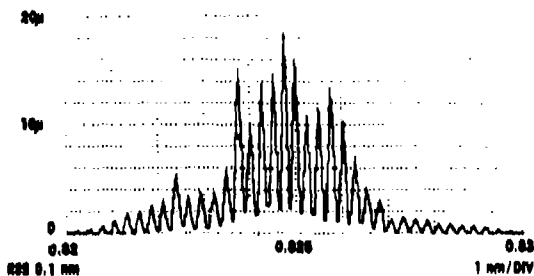


Figure 3. Multimode laser diode spectrum.

Electronics

The servo electronics is straightforward except for one point, the phase detector includes a bandpass filter that has notches at the second and fourth harmonics of the reference frequency. This is necessary because the photodiode output contains large components at even harmonics of the reference frequency and real phase detectors are sensitive to these signal components. This will cause an offset in the gyro output that is proportional to intensity. In order to obtain some criterion for specifying even harmonic rejection requirements let the offset be no larger than the shot noise amplitude with an integration time of 100 seconds. For the breadboard gyro the second harmonic rejection must be better than 130 dB. As the fourth through eighth harmonics are not negligible with respect to the second, attention must be paid to them also. It must be appreciated that this second harmonic rejection criterion is arbitrary and in fact is not good enough for high accuracy applications. It is also worth emphasizing that the required value of second harmonic rejection is a function of peak photocurrent, peak phase modulation, and fringe visibility factor.

Now that an estimate has been made of the tolerable magnitude of even harmonic sensitivity, the performance that can be expected of real phase detectors must be examined. One form of phase sensitive detector is an analog multiplier with one input a low distortion sine wave. This suffers from two problems: even harmonics in the reference sine wave, and even harmonic sensitivity in the modulator. Measurements made on the very high accuracy Analog Devices AD534 analog multiplier give low frequency second harmonic rejection of somewhat more than 70 dB. Unfortunately not only is this figure much too low but it degrades as the frequency increases. There is not much point in looking for a better multiplier as it is very difficult to generate a reference sine wave that has a second harmonic that is more than 60 dB below the fundamental.

Switching synchronous rectifiers are not much better but at least are cheaper, simpler and require a square wave reference rather than a high quality sine wave. A principle source of even harmonic sensitivity in this type of phase sensitive detector is asymmetry in the reference "square" wave. If the rectifier is modelled as a polarity reversing switch with the non-inverting half cycle d seconds shorter than one half of the period of T seconds, and if d is very small, the ratio between the $2k$ th harmonic and the fundamental is approximately $2kd/T$. Note that this approximation is independent of the order of the harmonic. For $d = 1$ nanosecond and $T = 5$ microsecond (200 kHz), the even harmonic sensitivity is -58 dB with respect to the fundamental. It is possible that with careful component selection and circuit layout that d could be reduced to 0.1 nanosecond. This would provide a 20 dB improvement in even harmonic sensitivity. These figures assume there are no nonlinearities in the switching circuit that could produce a degradation in the even harmonic rejection. Measurements on this type of phase detector show 70 dB appears to be a practical upper limit at a reference frequency of 200 kHz.

The phase sensitive detectors are so far short of the required performance that some form of filtering to reduce the even harmonics is clearly required. The filter should be a bandpass type with notches at the low even harmonics. The pass band, centred on the reference frequency, should have arithmetic symmetry, a bandwidth of twice the required servo open loop bandwidth and a linear phase response. A simple filter with these characteristics (second and fourth harmonic notches only) was developed.

In order to allow drift runs to be performed under the control of a laboratory computer a custom interface to the AOM driver generators was constructed. This contains two high speed 32 bit counters that count the frequencies of the AOM drivers. At selectable intervals the counter contents are stored without resetting the counters and then transferred to the computer over an IEEE 488 General Purpose Interface. In the computer counter overflows are compensated and the two counts are subtracted to give gyro output angle. Because one of the frequencies is frequency modulated by the reference it is important that the count transfer intervals be integral multiples of the reference period. The interface logic provides this function.

Polarization control

The original gyro design was based upon the expectation that the extinction ratio of the fiber polarizer would be high. Thus it was proposed to control loop polarization by a simple hill climbing process to maintain the interferometer output intensity approximately constant in the face of temperature changes. Unfortunately, in the early gyro test phase, the bias stability was poor. An estimate of the operational extinction ratio of the fiber polarizer was made and found to be only about 35 dB. Thus it was evident that improved polarization control must be provided. A polarization controller was added in series with the source and a higher accuracy control algorithm was developed.

Gyro drift performance

With the computer interface described above it is an easy matter to accumulate bias stability data over long drift runs. Because the frequency counters are not reset when their contents are transferred to the computer, the data in the computer is proportional to accumulated angle. Thus it can be sampled at any convenient multiple of the transfer period with a minimum of quantization error.

Figure 4 shows the results of a six hour drift run. The rotation rate bias is stable to within 1 $^{\circ}/\text{hr}$ during this period. Figure 5 displays the noise amplitude spectrum corresponding to the same run. The spectrum shows a low frequency spike and graphically indicates at what frequency our long term noise problems begin. The spectrum is white above .01 Hertz. The noise amplitude vs integration time curve is given in Figure 6. The short term noise is 5.0 $^{\circ}/\text{hr}$ (1 second) while the long term rate noise is 0.55 $^{\circ}/\text{hr}$ (100 second). The extrapolated drift (E.D.) = 0.093 $^{\circ} / \sqrt{\text{hr}}$ whereas we expect 0.015 $^{\circ} / \sqrt{\text{hr}}$ from shot plus quantization noise. The random walk coefficient is 0.22 $^{\circ} / \sqrt{\text{hr}}$.

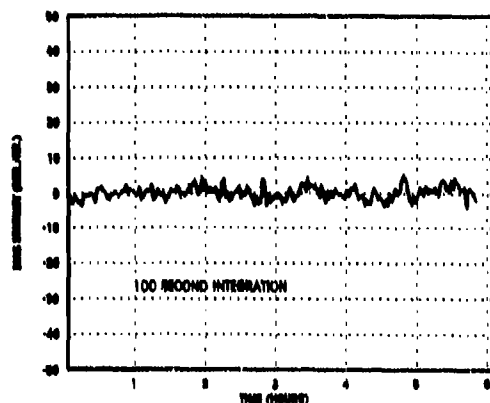


Figure 4. Gyro bias stability.

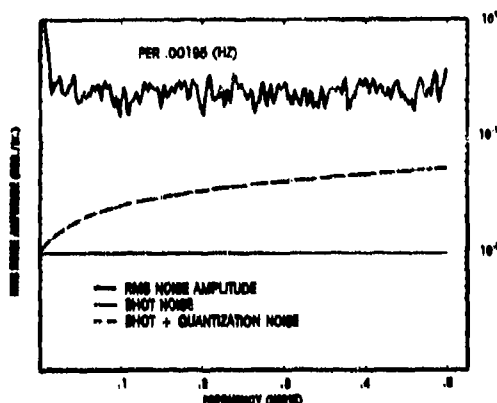


Figure 5. Gyro noise spectrum.

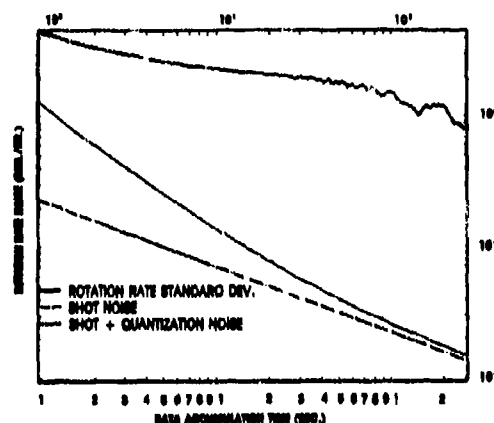


Figure 6. Gyro noise vs integration time.

Summary

We believe our results to be unique in that we have shown that good long term stability is achievable in a closed loop system using AOMs, a multimode laser diode and ordinary single mode fiber. These last two components are considerably less expensive than the more exotic superluminescent diodes and polarization holding fibers used by other researchers^{11,12}. We have determined that our short term performance is limited by electronic noise which at present is almost an order of magnitude above quantization noise.

References

1. V. Vali and R. W. Shorthill, "Fiber ring interferometer", *Applied Optics*, Vol. 15, No. 5, pp 1099-1100, 1976.
2. R. A. Bergh, H. C. Lefevre, and H. J. Shaw, "All-single-mode fiber-optic gyroscope", *Optics Letters*, Vol. 6, No. 4, pp 198-200, 1981.
3. R. A. Bergh, H. C. Lefevre, and H. J. Shaw, "All-single-mode fiber-optic gyroscope with long-term stability", *Optics Letters*, Vol. 6, No. 10, pp 502-504, 1981.
4. J. L. Davis and S. Ezekiel, "Techniques for shot-noise-limited inertial rotation measurement using a multiturn fiber Sagnac interferometer", *Proc. Soc. Photo-Opt. Instrum. Eng.*, Vol. 157, pp 131-136, 1978.
5. R.F. Cahill and E. Udd, "Phase-nulling fiber-optic laser gyro", *Optics Letters*, Vol. 4, No.3, pp 93-95, 1979.
6. J. L. Davis and S. Ezekiel, "Closed-loop, low-noise fiber-optic rotation sensor", *Optics Letters*, Vol. 6, No. 10, 1981.
7. R. Ulrich, "Fiber-optic rotation sensing with low drift", *Optics Letters*, Vol. 5, No. 5, pp173-175, 1980.
8. H. C. Lefevre, "Single-mode fibre fractional wave devices and polarisation controllers", *Electronics Letters*, Vol. 16, No. 20, pp 778-780, 1980.
9. M. Johnson, "In-line fiber-optical polarization transformer", *Applied Optics*, Vol. 18, No. 9, pp 1288-1289, 1979.
10. F. A. Mohr and U. Scholz, "Polarization control for an optical fiber gyroscope," in *Proceedings of the International Conference on Fiberoptic Rotation Sensors and Related Technologies*, Springer-Verlag, New York, pp 163-168, 1982.
11. W. Auch and E. Schlemper, "Drift behaviour of a fiber-optic rotation sensor using polarization preserving fiber", *Proc. First Intl. Conf. on Optical Fiber Sensors*, I. E. E., London, 1983.
12. W. K. Burns, R. P. Moeller, C. A. Villarruel, and M. Abebe, "All-fiber gyroscope with polarization holding fiber", *Optics Letters*, Vol. 9, No. 12, pp 570-572, 1984.

Acknowledgments

The authors appreciate the many informative discussions that we have had with S. Ezekiel of M.I.T. and with G. Pavliath of Litton G.C.S.D. This work was supported by a Canadian government N.R.C. grant.

DISCUSSION

H. Lefevre, Fr

What kind of optical power do you get back to the detector?

Author's Reply

60 nanowatts.

PROGRESS WITH MULTIPLEXED SENSOR ARRAYS BASED ON
REFLECTION AT SPLICED JOINTS BETWEEN SENSORS

J. P. DAKIN C. A. WADE P. B. WITHERS

PLESSEY ELECTRONIC SYSTEMS RESEARCH LTD
ROKE MANOR, ROMSEY, HANTS, U.K.

SUMMARY

This paper reports recent progress made in developing a time-division-multiplexed, fibre optic hydrophone array using optical time domain reflectometry (OTDR) techniques.

INTRODUCTION

Interferometric fibre optic sensors are attractive because of their high sensitivity relative to other types, such as those based on intensity modulation. Most reported to date have been single sensors, but there is currently considerable interest in using multiplexing techniques to drive an array of passive sensors from one source and detector. Such a system was recently reported by the authors (ref 1).

The basic operating principle is shown in figure 1. The system consists of a concatenated series of identical optical fibre sensors (which in the simplest case would be coils of fibre), each joined to the next by a partially-reflecting joint. Pairs of optical pulses, generated by applying pulses of RF to the Bragg cell, are launched into one end of the array. The first and second pulses of each pair have slightly different frequencies $f(1)$ and $f(2)$ respectively. As the transmitted pulses propagate down the array, a small proportion is reflected back from each partially-reflecting joint, and a series of reflections is received on a photodiode (figure 2). The delay between the two transmitted pulses is chosen to be equal to the two-way propagation time through each sensing section, so that the reflection of the first pulse from a particular joint is received simultaneously with the reflection of the second pulse from the preceding joint. The two therefore mix on the photodiode and generate a heterodyne signal, whose phase depends on the difference in optical paths. However their paths only differ by twice the length of the sensor that separates the two relevant reflecting joints, and therefore changes in the length of this sensor, caused for example by acoustic signals, modulate the phase of the heterodyne signal. The photodiode output consists of a sequence of short bursts of phase-modulated heterodyne signal, each corresponding to a particular sensor in the array. If the whole cycle is repeated continuously the photodiode output consists of a set of phase-modulated carriers time-division-multiplexed together. The acoustic signal on a particular sensor can then be recovered by demultiplexing and phase-demodulating the photodiode output.

Recently, improvements have been made in four main areas: development of partially reflecting splices; development of a high power single mode gas laser for use in the present system; development of a balanced-optical-path arrangement to allow shorter coherence length sources to be used in future systems; and development of an all-fibre frequency shifter, with the ultimate aim of producing a complete all-fibre system.

Partially reflecting splices

The fabrication of suitable low-loss, partially reflecting joints is crucial to the system. There is an optimum value for the size of reflection required, which depends on the number of sensors in the array.

For an array of ten sensors the optimum reflectivity is calculated to be in the range 0.1% to 2.0%, depending on the source power and system losses. A convenient way of producing a small reflection with low excess loss, is to introduce a refractive index mismatch into the optical beam. Fresnel reflection then occurs at each interface. Early breadboard systems, constructed to show the feasibility of the technique, used fibre joints with a small air gap between the fibre ends. This produced a pair of silica/air interfaces, each having a reflectivity of approximately 4%, in effect forming a low-finesse Fabry Perot cavity. The total reflectivity of such a splice is approximately a sinusoidal function of the fibre end separation, having maxima approaching 16% and minima close to zero. Splices fabricated in this way were rather lossy, and the reflection coefficient was highly sensitive to environmental effects such as temperature and strain on the splice support. This latter effect was due to the difficulty of adequately supporting the fibre ends and maintaining their separation.

Improved splices, having greater stability and lower transmission losses, have recently been produced by setting the fibre ends in transparent media having a different refractive index from silica (figure 3). This technique still produces a double reflection and splice reflectivity is therefore still a function of end separation, but once the potting medium has set the splice is quite stable and relatively insensitive to environmental effects.

Various different potting media have been tried, including UV-setting cement (ref index = 1.51), visible light cured adhesive (ref index = 1.59) and polystyrene (ref index = 1.6). The optically cured adhesives are particularly convenient to use and give maximum theoretical reflectivities of 0.16% and 1% for the types mentioned above. Polystyrene gives a theoretical maximum reflectivity of 1% but must be melted in order to make the

joint, although this can be done easily with a small electrical heater element. In this way polystyrene splices have been made with reflection coefficients of 0.5% to 0.8% and a transmission loss of 0.3 dB.

High power single mode gas laser.

The laser used for initial experiments on the sensor array was a 1mW HeNe device operating at a wavelength of 1152 nm. This had a multi-longitudinal mode output which was responsible for a certain amount of fading of the received heterodyne signal, due to drifting of the modes within the laser gain curve. Additionally, the 1mW output power was only sufficient to drive an array of up to two sensors plus a download. An improved source was therefore developed, with the aim of producing 10mW output in one longitudinal mode.

Conventional gas lasers have an output spectrum consisting of a set of discrete lines or modes, whose frequency separation is dependent on the length of the cavity. The total number of these modes in the spectrum depends on the Doppler-broadened linewidth.

Lasing can be confined to a single longitudinal mode by replacing one of the cavity mirrors with a pair, thus forming a secondary cavity (figure 4). The secondary cavity behaves like a single mirror with wavelength dependent reflectivity, maxima occurring when the cavity length is an integral number of half wavelengths. Laser modes having wavelengths that do not coincide with these reflection maxima will be suppressed. Thus by judicious choice of mirror reflectivities and spacings, a three mirror single mode laser can be constructed.

Such a laser was constructed to operate at 1152 nm. A rigid structure of Invar rods was used to support the gas discharge tube and the three mirrors. The low thermal expansion coefficient of Invar helped to minimize the effect of temperature fluctuations on the mirror separations, but a piezoelectric support for one of the mirrors was still necessary to control the length of the secondary cavity and maintain single mode operation.

Figure 5 shows the emission spectra of the laser with two and three mirrors: an interference filter was used to remove low intensity lines at wavelengths other than 1152 nm. The laser had a total output power of 13mW, with 9mW concentrated in a single mode at 1152 nm.

Balanced optical path interferometer.

In the basic system described in the introduction, the two light beams that interfere on the photodiode to produce a signal originate in the laser consecutively with a time difference t . This means that the coherence time of the laser must exceed t , or the beams will not interfere. On current systems t is of the order of 1 μ s and the coherence requirement has therefore precluded the use of short coherence length sources such as semiconductor or solid state lasers, both of which are more compact and rugged than gas lasers. A second consequence of the time difference between the generation of the two interfering pulses, is that any fluctuations in laser frequency will cause fluctuations in the heterodyne frequency, which are indistinguishable from phase modulation due to sound on the sensor. The balanced optical path configuration, described below, avoids both these problems and is expected to reduce laser microphony in current systems and enable Nd:YAG or semiconductor lasers with phase-noise reduction to be used in future systems.

A balanced optical path is achieved by generating the transmitted optical pulse pair from a single initial pulse, which is split into two paths, one of which contains a delay and a frequency shifter. The two paths are then combined, producing the required pairs of pulses. This "pre-delay" is matched to the differential delay in the sensor array, thus forming a balanced system, with the minimum source coherence length being determined by the error in matching the delays.

Figure 6 shows an all-fibre configuration of the balanced system using a fibre acousto-optic frequency shifter currently under development. This device is described in the next section.

All-fibre frequency shifter

It is well known that an optical phase shifter can be driven with a ramp waveform to produce a frequency shift (ref 2). A simple optical fibre phase shifter can be constructed by winding fibre on to a PZT cylinder (ref 3); voltages applied to the PZT strain the fibre and produce a phase shift in the propagating light. However, if such a PZT is driven with a sawtooth waveform to produce a frequency shift, severe ringing occurs, particularly on the flyback, resulting in a badly distorted phase ramp. We have devised three modifications to this simple idea, for reducing the resonances and improving the fidelity of the response.

A small strain gauge was attached to the PZT cylinder in order to monitor its response. The basic intention was to apply feedback to force the PZT to follow the applied drive signal accurately. Initially the transfer function of the PZT was found to have large phase shifts coinciding with its resonances, and these had to be reduced by mechanical damping before feedback could be applied, or the system would have oscillated. This was achieved by packing the PZT in a proprietary plastic damping compound. Modification of

the ramp waveform used to drive the PZT so as to remove the sharp edges without affecting the linear portion also helped. Negative feedback was then applied (figure 7) and resulted in a considerable improvement, the output of the strain gauge accurately following the PZT drive signal at ramp repetition rates up to 10KHz.

The device was incorporated into one arm of a fibre Mach Zehnder interferometer so that its optical performance could be investigated. The heterodyne signal generated at the output of the interferometer during the linear ramp sections was found to be slightly distorted, indicating that the optical fibre was not experiencing quite the same strain as the strain gauge. Further modifications are therefore required before the device will be of practical use; however these early results are highly encouraging and subsequent devices are expected to give improved performance.

Conclusion

We have described a fibre optic hydrophone array, consisting of a chain of passive sensors addressed by coherent optical time domain reflectometry, and recent progress made in improving the system. The areas in which improvements were described are: fabrication of reflective splices between sensors; the construction of a high performance gas laser source; modifications to the optical system to enable short coherence length sources to be used in subsequent systems; and an all-fibre heterodyne frequency shifter.

References

- 1 Dakin J P, Wade C A, and Henning M L, "Novel optical fibre hydrophone array using a single laser source and detector." Electronics Letters, vol 20, No 1, pp 53 - 54, Jan 1984.
- 2 Wong K K, and Wright S, "An optical heterodyne frequency translator", Proceedings of First European Conference on Integrated Optics, London, pp 63 - 65, Sept 1981.
- 3 Jackson D A, Priest R, Dandridge A, Tveten A B, "Elimination of drift in a single mode optical fibre interferometer using a piezoelectrically stretched coiled fibre", Applied optics, Vol.19, No 17, pp 2926 - 2929, Sept 1980.

Acknowledgement

This work has been carried out with the support of Procurement Executive, Ministry of Defence.

© 1985 The Plessey Company plc

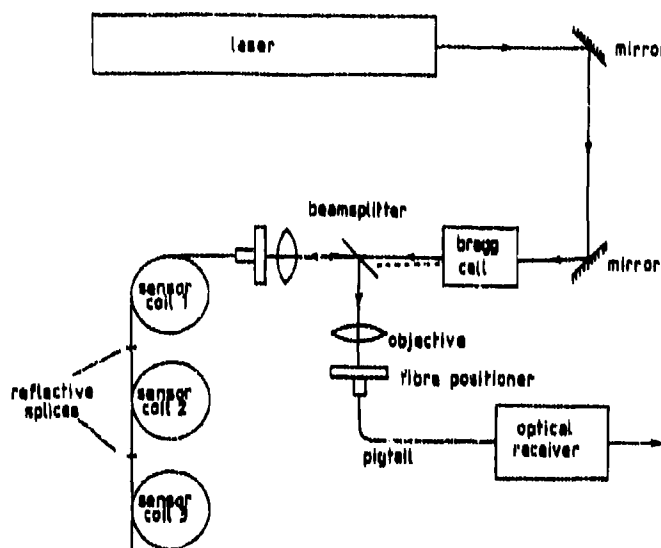


Figure 1. The basic reflectometric sensor array.

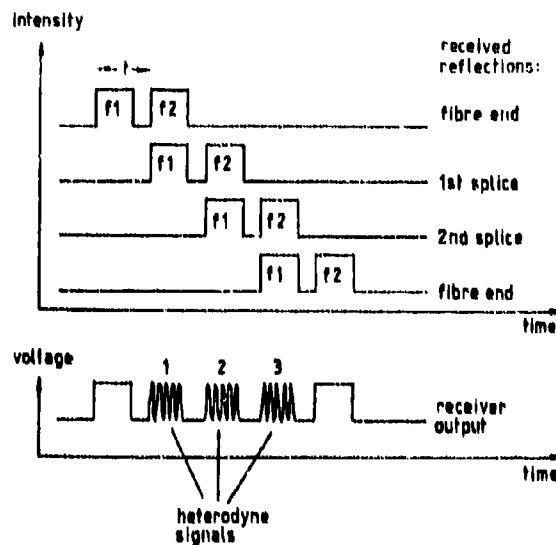


Figure 2. Timing diagram of reflections received, and corresponding receiver output for the array shown in Figure 1.

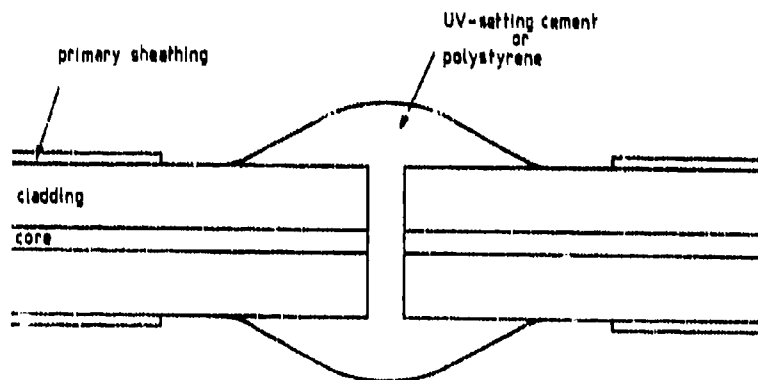


Figure 3. Construction of partially-reflecting splices using UV-setting cement or polystyrene.

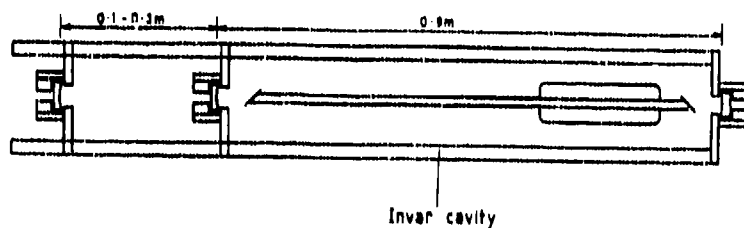


Figure 4. Construction of single-mode, 9mW, 1152nm HeNe laser.

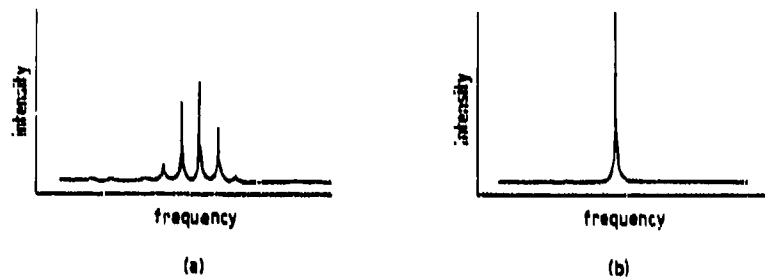


Figure 5. Fabry Perot interferometer scans of laser output:
 (a) Multimode, two mirrors, 0.9m cavity
 (b) Monomode, three mirrors, 0.9m & 0.18m cavities

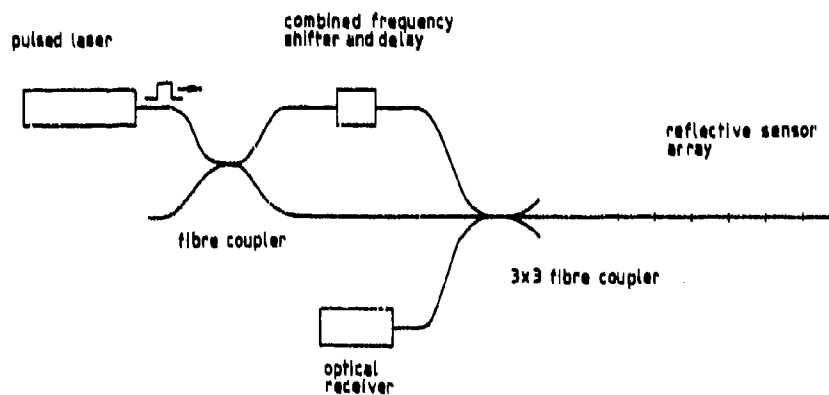


Figure 6. All-fibre sensor array, using short coherence laser and combined frequency-shifter and delay.

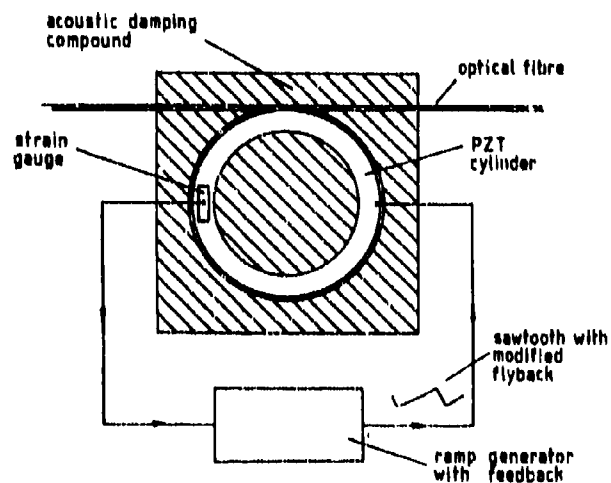


Figure 7. Optical fibre sawtooth frequency shifter.

DISCUSSION

S. Watanabe, US

Do you see significant variations in mixing efficiencies among the multiplexed sensors?

Author's Reply

Yes, this is due to polarisation fluctuations. We have ways to compensate for this but we are not compensating at present. An expensive way to cure the problem is polarization preserving fibres.

MAGNETIC AND PRESSURE SENSORS USING THE COMPENSATED POLARIMETRIC SENSOR CONFIGURATION

J P DAKIN, C R BATCHELLOR AND J A REX

PLESSEY ELECTRONIC SYSTEMS RESEARCH LIMITED
ROKE MANOR, ROMSEY, HAMPSHIRE, ENGLAND

ABSTRACT

Two identical lengths of high birefringence fibre spliced together with a 90° axial rotation to couple their orthogonal birefringent axes form the basis of a compensated polarimetric optical fibre sensor. This can be used to detect differential strains in the two fibre lengths caused by such phenomena as hydrostatic pressure or magnetic fields (the strain being introduced by magnetostrictive material bonded to the fibre). Magnetic and pressure sensors have been constructed using this principle and have shown good sensitivity yet better stability than Mach-Zehnder arrangements.

INTRODUCTION

The polarimetric optical fibre sensor was first proposed by Rashleigh of the U.S. Naval Research Laboratory and has been used to detect acoustic and magnetic fields, temperature, electrical current and strain (Ref. 3). The compensated version developed at Plessey ESR (Ref. 1) offers two main advantages over the original polarimetric sensor. Firstly, the original sensor of reference 3 could show an undesirable response to changes in its ambient conditions, as well as detecting the parameter required, whereas the compensated polarimetric sensor (CPS) is insensitive to any common-mode change of ambient conditions affecting both halves of the fibre. Secondly, the CPS is much less sensitive to phase noise in its light source, and can even employ a relatively incoherent LED source when well balanced (Ref 2).

We will first describe the theory of operation and the construction of a compensated polarimetric optical fibre sensor system, and then the application of this system to the measurement of AC and DC magnetic fields, and to the measurement of differential hydrostatic pressure. Finally, we will briefly describe a method for conferring download insensitivity to these sensors.

Theory of Operation of the Compensated Polarimetric Sensor System

A conventional polarimetric sensor (Fig. 1) uses a length of polarisation-maintaining optical fibre, which transmits light in two orthogonally polarised modes which have different propagation velocities. Plane-polarised light launched into the fibre at 45° to its polarisation axes will couple equal optical power into each of the two modes. The fibre introduces a phase delay between the two modes propagating along it. Changes in this delay can be observed simply by using an analyser at 45° to the polarisation axes. The light intensity passing through the analyser is proportional to $1 + \cos \phi$ where ϕ is the relative phase delay between the two polarisation modes. External physical fields can be made to change this phase delay, and are hence detected as cyclic variations of the analyser output. More sophisticated polarisation analysers can provide compensation for intensity changes and even allow tracking of phase changes over more than 2π radians. The simple polarimetric sensor has two disadvantages. Firstly its phase delay and hence output signal respond to changes both in temperature and strain in the fibre. Secondly, the differential phase delay introduced by the fibre may be as great as 3.10^6 radians in 100 metres, so that light launched into the fibre must be highly coherent in order to give high fringe contrast and low phase noise at the output from the analyser.

The compensated polarimetric sensor (Fig. 2) overcomes both these disadvantages. It consists of two identical lengths of polarisation-maintaining fibre which are spliced together with a 90° axial rotation in order to couple orthogonal polarisation axes. Light is input as before, but the phase delay between modes introduced in the first fibre length is exactly cancelled in the second. The fast mode in the first length couples into the slow mode of the second, and vice versa, so there is no net phase delay at the output.

Any uniform change in the physical conditions of the whole sensor will not affect the output signal, because the resulting change in the first length's phase delay is cancelled by an identical change in the second fibre length. The parameter to be sensed is allowed to change the phase delay in one of the fibre lengths relative to the other, causing an overall phase delay which is detected at the analyser. Hence the CPS is sensitive to differential mode but not common mode changes.

As the overall phase delay in a well compensated sensor will always be small, a light source of relatively high phase noise will normally give insignificant excess noise at the analyser. Reference 2 describes the successful operation of a CPS with an LED source showing that high fringe contrast may be achieved even using relatively broad linewidth sources.

Construction of Basic System

The layout of the basic CPS system is shown in Fig. 3.

The polarisation-maintaining optical fibre used in this study was type HB 800/1 made by York Technology Ltd., with core diameter 8 μ m and cladding diameter 128 μ m. It has a "bowtie" pattern of borosilicate glass within the cladding region our particular example having a beat length of 2.4mm at a wavelength of 633nm.

To make the CPS fibre, two equal lengths of polarisation-maintaining fibre were cut and their ends bared of coating. The polarisation axes at the fibre ends could then be located by viewing the bowtie pattern on the fibre endface under a microscope. Using this technique, the fibre lengths were aligned end to end with a relative 90° twist. The ends were then laterally adjusted to bring the fibre cores into line, using maximisation of light transmission between the lengths. Finally the ends were butted together and fusion spliced.

The CPS fibre requires an input light beam either circularly polarised or plane-polarised at 45° to each polarisation axis. This ensures that an equal intensity of light is launched into each polarisation mode of the fibre. The light source used was a Hitachi HL 7801E laser diode which emitted infrared light at a wavelength of 780nm, and was plane-polarised horizontally with an extinction ratio of 40.

The polarisation axes of the fibre were aligned at 45° to the laser junction. For initial experiments, discrete optical components were used to efficiently launch the laser into the fibre. Naturally in a practical sensor the launching system may be greatly simplified by using a packaged laser with a factory-aligned polarisation-maintaining fibre tail.

The polarisation state leaving the CPS fibre may be most simply analysed by a linear polariser at 45° to the polarisation axes, and the transmitted light measured to give the sensor's output signal. This was performed by a silicon PIN photodiode covered with an infrared polariser, while a second uncovered silicon photodiode within the same package measured the total light intensity leaving the fibre to allow compensation for source intensity fluctuation. The fibre end was fixed in a ferrule and held firmly in place so that its (unfocused) output cone of light illuminated both photodiodes, with its polarisation axes aligned at 45° to the axis of the linear polariser (Fig. 4). Although this arrangement has higher losses than a polarisation dependent beam splitter, it has significant savings in both cost and complexity, and hence is a more practical proposition for many low cost sensor applications.

The photodiode photocurrents are converted to proportionate voltages by transimpedance amplifiers. Thus the "analysed" output, V_p , is proportional to $1 + \cos \phi$ (ϕ = phase delay introduced in the fibre as before) and the bare photodiode output, V_t , is proportional to the total output intensity. These two signals may be electronically divided, and as V_t is also proportional to total output intensity, the divider output is therefore again proportional to the factor $(1 + \cos \phi)$, but is now independent of the total light intensity in the fibre and amplitude noise is eliminated.

Application of the Compensated Polarimetric System to Magnetic Sensing

A magnetic field can be made to strain an optical fibre simply by bonding the fibre to a magnetostrictive material.

Magnetostrictive material deforms parallel to an applied magnetic field, with the deformation approximating to a parabolic function of field strength. The magnetic sensor was constructed by bonding strips of magnetostrictive metallic glass on opposite sides of a polarisation-maintaining fibre, forming a "sandwich" as illustrated in Fig. 5. Metglass 2605UC metallic glass supplied by Allied Corporation was used, and the best bonding agent was found to be a rubber-based contact adhesive.

The magnetostrictive element was placed in a solenoid to produce a magnetic field parallel to the fibre. Measurements were made of the change of phase delay, $\Delta\phi$, resulting from the application of magnetic field, ΔB . The DC response is plotted in Fig. 6; the curve was a reasonable approximation to the expected parabolic shape, except it did not pass through the origin, due to an offset in the readings. The ordinate offset was believed to be due to magnetic remanence in the magnetostrictive material, which had not been annealed, whereas the abscissa offset was probably caused by a systematic phase offset from the point of quadrature of the CPS. From the shape of the curve, it is apparent that the small-signal AC sensitivity improves with increasing DC bias field as anticipated. Earlier workers have already reported the possibility of annealing the magnetostrictive material to reduce remanence but the long-term effectiveness of this process during magnetic "cycling" must remain in question. The frequency response of the magnetic sensor is shown in Fig. 7; the amplitude of alternating phase delay resulting from an AC field amplitude of 57uT, plus a DC bias field of 339uT, is plotted against frequency. There are several peaks of response due to mechanical resonances of the magnetostrictive element, and a region of high sensitivity around 20kHz to 50kHz. Here the sensitivity per unit length (with a DC bias of 339uT) is given by:-

$$\frac{\Delta\phi}{L\Delta B} = 1900 \text{ radians. T}^{-1}\text{.m}^{-1}$$

where L is the length of fibre bonded to the magnetostrictive strips (10cm) and ΔH is the AC field amplitude. The minimum detectable field of the magnetic sensor is $25nT$, Hz (based upon the minimum detectable phase change of the detector system of 5×10^{-6} radians. Hz $^{-1}$).

Clearly, the magnetic sensor's response could be increased by bonding greater lengths of fibre to the magnetostrictive element, using configurations such as illustrated in Fig. 8.

The application of the compensated polarimetric system for sensing pressure

Isotropic pressure will cause strain in polarisation-maintaining optical fibre, and hence a differential mode delay. Therefore a CPS for sensing pressure can be made simply by enclosing one of the fibre lengths in a chamber, which can be pressurised with the second length in close thermal contact, but unpressurised. For this study, both fibre lengths were enclosed (Fig. 9) so that they could be independently pressurised in order to demonstrate the differential and common-mode response of a compensated sensor. The sensor was arranged in the basic CPS configuration, and the changes of phase delay, $\Delta\phi$, resulting from step changes in the differential pressure between the chambers, ΔP , were measured. When the chambers were air-filled, the sensor was found to respond more to the transient temperature rise caused by adiabatic compression than to the pressure rise itself. However, temporarily covering the fibre with water virtually eliminated the transient component of the response due to this temperature rise. (A practical sensor may utilise a compliant silicone rubber filling). The sensitivity per unit length was found to be

$$\frac{\Delta\phi}{L\Delta P} = 4.96 \times 10^{-6} \text{ radians. Pa}^{-1}.\text{m}^{-1}$$

where L is the length of the fibre pressurised (1.8m). Fig. 10 compares the differential and common mode responses of the pressure sensor. Both photographs show a trace of output voltage V_o , against time over a 40kPa step decrease in pressure. The common mode response is less than 3% of the differential response. This common mode response may have been due to a slight imbalance between the lengths of fibre in the two chambers. The pressure sensor's response may be increased simply by increasing the length of fibre pressurised, as its sensitivity is proportional to this length. In addition, this is likely to improve the common mode rejection ratio as small errors in matching their lengths, or positioning of the fibre within the chambers will be less significant.

A Compensated Polarimetric Sensor with Insensitive Downloads

The compensated polarimetric sensors described so far have been sensitive to localised strains or temperature changes over their whole lengths from source to detector. This was exploited in bringing them to a quadrature point by localised heating, but it would not be desirable in a practical sensor. A configuration for a CPS with insensitive downloads from source to sensing element and sensing element to detector is shown in Fig. 11. This is an extension of a previously published method for remoting a conventional polarimetric sensor (Ref. 4).

The sensing element consists of two identical fibre lengths joined by a 90° splice as before, whereas the extension leads are further lengths of polarisation-maintaining fibre spliced to the sensing fibre, with a 45° relative rotation about their axes at each splice. The light source system is now arranged to launch light into only one plane-polarised mode of the first download. Thus the light transmitted to the sensing pair of fibres is plane-polarised at 45° to their polarisation axes, as required. The light leaving the sensing element would be analysed into components at 45° to the element's polarisation axes by the second download. The intensity of either of the plane-polarised modes leaving the second download would be measured, to give an output signal proportional to $1 + \cos \phi$. The total light intensity leaving the return lead would also be measured, and used as a reference to confer insensitivity to intensity changes on the system.

Since light in only one mode of each of the extension leads is used to determine the phase delay in the sensor element, changes in the phase delays of the downloads cannot affect the output. Hence the sensor system is insensitive to any changes in temperature, pressure etc. that may be experienced by the downloads, provided that this is not significant enough to cause differential attenuation between the two modes.

Conclusions

A basic compensated polarimetric sensor system has been constructed and adapted to measure magnetic fields and pressure giving sensitivities per unit fibre length of 1900 radians.T $^{-1}.$ m $^{-1}$ and 4.96×10^{-6} radians.Pa $^{-1}.$ m $^{-1}$ respectively. With the detector system capable of resolving phase changes of 5×10^{-6} radians.Hz $^{-1}$, the minimum detectable magnetic field was $25nT$.Hz $^{-1}$, and the minimum detectable pressure change was 0.67 Pa.Hz $^{-1}$. These are both quite sufficient for many practical sensing applications, and greater sensitivities can be achieved simply by using higher lengths of optical fibre. In addition, a method of making the sensing element remote from the source and detector system has been presented.

References

1. Dakin, J.P., Wade, C.A. "Compensated Polarimetric sensor using polarisation-maintaining fibre in a differential configuration". Electron. Letts., Vol. 20, No. 1 Jan. 1984 pp 51-53.
2. Dakin, J.P., Broderick, S., Carless, D.C., Wade, C.A. "Operation of a compensated polarimetric sensor with semiconductor light source". Proc. 2nd Int. Conf. on Optical Fiber Sensors, Stuttgart 1984, pp 241-245.
3. Rashleigh S.C. "Polarimetric Sensors: Exploiting the axial stress in high birefringence fibers". 1st International Conference on Optical Fibre Sensors, London, April 1983.
4. Varnham M.P. et al. "Polarimetric strain gauges using high birefringence fibre". Electronics Letters, Vol. 19, No. 17, pp 699-700.

© The Plessey Company plc 1985

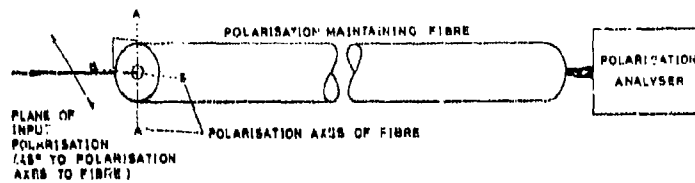


FIGURE 1: THE CONVENTIONAL POLARIMETRIC SENSOR

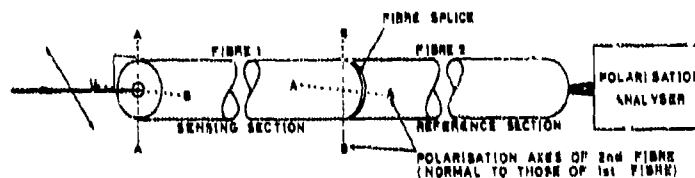


FIGURE 2: THE COMPENSATED POLARIMETRIC SENSOR

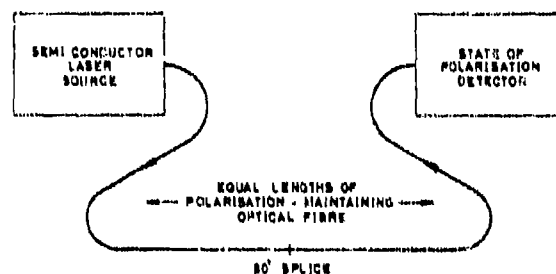


FIGURE 3: BASIC GPS CONFIGURATION

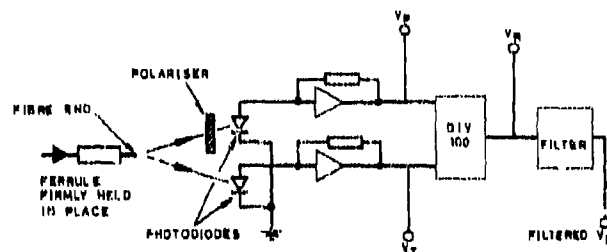


FIGURE 4: STATE OF POLARISATION DETECTOR

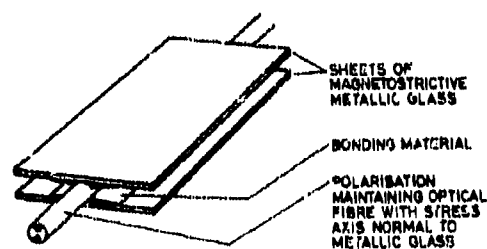


FIGURE 5: EXPERIMENTAL FIBRE OPTIC MAGNETOMETER

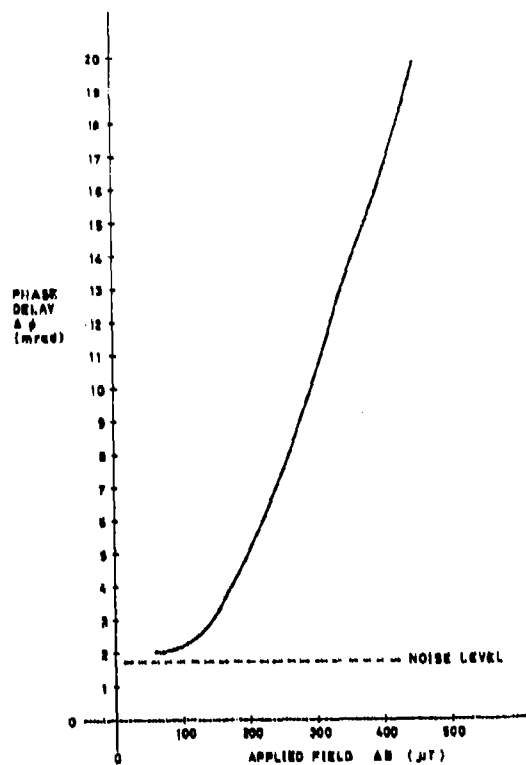


FIGURE 6: DC RESPONSE OF MAGNETIC SENSOR

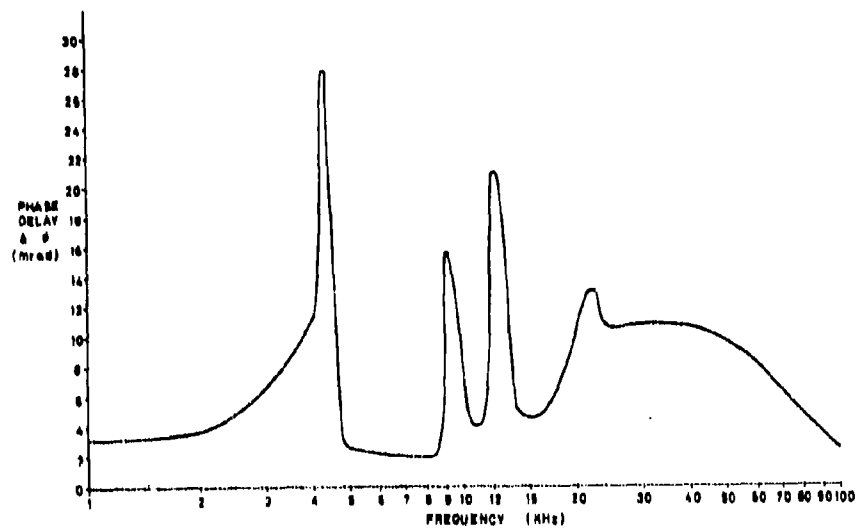


FIGURE 7: FREQUENCY RESPONSE OF MAGNETIC SENSOR.

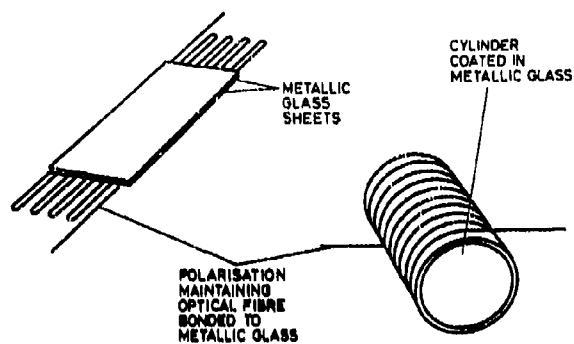


FIGURE 8: MAGNETOMETERS WITH IMPROVED SENSITIVITY

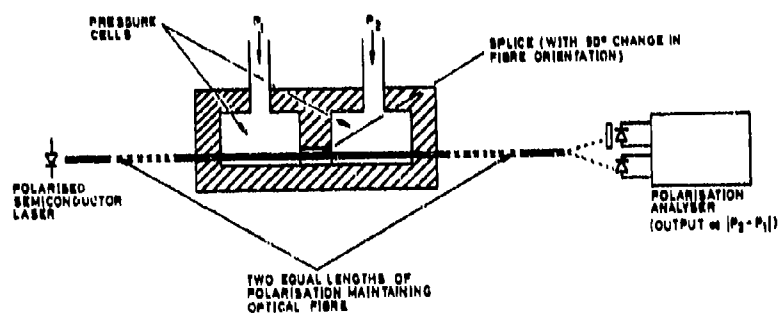


FIGURE 9: THE PRESSURE SENSOR

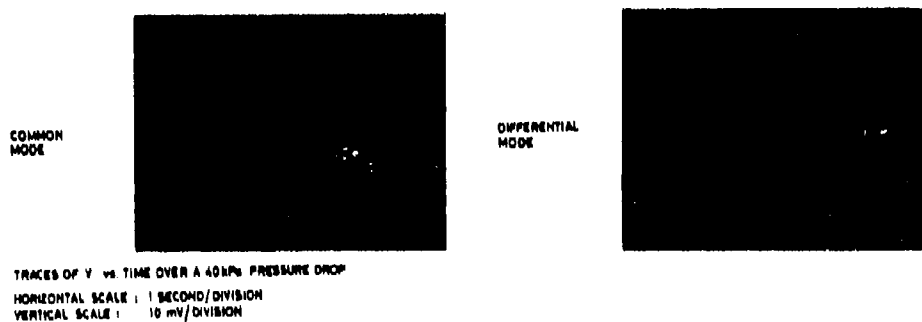


FIGURE 10: PRESSURE SENSOR RESPONSE IN DIFFERENTIAL AND COMMON MODES

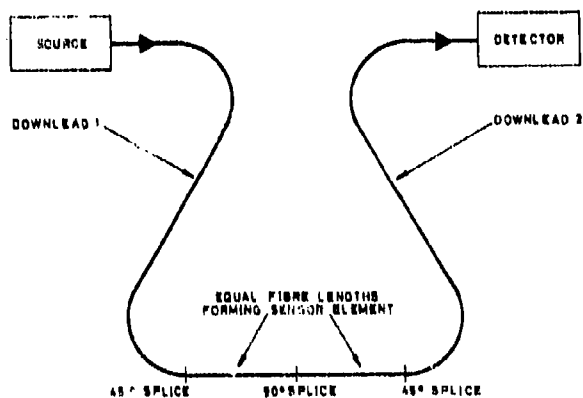


FIGURE 11: CPS WITH INSENSITIVE DOWNLOADS

FIBER OPTIC DEVICE FOR TEMPERATURE REMOTE SENSING

A.M. Scheggi, M. Brenci, G. Conforti, F. Così, R. Falciai, A.G. Mignani

Istituto di Ricerca sulle Onde Elettromagnetiche del C.N.R.
Via Panciatichi, 64 - 50127 Florence, Italy

SUMMARY

An optical-fiber temperature sensor is presented which is based on light amplitude modulation induced by a thermosensitive cladding applied on the distal end of the fiber. The experimental set-up for detecting and processing the signal is described, and the measured characteristics of the thermometer are reported.

INTRODUCTION

Since a few years optical fibers sensors are under investigation and application in many fields for measuring various physical and chemical parameters. The use of optical fibers offers the same advantage to sensing systems as they do to telecommunication systems, that is low attenuation, flexibility and reduced dimensions. Further, transmission over optical fibers is unaffected by external interference, so that optical fiber systems can be used in high voltage, electrically noisy, high temperature, corrosive or other stressing environments. They often offer an increased sensitivity over existing techniques. Two main classes of optical fiber sensors are usually defined: phase sensors and amplitude sensors, depending on how the physical or chemical variable to be measured modulates the intensity or the phase of the light in the fiber.

The phase sensors offer order of magnitude increased sensitivity over existing technology, but usually the more complicated single mode technology prevails, while the advantage of the intensity sensors are the simplicity of construction and the compatibility with multimode fiber technology.

A variety of multimode fiber sensors have been proposed and tested for measurements of different parameters ranging from displacements, vibrations, pressure, temperature, to blood velocity and flow, blood pH, oximetry, etc. These sensors present a relevant practical interest either in industrial and biomedical applications.

In the industrial field optical fiber thermometers can be utilized for temperature monitoring (also remote) in high voltage and electrical equipments or in the framework of semiconductor and other electronic material fabrication processes as well as in RF and microwave heating of food or of other materials (for instance for bonding or sealing purposes).

Other interesting applications are in the biomedical field, typically for temperature monitoring and for thermal distribution determination in RF or microwave hyperthermia or in photoradiation therapy of malignant tumors, but also for blood flow measurements by thermodilution technique. The main requirements for biomedical applications are high accuracy in the physiological range 30-50°C, small probe dimensions (for insertion in catheters and hypodermic needles) and biocompatibility of probe materials. Conversely industrial applications may require larger temperature working ranges but with a lower accuracy while the probe must be sturdy even if less miniaturized.

The majority of the proposed thermometers utilize the fiber only for light transmission to and from the sensor. The transducer can be of different type: for instance a Fabry-Perot optical cavity, a liquid crystal compound, a semiconductor, a birefringent crystal or a phosphor grain¹⁻⁸. Only a few thermometers make use as the sensing element of the fiber itself and in particular of its terminal portion: for example, by using a thermosensitive cladding^{9,10,11} or a rare earth doping on the tip¹² it is possible to obtain back-transmitted light signal intensity modulated by the temperature.

The present paper deals with a new temperature sensor previously proposed^{9,10,11} which utilizes the attenuation of the light transmitted along a multimode fiber, induced by a temperature sensitive liquid clad applied on a terminal portion of the fiber itself.

Details on the probe construction will be given along with a description of the optoelectronic detection and processing system. Furthermore results will be reported on the

characterization of the thermometer over different temperature intervals.

1. EXPERIMENTAL SET-UP

The used fiber is a PCS fiber and the replacing liquid clad is an oil exhibiting a temperature dependence on the refractive index (Fig. 1). When the temperature increases the refractive index of the liquid decreases with a consequent increase of the NA of the liquid clad fiber portion. Then the light backreflected undergoes an attenuation which decreases by increasing temperature within definite intervals depending on the used liquid. By utilising different liquids with different refraction index at room temperature, it is possible to make the device sensitive over different temperature ranges. The probe experimental configuration is shown in Fig. 2. The end face is mirrored and the

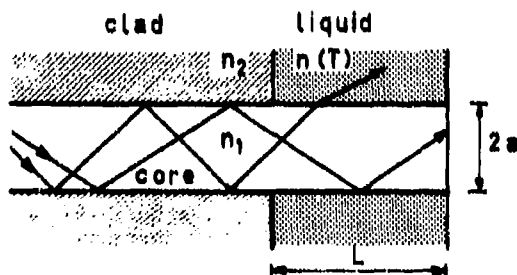


Fig. 1 - Working principle sketch.

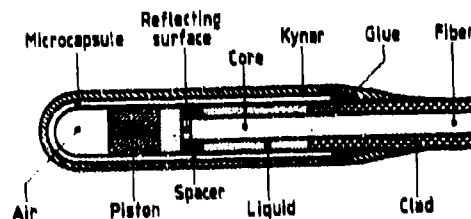


Fig. 2 - Probe experimental configuration.

liquid is contained in a glass microcapsule cemented to the fiber. In order to avoid deterioration of the cement, due to pressure by the liquid clad expansion with increasing temperature, the bottom of the capsule is left empty. A piston separating the empty from the liquid filled region allows the liquid expansion towards the empty region. An open ring plastic spacer provides fiber centering. The capsule and a portion of the fiber are coated with a plastic layer for protection. By using a 200 μm core fiber it was possible to realize miniaturized probes (1 cm long, and with an overall external diameter less than 1.5 mm).

Fig. 3 shows the schematic view of the sensor. The modulated light from a LED is coupled into the fiber. A four way optical fiber coupler provides a reference signal and a direct signal which is sent to the distal end of the fiber constituting the sensor. The light reflected backwards is sent along the same fiber through the beam splitter to the signal detector. A biased PIN photodiode (Fig. 4) is used as signal detector and the resultant voltage is amplified as a.c. signal. A good suppression of the noise is given by a narrow band active filter tuned on the fundamental frequency of the signal, followed by a rectifier which gives a continuous voltage V_s function of the measured temperature. The same processing is applied to the reference signal, and the continuous voltage V_r at the output of the channel results proportional to the source intensity alone. The two analog signals along with a calibration thermocouple analog output, digitalized by a multichannel 12 bit A/D converter, are processed by a microcomputer which evaluates the ratio V_s/V_r as a function of the temperature, thus eliminating short and long term source fluctuations.

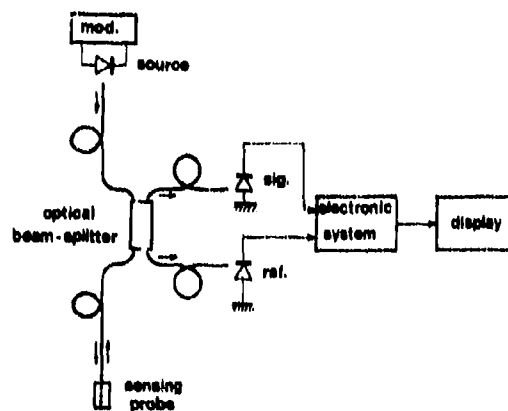


Fig. 3 - Sketch of the temperature sensor system.

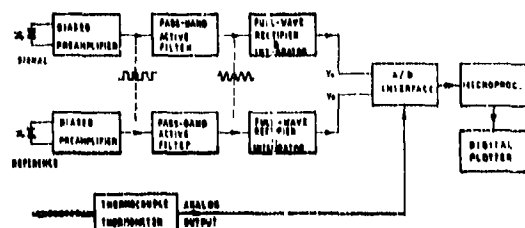


Fig. 4 - Analog section and calibration thermocouple.

2. EXPERIMENTAL RESULTS

The characterization of the thermometer was performed by calibration and response time curves recording and by stability tests. The calibration curves were obtained by immersing the probe in a thermostatic water or oil bath (depending on the considered temperature interval) along with an accurate calibration thermocouple (OMEGA) and by plotting the sensor output V_s/V_r versus thermocouple temperature on a digital plotter connected to the microcomputer.

The time response curves were obtained by measuring the sensor output when the probe is quickly replaced between two preset thermostated baths, while stability tests were performed by immersing the probe in a preset bath at a constant temperature and continuously recording and plotting the sensor output during the test period. Temperature fluctuations detected with this type of measurements include also the influence of temperature variation of the external environment on the optoelectronic system.

Fig. 5 shows a typical response curve which is linear in the 30-60°C temperature interval with a resolution within 0.1°C as required for biomedical applications.

Fig. 6 shows another calibration curve obtained with a probe where a different liquid (machine oil) was used as clad. In this case the curve exhibits the best linearity over the 100-130°C interval and the resolution results better than 1°C which is quite good for industrial applications. In both cases 5-7 m long fibers were used; however longer fibers for remote measurements can be used with a resultant lower accuracy. The measured rise time resulted of 1 sec and the accuracy derived from stability test over 6 hours resulted of $\pm 0.3^\circ\text{C}$.

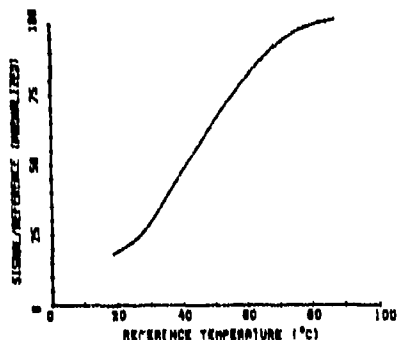


Fig. 5 - Typical response curve (biomedical applications).

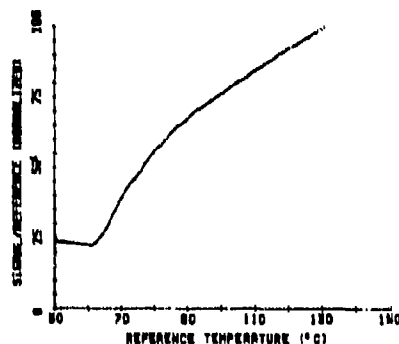


Fig. 6 - Typical response curve (industrial applications).

3. FURTHER IMPROVEMENTS

In order to obtain a more compact system with digital display of the measured temperature, the electronic and processing system of the sensor, was modified by replacing the microcomputer and the A/D interface before described with a simple voltage-to-time converter followed by a microprocessor and a display unit (Fig. 7). The voltage-to-time converter produces a time interval proportional to the ratio between the signal and the reference. This time interval is measured by the microprocessor which provides to drive the display. Assuming an interval where the temperature T is a linear function of the ratio between the signal and the reference, it is possible to select the time constants so to obtain a displayed number representing the temperature value. Of course the micro

processor could be programmed so to make a calibration also over a temperature range where the response curve is not linear.

Fig. 8 shows the package of the optoelectronic system (LED, beam splitter, detectors with electronic circuits) connected to the sensor and to the processing and display unit. The system was also provided with a convenient shielding and with filters so to be insensitive to the electromagnetic noise.

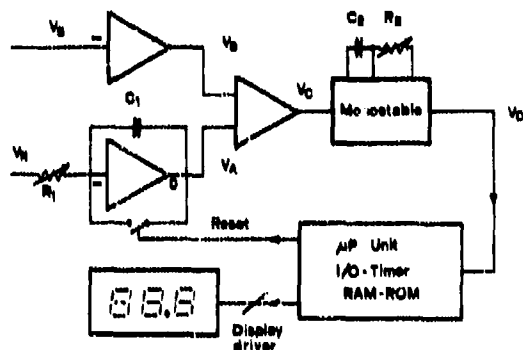


Fig. 7 - Voltage-to-time converter and display unit.



Fig. 8 - Thermosensitive-clad optical fiber temperature sensor.

REFERENCES

- 1 W.H. Quick, K.A. James, J.E. Coker: Fiber Optics Sensing Techniques - Proceedings IRE of the First International Conference on Optical Fiber Sensors, London, 26-28 April 1983, vol.221, 6-9.
- 2 R. Xist, S.Drope, H. Wölflschneider: Fiber Fabry Perot Thermometer for Medical Application - 2nd International Conference on Optical Fiber Sensors (Stuttgart, Sept. 1984) - Conference Proceedings VDE-VERLAG GmbH (Berlin) p.165 (1984).
- 3 C.C. Johnson, T.C. Rossel: Liquid-Crystal Fiberoptic RF Probes - Microw. Journal, August 1975, 55-57.
- 4 K. Kyuma, S. Tai, T. Sawada, M. Nunohita: Fiber Optic Instrument for Temperature Measurement - IEEE QE-18(4), April 1982, 676-679.
- 5 C. Ovrén, M. Adolfsson, B. Håk: Fiber-Optic Systems for Temperature and Vibration Measurements in Industrial Application - International Conference on Optical Techniques in Process Control (The Hague, The Netherlands), Paper B2 (1984).
- 6 T.C. Cetas: Biological Effects of Electromagnetic Waves - Proceedings 1975 USNC/URSI Symposium, vol. II, 239.
- 7 K.A. Wickersheim, R.B. Alves: Optical Temperature Measurement - Ind. Res./Dev., December 1979, 82-90.
- 8 R.B. Alves, K.A. Wickersheim: Fluoroptic Thermometry: Temperature Sensing Using Optical Fibers - Proceedings of SPIE 403, 146 (1983).
- 9 M. Brenici, R. Falcini, A.M. Scheggi: Termometro a fibra ottica - Italian Patent No. 84155 A/82 (1982) under extension.

- 10 A.M. Scheggi, M. Brenzi, G. Conforti, R. Falciai, G.P. Preti: Optical Fiber Thermometer for Medical Use - Proc. IEE of the First International Conference on Optical Fiber Sensors, London, 26-28 April 1983, vol. 221, 13-16.
- 11 A.M. Scheggi, M. Brenzi, G. Conforti, R. Falciai: Optical Fiber Thermometer for Medical Use - IEE Proc. 131, 270-272 (1984).
- 12 E. Snitzer, W.W. Morey, W.H. Glenn: Fiber Optic Rare Earth Temperature Sensor - Proceedings IEE of the First International Conference on Optical Fiber Sensors, London, 26-28 April 1983, vol. 221, 79-81.

DISCUSSION

J.Fridman, US

(1) You are using a thermocouple to calibrate your fibre optic sensor, and in that sense you are limited by the resolution and response time of the thermocouple to calibrate a much more sensitive device, with a potentially much higher accuracy and resolution. Why couldn't you use an absolute calibration that makes use of the change of NA as a function of $n(T)$, rather than depend on a thermo-mechanical device? (2) In medical applications that we have encountered e.g. temperature field around laser probe when illuminating skin, muscle tissue or blood vessels a probe response smaller than milliseconds is required. Why does your device have such a high response time of 1 second?

Author's Reply

(1) The performance of our sensor is widely sufficient for the application we had in mind, such as hyperthermia, where there is the problem of interference of R.F. with thermocouple. However the resolution of thermocouple we used for calibration (OMEGA) was 0.01°C and therefore sufficient for calibrating our sensor. (2) The time response can be improved by miniaturizing the probe and making the capsule of silver.

OPTICAL FIBER SENSORS FOR THE MEASUREMENT OF PULSED ELECTRIC CURRENTS*

G. W. Day and J. D. O. McFadden
National Bureau of Standards
Boulder, CO 80303

L. R. Vesser and G. I. Chandler
Los Alamos National Laboratory
Los Alamos, NM 87545

R. W. Cernosek
Sandia National Laboratory
Albuquerque, NM 87185

SUMMARY

Recent progress in the design of fiber sensors for pulsed electric currents is reviewed. Several of the most useful sensor configurations are described and compared. Models are used to predict the transfer function of these sensors, their sensitivity to non-ideal fiber properties, particularly linear birefringence, and methods for overcoming these problems. Other recent research is examined to suggest the prospect for sensors with improved sensitivity and stability.

INTRODUCTION

In the development and testing of weapons and weapon delivery systems and in controlled fusion research, the need to measure very large pulsed electric currents arises frequently. These measurements must often be performed in the presence of substantial electromagnetic interference, making the use of conventional sensors difficult. Optical sensing techniques can effectively eliminate this interference.

In this paper we describe recent progress in the design of current sensors based on the Faraday effect in single mode optical fiber. These sensors are being used successfully in several measurement systems at Los Alamos and Sandia National Laboratories where the pulse amplitudes range from about 100 A to 50 MA with durations as short as 1 μ s.

BASIC SENSOR DESIGNS

The Faraday effect is a magnetically induced rotation of the plane of polarization of linearly polarized light, given by

$$\theta = V \int \vec{B} \cdot d\vec{z} \quad (1)$$

where θ is the rotation, V is a material parameter known as the Verdet constant, $B = \mu_0 H$ is the magnetic flux density, and z is the direction of propagation. In an optical fiber current sensor [1,2,3] one or more loops of single mode optical fiber surround the electrical conductor. Then, since

$$\oint \vec{H} \cdot d\vec{z} = I \quad (2)$$

about any closed path around a conductor carrying a current I , the plane of polarization of light propagating in the fiber is rotated by an amount

$$\theta = \mu_0 V N I \quad (3)$$

where N is the number of turns of fiber around the conductor. For a single turn of fused silica fiber the ratio of rotation to current is approximately 265 deg/MA.

To measure this rotation the fiber is usually placed between polarizers and the transmitted light monitored with a high speed photodiode (Fig. 1). The transmittance of the sensor as a function of current depends on the relative orientation of the polarizers. For two important cases, namely crossed polarizers and polarizers at 45 deg to each other, the transfer functions are given by (Fig. 2)

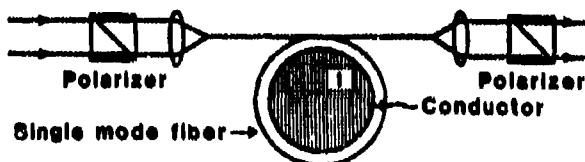


Figure 1. Schematic of an optical fiber current sensor. Linearly polarized light passing through one or more turns of fiber surrounding the conductor is rotated in proportion to the current. A polarizer at the output allows the rotation to be detected as a change in transmittance.

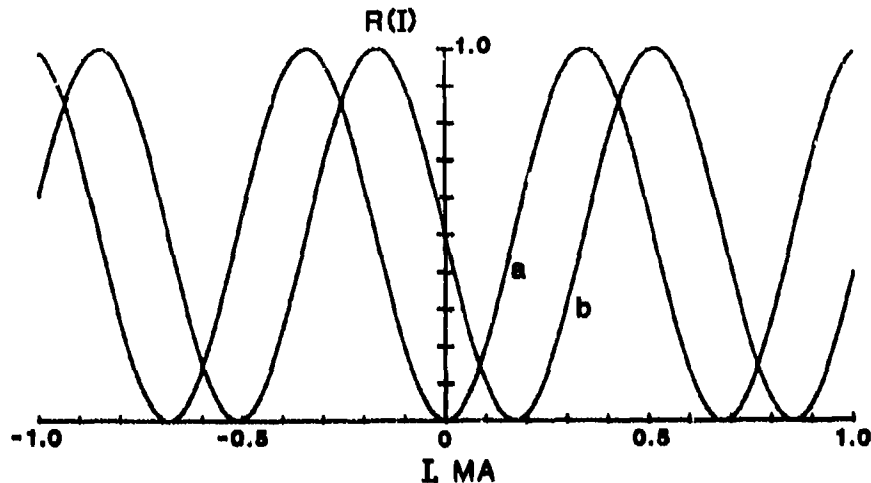


Figure 2. Computed transfer functions for the sensor shown in Fig. 1 for the case of polarizers aligned for minimum transmittance at zero current (a) and for polarizers oriented for a transmittance of 0.5 at zero current, i.e., the output polarizer at 45 deg to the minimum transmittance orientation (b).

$$R(\theta) = \frac{1}{2} (1 - \cos 2\theta) \quad (4)$$

and

$$R(\theta) = \frac{1}{2} (1 + \sin 2\theta), \quad (5)$$

respectively. The latter case obviously provides greater sensitivity (near $\theta = 0$) and is normally used for the detection of small currents.

When the currents to be measured are large, the multivalued nature of the transfer function may be a problem. Often, however, the general shape of the waveform is known in advance so that ambiguities can be resolved by inspection. Examples of such cases are illustrated in Figures 3 and 4. Figure 3 shows raw data from an experiment in which a capacitor bank was discharged into a very low resistance load. With the prior knowledge that the current waveform should approximate a damped sinusoid, it is easy to recognize the peak of the first half cycle at about 5 μ s and the first zero-crossing at about 10.5 μ s. Figure 4 shows some processed data from a two stage explosively driven flux compression generator. The current was initiated by capacitive discharge yielding a peak current of about 1 MA. After one stage of flux compression the peak current increased to about 10 MA (Fig. 4a) and after the second stage to more than 50 MA (Fig. 4b). Good agreement between the optical sensors and conventional sensors (Rogowski coils) also used in this experiment was observed except that the Rogowski coils in the second stage failed slightly earlier than the optical sensor.

When the general shape of the current waveform is not known in advance or when the data is processed automatically, a two polarization detection scheme can be used to resolve ambiguities [4]. Figure 5 shows such a system. The output of the fiber is split with a polarization-independent beamsplitter, allowing the detection of two separate polarization components. One polarizer-detector combination is oriented for minimum transmittance at zero current and therefore provides a cosinusoidal transfer function of the form of Eq.(4). The other polarizer-detector combination is oriented for a

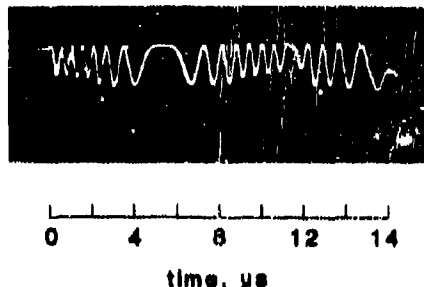


Figure 3. Raw data from a sensor similar to that shown in Fig. 1. The current was produced by a capacitor bank discharged into a low resistance load and approximates a damped sinusoid with a peak amplitude of about 2.4 MA.

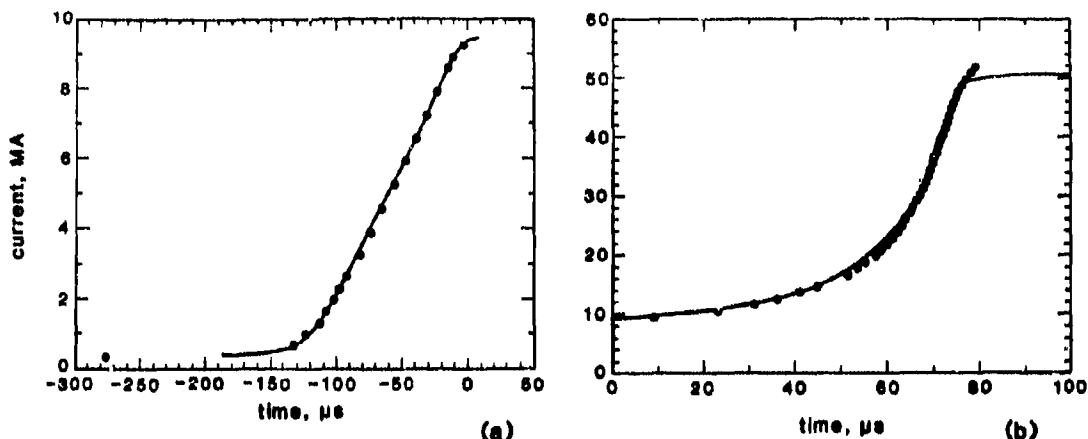


Figure 4. Processed data from a two stage high-explosive-driven flux compression generator. The left curve is the current measured at the output of the first; the right curve is the current at the output of the second stage. Time zero is the firing of the second stage. Points are from the optical sensor; solid lines are from a Rogowski coil.

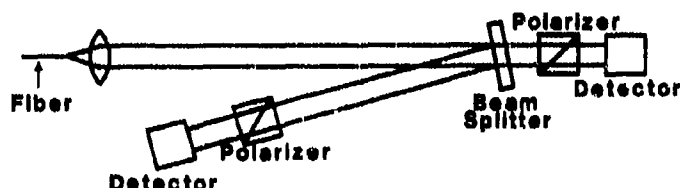


Figure 5. A two polarization detection scheme that provides both sinusoidal and cosinusoidal transfer functions and therefore allows resolution of ambiguities resulting from the multivalued transfer function.

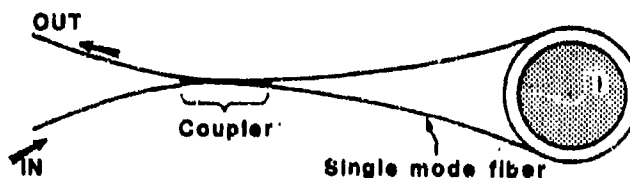


Figure 6. Schematic of a Sagnac interferometer used as a current sensor. No polarizers are required. The transfer function, which is identical to that shown in Figure 2b, is independent of the input polarization state.

transmittance of 0.5 (i.e., at 45 deg to the first) and provides a sinusoidal transfer function of the form of Eq.(5). The rotation can be determined unambiguously within the range $-90^\circ < \theta < +90^\circ$ by examining the sign of the sine and cosine signals. Furthermore, if the signals are sampled at least once within each 90 deg of rotation, multiple rotations can be identified [4].

An alternative sensor configuration that avoids the use of polarizers entirely is the Sagnac interferometer [5] shown in Figure 6. As in an optical fiber gyroscope, a coupler divides the input light into equal amplitude, counter-propagating waves in a fiber coil. The coupler, like a beamsplitter in an interferometer, introduces a 90 degree phase shift between its two output beams. Therefore, if the coil acts on the counter-propagating waves reciprocally the two components combining at the output port cancel and all the power is returned to the input port. Any nonreciprocal effects in the coil, specifically those produced by rotation or a magnetic field, cause power to appear at the output port. For the case of Faraday rotation, the transfer function can be obtained either by considering the change in polarization state of the counter-propagating beams or by resolving the input state into orthogonal circular states and considering the induced phase shifts. The result, somewhat surprisingly, is the same for any input polarization state, and is identical to that found for a coil placed between crossed polarizers [Eq.(4)].

EFFECT OF LINEAR BIREFRINGENCE IN THE FIBER

The sensor characteristics described in the preceding section can be achieved only when, in the absence of applied field, the propagation characteristics of the fiber are independent of polarization state. This is not, in general, a good assumption. Indeed, the primary difficulty with fiber current sensors is that linear birefringence in the fiber, resulting from inherent geometrical imperfections and stress or induced by applied stress, can seriously distort the transfer function.

Inherent linear birefringence can be effectively eliminated using certain manufacturing techniques. Birefringence resulting from applied stress, particularly from bending, remains a problem. Bend-induced linear birefringence can be predicted analytically [6] and is highly reproducible [7]. It is given by

$$\Delta\delta = K_{\lambda} r^2/R^2 \quad (6)$$

where r is the fiber radius, R is the bend radius, and K_{λ} is a parameter equal to about 7.7×10^7 deg/m for silica fibers at a wavelength of 633 nm.

Faraday rotation in a linearly birefringent medium such as a fiber coil can be modeled using Jones calculus. The relationship between the input and output polarization states is given by [8]

$$\begin{bmatrix} E_x(z) \\ E_y(z) \end{bmatrix} = \begin{bmatrix} \cos \frac{\phi z}{2} - j \frac{\Delta\delta}{\phi} \sin \frac{\phi z}{2} & -\frac{2F}{\phi} \sin \frac{\phi z}{2} \\ \frac{2F}{\phi} \sin \frac{\phi z}{2} & \cos \frac{\phi z}{2} + j \frac{\Delta\delta}{\phi} \sin \frac{\phi z}{2} \end{bmatrix} \begin{bmatrix} E_x(0) \\ E_y(0) \end{bmatrix} \quad (7)$$

where E_x and E_y are complex electric field amplitudes, $\Delta\delta$ is the birefringence per unit length, F is the Faraday rotation per unit length, and

$$\left(\frac{\phi}{2}\right)^2 = \left(\frac{\Delta\delta}{2}\right)^2 + (F)^2. \quad (8)$$

Inspection of Eqs. (7) and (8) indicates that when $F \ll \Delta\delta$ the matrix in Eq. (8) approaches that of a purely linear retarder, indicating that the rotation is effectively quenched. When $F \gg \Delta\delta$ the matrix approaches that of a pure rotation (circularly birefringent) element.

This behavior can be observed in the computed transfer functions shown in Figure 7. Figure 7a shows the transfer function of a sensor consisting of a single 3 cm diameter turn of 125 μ m diameter fiber between crossed polarizers and operated at 633 nm. The bend-induced birefringence is approximately 127 deg, leading to significant distortion in the amplitude of the transfer function for rotations less than about 180 deg (about 0.7 MA). Figure 7b shows the transfer function for a 10 turn, 10 cm diameter coil of the same fiber, in which the total birefringence is about 382 deg. In this case both the amplitude and the periodicity of the transfer function show significant distortion.

TWISTED FIBERS

One technique for overcoming induced birefringence is to twist the fiber. Twisting, like the Faraday effect, induces a rotation or circular birefringence in the fiber. The magnitude of the rotation is given by [9]

$$\alpha = g' \xi \quad (9)$$

where α is the rotation per unit length, ξ is the twist per unit length, and g' is a material parameter which at a wavelength of 633 nm is equal to about 0.08. The twist-induced rotation may be added algebraically to the magnetically induced rotation in Eq. (7). This is illustrated in Figure 8 which shows that the effect of twisting is, in essence, to bias the sensor away from the distorted part of the transfer function. The extent to which the transfer function can be shifted depends on the relative magnitude of the linear birefringence and twist-induced rotation per turn. Since for a given twist per unit length the twist per turn increases (linearly) with coil diameter and bend-induced birefringence per turn decreases (inversely) with the coil diameter, twisting becomes much more effective with larger coil diameters (Fig. 8b versus Fig. 8a).

Many 125 μ m silica fibers will withstand twists of between 40 and 50 turns per meter; with care, some will reach 80 or 90 turns per meter. For small coils this may not bias the transfer function sufficiently to measure dual polarity waveforms, though for single polarity waveforms less bias is required (Fig. 8a).

Another difficulty with twisting is that the parameter g' defined in Eq. (9) is slightly temperature dependent so that when large amounts of twist are used the bias in the transfer function may drift. One technique for eliminating this problem is to twist the fiber in opposite directions about its center [2]; any drift in the twist-induced rotation in one half tends to be compensated by an equal drift in the other half. The effect of alternate twisting on the transfer function is to shift the distortion in both

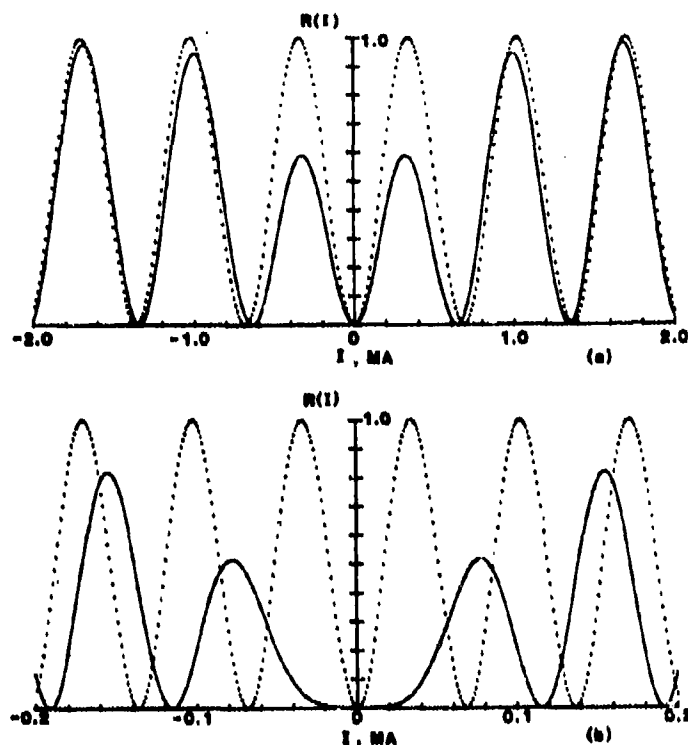


Figure 7. Computed transfer functions of fiber current sensors showing the effect of bend-induced linear birefringence in the fiber. (a) One turn, 3 cm coil diameter, 125 μ m fiber diameter, 633 nm operating wavelength. (b) 10 turns, 10 cm coil diameter, 125 μ m fiber diameter, 633 nm operating wavelength. Dotted curves show the transfer functions that would be observed if linear birefringence were not present.

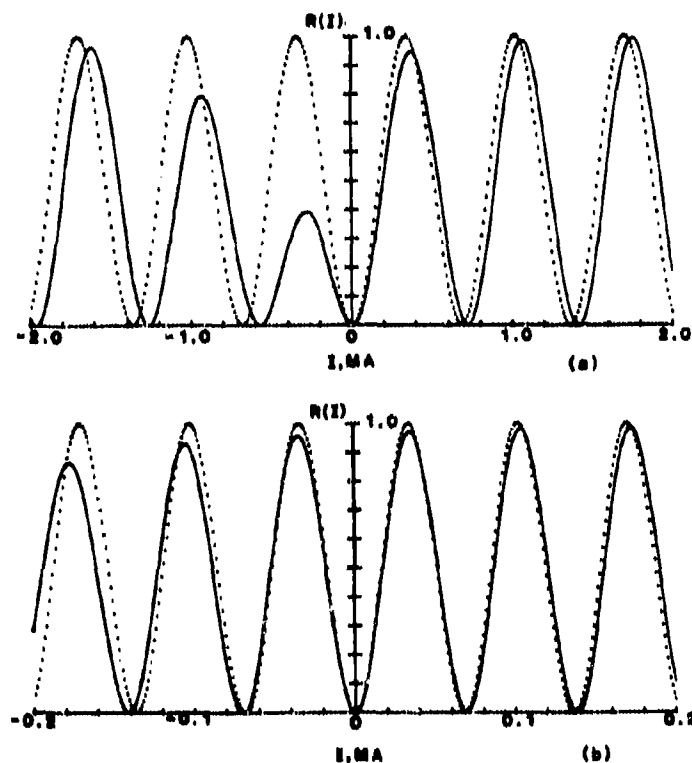


Figure 8. Computed transfer functions of the same sensors illustrated in Figure 7 showing the effect of twisting the fiber. (a) The 3 cm diameter coil using a twist rate of 50 turns/m. (b) The 10 cm diameter coil using a twist rate of 10 turns/m. Dotted curves assume no linear birefringence.

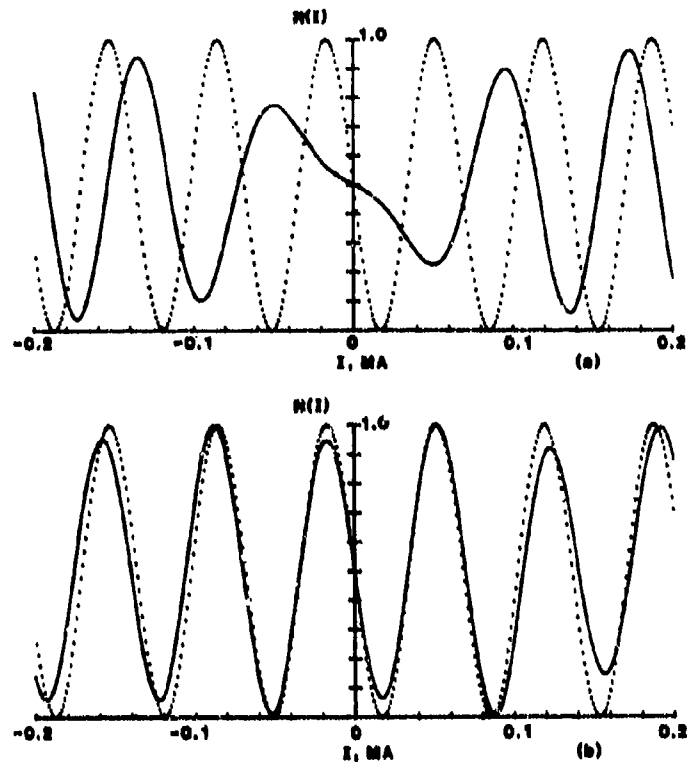


Figure 9. Computed transfer function showing the effect of alternate twisting. Coil is the same as in Figures 7b and 8b except that the polarizers are oriented for a transmittance of 0.5 at zero current. (a) The fiber is not twisted. (b) The fiber is twisted at a rate of 10 turns/m about its center. Dotted curves assume no linear birefringence.

directions from the origin. Thus it is most useful in sensors designed to measure small currents and which therefore use polarizers oriented at 45 deg. The transfer function of a 10 turn, 10 cm diameter coil in that configuration, without twisting and with alternate twisting is shown in Figure 9.

The effect of twisting on a Sagnac current sensor is qualitatively similar to the effect of alternate twisting in a polarimetric sensor. Specifically, the transfer function remains symmetric about zero current and the distortion caused by linear birefringence shifts away from the origin (Fig. 10). One of the most important properties of the Sagnac, its insensitivity to input polarization state, is retained, at least for the symmetric geometry considered here.

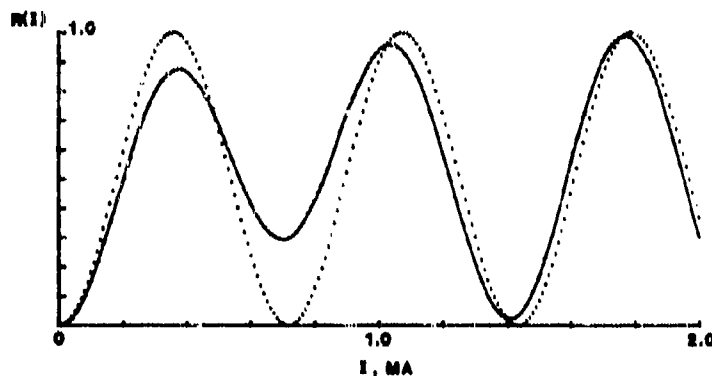


Figure 10. Computed transfer function for a Sagnac interferometer configuration showing the effect of twisting. Coil is the same as in Figures 7a and 8a. Twist rate is 50 turns per meter. Dotted curve assumes no linear birefringence.

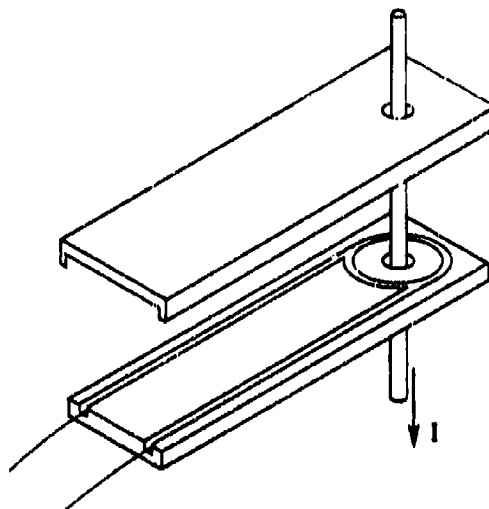


Figure 11. Fixture used for annealing bend birefringence. The material is machinable ceramic. The fiber lies in a 3 mm wide channel and makes several 3 cm diameter turns around a hole through which a conductor can be placed.

OTHER TECHNIQUES: ANNEALING AND HELICAL CORE FIBERS

For small multiple turn coils, where twisting is not very effective in eliminating the effects of linear birefringence, two recently developed techniques show promise.

One is to form the fiber into the desired sensor configuration and then reduce the bend-induced birefringence by annealing (Fig. 11) [10]. Temperatures between 600 and 700 deg C, maintained for periods from several hours to several days have been effective in decreasing the birefringence between one and two orders of magnitude. Coils with diameters of 3 cm and $5\frac{1}{2}$ turns have been tested to date. Such coils retain their shape and strength after annealing, and can be removed from the annealing fixture, if desired. Measured transfer functions at low frequency and low current demonstrate theoretical response.

Another recent development is a helical core fiber [11]. Such a fiber exhibits circular birefringence and thus behaves much like a twisted fiber. Potentially, it is much superior to twisting in that a higher degree of circular birefringence can be obtained (a beat length of less than 10 nm has been achieved to date) and, because the birefringence is induced by the helical geometry, it should be insensitive to temperature.

CALIBRATION

An advantage of Faraday rotation current sensors is that, aside from the difficulties introduced by linear birefringence, a knowledge of the Verdet constant is sufficient to provide calibration [Eq.(3)]. The Verdet constants of many bulk glasses are known but relatively little data has been available on optical fibers.

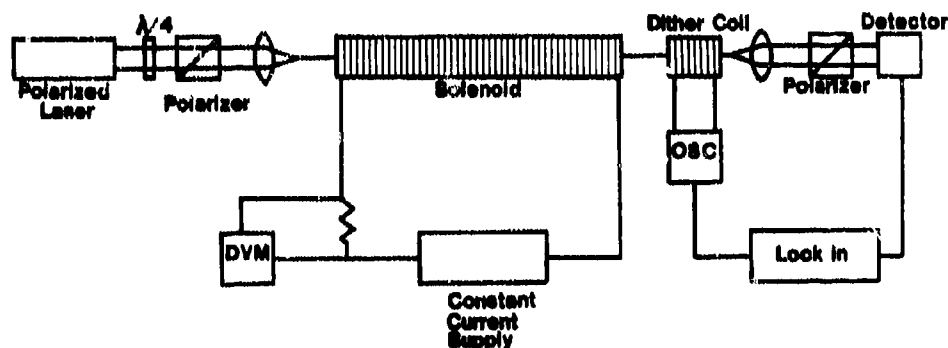


Figure 12. Schematic of a system used to measure the Verdet constant of optical fiber. The magnetic field is supplied by a 1 m long solenoid having about 3100 turns and operated at about 30 A. The second coil is operated at 100 Hz and provides a dither signal to facilitate alignment of the polarizers.

Figure 12 shows a solenoid system recently constructed at NBS to measure the Verdet constants of fibers. An advantage of using a solenoid is that, provided the fiber extends beyond the fringing fields, only the exact number of turns and the current need to be known (i.e., neither the length of fiber in the field nor the magnetic field as a function of length). The solenoid presently used is 1 m long, has about 3100 turns, and is driven at about 30 A. The fiber is placed in the solenoid with polarizers at the input and output. The fiber also passes through a smaller coil, which is driven at about 100 Hz and provides a dither signal to facilitate orientation of the polarizers.

To date, most of the fibers tested have shown Verdet constants within a few percent of the value for fused silica, 2.1 deg/cm·T at 633 nm. This includes the two types generally used in our laboratories for current sensors--a silica core, fluorine-doped inner cladding fiber, and a germanium-doped core, all-silica cladding fiber.

IMPROVED SENSITIVITY

It is widely believed that the relatively small Verdet constant of fiber limits the application of fiber current sensors to applications involving very large currents. Actually, if other noise sources can be reduced to the point that shot noise in the detector is the limiting factor, quite small currents can be measured.

For a sensor based on a single turn of fiber, with polarizers oriented at 45 deg (and therefore a transfer function of the form of Eq.(4)), and operated at 633 nm with sufficient optical power to produce an average current of 1 mA in the detector (which, for a 50 Ω system makes shot noise approximately equal to Johnson noise) the minimum detectable current can be computed to be about 2 nA/Hz^{1/2}. The primary obstacle in achieving this level is amplitude noise in the laser. One approach to reducing laser noise is active amplitude stabilization with an external modulator on the laser. Another is to detect both the +45 deg and -45 deg polarization outputs. Subtracting these signals not only yields reduced noise but a factor of two increase in sensitivity [Eq.(4)].

Simply increasing the number of turns of fiber to improve the sensitivity is limited by the extent to which linear birefringence can be controlled and to which a reduction in the response time of the sensor can be tolerated. Calculations similar to those presented above suggest that, using relatively large (e.g., 10 cm diam) coils of twisted fiber, it may be practical to use more than 100 turns. The response time of a 100 turn, 10 cm diameter coil, assuming transit time to be the limitation, is about 160 ns.

Several research groups are now exploring the possibility of producing fibers with a higher Verdet constant [12,13,14,15]. Among the possibilities are fibers containing lead and various rare-earth elements. An examination of data for various commercial bulk glasses suggests that an increase in the Verdet constant of a factor of 10 to 20 might be achieved in this way.

CONCLUSION

Substantial progress has been made in the development of optical fiber sensors for pulsed electric currents and these sensors have now become the preferred technology for the measurement of very large amplitude pulses. Recent developments, including the availability of optical fiber with improved polarization properties and more complete modelling of the fiber and sensor configurations, and research results on annealing, helical core fibers, and increased Verdet constant fibers leads to optimism toward further improvement, particularly in stability and sensitivity. The development of a sensor with a diameter of 1 cm and a minimum detectable current of the order of a few nA/Hz^{1/2} seems possible.

REFERENCES

1. A. M. Smith, Polarization and magneto-optic properties of single-mode optical fiber, Appl. Opt. 17, 52-56 (1978).
2. S. C. Rashleigh and R. Ulrich, Magneto-optic current sensing with birefringent fibers, Appl. Phys. Lett. 34, 768-770 (1979).
3. A. Papp and H. Harms, Magneto-optical current transformer. 1: Principles, Appl. Opt. 19, 3729-3734 (1980).
4. W. F. Hemsing, VISAR: 2 1/2 minutes for data reduction, Proc. SPIE 427, San Diego, CA (1983).
5. H. J. Arditty, Y. Bourbin, M. Mapuchon, and C. Puech, Current sensor using state-of-the-art fiber-optic interferometric techniques, Technical Digest, third International Conference on Integrated Optics and Optical Fiber Communications, San Francisco, CA (1981).
6. R. Ulrich, S. C. Rashleigh, and W. Eickhoff, Bending-induced birefringence in single-mode fibers, Opt. Lett., 5, 273-275 (1980).
7. G. W. Day, D. N. Payne, A. J. Barlow, and J. J. Ramakov Hansen, Design and performance of tuned fiber coil isolators, IEEE J. Lightwave Tech., LT-2, 56-60 (1984).
8. W. J. Tabor, A. W. Anderson, and L. G. VanUitert, Visible and infrared Faraday rotation and birefringence of single-crystal rare-earth orthoferrites, J. Appl. Phys., 41, 3018-3021 (1970).
9. R. Ulrich and A. Simon, Polarization optics of twisted single-mode fibers, Appl. Opt., 18, 2241-2251 (1979).
10. G. W. Day and S. M. Etzel, Annealing of bend-induced birefringence in fiber current sensors, Technical Digest, IOOC/ECOC 1985, Venice (to be published).

11. M. P. Varnham, R. D. Birch, and D. N. Payne, Helical core circularly birefringent fibers, Technical Digest, IOOC/ECOC 1985, Venice, Italy (to be published).
12. P. Sanders, D. Krohn, and M. Maklad, Faraday rotator single-mode fiber, Proc. SPIE 566, August 1985, San Diego, CA (1985).
13. K. Shiraishi, K. Nishino, and S. Kawakami, Temperature-insensitive fiber Faraday rotator, Appl. Opt. 24, 1896-1897 (1985).
14. K. Shiraishi, S. Sugaya, and S. Kawakami, Fiber Faraday rotator, Appl. Opt. 23, 1103-1106 (1984).
15. S. B. Poole, D. N. Payne, Fabrication of optical fibers containing low levels of rare-earth ions. Technical Digest, IOOC/ECOC 1985, Venice (to be published).

ACKNOWLEDGEMENTS

Research on optical fiber current sensors at NBS has been supported in part by the U.S. Department of Energy through Los Alamos National Laboratory, Sandia National Laboratory, and Bonneville Power Administration.

NONLINEAR ELLIPSE ROTATION IN A LOW-BIREFRINGENCE OPTICAL FIBER

B. Crosignani, S. Trillo
Fondazione "Ugo Bordonì", Istituto Superiore P.T., Viale Europa
160, Roma, Italy, and Dipartimento di Fisica, Università di Roma
"La Sapienza", P.le Aldo Moro 2, Roma, Italy

P. Di Porto
Fondazione "Ugo Bordonì", Istituto Superiore P.T., Viale Europa
160, Roma, Italy, and Dipartimento di Fisica, Università del
l'Aquila, L'Aquila, Italy

S. Wabnitz
Fondazione "Ugo Bordonì", Istituto Superiore P.T., Viale Europa
160, Roma, Italy

SUMMARY

The rotation of the polarization ellipse taking place in a low-birefringence single mode optical fiber and associated with the nonlinear optical Kerr effect is theoretically investigated. A detailed description of a proposed experiment for measuring the nonlinear refractive index n_2 through the ellipse rotation is also furnished.

1. INTRODUCTION

Optical fibers with silica cores are extensively used for the experimental demonstration of many nonlinear optical phenomena.¹ This is basically due to the relatively long propagation lengths along which the nonlinear interaction takes place in fibers. Correspondingly, the power levels required to produce observable nonlinear effects are much lower in fibers than in bulk media.

The optical Kerr effect, associated with a refractive index change linearly dependent on the field intensity, has been both theoretically and experimentally investigated in the case of high-birefringence fibers.² If the birefringence is high, the nonlinearity will not couple the intensities of the two orthogonal modes, but will only affect their relative phase-shift. The advent of extremely low-birefringence fibers for fiber optic devices and sensors requires ellipse rotation to be taken into account. In this paper, we will extend the well-known results obtained for the intensity-dependent rotation of the polarization ellipse in an isotropic bulk medium³ to the case of a low-birefringence fiber (see also Ref.4). We will also discuss the feasibility of an experiment apt to measure the ellipse rotation angle at a fixed propagation length as a function of the input power, which could be used as a method to determine the nonlinear refractive index n_2 .

2. KERR EFFECT AND NONLINEAR PROPAGATION IN A LOW-BIREFRINGENCE FIBER

The electric field $\underline{E}(\underline{r}, z, t)$ propagating in a single mode optical fiber can be expressed as

$$\underline{E}(\underline{r}, z, t) = E_1(\underline{r}) \exp(i\omega_0 t - i\beta_1(\omega_0)z) \hat{\phi}_1(z, t) \hat{x} + E_2(\underline{r}) \exp(i\omega_0 t - i\beta_2(\omega_0)z) \hat{\phi}_2(z, t) \hat{y}, \quad (1)$$

where $E_1(\underline{r}) \hat{\phi}_1$ and $E_2(\underline{r}) \hat{\phi}_2$ represent the two orthogonal linearly polarized states supported by the fiber and $\beta_1(\omega_0)$, $\beta_2(\omega_0)$ their relative propagation constants evaluated at the central angular frequency ω_0 of the carrier. Whenever chromatic dispersion and mode-coupling can be neglected, the complex amplitudes $\hat{\phi}_i(z, t)$ are given by

$$\hat{\phi}_i(z, t) = \hat{\phi}_i(z=0, t-z/v_i), \quad i = 1, 2, \quad (2)$$

$v_i = d\beta_i/d\omega|_{\omega_0}^{-1}$ being the group velocity of the i -th mode. This situation of free propagation is altered by the presence of a nonlinear contribution to the refractive index proportional to the field intensity (optical Kerr effect), so that

$$n = n_1 + n_2 |E|^2, \quad (3)$$

where n_1 is the linear refractive index of the core and n_2 is a coefficient dependent on the fiber material (typically $n_2 \approx 10^{-22} \text{ m}^2/\text{V}^2$ for silica). Over large lengths and for reasonable power levels (e.g., 1 Km and 100 mW respectively) Eq.(2) no longer applies, and $\hat{\phi}_1$ and $\hat{\phi}_2$ obey a set of coupled equations which express their mutual influence through the nonlinear interaction provided by Eq.(3). This set of equations takes on different forms according whether the fiber possesses a high or a low birefringence. In the latter case, one can assume $\beta_1 = \beta_2 = \beta$, $E_1 = E_2 = E$ and the corresponding set of equations reads⁽⁴⁾

$$\begin{aligned} (\partial/\partial z + (1/V)\partial/\partial t)\phi_1 &= -iR(|\phi_1|^2 + 2|\phi_2|^2/3)\phi_1 - iR\phi_1^*\phi_2^2/3, \\ (\partial/\partial z + (1/V)\partial/\partial t)\phi_2 &= -iR(|\phi_2|^2 + 2|\phi_1|^2/3)\phi_2 - iR\phi_2^*\phi_1^2/3, \end{aligned} \quad (4)$$

where V is the common group velocity of the two modes and

$$R = (\omega_0 n_2/c) \int_{-\infty}^{+\infty} E^4(x) dx dy, \quad (5)$$

with $\int_{-\infty}^{+\infty} E^2(x) dx dy = 1$.

In order to solve the set of Eqs.(4), it is convenient to introduce the circularly polarized states (clockwise and counter-clockwise, respectively) $E(x)\hat{e}^+$ and $E(x)\hat{e}^-$, where

$$\hat{e}^+ = (\hat{e}_x + i\hat{e}_y)/2^{1/2}, \quad \hat{e}^- = (\hat{e}_x - i\hat{e}_y)/2^{1/2} \quad (6)$$

and write accordingly the field as

$$E(x, z, t) = E(x) \exp[i\omega_0 t - i\beta(\omega_0)z] (\phi^+ \hat{e}^+ + \phi^- \hat{e}^-). \quad (7)$$

By comparing Eq.(7) with Eq.(1) (written for $n_1 = n_2 = n$ and $\beta_1 = \beta_2 = \beta$), it is immediate to obtain

$$\phi^+ = (\phi_1 - i\phi_2)/2^{1/2}, \quad \phi^- = (\phi_1 + i\phi_2)/2^{1/2}. \quad (8)$$

In terms of the amplitudes ϕ^+ and ϕ^- , the set of Eqs.(4) can be rewritten in the simpler form

$$\begin{aligned} (\partial/\partial z + (1/V)\partial/\partial t)\phi^+ &= -(2/3)iR(|\phi^+|^2 + 2|\phi^-|^2)\phi^+, \\ (\partial/\partial z + (1/V)\partial/\partial t)\phi^- &= -(2/3)iR(|\phi^-|^2 + 2|\phi^+|^2)\phi^-, \end{aligned} \quad (9)$$

which shows, in particular, that the two circularly polarized states can mutually influence their phases but not their amplitudes (the nonlinear interaction provided by the Kerr effect does not produce power exchange between them).

The set of Eqs.(9) can be solved in general.⁵ In a stationary situation, its solution takes on the simple form

$$\phi^+(z) = \phi_0^+ \exp(i\psi^+(z)), \quad \phi^-(z) = \phi_0^- \exp(i\psi^-(z)), \quad (10)$$

where

$$\psi^+(z) = (-2/3)R(|\phi_0^+|^2 + 2|\phi_0^-|^2)z, \quad \psi^-(z) = (-2/3)R(|\phi_0^-|^2 + 2|\phi_0^+|^2)z. \quad (11)$$

From Eqs.(10) and (11), it is immediate to generalize the well-known results concerning the intensity-induced rotation of the polarization ellipse in a bulk medium³ to the case of a low-birefringence fiber: the ellipse rotates, without changing its area and shape, by an angle $\psi(z)$ given by

$$\psi(z) = \frac{1}{2}(\psi^+ - \psi^-) = (R/3)(|\phi_0^+|^2 - |\phi_0^-|^2)z. \quad (12)$$

3. A PROPOSED EXPERIMENTAL CONFIGURATION

Equation (12) can be rewritten by expressing $\psi(z)$ as a function of the relevant physical quantities which are actually measurable in an experiment. More precisely, in MKSA units we have

$$\psi(\text{degrees/m}) = 2.88 \times 10^4 \pi (1/\lambda) (n_2/n_1) (1/A_{\text{eff}}) P f(e), \quad (13)$$

where P is the total power injected in the fiber, A_{eff} is the effective area of the fundamental mode which is reasonably close to the fiber-core area⁶ and $f(e) = \sin(2\pi e^{-1})$ shows the dependence of ψ on the eccentricity e of the input polarization (defined as the ratio a/b , where $2a$ and $2b$ are the lengths of the minor and major axes of the ellipse, respectively). By specifying Eq.(13) to a typical singlemode silica-core fiber, it turns out that the effect becomes observable, for instance, at a power level of some hundreds of mW for a propagation length of about 100 m.

An experimental demonstration of the effect will be carried out by using a low-birefringence fiber about 20 m long. The experimental setup, similar to the one already used by Owyung et al.,⁷ is shown in Fig.1. The linearly polarized light emerging from a cw transverse single mode Nd-YAG laser is passed through a variable retarder C1 to obtain elliptically polarized light and is coupled to the fiber by means of a microscope objective. The optical power coupled to the fiber can be varied by means of a stack of neutral-density filters and a variable attenuator (A), and the output power is measured via a beamsplitter (BS) into a calibrated

power meter.

The output polarization is analyzed by using the compensator C2 followed by the Wollaston prism WP which splits the two orthogonal linear polarizations. Two avalanche photodiodes, D1 and D2, are used to detect the beams emerging from WP. Synchronous detection is employed in order to increase the signal-to-noise ratio. The system is calibrated at low power level by adjusting C2 and WP in such a way that, in the absence of induced nonlinearity, the signal in D1 is maximized and the "orthogonal" one in D2 is made to vanish. Any rotation of the polarization ellipse will be detected as an increase of the signal level in D2. Particular care must be taken in posing the fiber, in order to avoid any coupling between the two polarization states due to fiber imperfections, such as induced stresses and geometrical effects (twists and bends).

Finally, we note that the ellipse rotation, besides furnishing the possibility of a precise determination of the nonlinear refractive index coefficient n_2 by employing a low-birefringence fiber, is also responsible for polarization fluctuations (associated with amplitude fluctuations), which can limit the sensitivity of polarimetric fiber sensors.

4. REFERENCES

1. R.H. Stolen, "Nonlinear properties of optical fibers", in "Optical Fiber Telecommunications", edited by S.E. Miller and A.G. Chynoweth, Academic Press, New York, 1979 (125-150).
2. see, for example, L. Crosignani, P. Di Porto, S. Piazzolla, and P. Spano, "Direct measurement of the nonlinear phase shift between the orthogonally polarized states of a single-mode fiber", Opt. Lett., 10, 1985, 89-91; J.M. Dziedzic, R.H. Stolen, and A. Ashkin, "Optical Kerr effect in long fibers", Appl. Opt., 20, 1981, 1403-1406, and references therein.
3. P.D. Maker, R.W. Terhune, and C.M. Savage, "Intensity-dependent changes in the refractive index of liquids", Phys. Rev. Lett., 12, 1964, 507-509.
4. B. Crosignani and P. Di Porto, "Intensity-induced rotation of the polarization ellipse in low-birefringence single-mode optical fibers", Optica Acta, 1985 (to be published)
5. B. Crosignani and P. Di Porto, "Self-phase modulation and modal noise in optical fibers", J. Opt. Soc. Am., 72, 1982, 1553-1554.
6. R.H. Stolen and Chinlon Lin, "Self-phase modulation in silica optical fibers", Phys. Rev. A, 17, 1978, 1448-1453.
7. A. Ouyang, R.W. Hellwarth and N. George, "Intensity-induced changes in optical polarizations in glasses", Phys. Rev. B, 5, 1972, 628-633

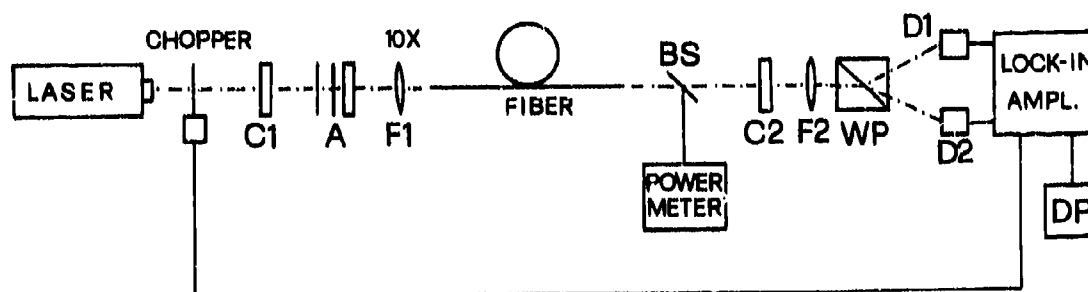


Figure 1 : Setup of the proposed experimental configuration. C1 : variable retarder - A : stack of neutral density filters and variable attenuator - F1 : microscope objective - BS : calibrated beamsplitter - C2 : compensator - F2 : focussing lens - WP : Wollaston prism - D1,D2 : Germanium avalanche photodiodes - DP : desktop computer

PROGRESS IN OPTICAL FIBER GYROSCOPES USING INTEGRATED OPTICS

H.C. LEFEVRE, J.P. BETTINI, S. VATOUX and M. PAPUCHON

Laboratoire Central de Recherches THOMSON

Domaine de Corbeville

91401 ORSAY

France

SUMMARY

We describe a quarter of a liter brass-board of a fibergyro using a multifunction integrated optic circuit (splitter, polarizer and phase modulator), a superluminescent diode and 250 meters of polarization holding fiber. The photon noise limited random walk performance is 0.004 deg/Vh. We also present a simple model to evaluate birefringence induced non-reciprocities, and an original method of signal processing, the "digital phase ramp", to solve the problem of scale factor linearity and accuracy.

I - DESCRIPTION OF THE BRASS-BOARD

Integrated optics was advocated very early as the privileged technology to make optical fiber gyroscopes (1), because the various optical functions needed in the system could be implemented on a single mass-duplicated circuit which would be connected to a fiber coil, a pigtailed source and a detector. However, the first brass-board which used this approach (2), had bad performances compared to classical optic (3) or all-fiber gyros (4). Since this time we have analysed the limitations of the initial scheme, and defined drastic improvements which have yielded 4×10^{-3} deg/Vh random walk performances. Our dedication to integrated optics was motivated at the beginning by its potential low cost, but also by specific technical advantages, with in particular, the possibility to fabricate phase modulators with low driving voltage and large bandwidth (DC to hundreds of MHz). This allowed us to demonstrate an original method of signal processing, the so-called "digital phase ramp" (5) to get a closed-loop operation of the gyro without any additional components, with respect to the usual open-loop reciprocal configuration.

In this paper, we describe the improvements brought to the device to get a good sensitivity and bias stability and we explain the principle of our method of signal processing.

We made a brass-board of 100 mm diameter and 35 mm height (figure 1-a) composed of a superluminescent diode (SLD), a coil of polarization holding fiber (250 m long, 85 mm diameter), a multifunction integrated optic circuit (Y junction for splitting, metallic polarizer and phase modulator), a fiber coupler and a PIN detector (figure 1-b). All the optical components (source, fiber, IO circuit and coupler) were fabricated in our Corporate Research Center.

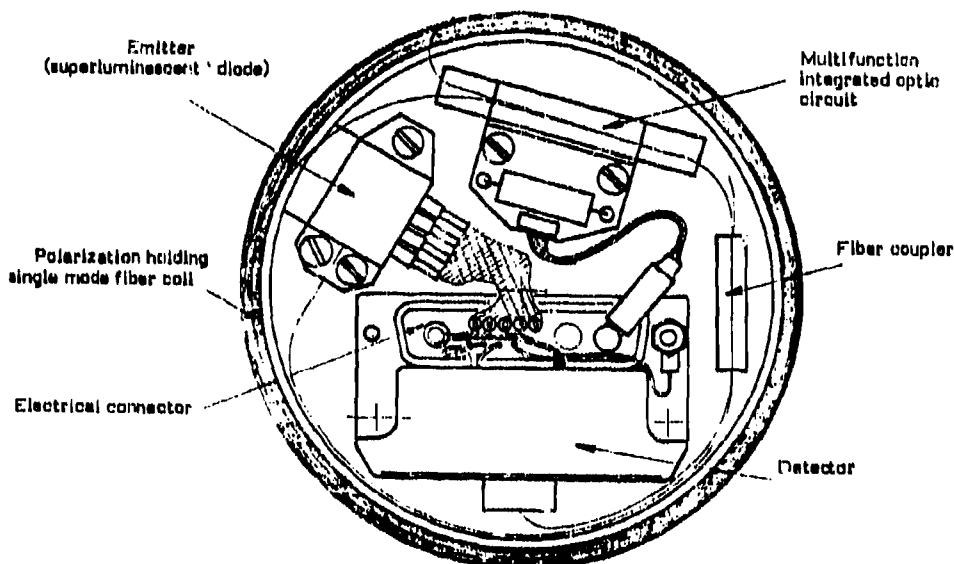


Figure 1-a

Actual configuration of a quarter of a liter fiber gyro brass-board

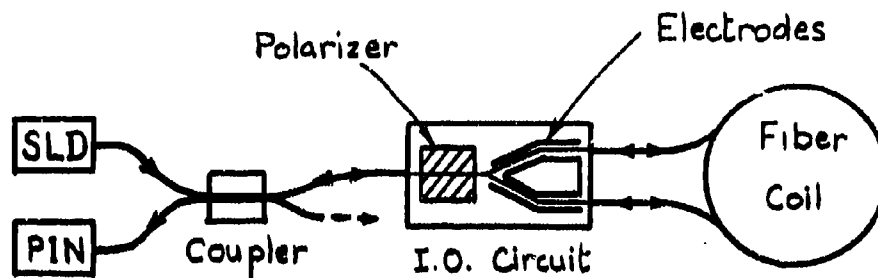


Figure 1-b

Operating schematic of the fiberygyro

The spatial filtering is realized with the coupler lead which ensures a quasi-perfect singlemode rejection. The sensitivity is limited by the photon noise of the $4 \mu\text{W}$ reaching the detector (there is a total loss of 19 dB in the interferometer : 6 dB for the reciprocal configuration, 5 dB for the IO circuit, 0.5 dB for the coupler, 2 dB for the fiber coil). The short term noise density is $0.06 (\text{deg/h})^2/\text{Hz}$ which corresponds to $7 \times 10^{-7} \text{ rad/VHz}$. The figure 2 gives the output signal when the axis of the coil is parallel (sensitive) or orthogonal (insensitive) to earth rotation axis with a time constant of 1 second. The bias offset of about 1 deg/h ($3 \times 10^{-6} \text{ rad}$) is due to the Michelson interferometer created by the residual backreflections at the $\text{LiNbO}_3\text{-SiO}_2$ interface. Compared to the 4% Fresnel reflection, this proves that a 100 degree edge angle provides a 40 dB improvement with respect to perpendicular edges (figure 3) (6). This could be further decreased with a larger angle.

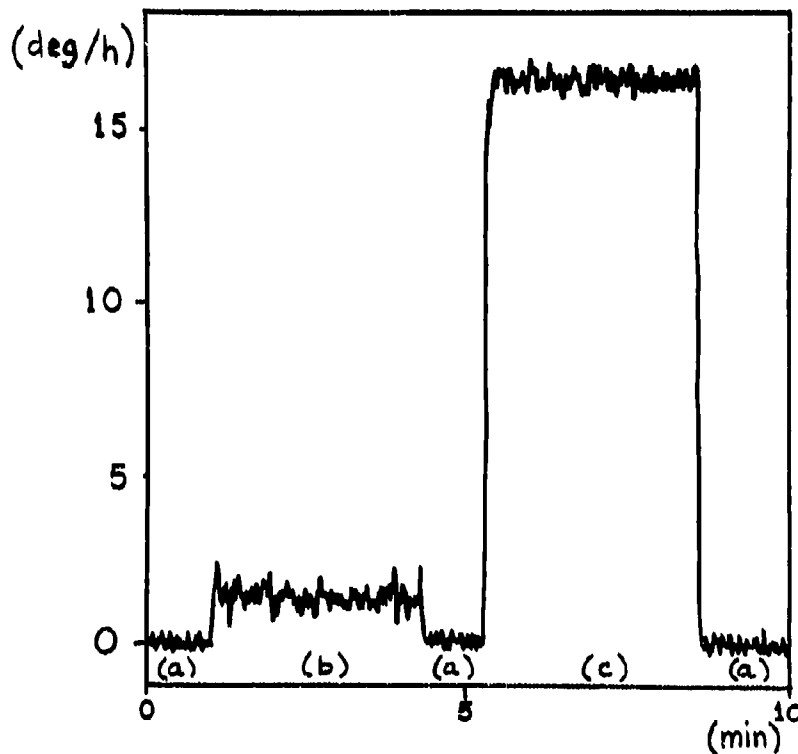


Figure 2

Fiberygyro output rate signal with 1 second time constant :

- a - electrical zero
- b - optical bias offset ($1 \text{ deg/h} \rightarrow 3 \mu\text{rad}$)
- c - earth rotation rate (15 deg/h)

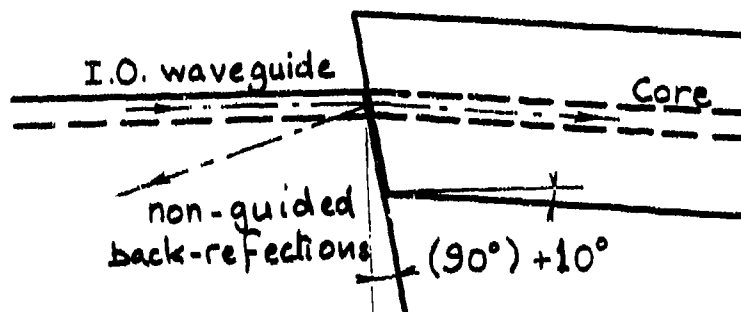
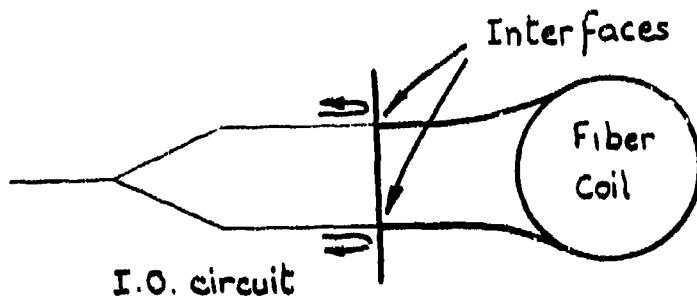


Figure 3

Elimination of back-reflections with non-orthogonal edges

We tested the long term bias drift with a sampling and averaging program. The figure 4 gives a typical example of the drift of the signal mean value over 1 hour, during 9 hours. The standard deviation is 0.12 deg/h, when the random walk performance corresponding to the short term noise density is 0.004 deg/ $\sqrt{\text{h}}$. By eliminating the residual bias offset the standard deviation should reach the theoretical value of 0.004 deg/h given by the random walk. The only source of bias is the residual Michelson interferometer, within the precision of our measurement. There is no non-reciprocity induced by Kerr effect, Faraday effect or lack of polarization filtering. We are now going to analyse this last problem.

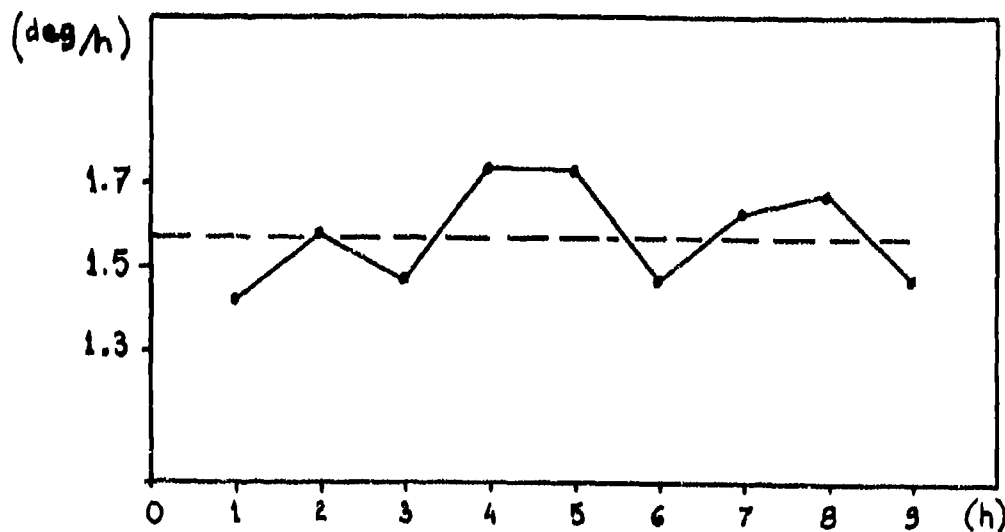


Figure 4

Long term drift of the gyro bias

II - PROBLEM OF BIREFRINGENCE INDUCED NON-RECIPROCITIES

1 - Introduction

If a single-mode fiber can be considered as a quasi-perfect spatial filter, actual polarizers (bulk, integrated optics or all-fiber) have limited performances to reduce the birefringence induced non-reciprocities to values compatible with the bias stability and repeatability needed for inertial navigation (less than 10^{-2} deg/h which corresponds typically to a phase shift of 10^{-7} to 10^{-8} rad). Kintner (7) showed that the bias error depends on the amplitude rejection ratio of the polarizer with ordinary fibers, which means that a polarizer rejection better than 140 to 160 dB should be required. Such numbers are clearly not reasonable and it has been thought that polarization-holding fibers should improve the performances of the system. But a typical 20 dB polarization conservation brings only a factor 10 improvement on the ratio of the amplitudes of both cross-polarised waves, which does not reduce considerably the requirement for the polarizer. However, this amplitude dependence is due to coherent parasitic interferences between the reciprocal primary waves and cross-polarised coupled waves and one should expect an important improvement with the use of a broadband source, e.g. super-luminescent diode (SLD), because of depolarization effects due to different propagation velocities of cross-polarised modes in polarisation-holding fibers which are also highly birefringent. Fredericks et al. (8) and Burns et al. (9) proposed two analysis of the problem which show that small bias errors can be obtained with reasonable demand on polarizer rejection, alignment tolerance and depolarization in the fiber coil. However, they were only concerned by the parameters which could reduce the dependence of the amplitude rejection ratio of the polarizer.

In this paper, after summarizing their results, we will present a simple model using discrete polarization coupling points randomly distributed along the fiber. This provides a good understanding of the problem and allows one to evaluate the required alignment tolerance and rejection ratio of the polarizer as a function of the fiber and source characteristics (beatlength, polarization conservation, coherence length).

The amplitude rejection dependence found in Kintner's result (7) has been explained simply by Fredericks et al. (8). This is due to coherent interference between the primary waves, which entered the interferometer in this axis of the polarizer and which are still in the same state of polarization at the output, and the part of the input waves which were crossed-polarized and attenuated at the input because of misalignment and which were coupled in the coil to be in the same polarization state as the primary waves at the output (figure 5). These parasitic waves have followed non-reciprocal paths, and, are coming back in the axis of the polarizer. They are not attenuated at the output and can interfere with the primary waves. The bias error signal carried by these parasitic waves is then magnified by coherent detection, considering the primary waves as the equivalent of a local oscillator. The error signal, which depends on the amplitude of the parasitic waves, is related to the input wave polarization misalignment and the amplitude extinction ratio of the polarizer.

Fredericks et al. (8) pointed out that the bias error depends on the phase difference between both eigen polarizer modes at the input. They suggested to average out this error by applying a variable stress on the input fiber lead after the polarizer in the axis which correspond to its eigen modes. We noticed that it is possible to do so before the polarizer in a fiber polarizer is used. In both cases, this does not modify the polarization coupling in the fiber coil and the bias error signal carried by the parasitic waves, but, varying their phase difference with the primary waves, this modulates the actual signal in the coherent detection process. This is a way of evaluating this effect but also to reduce it by shifting its carrier frequency outside of the detection bandwidth. They also explained that the birefringence of the input lead between the polarizer and the coil splitter reduces the degree of correlation between these waves and drastically limits the contrast of the interferences involved in the coherently detected bias error. They related the upper limit of the residual error to the degree of polarization of the waves returning to the polarizer. We will present here a simple model to evaluate more precisely this limit as a function of the characteristics of the various components of the system.

On the other hand, Burns et al. did not consider any depolarizing effect due to the birefringence of the input lead (9). Then, they found that the main source of bias error is the polarization coupling in the first depolarization lengths of the fiber coil.

2 - Model to evaluate the birefringence induced bias error of the fiber coil

a) Simple model with two coupling points

Let us first consider a loop interferometer with a perfect birefringent polarization holding fiber and one polarization coupling point M at a distance l from the splitter (figure 6). If light is inserted in mode 1 in the interferometer, four waves will come back at the output :

- 2 reciprocal primary waves which are still in mode 1. They have propagated along the same optical path in opposite direction and they are perfectly in phase
- 2 waves coupled in mode 2. They have propagated along different paths : $n_1 l + n_2 (L-l)$ and $n_1 (L-l) + n_2 l$ where L is the length of the coil and n_1 and n_2 the equivalent indices of both polarization modes.

If a broadband source is used and the path difference $(n_1 - n_2) \cdot (L - 2l)$ is longer than the coherence length L_C , these two coupled waves are not coherent and do not give any spurious interferometric signal. Non-reciprocal signals can be produced only by coupling in the middle of the coil over the depolarization length $L_D = L_C / (n_1 - n_2)$.

Now, if we consider two coupling points M_1 and M_2 (figure 7), six waves will come back at the output :

- 2 reciprocal primary waves which are still in mode 1
- 4 waves coupled in mode 2 at M_1 or M_2 and which have propagated along different paths.

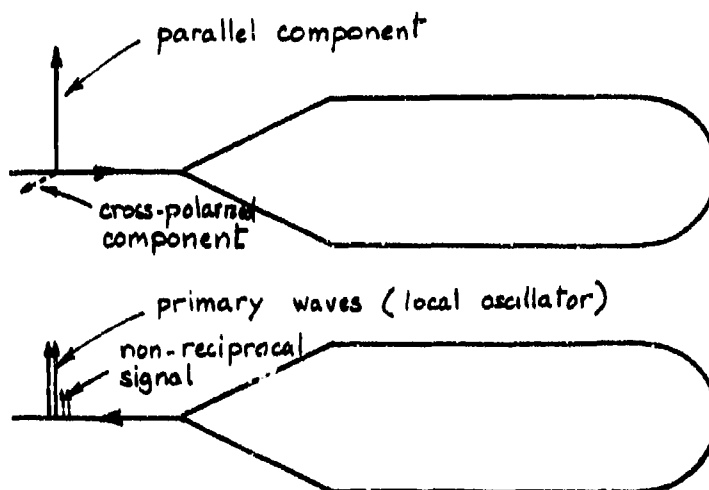


Figure 5

Problem of coherent detection of birefringence induced non-reciprocities



Figure 6

One polarization coupling point case

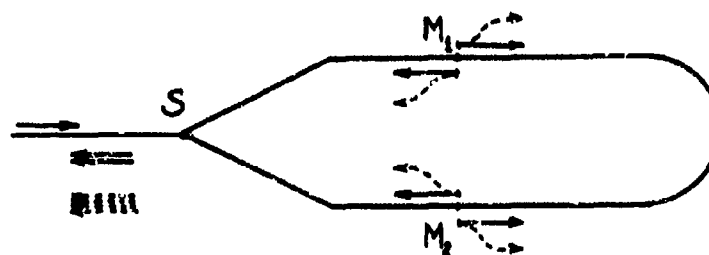


Figure 7

Two polarization coupling points case

These coupled waves are not coherent together excepted if the two coupling points are symmetrical with respect to the loop within the length of depolarization L_D . In this case, both waves coupled at the beginning of the loop in M_1 and M_2 interfere together as both waves coupled at the end. For each set, the waves propagate along the same path between both coupling points M_1 and M_2 but they propagate along cross-polarized paths between the splitter S and these coupling points. They experience a non-reciprocal phase difference $\Delta\Phi$ depending on the difference between the total birefringences of both branches SM_1 and SM_2 . This creates a parasitic bias offset signal $V\alpha_1\alpha_2\sin\Delta\Phi$ where α_1 and α_2 are the energy coupling coefficients at M_1 and M_2 . We have to notice that the waves which are coupled twice (at the beginning and at the end) are reciprocal. Both propagate in mode 1 between the splitter and the coupling points, and in mode 2 between both coupling points.

b) Experimental evidence

This analysis can be verified experimentally using an integrated optic Y junction fabricated on a LiNbO_3 substrate as a splitter, a linear polarization holding fiber coil and a SLD as a source. Light is fed in the Y Junction through a bulk-optic polarizer and a polarization holding fiber to ensure perfect spatial filtering and a good degree of linear polarization in the Y junction (less than 10^{-4} energy ratio between the TM and TE modes). The birefringence axis of the fiber coil ends are misaligned by 0.1 radian (≈ 6 degrees) with respect to LiNbO_3 substrate axis which provides two coupling points with $\alpha_1 = \alpha_2 = 10^{-2}$. Light is sent back to a detector with a bulk beamsplitter placed between the polarizer and the input fiber lead (figure 8).

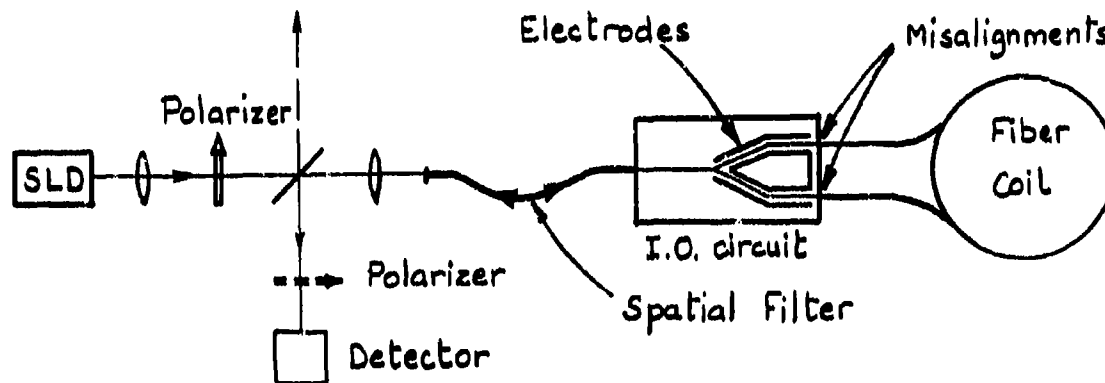


Figure 8

Experimental set-up to analyse the non-reciprocity induced by fiber-IO waveguide birefringence axis misalignment

Furthermore the interferometric signal is biased about $\pi/2$ with the conventional phase modulation technique (10, 11), applying an AC voltage on the electrodes fabricated on the substrate. We can neglect, for the moment, polarization coupling in the LiNbO_3 waveguides and in the fiber. The two coupling points should give a non reciprocal bias of $V\alpha_1\alpha_2\sin\Delta\Phi$, where $\Delta\Phi$ is the difference of birefringence induced phase between both branches of the LiNbO_3 Y junction. This parasitic bias could be as high as 10^{-2} rad when $\Delta\Phi = \pi/2$ because $\alpha_1 = \alpha_2 = 10^{-2}$. The observed bias was actually less than 10^{-4} rad, without any analyser in front of the detector which indicates that both branches are very similar. This can be expected because these branches have the same length and are only 200 μm apart on the same crystal substrate. Now when a DC voltage is added to the AC modulation, the bias follows a sine response with a maximum of about 10^{-2} rad. This is explained by the fact that the phase shift experienced by the TE mode is about half the one experienced by the TM mode. The DC voltage produces a scanning of the difference of total birefringence between both branches and the parasitic bias varies between $+V\alpha_1\alpha_2$ and $-V\alpha_1\alpha_2$. With an analyser placed in front of the detector, one can check that this parasitic bias is cross-polarized with the primary reciprocal waves. This confirms the previous analysis but this also gives a sensitive way to carefully align the fiber axis with respect to LiNbO_3 for reducing polarization coupling at the interface.

c) Model for an actual fiber with random coupling points

We assume for the moment that the splitter is perfect to evaluate the proper effect of a fiber coil with randomly distributed polarization coupling points. Instead of continuous coupling, we can consider that there is a discrete coupling point M_1 for each depolarization length L_D along the fiber (figure 9). The coupling coefficient α_1 is equal to the total power extinction ratio α of the coil divided by the number N of depolarization lengths L_D along the length L of the coil : $N = L/L_D$ and $\alpha_1 = \alpha/N$. This can be also expressed in term of h parameter (12) $\alpha_1 = h \cdot L_D$. The system can be decomposed in N pairs of waves coupled at points M_1 and M_1' which are symmetrical within the coil in terms of birefringence. When a biasing modulation is used, each pair gives a signal $\sqrt{\alpha_1 \cdot \alpha_1} \sin \Delta\Phi_1$ where $\Delta\Phi_1$ is the phase shift due to the difference of birefringence between both branches SM_1 and SM_1' as we saw earlier. We can assume that the random phaseshifts $\Delta\Phi_1$ of the N pairs are equally distributed over 2π radian. Then the rms value of the residual polarization induced non-reciprocal phase shift signal is equal to :

$$\Delta\Phi_P = \sqrt{N} \frac{\Delta\Phi_1}{\sqrt{2}}, \quad \Delta\Phi_P = \frac{\alpha}{\sqrt{2N}}$$

$\Delta\Phi_P$ is not equal to the total extinction ratio α of the fiber coil. It is reduced proportionally to the square root of the number of depolarization lengths along the fiber coil.

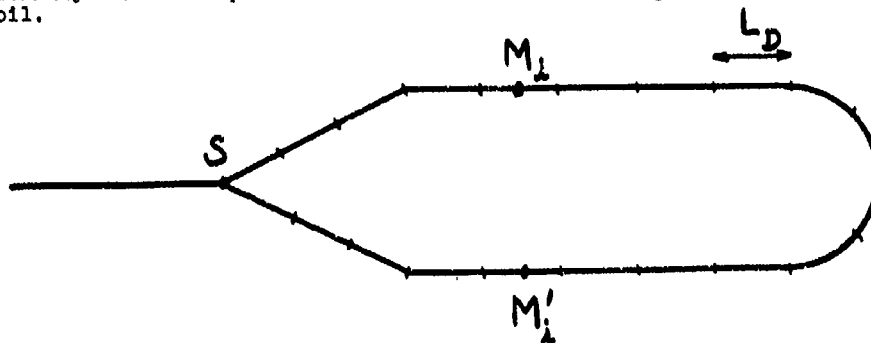


Figure 9

Simple model of discrete coupling points
for each depolarization length L_D

We can give typical values : a 2 mm beatlength and a 50 μ m coherence length lead to $L_D = 10$ cm ; over 250 meters, $N = 2.5 \times 10^3$ and an extinction ratio of 20 dB/km leads to $\alpha = 2.5 \times 10^{-3}$. In this particular case the rms value $\Delta\Phi_P$ is equal to 3.5×10^{-5} rad and not to 2.5×10^{-3} rad as it could be thought with $\alpha = 2.5 \times 10^{-3}$. We have to notice that the mean value is zero, and that $\Delta\Phi_P$ produces a bias offset if the fiber is stable, but in a real environment with thermal and acoustic perturbations, this produces noise which can be spread over a wide spectrum and further reduced in the detection bandwidth of the system.

If there are splices in the fiber coil, they must be non-symmetrical. The coupled wave will interfere only with the wave coupled in the fiber along the depolarization length which is symmetrical to the splice and the induced non-reciprocity will be limited to $\pm \sqrt{\alpha_1 \cdot \alpha_S}$ instead of $\pm \alpha_S$, the polarization coupling in the splice. When an integrated optics Y junction is used this cannot be avoided, which requires a careful alignment to take advantage of the low intrinsic non-reciprocity induced by the fiber. For $\Delta\Phi_P = 3.5 \times 10^{-5}$ rad, the coupling coefficient should be lower than 5×10^{-5} which means an alignment accuracy of the birefringent axis of the fiber and the waveguide of 0.4 degree.

d) Effect of a polarizer

For simplicity we are going to consider a perfect splitter and a polarizer with its transmission axis aligned with birefringence axis of the fiber coil. Most of the light, which entered the interferometer through the polarizer, comes back in phase and in the same polarization state after propagating along identical paths in opposite direction. The part coupled in the crossed state carries a non-reciprocal signal equivalent to a bias error of $\Delta\Phi_P = \alpha/\sqrt{2N}$. This spurious signal is attenuated through the polarizer at the output, and is added in intensity to the primary signal. The residual bias error becomes then $\epsilon^2 \Delta\Phi_P = \epsilon^2 \alpha/\sqrt{2N}$ where ϵ^2 is the intensity extinction ratio of the polarizer.

Now the polarization of the light entering the polarizer at the input is never perfectly aligned with the transmission axis. Part of it is cross-polarized and attenuated at the input. Similarly to the previous case, a small fraction will be coupled back in the polarization state corresponding to the transmission axis of the polarizer. The spurious wave carries a bias error signal equal to $k^2 \epsilon^2 \alpha/\sqrt{2N}$ where k^2 is the

ratio in intensity of the input power in the crossed-polarization and the one in the transmitted polarization entering the polarizer. This signal is smaller than the main bias error by a factor k^2 (typically 10^{-2} to 10^{-3}), but, as we saw earlier, problems arise if it is coherent with the primary waves which act as a local oscillator for coherent detection of this spurious effect.

This is the kind of effect pointed out by Burns et al. (9) when they found that the coupling in the first depolarization length at each end of the coil is critical. The use of a birefringent lead between the polarizer and the splitter avoids to first order coherent interference between this bias error signal $k^2 \epsilon^2 \alpha / \sqrt{2} N$ and the main part of the primary wave which has travelled always in the same slow or fast mode (we actually use the slow TE mode in a z-cut LiNbO₃ circuit and the corresponding mode in the fiber). However, light which is coupled an even number of times along the fiber has a reciprocal path, but its transit time through the loop is such that it can serve as a local oscillator to increase coherently the parasitic signal due to the term $k^2 \epsilon^2 \alpha / \sqrt{2} N$.

To clarify this statement we are going to consider how an input wave train propagates through the system using the previous model with N discrete coupling points (figure 9) (the use of autocorrelation functions is more elegant mathematically but does not help as much to understand the problem). At the input there is a wave train of intensity I_S transmitted by the polarizer which will propagate in the slow mode and another one I_F which was attenuated and which will propagate in the fast mode. At the output most of the power is still in the same wave train I_{SS} which corresponds to light which remained continuously in the slow mode, but there is also a series of wave trains I_{SSn} which correspond to light which experienced two couplings (slow \rightarrow fast, fast \rightarrow slow). The train I_{SSn} propagates along nL_p in the fast mode and $(N-n)L_p$ in the slow mode. I_{SSn} comes back at a time $n\tau$ earlier than I_{SS} (τ is the coherence time).

There is $(N-n)$ pairs of coupling points which can contribute to I_{SSn} , also it is equal to $(N-n) \cdot \alpha^2 / N^2 \cdot I_S$ (the contribution of the different pairs are not coherent, also they add in intensity). Light coupled just once comes back in the crossed state in a series of wave trains $I_{SFn} = \frac{\alpha}{N} I_S$ spaced also by the delay τ . Similarly the wave train I_F produces:

$$I_{FF} \approx I_F = \epsilon^2 k^2 I_S, \quad I_{FFn} = (N-n) \frac{\alpha^2}{N^2} I_F \quad \text{and} \quad I_{FSn} = \frac{\alpha}{N} I_F$$

This analysis is summarized in figure 10.

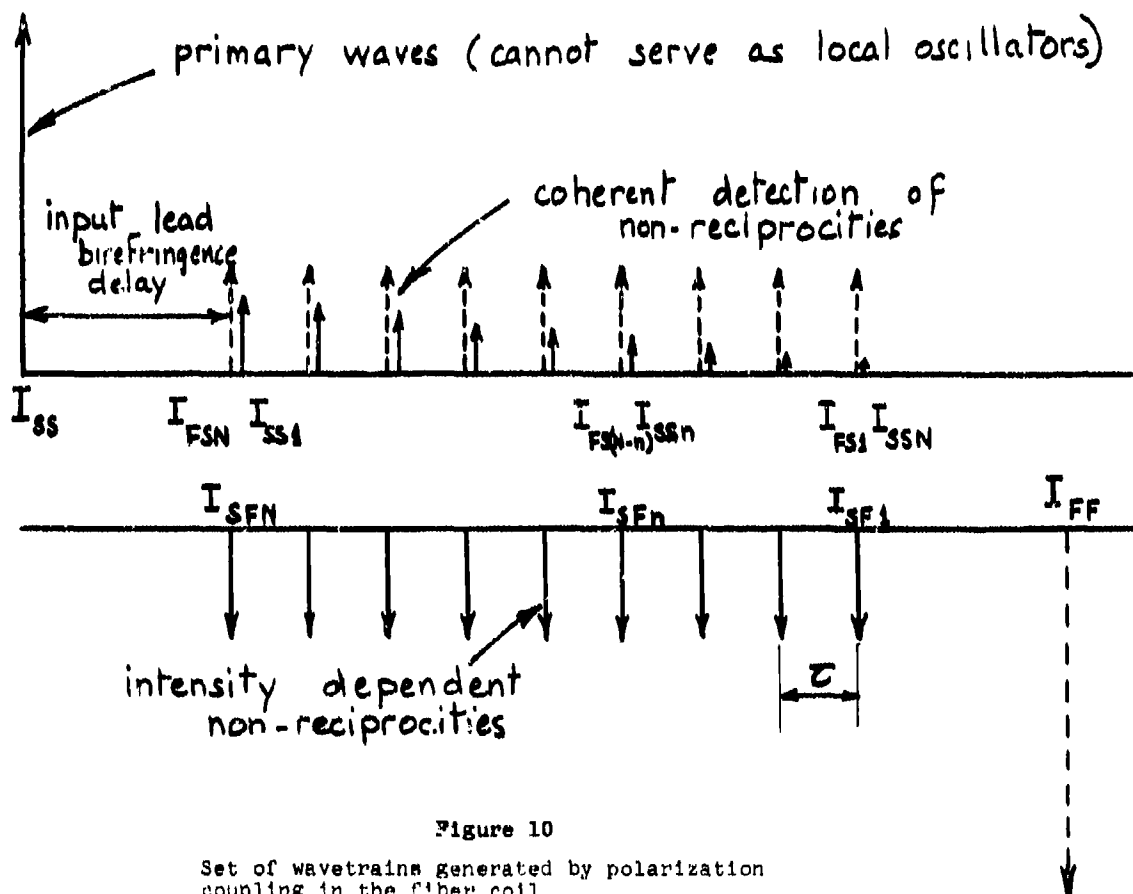


Figure 10

Set of wavetrains generated by polarization coupling in the fiber coil

There are two sources of birefringence non-reciprocities :

- an intensity rejection effect $\Delta\Phi_{\text{int}}$ as we saw earlier, created by the wave trains I_{SPN} and attenuated by the polarizer at the output. It is equal to $\epsilon^2 \cdot \alpha / \sqrt{2N}$
- an amplitude rejection effect $\Delta\Phi_{\text{amp}}$, due to coherent detection of the non-reciprocal wave train I_{SPN} with the local oscillators $I_{\text{SS}}(N-n)$. It can be shown that it is limited by $k \cdot \sqrt{\alpha} \cdot \epsilon \cdot \alpha / \sqrt{2N}$

Their relative influence will depend on the respective values of $(k \cdot \sqrt{\alpha})$ and ϵ . The input misalignment k^2 has to be smaller than ϵ^2 / α to avoid amplitude rejection effect.

With the numerical example used earlier ($\alpha = 2.5 \times 10^{-3}$ and $N = 2.5 \times 10^3$), an intensity rejection of 35 dB ($\epsilon^2 = 3 \times 10^{-4}$) leads to $\Delta\Phi_{\text{int}} = 10^{-8}$ rad which corresponds to 0.004 deg/h with our brass-board and $\Delta\Phi_{\text{amp}} < \Delta\Phi_{\text{int}}$ if $k^2 < \epsilon^2 / \alpha \approx 0.1$, which is obviously easy to get.

But, with a low polarization holding quality ($\alpha' = 0.1$ for example), an intensity rejection of 51.5 dB ($\epsilon^2 = 7 \times 10^{-6}$) is required to limit $\Delta\Phi_{\text{int}}$ to 10^{-8} rad, and $\Delta\Phi_{\text{amp}} < \Delta\Phi_{\text{int}}$ if $k^2 < 7 \times 10^{-5}$ which is now very difficult to get because of the limited polarization preservation of the first fiber coupler which is equivalent to an input misalignment.

In conclusion, depolarization and averaging process in high birefringence polarization holding fiber used with low temporal coherence source limits polarization non-reciprocities to very low level even without a high rejection of the polarizer, but a bad quality of polarization preservation can degrade this result very fast. The integrated optic polarizer (metallic layer with a dielectric buffer) (13) used in our experiment has the required rejection of 35 dB to be used with a 20 dB/km polarization preservation of the fiber coil. Finally we have to notice that the same kind of analysis with wavetrains can be used to explain the effect polarization coupling in the splitter and misalignment between the polarizer and the loop interferometer, but when a multifunction IO circuit is used these problems are avoided because all the components are automatically aligned with the substrate axis and the polarization coupling in a Y junction is extremely small (less than 50 dB). This is, with the wideband phase modulator, the second important technical advantage of integrated optics.

III - PRINCIPLE OF THE "DIGITAL PHASE RAMP"

The most popular method for biasing a fiber gyro is to apply a reciprocal phase modulation at one end of the fiber coil (10, 11). If the so-called proper frequency is used (4) ($f_p = 1/2T$ where T is the group delay through the coil), this provides a very stable biasing point which is perfectly centered about zero, even with an imperfect modulator. But when the system is rotating, the analog sine response is not linear over a wide range, and depends on many parameters as the optical power and the detector gain.

This calls for a closed-loop operation of the system. The best method is to apply a frequency shift (3) at one end of the loop to compensate the Sagnac effect which can be interpreted as a double Doppler effect on the beam splitter (14, 15). But this shift must vary between -1 MHz to 1 MHz for a dynamical range of 1000 deg/s. It has been proposed to get this shift with two acousto-optic Bragg cells (3), which increases the complexity of the system but above all introduces a basic non-reciprocity due to the high operating frequency of the cells. Its cancellation requires a precise positioning which will change with temperature, and then produces a bias drift. A stability of 1 deg/h needs relative mechanical stability of both cells on the order of $1 \mu\text{m}$ for a 100 MHz operating frequency. On the other hand, it is well-known in radar signal processing that frequency shifting can be simulated with a phase ramp. This requires wideband phase modulators : the main technical advantage of integrated optics. But this so-called serrodyne modulation demands an infinitely fast flyback and a reset perfectly equal to 2π radian, to ensure pure single sideband shifting. Our digital approach avoids these drawbacks because we take advantage of the fact that the system is working over a given length : the length of the fiber coil. Instead of a ramp, phase steps are generated at one end of the coil with a duration equal to the transit time. This creates a phase difference equal to the step value between both counterpropagating waves which have seen the modulation respectively at the beginning or at the end of the coil (figure 11). A closed loop is used to compensate exactly the Sagnac phase shift. The step fronts and resets of the phase of both waves are simultaneous and can be gated out from the detector signal which eliminates the requirement for infinitely fast flyback. Now just after the reset $\Delta\Phi_R$, the phase difference becomes ($\Delta\Phi_S - \Delta\Phi_R$) where $\Delta\Phi_S$ is the value of the steps. This does not produce any effect if $\Delta\Phi_R$ is equal to 2π , the periodicity of the fringes. This can be conveniently used as an error signal at the frequency of the reset to control that its value is precisely equal to 2π . With these two servoloops, the measurement of the phase step does not rely on the phase voltage response of the modulator but on the counting of the number of step durations between two resets. For a reset happening after n clock times, the measurement of the phase step is $2\pi/n$. The analog part of the processing is servo-controlled to keep both error signals equal to zero and the counting provides a digital measurement yielding linearity and stability of the scale factor over a large dynamical range.

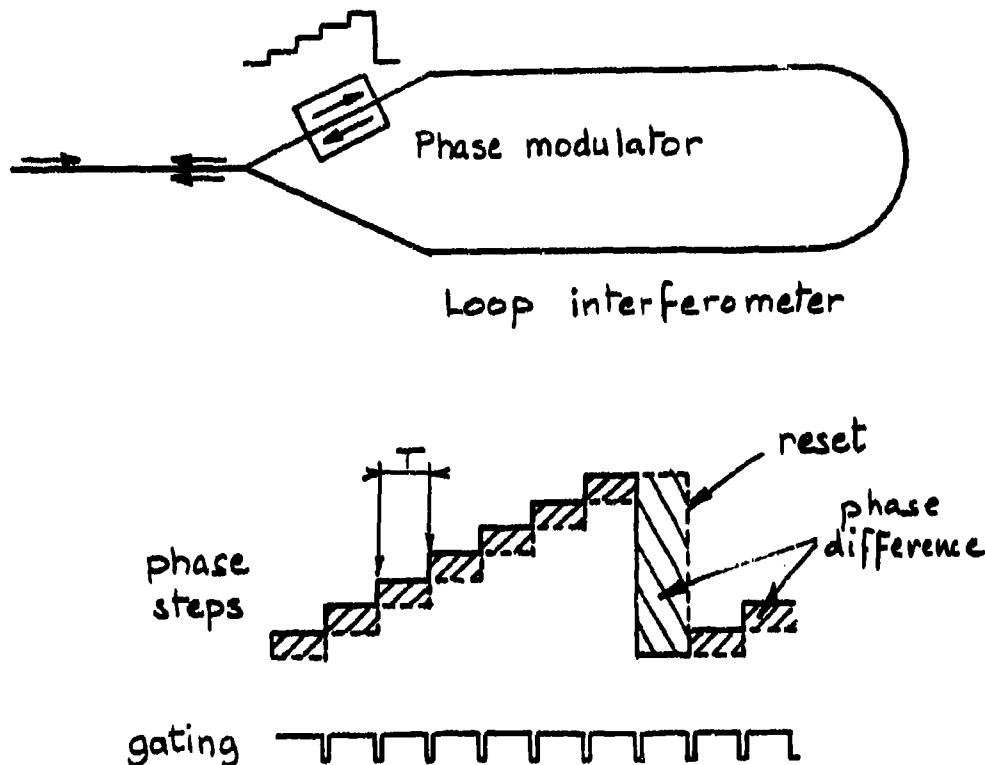


Figure 11

Effect of phase steps on the fibergyro

This method has another interesting feature compared to frequency shifting or analog phase ramp: the measurement of the phase does not depend directly on the transit time through the fiber coil. The step duration has to be approximately equal to this transit time to minimize the width of the spikes generated by the finite slew rate of the steps, but small temperature dependent changes of the transit time does not modify the measurement of the phase step equal to the opposite of the Sagnac phase shift. Then, the accuracy of the rotation rate will depend on stability of the geometrical length of the fiber coil ($\approx 10^{-6}/^{\circ}\text{C}$) and not on the stability of the index of refraction ($\approx 10^{-5}/^{\circ}\text{C}$). It will also depend on the stability of the wavelength of the source which must be temperature controlled. Furthermore it need not have two separate modulators for the biasing modulation and the phase steps. Both driving voltages can be added synchronously because the step duration is equal to the half period of the proper frequency required for the biasing modulation which works with sine wave but also square wave. The figure 12 describes a convenient scheme to implement this method of signal processing. The signal of the detector is measured with a lock-in amplifier. The output voltage is connected through an amplifier to an A/D converter which gives the digital value of the phase step. A logic circuit driven by a clock generates the digital ramp and adds the biasing modulation. This is sent to a D/A converter which feeds the phase modulator through a buffer amplifier. The reset is automatically done by the overflow of the D/A converter. The figure 13 shows the error signal generated at the frequency of the reset if its value does not corresponds to a 2π phase step. A second independent loop acting on the gain of the buffer amplifier allows one to servo-control this error signal to zero. This system provides a digital measurement of the rotation rate (related to the digital value of the phase step at the output of the A/D) or an incremental integrated output by counting the positive and negative resets (one count for about 3 seconds of arc with a coil diameter of 85 mm). The quality of our present processing electronics limits the scale factor accuracy to 1000 ppm, but 10 to 100 ppm are expected with a new design under study.

CONCLUSION

We have described the recent progresses made in the design of fiber gyroscopes using integrated optics, emphasizing the problem of polarization non-reciprocities. This technology has now proven that it is suitable for high performance applications. The final configuration is relatively simple and our signal processing using digital phase ramp will solve the problem of scale factor accuracy without degrading the low bias drift obtained because of reciprocity.

ACKNOWLEDGMENTS

We would like to thank H.J. ARDITTY and Ph. GRAINDORGE for their decisive contribution when we collaborated to this study, J. GIRAULT and A. BECH for fruitful discussions about the design of the electronics, M. KRAKOWSKI and Y. COMBEMALLE for providing the pigtailed superluminescent diodes, M. WERNER for designing the circuit masks, J.M. ARNOUX, S. BANN, S. BOTTI, G. DUTREY, A. ENARD, D. PAPILLON and D. ROLLY for their qualified technical assistance.

This work has been sponsored by D.R.E.T.

REFERENCES

- 1 M. PAPUCHON and C. PUECH, "Integrated Optics : a possible solution for the fiber gyroscope", Proceedings of SPIE, 157, 218-219, (1978)
- 2 H.J. ARDITTY et al., "Test results of an integrated fiber-optics gyroscope brass-board", Proceeding of OFS 1, 147-150, London, (1983)
- 3 J.L. DAVIS and S. EZEKIEL, "Closed-Loop low-noise fiber-optic rotation sensor", Optics Letters, 6, 505-507, (1981)
- 4 R.A. BERGH, H.C. LEFEVRE and H.J. SHAW, "All single-mode fiber-optic gyroscope with long term stability", Optics Letters, 6, 502-504, (1981)
- 5 H.C. LEFEVRE et al., "Double closed loop hybrid fiber gyroscope", Proceedings of OFS 3, Post-deadline paper PSD 7, San Diego, (1985)
- 6 H.J. ARDITTY et al., "Integrated-optic fiber gyroscope : Progresses towards a tactical application", Proceedings of OFS 2, 321-325, Stuttgart, (1984)
- 7 E.C. KINTNER, "Polarization control in optical fiber gyroscope", Optics Letters, 6, 154-156, (1981)
- 8 R.J. FREDERICKS and R. ULRICH, "Phase error bounds of fibre gyro with imperfect polariser/despolariser", Electronics Letters, 20, 330-332, (1984)
- 9 W.K. BURNS and R.P. MOELLER, "Polarizer requirements for fiber gyroscopes with high-birefringence fiber and broad-band sources", Journal of Lightwave Technology, LT-2, 430-435, (1984)
- 10 J.M. MARTIN and J.T. WINKLER, "Fiber-Optic laser gyro signal detection and processing technique", Proceedings of SPIE, 139, 98-102, (1978)
- 11 R. ULRICH, "Fiber-Optic rotation sensing with low drift", Optics Letters 5, 173-175, (1980)
- 12 I. KAMINOW, "Polarization in optical fibers", IEEE Journal of Quantum Electronics, QE-17, 15-22, (1981)
- 13 K. THYAGARAJAN et al., "Experimental demonstration of TM mode-attenuation resonance in planar metal-clad optical waveguides", Optics Letters, 10, 288-290, (1985)
- 14 R.A. BERGH, H.C. LEFEVRE and H.J. SHAW, "An overview of fiber-optic gyroscopes", Journal of lightwave technology, L-T2, 91-107, (1984)
- 15 H.J. ARDITTY and H.C. LEFEVRE, "Fiber-Optic gyroscopes", New directions in Guided Wave and Coherent Optics, Edited by D.B. OSTROWSKY and E. SPITZ, Nato Asi Series E : Applied Sciences N° 78, Published by Martinus NIJHOFF, The Hague, 1, 299-333, (1984)

DISCUSSION**G. Winzer, Ge**

You have used 3 dB-fibre couplers and a Y-branch in LiNbO_3 . Considering the loss budget, it seems that this hybrid solution is not advantageous. What is the reason for not integrating both branches on the LiNbO_3 , is it the difficulty to adjust the splitting ratio of the 3 dB-couplers or is it for spatial filtering?

Author's Reply

The spatial filtering is done by a 10 mm single-mode waveguide and it is too short to get a good rejection. So, the problem is not that you have to use a larger integrated optics circuit but a very long one, which is not so easy.

B. Schwaderer, Ge

Can you split off the loss figure of 5 dB of the I.O. to coupling loss and insertion loss?

Author's Reply

5 dB total extra loss fibre to fibre: 1 dB for each fibre-waveguide end-fire coupling, 1.5 dB for the Y-junction, 1.5 dB intrinsic waveguide loss, 1 dB is missing (uncertainty between the various parts).

SUMMARY OF SESSION II

DEVICES AND TECHNIQUES

(Transcript of closing remarks) by

T.G. Giallorenzi, Chairman

In the work done by the AT&T group (first paper) a very good cross-talk isolation of about 38 dB in the device itself was obtained even though they were able to see only 23 dB when they put both the transmitter and the receiver together. One needs to do much better than 23 dB in practical systems of course but the numbers are really very encouraging and show that with a little bit of engineering you can indeed come up with something very impressive.

The group from IROE-Firenze has shown an integrated optics geodesic lens approach to the wavelength division multiplexing and they did a very good job on fabricating the depression limited lens. The number they didn't have in the paper was the cross talk between channels, which makes it very difficult to compare an integrated optics lens type design with the bulk optics of the AT&T group; one would however guess that the bulk optics design would be probably at least 10 dB better because of the scattering in the planar waveguide. The third talk was about a method of phase noise reduction and it was shown that by feeding amplitude and phase information back to the laser one can reduce the laser phase noise of about 30 dB. Since the conventional wisdom has that there is very little correlation between the front facet and the rear facet noise terms, this demonstration clearly shows that there are more things going on than expected.

The McDonnell Douglas paper on optical quadrature modulator show a very clever idea of making a grating in front of your detector and besides it was able to demonstrate how the technology developed in the sensor is directly applicable to coherent communications.

The fifth talk was on the effects of optical feedback on the performance of high data rate systems, a problem encountered many times by anybody who works with diode lasers; even small percentages of feedback can dramatically destabilize your laser. The authors have shown that lensing the fiber can reduce the reflection and, accordingly, the effect. They went on showing that when instabilities are present in the laser, the effect should increase error rate quite dramatically.

The next paper addressed the use of ion milled alignment grooves for fiber-to-chip coupling. The losses are now getting down below the dB range for connector losses and this is very encouraging because one of the big barrier to the utilization of LiNbO_3 waveguides has been the coupling to fiber. The ion milling approach is technologically elegant but also difficult and it still remains to be seen whether ion milling or "V" groove on silicon are competitive with each other.

Three papers were on the theory of nonlinear effects in waveguides and they show a number of effects which can happen. In my opinion, this is very important for the large number of people interested in optical computing which still miss the technological base to build an optical computer (even if there are one or two big programs getting off the ground at the present time); the work done at a number of Universities, like the University of Rome and the University of Arizona, is probably the foundation for building potential optical computers.

The next talk was on the PIN-FET pre-amplifier for high-speed optical communication systems, and represents work in the main stream of data transfer community. There was a short discussion on high impedance versus transpedance amplifiers for the different frequency ranges and a very good engineering result was shown for 170 to 565 megabits receivers.

The next talk, from the CRC Canadian group, was an optoelectronic broadband switching. Cross-bar switches have been of interest to the community from the beginning and the Canadian group is probably the leader in developing this type of switches. They pointed out that if one is going to do a ten by ten switch on a LiNbO_3 , one would need about a square meter of it and it is probably beyond the technology to get crystals that are that large. However, if one has a ten by ten cross-bar switch, there are quite a number of applications in the computer area and in signal processing that would be opened up and the work the group is doing is quite significant and very important.

The next paper was about an acousto optic spectrum analyser using LiNbO_3 , a problem which has been treated in a number of groups for a number of years. The work was very well engineered and the progress achieved represents the state of the art on the subject, the 26 dB dynamic range which was reported being right up with the companies in the USA. The problem is of course that one needs specialized componentry beyond that one can buy; for example, the use of a Reticon detector which you basically glue at the end of the waveguide is not optimal but probably is the best choice commercially available.

Finally, we heard a review paper on modulators and detectors for high bandwidth applications. A great deal of interest exists in studying the possibility of moving fiber optic technology out to the millimeter wave and microwave regions; however in going beyond 15 GHz modulation becomes very difficult. But, given the progress both in the lasers, which can be modulated up to 17 GHz and integrated optics, one can think of doing things up to about 18-20 GHz.

To summarize the session, there were some very significant advances. The papers ranged from very theoretical, which basically form the foundations for all the things we'll do in the future, to fairly applied.

And when you get to the applied topics you really start seeing the problems, a lot of which have been swept under the rug. In telecommunication industry they have very few bumps now but in the military area, where we are trying to do some very demanding things with fiber optics, the rug is still very bumpy and there have to be several conferences like this one before all our bumps are smoothed out.

Wavelength Division Multiplexing at 1.5 μm for High Capacity Optical Transmission

by

J. Hegarty, N. A. Olsson and R. A. Logan

AT&T Bell Laboratories
Murray Hill, New Jersey 07974

ABSTRACT

We describe a method for multiplexing several channels of information, closely spaced in wavelength, together in one single-mode fiber. We report the results of a recent 10-channel experiment at 1.5 μm in which 10 distributed feedback lasers, modulated at 2 Gbits/s, were multiplexed together and transmitted over 68.3 km of fiber giving a system capacity of 1.37 terabit-km/s. The channel spacing was 1.35 nm and the multiplexer insertion loss was 3 db. Crosstalk, including Raman crosstalk, was found to be negligible.

I. INTRODUCTION

The advances in lightwave technology in recent years has demonstrated the vast potential of light as a carrier of information. The development of high speed lasers and detectors on the one hand and low loss fiber on the other has led to a series of records being set and quickly broken both in terms of repeaterless distances and in bits/second. Since the minimum loss region in silica fiber is in the 1.55 μm region, most of the record breaking advances have centered around this wavelength. Repeaterless distances of 203 km at 420 Mbit/s [1], bit rates of 1.2 Gbit/s over 113.7 km [2] and 4 Gbit/s over 117 km [3] have recently been achieved in single mode systems. To overcome dispersion effects over such long distances, narrow linewidth lasers have been necessary, such as the C^3 [4] and DFB [5] lasers. Despite the phenomenal bit rate-length products that have been achieved, only a small fraction of the potential system capacity has been realized. Silica fibers have very low loss over a broad spectral width at 1.55 μm , on the order of 50-80 nm. Consequently, many channels of different wavelengths could be multiplexed together on a single fiber [6]. Methods to achieve wavelength division multiplexing have only recently begun to be explored, however, in single mode systems. Multiplexing of three single mode channels, widely spaced over the 1.3-1.5 μm range was reported in 1984 [7]. To avail of the low loss window near 1.5 μm it is desirable that all channels lie within this window. Consequently, it is advantageous to minimize the channel spacing in order to increase the channel number. As an example, for directly modulated lasers with a linewidth of 1A, several hundred channels could be accommodated within the low loss window. Only recently has a 2-channel, closely spaced system been demonstrated [8].

The key to achieving such a concentrated system in the wavelength dimension is a multiplexer and lasers whose wavelengths can be tuned to the individual channels. The requirements on the multiplexer are low insertion loss and low crosstalk. As a step in this direction we have recently demonstrated an ultra-high capacity system satisfying all of the above criteria [9]. The system consisted of a 22 channel multiplexer through which 10 single frequency DFB lasers were efficiently multiplexed to give a system capacity of 1.366 Tbit-km/sec, which is about a factor of five greater than the current single channel record [3].

Details of the system are explained in the following sections. In section II the operation of the multiplexer and demultiplexer is outlined while in section III details of the lasers and receiver are described. Section IV deals with the fiber characteristics. The overall system performance is given in section V in terms of bit error rate measurements, crosstalk in the multiplexer/demultiplexer, fiber Raman crosstalk, and penalties.

II. MULTIPLEXING/DEMULTIPLEXING

The multiplexer used in the experiment was similar in design to that described previously [10]. The basis of the design is a diffraction grating which can combine spatially separate but collimated beams into one beam provided that the wavelengths satisfy the usual grating condition

$$m\lambda = nd (\sin \theta_1 + \sin \theta_2)$$

where θ_1 and θ_2 are the incident and diffracted angles, respectively, d is the grating spacing, n is the refractive index of the medium and m is the grating order which we will assume to have the value 1 henceforth. In the multiplexing process the diffracted angle θ_2 is the same for all wavelengths so that the two wavelengths separated by $\Delta\lambda$ must have their incident angles θ separated by $\Delta\theta$ given by

$$\Delta\lambda = nd \cos \theta \Delta\theta$$

It is evident that to minimize $\Delta\lambda$, $\Delta\theta$ should be as small as possible. The key to achieving this is to bring the incident beam sources as close together spatially as possible. A concentrator based on waveguiding in LiNbO_3 has been proposed [11] in which individual wavelengths are coupled into an array of waveguides on a single substrate. The waveguides are fanned in towards each other so that the beams emerging at the other ends of the waveguides are arbitrarily close together. Since the concentrating function is purely passive and to avoid the sizable bending losses in LiNbO_3 we have adopted instead a much simpler type of concentrator based on optical fibers whose loss is negligibly low.

A schematic of the 22-channel multiplexer used in the experiment is shown in Fig. 1. The concentrator consisted of 23 single mode fibers which were brought together at one end in a

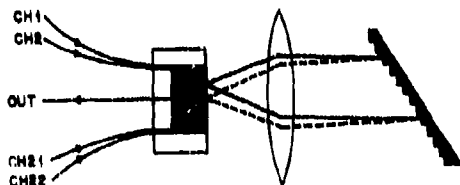


Figure 1. Multiplexer schematic diagram showing the 23 fiber array, collimating lens and grating.

linear array [10]. 22 of the fibers were input channels and the other fiber was the output channel carrying the multiplexed information. The fiber had a step index profile with a core diameter of $8.2 \mu\text{m}$. By etching the fibers in dilute HF acid the core-to-core spacing in the array was reduced, in this case to $24 \mu\text{m}$. The outputs of the semiconductor laser sources were coupled individually into the free fiber ends. The beams emerging from the array were collimated by a 25.6 mm focal length lens and diffracted off the grating back through the lens. The combined beam was refocused onto the output fiber in the array. The grating had a 600 l/mm ruling and was blazed for $1.5 \mu\text{m}$.

The important parameters in the operation of the multiplexer are insertion loss and crosstalk. The insertion loss is a function of bending losses in the fibers, linearity of the array, loss in the lens and efficiency of the grating. Crosstalk is a function of spurious scattering and coupling between adjacent channels. To measure these parameters the following experiment was performed. The output of a color center laser tunable from 1.4 to $1.57 \mu\text{m}$ and with a linewidth of 0.01 nm was coupled into one of the fibers and the output of all the other fibers together was monitored as a function of laser wavelength. As the laser was tuned the diffracted light was coupled consecutively from one fiber to the next. The results are shown in Fig. 2 where the vertical scale shows the

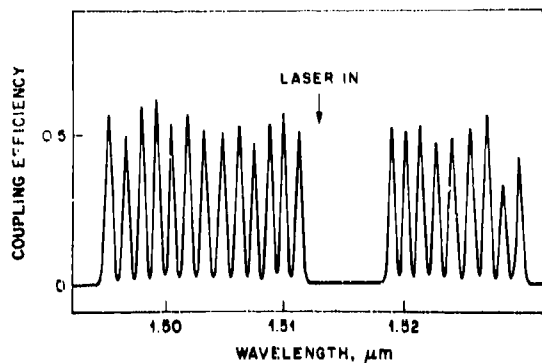


Figure 2. A plot of the multiplexer input fiber-to-output fiber coupling efficiency. The position of the channel used to couple in the tunable source is indicated by the arrow.

coupling efficiency from input to output fiber and hence the overall insertion loss of the multiplexer. This plot yields directly not only the loss but also the channel spacing and channel width. The break in the middle of the array is a result only of the particular way in which the array was fabricated. Two $30\text{ }\mu\text{m} \times 300\text{ }\mu\text{m}$ capillary tubes were used to align the etched fibers and the break is due to the wall thickness between the two sections. This could easily be eliminated. While the insertion loss fluctuates from channel to channel the average loss is only about 3 db. The grating accounts for 0.5-1 db of this and the remaining is most likely due to microbending in the fibers in the array. The channel spacing is 1.35 nm and the channel width between 1 db points is 0.3 nm. From Eq. 1 the difference in angle of adjacent channels impinging on the grating is a function of lens focal length f and core-to-core spacing x so that

$$\Delta\lambda = (xd/f)\cos\theta$$

Inserting the values of the parameters gives $\Delta\lambda = 1.4\text{ nm}$ in close agreement with that measured. The channel width $\delta\lambda$ is determined by two factors: 1) how rapidly the refocused spot is displaced from the core of the output fiber as the wavelength is varied and 2) the sensitivity of coupling into the core to the displacement, y . The latter dependence can be calculated using the theory of Marcuse [12]. For a fiber with a V -number of 2.2, y is about $3\text{ }\mu\text{m}$ for a 1 db allowed loss increase. Since

$$\delta\lambda = (2yd/f)\cos\theta$$

$\delta\lambda = 0.35\text{ nm}$, close to the measured value. The narrow width means that each semiconductor must be precisely tuned to match the channels. The channel width can be increased by using a coarser grating or by using a shorter focal length lens. This, of course, also increases the channel spacing. The figure of merit (mark/space ratio) for the multiplexer can be taken as $\delta\lambda/\Delta\lambda$ which in this case is 0.22.

The crosstalk in the multiplexer was measured by monitoring the output of only one fiber as the laser wavelength was scanned. A typical trace is shown in Fig. 3. An increase in the vertical scale by a factor of 100 reveals that the monitored channel picks up a small amount of signal when the laser is tuned to adjacent channels. This crosstalk is $< -36\text{ db}$, however, and is negligible.

The demultiplexer is similar in concept to the multiplexer and is shown schematically in Fig. 4. The individual channels are separated by a grating and focussed to an array of spots by a 10 cm focal length lens. A detector was placed at the focus of the lens and, with a free aperture of $50\text{ }\mu\text{m}$, acted as its own spatial filter to detect the channels in turn. The spectral passband of this arrangement was about .8 nm. The crosstalk between adjacent channels was less than -23 db and the demultiplexer insertion loss was 2.5 dB.

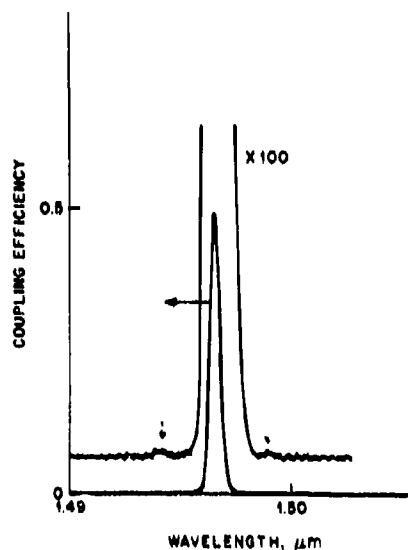


Figure 4. Schematic of the demultiplexer.

Figure 3. Plot of the laser power coupled from the input fiber to one of the other fibers in the array as a function of wavelength. The arrows indicate the wavelengths at which the laser is coupled to fibers adjacent to the monitored fiber.

The interface in the multiplexer between the array (glass) and air gave rise to a 4% reflection back along the input fibers. Since any part of this reflection coupled into the laser could give rise to mode-partition noise [13], it was essential to minimize it. A three layer anti-reflection coating reduced the reflectivity to the .15-.2% range.

III. LASERS

The lasers used in this experiment were heteroepitaxially ridge overgrown (HRO) distributed feedback lasers [14] and were chosen from several wafers with different design wavelengths. The wavelength distribution of the lasers was between 1.529 and 1.561 μm . The lasers had threshold currents in the 50-100 mA range as shown in Fig. 5 where the output versus current characteristics are drawn for a random selection. The quantum efficiency was typically 12% per facet. Distributed feedback was achieved by a second order diffraction grating with both facets cleaved. The mode rejection ratio at 2 Gbits/s modulation was between 26 dB and 40 dB. The pure single-longitudinal-mode operation, even at such high speed modulation, was essential for achieving the narrow channel spacing, low crosstalk and error free operation in the experiment. The sensitivity of

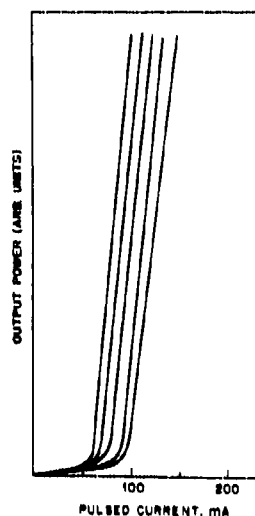


Figure 5. Light versus current curves for a random selection of the DFB lasers.

the lasers to reflections from outside was extremely small. Nevertheless, care was taken to reduce any such reflections, especially in the multiplexer, as discussed in the previous section.

The receiver used in the experiment had a high-impedance GaAs FET front end and a high-performance SAGM avalanche photodetector [15]. The receiver sensitivity for 10^{-9} BER at 2 Gbit/s was -32 dBm.

IV. FIBER

68.3 km of almost pure silica-core single mode fiber was used for transmission. The silica core fiber is a new lightguide design [16] which minimizes intrinsic Rayleigh scattering losses by reducing the amount of dopants in the core. It was made by the Modified Chemical Vapor Deposition (MCVD) process by totally depressing a fluorosilicate cladding between the silica core and the silica substrate tube. The deposited cladding to core diameter ratio (D/d) was >9.5 in order to minimize radiative leaky-mode losses that can occur in depressed cladding lightguides. Extrinsic losses due to micro-deformations, such as microbending, depend on the power confinement of the guide mode. Such losses can be greatly reduced by keeping the mode-field-radius small. This was accomplished by increasing the core-cladding index difference and decreasing the core diameter. The resultant cut-off wavelength, $\lambda_c \sim 1.42 \mu\text{m}$, was close to the operating wavelengths in order to provide good mode confinement by keeping the mode-field-radius small.

The fibers were fabricated to minimize loss without any constraint on dispersion. Zero chromatic dispersion occurred near $\lambda = 1.29 \mu\text{m}$ but it had a relatively high value, 17.5 ps/km-nm, near the minimum loss wavelength. Resultant losses were as low as 0.16 dB/km and median values, over long lengths, were about 0.19 dB/km within the $1.57 \mu\text{m} < \lambda < 1.58 \mu\text{m}$ region. The average loss of the fiber at the ten laser wavelengths used in the experiment (range 1.529-1.561 μm) was 15 db.

V. RESULTS

A schematic of the full system setup is shown in Fig. 6. The lasers were selected so that their wavelengths roughly corresponded to the individual channels. It is to be noted that choice of the first laser determined the wavelengths of all the other channels. Each laser was precisely temperature tuned to exactly match the channel. Ten lasers were used in the experiment and Fig. 7 shows how they were matched up with the multiplexer channels. The channel selected for output is also indicated. Coupling of the lasers to the fibers was accomplished by microlensing the fiber ends [17]. About 30% of each laser was coupled into the fiber.

The bit error rates (BER) were measured for each channel sequentially. Modulation was provided by an Anritsu test set and consisted of a $2^{15} - 1$ NRZ pseudorandom word at a data rate of 2 Gbit/s. The modulated channel was chosen for detection at the receiver by a rotation of the demultiplexing grating. During the BER measurement one of the other channels was modulated sinusoidally at 1 GHz and the rest were operated cw with full power coupled into the fiber. A received power between -29.0 dBm and -24.6 dBm, depending on the channel, was necessary to obtain a BER of 1×10^{-9} . The difference between the channels was a result of different extinction ratios and dynamic linewidths. Fig. 8 shows the BER curves and eye diagrams for the channels requiring the least (ch. 5) and most (ch 9) received power. In all cases the BER was independent of the presence of the other channels, showing that the overall crosstalk was minimal. From a baseline run with only 10m of fiber, we determined the power penalty arising from a combination of dynamic linewidth (chirping) of the lasers and the fiber dispersion. The greater the chirping the more dispersed is the received pulse and the greater the power penalty. The dispersion penalty was between 0.9 dB and 3.5 dB for the 10 channels. Extinction ratio and other penalties ranged from 2.1 to 5.2 dB. Table I contains a summary of the power budget for the system. The average loss including fiber was 25 dB and the average penalty was 5.5 dB.

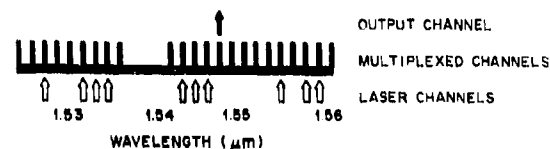
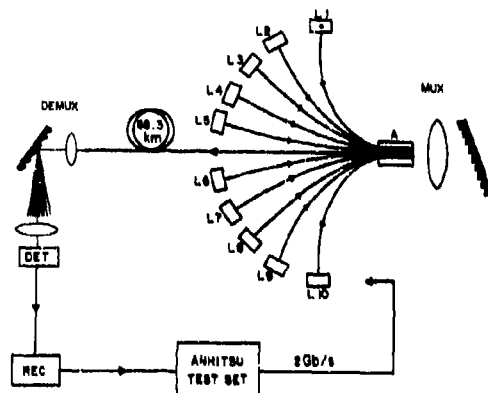


Figure 7. Chart of the available multiplexer channel wavelengths (solid bars) showing the output position (solid arrow). The wavelengths of the 10 lasers used are shown by the open arrows.

Figure 6. Schematic diagram of the transmission system. L1-L10 are the laser diodes, A is the fiber array, MUX and DEMUX indicate multiplexing and demultiplexing stages, respectively, and rec is the receiver.

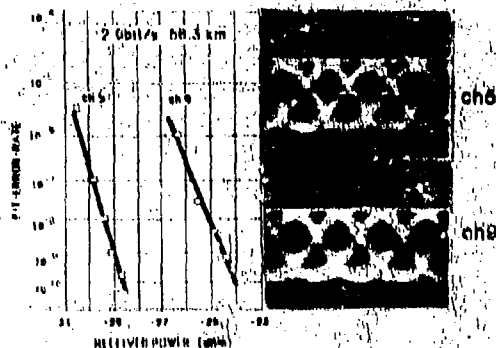


Figure 8. BER curves and eye diagrams after 68.3 km of fiber for the channels requiring the least (ch.5) and most (ch.9) received power for a 1×10^{-9} BER.

A measurement of the overall system crosstalk was made as follows. A channel having two nearest neighbor active channels was chosen for detection by the demultiplexer. This channel was laser channel 3 in Fig. 7. One of the nearest neighbor channels was modulated with the 2 Gbit/s data stream while the other was modulated with the 1 GHz sinusoidal signal. The other seven channels were operated cw and coupled into the fiber. The laser corresponding to the selected channel was switched off and the net photocurrent was measured. The ratio of this photocurrent to that measured when the selected laser was switched on was < -23 dB. That this amount of crosstalk is negligible was confirmed by the BER measurements. Since the multiplexer crosstalk was less than -36 dB, the overall crosstalk was mainly due to imperfect spatial filtering at the receiver.

A further source of possible crosstalk in a wavelength division multiplexed system arises from the stimulated Raman effect [18] which can couple power from one channel to another and so degrade the system performance. The magnitude of Raman crosstalk is a function of power/channel, number of channels, channel separation and fiber material. In a separate experiment [19] we have measured the worst case penalty on a single channel by the presence of a second channel whose power and wavelength could be varied over a large range. From these measurements we deduce that the worst case penalty in a 10-channel multiplexed system with coupled power/channel of 1 mW, is .08 dB. Since the powers coupled into the output fiber were in all cases less than 1 mW, Raman crosstalk is negligible. This is borne out by the BER measurements where no evidence of Raman crosstalk could be observed. The Raman effect is a fundamental limit, however, to the

channel power and density that can be used in wavelength division multiplexing.

In conclusion, we have demonstrated the first terabit kilometer/second capacity lightwave system. The ultrahigh capacity of 1.366 Tbit-km/s was made possible by multichannel WDM with a very high bit rate modulation and ultralow loss fiber. The system satisfies the criteria for BER performance and the various sources of crosstalk are negligible. Since the multiplexer is a 22-channel unit all channels could easily be operated with appropriate lasers giving a much higher capacity. In this experiment we have not attempted to integrate all of the elements in the multiplexer but since the elements are all based on the same material, an all-glass integrated multiplexer is possible. This would eliminate all interfaces and consequently spurious reflections which can be detrimental to the lasers' performance.

We wish to thank L. F. Johnson for lithography in the preparation of the lasers, K. L. Walker and L. G. Cohen for the fiber and B. L. Kasper and J. C. Campbell for the receiver. We also thank R. T. Ku for the fiber microlenses and Evaporated Coatings for the antireflection coating of the array and K. A. Jackson, D. V. Lang, P. A. Fleury, V. Narayanamurti and C. K. N. Patel for continued encouragement.

REFERENCES

- [1] V. J. Mazurczyk, et al., Postdeadline paper #6, ECOC 84, Stuttgart, 1984.
- [2] P. J. Chidgey, B. R. White, M. C. Brain, R. C. Hooper, D. R. Smith, P. P. Smyth, P. J. Fiddymont, A. W. Nelson and L. D. Westbrook, *Electron. Letts.*, **20**, 707 (1984).
- [3] S. K. Korotky, G. Eisenstein, A. H. Gnauck, B. L. Kasper, J. J. Veselka, R. C. Alferness, L. L. Buhl, C. A. Burrus, T. C. D. Huo, L. W. Stulz, L. G. Cohen, R. W. Dawson and J. C. Campbell, Postdeadline Paper, OFC'85, San Diego, 1985.
- [4] W. T. Tsang, N. A. Olsson, and R. A. Logan, *Appl. Phys. Letts.* **42**, 143 (1981).
- [5] H. Kogelnik and C. V. Shank, *Appl. Phys. Letts.* **22**, 515 (1983). For a review see Y. Suematsu, S. Arai, and K. Kishino, *Jour. of Lightwave Tech.*, LT-1, 161 (1983).
- [6] W. J. Tomlinson, *Appl. Opt.* **16**, 2180 (1977).
- [7] N. K. Cheung, C. R. Sundahl, J. Lipson and N. A. Olsson, *Proc. OF'84*, New Orleans, LA, 1984.
- [8] N. A. Olsson, R. A. Logan and L. F. Johnson, *Electron Letts.* **20**, 673 (1984).
- [9] N. A. Olsson, J. Hegarty, R. A. Logan, L. F. Johnson, K. L. Walker, L. G. Cohen, B. L. Kasper and J. C. Campbell, *Electron Letts.* **21**, 105 (1985).
- [10] J. Hegarty, S. D. Poulsen, K. A. Jackson and I. P. Kaminow, *Electron. Letts.* **20**, 685 (1984).
- [11] W. J. Minford, J. Lipson, E. J. Murphy, T. C. Rice and R. A. Linke, *Tech. Digest, Integrated and Guided Wave Optics Conference*, Kissimmee, Florida, 1984.
- [12] D. Marcuse, *Bell System Tech. Dig.* **56**, 703 (1977).
- [13] V. J. Mazurczyk, *Electron. Letts.* **17**, 143 (1981).
- [14] W. T. Tsang, R. A. Logan, N. A. Olsson, L. F. Johnson and C. H. Henry, *Appl. Phys. Letts.* **45**, 1272 (1984).
- [15] J. C. Campbell, A. G. Dentai, W. S. Holden and B. L. Kasper, *Electron. Letts.* **19**, 818 (1983).
- [16] K. Ciemiecki-Nelson, D. L. Brownlow, L. G. Cohen, F. D. DiMarcello, R. G. Huff, J. T. Krause, W. A. Reed, D. S. Shenk, E. A. Sigety, J. R. Simpson, and K. L. Walker, *OFC '85*, San Diego, USA, 1985.

- [17] L. G. Cohen, Bell System Tech. Jour. 51, 573 (1972).
- [18] R. H. Stolen, Proc. IEEE 68, 1232 (1980).
- [19] J. Hegarty, N. A. Olsson and M. McGlashan-Powell, Electron. Letts.

DISCUSSION

B.G. Winzer, Gc

Did you use a DFB laser with an internal phase shift and how did you produce this laser? What is the observed variation in wavelength for this DFB-laser on the same chip?

Author's Reply

No; with a regular grating side-mode suppression was consistently better than 400:1. The variation is typically about 200 angstroms even though the same grating is written on the whole wafer.

J. Dakin, UK

Were the crosstalk figures you mentioned (-23 dB overall and -36 dB for a single channel) optical figures or electrical figures? How are these figures consistent with the >400:1 mode rejection ratio for *each* laser? Did not the combined background from the unwanted laser modes and "in addition" the combined superluminescent background lead to crosstalk problems?

Author's Reply

The crosstalk was all optical. The -23 dB overall crosstalk was due mostly to the demultiplexer where the spectral resolution was about 10 angstroms and the tails from neighbouring channels overlapped the detected channels by a small amount. The suppressed side modes of the laser were not matched to adjacent channels and the pick-up from these was negligible. The superluminescent background was also negligible.

Unknown Questioner

(a) How large were detectors and what was their spacing? (b) Was any care necessary to limit back-coupling of laser power from the multiplexer?

Author's Reply

(a) Use only one detector; looked at one channel at a time. Crosstalk measured by turning off input to channel in question, leaving other channels on. (b) An AR coating with a reflectance less than 0.2 per cent was adequate.

S. Walker, UK

What factors limit the maximum achievable BER in this W.D.M. system?

Dr J. Hegarty

This is a laboratory experiment. The laser wavelength drifts and the mux-Demux is temperature sensitive.

A SPHERICAL WAVEGUIDE MULTIPLEXER - DEMULTIPLEXER

V. Russo, S. Sottini, G. C. Righini, S. Trigari
 Istituto di Ricerca sulle Onde Elettromagnetiche (IROE)
 del Consiglio Nazionale delle Ricerche
 Via Panciatichi, 64
 50127 Firenze-ITALY

SUMMARY

A wavelength multiplexer-demultiplexer (MUX - DEMUX) which can work also as a tapping element has been suggested and tested. This device is based on the imaging properties of a hemispheric geodesic lens. The aberrations of this lens have been evaluated and some examples of the potential performance of the device are given: in particular the MUX - DEMUX seems to be quite interesting in the case of monomode fibers, showing a diffraction limited performance. Experimental tests are in progress, utilizing a spherical waveguide fabricated by ion exchange on a glass substrate, and gratings with 540 or 1200 grooves/mm. The results already available are quite encouraging and confirm the expected advantages of this approach with respect to previous devices.

INTRODUCTION

Wavelength division can dramatically increase the transmission capacity of optical fibers. Multiplexing - demultiplexing devices (MUX - DEMUX) are therefore of great interest. In general they consist of a dispersing element and of a focusing one. Important characteristics are efficiency, reliability, cost, size and an easy coupling to input and output fibers.

In the case of multimode fibers a simple MUX can be fabricated, for example, by a plane grating and GRIN-rod optics, while for monomode fibers more complex devices have been proposed. In particular, Tomlinson (1) suggested a waveguide geodesic lens as focusing element coupled to an external diffraction grating. The operation of this MUX - DEMUX is described referring to Fig. 1, where, for sake of simplicity, only two wavelength channels, λ_1 and λ_2 , are considered. Light from the input fiber, including the two signals at λ_1 and λ_2 , is coupled to the thin film waveguide and is collimated by the geodesic lens. At the guide edge, this beam is diffracted back from the grating. Each signal is reflected at an angle which depends on its wavelength and is focused by the geodesic lens into the appropriate output fiber.

Recently this MUX - DEMUX has been realized by using a geodesic lens printed in glass and an ion-exchanged waveguide (2). This technique satisfies the requirements of a low cost and simple technology. Unfortunately the relatively high fabrication errors which can give rise to focal length shift and spherical aberrations limit the use of this technique to multimode fibers.

For this reason we have considered a MUX - DEMUX device based on the same working principle of the previous one, but characterized by a spherical geodesic lens as focusing element, that is a waveguide laying on a quarter of sphere. It can act either as a MUX or a DEMUX device; moreover it can operate simultaneously as a demultiplexer and a tapping element, the tap ratio depending on the diffraction efficiency of the grating.

THE SPHERICAL GEODESIC MUX - DEMUX

To investigate the features of the MUX - DEMUX with spherical waveguide, let us refer to the sketch in Fig. 2, which is limited to the case with only two wavelengths, λ_1 and λ_2 ; however, our considerations are valid for any number of channels.

The beam from the input fiber is coupled to the spherical guide and then is partially reflected by the grating positioned at the other guide edge, so that the output fiber on the right can act as a tap of the input signal. At the same time, the grating diffracts the remaining part of the light into monochromatic beams which are focused back by the spherical lens into separate fibers, so performing the multiplexing operation. The input and output fibers have to be coupled to the same edge of the spherical lens guide by butt joints secured by transparent glue. Of course the operation can be reversed, the device acting as a MUX.

In general, the 0th-order beam, reflected by the grating, is aberration free, as it can be easily proved by considering a hemispherical guide divided into two halves by a transmission grating and by recalling its imaging properties (3). Let us consider now the aberrations of the diffracted beams (4, 5). Referring to FIG. 3, let S_0 be a point source at the edge of the spherical guide so that the rays from S_0 , propagating along the meridians, incide normally on the MM' line, where the reflecting grating is placed. The diffracted beam is then focused back in S_1 . Since the following calculations are still valid if the position of S_0 and S_1 are reversed, this assumption is satisfied in most cases, at least approximately. Let α be the diffraction angle for the order considered and a the beam aperture. Since all the rays from S_0 form the same angle with the grating (all of them are perpendicular to it) the rays in the diffracted beam are still parallel to each other: they behave like a parallel beam coming from the outside the quarter-of-sphere lens and inciding on the MM' line at an angle α . The phase delay of the i -th ray S_1A with respect to the principal ray S_1O is therefore expressed by the optical path difference

$$n_1 \overline{BA} = n_1 \widehat{OA} \sin \alpha \quad (1)$$

where n_1 is the refractive index of the waveguide, BA is the virtual length travelled in a planar waveguide and the aperture angle α is assumed to be small in order to be able to use in the computations the length

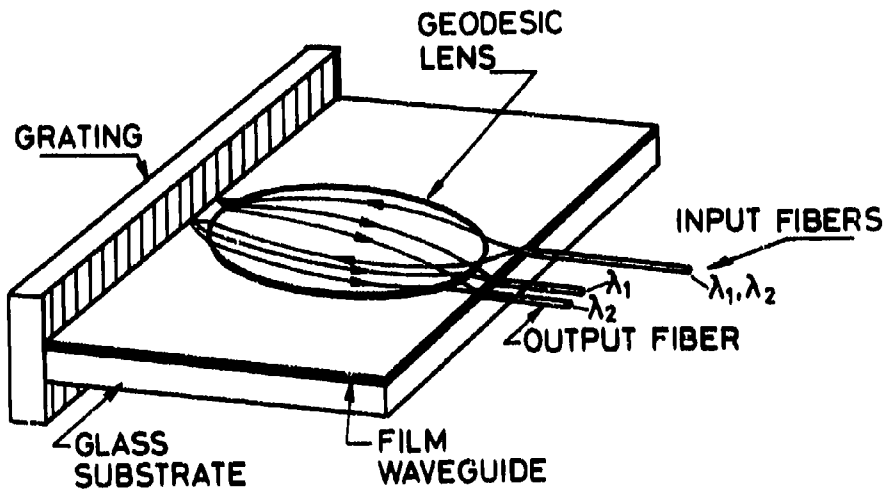


Fig. 1 The MUX-DEMUX device proposed by Tomlinson.

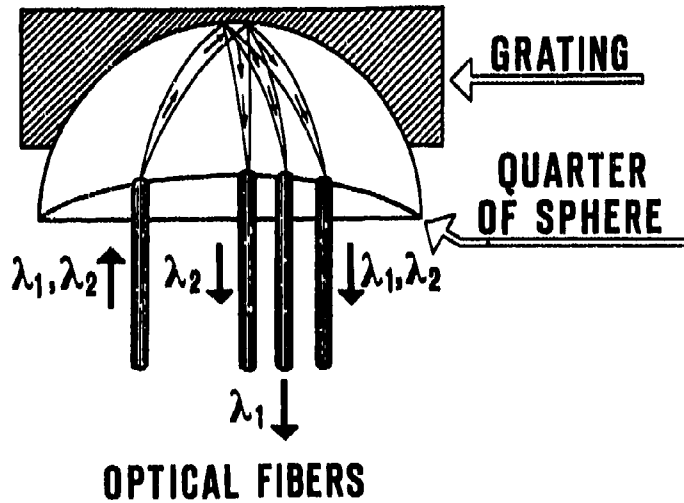


Fig. 2 Top view of the MUX-DEMUX device utilizing an external grating coupled to a spherical waveguide geodesic lens. This device can be used also as a tapping component. For simplicity only two wavelengths are considered.

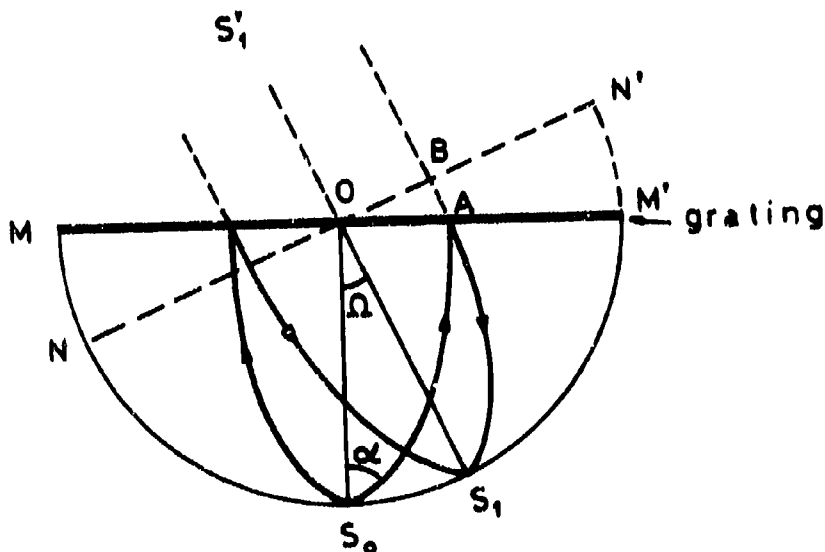


Fig. 3 Top view of the spherical waveguide lens. A guided beam from the point source S_0 (aperture a) impinges normally on the grating MM' . The corresponding diffracted beam, at an angle θ , is focused back in S_1 .

of the arc of circle \widehat{OA} .

The diffracted beam is not focused perfectly in S_1 . In fact, to have a point image S_1 , it is required that the rays have equal phases at the line NN' ; this condition implies a phase delay at the line MM' given by the optical path BA travelled along a meridian of the sphere. We can define the wave aberration W of this optical system, including also the grating, as the phase difference between the wavefront existing at MM' after the diffraction, and the wavefront that should be there to have a point image in S_1 .

$$W = n_1(\widehat{OA} \sin \alpha - BA) \quad (2)$$

By applying the sine-formula for the spheric triangle OAB we can write:

$$\sin \widehat{OA} = \sin \alpha / \sqrt{1 - \cos^2 \alpha \sin^2 \alpha} \quad (3)$$

$$\sin \widehat{AB} = \sin \alpha \sin \alpha / \sqrt{1 - \cos^2 \alpha \sin^2 \alpha} \quad (4)$$

and therefore

$$W = n_1 \sin^{-1}(\sin \alpha / \sqrt{1 - \cos^2 \alpha \sin^2 \alpha}) \cdot \sin \alpha - \sin^2 \alpha (\sin \alpha \sin \alpha / \sqrt{1 - \cos^2 \alpha \sin^2 \alpha}) \quad (5)$$

Expanding in series the trigonometrical functions in Eq. (5) and neglecting the terms of order higher than the 5th, W can be approximately expressed as:

$$W = n_1 \frac{1}{6} \alpha^3 \quad (6)$$

This simple formula clearly shows that the wave aberration corresponds to the coma in bulk optics. On the other hand, it must be pointed out that this geodesic system is perfect for on-axis sources, that is in absence of perturbing elements; any wavefront distortion at the MM' line is completely compensated in the second half of the hemisphere, due to symmetry reasons.

The expressions of W given by Eq. (5) and (6) are valid for the unity sphere; more in general, Eq. (6) becomes:

$$W = n_1 R \alpha^3 / 6 \quad (6a)$$

In the case of a MUX - DEMUX for optical communications, one has to do with relatively large field angles α (typically $0.5 - 0.7$ rad) and with apertures α about 0.15 rad. Hence expression Eq. (6) can give W values far from the exact ones and the use of formula (5) becomes compulsory. However, a numerical analysis has shown that for α values up to 25° and α ranging between 0° and 50° the relative error is smaller than 7%.

In order to get an idea of the influence of the aberrations on the performance of the MUX - DEMUX, let us consider, for example, a grating with 540 grooves/mm, a lens with radius $R = 10$ mm, and monomode fibers with $NA = 0.1$, corresponding to an aperture in the guide $\alpha = 0.067$ rad (refractive index of the guide $n_1 = 1.5$). At $\lambda = 0.633 \mu\text{m}$, α turns out to be 0.35 and $W = 0.26 \mu\text{m} = \lambda / 2.41$; moving to the infrared, at $\lambda = 0.87 \mu\text{m}$ we get $\alpha = 0.47$ rad and $W = 0.26 \mu\text{m} = \lambda / 2.46$, while at $\lambda = 1.3 \mu\text{m}$, $\alpha = 0.7$ rad and $W = 0.52 \mu\text{m} = \lambda / 2.47$. In other words, it turns out that the wave aberration has a value close to that required by the Rayleigh's quarter wavelength rule and smaller than the tolerance condition which is 0.6λ in the case of coma (6). Therefore, in the case of monomode fibers a performance very near to the diffraction limit has to be expected. If, on the other hand, we use graded index fibers with core diameter $50 \mu\text{m}$ and $NA = 0.2$, the beam aperture in the guide turns out to be $\alpha = 0.13$ rad. As a consequence with the same conditions of the previous example, $W = 1.92 \mu\text{m}$ at $\lambda = 0.633 \mu\text{m}$, $W = 2.58 \mu\text{m}$ at $\lambda = 0.87 \mu\text{m}$ and $W = 3.84 \mu\text{m}$ at $\lambda = 1.3 \mu\text{m}$. The wave aberration being larger than the wavelength, it is worthwhile considering also the amount of transversal coma (7):

$$C_T = \frac{dW}{d\alpha} = 0.5 n_1 R \alpha^2 \quad (7)$$

In our example the coma values turn out to be: $C_T = 44 \mu\text{m}$; $C_T = 59 \mu\text{m}$, and $C_T = 89 \mu\text{m}$ respectively. If compared with the core diameter of the fiber, the results at $\lambda = 0.633$ and $0.87 \mu\text{m}$ are reasonably good. As to the employment of this device at $\lambda = 1.3 \mu\text{m}$, in most cases it is convenient to reduce the amount of coma by using a wider grating pitch. Current requirements of wavelength channels spacing (in the order of $40-60$ nm) (8) are fully satisfied by a grating period as low as 300 grooves/mm: the resulting coma becomes lower than the fiber diameter. A further example is shown in Fig. 4, where the C_T is plotted versus α , for $\alpha = 4^\circ, 6^\circ, 8^\circ$ and 10° , having assumed $R = 10$ mm, $n = 1.58$ and $\lambda = 870$ nm.

As to the channel spacing, it depends on the linear dispersion of the grating, which is given by:

$$R \frac{d\theta}{d\lambda} = m / \Lambda \cos \theta \quad (8)$$

where m is the diffraction order, Λ is the grating pitch, and θ is the angle of diffraction. A blazed grat-

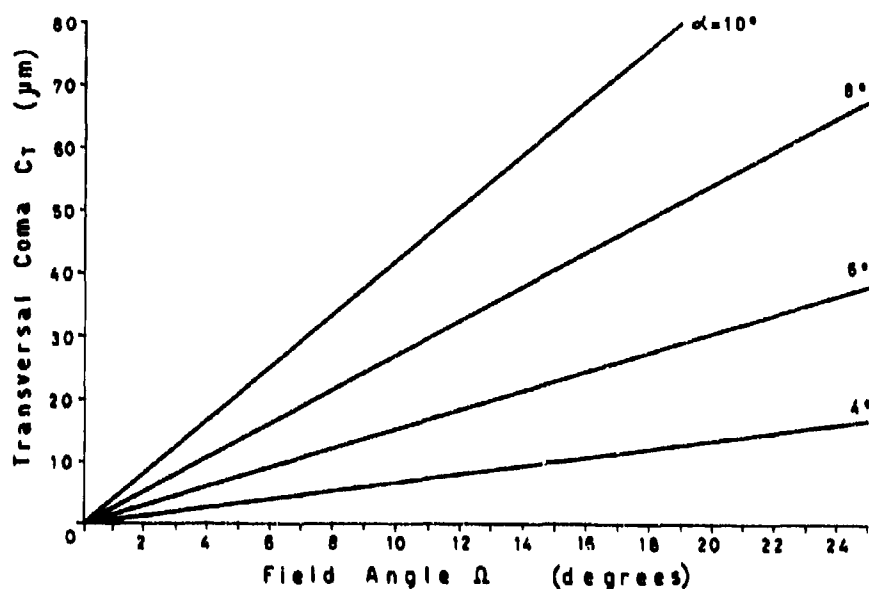


Fig. 4 Transversal coma C_T plotted versus the diffraction angle Ω for different values of the aperture α .



Fig. 5 Experimental set up utilizing a spherical waveguide made of epoxy resin deposited on a glass quarter of sphere. The quarter of sphere is laid and glued to a reflection grating partially visible in the bottom of the picture. The input light from a microscope objective included two wavelengths; $\lambda_1 = 0.633\mu\text{m}$ and $\lambda_2 = 0.488\mu\text{m}$. The bright lines at the lens edge are due to the light outputs from the film guide which is tapered.

ing is often convenient to increase the efficiency. In our case the Littrow mounting of such a grating can be easily achieved moving the input fiber along the circular edge of the guide. It avoids the cutting of the lens substrate, at the proper slant angle, as required in the planar case.

Eq.(6) can be still used as a first approximation with $n = 2\phi$ where $\phi = \sin \lambda/\Lambda$ is the blaze angle. From Eq.(8), substituting θ with ϕ , we have a linear dispersion:

$$Rd\phi/d\lambda = R/\Lambda^2 - (\lambda/2)^2 \quad (9)$$

With the same grating and geodesic lens as in the example described above, the values of the linear dispersion turn out to be: 5.48 $\mu\text{m}/\text{nm}$, 5.55 $\mu\text{m}/\text{nm}$ and 5.77 $\mu\text{m}/\text{nm}$ at $\lambda = 0.633\mu\text{m}$, 0.87 μm and 1.3 μm respectively. As a further example, if a fiber core spacing of 100 μm is requested, the minimum channel separation $\Delta\lambda$ is 180 \AA at $\lambda = 0.87\mu\text{m}$.

EXPERIMENTAL TESTS

Preliminary experiments have been carried out by using a multimode waveguide made of epoxy resin which was deposited on a glass quarter of sphere with radius 25mm. The input beam, coupled to the lens guide by a microscope objective (Fig. 5), included two wavelengths, $\lambda_1 = 6328\text{\AA}$ (He - Ne laser) and $\lambda_2 = 4888\text{\AA}$ (argon laser). A reflection phase grating with 540 lines/mm, glued at the lens output, reflected back a 0th - order beam and diffracted λ_1 and λ_2 beams into at least 2 orders, as shown in Fig. 6, where the output edge is imaged. The bright lines in Figg. 5 and 6 are due to the light output from the film guide which is tapered at the edge. The 1st order λ_1 and λ_2 foci turned out to be $\sim 2\text{mm}$ apart, which is in good agreement with the theory. In this test, carried out with a spherical waveguide already available, it was impossible to obtain the measures of the widths of the output spots, due to the disuniformity of the guide, which was also tapered at the edges as already mentioned.

More meaningful experiments are in progress, utilizing BK7 glass substrates with $R = 15\text{mm}$ and ion-exchanged waveguides. A first sample has been actually fabricated by dipping the spherical substrate, conveniently polished, in a 5% M solution of $\text{AgNO}_3/\text{NaNO}_3$ at $T = 325^\circ$. The ion-exchange time was 1h. Then the guide has been characterized with an indirect procedure which utilized some planar samples of BK7, whose guides were fabricated with the same recipe. In conclusion, at $\lambda = 6328\text{\AA}$, the guided modes were two and the losses were in the range 1.2 - 1.3db/cm.

The quarter of sphere has been laid on a 1200 lines/mm grating and fed by monomode fiber with core diameter 10 μm . Fig. 7 shows a top view of the device: on the top the input signal is visible, which includes three wavelengths: $\lambda_1 = 6328\text{\AA}$ (He - Ne laser), $\lambda_2 = 4888\text{\AA}$ and $\lambda_3 = 5145\text{\AA}$ (argon laser). Then, going to the bottom, there are the three 1st-order beams. The λ_1 beam is less bright due to the limited power available from the He - Ne laser, while the two beams from the argon source can be distinguished only in the focal zone, near the guide edge, having a wavelength difference of only 257 \AA . Finally the tapping beam, reflected by the grating, is clearly visible on the bottom. The microscope objective allows the imaging of the output line. In this way, feeding the device with the Ne-He laser only, and using a grating with 540 grooves/mm, the intensity distribution of the output spots has been measured. The results are shown in Figg. 8a (0th-order beam) and 8b (1st-order beam). It is evident that in both cases the spot width at 3db is of the same order as the input fiber core; that means that the expected aberration of the diffracted beam has no noticeable effect (the hump on the right of Fig. 8a is clearly due to the scattering of some micro-defects of the guide edge). Analogously, Fig. 9 shows the intensity distribution of the 1st-order diffracted beam, in the case with the 1200 lines/mm grating. Also in this case no spread of the beam focus has been noticed. In conclusion, the aberration effects are below the noise level.

Tests are still in progress with the aim of reducing the guide noise and improving the coupling with the grating and the input fiber.

CONCLUSIONS

A MUX - DEMUX device which can work also as a tapping element has been suggested and tested. This device is based on the imaging properties of a hemispherical geodesic lens. The main advantage of the present approach with respect to previous devices is given by the great accuracy - at low cost - available in the fabrication of the spherical geodesic lens so that the performance figured out by the theory should be actually achieved in experimental tests. Therefore this MUX - DEMUX device seem to be particularly interesting in the case of monomode fibers which are characterized by small core diameter and aperture angle. In practice, the spheric geodesic lens can assure diffraction limited performance also with large diffraction angles.

With multimode fibers having wider apertures, the aberration of the diffracted beams increases but it is still acceptable for gratings up to 600 lines/mm. On the other hand, current requirements for wavelength channel spacing are in the order of 40 - 60nm and therefore gratings with periods as low as 300 lines/mm are fully suitable: in this case the amount of coma is much lower than the fiber core diameter. However, if a higher dispersion is required, and therefore gratings with frequencies $\gg 600$ lines/mm. are to be used, the aberration of the lens becomes not negligible due to the high value of n , but it could be corrected anyway by designing a suitable holographic grating (9, 10).

Although meaningful measurements of the insertion losses and of the cross talk attenuation are not yet available, there are good reasons to believe that, potentially, they are at least as good as those achievable with an aspherical geodesic lens. Moreover, the choice of a spherical waveguide structure should assure a more rugged configuration with respect to the planar one.

Finally, the possibility of tapping operation is peculiar to this device, due to the property of the spherical guide to assure in any case an aberration-free 0th-order beam, which can be easily coupled back to a monomode fiber. The tap ratio depends on the efficiency of the reflection grating.

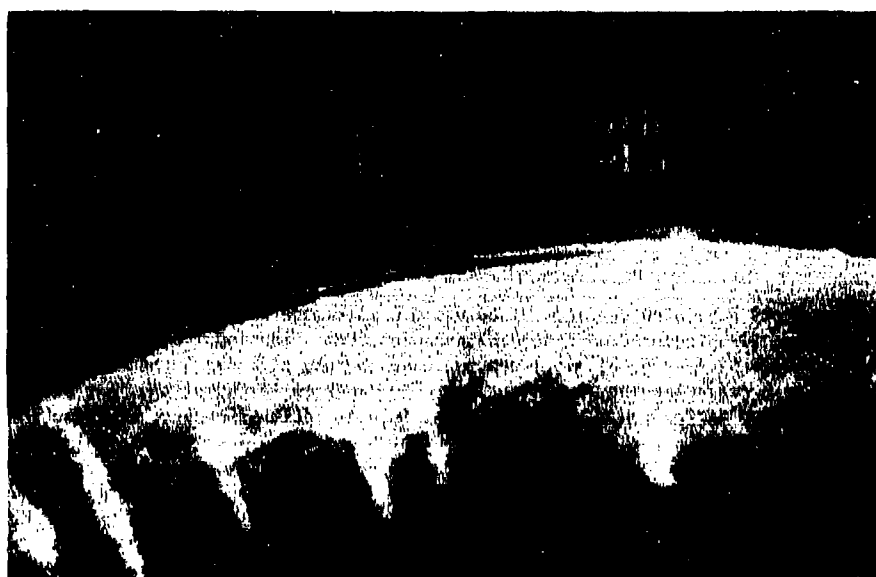


Fig. 6 Output edge of the spherical geodesic lens. The 0th, 1st and 2nd order diffracted beams are clearly visible.

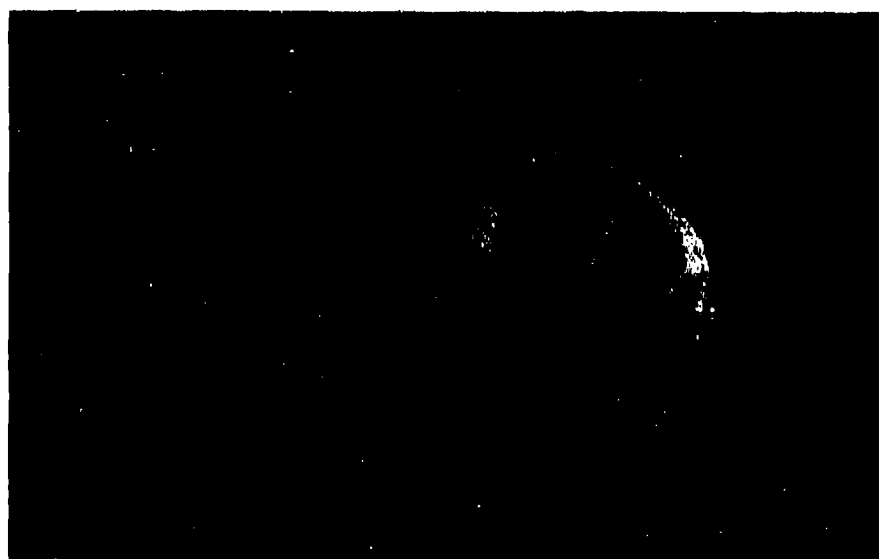


Fig. 7 Top view of the MUX-DEMUX consisting of a waveguide fabricated by ion-exchange on a glass quarter of sphere. The quarter of sphere, whose radius is $R = 16\text{mm}$, is laid on a blazed grating with 1200 grooves/mm. From the top to the bottom, at first the input monomode fiber is clearly visible (core diameter $10\text{ }\mu\text{m}$), which feeds the device with a signal including three wavelengths: $\lambda_1 = 6328\text{ }\text{\AA}$, $\lambda_2 = 4888\text{ }\text{\AA}$, and $\lambda_3 = 5145\text{ }\text{\AA}$. Then there are the three monochromatic beams diffracted by the grating and focused at the lens edge. Finally on the bottom, there is the 0th-order reflected beam, which can be used as a tapping.

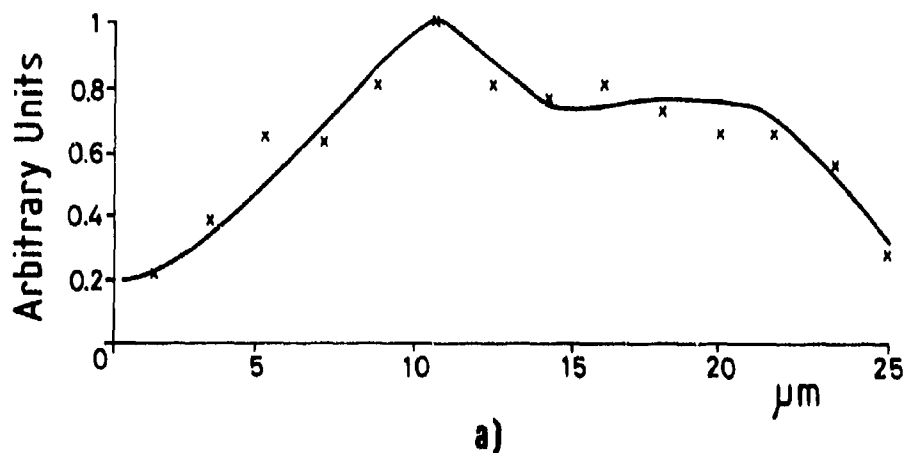


Fig.8 Output intensity distribution of the reflected (a) and of the diffracted beam in the case of a monochromatic signal $\lambda_1 = 6328\text{\AA}$ and of a grating of 540 grooves/mm (the hump on the right of Fig. 8a is clearly due to the scattering of some micro-defects of the guide edge).

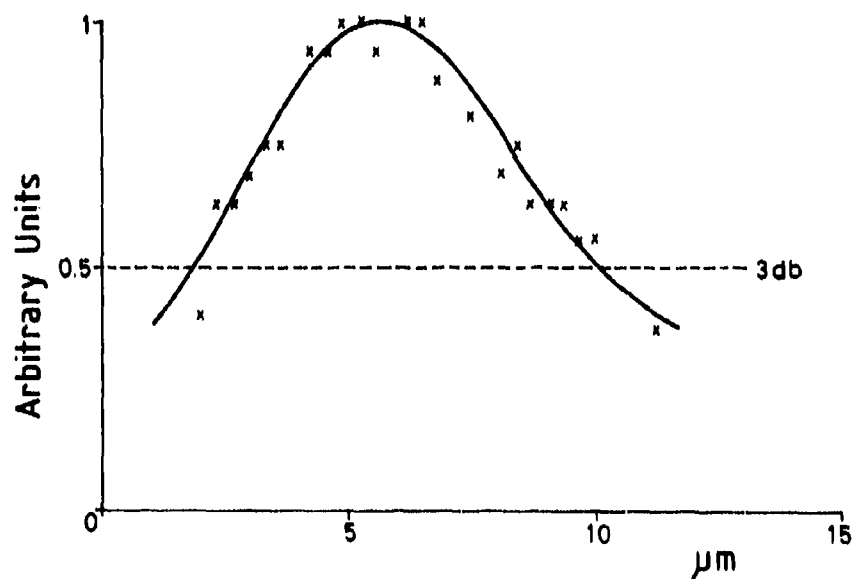
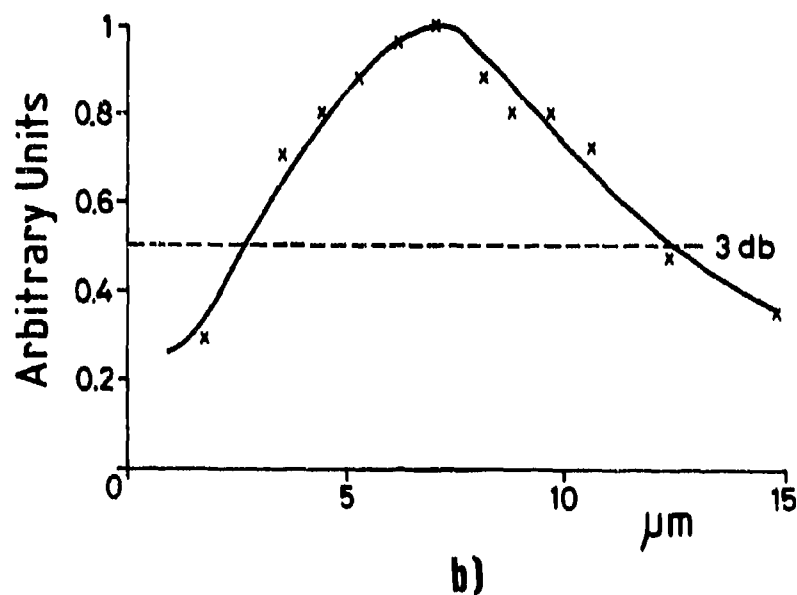


Fig.9 Output light distribution of the diffracted beam in the case of a signal at $\lambda_1 = 6328\text{\AA}$ and of a 1200 lines/mm grating.

REFERENCES

- 1) Tomlinson, W.J., 'Simple-Mode wavelength division Optical Multiplexer', U.S. Patent No. 4,153,330, 1979.
- 2) Lillienhof, H.J., Voges, E., Schultz, D., 'Grating Demultiplexers with Printed Geodesic Lenses in Glass', Proc. ECOC '82, Cannes, 1982, p. 321.
- 3) Righini, G.C., Russo, V., Sottini, S., Toraldo di Francia, G., 'Thin Film Geodesic Lens', Appl. Opt., II, 1972, p. 1442.
- 4) Righini, G.C., Russo, V., Sottini, S., 'Thin Film Integrated Signal Processors', AGARD Conf. Proc., No. 219, London, 1977, p. 25-31.
- 5) Righini, G.C., Sottini, S., Russo, V., 'Aberration Analysis in a Hemispheric Waveguide Geodesic Lens' submitted to Optica Acta.
- 6) Born, M., Wolf, E., 'Principles of Optics', sixth Ed., Oxford, Pergamon Press, 1980, chap. IX.
- 7) Toraldo di Francia, G., 'La Diffrazione della Luce', Torino, Einaudi, 1958, cap. XIII.
- 8) Winzer, G., 'Wavelength Multiplexing Components - A Preview of Single Mode Devices and their Applications' IEEE-J., Lightwave Techn., Vol. LT-2, 1984, p. 369-378.
- 9) Russo, V., 'Corrections of Optical Instruments by Holography', Optical and Acoustical Holography, E. Camatini Ed., Plenum Press, New York, 1972, pp. 127-150.
- 10) Hayford, M.J., 'Holographic Optical Elements', A Guide for Use in Optical System Design, Technical Bull. Optical Research Associates, Aug. 27, 1981.

A STUDY OF METHODS OF PHASE NOISE REDUCTION OF SEMICONDUCTOR LASERS FOR SENSOR APPLICATIONS

J. P. DAKIN AND P. B. WITHERS

PLESSEY ELECTRONIC SYSTEMS RESEARCH LIMITED
ROKE MANOR, ROMSEY, HAMPSHIRE, ENGLAND

SUMMARY

This paper describes methods of reducing semiconductor laser phase noise using (a) passive optical feedback from an array of mirrors or optical fibres, and (b) active control of the laser drive current from the output of an interferometer monitoring the laser emission.

1. INTRODUCTION

Many optical sensors based on fibre interferometry have been proposed. The majority of these use interferometers of the Mach-Zehnder or Michelson type, in which the optical path lengths of the two arms are often unequal. Under these conditions, a highly coherent light source is necessary to avoid signal/noise degradation due to fluctuations in the phase or frequency of the source. Single mode gas lasers are sufficiently coherent, but their large size, critical alignment requirements, and cost, limit their appeal as light sources for optical sensors. Semiconductor lasers, however, are compact, rugged and potentially low-priced devices, but the magnitude of the phase noise is such that, to obtain microradian sensitivity in interferometric sensors, only path differences less than one millimetre between the signal and reference arms can be tolerated. This imbalance may be increased if the magnitude of the laser phase noise can be reduced using either passive optical feedback or active control of the laser drive current. Both approaches are described in this paper.

Described first are proposed experiments to examine the feasibility of using an array of suitably spaced mirrors to provide passive optical feedback. Secondly, experiments to measure phase noise reduction produced by active control of the laser drive current are reported together with their results.

2. PASSIVE OPTICAL FEEDBACK

Goldberg (1) has demonstrated that optical feedback from a single external mirror, 80cm from the laser, produces significant levels of laser line narrowing and an associated decrease in the phase noise of 15dB. The additional reflector forms a Fabry-Perot cavity with the laser output mirror and the intensity of the reflected light is dependent on wavelength, as shown in figure 1, limiting the possible frequency excursions of the laser emission.

However, the cyclic nature of the Fabry-Perot reflectivity function can lead to additional laser emission lines whose spacing is determined by the position of the external mirror. These are generally referred to as external cavity modes (XCMs) and their spacing is given by

$$\Delta\nu = c/2L$$

where L is the separation of the additional mirror and the laser output window. If the external mirror reflectivity is sufficiently high, the laser will operate multimode, the emission spectrum comprising groups of XCMs, centred on the longitudinal modes of the free running laser.

In order to prevent multiple XCM emission lines, the external mirror should be placed close to the laser output window. The additional lines will then be positioned remotely from the free running laser modes and will be unlikely to oscillate. This, however, will produce a Fabry-Perot reflectivity function with very broad peaks, having little effect on decreasing the phase noise. In order to produce narrow reflectivity peaks, the mirrors of the Fabry-Perot cavity should be widely spaced. These conflicting requirements of widely spaced XCMs and narrow linewidth could be satisfied simultaneously by using an array of external mirrors.

2.1 Multiple External Mirrors

A Fabry-Perot interferometer comprising two plane parallel mirrors possesses reflection peaks for wavelengths $\lambda = 2L/N$, where L is the mirror spacing and N is a positive integer. If further mirrors are added to form an array, as in figure 2a, such that their spacings are submultiples of L (L/2, L/4, L/8...), the reflected beams will add coherently. As more mirrors are added to the array, alternate peaks will be attenuated and those remaining will be augmented, making the source less sensitive to other reflections when used in a sensor system. Thus an array of several mirrors with carefully chosen spacings will produce reflectivity peaks which are widely spaced in frequency and yet are still narrow.

A simple computer model was developed to demonstrate this, and the results are shown in figure 3. (These graphs were constructed by linear interpolation between sets of discrete points and are therefore approximations to, what in reality, are smooth, continuous functions).

The reflectivity function of the Fabry-Perot cavity formed between the laser output window and one external, low reflectivity, mirror is approximately sinusoidal. Figure 3 also shows the effect of an additional three mirrors spaced at $L/2$, $L/4$ and $L/8$ - the frequencies at which the reflectivity peaks occur become progressively wider spaced whilst the peaks themselves remain narrow, and increase in magnitude. If sufficient elements are incorporated the laser emission should comprise a single, narrow, line.

2.2 Randomly-spliced external fibre cavity

The array of mirrors discussed above would require high dimensional accuracy and stability which may in practice be difficult to achieve and maintain.

An alternative approach would be to use a reflecting array of random lengths of optical fibres as shown in figure 2b. The laser would oscillate at an optimum frequency within its gain curve at which the reflections from the splices add coherently. This technique is a modification of that described by Epworth (2), in which Rayleigh backscattering from a long fibre (100m or more) is used to produce laser line narrowing. In Epworth's system the laser locks on to peaks in the coherent backscatter vs. wavelength response. However, in our case, the reflection coefficient should be enhanced, even when using relatively short fibre lengths, making the device less sensitive to other reflections when the source is used in a system.

This fibre optic approach would remove the requirement for accurate alignment, but acoustic isolation would be necessary. For most dynamic sensor applications, such as hydrophones, occasional mode "hopping" due to thermal fluctuations would not cause problems provided the "hopping" rate were low (i.e. 1Hz). This would be ensured by thermal lagging of the fibre to reduce the rate of temperature variation.

3. ACTIVE CONTROL OF THE LASER CURRENT

3.1 Introduction

The frequency of the laser emission is strongly dependent on the drive current. Active control of this, by feedback from an interferometer used as a frequency discriminator monitoring the laser output, is known to reduce the phase noise (3,4).

In the present work, feedback from both an unbalanced Michelson (with a 26.5cm path difference) and a Fabry-Perot interferometer were studied as means of decreasing the phase noise of a semiconductor laser.

3.2 Experimental

The experimental arrangements are shown in figures 4 to 6. The source of illumination was a Hitachi 7801E laser diode with an output power of 2.6mW. The laser can be operated at up to 5mW output, but it was used at a lower power to obtain a longer life. This device produces a single mode emission at a wavelength of 780nm. The output from the Michelson interferometer was first divided by a source intensity signal, derived from a second detector, to minimize the effects of amplitude noise on the interferometer output. This arrangement is preferable to a subtraction approach, (see (3), for example) as the need for balancing the phase and amplitude noise signals is obviated. The resulting signal was fed back to control the laser current, and a spectrum analyser was used to monitor the output from the divider with and without feedback applied to the laser.

The bulky nature of the Michelson interferometer renders it unsuitable for phase noise reduction in sensor applications. The Fabry-Perot however is more convenient, being particularly robust and compact. When this interferometer was used in place of the Michelson, as shown in figure 5, the frequency discrimination slope was so high that the divider could be removed as it was found to have little, if any, measurable effect on the phase noise reduction; the interferometer output alone could be used as the feedback signal. In addition to the phase noise feedback, in all experiments simple intensity feedback was simultaneously applied from the laser's integral monitor photodiode, via a lower gain feedback loop. In this dual-loop system the latter loop ensured the laser operated near the correct region. Then the higher gain phase noise control loop dominated, allowing small phase changes from the laser to be rapidly corrected for.

In the experiments described so far, the interferometer and detector in the feedback loop intercepted all the light emitted by the laser. This is, in fact, unrealistic, as in any sensor application only a small proportion of the laser emission would be used in the noise reduction system. Further experiments were performed in which approximately 4% of the laser beam was diverted into the feedback system and the remainder was monitored by a second Fabry-Perot, the output of which was displayed on the spectrum analyser. This arrangement is shown in figure 6.

The output from the semiconductor laser was strongly divergent and had to be collimated before entering the interferometers. This was achieved using an 80mm FL, f/4 air-spaced doublet lens in the Michelson experiments, and a x20 microscope objective in those involving the Fabry-Perot. Optical feedback, from the interferometers and other components, was minimized in the former case by placing a 5mm aperture between the laser and collimating lens, and by slightly misaligning the Fabry-Perot interferometers and the laser beam in the latter. Uncontrolled optical feedback must be avoided; otherwise a multimode output and mode hopping may result.

3.3 Results

The graphs presented in figures 7 to 9 show the noise spectra, in a 1Hz bandwidth, for the three experimental arrangements described previously. The spectra plotted in each figure were produced with the following conditions:

- a) No feedback from the interferometers, the intensity feedback signal from the integral photodiode heavily damped by a low pass filter (3 dB point 0.1 Hz). This is the natural spectrum of the laser emission.
- b) No feedback from the interferometer. Amplitude noise feedback from integral photodiode applied.
- c) Feedback from interferometer providing phase noise correction. (Undamped signal from integral photodiode still applied although heavily dominated by interferometer signal under normal operating conditions).

The interferometer output is expressed in dBm relative to a 1 volt rms signal. The resulting phase shift which would occur in an interferometer with an optical path difference of 1cm is also shown.

In addition, figure 7, showing the Michelson results, also includes a graph of the noise output from the interferometer adjusted to zero path difference.

Table 1 compares the reduction in phase noise achieved from the three experimental arrangements at a frequency of 1KHz.

4. DISCUSSION OF EXPERIMENTAL RESULTS ON ACTIVE PHASE NOISE CONTROL

The results undoubtedly demonstrate that active control of the laser current, by feedback from an interferometer, leads to a significant improvement in the level of laser phase noise. However, any results obtained using the same interferometer to produce the feedback signal and monitor the laser output should be treated with caution as environmental vibrations causing variations in the interferometer mirror spacings will be corrected for.

That environmental vibrations affect the interferometer output is illustrated by comparing results obtained using the Michelson, adjusted to zero path difference without feedback, with those obtained with feedback and a path difference of 26.6cm (figure 7). At low frequencies, the former actually measures more noise, even though of course with a balanced interferometer contributions due to laser phase noise must be absent. This low frequency noise is thought to be due to local environmental vibrations. When feedback is applied, with the unbalanced interferometer, these are compensated for by appropriate changes in the laser emission frequency. As expected, noise reduction measured with a separate interferometer is less than that measured in the feedback loop.

It is considered that the results obtained using separate monitoring and control interferometers are the more realistic for real sensing systems. Comparing the results presented in figures 8 and 9, phase noise reduction is approximately 8dB less when measured with a separate interferometer. However, an improvement of up to 45dB was still observed and the resulting phase shifts that would be produced in an unbalanced interferometer are $1\mu\text{rad.cm}^{-1} \cdot \text{Hz}^{-1/2}$ for frequencies greater than 100 Hz, and less than $0.2\mu\text{rad.cm}^{-1} \cdot \text{Hz}^{-1/2}$ for frequencies greater than 1KHz.

Surprisingly, simple intensity feedback from the integral monitor photodiode of the laser was found to reduce the phase noise by up to 29dB. This was a considerably greater reduction than that observed by Dandridge and Tveten (5), who reported virtually no improvement with intensity feedback. It is possible to speculate that a Fabry-Perot cavity may have been formed between the laser chip and the integral monitor photodiode, resulting in a frequency dependent photodiode output.

Reflections from all the interferometers back into the laser cavity were found to cause unpredictable multimode operation, with an associated increase in phase noise. Although with careful alignment (or perhaps more strictly, misalignment) this could be eliminated, it is anticipated that an anti-reflection coated optical isolator would have to be incorporated to eliminate the problem completely.

5. CONCLUSIONS

The feasibility of using passive optical feedback from an array of spliced optical fibres to reduce laser phase noise has been demonstrated but, as yet, not confirmed in practice. The use of random lengths of fibre is attractive as it would be particularly simple to implement.

Active feedback control of the laser drive current reduced the phase noise by up to 45dB and the resulting phase shift, which would be produced in an unbalanced interferometer is less than $1 \mu\text{rad. cm}^{-1} \cdot \text{Hz}^{-1/2}$ for frequencies greater than 100Hz. This is considered to be sufficient for sensor applications.

REFERENCES

1. Goldberg, L. et al. "Spectral Characteristics of Semiconductor Lasers with Optical Feedback" IEEE J. Quantum Electronics, QE-18 (4) pp555-564 (April 1982).
2. Epworth R.E. et al. "A Practical 1.3 μm Semiconductor Source with Significantly Better Short Term Coherence Than a Gas Laser" 10th European Conf. On Optical Communication. Stuttgart, pp132-3 (Sept. 1984)
3. Cobb KW & Culshaw B. "Reduction in Optical Phase Noise in Semiconductor Lasers". Electronics Letts, 18 (8) pp 336-7 (1982)
4. Dandridge A. et al. "Fibre Optic Interferometric Sensor Development at NRL". 1st Int conf. on Optical Fibre Sensors. IEE London. pp48-52 (1983).
5. Dandridge A & Tveten A.B. "Properties of Diode Lasers With Intensity Noise Control". Appl. Optics, 22 pp. 310-2 (1983).

© THE PLESSEY COMPANY PLC

TABLE 1

EXPERIMENTAL ARRANGEMENT	PHASE NOISE AT 1KHz (1Hz BW) dBV			
	FREE RUNNING LASER	AMPLITUDE NOISE FEEDBACK VIA INTEGRAL PHOTO- DIODE	AMPLITUDE & PHASE NOISE FEEDBACK	(c-a) PHASE NOISE DE- CREASE PRODUCED BY CURRENT FEED- BACK FROM THE CONTROL INTER- FEROMETER
	a	b	c	
SINGLE MICHELSON (26.5 cm PATH IMBALANCE)	-55	-80	-100	45
SINGLE FABRY- PEROT	-48	-78	-100	52
SEPARATE CONTROL & MONITOR FABRY- PEROTS	-40	-69	-85	45

ALL FIGURES \pm 3dBV

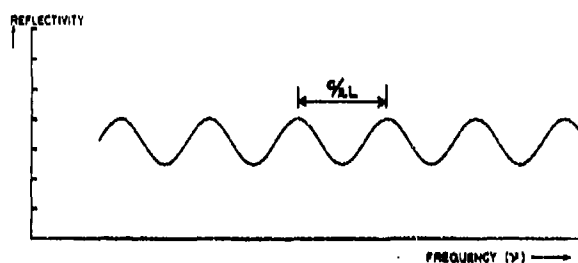


FIG. 1 REFLECTIVITY FUNCTION OF A FABRY-PÉROT CAVITY FORMED BY THE LASER OUTPUT MIRROR AND ONE ADDITIONAL PARALLEL REFLECTOR

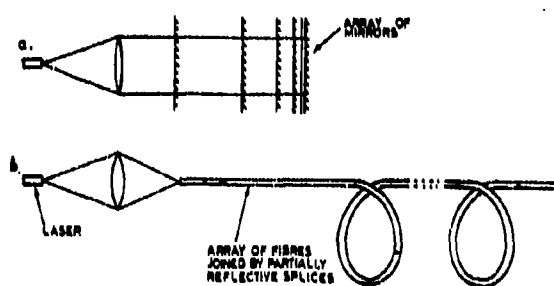


FIG. 2 PROPOSED TECHNIQUES TO REDUCE LASER PHASE NOISE USING PASSIVE OPTICAL FEEDBACK

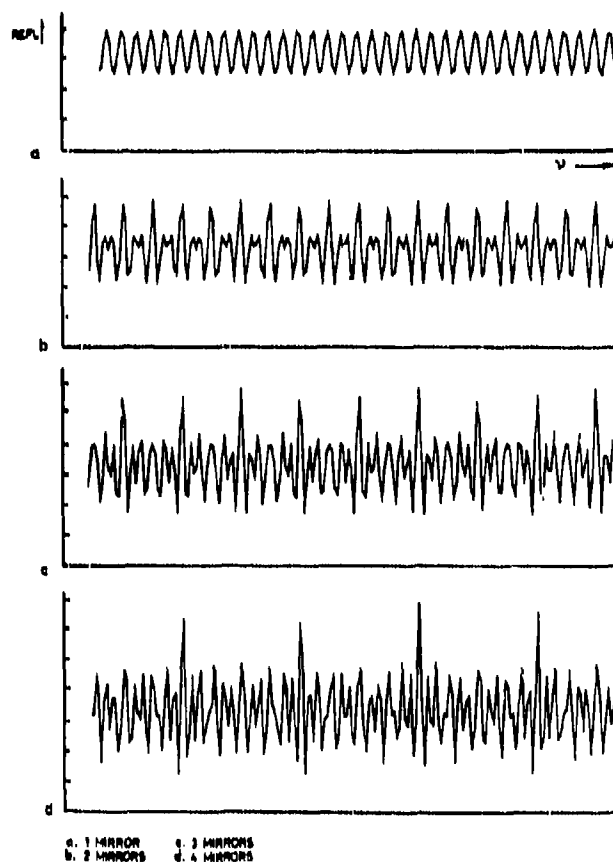


FIG. 3 REFLECTIVITY OF MIRROR ARRAY SHOWN IN FIGURE 2a.

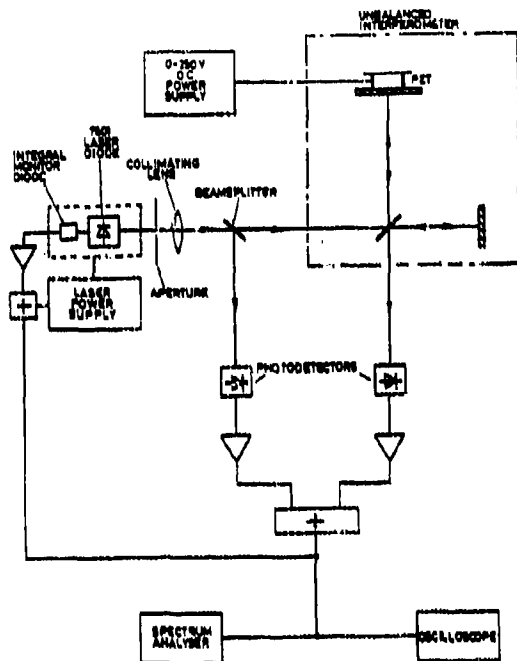


FIG. 4 SEMICONDUCTOR LASER PHASE NOISE REDUCTION USING FEEDBACK FROM A MICHELSON INTERFEROMETER

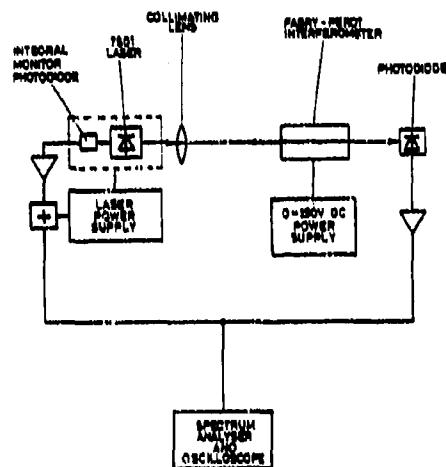


FIG. 5 SEMICONDUCTOR LASER PHASE NOISE REDUCTION USING FEEDBACK FROM A FABRY-PÉROT INTERFEROMETER

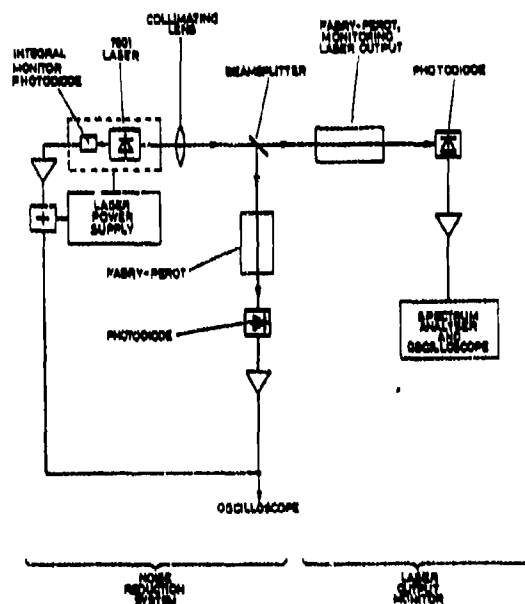


FIG. 6 SEMICONDUCTOR LASER PHASE NOISE REDUCTION USING FEEDBACK FROM A FABRY-PÉROT INTERFEROMETER WITH A SEPARATE MONITORING INTERFEROMETER

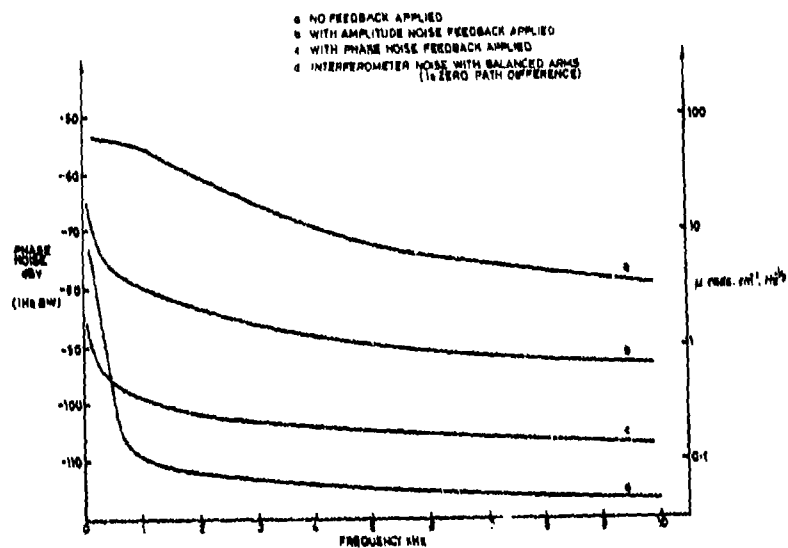


FIG. 7 LASER PHASE NOISE REDUCTION ACHIEVED USING FEEDBACK FROM A MICHELSON INTERFEROMETER WITH A 25-cm OPTICAL PATH DIFFERENCE

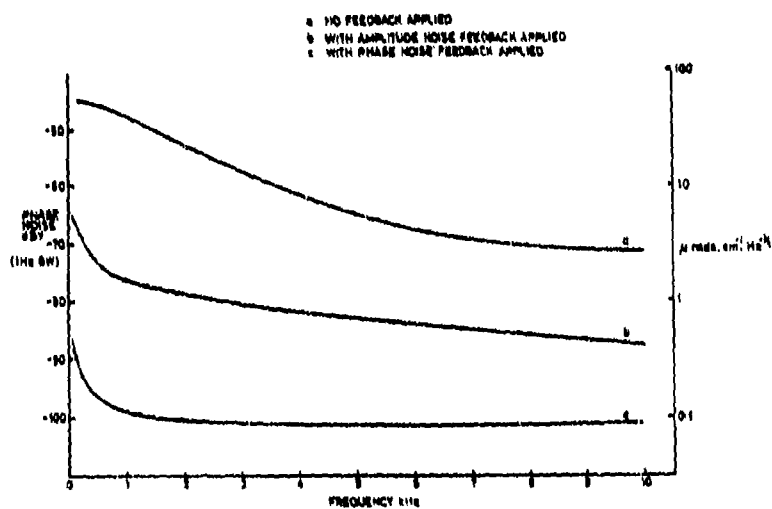


FIG. 8 LASER PHASE NOISE REDUCTION ACHIEVED BY USING FEEDBACK FROM A FARRY-PIROT INTERFEROMETER

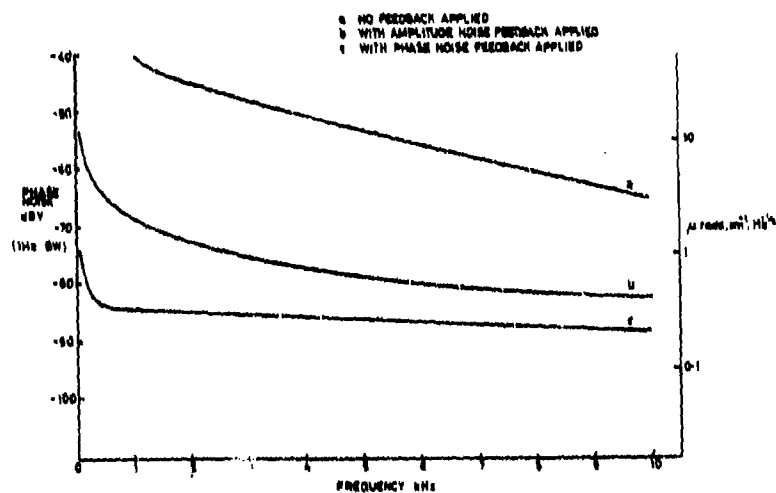


FIG. 9 LASER PHASE NOISE REDUCTION ACHIEVED USING FEEDBACK FROM A FARRY-PIROT INTERFEROMETER, SEPARATE MONITORING INTERFEROMETER

OPTICAL QUADRATURE DEMODULATOR FOR COHERENT DETECTION AND SENSOR APPLICATIONS

S. F. Watanabe, A. A. Joseph, H. B. Turner
S. A. Holmes, J. T. Freidah
McDonnell Douglas Astronautics Company
5301 Bolsa Avenue
Huntington Beach, CA 92647

ABSTRACT

A new device has been designed, built and demonstrated which provides exceptional performance in a very small, potentially very low cost unit. Balanced quadrature detection for homodyne or heterodyne detection of phase or frequency encoded signal information is accomplished with microradian phase sensitivities over a broad range of environments and for a broad dynamic range of signal levels and frequencies. Results of current development testing will be presented along with brief discussions of potential applications to coherent detection for interferometers, sensors, and communications.

INTRODUCTION

An innovative optical mixer/detector has been developed to provide balanced quadrature demodulation of optically encoded phase, frequency, and/or amplitude signals. The original motivation was to develop a compact, very sensitive device for detecting microradian optical phase shifts in fiber-optic interferometric sensors.

FIBER-OPTIC SENSOR APPLICATION

A typical fiber sensor, based on Mach-Zehnder interferometry (Figure 1), detects the influence field of interest (e.g., pressure, temperature, electric/magnetic field, etc.) by incorporating a transduction mechanism into the sensing fiber which generates an optical phase shift in response to that influence (Reference 1). For our sensor applications to date, the important design requirements have been that the device accept optical fiber inputs at AlGaAs laser wavelengths (830 nm), achieve very low phase detection noise floors (e.g. $<1 \mu\text{rad}/\sqrt{\text{Hz}}$) operate over a moderate temperature range ($0^\circ\text{C} < T < 60^\circ\text{C}$), and provide quadrature detection from DC to 100 kHz frequencies.

OPTICAL DEMODULATION

These performance levels have now been achieved using a proprietary optical demodulator concept to convert the optical phase signal into four balanced, quadrature electrical outputs proportional to $\pm \cos\theta$ and $\pm \sin\theta$. The construction of this device is extremely simple and the most costly element is the custom photo-detector. Obvious advantages of this design are its small size (Figure 2) and potentially low production cost -- both are consequences of the basic design simplicity. Another benefit of the compact package is an added degree of mechanical stability against optical misalignment in extreme thermal, shock, and vibration environments.

Great care is taken in the design to suppress back-reflection from the fiber ends or any other elements within the optical demodulator package, due to the extreme susceptibilities of most laser types to back-reflection. Excessive phase noise and strong parasitic oscillations will generally occur in the presence of back-coupled power levels in excess of only about 0.02% (Reference 2) of output power.

Frequency response of the silicon detector (1 mm diameter) has been measured to be in excess of 50 MHz; with smaller geometries and specific design attention to high-speed, Si, GaAs and other detector types (e.g., InGaAsP, Ge for longer wavelength carriers) can be made to perform at GHz frequencies if required.

ELECTRONIC DEMODULATION

The demodulation electronics (Figure 3), rather than the detector/preamps, will usually determine system dynamic range and frequency response. Circuits implemented for sensor applications are demonstrating 120 dB single frequency dynamic range with 50 kHz frequency response.

The benefits of balanced mixing are apparent in a measured 20 dB rejection of noise due to optical source amplitude fluctuations. This is essential to the achievement of quantum-limited performance for any coherent detection application. In order to enhance the packaging versatility of this passive demodulation technique, an integrated circuit (Figure 4) is under development to provide a compact, environmentally stable, self-contained unit for broad application to interferometric sensor, coherent communication, and high bandwidth optical-fiber telemetry applications.

DEMODULATION PERFORMANCE

Data in Figure 5 are from an optical demodulator fabricated and tested for use at audio frequencies with a fiber-optic acoustic sensor. Unfortunately, noise levels measured at frequencies below about 100 Hz are due to background laboratory acoustics and seismic levels. For frequencies above 500 Hz, the test system is laser phase noise limited at a level approximately 20 dB above demodulation shot-noise limits. For the AlGaAs laser diode types used in this system, this noise level is expected to vary like $(\text{frequency})^{1/2}$ (References 3 and 4). In a coherent detection system operating at the shot-noise limit, e.g., through the use of a strong local oscillator field, the noise level will decrease as $(\text{frequency})^{-1}$. The saturation dynamic range measurements shown in Figure 5 suggest that the demodulation dynamic range under shot-noise limited operation is on the order of 120 dB. Signal saturation occurs first in the multiplier function (refer to Figure 3) and exhibits a $1/f$ characteristic due to the differentiation function which takes place just prior to the multiplier stages.

In order to cope with optical modulation depth variations due to optical misalignment or polarization fading due to environmental effects, an AGC function has been incorporated which acts to hold constant, the phasor magnitude measured at the quadrature demodulator outputs. With this in place, system gain with a demodulator, such as shown in Figure 2, is routinely held constant to within ± 0.5 dB over a full 0° to 60°C external temperature range. The data of Figure 6 demonstrates this signal level stability using a 1 mrad, rms tonal operating at 1 kHz.

OTHER APPLICATIONS

Several frequency and phase demodulation applications for the compact fiber-optic demodulator are shown in Figure 7. The most obvious application is phase-shift-keyed (PSK) or frequency-shift-keyed (FSK) digital data transmission at very high bit rates over optical fiber links.

An important application arises when a local oscillator arrangement is used for homodyne or heterodyne detection. By sampling the signal carrier and the local oscillator, the optical quadrature demodulator can be used as the phase detector in a feedback loop which continuously adjusts the local oscillator to track the signal carrier. It is expected that such techniques will be required to reduce laser phase noise to the small bit-jitter tolerances (approximately $10^\circ - 15^\circ$) allowable for low error rate coherent digital communication (Reference 5).

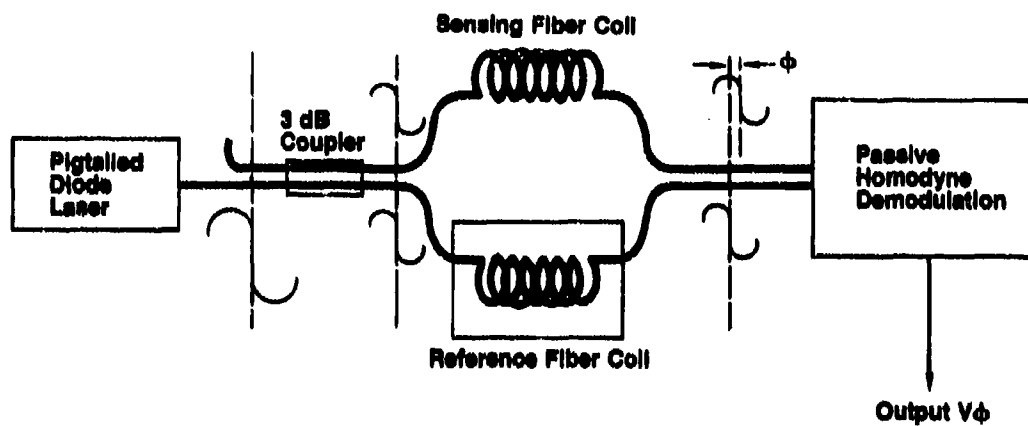
A convenient means for direct homodyne detection of a frequency modulated signal is to introduce a path length difference, ΔL , between two inputs of the same signal, $\Delta\omega(t)$, to the mixer/demodulator; the output is just proportional to $\Delta L \cdot \Delta\omega(t)$.

Multiplexed signals may be detected in several different straightforward configurations using the grating device. Multiple local oscillators and, possibly multiple optical demodulators, may be required when optical multiplexing is used; i.e., channel spacings greater than about 10 nm, as dictated by current optical filter isolation capabilities. More typically, it is expected that the full advantages of coherent detection will be obtained by the use of electronic multiplexing onto a single optical carrier; i.e., channel spacings of less than a GHz are easily demultiplexed at the intermediate frequencies of a heterodyne system. Something on the order of ten thousand "electronic" channels would then reside within each "optical" channel.

The optical demodulator is proving to be of great value wherever low-cost, self-contained, compact, passive balanced quadrature optical demodulation is a requirement. Interferometry, interferometric sensors, and coherent communications are likely to benefit most immediately from the availability of this new device.

REFERENCES

1. T. G. Giallorensi, et al, "Optical Fiber Sensor Technology," IEEE J. Quant. Elec., Vol. QE-16, April 1982, p. 626.
2. R. O. Miles, et al, "Low-Frequency Noise Characteristics of Channel Substrate Planar GaAlAs Laser Diodes," Appl. Phys. Lett., Vol. 38, June 1981, p. 848.
3. A. Dandridge and A. B. Tveten, "Phase Noise of Single-Mode Diode Lasers in Interferometer Systems," Appl. Phys. Lett., Vol. 39, October 1981, p. 530.
4. L. Goldberg, et al, "Spectral Characteristics of Semiconductor Lasers with Optical Feedback," IEEE J. Quant. Elec., Vol. QE-18, April 1982, p. 555.
5. P. S. Henry, "The Promise of Coherent Transmission," Lightwave, May 1983, p. 12.



■ Typical Requirements		Optical Fiber
Passive Quadrature Demodulation:	Implementation	
Noise Floor:		$< 1 \mu\text{rad}/\sqrt{\text{Hz RMS}}$
Dynamic Range:		$> 120 \text{ dB in } 1 \text{ Hz}$
Frequency Response:		$\text{DC} < f < 100 \text{ kHz}$
Operating Temperature:		$0^\circ\text{C} < T < 60^\circ\text{C}$

Figure 1. Fiber-Optic Interferometric Sensor Demodulation

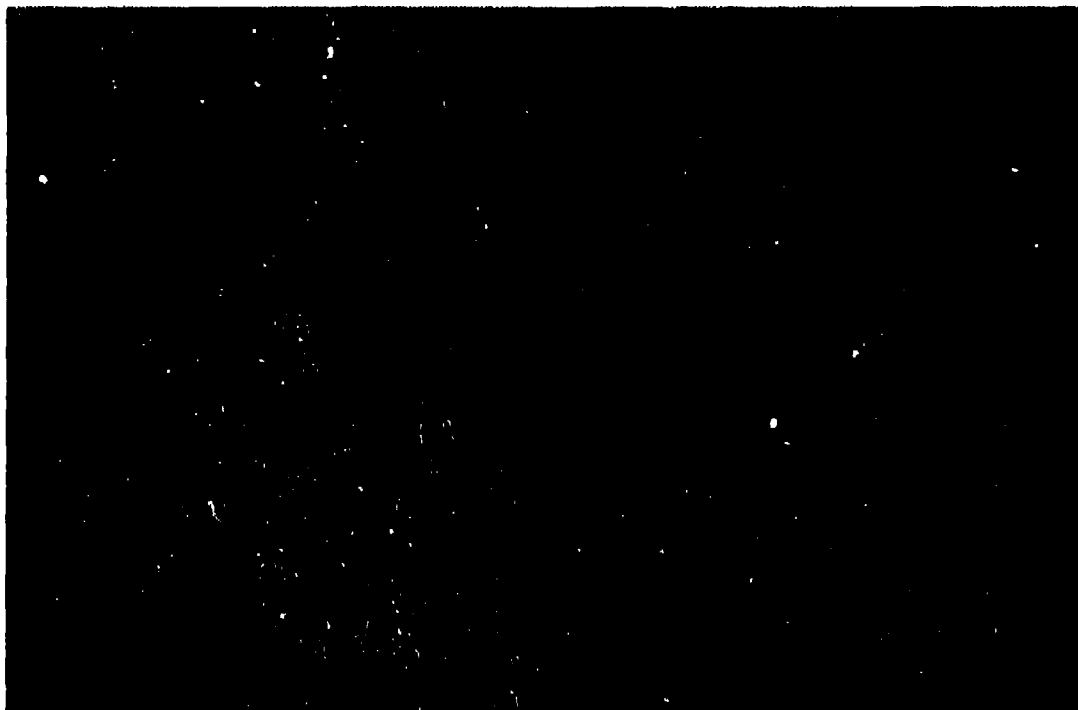
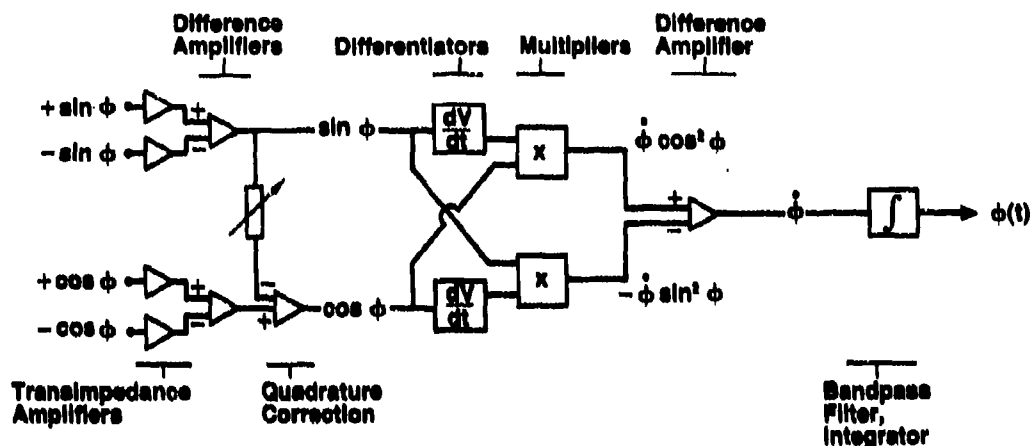


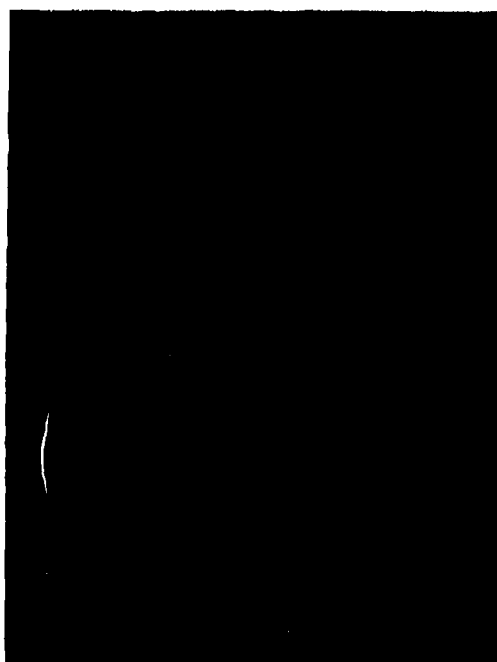
Figure 2. Ruggedized Optical Quadrature Demodulator



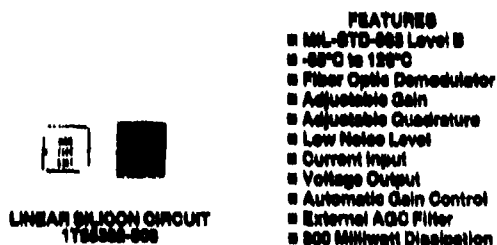
■ Demonstrated Performance:

- Dynamic Range: ~120 dB in 1 Hz Band (0.5% THD)
- Frequency Response: 10 Hz < f < 50 kHz Electronics
f > 50 MHz SI Detectors
- Amplitude Noise Rejection ~20 dB

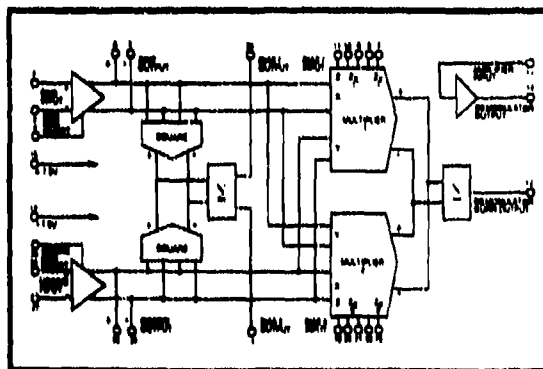
Figure 3. Balanced Quadrature Demodulation Electronics



BREAD BOARD ELECTRONICS



- #### FEATURES
- MIL-STD-883 Level B
 - -55°C to 125°C
 - Fiber Optic Demodulator
 - Adjustable Gain
 - Adjustable Quadrature
 - Low Noise Level
 - Current Input
 - Voltage Output
 - Automatic Gain Control
 - External AGC Filter
 - 200 mWatt Dissipation



BLOCK DIAGRAM

Figure 4. Passive Homodyne Demodulator Electronics

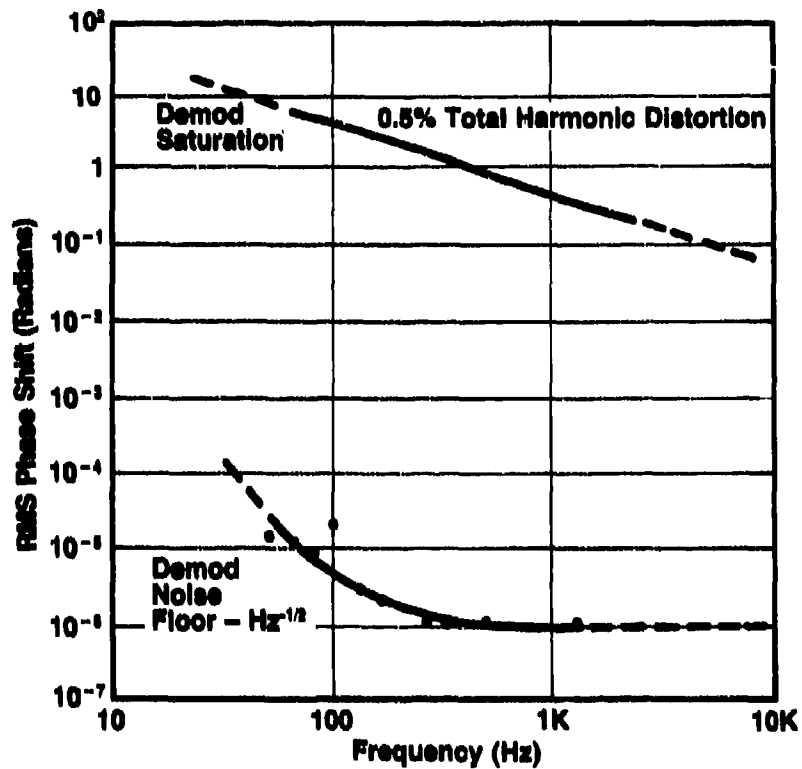


Figure 5. Optical Quadrature Demodulator Noise Data

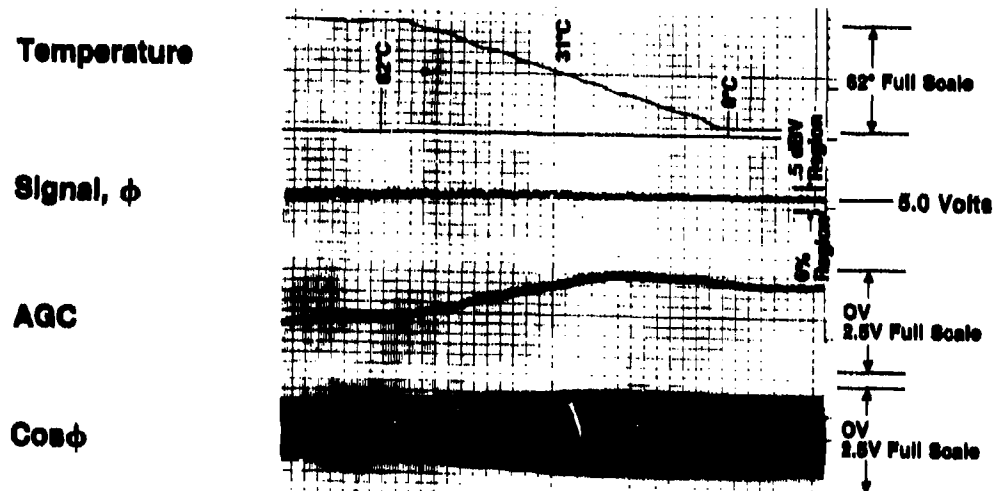


Figure 6. Optical Quadrature Demodulator Thermal Stability

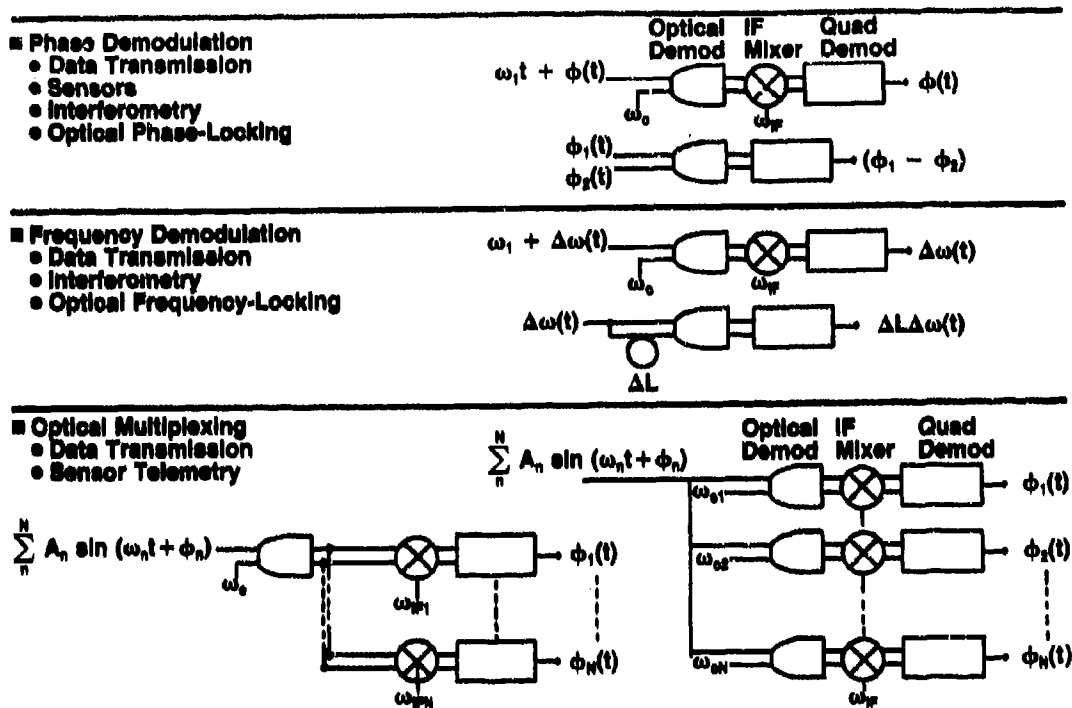


Figure 7. Coherent Detection Applications

DISCUSSION

T.Bakker, Ne

What is the influence of acoustical and mechanical vibrations on the performance of the optical quadrature demodulator you discussed?

Author's Reply

None observed to date, but no extensive environmental testing has been completed.

EFFECTS OF OPTICAL FEEDBACK ON THE PERFORMANCE OF HIGH DATA RATE SINGLE-MODE FIBER SYSTEMS

R. Keil, K. Mathyssek, E. Hörmann
Research Laboratories of Siemens AG
Otto-Hahn-Ring 6, D-8000 München 83, W-Germany

ABSTRACT

This paper presents performance measurements data accomplished on a 678 Mbit/s single-mode fiber optic transmission system for various laser diode structures and most importantly under different near- and far-end optical feedback conditions. Specifically, for two integral coupling schemes i.e. the drawn fiber taper with a lens and hemispherically ended graded index fiber lens (GRINF-lens) the near-end optical feedback have been modelled and simple method for its experimental assessment has been given. Feedback induced variations of lasing spectra and of mode partition noise and their influences on bit error rate (BER) data have been experimentally determined for a dispersive single-mode fiber transmission link with the two coupling arrangements.

Comparative measurements have been done with a butt-coupled fiber and with a non-dispersive fiber system. Furthermore, far-end reflections from a connector joint and their quantitative influence on BER data have been investigated.

INTRODUCTION

One of the main problems of single mode fiber communication systems for high data rates (>500 Mbit/s) is the modification of the intrinsic laser diode characteristics by optical feedback. Depending on both the intensity and phase of the light fed back into the laser mode strong changes of the threshold current, emission wavelength, spectral width and the line width of the longitudinal modes arise [1-4].

The change of the laser noise [5-8] and the mode partition noise [9,10] according to phase and intensity fluctuations of the reflected light deteriorates the bit error rate performance of high data rate systems [11,12]. In case of a laser diode coupled to a single mode fiber with a lens on its end optical feedback is mainly caused by reflections from the fiber lens surface, fiber connectors, fiber splices and fiber end. Coherent reflections from the near fiber end (fiber lens) cause both a shift and a broadening of the laser spectra as well as a change in the laser output power. The latter also occurs in spite of the stabilizing means of the laser output power realized by a monitor photodiode placed at the rear laser facet. Reflections from the far fiber end induce an enhancement of the intensity noise and especially of the mode partition noise.

THEORETICAL DETERMINATION OF NEAR-END OPTICAL FEEDBACK

Fig. 1 shows schematically a laser diode coupled to a single-mode fiber by a fiber lens. Yet different kinds of fiber lenses have been investigated with respect to the above mentioned feedback effects [13-17]. Assuming a spherically shaped lens surface the ratio of the reflected power P_b (coupled back into the laser mode) to the laser output power P_f is given by [18]

$$\frac{P_b}{P_i} = \frac{r_2}{\left[1 + \left(\frac{k w_x^2}{2}\right) \cdot \left(\frac{1}{R_x} + \frac{1}{R_L}\right)\right]^2 \cdot \left[1 + \left(\frac{k w_y^2}{2}\right) \cdot \left(\frac{1}{R_y} + \frac{1}{R_L}\right)\right]^2} \quad (1)$$

with the lens radius R_L , the power reflection coefficient at the lens surface r_2 and the wave number $k = 2/\lambda_0$ with λ_0 , being the vacuum wavelength. w_x , w_y and R_x and R_y denote the beam width spot radii and the radii of curvature of the phase front of the laser field strength at the lens vertex in the transverse directions, respectively /19/.

Fig. 2 represents the calculated results of the optical feedback ratio $\eta_{FB} = 10 \cdot \lg P_b/P_i$ due to reflection at the fiber lens surface versus the laser-lens distance d that is to be expected for various coupling arrangements as depicted in Fig. 3. The optimum distances d_{opt} are indicated by circles in Fig. 2. For an optimally coupled drawn fiber taper with a fused lens ($R_L \approx 10 \mu\text{m}$, $d_{opt} \approx 15-20 \mu\text{m}$, $r_2 \approx 0.04$) as shown in Fig. 3a the optical feedback amounts to roughly $\eta_{FB} \approx -40$ dB. Whereas for a fiber taper with a high-index microlens ($R_L \approx 12 \mu\text{m}$, $d_{opt} \approx 10-15 \mu\text{m}$, $r_2 \approx 0.09$) as outlined in Fig. 3b the calculated feedback is approximately $\eta_{FB} \approx -30$ dB. The third coupling arrangement as drawn in Fig. 3c consists of a piece of spherically shaped graded index fiber (GRINF-lens) being spliced onto the single-mode fiber end /20/. The graded index fiber acts like a quarter-pitch graded index lens. To obtain the optimum radius of curvature of the hemispherical lens, the graded index fiber (GIF) is etched down to the proper end diameter and finally melted to a lens in an arc discharge. For some typical parameters ($R \approx 25 \mu\text{m}$, $d \approx 50-70 \mu\text{m}$, $r_2 \approx 0.04$ and a GIF with N.A. ≈ 0.14) the expected feedback assumes the value of $\eta_{FB} \approx -50$ dB.

EXPERIMENTAL EVALUATION OF NEAR-END OPTICAL FEEDBACK

The influence of the coherent reflections on the power and spectrum fluctuations depends on the distance d , i.e. on the length of the external resonator cavity formed by the laser mirror and the first fiber lens surface. The external resonator changes the intrinsic laser mirror reflectivity r_1 as a periodic function of d and so does the output power (Fabry-Perot fluctuation).

Neglecting the multiple reflections an effective reflectivity r_{eff} may be derived and is given by /13/

$$r_{eff} = \left[\sqrt{r_1} \cdot (1 - r_1) \sqrt{\epsilon} \right]^2 + 4(1 - r_1) \sqrt{r_1} \epsilon \cdot \cos^2(kd) \quad (2)$$

with $\epsilon = P_b/P_i$.

The ratio between the laser output power P_i and the monitor power P_m at the rear laser facet is expressed as

$$\frac{P_i}{P_m} = \frac{1 - r_{eff}}{1 - r_1} \frac{\sqrt{r_1}}{\sqrt{r_{eff}}} \quad (3)$$

Inserting equation (2) into (3) and assuming a power stabilised laser operation ($P_m = \text{const.}$) we attain an expression for a periodic variation of the laser power

$$\frac{\Delta P_i}{P_{i0}} \approx \frac{2\sqrt{\epsilon}(1 + r_1)}{\sqrt{r_1}} \quad (4)$$

where P_{f0} is the laser output power without feedback. Fig. 4 shows the measured coupling efficiency η as a function of the laser-lens distance d for a typical drawn fiber taper with a fused lens and for a GRINF-lens coupling scheme. The maximum coupling efficiency for both is about 40 %. The optimum coupling distance d_{opt} is about 18 μm and 45 μm , respectively. The Fabry-Perot fluctuation with a period of $\lambda_0/2$ is visibly superimposed onto the axial alignment tolerance curve. It is a measure for the optical feedback and may be used to quantize it. Setting the measured ripple $\Delta P_f/P_{f0}$ into equation (4) we can easily evaluate the feedback parameter

$$\eta_{FB} = 10 \cdot \lg \frac{P_f}{P_i} \quad (5)$$

Corresponding to different coupling efficiencies the experimentally determined peak-to-peak amplitude of the ripple $\Delta P_f/P_{f0}$ for fiber tapers with fused lenses was found in a range of about 4-7 %, i.e. -42 dB to -38 dB for η_{FB} , respectively. For fiber tapers with high index lenses we measured $\Delta P_f/P_{f0}$ of about 7-12 % or in feedback terms $\eta_{FB} \approx -38$ dB to -36 dB. For the coupling scheme with a GRINF-lens the $\Delta P_f/P_{f0}$ ratio ranges between 1-2 % or $\eta_{FB} \approx -55$ dB to -51 dB, respectively. For comparison, in the case of a plane ended fiber the Fabry-Perot fluctuation ratio amounts typically to $\Delta P_f/P_{f0} \approx 30$ -35%.

In addition to the fluctuation of the emitted laser power one also observes periodically occurring changes of the spectral width and center wavelength of the optical spectra as the distance between laser and lens is varied. Fig. 5 gives an example of the measured optical spectrum variations with distance for MCRW-laser diode when coupled to a plane-ended fiber. The respective center wavelength positions are marked by a star. One can realize a center wavelength shift $\Delta\lambda$ of about 1.5 nm with a period of $\lambda_0/2 \approx 0.65 \mu\text{m}$. Center wavelength shifts up to 2 nm were observed. For a fiber taper with a fused lens and a GRINF-lens the measured center wavelength excursions were 0.8 nm and 0.6 nm, respectively. The change of the spectral half width σ strongly depends on the laser pump current and on the spectral width of the undisturbed laser. The experimentally observed variations $\Delta\sigma$ amount to 20-30 % where the half width of the optical spectra σ for different laser diodes being made available varies within a range of 1-2 nm.

MEASUREMENT SETUP FOR THE INVESTIGATION OF SYSTEM PERFORMANCE DUE TO OPTICAL FEEDBACK

The measurement setup for the investigations of optical feedback influence on the intensity noise spectra and the bit error rate (BER) performance characteristics is schematically shown in Fig. 6.

For transmission experiments different BH-, CSP- and MCRW-laser diodes with an emission wavelength of approximately 1.3 μm were employed. The lasers were modulated with a 678 Mbit/s pseudorandom pattern generator and the modulation depth was adjusted to 100 % every time. In the course of our experiments two different coupling arrangements, i.e. a fiber taper with a fused lens and a GRINF-lens have been utilized. For comparison a butt-coupled fiber was also used. In order to judge the feedback influence of the fiber lens surface next to the laser diode, the distance d between the laser mirror and that surface is continuously varied by a positioning system with a resolution of smaller than 0.1 μm . The connectorized fiber pigtail roughly 2 m long is coupled to a mono-mode fiber link. The feedback at the connector joint can be either tuned by slightly changing the gap between the fiber end faces or greatly reduced by index-matching.

Two different monomode fibers, i.e. a 30 km fiber with the dispersion minimum at $\lambda_0 = 1.3 \mu\text{m}$ and a 13 km dispersion shifted fiber with a total dispersion of 350 ps/nm at $\lambda_0 = 1.3 \mu\text{m}$ have been alternately implemented in the system. The dispersion shifted fiber has been introduced to evaluate the system degradation caused by the mode partition noise as expected most severely at $1.5 \mu\text{m}$.

The output of the fiber link is coupled into a monochromator and detected with a fast InGaAs/InP-avalanche photodiode and followed by a cascade of broadband amplifiers and an equalizer circuit. Depending on the adjustment of the monochromator one can monitor the intensity noise spectra of either the total received signal or selected longitudinal modes. The bit error rate performance measurements may also optionally be carried out.

FAR-END INFLUENCE OF OPTICAL FEEDBACK ON BER DEGRADATION

According to McCumbers theory [21] the intensity noise spectra, its amplitude and frequency characteristic for a laser diode depends strongly on the number of longitudinal modes examined. Furthermore it is also heavily influenced by the optical feedback (including distributed feedback within the fiber itself) and modulation format the laser diode is driven with.

Fig. 7a presents noise spectra of a continuously operating BH laser diode for both the total modes and for the dominant longitudinal mode. The drawn fiber taper with a lens yielding a coupling efficiency of 40 % has been used and the laser diode was biased at $1.2 I_{th}$. For this particular case the feedback to the laser was set to a maximum by appropriately adjusting the gap at the connector. The clearly visible comb structure in the dominant longitudinal mode is caused by the Fresnel reflection from the external cavity consisting of the fiber pigtail. The mode spacing of the intensity noise peaks is the inverse of the round trip time of the external cavity

$$f = \frac{c}{2nL} \quad (6)$$

where L , c and n are the external cavity length, the vacuum light velocity and the refractive index of the fiber material, respectively. One recognizes that the noise spectrum of the dominant longitudinal mode is not flat within the entire frequency range of the spectrum analyzer. Qualitatively, one observes similar relative noise spectra with a superimposed comb structure for all individual lasing modes the only difference being the noise power. The difference between the noise power for dominant mode (curve 1) and the one for total modes (curve 2) is larger than 20 dB for frequencies up to 600 MHz and is caused by mode partitioning. The intensity noise peaks are also present in the total modes (curve 2) but not so prominent concerning their amplitudes. The difference in their comb characteristics are attributed to strong anti-correlation between the individual longitudinal modes. The mutual compensation of the intensity fluctuations of the laser modes occurs for short or non-highly dispersive fiber lengths as is here the case. From the aforesaid it is evident that the RF spectrum of a single longitudinal mode also contains the information about mode partition noise (MPN). Due to the deteriorating influence of the optical feedback on the optical spectra leading for instance to wavelength shifts of the longitudinal modes accurate in-situ signal-to-noise measurements on single longitudinal modes in the RF-frequency domain are difficult to be carried out and above all then time-consuming.

Therefore, to circumvent this difficulty, we utilize a strong dispersive single mode fiber which abolishes the compensation of the intensity fluctuations due to the different propagation velocities of the individual modes along the dispersive fiber. With increasing fiber length the anti-correlation is lost leading to an increase of the total noise power. Under such experimental conditions the measurement of MPN can even be performed from the RF spectra in total modes. Fig. 7b visualizes such an RF spectrum of a BH-laser diode after a transmission along 13 km dispersion-shifted fiber. By varying the gap of the connector joint the amount of feedback is adjustable to maximum or minimum inducing intensity noise peak changes of approximately 5 dB.

Index-matching fluid in the connector markedly suppresses the comb structure but instead strong low frequency fluctuations in the kHz region of the RF spectrum arise (Fig. 7c). Qualitatively, this seems to be effectuated by one or a combination of the following effects: fiber backscattering, polarization variations and refractive index changes due to ambient temperature changes. However, these fluctuations will be greatly reduced by sinusoidally modulating the laser diode with both an appropriate frequency and modulation amplitude.

Fig. 8 shows both the eye-diagrams (upper row) and the RF intensity noise spectra (lower row) of a CSP laser diode modulated by a 678 Mbit/s NRZ pulse pattern. Two different fiber lengths (30 km non-highly dispersive and 13 km highly dispersive single mode fiber) have been successively used in the system measurements. The receiver power level was kept constant at -30 dBm each time. Fig. 8a-b and Fig. 8c-f demonstrate the results for the two fiber links, respectively. The system performance degradation caused by MPN (Fig. 8c-f) appears quite clearly even in the differences of the eye-pattern's closure. The eye-opening can still more close as indicated in Fig 8e-f when the index-matching fluid is removed from the connector joint and the gap width set then to maximum feedback.

The BER characteristics under various feedback conditions made adjustable at the connector site are shown in Fig. 9. The results pertain to the CSP laser diode. One observes that there is no impairment in the BER-performance after the transmission along 30 km single mode fiber (Fig. 9a,d). On the other hand, BER degrades quite rapidly when 13 km dispersion-shifted fiber is employed as a transmission medium due to MPN /22/. In that particular case, the best BER value is limited to 10^{-4} and belongs to the case of having no optical feedback at the connector joint (Fig. 9c). Fig. 9a,b refer to experimental results under the condition of maximum and minimum optical feedback as selected at the connector joint. One order of magnitude improvement in the BER seems to be feasible by properly adjusting the connectorized fiber ends. The deterioration in the BER-performance manifests itself in the appearance of the floor characteristics at high average optical power levels. Such a behavior and especially the absolute value of BER at high optical power levels is predominantly created by two laser parameters: the MPN k-factor and the width of the spectrum envelope of the time averaged spectrum providing all other relevant system parameters (dispersion and length of the fiber, data rate) being kept constant. Since both vary with optical feedback so does simultaneously the saturation value of BER also. Using the expression relating the power penalty to Q as defined in /23/ the saturation value for Q designated as Q_s may straightforwardly be rewritten as

$$Q_s \sim \frac{1}{k \sigma^2} \quad (7)$$

The inverse proportionality of Q_0 on σ^2 suggests that asymptotic error rate value is more dramatically determined by the spectral width than by the k-factor. Both quantities are susceptible to optical feedback. Measurements indicate that the k-factor as evaluated by the statistical sampling method /24/ increases by up to 30 % depending on the amount of the optical feedback from the connector /10/. Under similar experimental conditions, the lasing spectrum broadens by approximately 40 %. An alternative method for the determination of the MPN k-factor consists as can be seen from equation (7) in measuring both the spectral width and the Q-value in a system under real operating conditions /10,25/.

NEAR-END INFLUENCE OF OPTICAL FEEDBACK ON BER DEGRADATION

Since the optical spectrum width of a laser diode is influenced by the near-end reflections BER degradation resulting from such changes will be expected.

In order to judge the influence of various coupling optics on BER impairment three coupling structures have been chosen and quantitative BER measurements performed. The following coupling arrangements have been looked at: the drawn fiber taper with a fused lens and a fiber with a GRINF-lens both of comparable coupling efficiencies. For comparison purposes BER measurements with a butt-coupled fiber have also been done using the dispersion-shifted fiber in every case.

Fig. 10b,d show the BER characteristics versus the average received optical power for the fiber taper with a lens and the GRINF-lens, respectively. At least for modulation rates up to 678 Mbit/s the improvement in favour of GRINF-lens is not so remarkable. No measurable BER degradation have been produced by slightly traversing (few multiples of $\lambda_0/2$) the fiber lens along the axial direction for both coupling arrangements. Relatively low back reflections for the two coupling techniques are held responsible for this result under that specific modulation rate. On the contrary for the butt-coupling case the saturation value of BER strongly depends on laser-fiber alignment distance and is explainable by the heavily pronounced Fabry-Perot fluctuations superimposed on the axial alignment tolerance plot. Choosing the laser-fiber distance so that the fluctuation is adjusted to maximum or minimum the corresponding BER curves are shown in Fig. 10a or Fig. 10c, respectively. One order of magnitude improvement is attainable. Displacing the fiber by $\lambda_0/8$ for instance from the maximum the resulting BER plot is depicted in Fig. 10e.

CONCLUSION

The system characteristics of a 678 Mbit/s single-mode fiber optic transmission link operating at 1.3 μm are evaluated for various coupling arrangements and under different near-end and far-end optical feedback conditions. In order to judge any coupling optics regarding its optical feedback a simple external resonator model has been used to quantitatively specify the near-end reflections in a new and experimentally easy verifiable manner. The experimental results agree quite well with the theoretical predictions. Spectral variations i.e. center wavelength shifts and spectral envelope broadening due to the adjustable near-end reflections for distinct coupling schemes have been measured. Their implications on the system performance i.e. the BER characteristic have been experimentally evaluated for 13 km highly dispersive single mode transmission link. The highly dispersive single mode fiber in combination with 1.3 μm laser diodes has been employed to simulate fiber optic transmission in

the 1,55 μm wavelength region where laser mode partition noise becomes particularly dominant on attainable repeater spacing. Moreover, far-end reflections occurring at the laser's nearest connector joint and being made adjustable may also degrade the overall link properties. Quantitative BER measurements for various far-end feedback condition have been carried out using the highly dispersive single mode fiber. One order of magnitude BER difference between maximum and minimum feedback setting is realisable. The system measurements have been additionally accomplished with various laser diode structures (BH, CSP and MCRW) resulting in no favourable difference regarding both their sensitivity to optical feedback and their implications on system degradation between any of them at least at that specific modulation rate.

After implementing 30 km of non-highly dispersive single mode fiber into the system no BER degradation have been observed compared to the 5 m fiber length at 678 Mbit/s data rate notwithstanding any near- and far-end optical feedback.

ACKNOWLEDGEMENT

The authors would like to thank Dr. Trommer of Siemens Research Lab. for kindly supplying the fast photodiode used in the experiments, Mr. Marx for performing the spectral shift measurements and Mr. Trimmel for technical support and helpful discussions.

This work has been partly supported by the Federal Department of Research and Technology of the Federal Republic of Germany. The authors alone are responsible for the contents.

REFERENCES

- /1/ Kanada, T.; Nawata, K.:
Injection laser characteristics due to reflected optical power.
IEEE J. Quantum Electr., QE-15 (1979) pp. 559-569
- /2/ Lang, R.; Kobayashi, K.:
External optical feedback effects on semiconductor injection laser properties.
IEEE J. Quantum Electr., QE-16 (1980) pp. 347-355
- /3/ Goldberg, L.; Taylor, H.F.; Dandridge, A.; Waller, J.F.; Miles, R.O.:
Spectral characteristics of semiconductor lasers with optical feedback.
IEEE J. Quantum Electr., QE-18 (1982) pp. 555-564
- /4/ Miles, R.O.; Dandridge, A.; Tveten, A.B.; Taylor, H.F.; Giallorenzi, T.G.:
Feedback induced line broadening in cw channel-substrate planar laser.
Appl. Phys. Lett. 37 (1980) pp. 990-992
- /5/ Spano, P.; Plassolla, S.; Tamburrini, M.:
Theory of noise in semiconductor lasers in the presence of optical feedback.
IEEE J. Quantum Electr., QE-20 (1984) pp. 350-357

- /6/ Hirota, O.; Suematsu, Y.:
Noise properties of injection lasers due to reflected waves.
IEEE J. Quantum Electr., QE-15 (1979) pp. 142-149
- /7/ Hirota, O.; Suematsu, Y.; Kwok, K.-S.:
Enhancement effect of high-frequency noise of injection lasers with reflected waves due to direct modulation.
Opt. Commun. 33 (1980) pp. 136-138
- /8/ Ackat, G.A.; Lenstra, D.; Den Boef, A.J.; Verbeek, B.H.:
The influence of feedback intensity on longitudinal mode properties and optical noise in index-guided semiconductor lasers.
IEEE J. Quantum Electr. QE-20 (1984) pp. 1163-1169
- /9/ Anslow, P.J.; Farrington, J.G.; Goddard, I.J.; Throssell, W.R.:
System penalty effects caused by spectral variations and chromatic dispersion in single-mode fiber-optics systems.
J. Lightwave Techn. LT-2 (1984) pp. 960-967
- /10/ Mathyssek, K.; Hörmann, E.:
Parameter dependence of the mode partition noise and a new method for its evaluation.
11th Europ. Conf. on Opt. Commun., Venice, 1985
- /11/ Wenke, G.; Else, G.:
Investigation of optical feedback effects on laserdiodes in broad-band optical transmission systems.
J. Opt. Commun. 2 (1981) pp. 128-133
- /12/ Enning, B.; Wenke, G.:
Influence of optical feedback on the baseband spectra of a fiber-optic Gbit/s-transmission system.
J. Opt. Commun. 4 (1983) pp. 91-93
- /13/ Bludau, W.; Rossberg, R.:
Characterization of laser-to-fiber coupling techniques by their optical feedback.
Appl. Opt. 21 (1982) pp. 1933-1939
- /14/ Kuwahara, H.; Onada, Y.; Goto, M.; Nakagami, T.:
Reflected light in the coupling of semiconductor lasers with tapered hemispherical end fibers.
Appl. Opt. 22 (1983) pp. 2732-2738
- /15/ Wenke, G.; Zhu, Y.:
Comparison of efficiency and feedback characteristics of techniques for coupling semiconductor lasers to single-mode fiber.
Appl. Opt. 22 (1983) pp. 3837-3844
- /16/ Schwander, T.; Schwaderer, B.; Storm, H.:
Coupling of lasers to single-mode fibres with high efficiency and low optical feedback.
Electron. Lett. 18 (1982) pp. 1026-1028

- /17/ Mathyssek, K.; Wittmann, J.; Keil, R.:
Fabrication and investigation of drawn fiber tapers with spherical
micro lenses.
J. Opt. Commun. (accepted for publication)
- /18/ Keil, R.; Mathyssek, K.; Klement, E.; Auracher, F.:
Coupling between semiconductor laser diodes and single-mode optical fibers.
Siemens Res.- and Dev.-Rep. 13 (1984) pp. 284-288
- /19/ Kogelnik, H.:
Coupling and conversion coefficients for optical modes.
Microwave Research Institute Symposia Series Vol. 14
J. Fox, Ed., Brooklyn, N.Y.: Polytechnic Press, 1964
- /20/ Mathyssek, K.; Keil, R.; Klement, E.:
New coupling arrangement between laser diode and single mode fiber with
high coupling efficiency and particularly low feedback effect.
10th Europ. Conf. on Opt. Commun., 10A5, Stuttgart 1984
- /21/ McCumber, D.E.:
Intensity fluctuations in the output of cw oscillators.
Phys. Rev. 141 (1966) pp. 306-322
- /22/ Lerner, D.S.:
Effects of dispersion in a 565 Mbit/s optical fibre laboratory system.
Electron. Lett. 21 (1985) pp. 187-189
- /23/ Ogawa, K.:
Analysis of mode partition noise in laser transmission systems.
IEEE J. Quantum Electr. QE-18 (1982) pp. 849-855
- /24/ Liu, P.L.; Ogawa, K.:
Statistical measurements as a way to study mode partition in injection
lasers.
J. Lightwave Techn. LT-2 (1984) pp. 44-48
- /25/ Trimmel, H.:
Performance limitations for 565 Mbit/s single-mode fiber systems.
(to be published)

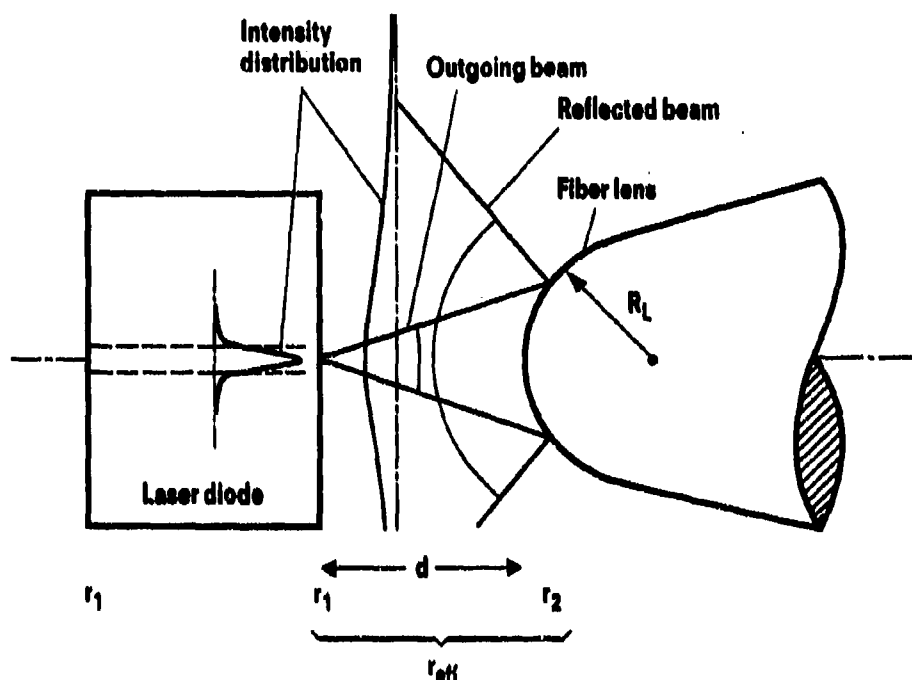


Fig. 1
Schematic representation of laser diode coupled to a tapered hemispherical fiber end for analyzing the near-end optical feedback effects. r_1 , r_2 and r_{eff} are the power reflection coefficients of the laser mirror, fiber lens and effective reflectivity of the external passive resonator, respectively. R_L and d designate the fiber lens radius and external resonator length, respectively.

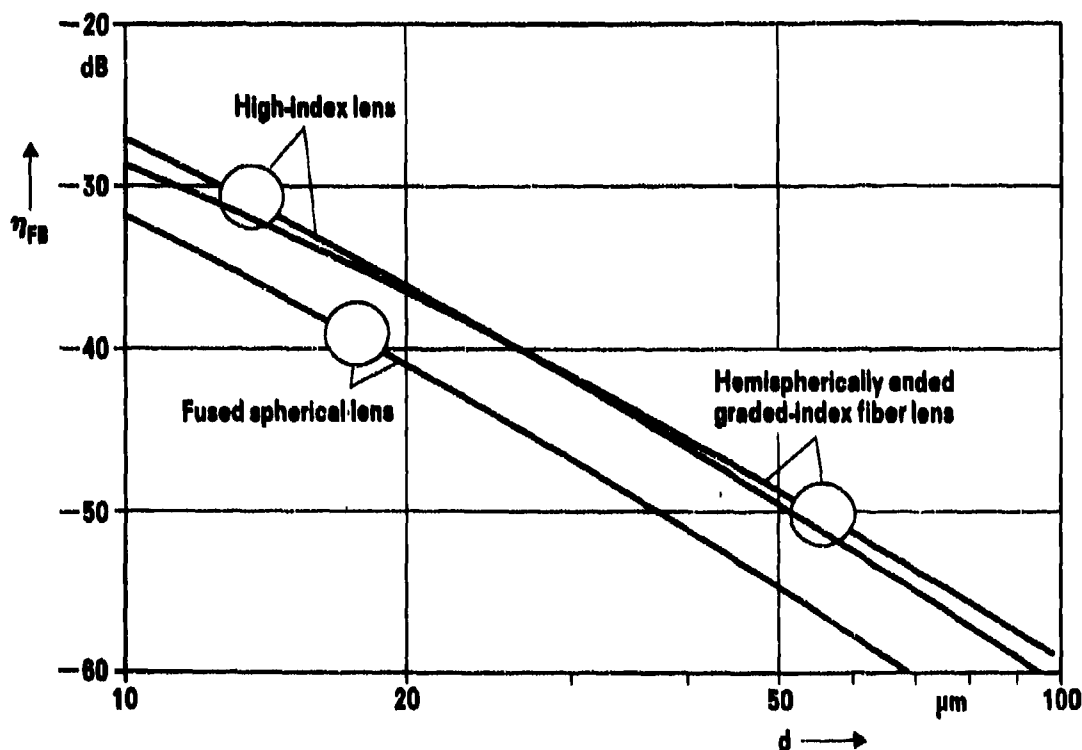


Fig. 2
Calculated feedback efficiency η_{FB} as a function of the external resonator length d for a SM-fiber with a fused spherical lens (Fig. 3a), a taper with a high-index lens (Fig. 3b) and SM-fiber with a spliced hemispherically ended GI-fiber lens (Fig. 3c). The typical optimum coupling distances experimentally obtained are marked by circles.

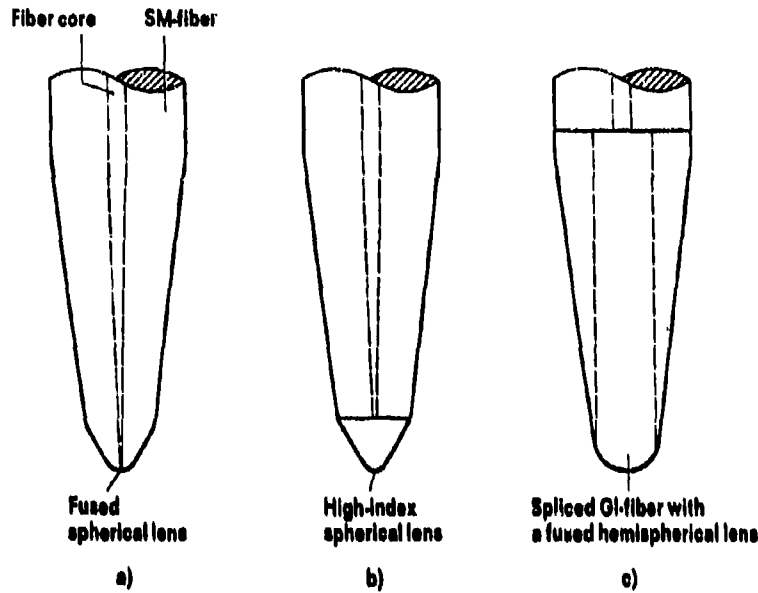


Fig. 3
Schematic representation of the investigated coupling schemes.
a) drawn fiber taper with fused spherical lens
b) drawn fiber taper with high-index spherical lens
c) SM-fiber with spliced hemispherically ended GI-fiber lens

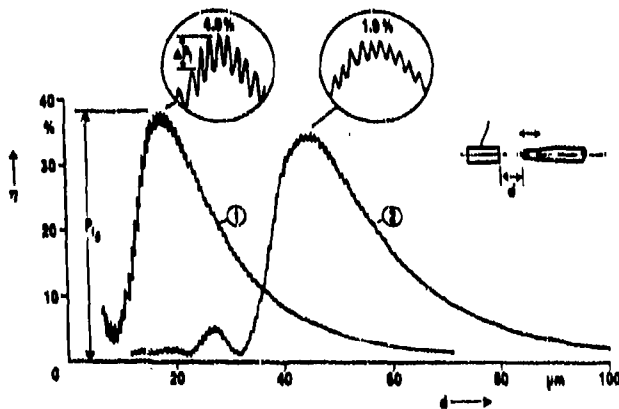


Fig. 4
Measured coupling efficiency versus axial alignment distance d for 1 - drawn fiber taper with fused spherical lens and 2 - hemispherically ended GI-fiber lens. The insets demonstrate the corresponding differences in the power fluctuation effect due to the external Fabry-Perot effect.

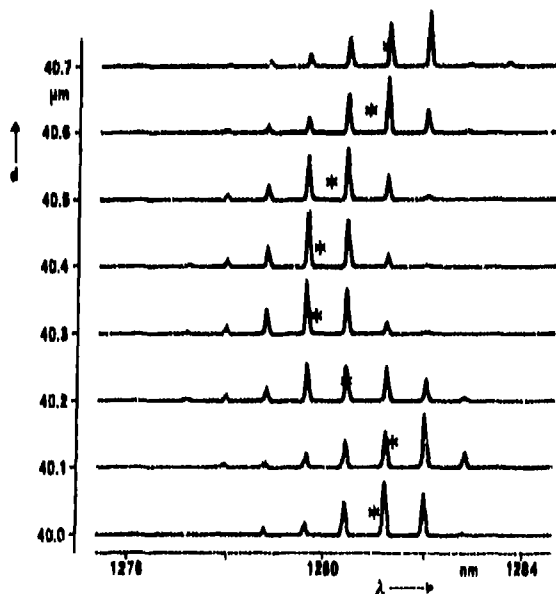


Fig. 5
Center wavelength shifts and envelope broadening of the optical spectrum as a function of the external cavity length for a MCRW laser diode butt-coupled to a SM-fiber. The stars denote the shift of the center wavelength.

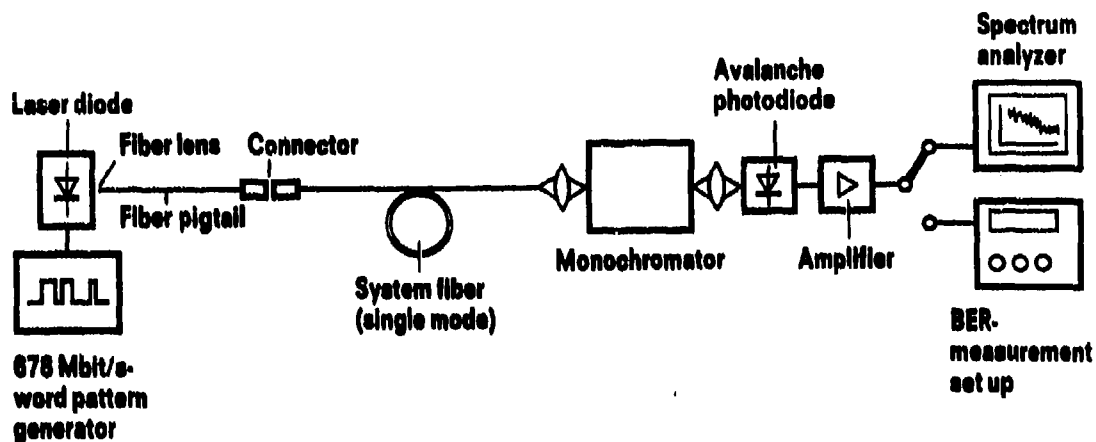


Fig. 6
Measurement set-up for system performance parameter analysis.

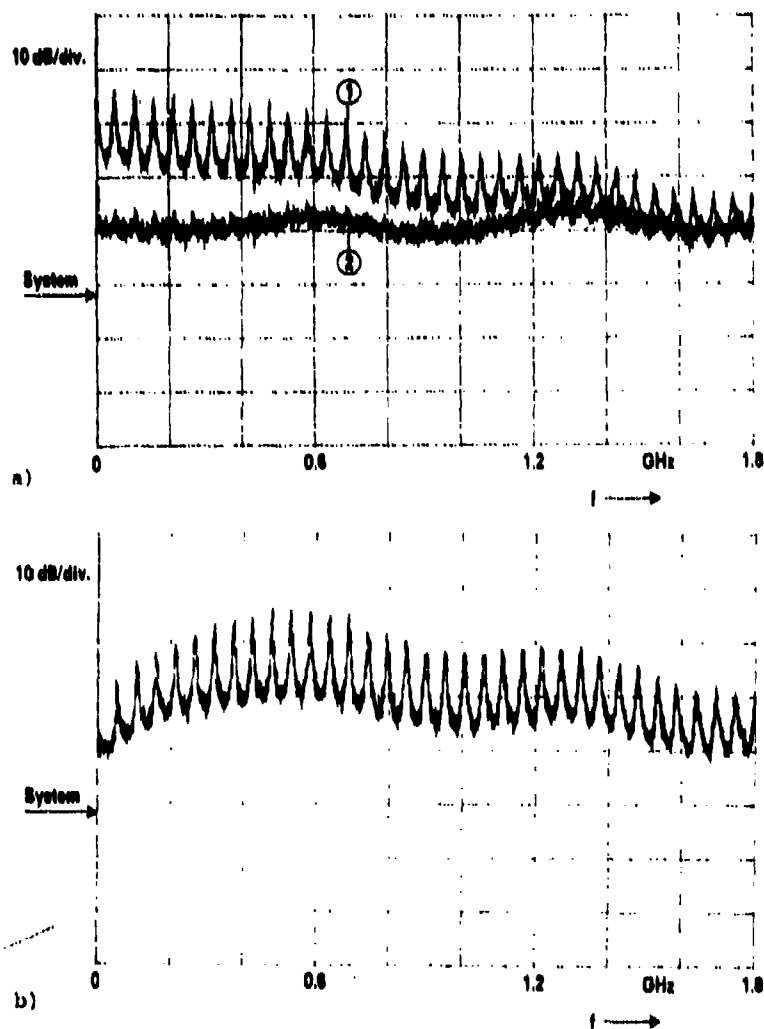


Fig. 7
a) Observed intensity RF noise spectra for 1 - the dominant mode and 2 - total output (all modes) of a SM-laser diode after transmission through 5 m fiber.
b) RF noise spectrum for all modes after transmission along 13 km of highly dispersive SM-fiber. In both cases, the connector joint is adjusted to maximum optical feedback.

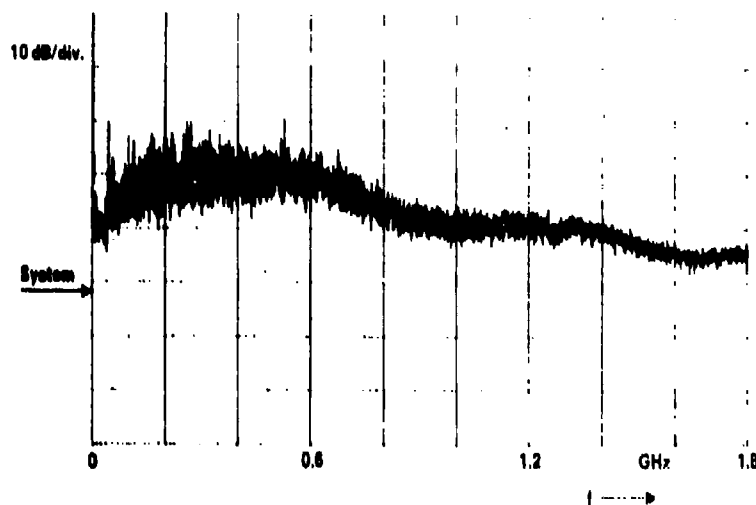


Fig. 7a

c) RF noise spectrum for total power (all modes) after transmission along 13 km of highly dispersive SM-fiber but with index matching fluid in the connector joint.

electrical

optical

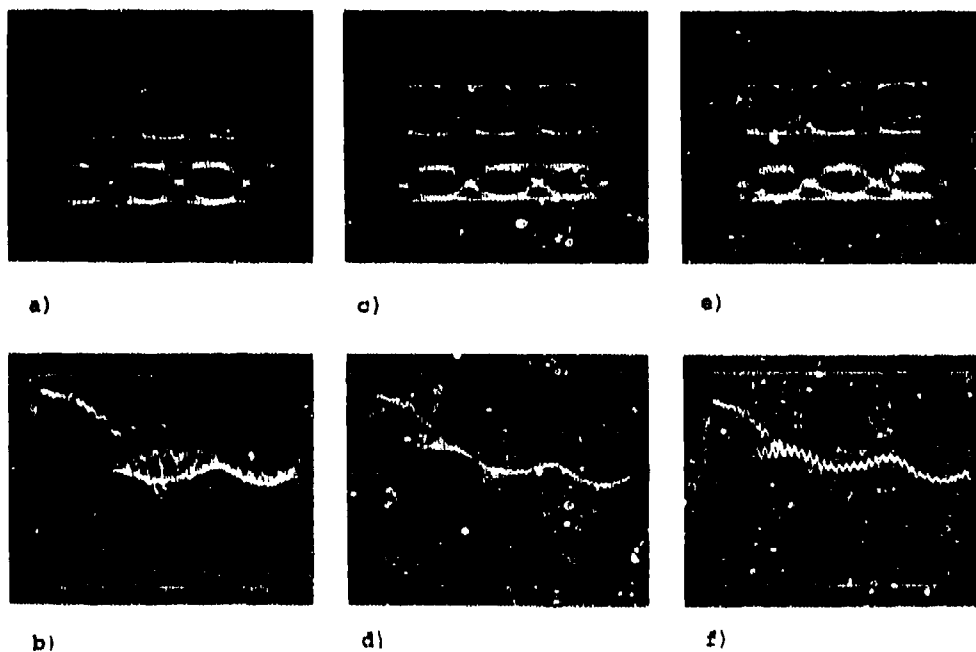


Fig. 8

Eye-diagrams (upper row) and the corresponding RF-spectra of total light output under various experimental conditions. (a-b) and (c-f) depicts the results for 30 km non-dispersive and 13 km strongly dispersive SM-fiber, (a-d) refers to no reflection at the connector, (e-f) as (c-d) but with an optical feedback at the connector set to maximum. The results pertain to a CSP laser diode 100 % depth-modulated at 678 Mbit/s and 1.2 I_{th} bias current.

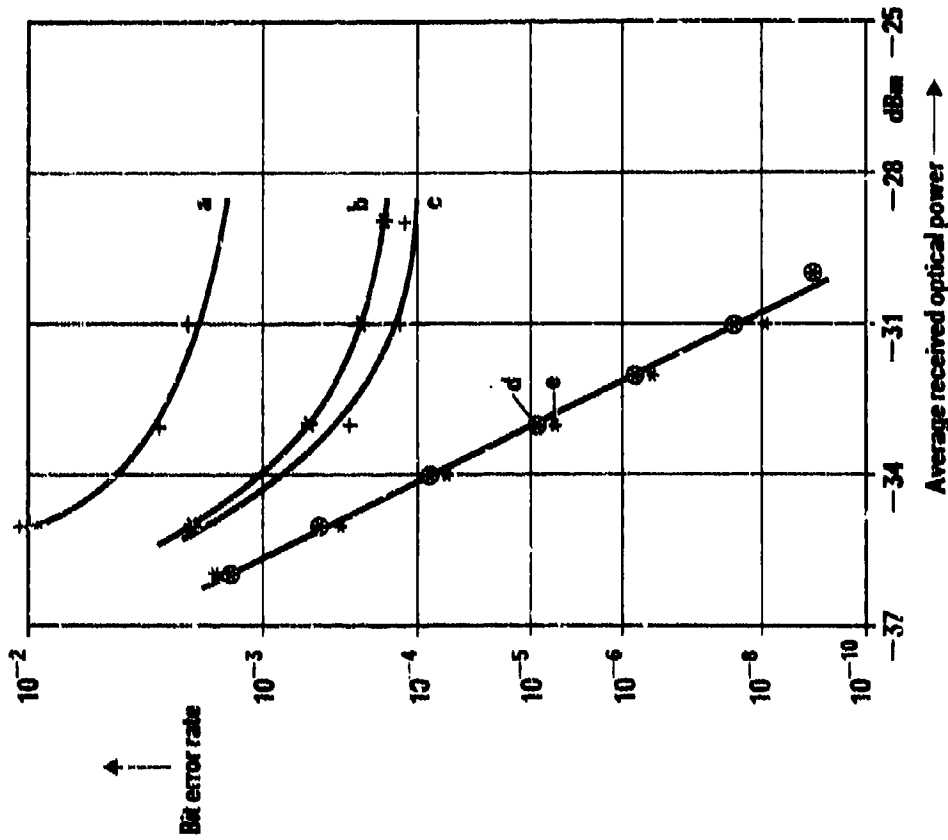


Fig. 9 BER performance versus average received optical power for a CSP laser under distinct connector feedback conditions and for three fiber link lengths. (a-c) presents the results for 13 km highly dispersive SM-fiber and high, low and no optical feedback at the connector joint. (d and e) belong to 30 km and 5 m nondispersive SM-fiber with no reflection at the connector.

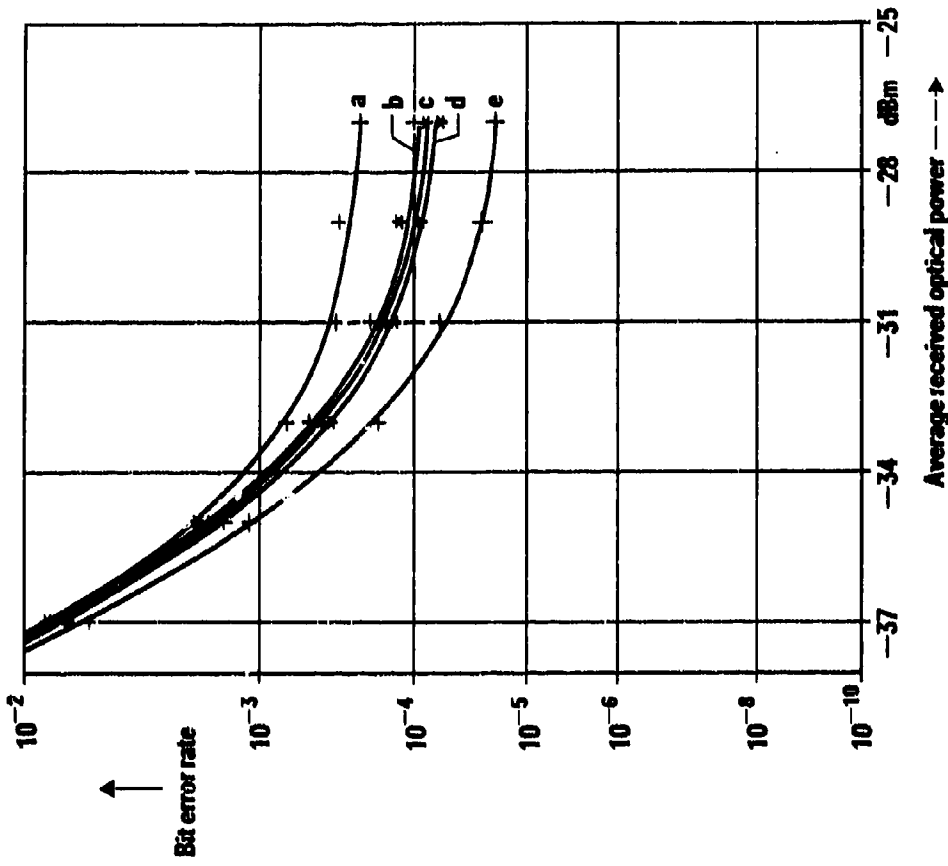


Fig. 10 BER versus average received optical power for various coupling structures and under various coupling distances. (a, e and c) demonstrate the results for the butt-coupled case and the laser-fiber distance set to maximum, minimum and in between of the Fabry-Perot fluctuation, respectively. (b and d) show the dependence for drawn fiber taper with a hemispherical lens and GRINP-lens, respectively. The measurements were performed with a CSP laser and operating conditions as stated in Fig. 8.

DISCUSSION

S.Walker, UK

(1) Have you performed any experiment with anti-reflection coated fibres? (2) Have you performed coupling experiments with DFB lasers.

Author's Reply

(1) We have not considered anti-reflection coatings. (2) No work with DFB lasers has been performed.

B.Schwaderer, Ge

You showed the tolerances (coupled power) of axial distance between laser and GRINF-lensed fibre. Can you comment on the tolerance of lateral adjustment?

Author's Reply

The lateral alignment tolerances for the GRINF-lensed fibre are in the same range as for a fibre taper with a fused lens. This means lateral misalignment of about $\pm 0.5 \mu\text{m}$ decreases the coupling efficiency approximately 1 dB.

H.Lefevre, Fr

What is the beatlength of the grating index fibre used as a lens?

Author's Reply

1 mm which leads to $250 \mu\text{m}$ length for $\lambda/4$ lens.

PERFORMANCE OF INTEGRATED OPTICAL FREQUENCY SHIFTERS
PIGTAILED TO HIGH BIREFRINGENCE FIBRES USING ION-MILLED GROOVES

Dr. I. Andonovic.
Dr. W. Johnstone.
Dr. D.N. Macfadyen.
Dr. A. McDonach. + *
Mr. M.S. Ner.
Dr. S. Beaumont. +

BARR & STROUD LIMITED
CAXTON STREET
ANNIESLAND
GLASGOW
G13 1NZ

UNIVERSITY OF GLASGOW
DEPT. ELECTRICAL AND
ELECTRONIC ENGINEERING
GLASGOW G12 8QQ

ABSTRACT

The practical application of lithium niobate integrated optical devices in the severe military environments that will be experienced by the fibre optic gyroscope, requires the development of a cheap, efficient and robust means of interconnecting optical fibres and integrated optical chips.

One technique for fibre to chip coupling which we have recently reported, is the use of ion-milled alignment grooves in the Lithium Niobate substrate to accurately locate the fibre end with the end of the waveguide. This technique uses a photolithographic process for the most precise alignment stages and is therefore amenable to mass production and automation.

Efficient coupling of light has been observed between optical fibres chemically etched to a diameter of about ten microns and waveguides formed by the indiffusion of titanium. The use of chemically etched optical fibres and ion-milled grooves allows a high packing density of chip/fibre connections, offering space savings in terms of device lengths as well as lateral separation.

Results are presented for the coupling of light to integrated optical waveguides from high birefringence optical fibres using ion-milled alignment grooves, and the degree of polarisation preservation achieved will be related to the performance of integrated optical phase modulators.

INTRODUCTION

The practical application of channel waveguide integrated optical devices in lithium niobate and other substrates will require rugged, reproducible, low loss, inexpensive coupling between fibres and waveguides. Low loss coupling can be achieved by the butt coupling technique¹ which requires the micro-alignment of the polished fibre with the polished end face of the waveguide. However, this arrangement is not very rugged, it is unsuitable for multiport devices and it involves the time consuming and costly micro-manipulation of the joint by a skilled operator. The use of silicon V grooves² permits repeatable multiport coupling. However, there is still a requirement for a manual micro-alignment stage.

An alternative, more attractive coupling technique using alignment grooves in the same substrate as the waveguide was proposed by Andonovic et al.³. The grooves of similar dimensions to and precisely aligned with the waveguides (Fig. 1) are fabricated through a mask defined by conventional photolithography. Coupling is achieved by inserting an etched fibre into the groove. In this technique the precision alignment is achieved at the photolithographic stage. Hence the technique is repeatable and the effort and precision of manipulation required at the waveguide coupling stage is considerably less than for the butt coupling technique thus reducing fabrication costs. Additional advantages of the ion-milled groove technique include its compatibility with multi-port fibre to chip coupling, its potential for automation, its ability to achieve high lateral packing densities and its thermal and mechanical stability since the fibre is supported by the substrate on which the waveguides are fabricated.

Standard single mode telecoms fibre to waveguide joints have been made by the ion-milled groove technique and losses (including Fresnel loss) from the input fibre to the waveguide output of 3.1dB have been achieved⁴. Many integrated optics device applications, however, require the use of high birefringence fibre with preservation of a single polarisation state throughout the system. This paper reports the coupling of a high birefringent fibre to a waveguide by an ion-milled groove technique. Aspects discussed include fibre preparation, groove fabrication, fibre to chip coupling and the degree of polarisation preservation in relation to the observed performance of a phase modulator addressed by high birefringent fibre.

FIBRE PREPARATION

Preparation of the high birefringence fibre involves its etching to a suitable geometry (10-15µm cross-section) for insertion into the ion-milled groove and the subsequent polishing of its end face. The cladding of high-birefringent fibre is inhomogeneous and preliminary experiments with Hydrofluoric acid etches revealed a large etch rate difference between the heavily doped stress-inducing regions of the cladding and their surroundings. This resulted in preferential etching and final fibre geometries which were not suitable for coupling. However, it was found that the stress inducing (bow-tie) regions were etched in preference to their surroundings by 40% diluted HF (Fig. 2) whereas the surrounding cladding was preferentially etched by Isoform buffered HF (ie. $\text{HF} + \text{NH}_4\text{F}$) (Fig. 3). Further studies then demonstrated that with an etch consisting of 60-70% by volume of 50% diluted HF and Isoform buffered HF the etch rates of the two distinct cladding regions were sufficiently similar to produce a suitably shaped fibre. Figure 4 illustrates the polished end face of an etched down high birefringence fibre embedded in Tan wax within a capillary. Measurements on such fibres showed an additional loss of 0.4dB associated with the etched down region and a reduction of the polarisation extinction ratio of 8dB. This depolarisation could represent either a scattering between modes (some of which may be caused by dirt on the fibre) or a loss of birefringence.

GROOVE FABRICATION

The grooves in the lithium niobate were fabricated by argon-ion-milling through a 20µm thick polyimide mask which has been appropriately patterned by reactive ion etching in oxygen. The polyimide, dissolved 20% by weight in an acetophenone/xylene mixture (1.56:1 by volume) is spun at 2000rpm to produce a 20µm thick film. After drying at 150°C for 0.5 hours and then at 250°C for 1 hour the polyimide is cross linked by curing at 350°C for 1.5 hours. Appropriate masking of the polyimide with aluminium is then achieved by standard optical photolithography and wet chemical etching. The polyimide mask for the argon ion-milling process is then created by oxygen reactive ion etching. The anisotropic nature of this etching process ensures that the walls of the polyimide are vertical (Fig. 5).

For the argon ion-milling of the LiNbO_3 it was found that an etch rate of 40nm/min could be obtained with a 1keV beam at a surface current density in the range of 0.6-1.0mA/cm². Under these conditions vertical side walled grooves up to a depth of 15µm can be produced in the lithium niobate (Fig. 6). It should be noted that good control of the groove dimensions, particularly the depth, in relation to the etched down fibre dimensions is required if accurate low loss alignment is to be achieved.

FIBRE TO WAVEGUIDE COUPLING

Waveguides fabricated in s-cut lithium niobate by indiffusion of 8µm wide by 700Å thick titanium stripes at 1050°C for 6 hours were used to make all of the fibre to chip coupling measurements. It was found that the loss associated with a single high birefringence fibre to waveguide joint made by the ion-milled groove technique was 2.3dB greater than a standard butt coupled joint. York HB 1200/1 fibre was used. The 2.3dB excess loss includes 0.4dB associated with the etched down fibre and 0.3dB loss resulting from the coupling of the evanescent field of the fibre to the walls of the groove. It is believed that the remaining excess loss of 1.4dB results from mis-alignment as a result of the groove dimensions not being ideal.

ACTIVE SYSTEM PERFORMANCE - POLARISATION EFFECTS

In a "polarisation conserving" birefringent fibre optic system incorporating channel waveguide lithium niobate integrated optical devices both the unwanted and the wanted polarisation states contain power and cross coupling between states occurs. Owing to the strong polarisation dependence of the phase modulation efficiencies of integrated optical modulators the power frequency content generated in each state will be different. In applications requiring control over the frequency spectrum and for which the detection is polarisation selective (as in the FOG) the coupling of power from the unwanted state to the selected state will be a source of error. It is therefore necessary to determine the power/frequency content of each polarisation state and the degree of cross coupling between them.

The active test system (Fig. 7) at Barr & Stroud enables the study of the polarisation effects discussed above. The system is basically a Mach-Zehnder interferometer illuminated by a 1.3µm beam from a Nd:YAG Laser or semiconductor diode laser. A device to be tested is mounted in one arm of the interferometer and addressed by high birefringent (York HB 1200/1) fibre (1 metre long pigtailed). Alignment of the polarisation axes of the fibres and the device is achieved by iterative rotational adjustments of the axes between crossed polarisers while monitoring the system for minimum output. An acousto-optic Bragg cell in the other arm of the interferometer translates the optical frequency by 80MHz. The 80MHz shifted beam and the modulated device output via the fibre are mixed on a beam splitter and focussed onto a 500MHz InGaAsP photo-diode. This heterodyne technique allows the optical frequency spectrum of the device output to be translated to an intermediate centre frequency of 80MHz for unambiguous analysis of the carrier and the positive and negative sidelobe levels displayed by a spectrum analyser.

The incorporation of half wave plate/polariser combination in the reference arm and the 50dB extinction ratio polariser at the fibre output facilitates the examination of the power/frequency content of the TE or the TM polarisation state of the system. Although the use of linear polarisation discriminators relates directly to most practical applications it should be remembered that, since the polarisation states of a birefringent waveguide are not linear, measurements made with the apparatus described above are a worst case approximation of the true discrimination between the waveguide polarisation modes of the system.

Figures 8 - 10 show frequency spectra generated by an integrated optical phase modulator under test in the apparatus described above. The waveguide of the modulator was fabricated in x-cut lithium niobate by the indiffusion of an 8 μ m wide by 700 thick titanium stripe at 1050°C for 6 hours. The electrode gap was 4 μ m. Electro optic figures of merit for the TM and TE modes were measured at 2.4 Vcm/radian and 13.2 Vcm/radian respectively. Figures 8 and 9 which are spectra for the TM mode demonstrate greater than 55dB and 45dB suppressions (relative to the carrier power) of the first and second harmonics respectively. Such suppressions were obtained by application of sine wave phase sweeps for which the Bessel function coefficients of these harmonics are zero. The levels of the suppressions were found to be insensitive to changes of $\pm 1^\circ$ in the alignment of the input fibre polarisation axis to the chip axes. From these results it can be concluded that the cross coupling of the frequency components generated by modulation of the TE carrier level within the chip into the TM mode contributes unwanted power to the levels of the first and second TM side bands of less than -55dB and -45dB respectively relative to the TM carrier power. Residual levels of suppressed harmonics will also include contributions from amplitude modulation.

Figure 10 is the frequency spectrum of the TE mode when a sine wave modulation is applied such that suppression of the first order TM harmonics is observed as in Figure 8. The lower level of the first harmonics in relation to the other components in the spectrum of Figure 10 suggests that the TE power/frequency content predominantly results from coupling from the TM mode and not from modulation of the TE carrier within the device. After adjustment to account for the relative sensitivities of the test system to TE and TM polarisation states the levels of the TE harmonics other than the first were determined to be approximately 20dB down on the corresponding TM harmonics. This is in good agreement with an independently measured TM to TE ratio of 23dB at the output fibre for TM carrier launched via a 50dB polarisation discrimination. This measurement reflecting the polarisation cross coupling was made for the unmodulated carrier using a second 50dB polariser and a Photodyne optical power meter.

CONCLUSIONS

A joint between a high birefringent fibre and a waveguide has been made by the ion-milled groove technique and has demonstrated a loss of 2.3dB in excess of a butt coupled joint. This early result is very encouraging and has established the feasibility of the ion-milled groove coupling technique to make joints using high birefringence fibre. In addition it has been demonstrated that useful measurements of the power/frequency content of both the orthogonal modes of a birefringent fibre/integrated optical system can be made with the apparatus described. Such measurements are invaluable to the determination of interference effects on signals resulting from the unwanted polarisation states of a given system.

Interference effects on a TM carried signal resulting from modulation of TE carrier within a phase modulator have been measured to be less than -55dB and -45dB relative to the TM carrier for two specific modulation conditions.

ACKNOWLEDGEMENTS

Barr and Stroud Ltd gratefully acknowledge the close collaboration with Glasgow University that made this project possible, and in particular the enthusiastic support of Professor J. Lamb. During the preparation of his contribution to this paper, Dr. McDonach was a Barr and Stroud Research Fellow at the University.

REFERENCES

1. R.C. Alferness, V.S. Ramaswamy, S.K. Korotky, M.D. Divino and L.L. Buhl, "Efficient Single-Mode Fibre to Titanium Diffused Lithium Niobate Waveguide Coupling for $\lambda = 1.32 \mu$ m" I.E.E.E. J. Quantum Electronics, Q.R-18, p1807, (1982).
2. C.H. Bulmer, S.K. Sheem, R.P. Moeller and W.K. Burns, "High-Efficiency Flip-Chip Coupling Between Single-Mode Fibres and LiNbO₃ Channel Waveguides" Appl. Phys. Lett., 37, p351, (1980).
3. I. Andonovic, M.B. Holbrook and A.D. McLachlan, "End-fire coupling between optical fibres and stripe waveguides" presented at the First European Conference on Integrated Optics, London, September 14-15, (1981).
4. A.C.G. Mutt, J.P.G. Bristow, A. McDonach and P.J.R. Laybourn "Fibre to Waveguide coupling using ion milled grooves in lithium niobate at 1.3 μ m wavelength" Optics Letters, 9, p463, (1984).

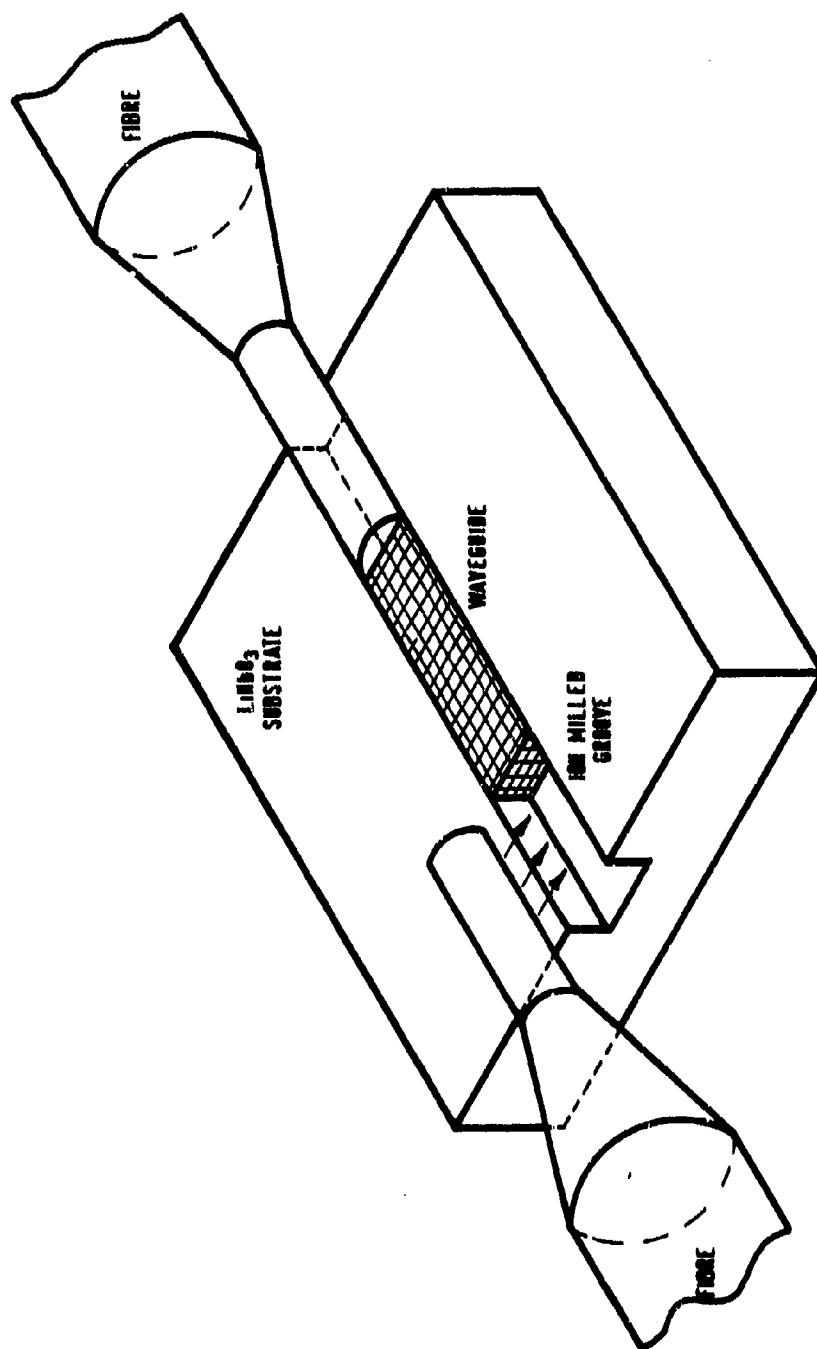


FIG1 FIBRE TO CHIP COUPLING BY THE ION - BEAM MILLED GROOVE TECHNIQUE



Fig.2 High Birefringent Fibre etched by
40% diluted HF



Fig.3 High Birefringent Fibre etched by
Isoform Buffered HF

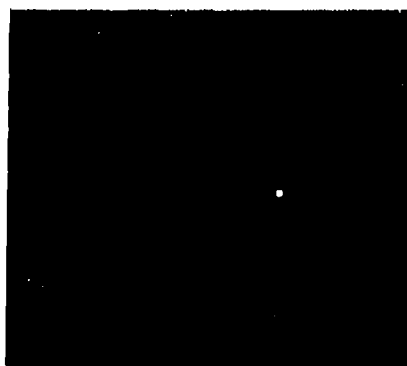


Fig.4 Polished Endface of etched
High Birefringence Fibre



Fig.5 Polyimide Mask

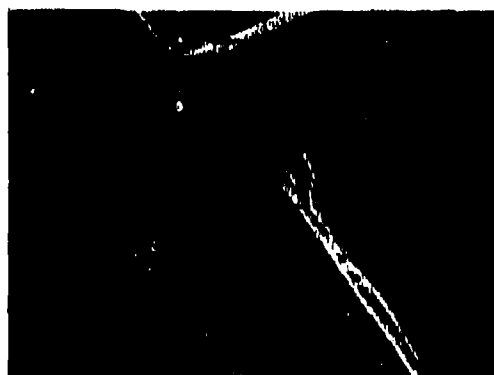


Fig.6 Ion Beam Milled Groove

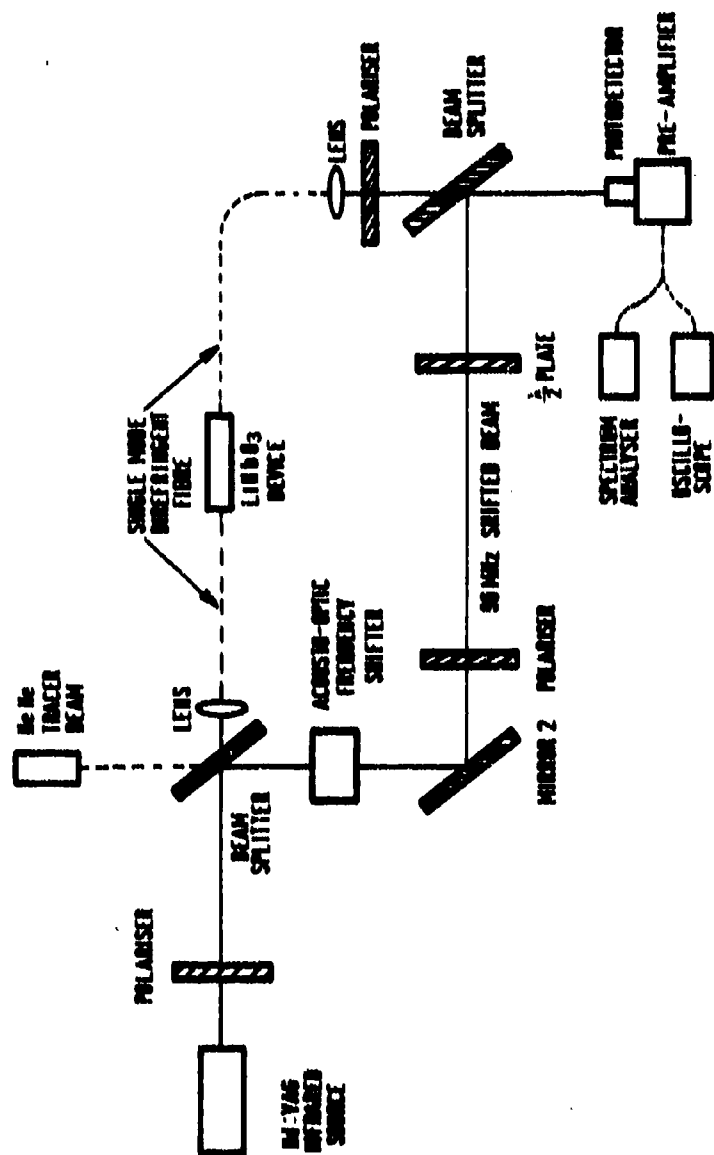


FIG.7 SCHEMATIC DIAGRAM OF ACTIVE DEVICE TEST EQUIPMENT



Fig.8 Output Frequency Spectrum of the phase modulator driven by a 7.7 radian (peak to peak) Sinewave phase sweep. The test system is TM selective.



Fig.9 Output Frequency Spectrum of the phase modulator driven by a 10.3 radian (peak to peak) Sinewave phase sweep. The test system is IM selective..

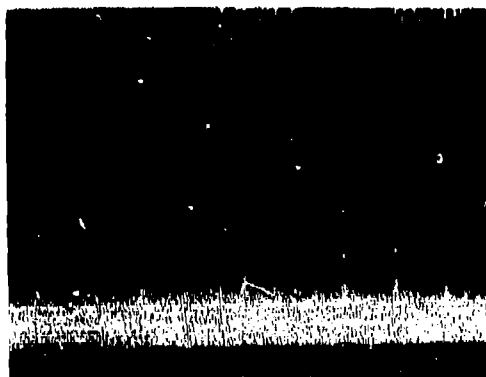


Fig.10 Output Frequency Spectrum of the phase modulator driven by a 7.7 radian (peak to peak) Sinewave phase sweep. The test system is TE selective.

DISCUSSION

G.Winzer, Ge

I didn't understand how you are doing the vertical adjustment of the fibre in the LiNbO_3 crystal; is this by control of the etching time and what is the etching rate in this case?

Author's Reply

Yes. Optimization of the fibre position is by control of the various etch parameters. Ion milling to better than 5 per cent. The fibre diameter is easier to control.

H.Lefevre, Fr

Did you perform temperature test of your coupling method?

Author's Reply

No.

NONLINEAR PLANAR GUIDED WAVE INTERACTIONS AND DEVICES

G. I. Stegeman and C. T. Seaton
Optical Sciences Center
University of Arizona
Tucson Arizona 85721

H. G. Winful
G. T. E. Laboratories Inc.
Waltham, Massachusetts 02254

SUMMARY

A variety of applications of third-order nonlinear integrated optics to optical signal processing are discussed. These include guided wave devices based on an intensity-dependent refractive index such as upper and lower threshold devices, all-optical switching devices, all-optical modulation devices, optical logic, and optical bistability. Multiple waveforms mixing with degenerate four-wave mixing to produce signal convolution and time inversion on a picosecond time scale are also discussed.

1. INTRODUCTION

The current rapid deployment of fiber communications systems means that information will soon be transmitted almost totally on optical waveforms. At present, the standard mode of operation for processing information is to detect the light with large bandwidth detectors, thus converting the information to electrical signals for subsequent processing in the electronics domain. If further transmission is necessary, the information is recorded onto optical waveforms by fast modulators and again coupled into optical fibers. This mode of operation is adequate as long as a) the data rate is not too high to tax the bandwidth of the electronics end of the system or b) jamming of the communications system by electromagnetic interference is not a potential hazard. A natural extension of fiber-optic communications would be to perform the signal-processing operations totally in the optical domain and therefore avoid problems with respect to electrical bandwidth and electromagnetic interference.

A very useful set of all-optical signal-processing operations would include a) simple binary logic gates, b) switching, c) modulation, d) thresholding, and e) convolution (which leads to a whole family of other processing functions). These operations can be based on the interaction of multiple waveforms with one another, which requires the presence of an optically nonlinear material. Nonlinear materials with very fast, probably picosecond, response times are necessary to process high data-rate signals with peak powers determined by the operating levels of semiconductor lasers. Although the "ideal" material is not currently available, encouraging developments have occurred in the materials area in the last few years. For all-optical signal processing, it is also possible to utilize the massive parallelism available in all-optical systems so that the total processing speed may still be very high with materials whose response times may be relatively slow. This however requires very fast serial-to-parallel and parallel-to-serial conversion, and very accurate clocking to implement -- factors which may mitigate against using parallel processing in an inherently serial system. (When the information being processed is already in parallel form, for example images, the parallelism can be better exploited.)

In this paper nonlinear optical phenomena that can be used in a waveguide format to implement a number of optical processing functions are described. The efficiency of any nonlinear interaction depends critically on the optical power density, that is, power per unit area. Therefore optical waveguides, with their inherent confinement of the light in one or two dimensions of the order of the wavelength of light, provide the optimum propagation geometry for nonlinear interactions in general, and nonlinear optical signal processing in particular. Furthermore, as shall be discussed here, waveguide geometries also lead to all-optical signal-processing operations that have no analogs in plane wave processing systems.

The signal processing operations discussed here are all based on the third-order susceptibility $\chi^{(3)}$, which involves the mixing of three optical fields.¹ This interaction produces the nonlinear polarization field

$$P^{NL}_i(\omega) = \epsilon_0 \chi^{(3)}_{ijkl} E_j(\omega) E_k^*(\omega) E_l(\omega) \quad (1)$$

Note that for the signal radiated by $P(\omega)$ to be at the system operating frequency, it is necessary to take the conjugate of one of the mixing fields (which also has repercussions for the final wavevector associated with the signal field.) If two of the required fields involve the product of an incident field with its own complex conjugate, then the phenomena are identified with an intensity-dependent refractive index. That is, including the linear susceptibility term $[\chi^{(1)}_{ij}(\omega) E_j(\omega)]$, the total polarization is given by

$$P_i(\omega) = \epsilon_0 [\chi^{(1)}_{ii} + \chi^{(3)}_{ijjj} |E_j(\omega)|^2] E_i(\omega) \quad (2)$$

$$P_i(\omega) = \epsilon_0 [n_0^2 - 1 + n_2 |E_j(\omega)|^2] E_i(\omega) \quad (3)$$

and, assuming that the optically induced change in the dielectric constant is small, the quantity in the square brackets can be written for plane waves as an intensity-dependent refractive index of the form

$$n = n_0 + n_2 I \quad (4)$$

where S is the local intensity, γ identifies the medium and $\alpha_{ij} = n_{\gamma}^2 \epsilon_0 n_{2\gamma}$. Equation (3) indicates that an intense field modifies the refractive index of a medium as seen by itself, as well as by other fields.

An intensity-dependent refractive index affects the propagation of light in a medium in two ways. First, changes in the index lead to changes in the optical wavevector k of light in the medium. For example, if an optical beam is propagated a distance L in the medium, the power-dependent phase change ΔkL can be tuned through π . That is an interference or phase-matching condition can be changed by increasing the intensity of a light beam. Another example is the Bragg condition for a grating that can be tuned optically. These two phenomena both have applications to all-optical signal processing which will be discussed here.

The amplitude distribution of a high-power optical field also changes with propagation distance in a waveguide with a medium characterized by an intensity-dependent refractive index. For a nonlinear medium, the field distributions depend on guided wave power which in turn affects the waveguide cut-off conditions. Furthermore, if both media bounding a thin film that guides light are nonlinear, there are multiple branches for the guided waves, a feature that can be used for switching. Devices based on these concepts will be discussed in this paper.

The other case of interest here for all-optical signal processing is degenerate four-wave mixing, which involves three input waves and one output wave.² Two or all three of the incident waves can contain information in the form of the temporal envelope of the waveforms. Therefore signal-processing operations are obtained in which waveforms interact when they pass through each other. As shall be shown later, these include signal convolution and time inversion.

2. INTENSITY DEPENDENT FIELD PHENOMENA

The variation in guide-wave field distribution with increasing power leads to signal-processing operations unique to guided waves.³ The prime example is that of a waveguiding film bounded on one or both sides by Kerr-like media, that is, media with refractive indices given by Eq. (4). The analysis is believed to be rigorously correct for TE polarized guided waves, but the TM polarized case is still the subject of debate as to the appropriate formulation.^{4,5}

(a) Nonlinear Guided Wave Threshold Devices

The geometry of interest has a film of thickness h ($0 < z < h$) and refractive index n_1 , a nonlinear cladding ($0 < z$) of index n_0 and nonlinearity n_{20} , and a substrate ($z > h$) of index n_2 (and in some cases nonlinearity n_{2s}). For a nonlinear cladding, the field distributions are⁶⁻⁸

$$E_y(z) = \frac{1}{2} \sqrt{\frac{2}{\epsilon_0}} \frac{q}{\cosh[k_0 q (z_1 - z)]} e^{i(\omega t - \beta k_0 x)} + cc, \quad n_{20} > 0, \quad (5)$$

and

$$E_y(z) = \frac{1}{2} \sqrt{\frac{2}{\epsilon_0}} \frac{q}{\sinh[k_0 q (z_1 - z)]} e^{i(\omega t - \beta k_0 x)} + cc, \quad n_{20} < 0, \quad (6)$$

where β is the effective guided wave index, $k_0 = \omega/c$ and $q^2 = \beta^2 - n_0^2$. The key parameter is z_1 , which depends on the power of the guided wave.⁶⁻⁸ At low powers, $z_1 \rightarrow \infty$ and the fields given by Eqs. (5) and (6) degenerate into exponentially decaying fields. However at high powers, z_1 decreases, and for the self-focussing case ($n_{20} > 0$), z_1 can even become negative. This leads a field maximum (a self-focussed field) in the nonlinear medium at high enough power levels. For the self-defocussing case, z_1 again decreases with increasing power, but never becomes negative (and hence the nonphysical case of divergent fields does not occur). The power dependence of the field distributions can be used to implement threshold devices, both upper and lower.

It is well-known⁹ that the usual power-independent asymmetric waveguide ($n_0 \neq n_2$) will not guide the lowest-order TE_0 mode below a certain minimum film thickness h_0 . As the film thickness is decreased towards the cut-off thickness, $\beta \rightarrow n_0$ (assuming $n_0 > n_2$) until $\beta = n_0$ at cut-off. However, at high powers, the index of the cladding medium is increased near the film-cladding interface and hence β , which is the field-weighted average of the guided wave index, can be larger than n_0 at thicknesses below the cut-off value. The higher the power, the thinner the film that will support a TE_0 guided wave. Therefore a direct relation exists between the film thickness and the threshold power above which a TE_0 solution can be propagated. Such a system acts as a minimum power threshold device.³ A sample calculation of power threshold versus film thickness is shown for a ZnS-based waveguide³ in Fig. 1.

If the cladding medium exhibits a self-defocussing nonlinearity ($n_{20} < 0$), then the effective index of a guided wave decreases with increasing power. Therefore, for a waveguide above cut-off for the TE_0 wave, increasing power forces the waveguide towards and eventually below cut-off (that is $\beta \rightarrow n_0$).¹⁰ The further the waveguide is initially above cut-off (that is the thicker the initial film thickness), the larger the power required to cut off the TE_0 wave. Detailed calculations³ for this effect are shown in Fig. 2.

We expect that such threshold devices can be used either in an end-fire (Fig. 3a) or a linear-nonlinear-linear waveguide geometry (Fig. 3b). In both cases, wave power transmitted by the thin-film waveguide will be the desired signal. One of the attractive features of such devices is that the fields of interest are established at the first transverse boundary at which the nonlinear medium is encountered. It is however necessary to strip of the unwanted fields, such as radiation modes, and propagation distances of tens of wavelengths will be required. Nevertheless, devices that require only tens of micrometers should be possible.

The threshold devices described above have not yet been implemented. The characteristic features of the fields discussed above have, however, been demonstrated experimentally for other geometries.^{11,12}

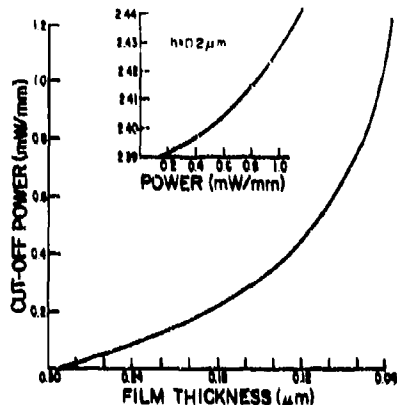


Fig. 1. The cut-off power above which the TE_0 wave can be propagated versus film thickness for a nonlinear self-focusing ZnS cladding medium. The inset shows the variation in effective index β with guided wave power for a film thickness of 0.2 μm .

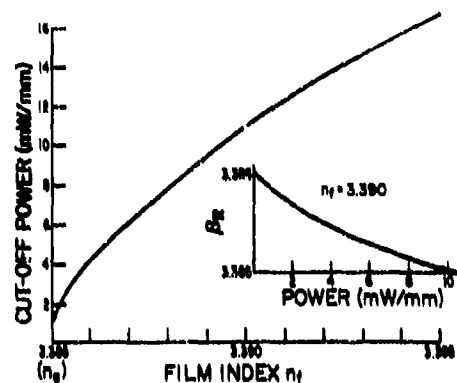


Fig. 2. The maximum TE_0 guided wave power which can be propagated versus index difference between the film and nonlinear GaAs-GaAl_xAs_{1-x} cladding. Inset is the effective index versus guided wave power for $n_1 = 3.39$ and film thickness of 1.07 μm .

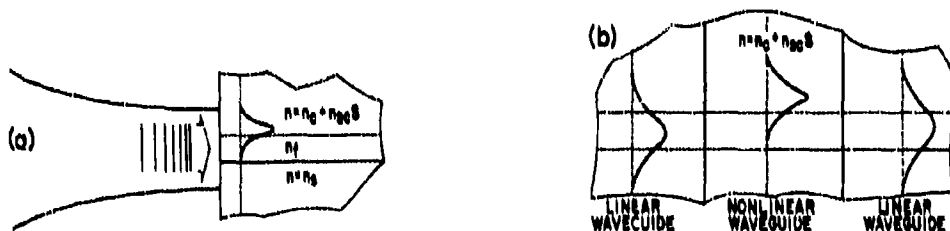


Fig. 3. Methods for exciting nonlinear guided waves with threshold characteristics. a) End fire excitation, b) Excitation by a linear guided wave incident onto a transverse boundary between a linear and nonlinear waveguide.

(b) Nonlinear Guided Wave Switching

Waves guided by a thin film bounded on both sides by self-focusing media also exhibit characteristics that appear promising for all-optical switching.^{3,6} Based on the previous discussion, at high powers one might expect fields that are self-focussed in either of the two nonlinear media or in both. Multiple solutions are obtained for the case when both bounding media have self-focussing nonlinearities. The details depend on the relative values of n_c and n_g , and n_{2c} and n_{2g} . At present it is not clear whether all of these solutions are stable. Nevertheless enough of the branches should be stable for all-optical switching to be possible.

We consider first the TE_0 case $n_c = n_g$, but with unequal nonlinearities, that is $n_{2c} > n_{2g}$. The solutions fall on two distinct branches, each characterized by its own field distributions, that is, self-focussing in different media at high powers. The example in Fig. 4a includes an estimate for the guided wave loss in terms of the imaginary component of β . The curves (in order of increasing β in the asymptotic limit) correspond to self-focussing in the medium with the highest nonlinearity (n_g), in the medium with the lowest nonlinearity (n_c), and in both media.⁸

A possible response of this system to guided wave power incident through a transverse boundary (Fig. 3b) is shown in Figs. 4a (dotted line) and 4b. As the guided wave power is increased, the wave excited follows the lower branch until it reaches the maximum value allowed for that branch. Subsequent increase in guided wave power can only be accomplished by switching the response to the upper branch. Because the attenuation of the upper branch is larger than that of the lower branch, this switching is accompanied by an instantaneous decrease in the signal transmission, as indicated in Fig. 4b.

If the guided wave power is now decreased, there is a minimum power that can be sustained by the waves corresponding to the upper branch. Further decrease in guided wave power requires switching to the lower branch, with again a subsequent increase in guided wave power (because of reduced attenuation). The net response curve closely resembles that of a bistable loop; there are two stable states, and which state the system is in depends on the previous history of how the light was guided.

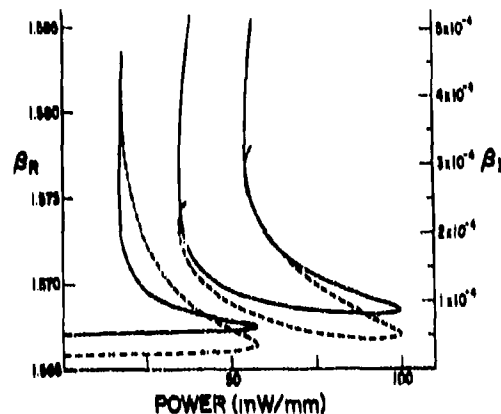


Fig. 4. Real (solid line) and imaginary (dashed line) parts of the effective index β versus TE_0 guided wave power for $h = 2.0 \mu\text{m}$, $n_1 = 1.57$, $n_c = 1.55$, $n_g = 1.55$, $n_{2c} = 0.002$, $n_{2g} = 2 \times 10^{-9} \text{ m}^2/\text{W}$, $n_{2c} = 1.55$, $n_{2g} = 0.001$, and $n_{2g} = 10^{-9} \text{ m}^2/\text{W}$.

If the material system is characterized by $n_c \neq n_s$ and by $n_{2c} \neq n_{2s}$, the resulting two branches become separated, and there is a range of powers over which guided wave power cannot be transported (see Fig. 5a). That is, when the guided wave power incident onto a transverse boundary (Fig. 3) is increased, the transmitted power remains a constant when the maximum of the lower branch is reached. However, when the power exceeds that required for excitation of the upper branch, switching to the upper branch occurs and the transmitted signal suddenly increases (Fig. 5b). Conversely when the guided wave power is decreased below that which can be sustained by the upper branch, the system switches to the lower branch and a sudden decrease in transmitted signal occurs. This response corresponds to all-optical switching.

Interesting possibilities also exist for the switching or modulation of one light beam by another. As indicated by Eq. (4), a high power guided wave (for example, of TE polarization), alters the spatial distribution of the refractive index in its vicinity. Therefore the propagation characteristics of an orthogonally polarized TM wave are also affected. (The change in refractive index for the TM wave will be less than that of the TE wave because the nonlinear effect makes the material optically anisotropic.) For a self-focussing nonlinearity, a strong TE wave can bring a TM mode above cut-off. Alternatively, in a self-defocussing medium, an increase in TE power can force a TM wave below cut-off. In both cases, a small modulation in the TE wave can produce a large modulation in a TM wave. This also leads to the switching of one optical beam by another.

To date, no experiments on thin films bounded by two nonlinear media have been reported.

3. INTENSITY DEPENDENT PHASE PHENOMENA

The curves shown in Figs. 1, 2, 4, and 5 exhibit a complicated behavior for the effective index β with guided wave power. However, at low guided wave powers the change in β is linear with power.¹³ That is,

$$\beta = \beta_0 + \Delta\beta_0 P_{gw} \quad (7)$$

where P_{gw} is the guided wave power per unit width along the wavefront and $\Delta\beta_0$ can be calculated either from the exact theory,⁸ or from normal mode analysis.¹³ In this limit, the total phase change experienced by a guided wave after it propagates a distance L contains two terms, namely

$$\Delta\phi = \beta_0 k_0 L + \Delta\beta_0 k_0 L P_{gw} \quad (8)$$

where $\Delta\phi^{NL} = \Delta\beta_0 k_0 L P_{gw}$ is the nonlinear power-dependent phase change. Typically an interference condition can change from constructive to destructive interference, or vice-versa, when $\Delta\phi^{NL} = \pi/2$ so that

$$P_c = \frac{\pi}{2\Delta\beta_0 k_0 L} \quad (9)$$

where P_c is a measure of the critical power required to produce power-dependent interference phenomena. In this section we discuss a number of devices that rely on such an intensity-dependent effective index and phase.

(a) Nonlinear Directional Coupler

An intensity-dependent refractive index can be used to alter the phase-matching condition between two coupled channel waveguides.¹⁴ For example, consider the channel waveguide directional coupler shown in Fig. 6. When light is injected into one channel, the overlap of that guided wave field with the adjacent channel waveguide results in power transfer into the second waveguide. As shown in Fig. 7 for low powers, the power oscillates between the two channels with propagation distance and, when terminated for the appropriate length, the device acts as a switch or a power splitter. For electro-optic materials, the transfer conditions can be tuned by applying an electric field to modify or modulate the refractive index, and this is the normal mode in which such a device is operated.

If one of the media in which the guided wave fields exist is characterized by an intensity-dependent refractive index, the cross-coupling conditions become power dependent and new signal processing devices become possible.¹⁴ That is, the response of the device depends on the intensity of the input waves. Assuming identical waveguides with guided field amplitudes described by $a_1(x)$ and $a_2(x)$ respectively and neglecting attenuation, the interaction can be described by the coupled wave equations:¹⁴

$$-i \frac{d}{dx} a_1(x) = \Gamma a_2(x) + [\Delta\epsilon_0 a_1(x)^2 + 2\Delta\epsilon_0' a_2(x)^2] a_1(x) \quad (10a)$$

$$-i \frac{d}{dx} a_2(x) = \Gamma a_1(x) + [\Delta\epsilon_0 a_2(x)^2 + 2\Delta\epsilon_0' a_1(x)^2] a_2(x). \quad (10b)$$

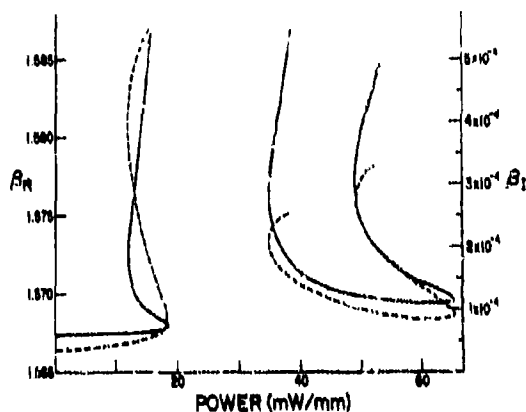


Fig. 5. The effective index versus TE_0 guided wave power for $h = 2.0 \mu m$, $n_c = 1.57$, $n_s = 1.56$, $\epsilon_{1c} = 0.002$, $n_{2c} = 2 \times 10^{-9} m^2/W$, $n_s = 1.55$, $\epsilon_{1s} = 0.001$, and $n_{2s} = 10^{-9} m^2/W$.

Here Γ is the usual linear-coupling coefficient between the two channels that leads to the oscillatory transfer between the channels shown in the low power regime of Fig. 7. Its value depends on the details of the channel geometry and separation. Note that in the absence of this coupling term, the remaining terms in the square brackets introduce an intensity-dependent contribution to the propagation wavevector for each channel. The parameters, $\Delta\alpha_0$ and $\Delta\alpha_0'$ respectively, quantify the nonlinear effect of each guided wave field onto itself because of its high intensity and the nonlinear effect of a strong field in one channel on the propagation characteristics of the neighboring channel.

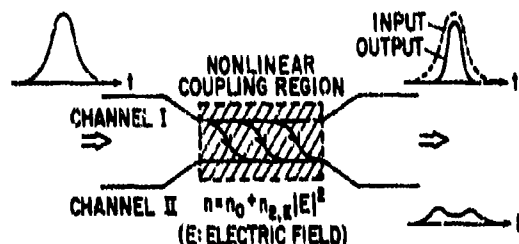


Fig. 6. A nonlinear coherent directional coupler consisting of two channel waveguides whose fields overlap in a medium characterized by an intensity-dependent refractive index.

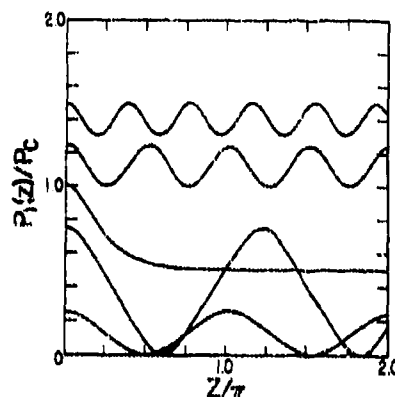


Fig. 7. The guided wave power (normalized to the critical switching power P_c) remaining in the incidence channel versus propagation distance at different incident power levels.

The solutions to these equations as obtained by Janssen¹⁴ are shown in Fig. 7 for a single input channel excited at different power levels. These results suggest a variety of possible applications. For example, if the device is set to produce complete transfer into the neighboring channel at low powers, at appropriately high input-power levels the transfer can be minimized. This corresponds to an intensity-dependent optical switch. A series of such switches can be used to demultiplex signals that are intensity coded. Alternatively, if the signals are of approximately equal intensity but are wavelength multiplexed, the signals can be demultiplexed if the material nonlinearity is strongly wavelength-dependent.

Intensity-dependent power transfer has recently been demonstrated using in-diffused channel waveguides in LiNbO_3 ,¹⁵ and in $\text{GaAs-Ga}_{0.7}\text{Al}_{0.3}\text{As}$ multiple-quantum-wall (MQW) channel waveguides.¹⁶ Although n_2 is quite small for LiNbO_3 (and in fact was measured in this experiment),¹⁵ a measurable transfer with picosecond time resolution has been observed by Haus and colleagues. The recent report¹⁶ of nonlinear switching in the MQW structures demonstrated partial switching of laser diode radiation at waveguide power levels of only 1 mW. In that case the two channel waveguides were strain-induced by depositing two gold stripes on top of a planar MQW waveguide. Although this device operated at a temperature of 180 K, it represents a very new and exciting development in this field.

The most promising application of nonlinear directional couplers appears to be to all-optical logic gates based on a Mach-Zender interferometer¹³ as sketched in Fig. 8. As indicated in the inset, the full set of logic functions can be implemented with this device.

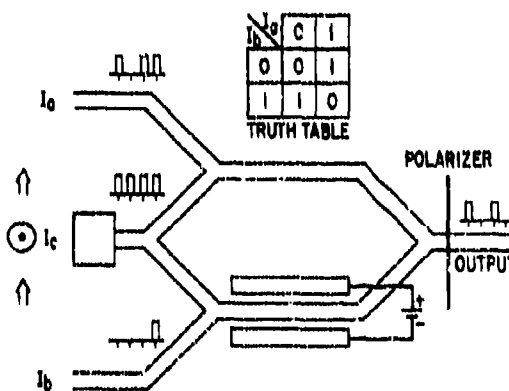


Fig. 8. A modified nonlinear Mach-Zender interferometer for implementing all-optical logic functions. The logic table is given in the inset.

(b) Nonlinear Grating Devices

All-optical tuning of gratings in nonlinear waveguides leads to a large number of potential applications to guided-wave all-optical signal processing. The underlying principle is very simple. When light is incident onto a grating (Fig. 9), it is strongly reflected (deflected) only when the Bragg condition

$$2k_{\text{grating}} = k_{\text{inc}} + k \quad (11)$$

is satisfied. The effective index k can be tuned optically by the incident beam itself, by another guided wave beam incident from another direction, or by illuminating the grating from above (or below). Therefore the Bragg condition, and hence the grating reflectivity, can be controlled optically. This phenomenon will prove to be very versatile because both the position and the intensity of the signal can be controlled optically.

Potentially one of the most important applications based on distributed feedback will be to optical bistability and switching.¹⁷ Consider first a single beam incident along the grating axis (beam 1 in Fig. 9). Because of a grating's reflection properties, there are always two waves present inside a grating that we label $a_+(x)$ and $a_-(x)$ for propagation along the $+x$ and $-x$ axes respectively. For a sinusoidal surface grating centered on the plane $z = 0$ (film-cladding interface) that produces a surface corrugation given by $u = u_0 \sin(kx)$ and includes both the forward and backward travelling waves, the appropriate coupled-mode equations including an intensity-dependent wavevector are¹⁷

$$i \frac{d}{dx} a_+(x) = \Gamma e^{-i\Delta\beta k_0 x} a_-(x) + \Delta\beta k_0 [a_+(x)^2 + 2a_-(x)^2] a_+(x) \quad (12a)$$

and

$$-i \frac{d}{dx} a_-(x) = \Gamma e^{i\Delta\beta k_0 x} a_+(x) + \Delta\beta k_0 [2a_+(x)^2 + a_-(x)^2] a_-(x), \quad (12b)$$

where Γ is the distributed reflection coefficient for a planar waveguide and the initial detuning from the Bragg condition is given by

$$\Delta\beta = 2\beta_0 - \kappa/k_0. \quad (12c)$$

These equations have been solved analytically.¹⁷ In terms of an incident switching power P_c for the $\Delta\beta = 0$ case,

$$P_c = \frac{2\beta}{3\Delta\beta_0^2 k_0 L}. \quad (13)$$

Typical numerical results for the transmission through the grating are shown in Fig. 10. As the incident power is increased past the turn-back point, the system switches to the upper branch. When power is reduced, switching to the lower branch occurs at the turn-back point for the upper branch. Hence a bistable loop is obtained. As shown in Fig. 10, switching occurs for $|a_+(0)|^2 = P_c$, provided that the feedback parameter is of the order of unity or larger. If two beams are incident onto the grating, the bistable switching of one beam will also produce bistable switching of the second beam. P_c for channel waveguides can be nanowatts for InSb waveguides,¹⁸ microwatts for GaAlAs MQW structures, and potentially tens of milliwatts for nonlinear organic used as the nonlinear material.¹⁸

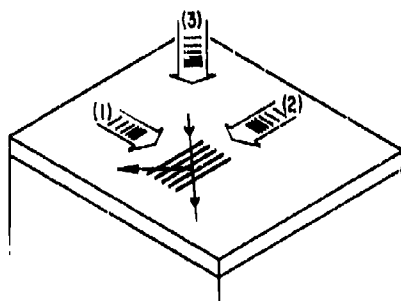


Fig. 9. General nonlinear grating geometry for switching guided waves. The grating can be tuned (in a bistable fashion) by a high power guided wave (control beam for example) along the grating axis, by a control guided wave incident parallel to the lines of the grating, or by illumination from above or below.

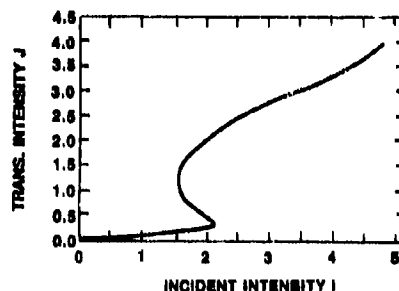


Fig. 10. Transmitted versus incident intensity for guided wave optical bistability for a given feedback ($\Gamma L = 2$) which characterizes the grating reflectivity, and grating length L .

If the grating is illuminated either from above or by a guided wave incident parallel to the grooves, the grating reflectivity can be tuned continuously with the control beam power, as shown in Fig. 11. That is, the operating point of the grating can be controlled optically. This property is useful for implementing a variety of all-optical logic functions. For example, if two input beams of power P_s are incident as control beams with the grating initially offset from maximum reflectivity (for a third weak signal beam) by $-P_s$, an XOR operation is obtained for a weak signal beam. Similarly, operations such as AND may also be implemented.

There are also applications to serial-to-parallel and parallel-to-serial conversion. For example, consider a serial data stream passing through a long grating which is initially tuned to zero reflectivity, as illustrated in Fig. 12. If at some instant in time the gratings are illuminated from above with sufficient power to tune the gratings to maximum reflectivity, the serial data stream is converted to a parallel data stream. Similarly a parallel data stream can be converted to a serial data stream.

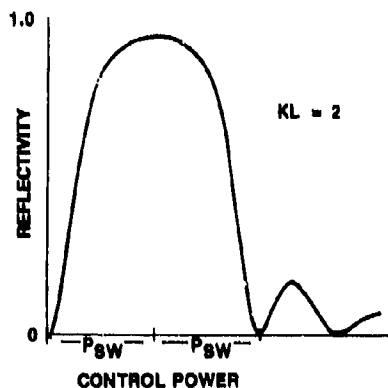


Fig. 11. Grating reflectivity versus control beam power for a nonlinear grating ($K = \Gamma$).



Fig. 12. Serial-to-parallel conversion of a data stream via a nonlinear grating. a) The data stream propagates through the grating which is detuned from the Bragg condition. b) The grating is illuminated from above with a beam of sufficient power to tune the grating to the Bragg condition. c) The data stream is deflected into a parallel one dimensional array. Parallel to serial conversion is obtained by effectively reversing the process in time.

Optically tuned nonlinear gratings are potentially very versatile elements. During the grating fabrication process, it is possible to stop the periodicity for some distance λ , which corresponds to phase shift of $n\lambda/4$ inside the grating. Thus phase-keyed processes such as correlation and coding and decoding, both well-known in surface acoustic wave devices,¹⁹ can be implemented optically with guided waves. Here the grating code could be either turned on optically with a control beam or actuated by the signal beam itself (providing that it lies within a specific power range). There are numerous other applications such as switching of arrays of parallel beams or the "slide" operation for optical computing which are not discussed here because of space limitations.

To date no devices based on nonlinear gratings have yet been reported.

4. DEGENERATE FOUR-WAVE MIXING

The key feature that leads to an intensity-dependent refractive index is a nonlinear polarization source field at the same frequency as the incident field. Such a polarization field can also be produced by the mixing of three input waves, see Eq. (1). If two of the input fields propagate in opposite directions, this process is called degenerate four-wave mixing.²⁰ Since these two fields propagate in opposite directions, their wavevectors cancel exactly. Therefore, for any angle of incidence of the third beam in this geometry, the process is always phase-matched (wavevector conserved) provided that the fourth wave is generated backwards along the incidence direction of this third beam. In a waveguide format,²¹ the process is phase-matched as long as beams 1 and 2 propagate in the same waveguide mode. This ensures that the signal beam 4 is radiated into the same mode as beam 3.

This interaction geometry introduces new signal-processing possibilities because the input beams can propagate in different directions relative to one another, and at different speeds (1 and 2 different from 3 and 4).²² For example, this allows the convolution of two waveforms to be produced in real time in the form of an optical guided wave signal. This case shown in Fig. 13a. The two input beams being convolved are 1 = a, pulse envelope $U_1(t)$; and 2 = b, pulse envelope $U_2(t')$; and beam 3 = c, is a control beam whose presence is required to make the process possible via degenerate four-wave mixing. The total radiated signal is of the form

$$U_4(t) = \int U_1(2t-\tau)U_2(\tau) d\tau, \quad (14)$$

which corresponds to the convolution of the two input waveforms with a time compression of a factor of two. Whether this process occurs or not is determined by the presence or absence of the control beam, a further advantage for controlled access signal processing.

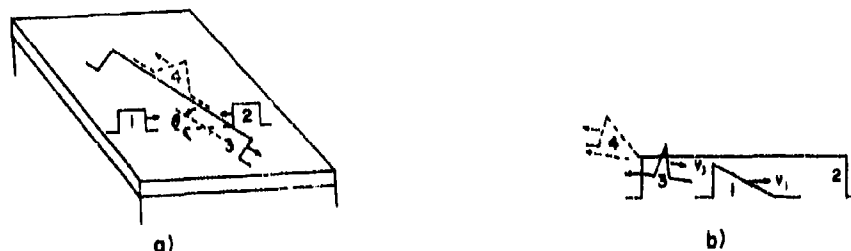


Fig. 13. The application of degenerate four wave-mixing to a) the convolution of pulses 1 (=a) and 2 (=b), and b) to the time inversion of beam 1 (=a).

Another example is time inversion²² with time compression or expansion, illustrated in Fig. 13b. The waveform to be inverted is coupled into a slow mode of the waveguide and a very short pulse (δ -function in time) into a fast mode that overtakes it essentially at a small angle from behind. Hence the trailing end of the input signal pulse is re-radiated back along the path of the δ -function pulse, and as the short pulse passes through waveform 1, a time inverted version of the input signal is produced. In this case the control beam is 2 and the radiated signal is beam 4. By adjusting the relative angles and the mode numbers of the various input wave, the signal can also be expanded or compressed in time.

Only one experiment on degenerate four-wave mixing in thin film waveguides has been reported.²³ The signal waves were tens of nanoseconds in duration and therefore no real time signal processing operations were demonstrated.

5. SUMMARY

We have discussed a number of potential applications to all-optical signal processing of nonlinear interactions in planar and channel waveguides. It should by now be clear that most, if not all, of the processing functions of interest can be implemented optically. The planar interaction geometries are mostly applicable to serial processing systems. Interactions involving channel waveguides (or fibers) can be used also for parallel processing operations. It is still very early in the waveguide all-optical signal-processing field, and to date only a few interactions have been verified experimentally.

The key to implementing such devices is the availability of appropriate materials. The requisite nonlinearities should be large enough that the various devices can be implemented at power levels of tens of milliwatts or less. Furthermore, once the optical signal is turned off, the nonlinearly induced polarization or refractive index should relax as quickly as possible, preferably in picoseconds. This nonlinearity relaxation time will ultimately limit the processing speed. (Usually the "turn-on" time for the nonlinearity is instantaneous, provided that enough power is supplied to the device.)

Some candidate materials already satisfy the above criteria, although not all optimally. For example, GaAs/GaAlAs MQW materials have more than adequate nonlinearities, although the relaxation time for the nonlinearity is still in the hundreds of picoseconds range.²⁴ Semiconductor-doped glasses relax in times of the order of picoseconds.²⁵ However, the powers required for signal processing are predicted to lie in the 10-mW to 1-W range. Both of these material systems have large losses and are therefore not ideal for serial processing involving multiple devices. The use of nonlinear organic materials that are very fast is one of the more interesting prospects on the horizon. The absorption in these materials should be controllable and they must now be engineered to increase their nonlinearities by several orders of magnitude to reduce device operating powers to reasonable levels.^{18,26}

We look forward over the next few years to both the demonstration of more all-optical signal processing operations, and to the development and incorporation of new nonlinear materials into guided wave formats.

This research was supported by the National Science Foundation (ECS-8304749, -8117483), Army Research Office (DAAO-29-83-K-0026), the Joint Services Optics Program (NICOM, BMDSC) and the Air Force Office of Scientific Research (AFOSR-84-0277).

6. REFERENCES

1. Y. R. Shen, The Principles of Nonlinear Optics (New York, J. Wiley, 1984); P.D. Maker and R. Terhune, Phys. Rev. 137, A801 (1964).
2. Recently reviewed in: R. A. Fisher, ed., Optical Phase Conjugation, New York, Academic Press, 1982).
3. C. T. Seaton, G. I. Stegeman, and H. G. Winful, review for Optical Engineering, in press.
4. V. M. Agranovich, V. S. Babichenko, and V. Ya. Chernyak, Sov. Phys. JETP Letters, 32, 512 (1981).
5. C. T. Seaton, J. D. Valera, B. Svenson, and G. I. Stegeman, Optics Lett., 10, 149 (1985).
6. A. E. Kaplan, Sov. Phys. JETP 45, 896 (1977).
7. N. N. Akhmediev, Sov. Phys. JETP 56, 299 (1982).
8. C. T. Seaton, J. D. Valera, R. L. Shoemaker, G. I. Stegeman, J. Chilwell, and S.D. Smith, J. Quant. Electron., in press.
9. See for example A. Yariv, "Propagation, Modulation, and Oscillation in Optical Dielectric Waveguides," in Quantum Electronics, 2nd Edition, (New York, Wiley, 1975) Chapter 19; or H. Kogelnik in Integrated Optics, Vol. 7 of Topics in Applied Physics, T. Tamir, ed. (Springer Verlag, Berlin 1975).
10. C. T. Seaton, J. D. Valera, R. L. Shoemaker, G. I. Stegeman, J. Chilwell, and S. D. Smith, Appl. Phys. Lett., 43, 1162 (1984).
11. H. Vach, C. T. Seaton, G. I. Stegeman, and I. C. Khoo, Optics Lett. 9, 238 (1984).
12. I. Benfion, M. J. Goodwin, and W.J. Stewart, Electron. Lett., 21, 41 (1985).
13. G. I. Stegeman, IEEE J. Quant. Electron. QE-18, 1610 (1982).
14. S. M. Jensen, IEEE J. Quant. Electron., QE-18, 1580 (1982).
15. A. Lottes, H. A. Haus, F. J. Leonberger, and E. P. Ippen, IEEE J. Quant. Electron., QE-19, 1718 (1983).
16. P. Li Kam Wa, J. E. Sitch, N. J. Mason, J. S. Roberts, and P. N. Robson, Electron. Lett., 21, 26 (1985).
17. H. G. Winful, J. H. Marburger, and E. Garmire, Appl. Phys. Lett. 35, 379 (1979).
18. G. I. Stegeman, C. Liao, and H. G. Winful, "Distributed feedback bistability in channel waveguides," in Optical Bistability II, C. M. Bowden, H. M. Gibbs, and R. L. McCall, eds. (New York, Plenum Press, 1984), p. 389.
19. E. A. Ash, in Acoustic Surface Waves, A. A. Clinger, ed. (New York, Springer-Verlag, 1978), p. 97.

20. D. M. Pepper, Opt. Eng. 21, 156 (1982).
21. C. Kevaguleff and G. I. Stegeman, IEEE J. Quant. Electron., QE-20, 716 (1984).
22. G. I. Stegeman, J. Opt. Comm. 4, 20 (1983).
23. C. Karaguleff, G. I. Stegeman, R. Zanoni, and C. T. Seaton, Appl. Phys. Lett. 7, 621 (1985).
24. Y. Silberberg, P. W. Smith, D. A. B. Miller, B. Tell, A.C. Gossard, and W. Wiegmann, Appl. Phys. Lett., 46, 701 (1985).
25. S. S. Yao, C. Karaguleff, A. Gabel, R. Fortenberry, C. T. Seaton, and G. I. Stegeman, Appl. Phys. Lett., 46, 801 (1985).
26. C. Sauteret, J.-P. Hermann, R. Yrey, F. Pradere, and J. Ducuing, Phys. Rev. Lett. 36, 956 (1976).

BISTABILITY IN NONLINEAR WAVEGUIDES

by

M. Bertolotti, C. Sibilia, I. Anselmi
 Dipartimento di Energetica-
 Sezione Fisica-Universita' di Roma I
 Via Scarpa n.16, 00161 Roma, Italy

SUMMARY

The propagation of electromagnetic waves (TE) in a nonlinear waveguide is studied. For simplicity a three layer structure is considered with the two external media of semi-infinite extent. The mode dispersion equation is derived together with the power carried by the single mode in the structure, showing that bistability can occur in some case.

1. INTRODUCTION

Propagation in nonlinear waveguides was considered since 1968 (1) when surface waves on the interface between two media one of which had a dielectric constant with a quadratic dependence on the wave field, were studied.

This situation was further considered in refs. 2 to 6 and extended to the case of both media nonlinear by Lomtev (7) or of a symmetric layered structure consisting of a layer having a linear dielectric constant between two layers of a medium whose dielectric constant depends quadratically on the amplitude of the wave electric field by N.N. Akhmediev (8).

A feature of the wave propagation in these structures is that the dispersion relation contains as a parameter, besides the frequency and the wave vector, also the square of the field of the electromagnetic wave. This means that at a given frequency it is possible to control the propagation constant of the wave by varying its energy flux. Moreover, wave solutions are obtained having no analogy in ordinary linear structures, and in a certain range of values of the carrying layer thickness or of the wavelength, in the case of a three layer structure, the nonlinear surface waves are bistable (8).

The study was subsequently extended to the case of guided waves in a three layer structure, in which one, two or all the media were nonlinear (9 to 30) and bistable behaviour was confirmed theoretically (8,11,13,18,30). Finally experimental evidence has been obtained (17,23,27).

In the present paper we discuss the propagation along a nonlinear guiding medium (see Fig.1), looking at symmetric ($\epsilon_2 = \epsilon_3$) and asymmetric ($\epsilon_2 \neq \epsilon_3$) configurations.

This structure has already been studied using the "coupled mode theory" (11, 16); because of the high intensities which can be present in the waveguide, this approach may not be useful and a general and exact theory must be considered to predict all the features of the behaviour of the structure.

2. WAVE EQUATIONS FOR THE STRUCTURE

Let us consider the case shown in Fig. 1 of a medium with a nonlinear refractive index ($\epsilon_1 = \epsilon_1 + \epsilon_1 |E|^2$). We restrict here to the study of TE modes. They have only the field components E_y, H_x, H_z . Since we are interested to the normal modes of the slab waveguide we assume that the z component of the mode field is given by the function $\exp(i\beta z)$. In this way the wave equations for the three layers become

$$\frac{\partial^2 E_3}{\partial x^2} - E_3 k_{30}^2 = 0, \quad x > 0 \quad (1a)$$

$$\frac{\partial^2 E_1}{\partial x^2} + E_1 k_{10}^2 + 1/2 \delta \epsilon_1 |E_1|^2 = 0 \quad 0 < x < -d \quad (1b)$$

$$\frac{\partial^2 E_2}{\partial x^2} - E_2 K_{20}^2 = 0, \quad x < -d \quad (1c)$$

where

$$\begin{aligned} \delta &= k \epsilon_{ML} \\ K_{10}^2 &= \beta^2 - \epsilon_{10} k^2 \\ K_{20}^2 &= \beta^2 - \epsilon_{20} k^2 \\ K_{30}^2 &= \beta^2 - \epsilon_{30} k^2 \\ k &= 2\pi / \lambda \end{aligned} \quad (2)$$

The minus sign in eq.(1b) is valid for $K_{10}^2 > 0$ (surface modes), otherwise the plus sign must be used and K_{10}^2 is redefined as

$$K_{10}^2 = \epsilon_{10} k^2 - \beta^2 \quad (3)$$

with the condition that $\epsilon_{10} > \epsilon_2 > \epsilon_3$

A first integration of eqs.(1) gives

$$\left(\frac{dE_3}{dx} \right)^2 - E_3^2 K_{30}^2 = 0 \quad x > 0 \quad (4a)$$

$$\left(\frac{dE_1}{dx} \right)^2 + E_1^2 K_{10}^2 + 1/2 \delta E_1^4 = 0, \quad 0 < x < -d \quad (4b)$$

$$\left(\frac{dE_2}{dx} \right)^2 - E_2^2 K_{20}^2 = 0, \quad x < -d \quad (4c)$$

The solutions of Eqs.(4) are the following

$$E_3(x) = E_0 \exp(-K_{30} x) \quad (5a)$$

$$E_1(x) = \pm \left(\frac{\gamma_1^2 - \alpha_1^2}{2\gamma_1 \delta} \right)^{1/2} \operatorname{sd}(\sqrt{\gamma_1} (x + x_{01}), t^2) \quad (5b)$$

$$E_2(x) = E_d \exp(K_{40} (x + d)), \quad (5c)$$

where

$$\gamma_1 = (\alpha_1^2 + 2\alpha_1 \delta)^{1/2} \quad (6a)$$

$$\alpha_1 = K_{10}^2, \quad (6b)$$

$$E_0 = E_3(x=0)$$

$$E_d = E_2(x=-d)$$

α_1 and x_{01} are integration constants and sd is a Jacobi Elliptic Function, with the parameter t^2 (31):

$$t^2 = \frac{\gamma_1 - \alpha_1}{2\gamma_1}, \quad (7)$$

Eq. (5b) (i.e. the solution of the nonlinear wave equation) describes both situations of surface ($K_{10}^2 > 0$) and guided ($K_{10}^2 < 0$) modes.

The integration constant x_{01} can be expressed as a function of the field E_0 at the boundary $x=0$:

$$x_{01} = \pm \left(\frac{1}{\gamma_1} \right)^{1/2} \operatorname{sd}^{-1} \left[E_0 \left(\frac{2\gamma_1 \delta}{\gamma_1^2 - \alpha_1^2} \right)^{1/2} \right]. \quad (8)$$

Using the continuity of the first derivative at this boundary, it is also possible to find the expression of the dispersion equation

$$\frac{\operatorname{sn}(\sqrt{\gamma_1} (x_{01} + d)) \operatorname{dn}(\sqrt{\gamma_1} (x_{01} + d))}{\operatorname{cn}(\sqrt{\gamma_1} (x_{01} + d))} = - \frac{K_{30}}{K_{40}} \frac{\operatorname{sn}(\sqrt{\gamma_1} x_{01}) \operatorname{dn}(\sqrt{\gamma_1} x_{01})}{\operatorname{cn}(\sqrt{\gamma_1} x_{01})} \quad (9)$$

The dispersion equation (9) is however not a convenient form to be

handled due to the presence of the two integration constants x_{01} and c_1 . Using eqs. (4) it is possible to eliminate x_{01} . So for asymmetric configuration ($\epsilon_2 \neq \epsilon_1$) all the modes of the structure are given by solving the following equation:

$$\frac{\operatorname{sn}(\sqrt{\gamma_1}(x_{01} + d)) \operatorname{dn}(\sqrt{\gamma_1}(x_{01} + d))}{\operatorname{cn}(\sqrt{\gamma_1}(x_{01} + d))} = - \frac{K_{20}}{K_{20}} \left\{ \frac{2\gamma_1 \left[-(K_{10}^2 + K_{20}^2) + \sqrt{(K_{10}^2 + K_{20}^2)^2 + 2c_1\delta} \right]}{1 + t^2 \left[\frac{-(K_{10}^2 + K_{20}^2) + \sqrt{(K_{10}^2 + K_{20}^2)^2 + 2c_1\delta}}{(\gamma_1^2 - \alpha_1^2)} \right]} \right\} \cdot \frac{1}{(\gamma_1^2 - \alpha_1^2) \left[1 - (1 - t^2) \frac{2\gamma_1 \left[-(K_{10}^2 + K_{20}^2) + \sqrt{(K_{10}^2 + K_{20}^2)^2 + 2c_1\delta} \right]}{(\gamma_1^2 - \alpha_1^2)} \right]^{1/2}} \quad (10)$$

where

$$\frac{1}{2} x_{01} = \pm d^{-1} \left\{ \left[\frac{2\gamma_1 \left[-(K_{10}^2 + K_{20}^2) + \sqrt{(K_{10}^2 + K_{20}^2)^2 + 2c_1\delta} \right]}{(\gamma_1^2 - \alpha_1^2)} \right]^{1/2} \right\} \quad (11)$$

In this way the dispersion equation for each β depends on ω , d , and $2c_1\delta$ (i.e. E_0).

In the linear limit ($\delta \rightarrow 0$) this equation reduces to the one for a linear slab waveguide.

In the case of a symmetric configuration ($\epsilon_2 = \epsilon_1$), the dispersion equation for symmetric and antisymmetric modes (the only possible kind of modes for this configuration) is given by:

$$\frac{\operatorname{sn}(\sqrt{\gamma_1} d/2) \operatorname{dn}(\sqrt{\gamma_1} d/2)}{\operatorname{cn}(\sqrt{\gamma_1} d/2)} = - f(x), \quad (12)$$

Where

$$f(x) = \frac{2\gamma_1 \left[- (K_{10}^2 + K_{20}^2) + \sqrt{(K_{10}^2 + K_{20}^2)^2 + 2C_1 \delta} \right]}{(\gamma_1^2 - \alpha_1^2) \left[1 - (1-t^2) \frac{2\gamma_1 \left[- (K_{10}^2 + K_{20}^2) + \sqrt{(K_{10}^2 + K_{20}^2)^2 + 2C_1 \delta} \right]}{(\gamma_1^2 - \alpha_1^2)} \right]} \left. \right\}^{1/2},$$

$$1 + t^2 \frac{2\gamma_1}{(\gamma_1^2 - \alpha_1^2)} \left[- (K_{10}^2 + K_{20}^2) + \sqrt{(K_{10}^2 + K_{20}^2)^2 + 2C_1 \delta} \right] \quad (13)$$

for antisymmetric modes ($E_0 = -E_d$), and

$$\frac{\operatorname{sn}(\sqrt{\gamma_1} d/2) \operatorname{dn}(\sqrt{\gamma_1} d/2)}{\operatorname{cn}(\sqrt{\gamma_1} d/2)} = \frac{1}{f(x)} \quad (14)$$

for symmetric modes ($E_0 = E_d$).

These dispersion equations describe both guided ($K_{10}^2 < 0$) and surface ($K_{10}^2 > 0$) modes, and can be solved via the usual graphics methods.

3. POWER FLUX

To know the behaviour of the modes inside the guide, it is more convenient to express the power flux through the structure calculated as

$$P = \frac{\beta_0 c^2 \epsilon_0}{8\pi\omega} \int_{-\infty}^{+\infty} E^2(x) dx. \quad (15)$$

Substituting the solution of the wave equation we have, for an asymmetric structure

$$P = P_C \left\{ \frac{E_0^2}{2K_{10}} + \frac{E_d^2}{2K_{20}} + \frac{\sqrt{2\gamma_1}}{\delta} \left[E(\sqrt{\gamma_1}(x_0 + d)) - E(\sqrt{\gamma_1}x_0) + \sqrt{\gamma_1}(x_0 + d) - (1-t^2)\sqrt{\gamma_1}d + \right. \right. \\ \left. \left. + t^2 (\operatorname{sn}(\sqrt{\gamma_1}x_0) \operatorname{cd}(\sqrt{\gamma_1}x_0) - \operatorname{sn}(\sqrt{\gamma_1}(x_0 + d)) \operatorname{cd}(\sqrt{\gamma_1}(x_0 + d))) \right] \right\}, \quad (16)$$

which reduces to the following expression in the case of a symmetric structure

$$P = P_c \left\{ \frac{\epsilon_0^2}{K_{10}} + \frac{\sqrt{2} \sqrt{\gamma_1}}{5} \left[- (1-t^2) \sqrt{\gamma_1} d + \right. \right. \\ \left. \left. + 2 E(\sqrt{\gamma_1} d) - 2 t^2 (1-q) \operatorname{sn}(\sqrt{\gamma_1} d/2) \operatorname{cd}(\sqrt{\gamma_1} d/2) \right] \right\},$$

with $P_c = \frac{\beta_1 c^2 \epsilon_0}{8\pi\omega}$ (17)

where $q=1$ for symmetric modes and $q=0$ for antisymmetric modes, and $E(x,t)$ is the elliptic integral of the second kind (31). It is easy to verify again that in the linear limit eq. (17) reduces to the power expression through the corresponding linear structure.

4. NUMERICAL CALCULATIONS AND RESULTS

We have calculated the mode behaviour in a waveguide made by a thin film of a nonlinear material with $\epsilon_0 = 12.92$, $\beta = 10^{-10}$ m/W, and thickness d , bounded by two media in a symmetric configuration with $\epsilon_1 = 4.1242$ for different values of the ratio d/λ : $d/\lambda = 0.5$, and $d/\lambda = 1$. At first we have solved (by intersection) the dispersion equation, then we have calculated the power carried by each allowed mode of the slab waveguide. The main result is an "N" shaped curve describing the behaviour of the propagation constant of the antisymmetric mode as a function of the normalised power P/P_c (in the case of symmetric configuration) (s. Fig. 2). This shape is characteristic of a bistable process which in this case shows itself as the presence of a critical power value at which two modes of the same kind appear.

There are several possible applications of these results. At low powers, below the critical value for the bistable behaviour a deflector can be made, use the change of β with power when extracting the mode from the waveguide. At the critical power two modes of the same kind appear and the system can be used as a 2switch2 between two states.

REFERENCES

- 1- A.G. Litvak, V.A. Mirov, Radiotekhnika 11, (1968), 1911
- 2- V.M. Agranovich, V.S. Babichenko, V.Ya. Cherny, JETP Lett. 32, (1980), 512
- 3- W.J. Tomlinson, Opt. Lett. 5, (1980), 323
- 4- A.A. Maradudin, E. Phys. B41, (1981), 341
- 5- A.E. Kaplan, IEEE J. Quant. El. QE 17, (1981), 336
- 6- D. Sarid, Appl. Phys. Lett. 39, (1981), 889
- 7- A.I. Lomtev, JETP Lett. 34, (1981), 60
- 8- N.N. Akmediev, Sov. Phys. JETP 56, (1982), 299
- 9- D. Sarid, G.I. Stegeman, Appl. Phys. 52, (1981), 5439

- 10-A.A.Maradudin, Second Intern. School on Condensed Matter
Physic, Varna, Bulgaria, 1982
- 11-G.I. Stegeman-IEEE J. Quant. El, QE-18, 81982), 1610
- 12-V.K. Fedyanin, Mihalache, Zeit. Phys. B47, (1982), 167
- 13-G.I. Stegeman-Appl. Phys. Lett. 41, (1982), 214
- 14-U. Langbein, F. Lederer, H.E. Ponath, Opt. Comm. 46, (1983), 167
- 15-F. Lederer, U. Langbein, H.E. Ponath- Appl. Phys. B31, (1983), 69, 187
- 16-G.I. Stegeman, C. Liao, Appl. Optic. 22, (1983), 2518
- 17- G.I. Stegeman, K. Fortenberger, C. Karaguleff, R. Moshrefzadeh,
W.H. Hetherington III, N.E. Van Wyck-Opt. Lett. 8, (1983), 295
- 18-A.D. Boardman, P. Egan-J. de Physique 45, C5, (1984), 291
- 19-A.D. Boardman, P. Egan-Phil. Trans. R. Soc. London, A313, (1984), 363
- 20-G.I. Stegeman, C.T. Seaton, H.G. Winful- Phil. Trans. R. Soc. London,
A313, (1984), 321
- 21-C. Sibilia, M. Betolotti, D. Sette-Phil. Trans. Roy. Soc. London,
A313, (1984), 361
- 22-G.I. Stegeman, C.T. Seaton-Opt. Lett. 9, (1984), 235
- 23-G.I. Stegeman, C.T. Seaton, J. Chilwell, S.D. Smith-
Appl. Phys. Lett. 44, (1984), 830
- 24-U. Langbein, F. Leder, H.E. Ponath, U. Trutschel, Appl. Phys. B36,
(1985), 187
- 25-V.J. Montemayor, R.T. Deck-JOSA, B2, (1985), 1010
- 26-H. Vach, C.T. Seaton, G.I. Stegeman, I.C. Khoo-Opt. Lett, 9, (1984), 238
- 27-K. Thyagarajan, Y. Bourbin, A. Erad, S. Vatoux, M. Papuchon-
Opt. Lett, 10, (1985), 288
- 28-A.D. Boardman, P. Egan- In publ. on IEEE J. QE
- 29-U. Langebein, F. Lederer, H.E. Ponath-Opt. Comm., 53, (1985), 417
- 30-G. Stegeman, C. Seaton, W.M. Hetherington, H.G. Winfull-Proc. ECIO'83-
Berlin- 1985, Springer & Verlag
- 31-E.T. Whittaker, G.N. Watson-"A Course of Modern Analysis" , Cambridge-
University Press-N.Y., -1962

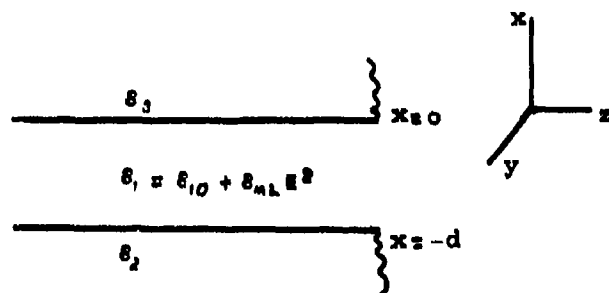


Figure 1

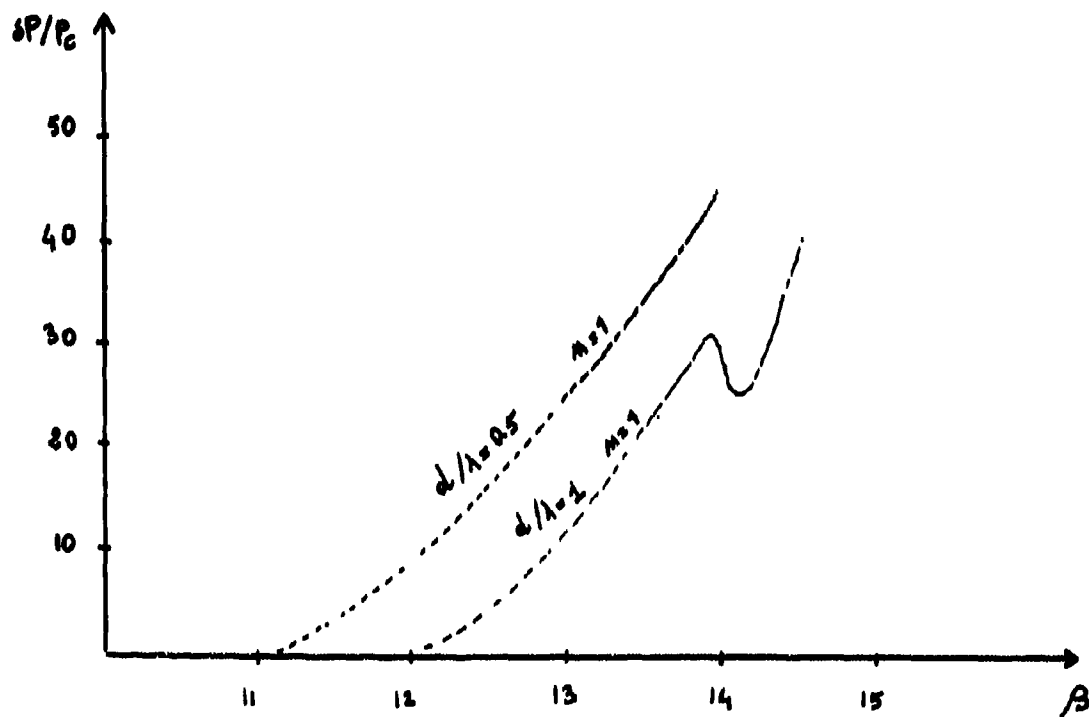


Figure 2

INTEGRATED OPTICS OPTICAL LIMITERS

by
C. T. Seaton, J. D. Valera, and G. I. Stegeman
Optical Sciences Center
University of Arizona
Tucson, AZ 85721
U.S.A.

SUMMARY

We have recently demonstrated two novel, passive, low-power, guided-wave optical limiters. Both are based on intensity-dependent refractive indices and involve phenomena unique to optical waveguides. The first utilizes newly discovered nonlinear guided waves that exhibit optical-limiting action for a film bounded by a nonlinear medium. The second relies on an intensity-dependent reduction in coupling efficiency when waveguide modes are excited by prism or grating couplers. In both cases, preliminary experiments have demonstrated optical limiting action.

1. INTRODUCTION

A totally passive optical limiter is very difficult to achieve for several reasons. A high-power incident optical field can a) cause a phase transition that changes a material's optical properties from transparent to reflecting, b) trigger a detector relay that closes a shutter or apply a voltage that causes a phase transition, or c) cause a change in the material refractive index that is usually translated via an optically resonant structure into a change in the reflective properties of an optical device. Only cases a) and c) belong to the passive category and can have response times limited essentially by those of the material nonlinearities. In case c) particularly, the optically induced change in the refractive index is typically given by $\Delta n = n_2 I$, where I is the local intensity in watts per meter squared and n_2 is in meters squared per watt. For a given amount of total power that is the quantity of interest in most applications, the intensity (power/area) can be optimized by reducing the beam cross-sectional area. Waves guided by single or multiple interfaces offer an ideal approach, since the beam cross-section can be reduced to the order of an optical wavelength in one or both dimensions. Guided wave versions of schemes first proposed for plane waves, for example bistability, offer operation at power levels reduced by two to four orders of magnitude relative to their bulk wave counterparts.¹ Unfortunately, they can suffer from the same problems as bulk devices, such as background level.²

An intensity-dependent refractive index affects the propagation of light in a medium in two ways. First, changes in the index lead to changes in the optical wavevector k of light in the medium. Therefore, if an optical beam is propagated a distance L in the medium, the net phase change kL can be tuned through $m\pi$, where m is an integer, by changing the power. That is, an interference condition can be changed from destructive to constructive and vice-versa by increasing the intensity of a light beam. Under appropriate conditions, this phenomenon can lead to optical limiters that operate over limited wavelength ranges, such as narrow-band limiters useful for blocking specific wavelengths.

An example of such a process is the coupling of radiation into a nonlinear optical waveguide via a distributed coupler such as a prism or a grating.^{3,4} Under such a coupler, the guided wave field grows with distance along the waveguide surface over the aperture of the incident beam. For efficient coupling, the projection of the incident field wavevector (plus the grating wavevector for grating couplers) onto the surface must match the wavevector β_0 of the guided wave being generated. However, if the guided-wave wavevector varies with guided wave power ($\beta = \beta_0 + \Delta\beta_{\text{PW}}$)¹ via an intensity-dependent refractive index in one of the guiding media, this synchronous coupling condition is spoiled and coupling efficiency is reduced. Hence increased incident power leads to decreased coupling. We have already demonstrated experimentally this phenomenon.⁴

The amplitude distribution of a high-power optical field also changes with propagation distance in a medium characterized by an intensity-dependent refractive index. For a self-focussing medium ($n_2 > 0$), an optical beam collapses at some point into a narrow filament that can be blocked off or transmitted, depending on the application. If the beam is guided by a single interface, or by multiple interfaces, the field maximum can move from one medium to another with increasing power and again the transmission properties can be controlled.⁵⁻⁷ Under different conditions, thermal effects in a bounding medium can cause a guided wave to become leaky at high powers, and again the waveguide transmission decreases with increasing intensity. These approaches can, if the material nonlinearity is broad-band, lead to large bandwidth optical limiters.

Optical waveguides therefore offer new opportunities for obtaining optical-limiter action caused by power-dependent amplitude distributions that occur under certain conditions. Consider waves guided by the thin-film waveguide shown in Fig. 1 for a film of refractive index n_f and thickness d , bounded by a cladding and substrate with indices n_c

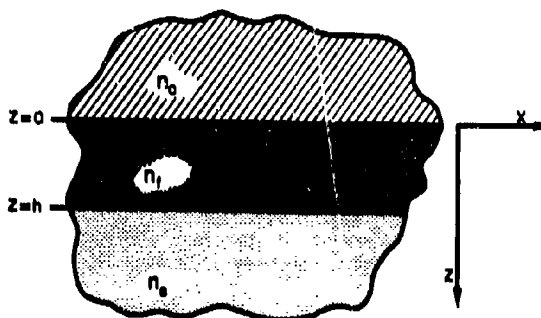


Fig. 1. Geometry pertinent to nonlinear guided waves.

and n_s , respectively. When the optically induced change in refractive index n_2 in one of the three media becomes comparable to $n_f - n_c$ or $n_f - n_s$, the guided wave fields and propagation wavevectors change dramatically from their low-power values.⁵⁻⁹ Fortunately, the nonlinear wave equation that includes an intensity-dependent refractive index has been solved analytically,⁵⁻⁸ and numerical solutions of the dispersion relations have shown that the resulting waves exhibit maxima in the power that can be transmitted by them. We have verified this basic prediction in a preliminary experiment.⁹

2. NONLINEAR GUIDED WAVES

(a) Self-focussing nonlinearities

In the geometry of Fig. 1, we assume that the cladding medium is characterized by a refractive index of the form $n = n_c + n_2 I$ where I is the local guided wave intensity. The nonlinear wave equation that must be solved, for example for T polarized waves (E_y), is

$$\nabla^2 E_y + k_0^2 [n_c^2 + n_2 E_y^2] E_y = 0, \quad (1)$$

where $k_0 = \omega/c$ and $n_2 = n_f^2 \epsilon_0 n_2$. For $n_2 > 0$, the field solutions in the nonlinear cladding are of the form⁵⁻⁸

$$E_y(x, z) = \frac{1}{2} \sqrt{\frac{2}{\epsilon_0}} \frac{q}{\cosh[qk_0(z_1 - z)]} e^{i(k_0 x - \omega t)} + cc, \quad (2)$$

where q is the effective guided wave index, $q^2 = \beta^2 - n_c^2$, and z_1 can be calculated from the power carried by the wave. In the film and substrate,

$$E_y(0, z) = E_y(0, 0) \left[\cos(\kappa k_0 z) + \frac{q}{\kappa} \tanh(qk_0 z_1) \sin(\kappa k_0 z) \right], \quad \beta < n_f, \quad (3a)$$

$$E_y(0, z) = E_y(0, 0) \left[\cosh(\kappa k_0 z) + \frac{q}{\kappa} \tanh(qk_0 z_1) \sinh(\kappa k_0 z) \right], \quad \beta > n_f, \quad (3b)$$

and

$$E_y(0, z) = E_y(0, d) e^{-\kappa(z-d)} \quad (3c)$$

respectively, where $E_y(0, 0)$ is given by Eq. (2), $\kappa^2 = \beta^2 - n_f^2$, and $\kappa^2 = |\beta^2 - n_s^2|$. Using standard integrated optics techniques, dispersion relations are obtained by

$$\tan(\kappa k_0 d) = \frac{\kappa[q \tanh(qk_0 z_1) + s]}{\kappa^2 - sq \tanh(qk_0 z_1)}, \quad \beta < n_f, \quad (4a)$$

and

$$\tanh(\kappa k_0 d) = \frac{\kappa[q \tanh(qk_0 z_1) + s]}{-\kappa^2 - sq \tanh(qk_0 z_1)}, \quad \beta > n_f. \quad (4b)$$

The total guided wave power per meter of wavefront is given by $P_c + P_f + P_s$, where

$$P_c = \frac{8q}{k_0 n_c^2 n_2} [1 - \tanh(qk_0 z_1)] \quad (5a),$$

$$P_s = \frac{80}{2\epsilon_0} \left| \frac{E_y(0, d)}{E_y(0, 0)} \right|^2, \quad (5b)$$

$$P_f = \frac{80}{2} \left[d \left(1 + \frac{q^2}{\kappa^2} \tanh^2(k_0 q z_1) \right) + \frac{\sin(2k_0 d)}{2k_0 \kappa} \left(1 - \frac{q^2}{\kappa^2} \tanh^2(k_0 q z_1) \right) + \frac{q}{\kappa^2 k_0} \tanh(k_0 q z_1) (1 - \cos(2k_0 d)) \right], \quad n_f > \beta, \quad (5c)$$

and

$$P_f = \frac{80}{2} \left[d \left(1 - \frac{q^2}{\kappa^2} \tanh^2(k_0 q z_1) \right) + \frac{\sinh(2k_0 d)}{2k_0 \kappa} \left(1 + \frac{q^2}{\kappa^2} \tanh^2(k_0 q z_1) \right) + \frac{q}{\kappa^2 k_0} \tanh(k_0 q z_1) (\cosh(2k_0 d) - 1) \right], \quad \beta > n_f, \quad (5d)$$

where S_0 is the guided wave Poynting vector at the film-cladding interface.

Since large material nonlinearities are usually accompanied by large loss in the material, it is useful to also estimate the power-dependent attenuation. The key assumption is that the field distributions obtained from solutions in lossless nonlinear waveguides are still valid if the loss is small. From the expansion of $\nabla \cdot (\epsilon \mathbf{E})$, and Maxwell's equations $\nabla \times \mathbf{E}$ and $\nabla \times \mathbf{H}$, it is easily shown that

$$\nabla \cdot (\epsilon \mathbf{E}) = \frac{1}{2} \epsilon_0 \epsilon_1 \mathbf{E}_y \cdot \mathbf{E}_y^* \quad (6)$$

in the y 'th medium where $\epsilon = n_y^2 - i\epsilon_1$, the relative dielectric constant has a small imaginary component. That is, $n_y^2 \gg \epsilon_1$. Integrating over a small-volume element dV and substituting in terms of the guided wave power will lead, after some manipulation, to

$$\beta_1 = \frac{c\epsilon_0}{4(P_c + P_f + P_s)} \int_{-\infty}^{\infty} \epsilon_1 E(z) \cdot E^*(z) dz \quad (7)$$

for the imaginary component of the effective index $\beta = \beta_R - i\beta_I$. Here P_γ is the power per unit distance along the wavefront propagating in the γ 'th medium. The subscripts c, f, and s refer to the cladding, film, and substrate, respectively. For s-polarized waves,

$$\beta_I = \frac{1}{2\beta_R(P_c + P_f + P_s)} \sum_{\gamma} \epsilon_{I\gamma} P_{\gamma} \quad (8)$$

Sample calculations⁷ are shown for $n_{2c} > 0$ in Fig. 2 for the effective mode index β versus guided wave power for the material system studied in our experiments,⁹ namely a glass film on a glass substrate with the nonlinear liquid crystal MBBA as the cladding. ($n_{2c} > 0$ corresponds to a nonlinearity in which the refractive index increases with increasing power.) For both the TE_0 and TE_1 modes that can be supported in this waveguide geometry there is a maximum in the power that can be transmitted by the waveguide for bounding media with a positive nonlinearity. For TE_0 , the transmitted power drops with increasing β after the peak is reached, and then rises again asymptotically to the power associated with a single interface s-polarized surface polariton.⁶ For TE_1 only, a single maximum in the guided wave power is predicted. The corresponding field distributions are shown in Fig. 3. The effect of increasing β is to localize the field in the cladding medium. Clearly, these nonlinear guided waves lead to optical limiter action.

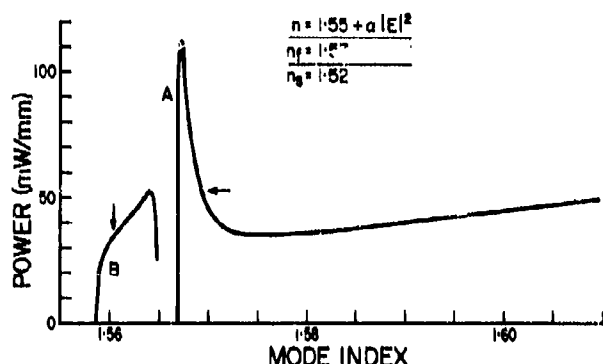


Fig. 2. TE_0 and TE_1 guided wave power versus the effective index β for waves guided by a Corning 7059 glass film ($h = 2.0 \mu m$) with a $n_s = 1.55$ substrate and a nonlinear cladding ($n_c = 1.55$, $n_{2c} = 10^{-9} m^2/W$).

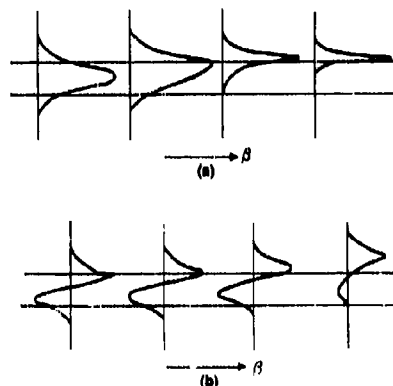


Fig. 3. The field distributions associated with TE_0 and TE_1 nonlinear guided waves for a nonlinear cladding.

The limiting action for the case $n_{2c} > 0$ has been demonstrated for TE_1 waves experimentally using the apparatus shown in Fig. 4. A bead of liquid crystal MBBA ($n_c = 1.55$, $n_{2c} = 10^{-9} m^2/W$) was placed on top of a glass ($n_g = 1.61$) waveguide deposited onto a microscope slide as a substrate ($n_s = 1.52$). Radiation from a 0.515- μm argon-ion laser was coupled into and out of linear portions of the waveguide by strontium-titanate coupling prisms.

The results⁹ are shown in Fig. 5. Both limiting action and hysteresis were observed. This hysteresis is a direct consequence of the lossy nature of the liquid crystal medium and is unrelated to the limiter action. The power-dependent loss occurs because of a power-dependent mismatch between the guided wave fields at the transverse, linear-nonlinear waveguide boundaries, and because of power-dependent attenuation in the nonlinear medium. Since the nonlinear bounding medium has a high absorption coefficient compared to that of the film, the attenuation of the guided wave should increase as an increasing fraction of the guided wave power is propagated in the nonlinear medium caused by self-focussing (Fig. 2). As the power is increased from zero, the wave follows the low β side of the dispersion curve (TE_1 in Fig. 2) up to the maximum power point where the transmitted power reaches a constant value. Hysteresis occurs when the incident power is decreased past the maximum transmission value and both branches of the β -versus-power curve are followed as the power is split between them (Fig. 2). The higher β branch corresponds to stronger localization in the liquid crystal and therefore higher net loss until the point where the high β branch terminates.

Therefore, the basic limiting action of the nonlinear guided wave solutions has been confirmed.

The nonlinear waves in this experiment were launched through the boundary between a normal and nonlinear waveguide. They could also have been excited by endfire coupling directly into the nonlinear waveguide. In both cases, the nonlinear field distributions are established at the linear (or air)-nonlinear waveguide transverse boundary, and typically all other fields are stripped (or radiated) away in at most a few tens of wavelengths. Therefore, only a few tens of micrometers are needed to establish the desired properties, and many such devices can be combined serially or in parallel.

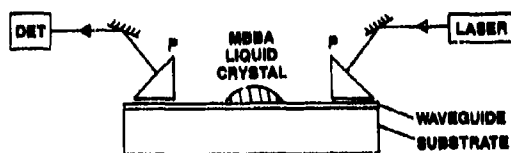


Fig. 4. The apparatus used to demonstrate nonlinear guided waves.

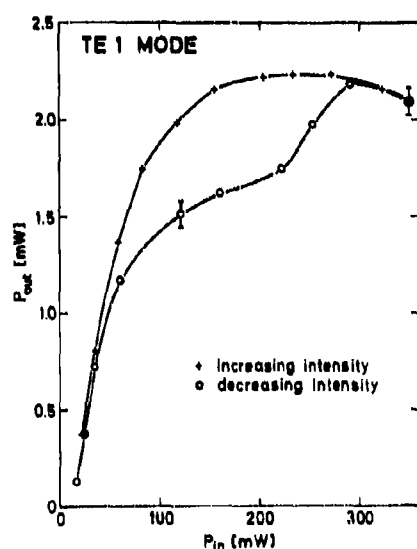


Fig. 5. The transmitted versus incident power for a nonlinear waveguide consisting of a liquid crystal used as a cladding on top of a thin film glass waveguide. The results are for the TE₁ wave.

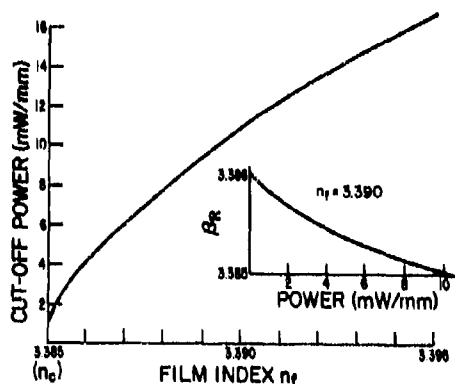


Fig. 6. The cut-off power for the TE₀ wave versus index difference between the film and nonlinear GeAsGaAl_xAs_{1-x} cladding. Inset is the effective index versus guided wave power for $n_f = 3.39$ and film thickness of 0.102 μm .

(b) Self-defocussing nonlinearities

The inherent problem with using self-focussing nonlinearities is that the lowest-order TE₀ solution exhibits only a local (and not absolute) maximum in the guided wave power. There is a maximum A_{sat} by which the refractive index of a material can be changed optically, and it is possible that inclusion of this saturation effect will lead to an absolute maximum in the power that can be transmitted by the TE₀ wave. However, a more attractive solution is to use nonlinear cladding media characterized by self-defocussing nonlinearities. As we now show, this leads to limiting action even with the lowest-order TE mode.

The nonlinear guided waves obtained in the material limit $n_{2c} < 0$ have been treated before.^{10,11} In this case, the solution to the nonlinear wave equation in the cladding is given by

$$E_{cy}(x, z) = \frac{1}{2} \sqrt{\frac{2}{|n_{2c}|}} \frac{q}{\sinh[qk_0(z_1 - z)]} e^{i(k_0 x - \omega t)} + \text{cc} \quad (9)$$

and the fields in the film and substrate are still given by Eq. (3), but with $\tanh(qk_0 z_1)$ replaced by $\cotanh(qk_0 z_1)$. The dispersion relations and power formulae are also still valid when the same substitution is made.

Optical limiting action can be obtained¹¹ if one ($n_c > n_s$, $n_{2c} \neq 0$), or both, of the bounding media is characterized by a self-defocussing nonlinearity ($n_{2c} < 0$). The results of a detailed calculation for a MQW (multiple quantum well) GaAs/GaAl_xAs_{1-x} guided wave structure are given here (Figs. 6 and 7). The nonlinear MQW material is assumed to be characterized by $n_{2c} = -2 \times 10^{-9} \text{ m}^2/\text{W}$ and $n_c = 3.385^{12}$; the substrate is the appropriate bulk GaAl_xAs_{1-x} composition for $n_s = 3.38$; and the film of bulk GaAl_xAs_{1-x} has variable index $n_f(x)$ and thickness. If the cladding is the only MQW material, then it is the only one that will have a significant nonlinearity at room temperature. We neglect losses, but do note that only a small length of guided wave structure is necessary since the nonlinear waveguide properties are all established at the nonlinear waveguide boundary. The decrease in β to waveguide cut-off with power is shown in the inset of Fig. 6. It can easily be shown that in this limit¹⁰

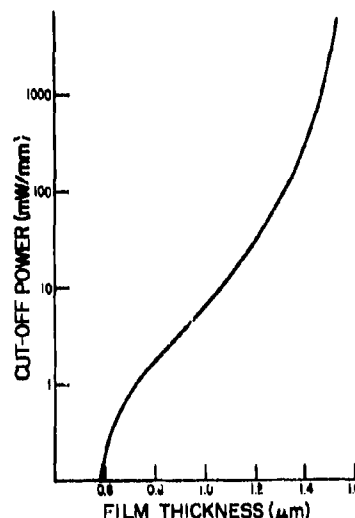


Fig. 7. The cut-off power versus film thickness for the TE₀ wave with β , the effective index fixed at $n_c + 0.2(n_f - n_c)$ for a GaAs-GaAl_xAs_{1-x} self-defocussing cladding.

$$P_c = \frac{1}{k_0^2 \epsilon_1 n_c n_{2c}} \quad (10)$$

$$\tan(k_0 kh) = \frac{\kappa[\kappa k_0 \epsilon_1 + 1]}{\kappa^2 k_0 \epsilon_1 - \kappa} > 0 \quad (11)$$

The second equation implies that $\epsilon_1 \neq 0$, which leads to a finite value of P_c at cut-off and optical limiter action, as shown in Fig. 6. Therefore, limiting action is obtained when the refractive index of the nonlinear bounding medium is larger than that of the linear bounding medium for negative nonlinearities. Note that this is the lowest-order mode, and when it cuts off, no power can be transmitted through the waveguide. The variation in cut-off power with index difference $n_f - n_c$ is also shown in Fig. 6. The thickness of the film was chosen to give $\beta = n_c + 0.2(n_f - n_c)$ for each case. A much more dramatic variation in cut-off power is produced (Fig. 7) by fixing n_f and varying the film thickness (and therefore β as well). Changes in limiting power of five orders of magnitude can be tuned by fixing the required film thickness. These results indicate that limiting action can be produced at usefully low power levels.

(c) Leaky wave cut-off

Optical limiting action can also be obtained by increasing the refractive index of a nonlinear cladding medium more or less uniformly until a guided wave becomes cut-off into a radiation field in either the cladding or substrate. That is, for a given thickness, the existence of a guided wave or a leaky wave in a guiding structure depends on the refractive index difference between the film and one or both of the bounding media. As the power in the nonlinear cladding increases, its index increases because of thermal effects, and the highest-order excited mode moves towards cut-off. At cut-off, energy leaks out of the guided wave in the form of radiation fields. If $n_c > n_f$, radiation occurs into the cladding medium. Alternatively, if $n_s > n_c$, power is radiated into the substrate.

The results of an experiment that appears to exhibit this type of behavior is shown in Fig. 8. The transmitted power initially rises linearly with incident power. Further increase in incident power leads to decrease in transmitted power until very little is transmitted by the waveguide via the mode being launched. Note that in this case the degree of limiting action depends on the propagation distance through the nonlinear part of the waveguide, contrasting with the previous two cases in which the limiting action was established at the transverse boundary.

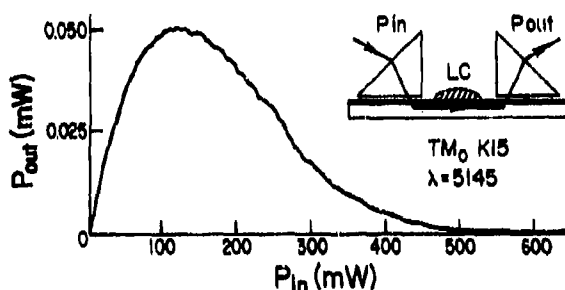


Fig. 8. The TM_0 guided wave power transmitted by a section of glass waveguide with a bead of the liquid crystal on top.

3. NONLINEAR DISTRIBUTED COUPLERS

A third unique guided wave approach to optical limiters is to exploit the very process by which radiation is coupled into a thin-film waveguide by distributed couplers such as a prism or a grating. The geometry we consider is shown in Fig. 9. Light is incident through a prism of refractive index n_p at an angle θ_p to the surface normal. One of the waveguiding media, the cladding (gap), film, or substrate, exhibits an intensity-dependent refractive index whose change with intensity is given by $n_2 I$, where I is the local guided wave intensity.

The coupling process by which a guided wave is launched is well known. The incident field is written as

$$E_{in}(x, z) = \frac{1}{2} E_{0a}(x) e^{ik_0 n_p (\sin \theta_p x - \cos \theta_p z)} - i\omega t + cc \quad (12)$$

where $a_0(x)$ describes the incident field distribution along the propagation direction, typically Gaussian. The guided wave field at the film-cladding interface is written as

$$E(x) = \frac{1}{2} a_g(x) e^{i(k_0 x - \omega t)} + cc \quad (13)$$

Here $a_g(x)$ is the guided wave field amplitude. Assuming that one of the guiding media has an intensity-dependent refractive index and that the principal effect of the nonlinearity is to produce a power-dependent guided-wave wavevector, this wavevector can be written in the form¹

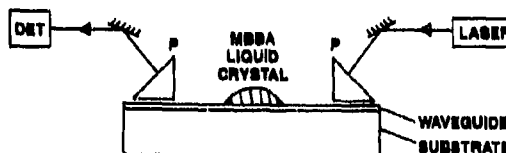


Fig. 9. The nonlinear prism coupler geometry.

$$\beta = \beta_0 + \Delta\beta_0 P_g \quad (14)$$

where P_g is the guided wave power per millimeter (measured along the wavefront) and the coefficient $\Delta\beta$, is calculated from the guided wave nonlinearities. The nonlinear coupling process discussed here usually occurs at power levels one order of magnitude less than that required for nonlinear guided waves. The variation in guided wave index with power corresponds to the linear portion of the curves in Fig. 2. A coupled-mode computational approach is adequate for the calculation of $\Delta\beta_0$. The coupling equation that describes the exchange of energy between the incident and guided wave is³

$$\frac{d}{dx} a_g(x) = i \tau_0(x) e^{i(n_p k_0 \sin \theta_p - \beta_0 - \Delta\beta_0 P_g)x} \cdot e^{-i a_g(x)} \quad (15)$$

where λ is the characteristic distance for reradiation of the guided wave field back into the prism and is the transfer coefficient that is easily calculable from the waveguide parameters.

A calculation of the in-coupled versus incident power is shown in Fig. 10. As the waveguide power grows with propagation distance, the wavevector mismatch between the incident and guided wave fields increases (that is, $\Delta\beta k_0 = -\Delta\beta_0 k_0 P_g \neq 0$ initially assuming $n_p k_0 \sin \theta_p = \beta_0$) and coupling synchronism (defined by $\Delta\beta = 0$) is lost. The net result is that coupling efficiency decreases with increasing power,⁸ leading directly to an optical limiter, as indicated in Fig. 10.

A preliminary experiment has been performed to test this concept.⁴ Liquid crystal MBBA was placed between a coupling prism and a Corning 7059 glass film deposited onto a silica glass substrate. The coupling efficiency was measured by comparing the power coupled out by a second linear coupler to the power incident on the input coupler. The results are shown in Fig. 11. There is clear indication of nonlinear coupling leading to optical limiting action.

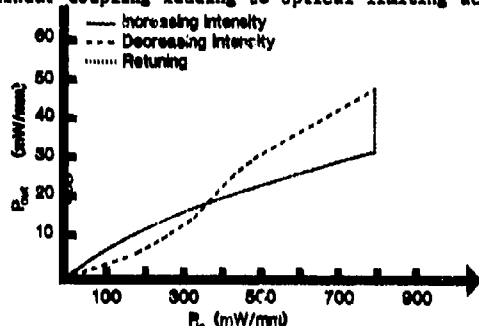


Fig. 10. Theoretical calculation of the waveguide versus incident power for a nonlinear prism coupler with $\lambda/w_0 = 1.5$, $w_0 = 0.63$ mm, and $\alpha = 100$ cm⁻¹. At an incident power of 800 mW, the coupling efficiency was re-optimized (by varying the incidence angle) and then the incident power reduced to zero.

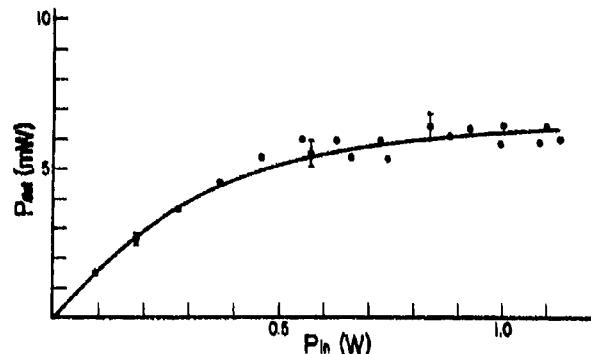


Fig. 11. The guided wave power versus power incident onto a coupling prism for a nonlinear coupler consisting of a liquid crystal (cladding), a Corning 7059 glass film, and a soda-lime glass substrate.

It is interesting to note that the operation of a nonlinear out-coupler is different from the input coupler. In the out-coupling process, the direction of the radiation field is determined by the local guided-wave wavevector. Therefore, it is automatically always synchronized to the guided wave. Reversing the input and output in Fig. 9, we found the transmitted intensity to remain linear with input power, as expected.

One of the key features of this type of limiter is the highly directional radiation accepted by the prism coupler. Therefore, not only does it limit the power accepted over a small solid angle, such as a distant source, it also very efficiently rejects electromagnetic energy that is not incident at the correct angle.

This research was supported by the National Science Foundation (ECS-8304749), Army Research Office (DAAG-29-85-K-0026), the Joint Services Optics Program (MICOM, BMDSC), and the NSF-Industry Center for Optical Circuitry.

References

1. G. I. Stegeman, IEEE J. Quant. Electron., QE-18, 1610 (1982).
2. D. A. B. Miller, S. D. Smith and A. Johnston, Appl. Phys. Lett., 35, 658 (1979).
3. C. Y. Liao and G. I. Stegeman, Appl. Phys. Lett., 44, 164 (1984).
4. J. D. Valera, C. T. Seaton, G. I. Stegeman, R. L. Shoemaker, Xu Mai, and C. Liao, Appl. Phys. Lett. 45, 1013 (1984).
5. N. N. Akhmediev, Sov. Phys. JETP, 56, 299 (1982).
6. A. A. Maradudin, "Nonlinear Surface Electromagnetic Waves", in Solids-Modern Topics, M. Borissav, ed., (Singapore, World Scientific Publishers, 1983) p. 72.
7. G. I. Stegeman, C. T. Seaton, J. Chilwell, and S. D. Smith, Appl. Phys. Lett., 44, 830 (1984).

9. H. Vach, G. I. Stegeman, C. T. Seaton and I. C. Khoo, Opt. Lett., 9, 238 (1984).
10. C. T. Seaton, J. D. Valera, R. L. Shoemaker, G. I. Stegeman, J. Chlilwell, and S. D. Smith, Appl. Phys. Lett. 45, 1162 (1984).
11. C. T. Seaton, Xu Mai, G. I. Stegeman, and H. G. Winful, Optical Engineering, in press.
12. D. A. B. Miller, D. S. Chemla, D. J. Eilenberger, and P. W. Smith, Appl. Phys. Lett., 41, 679 (1982).

DISCUSSION

A.Kohnle, Ge

You showed an optical limiter into which radiation is coupled by a prism. Can you say something about the acceptance angle restrictions or field of view of such a device?

Author's Reply

The typical numerical aperture is few minutes of arc.

PIN-FET PREAMPLIFIER FOR HIGH-SPEED OPTICAL TRANSMISSION SYSTEMS

B. Schwaderer
 ANT Nachrichtentechnik GmbH
 Gerberstraße 33, 7150 Backnang, FRG

Summary

The design of a hybrid integrated PIN-FET transimpedance preamplifier is given for long-haul optical transmission systems at 1.3 μm wavelength with bit rates of 140 Mbit/s and 565 Mbit/s. The preamplifier uses a GaInAs/InP PIN-photodiode with a dark current of less than 10 nA, a high spectral responsivity of greater than 0.7 A/W at 5V bias supply and a GaAs-MESFET with 45 mS transconductance and about 0.7 pF input capacitance. Using transimpedance-resistors of 50 k Ω and 25 k Ω the design goals of receiver sensitivities are -43 dBm for the 140 Mbit/s system and -36.7 dBm for the 565 Mbit/s system respectively for BER 10^{-9} . The measured values of -42.8 dBm and -35.8 dBm including connector losses are within the predicted ranges.

1. Introduction

The development of multi-mode graded-index fibers and single-mode fibers with low loss and high bandwidth in the long-wavelength region ($\lambda = 1.1 \mu\text{m} - 1.6 \mu\text{m}$) has spurred the demand for high-speed optical transmission systems, covering the PCM (Pulse-Code-Modulation) transmission systems hierarchy of 140 Mbit/s and 565 Mbit/s.

One of the key-elements of such systems is the optical receiver. As the transmitted output power of the laser diodes used is fixed because of life-time reasons, the receiver sensitivity is one of the main figures affecting the maximal transmission distance without repeaters.

At present time for bit rates up to 700 Mbit/s, the optical receiver is based on either a Germanium avalanche photodiode (Ge-APD) in conjunction with a low-noise bipolar transistor preamplifier or an Indium-Gallium-Arsenide PIN-photodiode (InGaAs PIN) hybrid integrated with a low-noise GaAs-MESFET preamplifier.

PIN-FET receivers can have a better receiver sensitivity than Ge-APD receivers [1] and they don't require a stabilization of the high voltage bias supply and of the temperature. Thus this paper shows the design of PIN-FET preamplifiers for optical receivers.

2. Basic Design Principles

The goal in the design of an optical receiver is to minimize the amount of optical power necessary at the receiver input to achieve a given bit error rate (BER) in digital systems. This optical power P is usually measured in dBm (0 dBm = 1 mW) and referred to as receiver sensitivity. To optimize the sensitivity, the photocurrent generated by the detected power P must be converted to a usable signal V_{out} for further processing with a minimum amount of noise added, Fig. 1a. The preamplifier is defined as the first stage or stages of amplification following the photodiode. Beside the detector the preamplifier is the dominant source of noise added to the signal. Thus the main noise sources are: the shot-noise of the photodiode current, the thermal noise of the resistor used to provide a dc-return-path for the detector current, the shot-noise of the gate leakage current and the noise contribution of the channel conductance of the FET.

Fig. 1b depicts the noise equivalent circuit of the receiver input stage. The signal current I_s is generated by the incident light of power P and given by

$$I_s = S_\lambda \cdot P \quad (1)$$

where the spectral responsivity S_λ of the photodiode depends on the quantum efficiency of the diode and of the photon energy or wavelength. S_λ ranges from 0.7 to 0.9 A/W at 1.3 to 1.6 μm typically. The shot noise current source i_d^2 with the density

$$\frac{d}{df} i_d^2 \approx 2q (I_s + I_0) \quad (2)$$

(q is the electronic charge) represents the noise contribution of the signal current I_s and the dark current I_0 of the diode. C_d is the depletion capacitance of the diode. The bias resistor R is associated with a thermal noise current i_R^2 of density

$$\frac{d}{df} i_R^2 = 4kT \frac{1}{R} \quad (3)$$

(Boltzmann's constant k , absolute temperature T). C_S is any stray capacitance of the circuit. The input equivalent noise sources of the FET with the input impedance Z_{in} originate from the gate current I_G .

$$\frac{d}{dt} \overline{i_G^2} = 2qI_G \quad (4)$$

and the channel conductance

$$\frac{d}{dt} \overline{v_G^2} = 4kT \left(\frac{r}{g_m} \right) \quad (5)$$

(g_m transconductance, r noise calculation factor; $r \approx 0.7$ for Si-FET, $r \approx 1.1 - 1.7$ for GaAs-MESFET [2]).

For signal frequencies up to 1 GHz the input impedance of FET will be capacitive,

$$Z_{in} \approx \frac{1}{2\pi f C_{in}} \quad (6)$$

where C_{in} is composed of the gate-source-capacitance and the drain-gate-capacitance. A detailed analysis shows, that the bit rate dependence of the total noise due to the bias resistor and the FET becomes [3/

$$\overline{i^2} = \left[\frac{4kT}{R} \left(1 + \frac{r}{g_m R} \right) + 2qI_G \right] I_2 f_B + 4kT r (2\pi)^2 \frac{C_F^2}{g_m} I_3 f_B^3 \quad (7)$$

($C_F = C_d + C_S + C_{in}$; I_2, I_3 calculation figures dependent on the shape of the signal pulses; f_B bit rate).

To minimize the noise contributions of the FET, a GaAs-MESFET is commonly used, selected for low input capacitance, high transconductance and low gate leakage current. To reduce the thermal noise contribution of the dc-return resistor R_B (Fig.2) for the photodiode, the value of the resistor should be as large as possible, typically 1 to 5 M Ω . When R_B is large the input admittance is dominated by the total input capacitance C_F and the frequency response of the front-end has a low cut-off frequency f_{CH} , typically 20 to 100 kHz. This design is referred to as high impedance front-end. For digital signals with clock frequencies $f_C \gg f_{CH}$ a carefully adjusted equalization is necessary to reshape the signal pulses. In many cases the equalization is done by using a differentiator which attenuates the low frequency components of the signal and thus restores a flat frequency response. Although the high impedance front-end is capable of reducing the noise to an absolute minimum [3/], this design has several drawbacks:

- o The equalization has to be adjusted to compensate the frequency dependence of the input admittance, which varies from front-end unit to unit.
- o The equalization exactness depends on the signal spectrum.
- o The dynamic range is reduced because the building up of the low frequency signal components within the front-end leads to saturation at high input signal levels.
- o Circuits for temperature compensation of the operating points have to be added.

These drawbacks are not given in the transimpedance front-end design (Fig.3), where the shunt feedback resistor R_F additionally acts as dc-return-resistor of the photodiode. If R_F has the same value as R_B , the noise of the transimpedance front-end is the same as that of the high impedance front-end. Assuming the same total input capacitance C_F and a frequency independent open loop gain A of the amplifier, the frequency response of the transimpedance front-end has a cut-off frequency f_{CT} which is by the factor A higher than f_{CH} . If f_{CT} is greater than half the signal clock frequency no additional signal equalization is needed.

In practice the noise performance of the transimpedance front-end is not as good as that achieved with the high impedance front-end. The reasons are:

- o The open loop gain is limited, thus R_F is limited if there is no equalization considered.
- o Shunt feedback amplifiers with high gain tend to oscillate with increasing feedback resistor.
- o The stray capacitance C_F of the feedback resistor increases the total input capacitance thus reducing the bandwidth.

These drawbacks of the transimpedance design are not so severe than those of the high impedance concept.

Thus in spite of somewhat reduced receiver sensitivity PIN-FET transimpedance preamplifiers are used in our optical transmission systems for bit rates of 140 and 565 Mbit/s.

3. PIN-FET Preamplifier for 140 and 565 Mbit/s

Fig.4 shows the principle circuit of the 140 Mbit/s front-end. The detector is a back-side illuminated mesa type InGaAs/InP PIN-photodiode for the 1.1 to 1.6 μm wavelength region. Within this wavelength region, the optical responsivity is greater than 0.75 A/W. The active area has a diameter of 90 μm . At a reverse bias of 5 V, the diode has a dark current lower than 10 nA and a depletion capacitance of about 0.4 pF. The preamplifier consists of a wellknown cascode stage with a GaAs-MESFET input transistor and a bipolar microwave Si-transistor of pnp-type and two additional emitter followers. The GaAs MESFET has a transconductance of $>40\text{ mS}$ and an input capacitance of $<0.7\text{ pF}$. The open loop total input capacitance C_T is in the range of 1.2 to 1.6 pF. The shunt feedback resistor $R_F = 50\text{ k}\Omega$ is a thin film hybrid integrated chip resistor with minimum stray capacitance C_F (compare Fig.3). The influence of C_F on the frequency response of the preamplifier is compensated within the feedback loop. The overall electrical 3-dB-bandwidth of this PIN-FET receiver is calculated to 110 MHz, the measured value is 109 MHz. Fig.5 shows the calculated and measured receiver sensitivity of the front-end. The minimum mean optical power for $\text{BER} = 10^{-9}$ is calculated and measured: -43.5 dBm and -42.8 dBm respectively. The measurements are performed at 1.3 μm wavelength, a bitrate of 170 Mbit/s (140 Mbit/s including a 5B6B line code) and a pseudo random signal with a period of 2^7-1 bit.

The circuit of the 565 Mbit/s front-end is given in Fig.6. In principle it is the same cascode stage as at 140 Mbit/s. The shunt feedback resistor is reduced by a factor of two to $R = 25\text{ k}\Omega$ and the receiver bandwidth is increased to 400 MHz. This bandwidth increase is reached by inserting an equalizing amplifier stage between the emitter followers. The overall electrical 3-dB-bandwidth is calculated to 400 MHz and measured to 425 MHz. Fig.5 shows the receiver sensitivity of this receiver as well. The minimum optical power for $\text{BER} = 10^{-9}$ is calculated and measured: -36.9 dBm and -35.8 dBm respectively.

These receiver sensitivities are comparable to published values reached by the use of Ge-APD-receivers with -40.5 dBm at 170 Mbit/s /1/ and -38 dBm at 565 Mbit/s /4/.

4. Conclusion

The design of hybrid integrated PIN-FET preamplifiers is given for optical transmission systems in the long wavelength region. Two amplifier-designs are commonly used with a GaAs-MESFET of high transconductance ($>40\text{ mS}$) and low input capacitance ($<0.7\text{ pF}$) as an input transistor: a high impedance design and a transimpedance design. The first one requires careful frequency response equalization and has low dynamic range. The second one shows about 1-2 dB lower receiver sensitivity than the first, but has higher dynamic range, no stability problems and is insensitive to tolerances of the used active components.

Transimpedance PIN-FET preamplifiers for optical transmission systems at 1.3 μm wavelength with bitrates of 170 Mbit/s (140 Mbit/s, line code 5B6B) and 565 Mbit/s are presented. With transimpedance-resistors of 50 k Ω and 25 k Ω the design goals of receiver sensitivities are -43 dBm and -37 dBm respectively for $\text{BER} \leq 10^{-9}$. The measured values of -42.8 and -35.8 dBm including connector losses are within the predicted ranges.

References:

- /1/ Smith, D.R.; Hooper, R.C.; Smyth, P.P.; Wake, D.:
Experimental comparison of a germanium avalanche photodiode and InGaAs PINFET receiver for longer wavelength optical communication systems
Electr.Lett., Vol.18, 1982, pp. 453-454
- /2/ Ogawa, K.:
Noise caused by GaAs MESFETs in optical receivers
BSTJ, Vol.60, 1981, pp. 923-971
- /3/ Smith, R.G.; Personick, S.D.:
Receiver design for optical fiber communication systems;
in Kressel, H: Semiconductor devices for optical communication; Springer Verlag, Berlin 1980, pp. 89-160
- /4/ Bambach, W.; Kremers, E.; Schwaderer, B.; Wernz, H.;
Wiesmann, Th.; Gruber, J.; Tränkle, G.:
565-Mbit/s single-mode transmission system with monolithic integrated circuits
10th ECOC '84, Stuttgart 1984, Conf.Proc., pp. 254-255

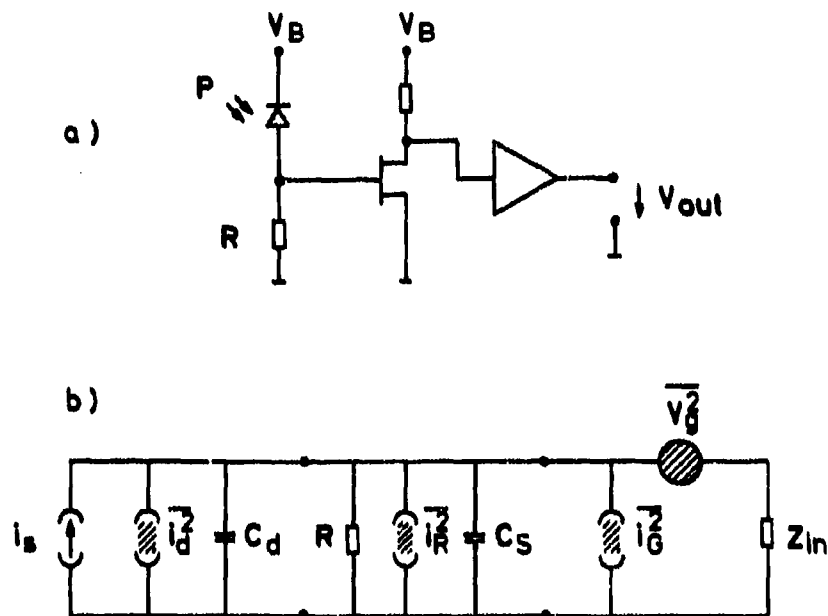


Fig.1: PIN-FET-Preamplifier and simplified noise equivalent circuit

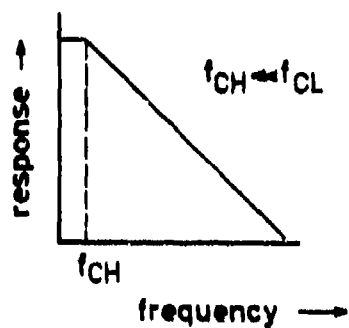
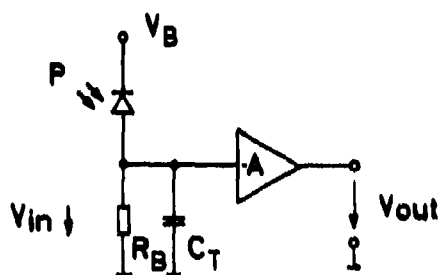


Fig.2: High impedance preamplifier

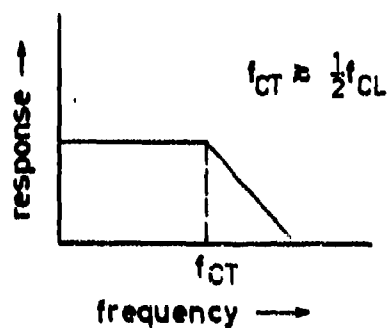
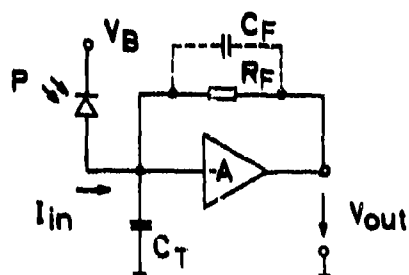


Fig.3: Transimpedance preamplifier

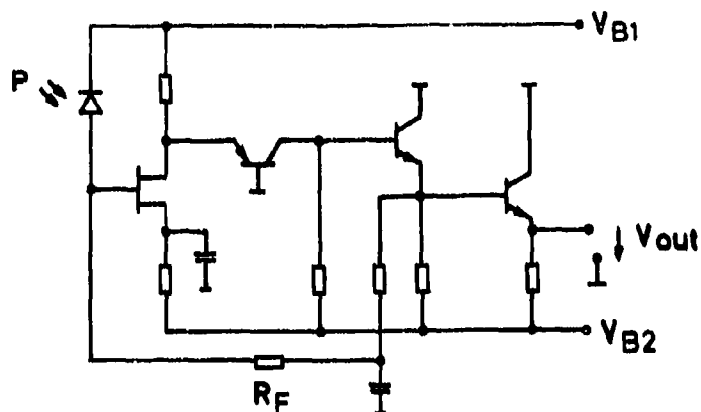


Fig.4: Optical receiver for 140 Mbit/s

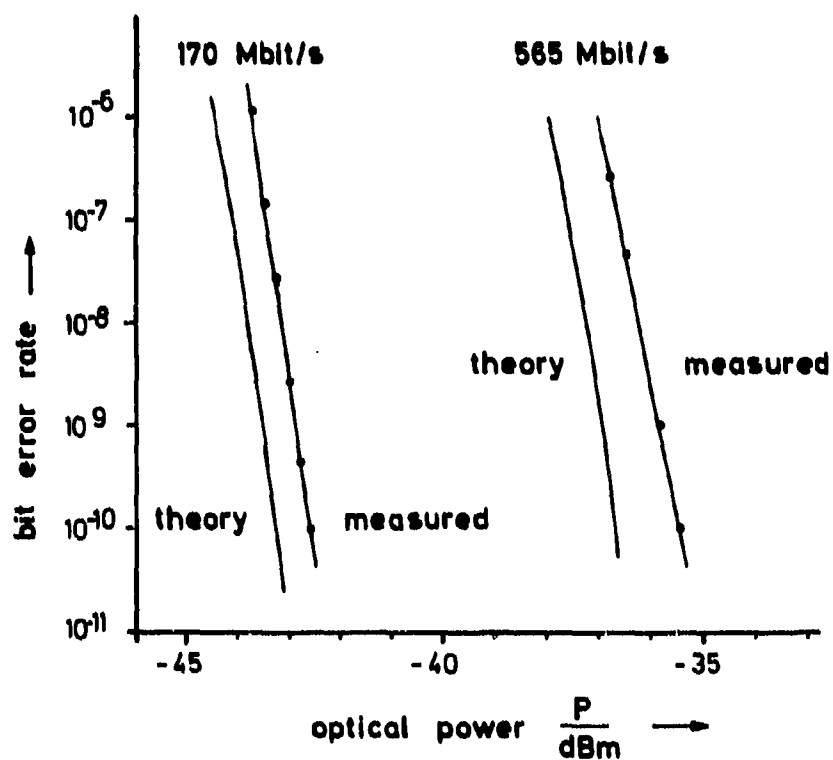


Fig.5: Predicted and measured receiver sensitivities at 170 and 565 Mbit/s

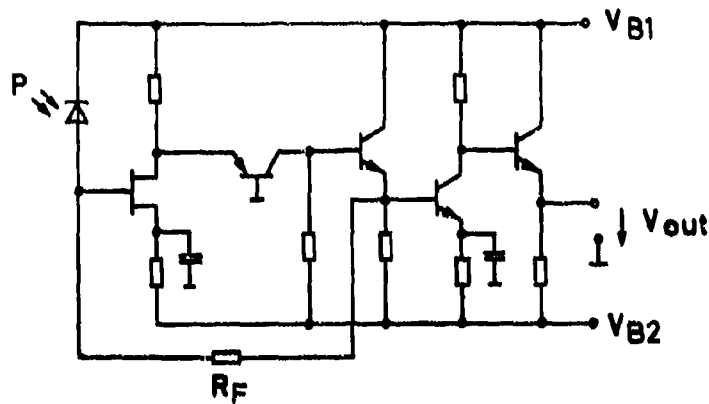


Fig.6: Optical receiver for 565 Mbit/s

DISCUSSION

S.Walker, UK

(1) Are $1/f$ noise terms important in your description? (2) Do you include intersymbol interference effects in your transimpedance bandwidth calculation?

Author's Reply

(1) The $1/f$ noise terms were not found to be important. (2) The receiver bandwidth is made large enough to remove I.S.I. effects.

P.Deimel, Ge

What is the advantage of FETs at high bit rates compared to bipolar devices?

Author's Reply

Two aspects have to be considered: the FET gate leakage current is of the order of 5,10 nA, where as the bipolar device needs a base current of 100 to 200 μ A this has higher shot-noise. To overcome this noise one has to use a sophisticated design APD, which is not yet available (in In-P-technology); the collector-base-capacitance of the transistor acts as Miller-capacitance. This capacitance has to be compared to the stray capacitance C_F of the feedback resistor. One has to optimize between these aspects which leads to a FET-input stage.

OPTOELECTRONIC BROADBAND SWITCHING FOR COMMUNICATIONS AND SIGNAL PROCESSING

by

R.I. MacDonald and D.K.W. Lam
Optical Communications Program
Department of Communications
Communications Research Centre
3701 Carling Avenue
P.O. Box 11490, Station H
Ottawa, Ontario, Canada
K2H 8S2

Summary

By employing a hybrid technology using electronic and optical integration, optical isolation levels can be attained in a switch matrix without the need to switch light. Bandwidths of several GHz, subnanosecond switching time and crosstalk below 50 dB have been demonstrated in monolithically integrated optoelectronic switch matrices. These devices show high promise as central switches in star configuration communication systems where very high bandwidth or very large array size is required. Advantages over foreseeable alternative technologies include size and power consumption as well as performance. In addition, optoelectronic switch matrices have unique properties that suggest their application in a number of signal processing situations where precise broadband signal delays are required, such as in the phasing of arrays, or the production of tunable filters. Recent work in these areas will be described.

1. Introduction

Optical transmission has advanced very rapidly in the telephone network because of the low losses and high digital rates that can be attained. The immunity of optical transmission to signal leakage has also been important for military applications where security is a concern. This feature can be of use in applications other than transmission. A notable example is in broadband matrix switches, where signal paths in close proximity must not crosscouple, even at high frequency.

Although the leakage immunity of optical waveguide signal distribution and the absence of any need to match the impedances of the distribution lines to switches are advantageous for matrix switch design, what is lacking at present is a suitable optical crosspoint switch. Light can be switched in a variety of ways. Optical switch matrices have been made with optomechanical switches in which fibres or prisms are physically moved [1,2], with electro optic devices employing controlled coupling between single mode waveguides [3], and with multimode waveguide switches based on total internal reflection [4]. None of these devices, however, is entirely suitable for large scale switching of high frequency signals, because of slow switching action, excessive crosstalk, high insertion loss or large size. All are in an experimental stage of development.

In this paper we report recent developments in an alternative form of photonic switch matrix that takes advantage of optical signal distribution but avoids the need to switch light. This method employs optoelectronic detectors as crosspoint switches. Signals are distributed to the detectors via an optical distribution network as shown in Fig. 1. The crosspoint photodetectors convert these incoming optical signals to electrical ones which are then summed up into output ports. Switching occurs because the detection of the optical signals is controllable: the photodetectors can be rendered sensitive or insensitive by appropriately biasing them [5,6]. The overall performance of the matrix is determined by the switching performance of the photodetectors and by the electromagnetic coupling among the output lines. In principle the latter can be made arbitrarily small because no electrical lines need cross: the only crossings occur between electrical and optical lines. Therefore any derived form of electrical isolation can be inserted between output lines. In practice, as we will show, the isolation can be very good even in very compact integrated arrays. Aspects of these switching matrices that are expected to be of importance in military applications are the simplicity, reliability and small size that can be achieved by integrated optoelectronic fabrication techniques for which these matrices are well suited, and the broad band performance available. Applications to signal processing may be of particular importance.

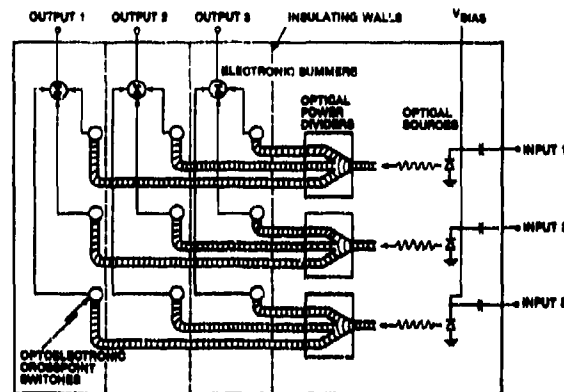


Fig. 1. Schematic diagram of an optoelectronic switch matrix. Input signals are converted to light and distributed in that form to the crosspoints. Output electrical signals are generated in the on-state crosspoint photodetectors and summed into the output lines.

2. Optoelectronic Switch Matrices

A number of different photodetectors have been reported as optoelectronic crosspoint switches [7-11]. In general very high isolation (over 90 dB at 1 GHz) can be obtained with bipolar devices, whereas more convenient fabrication and operation is achieved with photoconductors, which have isolation between 50 and 70 dB. Overall, GaAs photoconductors seem to be the most promising devices for optoelectronic switching, because of their very broadband response and the ease with which they can be integrated with each other [12] and with GaAs field effect transistors in monolithic optoelectronic integrated circuits. This paper will be chiefly concerned with GaAs photoconductor crosspoint switches.

A typical GaAs photoconductor switch that we have studied consists of a mesa of epitaxially grown GaAs ($n \sim 5 \times 10^{18} \text{ cm}^{-3}$, 1 μm thick) over which interdigitated contacts are formed with evaporated AuNiGe, with a contact spacing of 5 μm . The sensitive area has a 100 μm diameter. The frequency response of such a detector between 900 MHz and 1.8 GHz is shown in Fig. 3. The response is essentially flat from DC to 1.75 GHz. To obtain the response shown in Fig. 3 a nominal bias of 2 V was applied resulting in a bias current of 10 mA. The detector was mounted in a microstrip biasing and decoupling circuit. The optical signal was supplied by a current modulated laser diode operating at 0.82 μm wavelength, at an average incident power of 1 mW via a butt-coupled optical fibre. The overall responsivity of the detector is about 0.3 A/W, which is close to calculated values and shows evidence of internal photo current amplification due to the photoconductive gain mechanism. The noise equivalent power is about 10^{-11} W/Hz . The photoconductor thus has similar performance to a broadband p.i.n. diode but has higher bias current and correspondingly higher noise, as well as faster switching times and lower operating voltage.

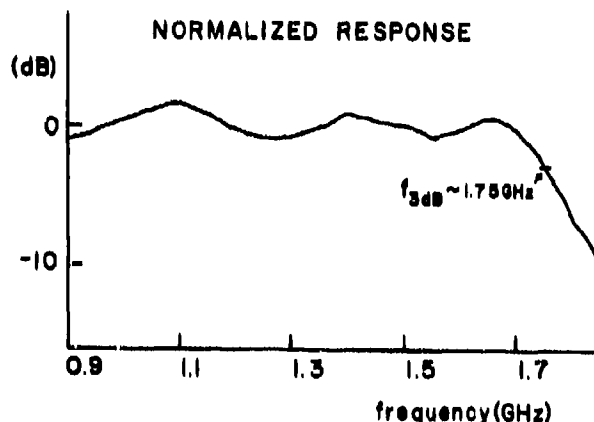


Fig. 2. Response of a microstripline-mounted GaAs photoconductor to 1 mW optical signal at 820 nm wavelength. Flat response is achieved between 1 MHz and 1.75 GHz. Bias voltage is 2 V, bias current 10 mA, contact spacing is 5 μm .

The switching performance is indicated in Fig. 3, which represents the response of the same device between 300 MHz and 1.3 GHz when the photoconductor is biased (upper trace) or unbiased, i.e. either in an open circuit, or with bias supply grounded (lower trace). The rolloff in on-state signal below 300 MHz is due to a high-pass circuit in the laser driver, and is not an intrinsic property of the photoconductor. The response to the optical signal is reduced by about 50 dB. The residual response in the unbiased off-state, which is about 10 dB above the detector noise floor, is attributed to photovoltaic effects, and may be eliminated by advances in fabrication technology. Other similar devices have up to 70 dB isolation. These results indicate that the photoconductor can be used as a crosspoint switch with high isolation over the frequency range 0-2 GHz.



Fig. 3. Switching performance of the above device. The upper trace shows the response when biased. The lower trace shows the response when unbiased. (The rolloff below 300 MHz is due to the transmitter drive circuit). More than 50 dB isolation is obtained. Other devices have shown up to 70 dB.

The speed with which the crosspoints can change state is important in many applications. Fig. 4 demonstrates the gating of a high speed pulse by a photoconductive crosspoint switch [13]. The detector's response to the pulse (which is offset by the right for clarity) is visible only if bias voltage is applied. Switching speeds below 1 ns were indicated by this method. Indirect measurements using a mixing technique suggest that the switching time is less than 250 p.s.



Fig. 4. (i) Bias pulse monitor : 1 v/div 1 ns/div.
 (ii) Laser pulse monitor : 5 mv/div 1 ns/div.
 (iii) Photoconductor response: 2 mv/div 50 ps/div.
 Response of GaAs photoconductors when: (a) (ii) is ahead of (i), off condition, (b) (ii) is within (i), on condition, (c) (ii) is after (i), off condition. The photoconductor response (iii) is deliberately offset to the right for clarity.

To test the concept of broadband matrix switching with photoconductors we have constructed a breadboard 3x3 photoconductive matrix switch [14] as shown in Fig. 5. Three shielded laser transmitters mounted on microstrip biasing circuits are in the brass housings at the left. The three optical signals are coupled into multimode optical fibres with 100 μ cores, and split by the three-way biconical taper optical fibre power dividers [15] mounted on glass slides at the centre. Each signal is delivered to one photoconductive detector connected to each output line at the bottom. The three photoconductor crosspoints serving each outgoing line are monolithically integrated and the optical fibres delivering the signal are butt-coupled and fixed with epoxy. The performance of each crosspoint is shown in Fig. 6, where all possible signal connections are depicted in a matrix. These results demonstrate the feasibility of optoelectronic matrices for handling very broadband signals. The results shown cover 0-1.3 GHz. Measurements at 3.8 GHz yielded 45 dB isolation for most crosspoints, the reduced value being due to rolloff in the laser output and detector response at high frequency. With new, high frequency laser diodes, optoelectronic matrices are expected to maintain at least 50 dB isolation over the bandwidth of the detectors.



Fig. 5. Breadboard 3x3 optoelectronic switch matrix for 1 GHz. Input signals drive three lasers at left. Optical power is divided 3 ways in each of the biconical taper couplers mounted on glass slides. Signals are delivered to monolithic 3x1 arrays. Control is by bias voltages applied to the detectors.



Fig. 6. Performance of the breadboard array. Each photo shows on-state and off-state for a signal applied to the corresponding input (at left) and transmitted to the corresponding output (along bottom).

The promise of optoelectronic switching depends on the integration of the detector arrays. Initial efforts to demonstrate monolithic arrays [12] have yielded excellent results up to about 100 MHz, as shown in Fig. 7. Isolation is 70 dB, crosstalk between electrical lines is below 80 dB. At higher frequencies, however, crosstalk among the electrical output lines posed a severe limitation. Further investigation using monolithic arrays mounted in carefully designed alumina microstripline biasing and decoupling networks have yielded very promising results.

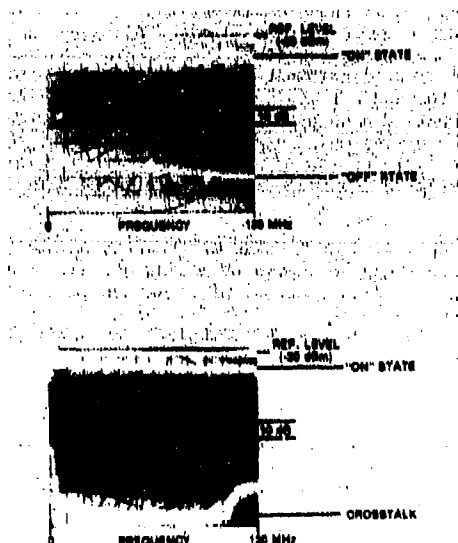


Fig. 7. Crosstalk measurements over the frequency range 0-130 MHz for an experimental monolithic 2x2 array - typical case. The output crosstalk is about 80 dB below the signal, and the switch crosstalk between 60 and 70 dB below the on-state response. The package actually contains a 5x5 crosspoint array of which only a submatrix is connected.

We have characterised the switching performance of monolithic GaAs photoconductor arrays consisting of elements spaced 100 μm apart. A shielding mesa and metallization was provided around the detectors and covering the area between them. Over the band 0-1.3 GHz, crosstalk is below 45 dB for nearest neighbours, and below 50 dB for detectors spaced by 500 μm [16]. This result shows the feasibility of integrated photodetector arrays to switch high rate data and wideband analogue signals, for example FM video.

The integrated fabrication of a developed optoelectronic switch array must ultimately include the summing points shown in Fig. 1, bias control circuits for the photodetectors, and preamplifiers for the detected signal, as well as the optical distribution waveguide. With detectors such as photoconductors whose off-state is a zero-bias condition, the summing of the signals is easily achieved onboard the chip by connecting all the photodetectors serving one output line to a common load. A single pre-amplifier is thus needed for each output line. The preamplifier and the bias control circuits can be made using GaAs FETs which are easily integrated using the photoconductor fabrication process. The optical waveguide is more problematic. We are presently experimenting with a hybrid integrated arrangement in which the distribution waveguides are fabricated by ionic interchange in a glass substrate. Light is coupled out of these waveguides normal to the surface by a perturbation. The integrated arrays of GaAs photoconductors are mounted face-down on the glass waveguide substrate so that a portion of the light in each waveguide is coupled by the perturbations into each detector. The glass substrate also carries a metallization and performs simultaneously the role of a circuit board on which numerous GaAs detector arrays can be mounted.

Each connection through an optoelectronic matrix can be viewed as an optical communications link with optical source, transmission waveguides, and receiver. On a per-crosspoint basis the power consumption of the matrix is low. Under ordinary conditions a maximum of one crosspoint per output line is in the on-state. The rest draw no current. Each output line requires an amplifier to raise the low-level detected signal to a voltage suitable for the following electronics, and each input line requires a laser and driver. The power consumed by input and output electronics dominates the power budget of the matrix, but it is not high. For a matrix of 100x100 lines designed to handle 100 Mb/s signals with a bit error rate of 10^{-9} the per crosspoint power consumption is calculated to be about 3 mW [17]. In comparing the optoelectronic matrix principle with purely optical switching it should be borne in mind that the optical transmitter and receiver must be present at each input and output in these devices also.

It has been demonstrated that optoelectronic crosspoints can have sufficient speed and isolation to be useful in many switching applications with analogue as well as digital signals. The performance of the optoelectronic crosspoints in fact compares favourably with that of the various all-optical switches mentioned previously. Optoelectronic switches generally have higher isolation than electro-optic coupled waveguide switches, and operate faster than optomechanical and liquid crystal switches. Their bandwidth and insertion loss can be viewed as equivalent to that of any optical switch because for most foreseeable applications, electrical input and output signals are required, and the performance of the necessary optical transmitters and receivers establishes these parameters.

3. Applications

3.1 Communications Switching

The principles involved in optoelectronic switching lead naturally to non-blocking elementary matrix sub-units of large dimension, particularly where digital signals are to be switched [17]. The number of output lines in such a sub-unit is set by the balance between the optical transmitter power and the power required by the detector to achieve the desired bit error rate. An average received optical power of the order of tens of microwatts provides a BER of 10^{-9} at 100 Mb/s with photoconductor detectors of the type discussed here. Semiconductor lasers that couple several tens of milliwatts into a multimode optical fibre are now commercially available. Allowing for excess loss in the optical power dividing network, a few hundred output lines can therefore be served by each input in an elementary matrix. The number of input lines that can be switched to a single output line is set by the accumulation of leakage through off state switches, and is at least of the same order. These large-dimension matrix elements can be used to build up a very large scale matrix switcher for high rate digital signals. One of the most interesting applications for such a device is the interconnection of computers for parallel processing. An optoelectronic digital exchange is a promising alternative to optical waveguide crossbar switches presently being studied for this purpose [18].

Analogue switching generally requires higher optical signal power at the crosspoints than digital switching, and the number of output lines that can be served by a single transmitter in an optoelectronic switch is correspondingly lower. Nevertheless, monolithic switching matrices suitable for routing signals with bandwidths of hundreds of MHz to several tens of output channels are foreseeable. Such a capability would be useful in a variety of communications applications involving the routing of FM or wideband video signals.

3.2 Delay Line Processors

The use of optoelectronic switch matrices to obtain control and flexibility in the use of optical fibre delay lines [19] is a very promising non-communications application. Wideband, precise and rapidly selectable delays can be provided in the delivery of a signal to a number of output lines, which might for example be connected to the elements of a phased array antenna, by placing optical delay lines in the signal distribution network of the switch matrix. This arrangement is different from optical delay generators for phased arrays that have been described in the literature [20], which employ an optical source for each required antenna phasing pattern, and establish that pattern with a fixed set of fibre delay lines fed by that source. The advantage of the matrix switching approach is that only one delay line is needed per delay, rather than a number equal to the product of the number of elements with the desired number of phasing patterns. The problem of coupling a large number of fibres to a single optical detector is also eliminated.

A variety of signal processing functions can be obtained by making delayed connections between the outputs and the inputs to form a Reflex Optoelectronic Switch Matrix (ROSM) [21] as shown in Fig. 8. Here all but one of the output ports of the switching matrix are connected back to corresponding input ports by means of delay lines of various lengths. Optical fibre delay lines can be employed by inserting them between the laser transmitters and the optical power dividing network of the switch matrix. The switch allows the delays to be combined in series or parallel. If each line is twice as long as the next, any of $2^N - 1$ delays, where N is the number of delay lines, can be composed by appropriately setting the crosspoint switches of the matrix. For example, making connections at crosspoints A, F and H in Fig. 8 provides for the serial connection of t_1 and t_2 .

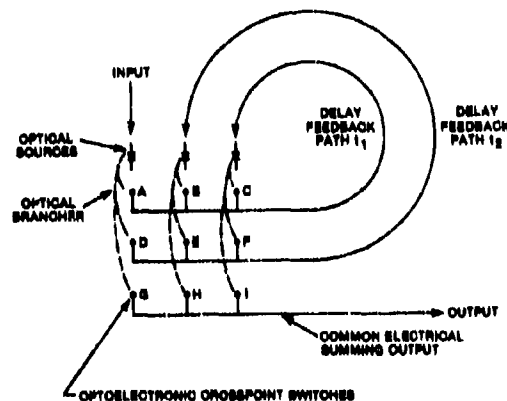


Fig. 8. Reflex optoelectronic switch matrix. The delays can be optical waveguide lines for precision.

An advantage of the optoelectronic switching technique in this application is that as a natural consequence of the partitioning of the optical signal power a 'broadcast mode' is available whereby any input can go to more than one output. This feature permits recirculation through the delay lines and their combinations, so that discretely tunable loop filters can be made. For example closing switches A, C and I in Fig. 8 provides recirculation through loop 1. This mode is peculiar to the ROSM. Reflex switching matrices using optical waveguide switches [22] cannot easily provide 'broadcast' mode because of the difficulty of attaining an efficient power dividing switch state. Electronic matrix switches can only provide the recirculation if each crosspoint also provides a high reverse isolation in the 'on' state, so that a direction is imposed on the signal.

The properties of a ROSM-controlled tunable loop filter are similar to those of a fixed hybrid filter using an optical delay line [23]. A typical frequency response is shown in Fig. 9. A loop gain of 26 dB was employed to feed the signal from the photoconductive crosspoint detector back to the loop input laser. The filter envelope extends over 1 GHz, and shows a dynamic range of 26 dB. The Q-factor is 300 at 600 MHz. The optoelectronic matrix requires that the signal undergo an optical-electrical-optical conversion on each circulation through the loop. While this conversion does add noise, it also provides an opportunity to control the loop loss and hence the sharpness of the filter by means of an electronic amplifier in the loop.

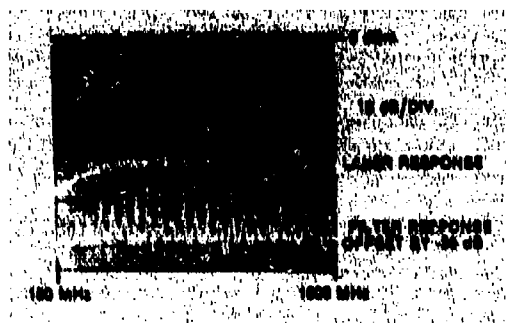


Fig. 9. Frequency response of a loop filter made with a ROSM.

Many signal processing applications can be envisaged for the ROSM. In processing digital signals the rapidity with which the switch can be reconfigured provides a novel capability that can be used to create high speed multiplexers, demultiplexers and correlators. All the basic elements of a fibre optic lattice structure are present [24], including feed-forward delay, which is equivalent to parallel combinations of delay lines with the matrix. A single optoelectronic matrix may therefore be programmed to act in a wide variety of ways in a signal processor.

3.2 Optoelectronic Mixer Arrays

It has been demonstrated that optical detectors can be used to switch signals off and on. If the switching can be done rapidly enough, then optoelectronic switches can be used as chopper modulators to achieve the mixing of signals. In an optoelectronic mixer one signal is applied as an intensity-modulated optical signal, while the other is an electrical signal added to the detector bias. The product is an electrical signal at the output of the detector. Optoelectronic mixing has been observed in avalanche photodiodes [25] and in photoconductive detectors [26], and mixing at frequencies up to 4.5 GHz has been observed [27]. By applying local oscillator signals to the crosspoints of an optoelectronic switching array one obtains an array of tuners. If frequency division multiplexed optical intensity modulation signals are applied to the input ports two independent types of switching are achieved in a single location. This mode makes optimum use of the bandwidth of optoelectronic switches to provide matrix switching of very large numbers of signals of moderate bandwidth. Experimental studies of monolithic mixer arrays similar to the photoconductor arrays shown in Fig. 2 [28] indicate that in comparison to the bias switching mode of operation crosstalk performance is degraded by about 10 dB by crosscoupling of the local oscillator signals.

Many other applications can be foreseen for optoelectronic mixer arrays, particularly in optical signal processing. For example photoconductors can operate in a bilinear mixing mode in which the amplitudes of the electrical bias signal and the optical modulation signal are multiplied. An array of photoconductors could thus act as a mixing detector for an optical frequency exciser [29] using an integrated optical Fourier transform generator and performing the discrete inverse transform by means of the mixing and signal summing properties of the detector array. The switching of the photoconductors here serves to delete and insert frequency components in the spectrum of the detected output.

4. Present Status

An optoelectronic matrix based on light emitting diode signal sources and p.i.n. crosspoint photodetectors was developed using discrete component construction as a commercial prototype by Foundation Instruments in 1981. This switcher provides over 60 dB isolation in the band 0-100 MHz for 1 volt p-p signals presented at the inputs. Internal gain is provided so that insertion loss is 0 dB. The basic configuration is a 7x7 matrix.

Work at the Communications Research Centre has focussed on photoconductor arrays as noted in this paper. Current projects are to increase the level of integration of the matrix elements and associated optics and to improve the performance of crosspoint photodetectors.

(a) Integration

The integration of photoconductive detectors with FET amplifiers has recently been reported [30] with receiver sensitivity as low as -42 dBm for error rate of 10^{-9} at 90 Mb/s. Such integrated receivers might considerably extend the number of crosspoints that could be used in a single matrix. The integration of numerous photoconductive detectors with a single amplifier is under study.

The integration of optical waveguides to distribute the signals with the detector array itself is an important matter for development. Various methods are promising. The distribution of light to arrays of InGaAs photodiodes by means of double heterostructure waveguide integrated on the reverse side of the substrate has recently been reported [31]. This technique gave optical crosstalk less than -40 dB between detectors. Another approach is to use waveguide fabricated in another material and form a hybrid optical/electronic structure. We are presently completing an experiment on using silver-diffused glass waveguide in this way.

The prospects for integrated optoelectronic switching arrays incorporating both optical and electronic integrated elements seems very good, and this area is an active one for research.

(b) Photodetectors

We have focussed on photoconductors as the most promising detectors for optoelectronic switching because of their zero-bias off-state and ease of monolithic co-fabrication with FET's. Remaining difficulties of photoconductors, however, are that they draw considerable dark current and are therefore power consuming and noisy, and they often have very high response at very low frequency, necessitating equalization. We have recently proposed and demonstrated a new type of photoconductor [32] that avoids these problems. The opportunity to use short wavelength light (~ 800 nm) in optoelectronic switching matrices arises because there is no need for long distance optical signal transmission. At these short wavelengths the absorption length of the light in GaAs is only about a micron, which is of the same order as the surface-depleted layer of an undoped crystal. We have fabricated photoconductors in 2 μ -thick layers of undoped GaAs grown on semi-insulating substrates and found that photoresponse similar to more conventional photoconductors is obtained (i.e. about 0.3 A/W with bandwidth over 1 GHz) but dark current is below 100 μ A. Furthermore, the response at DC is only about a factor of two greater than at 1 GHz, so that the need for equalization is reduced. We attribute this reduction in low frequency response to the extension of the surface depleted layer right through the photoconductive channel, preventing any back-gating or other phototransistor-like mechanisms.

5. Conclusion

This paper has attempted an overview of the principles of optoelectronic broadband matrix switches, their applications and the current state of research. These devices are very promising for large scale, very wideband network switching. We have recently completed a study which compares optoelectronic switching directly with optical waveguide matrix switching, and concluded that the optoelectronic form shows greater promise [33]. The advantage of optoelectronic switching over optical switching lies fundamentally in the smaller size of optoelectronic arrays, which permits much higher levels of integration. In view of the current state of interest in broadband switching, and in optical techniques in particular, it can be anticipated that there will be an increased activity to develop optoelectronic arrays in the near future.

6. References

- [1] W.C. Young and L. Curtis, "Cascaded Multiple Switches for Single and Multimode Optical Fibres", *Electron. Lett.* 17, pp. 571-573, 1981.
- [2] Y. Fujii, J. Minowa, T. Aoyama, K. Doi, "Low-Loss 4x4 Optical Matrix Switch for Fibre Optic Communication", *Electron. Lett.* 15, pp. 427-428, 1979.
- [3] M. Kondo, Y. Ohta, M. Fujiwara, M. Sakaguchi, "Integrated Optical Switch Matrix for Single Mode Fibre Networks", *IEEE J. Quant. Electron.* QE-18, p. 1759-1765, 1982.
- [4] R.A. Soref, "Multimode Achromatic Electro-Optic Waveguide Switch for Fibre-Optic Communications", *Appl. Phys. Lett.* 28, pp. 716-718, 1985.
- [5] R.I. MacDonald, E.H. Hara, "Optoelectronic Broadband Switching Array", *Electron. Lett.* 16, pp. 502-503, 1976.
- [6] R.I. MacDonald, E.H. Hara, R.H. Hum, "Fast Photoconductive Optoelectronic Broadband Switch with Low Control Voltage", *Electron. Lett.* 17, pp. 611-613, 1981.
- [7] R.I. MacDonald, E.H. Hum, "Switching with Photodiodes", *IEEE J. Quant. Electron.* QE-16, pp. 289-295, 1980.
- [8] R.A. Kiehl, D.M. Drury, "Performance of Optically-Coupled Microwave Switching kDevices", *IEEE Trans. Microwave Theory and Techniques* MTT-29, pp. 1004-1010, 1981.
- [9] E.H. Hara, S. Machida, M. Ikeda, H. Kanbe, T. Kimura, "Optoelectronic Matrix Switching Using Heterojunction Switching Photodiodes", *Electron. Lett.* 17, pp. 150-151, 1981.
- [10] E.H. Hara, R.I. MacDonald, Y. Tremblay, "Optoelectronic Switching with Avalanche Photodiodes", *IEEE Topical Meeting on Optical Fibre Communications*, Washington 1979.
- [11] E.H. Hara, R.I. MacDonald, "Characteristics of a Photoconductive Detector as an Optoelectronic Switch", *IEEE J. Quant. Electron.* QE-19, pp. 101-104, 1982.
- [12] R.I. MacDonald, D.K.W. Lam, R.H. Hum, J. Noad, "Monolithic Array of Optoelectronic Broadband Switches", *IEEE J. Solid State Circuits* SC-19, pp. 219-223, 1984.
- [13] D.K.W. Lam and R.I. MacDonald, "Fast Optoelectronic Crosspoint Electrical Switching of GaAs Photoconductors", *IEEE Electron. Devices Letters* EDL-5, p. 1-3, 1984.
- [14] R.I. MacDonald, R. Hum, R. Kuley, D.K.W. Lam, T. Noad, "Experimental Demonstration of an Optoelectronic Switch Matrix for SS/TDMA in the 0.3-4.0 GHz Band", *Communications Research Centre Technical Note* No. 171, 1984.
- [15] B.S. Kawasaki, K.O. Hill, "Low-Loss Access Coupler for Multimode Optical Fibre Distribution Networks", *Appl. Opt.* 16, pp. 1794-1796, 1977.
- [16] D.K.W. Lam, R.I. MacDonald, "Crosstalk Measurements of Monolithic GaAs Photoconductive Detector Arrays in the GHz Region", *Appl. Phys. Lett.*, June 15, 1985.
- [17] R.I. MacDonald, "Optoelectronic Switching in Digital Networks", *IEEE Journal of Selected Areas in Communication*, March 1985.
- [18] J.A. Neff, private commun.
- [19] K.P. Jackson, S.A. Newton, B. Moslehi, M. Tur, C. Cutler, J. Goodman, H. Shaw, "Optical Fibre Delay-Line Signal Processing", *IEEE Trans. Microwave Theory and Techniques* MTT-33, pp. 193-210, 1985.
- [20] P.G. Sheehan, J.R. Forrest, "The Use of Optical Techniques for Beamforming in Phased Arrays", *SPIE Vol. 477 Optical Technology for Microwave Applications*, pp. 82-89, 1984.
- [21] D.K.W. Lam, R.I. MacDonald, "A Reflex Optoelectronic Switch Matrix", *J. Lightwave Technol.* LT-2, pp. 88-90, 1984.
- [22] B-V. Chen, "Integrated Optical Circuits for Space Applications", *International Conf. on Comm.* Denver, 1981, *IEEE 0536-1486/81 0000-0081*.
- [23] J.E. Bowers, S.A. Newton, W.V. Sorin, H.J. Shaw, "Filter Response of Single-Mode Fibre Recirculating Delay Lines", *Electron. Lett.* 18, pp. 110-111, 1982.
- [24] B. Moslehi, J. Goodman, M. Tur, H. Shaw, "Fibre Optic Lattice Signal Processing", *Proc. IEEE* 72, pp. 909-930, 1984.
- [25] R.I. MacDonald, K.O. Hill, "Avalanche Optoelectronic Down-Converter", *Opt. Lett.* 7, pp. 83-85, 1982.
- [26] A.J. Foyt, F.J. Leonberger, R.C. Williamson, "InP Optoelectronic Mixers", *SPIE Vol. 269*, pp. 109-114, 1981.

- [27] D.K.W. Lam, R.I. MacDonald, "GaAs Optoelectronic Mixer Operation at 4.5 GHz", IEEE Trans. Electron. Devices ED-31, pp. 1766-1768, 1984.
- [28] D.K.W. Lam, R.I. MacDonald, "Crosstalk in Monolithic Photoconductive Arrays", to be presented at Device Research Conference, Univ. of Colorado, June 1985.
- [29] P.J. Roth, "Optical Excision in the Frequency Plane", SPIE 26th Symposium, San Diego, 1982.
- [30] C.Y. Chen, N.A. Olsson, C.W. Tu, P.A. Garbinski, "Monolithic Integrated Receiver Front End Consisting of a Photoconductive Detector and a GaAs Selectively Doped Heterostructure Transistor", Appl. Phys. Lett. 46, pp. 631-683, 1985.
- [31] R. Trommer, "Monolithic InGaAs Photodiode Array Illuminated Through an Integrated Waveguide", Electron. Lett. 21, pp. 382-383, 1985.
- [32] R.I. MacDonald, D.K.W. Lam, "Depleted Layer Photoconductor", to be presented at 11th European Conference on Optical Communications (ECOC'85), October 1985.
- [33] R.I. MacDonald, D.K.W. Lam, "A Comparison Among Photonic Switch Matrices", unpublished.

ACOUSTOOPTIC SPECTRUM ANALYZER USING A PLANAR BRAGG-CELL

M. Stockmann and P. Clemens
Research Laboratories of Siemens AG
Otto-Hahn-Ring 6, D-8000 Muenchen 83, W-Germany

SUMMARY

The design principles and the performance characteristics of a miniaturized acoustooptic RF-spectrum analyzer are presented. The device yields a time-bandwidth-product of more than 300. Using a planar Bragg-cell fabricated on a LiNbO_3 substrate and air between Bragg-cell and detector array the time-bandwidth-product has been doubled compared to the minibulk as well as the integrated optic spectrum analyzer for the same device length. The time resolution of the spectrum analyzer is 33 μsec and its linear dynamic range 28 dB.

1. INTRODUCTION

Due to its potential for parallel processing of information the acoustooptic RF-spectral analysis offers high speed of operation and high probability of intercept of signals in a dense environment. A device incorporating such abilities is of particular importance for radar warning application. Up to now many papers have been published on small and compact spectrum analyzers. Essentially two different paths have been walked along in developing such a processor. One leads to the minibulk spectrum analyzer /1/ and the other to the integrated optic spectrum analyzer /2/. Because of the limited size the angular resolution of these analyzer designs is relatively low, yielding only 50 /1/ to 100 /3/ resolved spots (i.e. time-bandwidth-product).

This paper describes a miniaturized spectrum analyzer with a time-bandwidth-product of more than 300. This high value was achieved in the following way. A planar Bragg-cell on a LiNbO_3 substrate is used as it is well known from several integrated optic spectrum analyzer device arrangements. The velocity of the surface acoustic wave (SAW) is about half the velocity of the bulk wave in LiNbO_3 . As a result the acoustic wavelength shortens by an amount of approximately two and hence the angle of the diffraction doubles. Unlike the integrated optic spectrum analyzer the medium between Bragg-cell and detector-array of our new version consists of air. The refractive index change of the interface Bragg-cell/air additionally increases the diffraction angle by a factor of about two. For a given size of the spectrum analyzer this hybrid setup produces a doubling of the time-bandwidth-product compared to the two types mentioned above.

2. DESIGN LAYOUT OF THE SPECTRUM ANALYZER

Figure 1 represents in a schematic way the basic arrangement of the spectrum analyzer. The planar Bragg-cell builds the basic element and is fabricated on a y-cut lithiumniobate-substrate with the acoustic wave propagating in the direction of the c-axis. The preparation of the titanium-indiffused, single mode, optical slab waveguide occurs in a conventional way /4/ (30 nm Ti-layer, 3 h diffusion time at 980 °C in wet oxygen atmosphere to suppress the lithium outdiffused waveguide).

The SAW-transducer is designed for a bandwidth of 500 MHz and 750 MHz center frequency. The octave bandwidth is attained by a "chirp design", i.e. the electrode spacing of the transducer varies smoothly so that each pair of electrodes is resonant for one frequency within the bandwidth. The electrodes are arranged in a "dog-leg" structure to gain acoustic aperture for increased diffraction efficiency /5/. To accomplish a flat frequency response of the Bragg-cell a weighted electrode overlap compensates the roll-off in the frequency response of the acoustooptic interaction. The electrodes are slightly tilted against each other to satisfy the Bragg-condition within the bandwidth. A standard planar photolithographic process, i.e. projection exposure and lift-off technique, has been applied to fabricate the transducer out of aluminium.

The light source of the spectrum analyzer is a commercially available laser diode (Hitachi HLP 1400) with a single longitudinal mode (0.1 nm spectral width and 830 nm wavelength). An achromatic lens with a focal length of 10 mm focuses the laser light onto the detector array thus collimating the laser light as well as Fourier-transforming the light diffracted by the Bragg-cell. Such an arrangement offers the advantage that no special waveguide lens is necessary to perform the Fourier-transformation. Up to now it is very difficult and expensive to fabricate such waveguide lenses of high quality. The collimated laser light is coupled into the waveguide via a lithiumniobate prism. This coupling method hardly generates in plane scattered light and it is easy to adjust.

The light exits the waveguide of the Bragg-cell by the polished endface. The beam path within the waveguide is very short to keep the in plane scattered light level as low as possible, whereas the distance in air from the endface of the waveguide to the detector array is approximately 150 mm and is determined by the commercially available detector array (Reticon CCPD 128X8). A cylindrical lens focuses the waveguide endface of the Bragg-cell onto the detector array. The cylindrical lens is necessary to collect the light exiting the Bragg-cell waveguide and diffracted into a beam that is divergent perpendicular to the waveguide plane. To keep the setup assembly compact the optical beam path between Bragg-cell and detector array is folded by means of two prisms. The cylindrical lens is cemented to the prism closer to the Bragg-cell.

The detector array in use processes 1024 elements read out via 16 parallel video channels thus achieving a shortest read out time of 10 μ sec. The proposed scheme of the spectrum analyzer fits into a housing having the dimensions 144 mm x 125 mm x 30 mm that has to be plugged into an electronic equipment for postprocessing of the spectral data.

3. PERFORMANCE CHARACTERISTICS

The parameters of the spectrum analyzer that were investigated are the frequency response, the frequency resolution, and the linear dynamic range. Figure 2 shows the frequency response of the spectrum analyzer. One recognizes that the 3 dB bandwidth amounts to 500 MHz. This value corresponds to the design goal of the SAW-transducer.

The Rayleigh-frequency resolution of a Bragg-cell is given by the reciprocal transit time of the acoustic wave traversing the optical aperture. As the optical aperture of the planar Bragg-cell is about 4 mm a theoretical frequency resolution about 1 MHz will be expected. In this case the optical aperture is given by the maximum width of the uniform gap provided by our prism-couplers. The measured frequency resolution is 1.5 MHz. There are two main reasons for the deviation from the expected value. Firstly the SAW is penetrated by a slightly convergent light beam causing that the Bragg-condition is not fully satisfied near the margin of the optical aperture. This effect apodizes the optical aperture thus broadening the focal spot and deteriorating the frequency resolution. Secondly, there is electrical crosstalk of roughly 8 % between adjacent detector elements, also broadening the measured signal.

The linear dynamic range of the spectrum analyzer is given by the ratio of the highest to the lowest detectable RF-power. In order to determine the highest detectable power the diffraction efficiency was measured as a function of the RF-power at center frequency applied to the Bragg-cell. The result is depicted in Figure 3. For low values of the RF-power the graph exhibits the expected linearity with a slope of 7.5 %/W. With increasing power the curve becomes non-linear because of thermal effects within the Bragg-cell. At the RF-power $P_{\text{max}} = +29$ dBm (800 mW) the deviation from linearity reaches 1 dB. Therefore P_{max} is called "linear limit" and it defines the highest RF-power that can be detected using this Bragg-cell. P_{max} is also the maximum detectable power for the spectrum analyzer, provided the detector array will be saturated by the deflected light corresponding to P_{max} . Selecting an appropriate integration time of the detector array this condition can always be fulfilled. The correct integration time depends on the optical output power of the laser, the higher the laser power the shorter the integration time. For this spectrum analyzer an integration time of 33 μ sec is obtained at 10 mW of laser output power. Because of the high losses occurring within the prism coupler employed to couple the laser light into the waveguide of the Bragg-cell, the shortest possible integration time (10 μ sec) of the detector-array could not be used. The lowest RF-power detectable with the spectrum analyzer is the noise equivalent power (NEP). Possible sources of noise are either electrical noise of the detector array or in plane scattered light. The NEP of this spectrum analyzer is determined by the detector noise to approximately +1 dBm. The noise signal produced by the scattered light is about 7 dB below the measured value of the NEP. Thus, the linear dynamic range of the spectrum analyzer amounts to 28 dB and is limited by the dynamic range of the detector array.

4. CONCLUSIONS

In table 1 the specifications of the spectrum analyzer are summarized. From the frequency resolution of 1.5 MHz and the bandwidth of 500 MHz a time-bandwidth-product of 330 is calculated. It would still be possible to significantly increase the frequency resolution and hence the time-bandwidth-product by widening the optical aperture. The optical aperture of our arrangement is limited by the quality of the prism-coupler used.

The time resolution of the spectrum analyzer is 33 μ sec. It is restricted by the available light power in the waveguide. Improving the coupling efficiency (by now only about 1-2 %) of the prism coupler would increase the optical power in the waveguide thus leading to a shorter time resolution. The prism coupler has proven to be the limiting device for the frequency resolution as well as the time resolution. A more advantageous alternative might be the grating coupler.

The linear dynamic range of the spectrum analyzer is 28 dB and is limited by the dynamic range of the detector array. The Bragg-cell itself would yield a linear dynamic range of about 35 dB.

Thus a miniaturized spectrum analyzer with a time-bandwidth-product of more than 300 is presented. This high number has been achieved by a design that yields the double time-bandwidth-product at a given size compared to both the minibulk- and the integrated optic spectrum analyzer types, respectively.

Table 1: Specifications of the spectrum analyzer.

Bandwidth	500 MHz
Center frequency	750 MHz
Frequency resolution	1,5 MHz
Time resolution	33 μ sec
Linear dynamic range	28 dB

5. REFERENCES

- /1/ J.P. Lindley: Application of Acousto-Optic Techniques to RF Spectrum Analysis Acousto-Optic Signal Processing, Ed.: N.J. Berg and J.N. Lee, Marcel Dekker Inc., New York, 1983, pp. 87-106
- /2/ T.R. Joseph et al.: Performance of the integrated optic spectrum analyzer. SPIE Vol. 321 Integrated Optics II (1982), pp. 134-138
- /3/ M. Kanazawa et al.: High Resolution Integrated Optic Spectrum Analyzer. IOOC '83, June 27-30, 1983, Tokyo, Technical Digest pp. 258-259
- /4/ J.L. Jackel et al.: Elimination of outdiffused surface guiding in titanium-diffused LiNbO₃. Appl. Phys. Lett. 38 (1981) pp. 509-511
- /5/ K.M. Lakin et al.: A New Interdigital Electrode Transducer Geometry. IEEE Transactions on Microwave Theory and Techniques, Vol. MTT-22 (1974) pp. 763-768

6. ACKNOWLEDGEMENT

We thank Mrs. G. Lindemann for doing the photolithographic work and Mr. G. Stadler for constructing the setup.

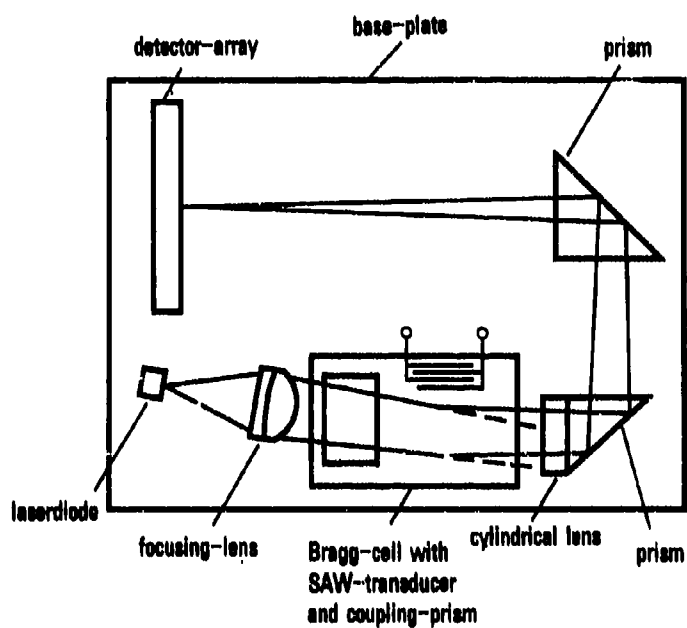


Fig. 1. Design layout of the spectrum analyzer

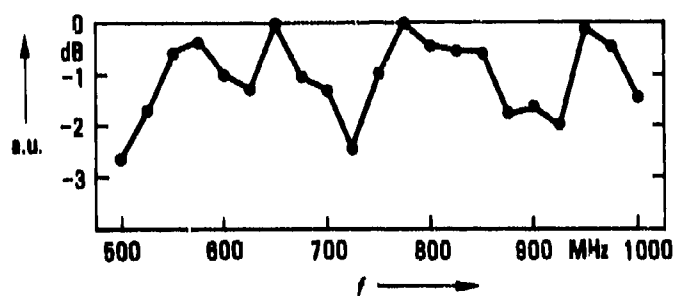


Fig. 2. Frequency response of the spectrum analyzer, i.e. detector signal (a.u.) versus frequency f

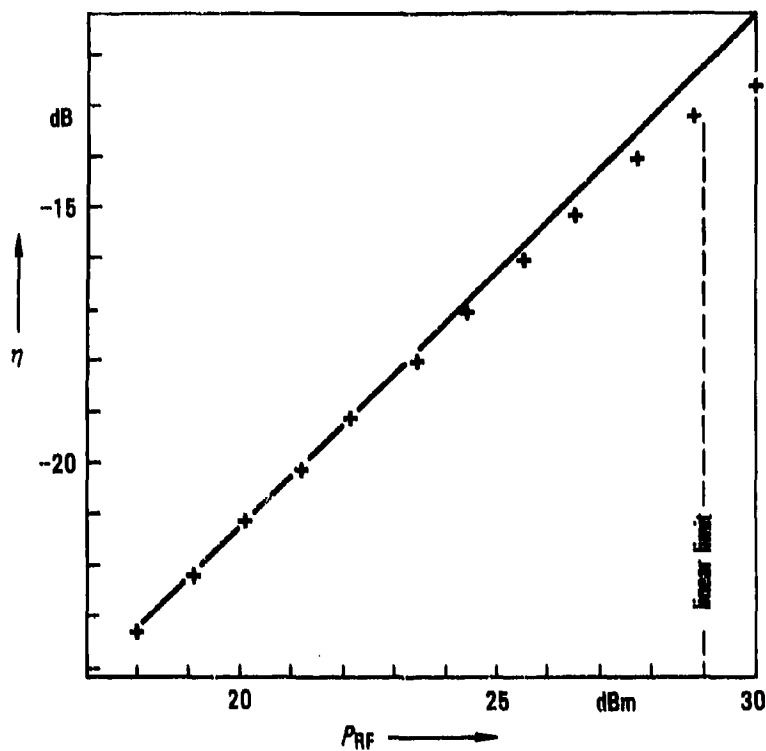


Fig. 3. Diffraction efficiency η of the Bragg-cell versus RF-power P_{RF} applied to the SAW-transducer

DISCUSSION

S.Walker, UK

What precautions did you take against bulk-wave effects?

Author's Reply

The mounting adhesive should absorb these waves, maybe they contributed some spurious responses.

R.MacDonald, Ca

What was the detector spacing and what was the mechanism of the crosstalk?

Author's Reply

18 μm . Mechanism not known.

MODULATORS AND PHOTODETECTORS FOR MICROWAVE/MILLIMETER-WAVE FIBER OPTIC SYSTEMS

by

J.J. Pan
E-Tek Dynamics, Inc.
250 East Drive
Melbourne, Florida 32901
USA

ABSTRACT

Growth of sophisticated military satellite communications, electronic warfare, and radar systems places increasing demands on microwave/millimeter-wave fiber optics for wide instantaneous bandwidth, immunity of EMI/EMP, deployment speed/simplicity, and low cost. The microwave fiber optic communication links using a direct-modulated laser diode (LD) and a PIN photodetector (PD) have been demonstrated at frequency of 7.5 GHz. A GaAlAs LD with a direct intensity modulation bandwidth of 11 GHz was recently achieved. Unfortunately, the LD operating at room temperature above 12 GHz is extremely difficult, if not impossible, to fabricate. Then, the laser beam modulated by an electro-optic modulator (EOM) provides the essential way of microwave or millimeter-wave fiber optic communications above 12 GHz. This paper will discuss the 20–60 EOMs and PDs; the design/fabrications of 20 GHz devices are particularly emphasized.

Both traveling wave and semiconductor waveguide EOMs are feasible to modulate LD beam above 20 GHz. The travelling wave EOM (TW-EOM) presently offers the advantage of low RF driving power. The Titanium diffused LiNbO₃ Mach-Zehnder interferometric TW-EOM has low propagation loss at 20 GHz, while an EOM fabricated on GaAs or InP substrates can operate in millimeter-wave frequencies, but suffering slightly higher propagation loss than LiNbO₃. We will describe the critical design parameters such as electrodes configuration, RF impedance optimization, optical/RF velocities matching, Ti diffusion time/temperature, etc. Velocity mismatch compensation, EOM RF performances, and efficient single-mode fiber to EOM interface technique/experimental results will also be reported.

We investigated GaAs MESFET, Schottky-Barrier PD, modified IMPATT PD and photoconductive PD for short wavelength (0.85 μm), and InP Schottky-Barrier PD and photoconductive PD for long wavelength (1.3 μm) low noise optical demodulation above 20 GHz. The RF package design, device design/fabrication, circuit optimization, and experimental characterizations/results of the selected PD are presented.

DISCUSSION

C. Gee, US

You have reviewed modulators that have been demonstrated up to 18 GHz at many laboratories. How do you plan to extend these devices to millimetre wave frequencies (i.e. 40 GHz, 60 GHz)?

Author's Reply

We have to pay attention not only to device problem but also the circuit technology.

G. Willson, UK

Do you foresee any limitation on the operating wavelength due to line broadening of the laser linewidth at GHz modulation frequencies?

Author's Reply

It is anticipated that optical phase-locked-loops will be required to give sufficiently stable source wavelength to compensate for temperature-induced drifts, mechanical vibrations, etc..

R. MacDonald, Ca

Can you comment on the depleted layer photoconductors that have been developed at Bell Labs and also at CRC. These reduce significantly the dark current.

Author's Reply

The devices are interesting but the performances at very high frequency are still unknown.

SUMMARY OF SESSION III

GLASS FLUORIDE AND CRYSTALLINE FIBERS

by

J. Lucas, Chairman

The main topic of the session was materials for infrared waveguides development. Four contributors presented a critical review on three kinds of waveguides including fluoride glasses, chalcogenide glasses and single crystal fibers. Dr DAHN TRAN, from N.R.L. (U.S.A.) and Pr. Jacques LUCAS, from the University of Rennes (F.) discussed the state of the art in the field of fluoride glasses which are promising candidates for the fabrication of repeaterless long telecommunication links. Scattering and multiphonon absorption measurements show that a potential loss of 10^{-2} dB/km in the window close to 2.55 μm is very realistic.

The candidate materials for reaching this target are ZrF_4 -based glasses called fluorozirconates. Many informations on fundamental properties of the material as well as the main characteristics of the fibers have been presented. The lowest attenuation, measured on fibers, reported by Dr. TRAN was 4 dB/km at 2.55 μm and less than 20 dB/km at the OH absorption peaking at 2.87 μm . Other applications of bulk sample fluoride glasses have been discussed more specially in relation with their applications in the mid IR laser domain, and for the traditional IR optics operating in the military window around 4 μm where those glasses are very transparent.

The second class of materials for I.R. fibers was chalcogenide glasses essentially those based on the association of As, Se, Ge, Te, ... Dr. PITT, from STL, showed that the attenuation measured at STL on these glasses was in the range 5 to 10 dB/m in the 10 μm region. These values make those fibers suitable for short distances applications in the 8-12 μm region and more specifically at the 10.6 μm of the CO_2 laser.

Finally, an overview of a new field of crystal growth science has been presented by Pr. FEIGELSON, from Stanford University (U.S.A.), who described the different technic for making single crystal fibers. Using laser-heated pedestal growth system, high melting oxides have been transformed in short length single crystal fibers. Among the different materials Nd/YAG fibers have been prepared for laser applications, LiNbO_3 fibers for non-linear technology and many others like sapphire or KRS_5 , a thallium bromo-iodide fibers have been developped for I.R. transmission.

The reasons of developping such I.R. waveguides have been clearly demonstrated; long distance repeaterless communications is the ultimate target but medium loss fibers offer also a lot of applications such as remote I.R. spectroscopy, I.R. sensor thermography, thermal imaging, endoscopy, surgery, laser machining, printing, etc....

PREPARATION AND PROPERTIES OF INFRARED TRANSMITTING HEAVY METAL FLUORIDE GLASS OPTICAL FIBERS

Danh C. Tran
Optical Sciences Division
Naval Research Laboratory
Washington, D.C. 20375-5000, USA

SUMMARY

In present silica fiber technology, optical attenuation at the intrinsic minimum level of about 0.16 dB/km at 1.6 μm has been attained. Non-oxide glasses based on heavy metal fluorides potentially can offer intrinsic minimum losses several orders of magnitude lower than that of silica, owing to a lower Rayleigh scattering loss contribution and an extended infrared absorption edge. As a result, heavy metal fluoride glasses are most promising for long distance repeaterless optical communication systems. The present paper will draw primarily from the published literature on fluoride glasses and fibers to provide a complete review of the present state-of-the-art in the field. Candidate fluoride glasses for fiberization will be evaluated on the basis of their infrared transparency as well as their glass forming ability. The synthesis of high optical quality bulk fluoride glasses by conventional casting and the fabrication of fibers using both preform and crucible techniques will be discussed. The optical properties of the fluoride glass fibers will be evaluated based on the absorption loss contribution associated with hydroxyl groups and transition metal/rare-earth impurities, and on the scattering loss component arising from both Rayleigh scattering and processing induced defects such as microcrystallization, phase separation and particle inclusions.

ULTRA-LOW LOSS OPTICAL WINDOWS FOR HEAVY METAL FLUORIDE GLASSES

The major thrust of mid-IR optical fiber research has been concentrated on ultra-low loss fiber applications. Heavy metal fluoride glasses based on ZrF_4 , discovered by Poulain, Lucas, and co-workers in 1975 [1], have been considered to be the primary candidate material for the next generation of optical communications fibers, owing to their higher transparency as compared to the oxide and chalcogenide glasses, and to their superior glass forming ability with respect to the chloride, bromide, and iodide based glasses. Fig. 1 illustrates the intrinsic loss minima for oxide, chalcogenide, and halide glass systems, which are determined by the $1/\lambda^4$ wavelength dependent Rayleigh scattering loss at shorter wavelengths and the multiphonon vibrational absorption edge at longer wavelengths. The predicted intrinsic minimum attenuation in heavy metal fluoride glasses based on ZrF_4 is $\sim 10^{-3}$ dB/km at 3.44 μm as compared to $\sim 10^{-2}$ dB/km at 4.54 μm for chalcogenide glasses and to 0.16 dB/km at 1.6 μm for silica [2]. In addition to the 3.44 μm window of maximum transparency predicted for ZrF_4 -based glasses, another optical window for ultra-low loss fluoride fiber applications appears to emerge at 2.55 μm [3, 4]. Fig. 2 illustrates the OH- absorption contribution in the mid-IR wavelength region obtained from a dry ZrF_4 -based glass fiber [4]. The fundamental OH-absorption band is centered at around 2.87 μm , and the two peaks at 2.24 μm and 2.42 μm are attributed to combination bands with metal fluorides such as ZrF_4 and BaF_2 . The actual data which are represented by the solid curve indicate that fluoride glass fiber having a low OH-absorption loss of less than 20 dB/km at 2.87 μm can be prepared using dry processing conditions. Moreover, based on the empirical multiple Gaussian fit - represented by the broken curve - to the absorption bands associated with OH of Fig. 2, it was expected that the loss contribution due to OH is less than 10^{-2} dB/km at 2.55 μm . Recent scattering measurements performed on bulk ZrF_4 -based glasses between 2.4 μm and 3.2 μm have demonstrated that the intrinsic scattering level as low as 10^{-2} dB/km can be achieved at 2.55 μm [5]. The determination of intrinsic multiphonon absorption edges in heavy metal fluoride glasses still presents some uncertainty due to background interferences arising from rare-earth impurity absorption in the infrared; but based on the best estimates and careful extrapolation of experimental data collected for a number of current "state-of-the-art" ZrF_4 -based glasses, the multiphonon absorption contribution is projected to be at most $\sim 10^{-2}$ dB/km between 2.3 and 2.8 μm [6]. Thus, in the absence of transition metal impurities whose absorption bands tail off toward the 2 μm to 3 μm wavelength region and neodymium impurities which exhibit a narrow absorption peak at around 2.55 μm , and of fiber processing induced scattering defects, it is expected that ultra-low optical losses in the order of 10^{-2} dB/km can be achieved in ZrF_4 -based glass fibers at 2.55 μm .

PREPARATION OF HEAVY-METAL FLUORIDE GLASSES AND FIBERS

Heavy metal fluoride glasses based on ZrF_4 , sometimes called fluorozirconate glasses, are commonly used in the preparation of potential ultra-low loss fibers because they are relatively stable, compared to other heavy-metal fluoride glasses. They generally contain 50-70 mol % ZrF_4 as the primary glass-forming component, 19-31 mol % BaF_2 as a glass network modifier, and lesser amounts of alternate fluorides which serve as glass stabilizers and refractive index modifiers. Table 1 lists some typical fluorozirconate glass compositions reported for the fabrication of infrared fibers.

GLASS	COMPOSITION (mol %)	REFERENCES
Zr-Ba-Gd-Al	61 ZrF ₄ -32 BaF ₂ -3.9 GdF ₃ -3.1 AlF ₃	[7]
Zr-Ba-La-Al-Li	53 ZrF ₄ -19 BaF ₂ -5 LaF ₃ -3 AlF ₃ -20 LiF	[8]
Zr-Ba-La-Al-Na	53 ZrF ₄ -20 BaF ₂ -4 LaF ₃ -3 AlF ₃ -20 NaF	[9]
Zr-Ba-La-Al-Na	55 ZrF ₄ -31 BaF ₂ -5 LaF ₃ -5 AlF ₃ -4 NaF	[10]
Zr-Ba-La-Al-Na-In	54.9 ZrF ₄ -22.55 BaF ₂ -3.92 LaF ₃ -14.71 NaF-3.73 AlF ₃ -0.19 InF ₃	[11]

Table 1. Typical Heavy Metal Fluoride Glasses for Infrared Fibers

The incorporation of PbF₂ or ThF₂ to the compositions listed in Table 1 will give rise to an increase in the glass refractive index, while the addition of HfF₄ or the reduction of AlF₃ content will decrease it.

Fluoride glasses can be prepared by fusing anhydrous fluorides at temperatures ranging from 800°C to 1000°C for about one hour, or by converting oxide raw materials to fluorides using ammonium bifluoride (NH₄F·HF) at around 400°C prior to the fusion process. They are melted in capped platinum, gold, or vitreous carbon crucibles in a dry inert atmosphere of argon or nitrogen and are usually formed by casting in pre-heated metal molds.

ZrF₄-based glass fibers have been prepared from both crucible and preform techniques. The crucible approach is most desirable because it allows the continuity of the drawing process; and in addition, glass melts can be rapidly quenched directly into fibers thus preventing any drawing induced crystallization. In contrast to oxide glasses, fluorozirconate glasses exhibit a shear viscosity of less than 10 Poises at temperatures just above the crystallization region (~450°C-550°C) and around 1 Poise at the liquidus temperature (~550°C); and as a result, crucible drawing directly from fluoride glass melt, i.e. above the crystallization point, cannot be easily achieved. Fluoride glasses also display one of the steepest viscosity-temperature profile coupled with a high tendency toward crystallization within the fiber drawing temperature, i.e. just below 400°C where the shear viscosity ranges from 10⁴-10⁶ Poises [8]; and consequently, crucible drawn fibers are subjected to non-uniformity, and microcrystallization which is generally induced by the crucible wall.

Present fluoride glass fiber technology relies strongly on the preform casting approach. In this approach, core melts are directly cast into cladding tubes to form waveguide preforms. Fluoride glass cladding tubes with uniform wall thickness and controlled bore size can be obtained by rotating cladding melts using metal molds prior to the solidification step. Fig. 3 illustrates the sequence of steps associated with the rotational casting process. Fluoride glass preforms are then drawn at around the glass softening point where again the rate of crystallization is relatively high. Stringent design of the draw furnace and tight control of the draw parameters are necessary to prevent fiber drawing induced microcrystallization. Both resistance and RF heating have been used in fiberizing fluoride glass preforms.

THE PROBLEM OF EXTRINSIC ABSORPTION ASSOCIATED WITH IMPURITIES

Within the 2 μm-4 μm spectral region where possible operating windows for the heavy metal fluoride glasses occur, extrinsic absorption originating from transition metal and rare-earth impurities is most detrimental toward achieving ultra-low loss optical fibers. The emergence of a transparent window at 2.55 μm as described earlier has stirred an emphasis toward purifying fluoride glass starting materials, specifically from transition metal impurities since the rare-earth elements - except for Nd - absorb more strongly at slightly longer wavelengths. Table 2 lists the level of each impurity causing a loss of 0.01 dB/km.

Impurity	OPERATIONAL WAVELENGTH			
	2.0 μm	2.5 μm	3.0 μm	4.0 μm
Fe	0.11	0.35	3	25
Co	0.08	0.32	10	50
Ni	0.11	1.67	80	100
Cu	7.5	71.50	1000	>5000
Nd	-	0.50	16.7	-
Ca	>5000	-	20	0.20
Pr	0.23	5.55	25	0.50
Sm	10	3.85	1.7	1.43
Tb	0.40	-	0.7	>5000

Table 2. Impurity Levels (ppb) Causing 0.01 dB/km Loss [Ref. 12]

High-purity fluoride chemicals, other than ZrF₄, have been generally prepared from direct conversion of metal carbonates or oxides to fluorides using hydrofluoric acid (HF). The carbonates of Ba, Na, Li, the oxide of Al, and Hf are commercially available with transition metal impurity level in the ppb range. Recently much emphasis has been placed on the purification of ZrF₄. Techniques such as sublimation [13, 14], ion-exchange [15], and chemical vapor purification [16] have been investigated, but the degree of purification cannot be readily assessed when the transition metal level is <500ppb; this is due to strong Zr interfering matrix lines associated with spectro-chemical emission techniques generally used in trace analysis of transition metal impurities. A recently developed purification approach based on recrystallization and extraction have demonstrated that the Fe content in ZrF₄ can be minimized to <1 ppb in the absence of contamination picked up during processing [17]. This result was confirmed by Fe isotopes tracer analysis. The extraction technique also allows an indirect assessment

of trace amounts of Cu remaining in the purified ZrF_4 which falls to around 3 ppb. The removal of Ni and Co is still under investigation; and the purification of rare-earth fluorides such as GdF_3 and LaF_3 from Nd is being conducted using zone refining techniques.

OPTICAL PROPERTIES OF HEAVY METAL FLUORIDE GLASSES AND FIBERS

Fluoride glasses are known to be prone to devitrification; but with the use of high purity starting materials, stable glass compositions, and stringent processing conditions, ultra-high optical quality and crystal-free ZrF_4 -based glasses can be prepared. Table 3 lists the light scattering loss data obtained from two ZrF_4 - BaF_2 - LaF_3 - AlF_3 -LiF bulk glass specimens measured directly in the infrared spectral region associated with ultra-low loss fluoride glass fiber applications, using a color center laser as an excitation source [5].

λ (μm)	$1/\lambda^4$ (μm^{-4})	Rayleigh scattering loss (dB/km) (theoretical)	Measured scattering loss (dB/km) for ZrF_4 -based glasses	
			Glass No. 1	Glass No. 2
2.4	0.0301	0.0113	0.0136	0.0168
2.5	0.0256	0.0097	0.0113	0.0148
2.6	0.0219	0.0083	0.0103	0.0132
2.8	0.0163	0.0060	0.0082	0.0098
3.0	0.0123	0.0044	0.0061	0.0070
3.2	0.0095	0.0033	0.0052	0.0061

Table 3. Infrared Light Scattering Losses in Heavy Metal Fluoride Glasses

The total scattering coefficients measured between 2.4 μm and 3.2 μm exhibit a typical $1/\lambda^4$ Rayleigh behavior and lie near the theoretically predicted intrinsic minimum values for these materials [5]. In addition, light scattering measurements performed in the visible spectral region have demonstrated that these high optical quality glasses exhibit total scattering loss 1/2 to 2/3 that of the best synthetic silica [5]. The low scattering levels obtained in both infrared and visible spectral regions were uniformly retained throughout the entire volume of the bulk fluoride glasses suggesting a high degree of homogeneity.

The spectral loss data obtained for a state-of-the-art fluoride glass fiber is shown in Fig. 4 [3]. The fiber structure consists of a ZrF_4 - HfF_4 - BaF_2 - LaF_3 - AlF_3 - NaF glass cladding, a ZrF_4 - BaF_2 - LaF_3 - AlF_3 - NaF glass core, and a teflon FEP polymer protective coating. The fiber numerical aperture of 0.1 was determined. The loss measurements performed on the 60 m long fiber show a minimum loss of 4 dB/km at the 2.55 μm transparent window - the lowest reported at this writing - with an OH-fundamental absorption of less than 30 dB/km at 2.87 μm . The scattering loss contribution, measured independently from the total optical loss, exhibit a $1/\lambda^4$ Rayleigh dependence and a wavelength independent loss of ~ 1 dB/km which can be attributed to the presence of small amounts of microcrystallites or bubbles. The absorption loss contribution of ~ 3 dB/km at 2.55 μm can be associated to the presence of about 20 ppb Fe, and trace amounts of Ni, Co, and possibly Nd. It is expected that further purification of the raw materials, clean room processing conditions to prevent trace level impurity contamination, and stringent control over preform casting and fiber drawing parameters will eventually lead to the 10^{-2} dB/km optical loss level expected in ZrF_4 -based glass optical fibers at 2.55 μm .

CONCLUSIONS

Heavy metal fluoride glasses based on ZrF_4 are considered to be prime candidates for ultra-low loss fiber applications owing to their superior glass forming ability with respect to other halide glasses. For the ZrF_4 -based glass system, it was predicted that a second operating window for ultra-low loss fiber applications exists at 2.55 μm , where the extrinsic absorption loss contribution from the rare-earth impurities is less severe. Extensive purification efforts have been devoted toward suppressing the transition metal impurities to the ppb levels in the fluoride raw materials. Purification techniques that have been investigated include sublimation, ion-exchange, chemical vapor purification, recrystallization, and extraction for the removal of transition metal impurities, and zone refining for the minimization of rare-earth impurities. OH-fundamental absorption of less than 20 dB/km has been achieved in ZrF_4 -based glass fibers and the expected loss contribution due to OH at the 2.55 μm transparent window is less than 10^{-2} dB/km. Light scattering measurements performed directly in the infrared spectral region associated with ultra-low loss fiber applications have confirmed the explicit $1/\lambda^4$ Rayleigh scattering behavior in both ZrF_4 -based glasses and fibers. The measured scattering loss level in bulk ZrF_4 -based glass specimens lies near the theoretically predicted intrinsic minimum values and is 1/2 to 1/3 that of the best synthetic silica. The spectral loss obtained for a state-of-the-art ZrF_4 -based glass fiber exhibits a low loss of 4 dB/km at the 2.55 μm window and an OH-fundamental absorption of less than 30 dB/km. The fiber scattering loss contribution of about 1 dB/km was attributed to small amounts of particle inclusions including microcrystallites or bubbles, and the 3 dB/km absorptive component at 2.55 μm was associated with trace amounts of Fe, Ni, Co and possibly Nd. It is expected that further purification of the fluoride raw materials, ultra clean room processing conditions to prevent trace level impurity contamination, and most stringent control over preform casting and fiber drawing parameters will eventually lead toward the 10^{-2} dB/km optical loss level expected in ZrF_4 -based glass optical fibers at 2.55 μm .

REFERENCES

1. M. Poulain, M. Poulain, J. Lucas, and P. Brun, "Verres fluores au tetrafluorure de Zirconium. Proprietes optiques d'un verre dope au Nd," *Mat. Res. Bull.*, **10**, 1975.
2. S. Shibata et al., "Prediction of loss minima in infrared optical fibres," *Electron. Lett.*, **17**, pp. 773-777, 1981.
3. D.C. Tran et al., "Fluoride glass optical fibers," *Proc. 3rd Int. Symp. on Halide Glasses*, Rennes, June 1985, invited paper.
4. P.W. France, S.F. Carter, J.R. Williams, and K.J. Beales, "OH-absorption in fluoride glass infrared fibres," *Electron. Lett.*, **20**, pp. 607-608, 1984.
5. D.C. Tran, K.H. Levin, R.J. Ginther, G.H. Sigel, Jr., and A.J. Bruce, "Light scattering in heavy-metal fluoride glasses in the infrared spectral region," *Electron. Lett.* (to be published).
6. L.G. Van Uitert, A.J. Bruce, W.H. Grodkiewicz, and D.L. Wood, "Minimum loss projections for oxide and halide glasses," *Proc. 34d Int. Symp. on Halide Glasses*, Rennes, June 1985.
7. T. Miyashita and T. Manabe, "Progress in fluoride glass fiber research and development in Japan," *Proc. 2nd Int. Symposium on Halide Glasses*, Troy, N.Y., 1983, invited paper.
8. D.C. Tran, R.J. Ginther, and G.H. Sigel, Jr., "Fluorozirconate glasses with improved viscosity behavior for fiber drawing," *Mat. Res. Bull.*, **17**, pp. 1177-1184, 1982.
9. Y. Mimura, H. Tokiwa, and O. Shinbori, "Fabrication of fluoride glass fibres by the improved crucible technique," *Electron. Lett.*, **20**, pp. 100-101, 1984.
10. G. Mass, V. Cardin, and M. Poulain, "Fluoride Glass infrared fibers for light transmission up to 5 μ m," *Proc. SPIE*, Arlington, Va, 1984, paper 484-16.
11. T. Shibata et al., "Fabrication of high-strength, low-loss fluorozirconate glass optical fibers," *Proc. 3rd Int. Symp. on Halide Glasses*, Rennes, June 1985.
12. Y. Ohishi, S. Mitachi, T. Kanamori, and T. Manabe, "Optical absorption of 3 d transition metal and rare-earth elements in zirconium fluoride glasses," *Phys. Chem. Glasses*, **24**, pp. 135-140, 1983.
13. S. Mitachi, Y. Terunuma and Y. Ohishi, "Reduction of impurities in fluoride glass optical fibers," *Japan J. Appl. Phys.*, **22**, pp. L537-L538, 1983.
14. M. Robinson, "Synthesis of high purity starting materials for heavy metal fluoride glasses," *Proc. 2nd Int. Symp. on Halide Glasses*, Troy, N.Y., 1983.
15. P.H. Klein, P.E.R. Nordquist, Jr., and A.H. Singer, "Removal of Fe, Co, Ni, and Cu from ZrF_4 to meet purity standards for 0.01 dB/km fluoride fiber," *Proc. SPIE*, Arling, Va, 1984, paper 484-15.
16. R.C. Folweiler and D.E. Guenther, "Chemical vapor purification of fluorides," *Proc. 3rd Int. Symp. on Halide Glasses*, Rennes, June 1985.
17. C.F. Fisher, D.C. Tran, P. Hart, and G.H. Sigel, Jr., "An extraction process for purifying fluoride glass starting materials," *Ibid.*
18. D.C. Tran, C.F. Fisher, and G.H. Sigel, Jr., "Fluoride glass preforms prepared by a rotational casting process," *Electron. Lett.*, vol. 18, pp. 657-658, 1982.

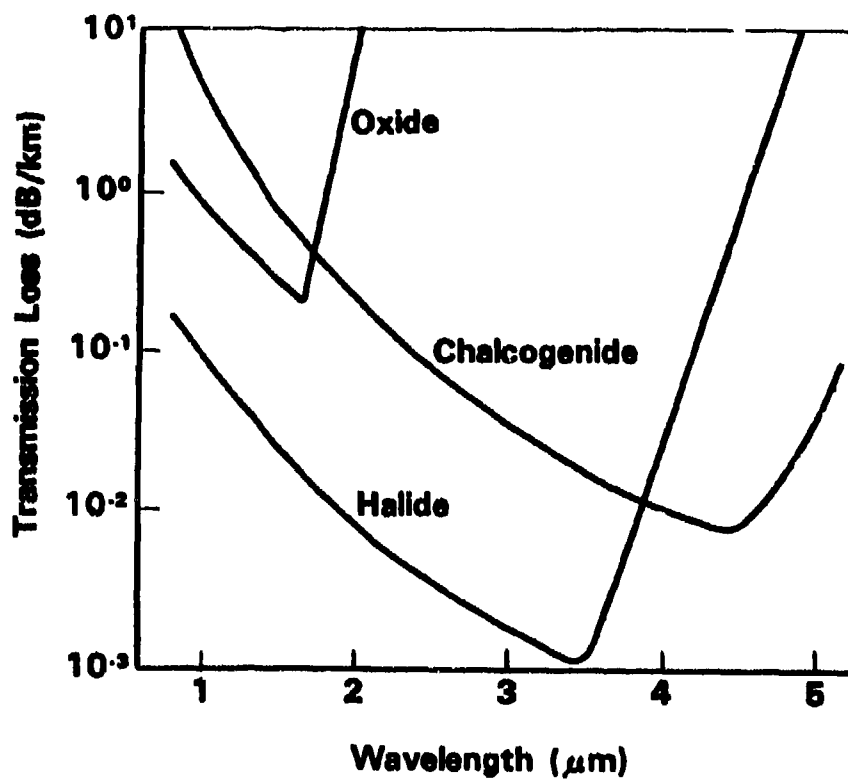


Fig.1 INTRINSIC OPTICAL ATTENUATION OF VARIOUS MATERIALS
(from T. Manabe)

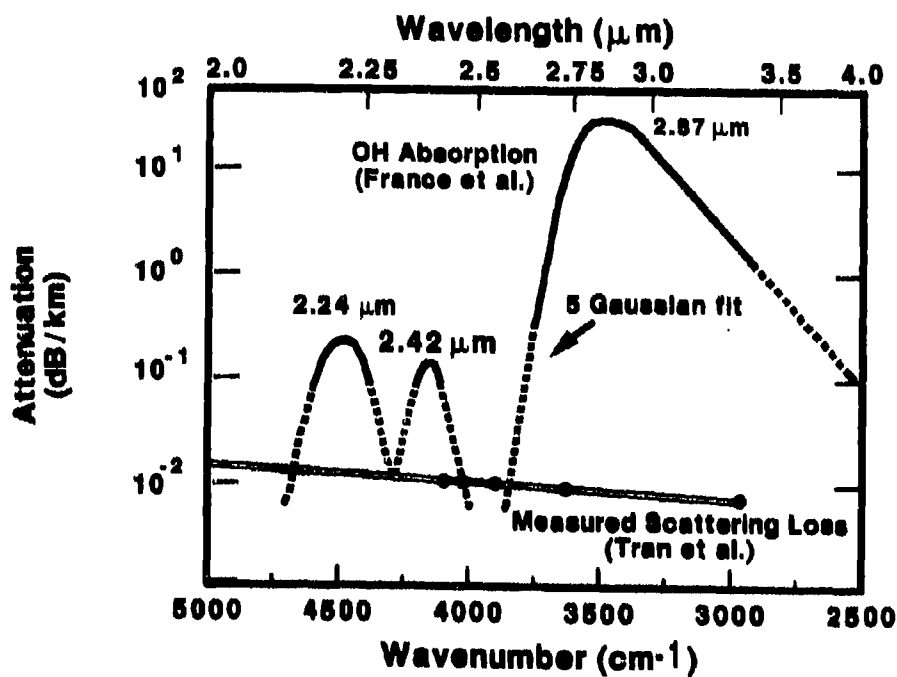


Fig.2 POTENTIAL OPTICAL WINDOW AT 2.55 μm FOR FLUORIDE GLASS FIBERS

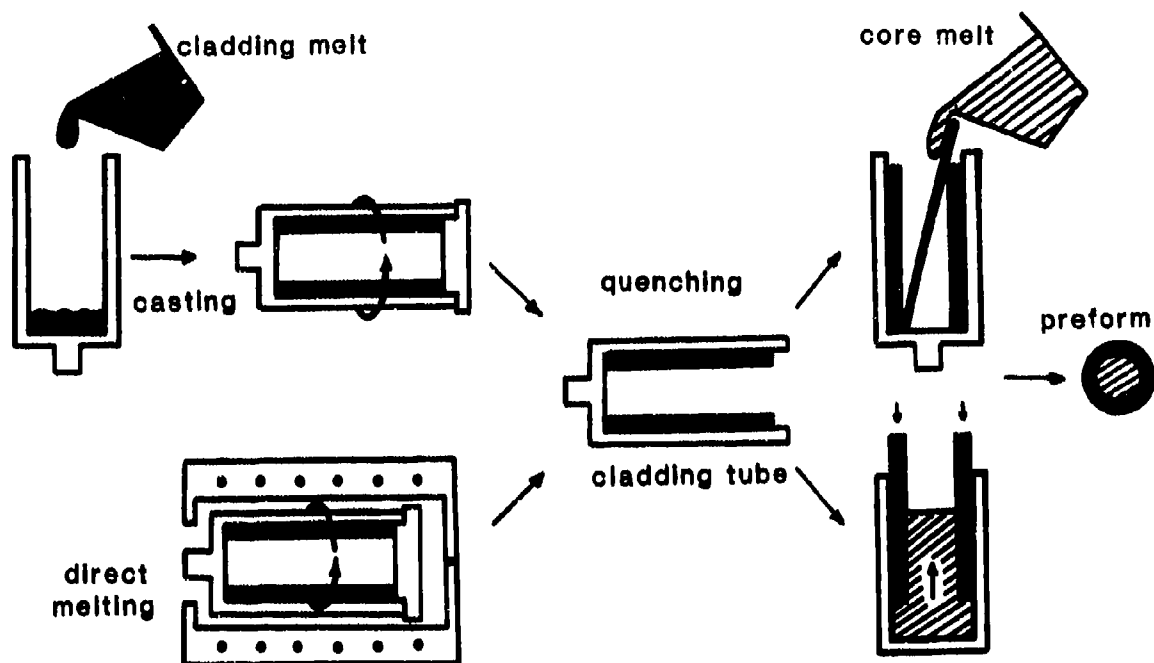


Fig.3 ROTATIONAL CASTING PROCESS (Ref.18)

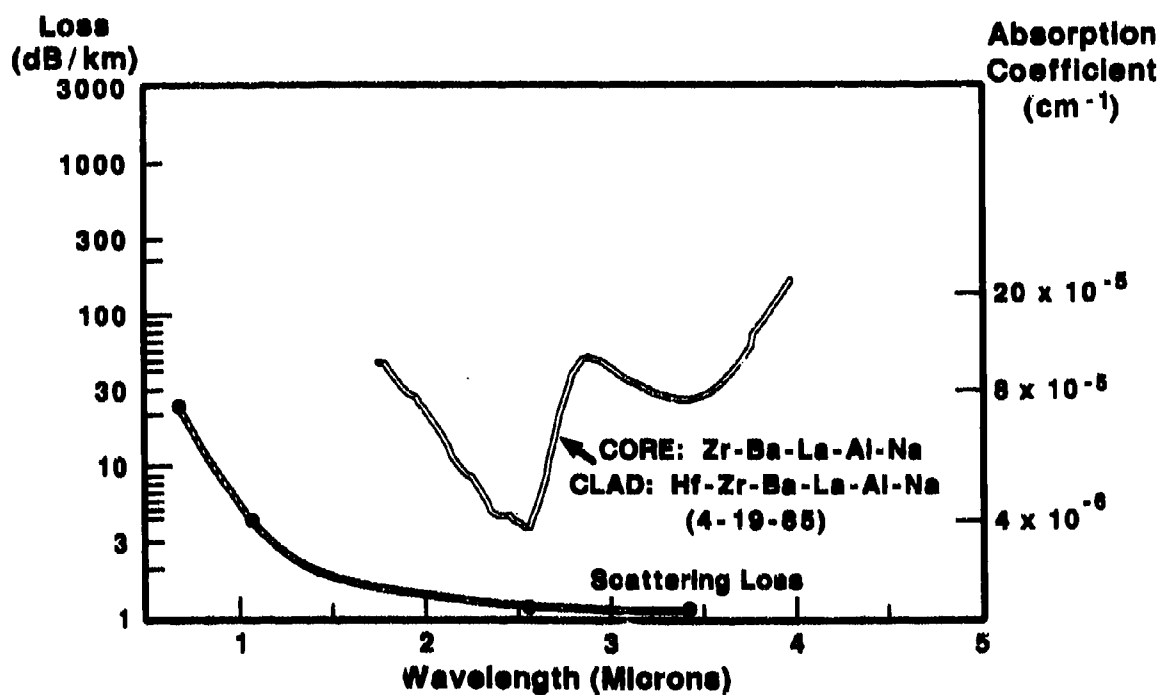


Fig.4 SPECTRAL LOSS OF A STATE-OF-THE-ART FLUORIDE GLASS FIBER (Ref.3)

GLASS FIBRES FOR TRANSMISSION IN THE 8 - 12 MICROMETRES WAVEBAND

N.J. Pitt and M.G. Scott

Standard Telecommunication Laboratories Limited,
London Road, Harlow, Essex, CM17 9NA, England

SUMMARY

Chalcogenide glasses, crystalline halides and hollow waveguides have been assessed for transmission in the 8 - 12 μm waveband. Of these, chalcogenide glasses have been selected for development of fibre optic materials. The bulk properties of a range of glasses have been studied and compositions chosen to optimise transmission and thermal stability. The role of major impurities and the procedures used to minimise them are described. Selected compositions have been drawn into long lengths of polymer coated fibre with diameters controlled accurately up to 500 μm . Current fibres transmit at CO_2 laser wavelengths with losses of 5 - 10 dB m^{-1} but potential for substantial improvement still exists. Mechanical testing has shown that with suitable coatings chalcogenide fibres are flexible enough to sustain a bend radius of the order of 1 cm.

INTRODUCTION

The 8 - 12 μm waveband is of interest for a wide range of military applications including laser range finders, thermal imaging, sensing and tracking systems. Most importantly it includes the output waveband of the tuneable CO_2 laser. The availability of suitable optical fibres for this waveband would not only allow significant savings in weight and space by the replacement of conventional lens-based optical systems but would open up new applications. In many cases fibre lengths of only a few metres will be required and, therefore, fibre losses of the order of 1 dB m^{-1} will be adequate. However, the development of lower losses would allow longer length applications and short length CO_2 laser power delivery, a requirement which is likely to increase with the development of rugged light-weight r.f. waveguide lasers.

CANDIDATE MATERIALS

The choice of materials that are transparent in the 8 - 12 μm waveband is limited to those comprising weakly bonded heavy atoms in order that the i.r. phonon edge should be at a wavelength much longer than 12 μm . Several groups of materials are of potential interest; of these chalcogenide glass and crystalline halide fibres have received much attention worldwide, but more recently hollow waveguides have been developed for CO_2 laser transmission.

Polycrystalline fibres, usually based on the halides of thallium or silver, are fabricated by extrusion, typically at rates of the order of centimetres per minute. This is much slower than in glass fibre drawing, where speeds of several metres per minute are more common. The prime advantage of crystalline fibres is their low loss: 0.1 dB m^{-1} at 10.6 μm has been reported [1]. The ability of these materials to deform plastically, which allows them to be extruded, makes the fibres susceptible to mechanical damage and limits the extent to which they can be bent before the formation of slip lines leads to rapid deterioration in transmission due to scattering. Typically a 500 μm fibre will have a minimum bend radius of approximately 10 cm.

Single crystal fibres offer the potential of reduced scattering losses due to the absence of grain boundaries. Alkali and thallium halides have been used, the lowest loss being 0.3 dB m^{-1} for CsBr fibre [2]. The modified EFG crystal growth techniques used for fabrication suffer from several disadvantages: the maintenance of stable growth conditions is difficult, growth rates are only millimetres per minute and the technique does not lend itself to production of fibres with a core/cladding structure. Minimum bend radii may be smaller than those attained using polycrystals but many of the materials best suited to single-crystal fabrication exhibit poor environmental stability, being rapidly attacked by moisture.

Hollow-core fibres offer an alternative approach to the problem of mid-i.r. waveguiding, and can be divided into two types. The first have a metallic inner cladding such as germanium, aluminium or nickel [3], which provides a surface that is highly reflective to low order modes. The second type is fabricated from glass and transmits because the real part of the complex refractive index can fall below unity in the region of a strong absorption. Hollow oxide glass fibres have only recently received attention but losses of 2 dB m^{-1} have been achieved at 10.6 μm using vitreous silica [4] and similar results have been reported for a $\text{GeO}_2\text{-ZnO-K}_2\text{O}$ glass [5], a commercial borosilicate [3] and a lead silicate glass [6]. The use of oxide glasses offers many advantages in terms of ease of

fabrication, environmental and thermal stability, strength etc.; but it is not clear whether such fibres can be optimised for wideband applications. A further disadvantage is their flexibility, which is restricted not only by the need to use relatively large fibre diameters to obtain low attenuation, but by the high sensitivity of this type of fibre to bending induced losses.

Although there is an extremely wide range of glass-forming chalcogenide compositions, those that transmit in the 8 - 12 μm waveband must generally consist of two or more of the elements Ge, As, Se or those below them in the periodic table. The use of such glasses offers the advantages of speed and control normally associated with oxide fibre-drawing techniques, and yields fibres that are both flexible and chemically durable. The lowest loss reported at 10.6 μm is 3 dB m^{-1} for a Ge-Sb-Se fibre [7]. The relative merits of chalcogenide glasses and other candidate materials are compared in Table 1. Although losses in chalcogenides are currently somewhat higher than those shown by crystalline fibres, the potential for improvement, combined with their several advantages over other fibre types, stimulated the development of chalcogenide fibre materials, which is reported in the rest of this paper.

TABLE 1 COMPARATIVE MERITS OF 8 - 12 μm FIBRE MATERIALS

	Chalcogenide glass fibre	Polycrystalline fibre	Single Crystal fibre	Hollow-core fibre
Attenuation	Medium	Good	Good	Medium
Flexibility	Good	Poor/Medium	Medium	Poor
Fabrication rate	Good	Medium	Poor	Good
Environmental stability	Good	Medium	Poor/Medium	Good

GLASS FABRICATION AND CHARACTERISATION

Glasses were synthesised from the elements germanium, arsenic, selenium and tellurium of 5 or 6 N purity. Batches of 15-40 g were weighed in an argon-flushed glove box and sealed inside evacuated silica ampoules before being melted in a rocking rotation furnace [8]. After melting for 18 hours, at 900°C or 825°C for glass with or without germanium respectively, the furnace was slowly cooled to 600°C before removing the ampoule to cool in air.

The glass transition temperature, T_g , and crystallisation temperature, T_x , of each glass were determined using a DuPont 1090 differential scanning calorimeter (DSC) on 20 mg samples heated at 10°C min^{-1} in argon. The glasses were then annealed at $T_g + 50^\circ\text{C}$ before cutting and polishing samples for infrared spectroscopy, which was carried out using a Nicolet 5 MX F.T. spectrometer.

INFRARED ABSORPTION IN BULK GLASSES

Figure 1a shows the absorption spectrum of a glass of composition $\text{Ge}_5\text{As}_{38}\text{Se}_{57}$. The peak at 12.8 μm can be attributed to oxide impurities, which react preferentially with Ge atoms to form Ge-O bonds [9]. It can be seen in Fig. 1b that by eliminating Ge from the glass this strong absorption is replaced by another at 15.4 μm , which can be attributed to As-O bonds [10]. In shifting the absorption to a longer wavelength its contribution to losses in the 8 - 12 μm band is reduced. Nevertheless there remain several oxide species that give rise to weak absorptions between 8 and 16 μm . These are barely distinguishable in bulk samples but contribute significantly to losses in fibres, thus making it necessary to reduce oxide impurity levels below 1 ppm.

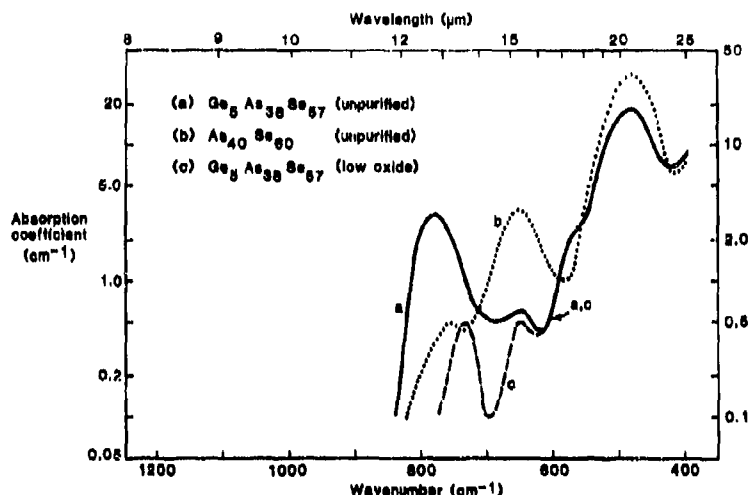


Fig.1 Effect of oxide impurity upon the infrared absorption edge

Standard techniques were used to remove surface oxide from the raw materials. Selenium was vacuum baked at 300°C [11] and tellurium was etched in a bromine/hydrobromic acid solution [12]. The germanium and arsenic, which was used in its amorphous form, showed little tendency to oxidise at room temperature and therefore received no further purification. Silica ampoules were prepared by cleaning in hydrochloric acid, rinsing in de-ionized water and vacuum baking at 350°C.

Oxide levels can be further reduced by the addition of gettering agents to which oxygen will preferentially bond. The use of aluminium has been widely reported [7, 13]. However, even when added in amounts less than 100 ppm we found aluminium to promote wetting and slight attack of the silica ampoule. Glasses of improved quality were obtained by adding aluminium in the form of its bromide, which was also found to lower hydride impurity levels, presumably by the formation of volatile HBr. Excess aluminium and bromine are believed to be incorporated into the glass but further work is required to establish whether such additions contribute to scattering losses. Figure 1c illustrates the improved transmission that was achieved by implementing these purification procedures.

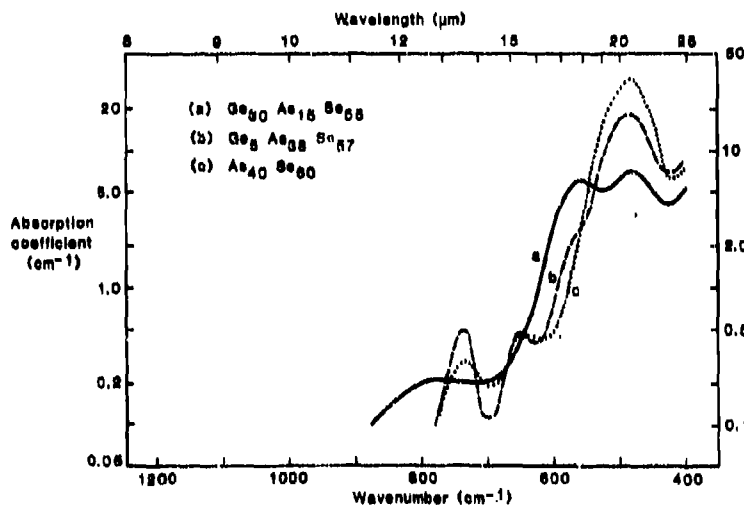


Fig.2 Effect of Germanium upon the infrared absorption edge

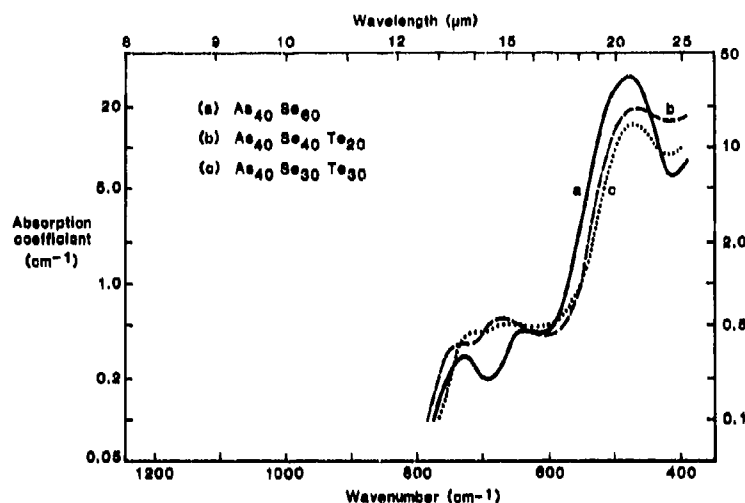


Fig.3 Effect of substitution of Te for Se upon the infrared absorption edge

Further reduction in losses at 8 - 12 μm can be achieved by shifting the intrinsic multiphonon edge to longer wavelengths. Figure 2 shows how the two-phonon absorption peak at 17.8 μm (due to Ge-Se bonds) was eliminated by reducing the germanium content of the glass from 30 to 0 atom %. At the same time the absorption at 20.6 μm was found to increase due to the consequent formation of more As-Se bonds. The absorption spectrum was further improved by substituting the heavier element tellurium for some of the selenium, as can be seen in Fig. 3. The absorption at 20.6 μm decreased by a factor of two as the Te content was increased to 30 atom %. Table 2 summarises the effect of composition upon the multiphonon edge and for comparison also shows data for a Ge-Sb-Se glass of a composition similar to that reported in reference [7]. The lowering of glass transition temperature with removal of germanium and addition of tellurium is an inescapable consequence of using heavier, more weakly bonded elements in order to extend the transmission range. Although the $\text{As}_{40}\text{Se}_{30}\text{Te}_{30}$ glass exhibited a weak DSC crystallisation exotherm, the glass containing 20% Te was found to be quite stable and is, therefore, a promising material for fabrication of low loss fibre.

TABLE 2 EFFECT OF COMPOSITION UPON OPTICAL AND THERMAL PROPERTIES

Composition	Magnitude of 2 phonon absorptions (cm^{-1})		Wavelength at which absorption = 2 cm^{-1} (μm)	T_g ($^{\circ}\text{C}$)	T_x ($^{\circ}\text{C}$)
	Ge-Se peak at 17.8 μm	As-Se peak at 20.6 μm			
$\text{Ge}_{30}\text{As}_{15}\text{Se}_{55}$	6.1	6.8	16.3	355	-
$\text{Ge}_5\text{As}_{38}\text{Se}_{57}$	1.5	18.6	17.4	203	-
$\text{As}_{40}\text{Se}_{60}$	-	33	17.8	185	-
$\text{As}_{40}\text{Se}_{40}\text{Te}_{20}$	-	19.4	18.5	146	-
$\text{As}_{40}\text{Se}_{30}\text{Te}_{30}$	-	14.5	18.7	139	280
$\text{Ge}_{15}\text{Sb}_{25}\text{Se}_{60}$	5.5	10 *	16.5	239	370

* Sb - Se absorption peak at 21.2 μm .

FIBRE FABRICATION

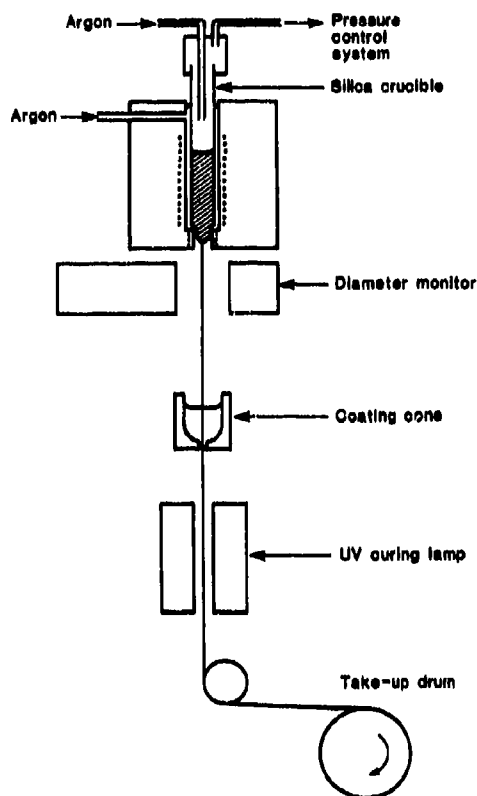


Fig.4 Pressurized crucible fibre drawing apparatus

The apparatus used for fibre drawing is illustrated in Fig. 4. The glass to be drawn was placed inside a clean dry vitreous silica crucible, which was slowly purged with argon in order to minimise contamination by oxygen and water vapour. The crucible was heated by a resistance furnace, the interior of which was also purged with argon. A secondary heating element around the crucible nozzle allowed the drawing temperature to be independently and accurately controlled. The fibre diameter was continuously monitored and controlled by adjusting the speed of the take-up drum. Fibres several hundred metres in length were pulled at rates of $5 - 10 \text{ m min}^{-1}$. The diameter of fibres could be controlled within a few microns up to $125 \mu\text{m}$. However, to achieve $\pm 5\%$ control on fibres up to $500 \mu\text{m}$ in diameter it was necessary to apply a controlled top pressure to the crucible by restricting the argon purge outlet. Fibres have been coated on-line with various uv-cured epoxy-acrylates having a range of mechanical properties. The tougher coatings improved the fibre strength and greatly enhanced the ease with which they could be handled.

MECHANICAL TESTING

An Instron tensile tester was used for mechanical testing. Ten centimetre gauge lengths of both coated and uncoated fibre were tested at room temperature using a constant 1 s min^{-1} strain rate. Several measurements were made and the results averaged, ignoring those in which the fibre was observed to have failed next to the cross-head. The results, which are shown in Table 3, indicate an increase from 1% to 1.6% in the average strain to failure due to the protective fibre coating. These are, however, preliminary results and are not expected to represent the best that might be achieved. It is anticipated that improvements to processing conditions will enable the relatively short lengths of fibre required to survive a $1.5 - 2.0\%$ proof-test. A $100 \mu\text{m}$ diameter fibre would experience a maximum strain of only 0.5% upon being subjected to a bend of 1 cm radius; however, an investigation of fatigue behaviour will be necessary in order to establish the level of strain that could be sustained during an extended period of service.

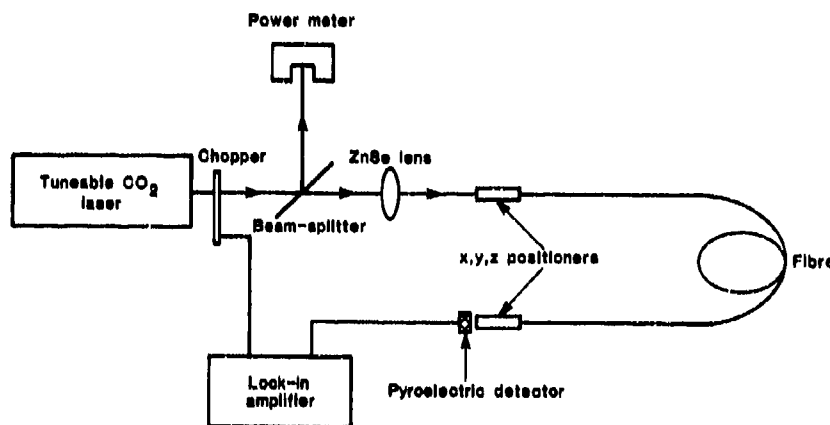
TABLE 3 MECHANICAL PROPERTIES OF $\text{Ge}_5\text{As}_{38}\text{Se}_{57}$ FIBRE

	COATED	UNCOATED
No. of samples	11	20
Diameter (μm)	82 ± 4	94 ± 6
Tensile strength (MPa)	285 ± 25	177 ± 40
Strain at failure (%)	1.61 ± 0.15	0.96 ± 0.15
Young's Modulus (GPa)	18^*	18 ± 3

* Value determined for uncoated fibre

FIBRE ATTENUATION MEASUREMENTS

The experimental arrangement used for attenuation measurements is shown in Fig. 5. A conventional cut-back technique was used, successive short lengths being removed from the output end of the fibre. By tuning the CO_2 laser the attenuation could be measured across the $9.3 - 11 \mu\text{m}$ wavelength range. Losses in $\text{Ge}_5\text{As}_{38}\text{Se}_{57}$ fibre were 10 dB m^{-1} at $10.6 \mu\text{m}$ and approximately 5 dB m^{-1} at $9.3 \mu\text{m}$. Optimisation of the techniques used to eliminate oxide impurities will enable substantially lower losses to be achieved and a potential order of magnitude reduction should be realised in As-Se-Te based fibres.

Fig.5 CO_2 laser attenuation measurement equipment

CONCLUSIONS

Chalcogenide glasses offer several advantages, in comparison with crystalline halides and hollow core fibres, which make them well suited as waveguide materials for the $8 - 12 \mu\text{m}$ waveband. Long lengths of fibre can be drawn at speeds of several metres per minute using a pressurised crucible technique that enables diameters to be controlled accurately up to $500 \mu\text{m}$. When protected by an epoxy-acrylate coating, fibres exhibit a significant improvement in strength and can sustain a bend radius of the order of 1 cm . Losses in fibres based on the Ge-As-Se system are currently below 10 dB m^{-1} at the CO_2 laser wavelength. However, more promising compositions have been identified in the As-Se-Te system, which, with further improvement in purification and oxide gettering techniques, offer a potential order of magnitude reduction in losses.

REFERENCES

1. Harrington, J.A., "Infrared Fibre-Optical Waveguides", IEEE/OSA Conf. on Laser and Electro-Opt.Syst., San Diego, 1980, Tech. Digest Paper Th EE 1.
2. Mimura, Y. and C. Ota, "Transmission of CO₂ Laser Power by Single-Crystal CsBr Fibres", Appl. Phys. Lett., 40 (9), 1982, pp. 773-775.
3. Miyagi, M., A. Hongo, Y. Aizawa and S. Kawakami, "Fabrication of Germanium-Coated Nickel Hollow Waveguides for Infrared Transmission", Appl. Phys. Lett., 43 (5), 1983, pp. 430-432.
4. Wilson, S.J., R.W.J. Devereux and R.M. Jenkins, Private Communication.
5. Hidaka, T., K. Kumada, J. Shimada and T. Morikawa, "GeO₂-ZnO-K₂O Glass as the Cladding Material of 940 cm⁻¹ CO₂ Laser-Light Transmitting Hollow Core Waveguide", J. Appl. Phys., 53 (8), 1982, pp. 5484-5490.
6. Hidaka, T., T. Morikawa and J. Shimada, "Hollow-Core Oxide-Glass Cladding Optical Fibres for Middle Infrared Region", J. Appl. Phys., 52 (7), 1981, pp. 4467-4471.
7. Katsuyama, T., K. Ishida, S. Satoh and H. Matsumura, "Low Loss Ge-Se Chalcogenide Glass Optical Fibres", Appl. Phys. Lett., 45(9), 1984, pp. 925-927.
8. Ford, E.B. and J.A. Savage, "A Furnace for the Synthesis of Chalcogenide Glasses", J. Phys. E9, 1976, pp. 622-625.
9. Ma, D.S., P.B. Danielson and C.T. Moynihan, "Bulk and Impurity Absorption in 0.5 As₂Se₃ - 0.5 GeSe₂ Glass", J. Non-Cryst. Solids, 37, 1980, pp. 181-190.
10. Moynihan, C.T., P.B. Macedo, M.S. Maklad, R.K. Mohr and R.E. Howard, "Intrinsic and Impurity Absorption in As₂Se₃ Glass", J. Non-Cryst. Solids, 17, 1975, pp. 369-385.
11. Savage, J.A., P.J. Webber, and A.N. Pitt, "An Assessment of Ge-Sb-Se Glasses as 8 to 12 μ m Infrared Optical Materials", J. Mater. Sci., 13, 1978, pp. 859-864.
12. Savage, J.A., P.J. Webber, and A.N. Pitt, "The Potential of Ge-As-Se-Te Glasses as 3-5 μ m and 8 - 12 μ m Infrared Optical Materials", Infrared Phys., 20, 1980, pp. 313-320.
13. Reichtin, M.D., A.R. Hilton and D.J. Hayes, "Infrared Transmission in Ge-Sb-Se Glasses", J. Electr. Mater., 4(2), 1975, pp. 347-362.

ACKNOWLEDGEMENTS

The authors wish to acknowledge the assistance of G.S. Sapsford in carrying out the fibre strength measurements, T.V. Clapp in fabricating several of the glasses and R.Worthington who carried out the attenuation measurements. We wish to thank J.A. Savage for many helpful discussions, and the Directors of STL Limited for permission to publish this paper. This work has been carried out with the support of the Procurement Executive, Ministry of Defence, sponsored by the Directorate of Components, Valves and Devices.

DISCUSSION

J. Fridman, US

(1) Your efforts for the improvement of the glass by the removal of Ge and the addition of Te show results in the 16—20 μm range and yet none in the more important 8-12 μm waves and where the CO_2 laser line at 10.6 μm is located. What can you do about that? (2) have you considered drawing fibres from ZnSe, say by a variation of the CVD process whereby you will achieve transmission at 10.6 μm in the tens of watts?

Author's Reply

(1) The results presented were based on spectrometric measurements on bulk samples and do not give precise definition of the shapes of the 3-phonon intrinsic and 1-phonon oxide absorption peaks in the 8—12 μm region. Further work is being carried out to clarify the situation. (2) We have not considered a fibre drawing process for ZnSe. However, I am aware of other workers having used ZnSe single crystal waveguides for CO_2 laser transmission.

SINGLE CRYSTAL FIBERS

Professor Robert S. Feigelson
 Director, Crystal Science Division
 Center for Materials Research
 Stanford University
 Stanford, CA 94305

SUMMARY

Single crystal fibers are just now emerging as a new frontier in both materials science and device technology. Various methods have already been developed for the preparation of single crystal fibers of a wide range of materials with useful properties. Along with discussions of fiber growth methods and potential applications for single crystal fibers, current research on the growth of laser, nonlinear optic, and IR transmitting single crystal fibers are also discussed.

INTRODUCTION

The spectacular development of silica glass fibers for optical communication and data transmission applications over the past two decades is well known. An extensive effort is now underway to extend the applicability of glass fiber technology into the mid-IR region for thermal imaging, radiometric sensing, and high power transmission for medical and industrial applications. For these uses, new types of materials are being investigated including chalcogenide and fluoride glasses, and to a much more limited extent polycrystalline solids such as the silver halides and KRS-5.

By comparison to the advances made with glass fibers and the extensive research and development effort which led to its commercialization, the field of single crystal fibers is still in its infancy. Even so, the work that has been done so far seems to indicate that the future for them is bright and that these fibers represent a new frontier in material science, crystal growth, and device research. They have the potential of being useful for a variety of optical, electronic, acoustic, and structural applications, because the materials which can be grown in single crystal fiber form have a wide range of physical-chemical properties. Goodman (1) in 1978 was one of the first to suggest a number of potential applications for single crystal fibers.

Most of the device research on single crystal fibers to date has centered on miniature fiber lasers, nonlinear materials for modulators, signal processors and parametric sources, high-temperature thermometry applications and fiber reinforced composite structures. Potential areas for fiber device research include doublers, isolators, and rotators as well as the use of single crystal fibers of ferroelastic and ferroelectric materials to produce domain wall grating arrays for interaction with and control of acoustic and optical waves, which could lead to programmable spatial filters for optical processing, tunable acoustic filters for signal processing and grating couplers and phase matching gratings for integrated and fiber optics. Some crystal fibers, to be useful, will have to be clad with a low index material to reduce their susceptibility to environmental damage and the number of guided modes. Glass coatings of controlled index are being developed for some fiber lasers and other methods for changing index and composition in the fiber surface by chemical reaction, doping, and selective vaporization are also being explored.

Over fifty different materials including oxides, halides, borides, carbides, semiconductors, and metals have been already prepared in single crystal fiber form by a variety of techniques, and some in crystal form for the first time. A representative list is given in Table I.

TABLE I

Representative List of Materials Grown in
 Single Crystal Fiber Form

<u>Oxides</u>	NdSiO ₃	Nb
Nd:Y ₃ Al ₅ O ₁₂ (YAG)	Mn ₂ SiO ₄	<u>Semiconductors</u>
Al ₂ O ₃ (Sapphire and Ruby)	ScTaO ₄	Ge
LiNbO ₃	<u>Halides</u>	Si
Li ₂ GeO ₃	BaF ₂	<u>Refractory Compounds</u>
Gd ₂ (MoO ₄) ₃	CaF ₂	TiC
Ca ₈ Si ₂ O ₄	AgBr	B ₂ O
Y ₃ Fe ₅ O ₁₂ (YIG)	KRS-5	LaB ₆
Y ₂ O ₃	<u>Metals</u>	TiB ₂
Nb ₂ O ₅	Fe	
BaTiO ₃	Co	

FIBER GROWTH

There are a number of methods which have been developed for the preparation of single crystal fibers. These include growth from the melt, solution, or the vapor phase. Only the melt growth method appears useful for preparing device quality fibers because of the greater ease with which the fiber diameter, length, and crystallographic orientation can be controlled. Melt growth methods which have been used for fiber growth include edge-defined and capillary-fed growth, solidification in capillary tubes, and the float-zone method. The first three approaches require a carefully manufactured die, crucible or orifice made from a material which is compatible (non-reacting, etc.) with the melt.

Unlike glasses, crystalline materials exhibit a large change in viscosity on melting, and therefore crystals are free to move about in the melt during growth unless constrained from doing so. Methods for growing small diameter fiber crystals must include some method of controlling the position of the growth interface, otherwise large diameter variations will occur.

While the first successful attempt to grow a fiber crystal was made by Von Gomper in 1922 (2), single crystal fiber growth really began in a meaningful way with the work of LaBelle and Mlavyky (3) in 1967 on the growth of sapphire filaments. This work led to the development of the important edge-defined, film-fed growth process (4). In 1972 Haggerty (5) reported on the development of a four beam laser-heated float zone process for the growth of sapphire, Y_2O_3 , TiC and TiB_2 fiber crystals. Gasson and Cockayne (6) were the first to demonstrate the use of laser heating for float zone growth of oxides. In 1975 Burrus and Stone (7) used this method, in a two-beam pedestal-growth geometry, for the growth of single crystal fibers for laser devices. The pedestal growth method is a variation of the float-zone technique in which the fiber crystal is smaller in diameter than the source rod from which it grows, rather than equal to it. In this method, which is illustrated in Figure 1, the top of a source rod of the material to be grown is melted with the laser beam and the fiber pulled from the molten droplet. As the fiber grows, the source rod has to be pushed into the laser beam to maintain constant melt volume. Initially, Burrus and Stone successfully grew Nd^{3+} :YAG fiber lasers as small as 50 μm in diameter and greater than 10 cm in length and shortly thereafter fibers of Nd^{3+} : Y_2O_3 (8). Burrus and Goldren (9) prepared sapphire-clad ruby fibers by a similar method, using the laser to evaporate the Cr dopant from the surface of the as-grown ruby fiber, creating a colorless Cr-free region which was separated from the heavily doped, higher index core by a sharp boundary.

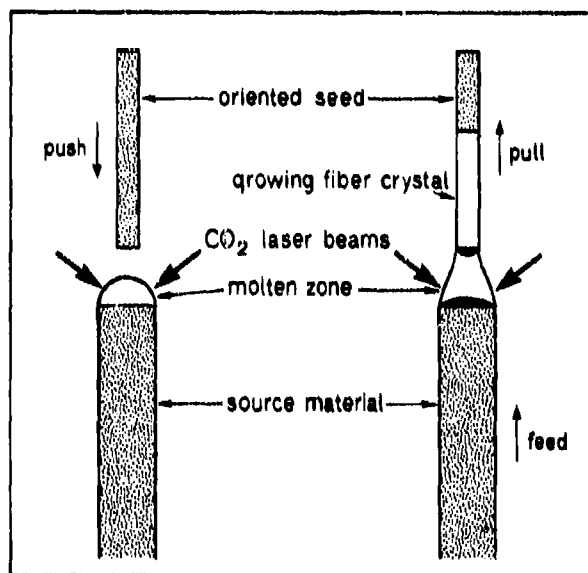


FIGURE 1: (a) Schematic of the laser heated pedestal growth method.
(b) Photograph of an actual fiber being grown by this method.

In 1980 Mimura et al. (10) described a gravity-fed capillary drawing technique (Figure 2), which is similar to the glass fiber drawing process, for growing single crystal fibers of the low melting material KRS-5 (thallium bromide). In the same year, Bridges et al. (11) developed a pressurized capillary-fed growth method for growing AgBr fiber crystals (Figure 3).

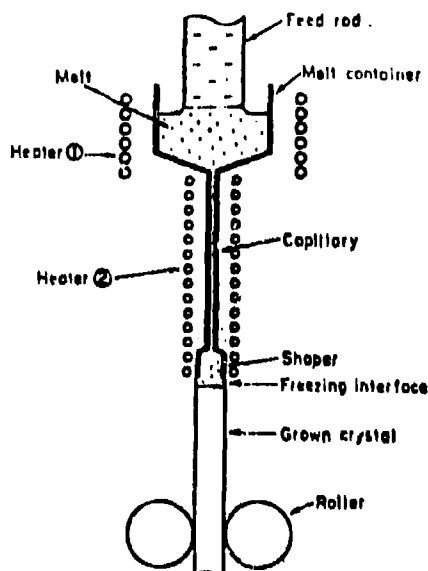


FIGURE 2: The capillary drawing method used by Mimura et al. (10) for growing KRS-3 single crystal fibers.

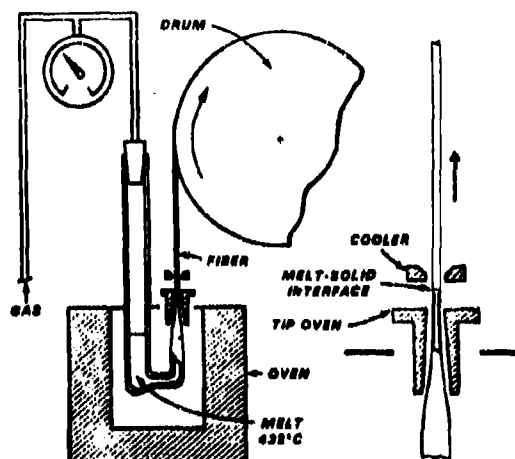


FIGURE 3: The pressurized capillary-fed fiber growth method of Bridges et al. (11).

Based on the work of several earlier investigators (4,6) a broad based multi-investigator program was developed at Stanford University a few years ago to explore the potential for using single crystal fibers in a variety of device applications and in material research. The pedestal growth method was chosen, together with laser heating, as our basic growth system because it appeared to be the most versatile method for growing fibers of a very large number of materials of different types, including very high melting compounds. It can also be used to grow crystals with a uniform, controlled composition, and even many incongruently melting compounds. Although the equipment for producing device quality single crystal fibers will be very sophisticated, the laser heated fiber growth method in its simplest configuration can be very useful for preparing single crystals of a wide variety of material for property evaluation. Single crystals can usually be produced much more quickly than with more conventional crystal growth methods and at much lower cost due to the minimal quantity of material required. Crucibles and furnaces are not required, which reduces contamination. The starting materials can be easily obtained from either polycrystalline samples or single crystals. For some materials, however, such as low-melting or volatile compounds, this method may not be satisfactory. In these cases other methods, such as capillary-fed growth, can be used more successfully.

This presentation will serve as an introduction to the subject of single crystal fiber growth.

EXPERIMENTAL PROCEDURE

A schematic of the first laser-heated pedestal growth system (LHPG) used at Stanford is shown in Figure 4. It incorporates two lead screw drives for independent fiber and source rod movement, an atmosphere control chamber and x-y positioners for fiber-source rod alignment. Both the fiber and source rod can be rotated and growth rates in the 0.01 to 100 mm/min. can be achieved. Usually growth rates vary from 1-3 mm/min. for pure melts to 0.1 to 0.3 mm/min. for growth from solution. The fiber diameters are usually 1/2 to 1/3 that of the source rod. Larger reduction ratios give rise to growth instabilities.

The original fiber growth system used a 50W CO₂ laser and a two beam arrangement similar to Burrus and Stone (7). Power is controlled by a three function proportional controller. The large temperature gradients inherent with the two beam heating system gave rise to a number of problems including poor diameter control, difficulties in forming uniform molten zones, and excessive volatilization of the melt at the hot spots formed where the laser beam hit the sample. To reduce these problems, Fejer et al. (12) developed a new type of laser optic system as shown in Figure 5 which gives a radially uniform annular hot zone. These optics were recently incorporated into the fiber growth system.

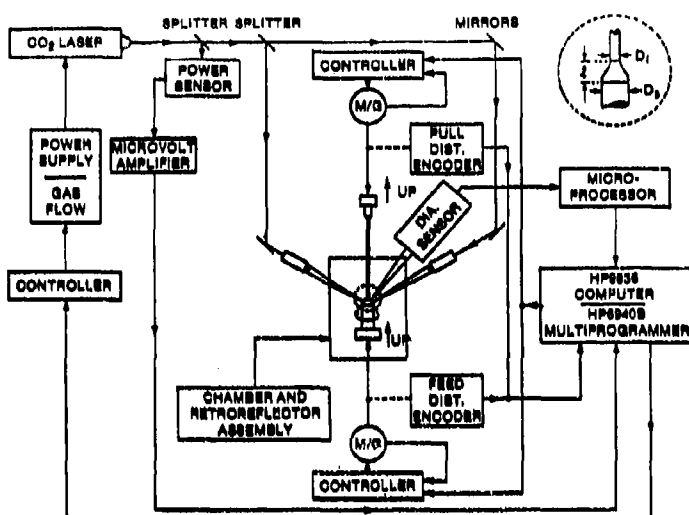


FIGURE 4: Schematic diagram of the first Stanford LNPG growth apparatus, including a planned automatic diameter control system.

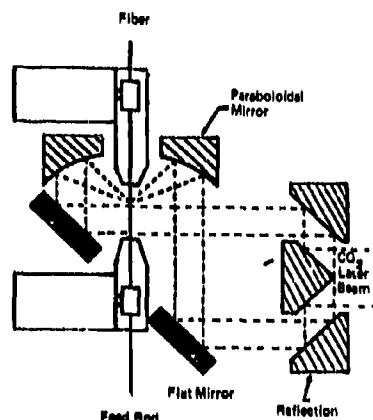


FIGURE 5: Schematic diagram of the new 360° axially symmetric focusing optics which replace the two-beam system (12).

The power required to melt a given material depends on its melting point, emissivity or optical absorption coefficient at $10.6\ \mu\text{m}$, and also the diameter of the crystal to be grown. The 50 watt CO_2 laser is capable of melting most oxides and fluorides, which absorb $10.6\ \mu\text{m}$ radiation efficiently at source rod diameters less than $2\ \text{mm}$. As the diameter decreases, less and less power is required to maintain a stable molten zone. As shown in Figure 6, high melting materials such as Al_2O_3 , $\text{Y}_3\text{Al}_5\text{O}_{12}$, and LiNbO_3 can be melted at a power level of only one watt or less when their diameter is less than $100\ \mu\text{m}$. For smaller diameters, too much power is available from the 50W laser, and it becomes difficult to control the laser power output and, therefore, the temperature accurately enough. To eliminate this problem, a power attenuator was incorporated into the beam line so that the laser can operate at a stable mid-range power level while at the same time allowing a low output power level to heat the sample.

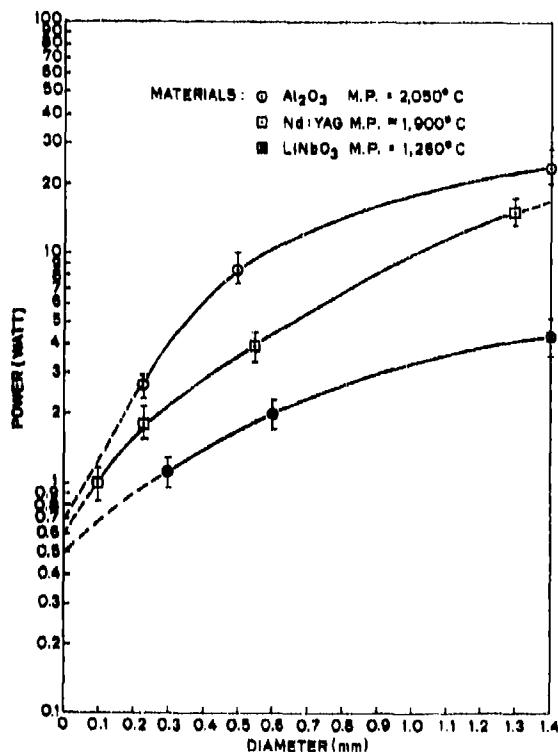


FIGURE 6: Laser power as a function of source rod diameter.

For highly reflecting metals and semiconductors which exhibit both free carrier absorption at $10.6\ \mu\text{m}$ and high thermal conductivity losses, the 50 watt laser is not powerful enough to form stable melts in these materials unless the diameter of the source rod is very small and/or the sample has a low melting point. Although fibers of some of these materials have been grown, a higher power laser would reduce many of the problems encountered.

The crystal growth process is monitored with both a binocular microscope at magnifications up to 70X and with the use of a video monitoring and recording system. These techniques allow a study of macroscopic defect formation during growth and zone stability.

The source material used for fiber growth can be in the form of single crystal or polycrystalline rods cut from existing samples. If such materials are not available, then the compound can be prepared into a dense polycrystalline solid by either cold pressing followed by high temperature sintering, or by hot pressing. Porosity in the starting material can lead to the formation of bubbles in the melt during growth and poor crystal quality. Source rods close to theoretical density are therefore highly desirable. A considerable effort may be required, however, to produce high density samples of certain materials. If porosity is a problem, then two simple methods can be used to minimize it. The first is to regrow the initial fiber, which although of poor quality is near maximum density. The fiber grown from this is usually of a much higher quality. The second technique involves densifying a fabricated source rod by passing it through the laser beam close to or just at its melting point.

Seeding the growth can be accomplished easily by using either single crystal or polycrystalline rods tapered to a sharp point. Since single crystals form so easily in these small diameter samples, even a dissimilar material such as a refractory metal wire can be used to initiate growth. Fibers can also be grown along specific crystallographic directions when oriented seeds are used.

FIBER LASERS

The laser-heated pedestal-growth method is ideally suited for the growth of solid-state laser crystals, most of which are high melting oxides. In addition to its use for preparing miniature laser devices, such as described originally by Murrus and Stone (7), it was found to be a powerful, relatively inexpensive technique which can be used for the rapid identification of promising new laser materials.

The major portion of fiber research at Stanford is focused on developing new laser materials and fiber laser devices. Both novel as well as conventional materials are being studied. To date efficient CW guided fiber lasers made from Nd:YAG have been developed (13) that operate at either 1.064 or $1.32\ \mu\text{m}$. Laser action was also demonstrated using a single laser diode as a pump source ($\lambda=817\ \text{nm}$), in a $250\ \mu\text{m}$ diameter, 4 mm long Nd:YAG fiber (13). These devices had slope efficiencies as high as 10% and output powers of up to $1/4\ \text{mW}$. Studies of the performance of various Nd:YAG fiber lasers led to the conclusion that two main optical loss mechanisms are present: 1) in fibers with $>200\ \mu\text{m}$ diameters, signal loss is mostly due to scattering by residual bulk defects; and 2) in small diameter fibers, optical losses arise from surface irregularities mostly because of fiber diameter variations which scatter the signal into unwanted higher order modes and radiation modes.

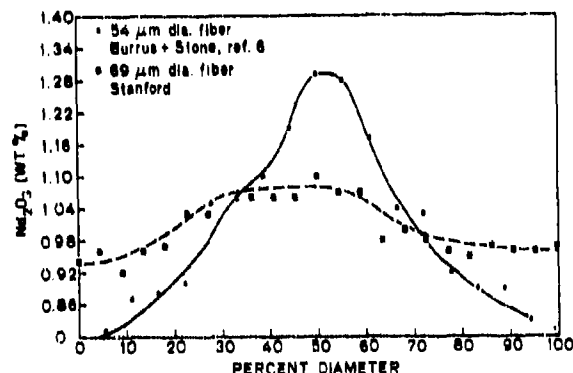
Continuing studies are aimed at reducing optical losses through improvements in fiber processing technology (improving diameter uniformity), cladding and in enhancing laser properties. To date, fiber diameter variations have been reduced from 5% to 1% using improved fiber growth equipment (12). This has been accomplished with manual diameter control and significant improvements are expected when automatic diameter control comes on line.

To reduce surface scattering losses in Nd:YAG fiber lasers and provide them with a protective jacket, a method of cladding these fibers with a suitable material has been under investigation (13). Because of their stability, hardness, and low melting temperatures, high refractive index glasses have been studied. While glasses with slightly lower index than Nd:YAG have been found, and techniques developed to coat them uniformly, the thermal expansion mismatch between the fiber and cladding, which although small ($\sim 1\%$) induces stresses and cracking of the fiber on cooling during the cladding process. These problems can be minimized by using thinner coatings, and/or glasses with thermal expansion coefficients similar to that of the crystalline fiber.

One of the important problems encountered with large Nd:YAG boules grown by the Czochralski method is related to facet formation at the growth interface leading to a cored region in the crystal. The facet region develops because of the different growth kinetics associated with the shape of the solid-liquid growth interface which is influenced by thermal gradients and growth anisotropy, a property of the material being grown. The facets represent slow-growing directions and often the incorporation of impurities and dopants will be different on the facet face than the edges, which will lead to sharp compositional inhomogeneities, stress and variations in birefringence. Since many device quality crystals can be cut from each boule, this problem can be circumvented by cutting around the cored region. With fiber crystals, however, the entire crystal is used as the laser and so if a core is present, laser performance would certainly suffer.

A study of interface faceting and compositional in homogeneities in Nd:YAG was undertaken by O'Meara et al. (14). Using optical microscopy with polarized light and electron microprobe techniques, facet formation and impurity segregation was studied. A number of interesting observations have been made to date. In Figure 7, the radial variation in Nd concentration of two fibers grown under different conditions but of approximately the same diameter is plotted. One of the fibers has a large concentration of Nd in the core region while the other is significantly more uniform. Note that the shape of the curves may reveal the presence of facets at the interface. The difference in Nd profile between these two fibers is believed to be related to the different processing conditions used. In general it appears that: 1) the Nd concentration is nearly uniform across the fiber cross section when the growth rate is small (around 0.25 mm/min or less). When the growth rate increases, so does the Nd concentration at the center of the fiber as seen in Figure 7 until a center concentration 1.5 times the edge is reached at growth rates of 2 mm/min. Also, it has been observed that the average Nd concentration also increases with growth rate. Growth striations (small compositional variations occurring in bands along the growth axis of the crystal which are due to growth rate fluctuations) were also found. At slow growth rates, facets seem to form only in larger diameter fibers and small fibers show no significant birefringence patterns.

FIGURE 7: Radial variation of Nd concentration in two Nd:YAG fibers grown under different conditions (14).



Other fiber lasers which have been grown and are currently undergoing analysis include Nd:CaSiO₄ (15), Nd:YAlO₃ (16), Nd:LiNbO₃ (15,17), NdSiO₃ (17), Mn₂SiO₄ (15) and Ti³⁺: Al₂O₃ (15,17).

NONLINEAR OPTICAL MATERIALS

One of the most important nonlinear optical materials for second harmonic generation, optical parametric oscillation, etc., is LiNbO₃, a ferroelectric material with a Curie temperature near its melting point of ~1260°C. It was chosen for study because of its potential use in fiber devices.

To be useful LiNbO₃ single crystals must have a single domain structure. Czochozalski grown crystals have to be poled after growth to achieve this result because they exhibit a multidomain structure whose morphology depends upon growth direction. In the growth of LiNbO₃ fibers it was found (18) that c-axis fibers less than 700 μm diameter were essentially single domain as grown and do not require poling (Figure 8). In addition, the built-in dipole moment in these c-axis fibers always points toward the melt. If a single domain seed crystal of reversed dipole orientation is used, the dipolar orientation reverses at the growth junction (Figure 9). The three 120° growth ridges also rotate by 60° due to a crystallographic faceting effect.

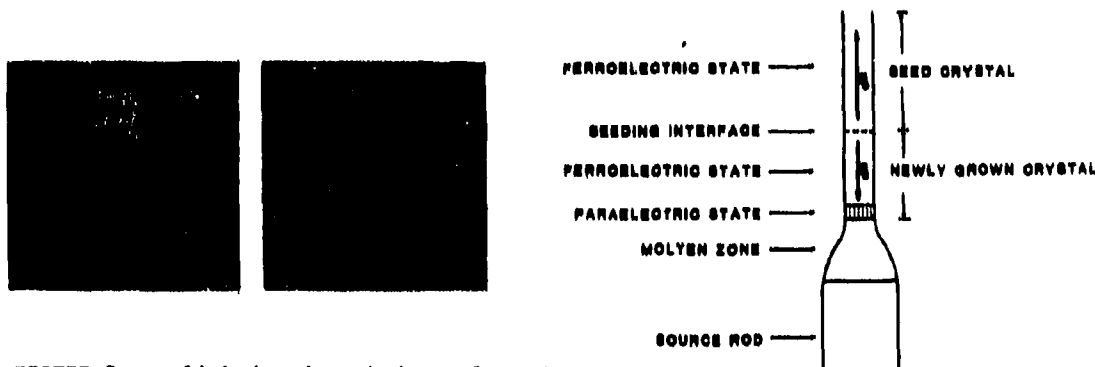


FIGURE 8: Polished and etched samples of c-axis LiNbO₃: (a) unpoled Czochozalski boule with cylindrical domains, (b) as-grown 700 μm single domain fiber with only thin anti-parallel surface domains (18).

FIGURE 9: Schematic showing c-axis domain reversal (18).

Small diameter LiNbO_3 fibers grown along the a-axis did not have a single domain structure but instead had an unusual bipolar nose-to-nose domain pattern with the anti-parallel domain boundary in the c plane and parallel to the growth axis (Figure 10).

FIGURE 10: Nose-to nose domain pattern of unpoled a-axis grown fibers. Polished and etched on "b" face (18).



A study of the various phenomena which could account for the observed domain structures in a- and c-axis LiNbO_3 fibers led to the hypothesis (19) that a self-induced poling voltage is present due to fiber growth and that it is caused by the thermoelectric effect where an electric potential (the poling potential) is generated by the temperature gradients present during growth. The large, axial temperature gradient is responsible for the single domain in c-axis fibers and its dipole orientation and the radial, temperature gradient is responsible for the bipolar domain structure in a-axis LiNbO_3 fibers. The requirement for single domain a-axis fibers has led to attempts to alter the radial temperature gradients by an asymmetric displacement of the fiber in the laser beam. This, however, was only partially successful with the domain boundary moving along the c-axis but not completely through the crystal. Other methods such as the use of external poling fields and impurity diffusion are being studied.

INFRARED TRANSMITTING FIBERS

A number of important applications exist for infrared transmitting fibers including transmission lines, spectroscopic analysis, thermometry and laser delivery systems. While the mixed fluoride and chalcogenide glasses under study are attractive candidates for long distance transmission lines, certain crystalline materials, including a number of halides and certain oxides like sapphire, may have more suitable properties for applications requiring shorter lengths and longer wavelengths.

The silver halides, AgBr and AgCl and KRS-5 (thallium bromiodide) are considered prime crystalline fiber candidates for IR transmission applications. Polycrystalline fibers of these materials have been made by extruding bulk single crystals through a die. Grain boundary scattering in polycrystalline fibers, however, leads to less than optimum optical transparency.

SILVER BROMIDE AND THALLIUM BROMIODIDE

The capillary-fed growth methods of Mimura (10) and Bridges et al. (11) were used for the growth of single crystal fibers of KRS-5 and AgBr respectively. The silver halide single crystal fibers, while having good optical properties, apparently suffer from poor mechanical properties. Work on KRS-5 single crystal fibers has not been extensive enough to draw definitive conclusions, but thallium containing compounds are limited to applications other than medical due to their toxicity.

Since AgBr and KRS-5 have relatively low melting points (AgBr , 432°C and KRS-5, 415°C), the laser heated pedestal growth method would not be as suitable for these materials as the capillary fed growth methods of Mimura et al. and Bridges et al.

A small study was undertaken by Route et al. (20) to see whether the capillary-fed method of Bridges et al. (11) could be used to grow KRS-5. It was first set up and successfully used to grow AgBr fibers and then adapted for the growth of KRS-5. The melt reservoir and capillary were made from fused silica and a silver cold finger was mounted above the capillary tip. The composition of KRS-5 is near the minimum melting composition in the $\text{TlBr} - \text{TlI}$ system with a composition of approximately 38 m/o $\text{TlI} - 42$ m/o TlBr . Growth was initiated by dipping a platinum wire into the melt and from that point the fiber grew readily. Growth rates varied from 1.5 - 8.4 mm/min. In some cases, it was easier to grow KRS-5 than AgBr . Surfaces were quite smooth but longer range diameter variations due to a poor mechanical fiber guiding system was a problem. Single crystal KRS-5 fibers 0.4 - 0.6 mm diameter and 22 mm in length were grown without serious difficulties (Figure 11). A condensate appeared on the cold finger which was analysed to be pure TlBr . The fibers therefore may be TlI -rich, although a shift in lattice constants could not be detected.

The optical quality of the fibers appeared quite good, except for the presence of a few dark inclusions at sites where the fiber diameter changed abruptly (Figure 12). The natural growth orientation for an unseeded KRS-5 fiber was found to be $\langle 110 \rangle$, the densest packed plane in the CsCl structure. Seeded growth was not attempted.

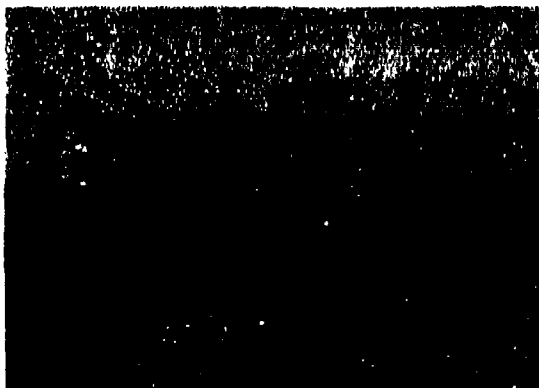


FIGURE 11: Photograph of optical quality KRS-5 fiber grown by the pressurized capillary growth method (21).

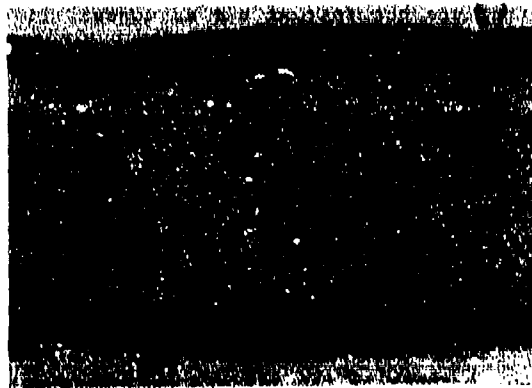


FIGURE 12: Photograph of KRS-5 fiber showing some typical scattering defects found in some regions of the fiber which appear to be voids and/or precipitates (21).

BARIUM AND CALCIUM FLUORIDE

Barium and calcium fluoride are both high melting compounds (MP= 1280°C and 1360°C respectively) and large crystals are grown commercially under a vacuum and/or reactive atmosphere to reduce O_2 and $(OH)^-$ contamination. Both compounds can easily be melted with the 50 watt CO_2 laser and were logical candidates for fiber growth by the LHPG method (21).

Optical quality single crystals were used as source rods and the growth of fiber crystals by the LHPG presented few problems, the most significant of which, however, was the formation of precipitates at a temperature several hundred degrees below the melting point. During growth, the crystals were clear and free of macroscopic scattering centers but as the crystal cooled, precipitates began to form 3-10 mm above the growth interface as illustrated in Figure 13. The precipitates are believed to be an oxide or oxyfluoride of Ba or Ca respectively even though the fibers were grown in a purified argon atmosphere. The scattering losses were more serious in BaF_2 than in CaF_2 as seen in Figure 14.

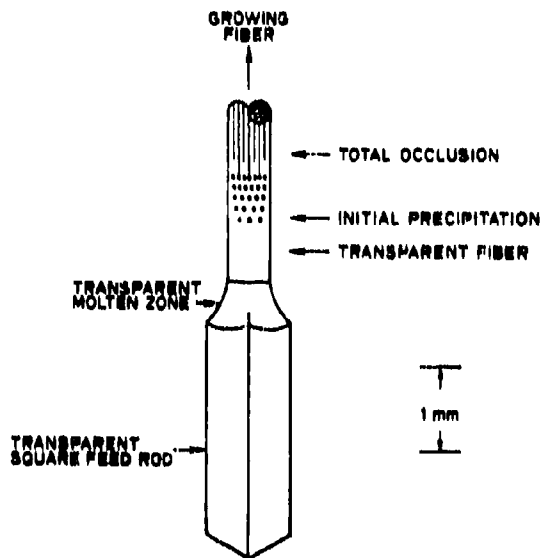


FIGURE 13: Schematic diagram illustrating the occurrence of precipitation in BaF_2 and CaF_2 crystal growth.

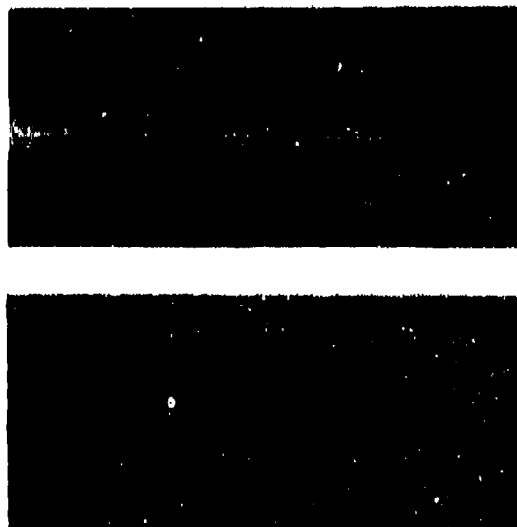


FIGURE 14: Photographs of a) BaF_2 fibers in reflected light showing total opacity, and b) two CaF_2 fibers in transmitted light revealing much lower density of scattering defects.

It is suspected that the molten zone acts as a getterer for reactive species present in the gas phase even when they are in low concentrations. A vacuum growth chamber or one in which a reactive gas such as HF can be used should reduce or eliminate this problem. Future plans call for such modifications.

SAPPHIRE

The high melting point and excellent optical properties of sapphire make it useful in fiber form for high-temperature thermometry applications (22), and in fact a commercial fiber thermometer has recently reached the market. The fiber thermometer is based on radiation emitted by a blackbody tip in the fiber and one or two color pyrometry can be used to analyze the radiation guided down the fiber. Although sapphire fibers were grown as far back as 1967 (4) and are very easy to grow in fiber form, two problems have limited their utilization in these type devices: 1) internal and surface scattering losses have been difficult to reduce to optimum levels; and 2) a stable, non-reactive blackbody tip has been difficult to find.

Byer et al. (23) have grown high optical quality sapphire fibers and have studied various metal alloy blackbody materials. In recent studies they have observed a temperature resolution of 10 mK in a 0.3 second bandwidth.

CONCLUSIONS

The field of single crystal fibers represents an emerging technology whose future appears promising. Some possible applications for single crystal fibers, the types of materials which can be produced in fiber form, and the current progress in fiber growth are discussed.

REFERENCES

1. C. H. L. Goodman, Solid State and Electron Devices 2, 129 (1978).
2. H. von Gompers, Z Physik. 8, 184 (1922).
3. H. E. LaBelle, Jr., and A. I. Mlavsky, Nature 216, 374 (1967).
4. H. E. LaBelle, Jr., and A. I. Mlavsky, Mater. Res. Bull. 6, 571 (1971).
5. J. S. Haggerty, Production of Fibers by a Floating Zone Fiber Drawing Technique, Final Report, NASA-CR-120948, May (1972).
6. D. B. Gasson and B. Cockayne, J. Mater. Sci. 5, 100 (1970).
7. C. A. Burrus and J. Stone, Appl. Phys. Lett. 26, 318 (1975).
8. J. Stone and C. A. Burrus, J. Appl. Phys. 49, 2281 (1978).
9. C. A. Burrus and L. A. Coldren, Appl. Phys. Lett. 31, 383 (1977).
10. Y. Mimura, Y. Okamura, Y. Komazawa, and G. Ota, Jap. J. Appl. Phys. 19, L269 (1980).
11. T. J. Bridges, J. S. Masiak, and A. R. Strnad, Opt. Lett. 5, 185 (1980).
12. M. M. Fejer, J. L. Nightingale, G. A. Magel, and R. L. Byer, Rev. Sci. Instrum. 55, (11) (1984).
13. H. J. Shaw, M. Digonnet, C. Gaeta, and A. Cordova-Plaza, 24th Annual Rpt. on Materials Research at Stanford University, CMR-85-2, July (1985).
14. D. L. O'Meara, H. J. Shaw, and R. S. Feigelson, 24th Annual Rpt. on Materials Research at Stanford University, CMR-85-2, July (1985).
15. W. L. Kway and R. S. Feigelson, unpublished.
16. Z-K. Tan and R. S. Feigelson, unpublished.
17. R. L. Byer, M. M. Fejer, and J. L. Nightingale, unpublished.
18. Y-S. Luh and R. S. Feigelson, 24th Annual Report on Materials Research at Stanford University, CMR-85-2, July (1985).
19. Y-S. Luh, M. M. Fejer, and R. S. Feigelson, *ibid*.
20. R. K. Route, Y-S. Luh, and R. S. Feigelson, Preparation of Infrared Optic Fibers Using New Materials, Final Report, NRL-M00014-82K-2001, August (1983).
21. W. L. Kway, R. K. Route, and R. S. Feigelson, *ibid*.
22. R. R. Dils, J. Appl. Phys. 54, 1198 (1983).
23. R. L. Byer, M. M. Fejer, and J. C. Nightingale, unpublished.

ACKNOWLEDGMENTS

Much of the work herein was supported in large part by the NSF-NRL program through the Center for Materials Research at Stanford University.

VERRES FLUORES POUR GUIDES D'ONDE INFRA ROUGE.

J. Lucas, Professeur
Laboratoire de Chimie Minérale D,
Campus de Beaulieu,
Université de Rennes
35042
France.

RESUME

La réalisation de guides d'onde optique est plus favorable à partir de matériaux existant à l'état vitreux qu'à partir de matériaux polycristallins ou monocristallins. Les verres qui actuellement correspondent au meilleur compromis entre la largeur de la bande de transmission, les potentialités d'ultra transparence, les faibles pertes par diffusion et la mise au point des conditions techniques de fibrage sont les verres fluorés. Les verres à base de tétrafluorure de zirconium permettent une transmission par fibres jusqu'à 4 μm , ceux à base de métaux plus lourds, thorium, indium, terres rares, etc..., jusqu'à 5 μm . Les applications potentielles en télécommunications longue distance sans répéteur dues aux très faibles pertes théoriques, 10^{-1} dB/km, sont discutées ainsi que les applications courtes distances dans les technologies capteurs et transport d'énergie.

INTRODUCTION

La réalisation de guides d'onde optique est grandement facilitée quand le matériau support de la transmission est vitreux. La mise en forme de verres à l'état de guides plan ou de fibres s'effectue généralement dans son domaine de plasticité maximum, c'est-à-dire à partir soit du bain liquide, soit de préformes solides en les fibrant après la température de transition vitreuse T_g , c'est-à-dire dans un domaine où la viscosité du solide est faible. Cette technologie introduit peu de contraintes et de défauts dans le matériau fibré et le guide obtenu conserve le plus souvent ses bonnes propriétés de transmission.

Ceci n'est pas le cas des matériaux cristallisés qui doivent être mis sous forme de guides d'onde par des techniques plus brutales, extrusion ou filage par exemple, qui entraînent le plus souvent de fortes contraintes dans le matériau, sources de dislocations, d'hétérogénéités, de joints de grains qui entraînent de fortes pertes par diffusion.

L'avantage du verre est cependant contrarié par le fait que très peu de matériaux existent à l'état vitreux et a fortiori des matériaux ayant une large bande de transparence. La chimie des verres est largement dominée, depuis des siècles, par la silice SiO_2 et les guides d'onde à base de SiO_2 ont atteint un développement unique ces dernières années, permettant d'atteindre les limites ultimes de transparence voisines de 0,15 dB/km à 1,3 μm . La largeur du domaine de transparence est cependant contrariée par la forte absorption multiphonon de la liaison Si-O qui diminue fortement la transparence après 1,8 μm . Il apparaît donc comme nécessaire pour augmenter le domaine spectral guidé, de passer des verres d'oxydes aux verres d'halogénures dont l'absorption multiphonon est nettement déplacée vers les grandes longueurs d'onde.

Dans la famille des halogénures M_xX_y (M = métal ; X = fluor F, chlore Cl, brome Br, iode I), seule la classe des verres de fluorures M_xF_y présente les conditions de stabilité, de résistance à la corrosion, suffisantes pour être préparés à l'état de fibres.

Hormis les verres fluorés à base de BeF_2 , connus depuis plusieurs dizaines d'années, la découverte de nouvelles familles de verres fluorés, stables, à l'Université de Rennes est récente (1), et a été suivie d'un développement technologique intense ces dernières années.

LA TRANSPARENCE D'UN MATERIAU

Comme indiqué sur la Figure 1, les origines des pertes optiques dans un matériau sont de deux types : intrinsèques et extrinsèques.

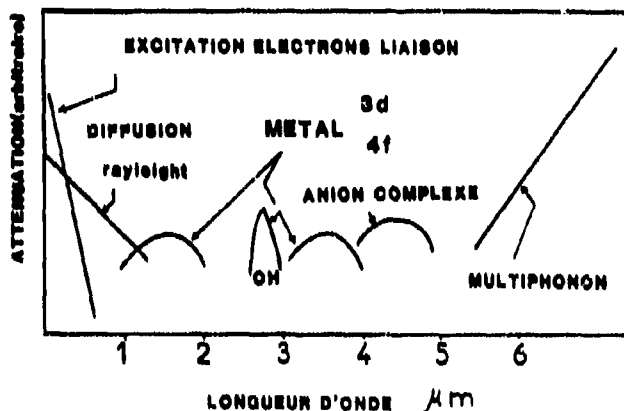


Figure 1.

Origine des pertes optiques dans un matériau.

Les mécanismes intrinsèques d'absorption correspondant à un matériau idéalement pur, sont :

- la diffusion Rayleigh, qui varie en général en λ^{-4} , et qui diminue donc très rapidement avec la longueur d'onde ;
- dans la région U.V., l'excitation des électrons de liaison par les photons très énergétiques, plusieurs électrons-volts, est également une source d'absorption, mais qui devient négligeable aux grandes longueurs d'onde ;
- le facteur déterminant est alors l'absorption multiphonon due aux vibrations des atomes liés les uns aux autres dans le solide, et qui augmente en fonction de la longueur d'onde.

On admet donc qu'entre ces deux frontières U.V. et I.R., il existe une zone théorique d'ultra transparence.

A ces raisons intrinsèques de pertes optiques, il faut malheureusement ajouter les facteurs extrinsèques qui sont liés à la pureté et à la qualité du matériau. Des pertes par diffusion peuvent en effet provenir de la présence de particules, de cristallites, de joints de grains, de dislocations, d'hétérogénéités de toutes sortes, qui sont générées au cours de la fabrication du matériau, ou de l'élaboration du guide d'onde. Ce facteur est très critique quand le verre à fibrer est sensible à la dévitrification, c'est-à-dire à l'apparition de nuclei et de microcristallites au cours du fibrage.

Les autres raisons de pertes de lumière dans le visible et le moyen infra-rouge sont :

- la présence d'ions paramagnétiques contenant des électrons célibataires qui, par excitation électronique, peuvent absorber des photons visibles ou I.R. Les ions des métaux de transition d, comme Fe^{2+} , Cu^{2+} , Co^{2+} , Ni^{2+} , etc... ou de terres rares f comme Nd^{3+} , Pr^{3+} , Ce^{3+} , Eu^{3+} , etc... sont, à cet égard, des poisons violents pour la transmission optique sur de grandes épaisseurs ;
- l'existence d'anions complexes comme OH^- , SO_4^{2-} , PO_4^{3-} , etc..., qui sont, par des mécanismes purement vibrationnels, autant de pièges à photons I.R., constitue un facteur de perte important le long du trajet de la lumière guidée.

LE CHOIX DES MATERIAUX

Il est clair que l'absorption multiphonon est le facteur déterminant pour obtenir un matériau ayant :

- un domaine de transmission le plus large possible
- une courbe d'ultra transparence la plus profonde possible permettant de diminuer les pertes jusqu'à des valeurs de l'ordre de 0,001 dB/km.

La Figure 2 montre comment varie l'absorption multiphonon pour différentes classes de matériaux cristallins ou vitreux, pour lesquels des tentatives de préparation de fibres optiques I.R. ont été faites.

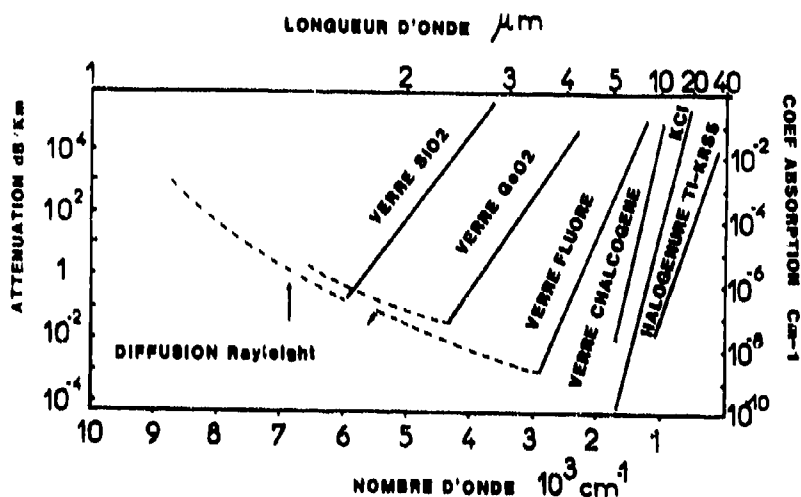


Figure 2. Absorption multiphonon pour différents types de matériaux vitreux ou cristallins

Les fibres à base de SiO_2 dominent très largement cette technologie des fibres optiques et les conditions de pureté et de préparation idéales ont été atteintes puisque les pertes théoriques minima de 0,15 dB/km ont été mesurées il y a quelques années. On voit sur cette courbe que l'absorption multiphonon augmente très vite à partir de 1,6 μm , et que, pour transmettre de la lumière au-delà de cette longueur d'onde, les verres à base d'oxydes de germanium GeO_2 sont mieux adaptés. Ces verres présentent toutefois deux inconvénients : une tendance à la cristallisation plus forte et la présence d'impuretés OH^- dont le maximum d'absorption se situe vers 2,9 μm .

Les verres de chalcogénures, en particulier ceux provenant de combinaisons adé-

quates des éléments suivants : S, As, Se, Te, etc..., sont aussi de très bons candidats pour le guidage I.R. L'avantage de ces verres réside dans leur grande stabilité vis-à-vis de la dévitrification et leur résistance à la corrosion par l'eau. Par contre, leur pollution par des impuretés H, O, créant des vibreurs parasites type SH, est très difficile à éviter.

Les autres matériaux mentionnés, tels que les halogénures alcalins type KCl, halogénures d'argent tel que AgCl/AgBr ou les halogénures de thallium tel que KRS₅ (cristaux mixtes de TlBr, TlI, ne peuvent pas être obtenus à l'état vitreux. Leur mise en forme à l'état de fibres à partir de lingots polycristallins ou monocristallins fait appel aux techniques d'extrusion qui, comme indiqué précédemment, introduisent des contraintes internes qui augmentent considérablement la diffusion et limitent la longueur des guides d'onde.

Les verres fluorés sont actuellement le meilleur compromis entre tous ces facteurs : état vitreux, absorption multiphonon reculée, bonne résistance à la corrosion et à la dévitrification, transmission dans le visible et dans l'I.R.

LES VERRRES FLUORES

Le seul fluorure susceptible d'être obtenu à l'état vitreux est le fluorure de beryllium BeF₂, mais ses verres ou leurs dérivés sont toxiques, souvent hygroscopiques avec une absorption multiphonon voisine de GeO₂.

Tous les autres verres fluorés sont issus de combinaisons dans lesquelles l'un des partenaires ou un couple de partenaires joue le rôle de vitrificateur alors que l'autre joue celui de modificateur de réseau.

Les fluorures dits "vitrificateurs" peuvent être classés de la façon suivante :

- 1) MF₂ où M est un petit cation polarisant créant une forte liaison covalente : BeF₂ en est le seul représentant ;
- 2) MF₃, avec M = Al, Fe, Cr, In, etc... Ici aussi, le cation M³⁺ petit et chargé, polarise fortement les ions F⁻ ;
- 3) MF₄, avec M = Zr, Th, U. La forte association dans l'état liquide nécessaire pour la formation de l'état vitreux est ici aussi possible avec ces cations fortement chargés. L'ion Zr⁴⁺, le plus petit, correspond au cas le plus favorable.

Un examen critique de ces différentes familles de verre pour la fabrication de fibres optiques amène aux remarques suivantes :

- a) Les verres de BeF₂ sont difficiles à manipuler, toxiques et leur largeur de transmission est peu supérieure à celle de SiO₂, 2 μm, correspondant à une limite pour du guidage sur de moyennes ou longues distances.
- b) Les verres à base de métaux trivalents MF₃ ont une forte tendance à la cristallisation et à la corrosion par la vapeur d'eau, ce qui explique qu'aucune tentative de fibrage de ces verres n'ait abouti. De plus, l'absorption multiphonon est légèrement inférieure à celle des verres à base de ZrF₄.
- c) Les verres à base de métaux lourds MF₄ sont actuellement dominés par les verres de fluorozirconate ZrF₄ pour lesquels des techniques de fibrage ont été récemment développées (2, 3, 4). Les matériaux vitreux à base de ThF₄ combiné à MnF₂ ou ZnF₂ (5) présentent un domaine spectral plus large, mais étant plus instables, ils n'ont pour l'instant pas fait l'objet d'études de fibrage.

1. Les verres fluorés à base de ZrF₄

Cette famille de verres découverte il y a une dizaine d'années a fait l'objet d'études intensives en raison de ses applications dans le moyen I.R. Le diagramme de la Figure 3 montre que des matériaux vitreux peuvent être obtenus simplement dans le binaire ZrF₄-BaF₂.

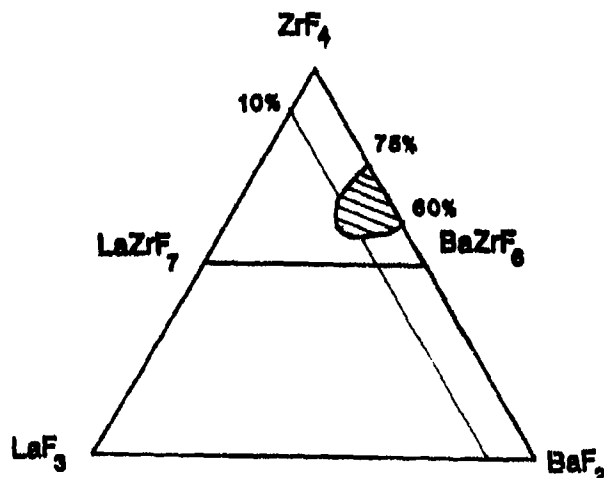


Figure 3.

Domaine d'existence de verres fluorés dans un diagramme ternaire à base de ZrF₄.

Ces verres sont toutefois instables et il est nécessaire d'utiliser d'autres adjuvants pour diminuer leur vitesse de cristallisation. L'addition de LaF_3 par exemple augmente le domaine vitreux, mais les verres qui ont été actuellement optimisés pour le fibrage sont des verres multicomposants dont une composition est par exemple : 56 ZrF_4 , 34 BaF_2 , 6 LaF_3 , ou GdF_3 et 4 AlF_3 . Ces verres ont un indice de réfraction n voisin de 1,5 qui peut être modifié par adjonction d'autres fluorures permettant ainsi la réalisation de structure à variation d'indice indispensable pour la technologie des guides d'onde.

La Figure 4 montre que le domaine de transparence de ces verres à base de ZrF_4 s'étend pour des épaisseurs de quelques millimètres de 0,2 à 7 μm . La Figure 5 représente la contribution de l'absorption multiphonon en fonction de la longueur d'onde.

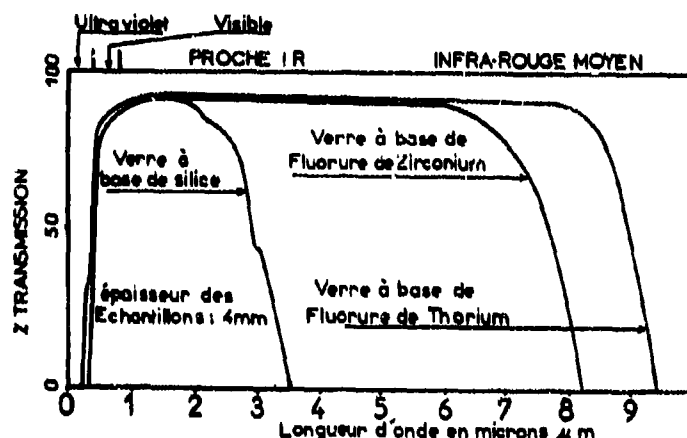


Figure 4. Domaine de transparence de verres fluorés à base de fluorure de zirconium ZrF_4 ou de mélange de fluorures $\text{ThF}_4/\text{MnF}_2$ ou ZnF_2 .

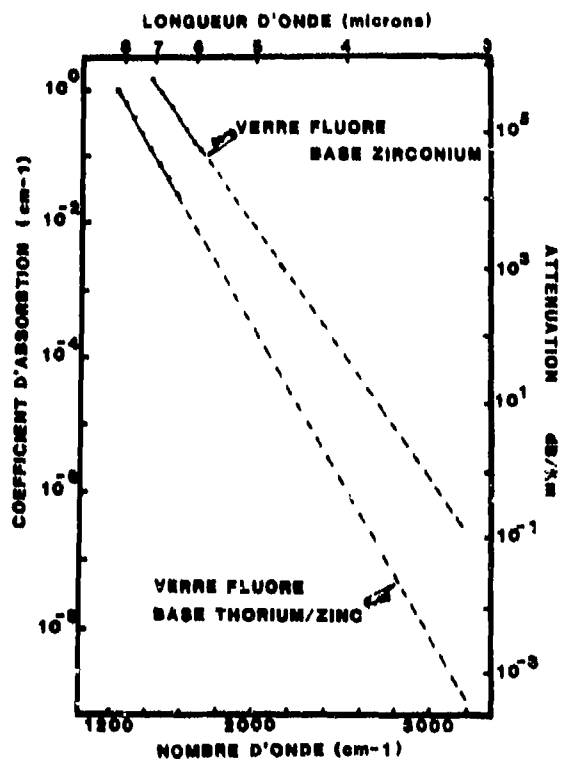


Figure 5.

Evolution du coefficient d'absorption α et des pertes optiques multiphonon en fonction de la longueur d'onde pour des verres base ZrF_4 et des verres base ThF_4 .

On voit que les pertes par absorption exprimées en dB/km augmentent très rapidement après 4 μm . A 5 μm , par exemple, les pertes théoriques sont de l'ordre de quelques milliers de dB/km . La Figure 6 représente les contributions diffusion Rayleigh et absorption multiphonon pour des verres à base de SiO_2 et à base de ZrF_4 . Il est clair que les verres fluorés présentent une courbe d'ultratransparence beaucoup plus profonde, atteignant des valeurs théoriques voisines de 0,001 dB/km dans la région spectrale 2-4 μm .

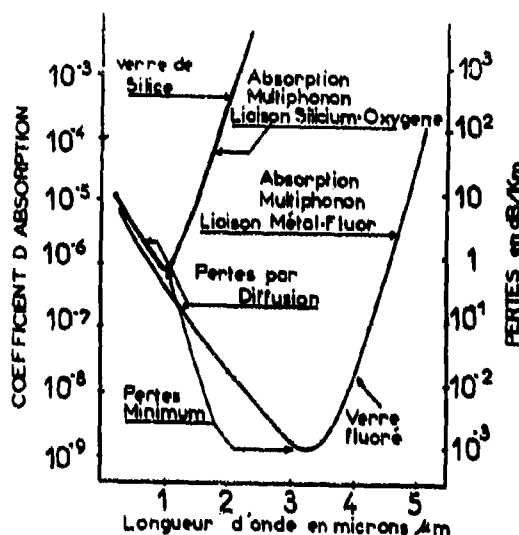


Figure 6. Evolution de la transparence de verre fluoré et de verre de silice en fonction de la longueur d'onde dans l'hypothèse d'un matériau idéal (pertes intrinsèques).

2. Les verres fluorés à base de métaux lourds, thorium, indium, terres rares

Les fluorures ThF_4 , LnF_3 (Ln = terres rares), InF_3 peuvent également conduire à des matériaux vitreux en abaissant le point de fusion des mélanges de fluorures par ZnF_2 ou MnF_2 . Plusieurs types d'association de fluorures conduisent à des verres que l'on peut obtenir avec des épaisseurs d'une dizaine de millimètres. Par exemple, la composition 28 ThF_4 , 28 YF_3 , 28 ZnF_2 , 16 BaF_2 est une des compositions qui présente la vitesse de dévitrification la plus basse, donc la plus facile à mettre en œuvre pour la réalisation de guides d'onde.

L'examen de la Figure 4 indique que l'absorption multiphonon est ici, du fait du poids des métaux, reculée de $1 \mu\text{m}$ à peu près par rapport aux verres à base de ZrF_4 . Leur domaine de transparence s'étend de $0,2$ à $8 \mu\text{m}$ pour des épaisseurs de quelques millimètres. L'extrapolation de la contribution multiphonon à l'absorption est représentée Figure 5 et indique clairement que les pertes par mécanisme multiphonon diminuent très rapidement vers les courtes longueurs d'onde. Par exemple, à $5 \mu\text{m}$, les pertes théoriques sont de quelques dizaines de dB/km , soit dix fois plus faibles qu'avec les verres base ZrF_4 . Le minimum théorique de pertes peut être évalué comme étant en-dessous de 10^{-1} dB/km , la région d'ultra transparence étant légèrement déplacée vers les grandes longueurs d'onde.

LES FACTEURS EXTRINSEQUES D'ABSORPTION

Comme indiqué au début de cet article, plusieurs facteurs liés à la pureté des matériaux utilisés, aux contraintes introduites lors des procédés de fabrication des guides, modifient très fortement l'ultra transparence théorique.

Les pertes par diffusion Rayleigh ont longtemps été considérées comme les plus dangereuses; compte tenu de la faible stabilité de l'état vitreux de ces matériaux comparés à la silice. D.C. Tran (6) et coll. ont montré que la loi de diffusion était bien du type Rayleigh et varie comme λ^{-4} . L'extrapolation de mesures effectuées dans le visible et le proche I.R. conduit bien à de très faibles pertes par diffusion dans la région d'ultra transparence ($\approx 0,02 \text{ dB/km}$).

Le risque de diffusion parasite dû à la formation de microcristallites au cours du fibrage n'est donc pas aussi critique lors de la fabrication de fibres en verre fluoré.

L'espace parasite la plus néfaste est sans aucun doute l'ion OH^- dont la bande de vibration à $2,9 \mu\text{m}$ se situe dans la région d'ultra transparence. De récentes études effectuées à Rennes (7) ont permis de calculer le coefficient d'absorption molaire de OH^- dans les verres fluorés. La contribution de l'ion OH^- à $2,9 \mu\text{m}$ est la suivante :

- environ 5000 dB/km/ppm pour les verres de fluorozirconate
- environ 10000 dB/km/ppm pour les verres à base de ThF_4 .

L'examen de ces valeurs montre l'extrême absorption parasite de ces ions OH^- et la nécessité de développer des traitements de purification.

Les métaux de transition 3d et 4f comme Fe^{3+} , Ni^{2+} , Co^{2+} , Nd^{3+} , Er^{3+} , Pr^{3+} sont aussi des facteurs d'absorption parasite importants. Le Tableau I montre les pertes introduites à différentes longueurs d'onde pour 1 ppm d'impureté de ces métaux. Il est clair que pour du guidage sur de très longues distances sans répéteur, il sera nécessaire d'atteindre des niveaux de pureté de l'ordre du ppb lors de la préparation des fluorures de départ et de l'élaboration des fibres.

départ et de l'élaboration des fibres.

TABLEAU I
Influence de traces de métaux 3d ou 4f sur les pertes optiques dans les verres fluorés. Les valeurs correspondent aux pertes en dB/km/ppm pour différentes longueurs d'onde

λ μm	2.0	3.0	4.0
Eléments (ppm)			
Fe	90	2	0,4
Co	130	4	0,2
Ni	90	0,5	0,1
Cu	3	0,001	-
Ce	--	8	50
Pr	43	0,4	20
Sm	4	6	7
Tb	25	14	-

PREPARATION, PURIFICATION DES VERRES FLUORES

La façon la plus simple de préparer les verres fluorés est la fusion du mélange de fluorures en atmosphère neutre en utilisant des creusets soit de carbone vitreux, soit d'or ou platine. La présence d'une atmosphère sèche exempte de traces de vapeur d' H_2O est indispensable pour éviter la pyrohydrolyse du bain fondu et la formation d'oxydes ou d'hydroxydes qui sont autant de sources de cristallisation parasite.

Il est également possible d'accéder au bain de fluorures fondus en utilisant des oxydes comme matériaux de départ et en les convertissant en fluorures par traitement à 300°C en présence de fluorure acide d'ammonium NH_4FHF . Après traitement de fluoration, l'excès de sel d'ammonium est éliminé par sublimation.

Lors de la préparation de verres fluorés par cette dernière méthode et même à partir de fluorures très purs, il est difficile d'éviter la formation d'ions OH^- et d'ions O^{2-} dans le bain. Les verres obtenus présentent alors une absorption caractéristique autour de $3 \mu\text{m}$, et des épanchements dans la région $6-7 \mu\text{m}$ due aux vibrateurs $\text{H}-\text{O}$. Des techniques de Reactive Atmosphere Processing RAP utilisant soit CCl_4 (8), soit CS_2 (9) ont été développées avec succès pour éliminer ces vibrateurs parasites. La Figure 7 montre comment, après un traitement RAP, se trouve améliorée la transmission d'un verre fluoré aussi bien dans la région $2,9 \mu\text{m}$ qu'aux environs de $7 \mu\text{m}$. Le traitement consiste à faire passer les vapeurs de CCl_4 ou CS_2 sur le bain de verre en fusion.

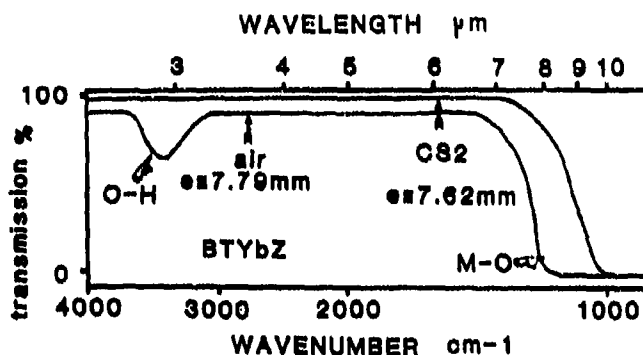


Figure 7. Transmission optique d'un verre fluoré à base de thorium préparé à l'air et ensuite soumis à un traitement de Reactive Atmosphere Processing sous CS_2 .

CONCLUSION. APPLICATIONS

Il ne fait aucun doute que l'importante activité de recherche sur les verres fluorés est motivée par la potentialité de préparer des fibres optiques ultra transparentes de quelques centièmes ou millièmes de dB/km autorisant de ce fait des télécommunications longues distances sans répéteur.

Ce type d'applications visant à mettre au point des fibres optiques de deuxième génération complémentaires des fibres de silice va nécessiter le développement d'une technologie nouvelle de préparation qui passera nécessairement par la voie gazeuse. Le défi technique posé étant la préparation de fibres dont le taux tolérable d'impuretés sera de

l'ordre de quelques parties par milliards, il est clair que des méthodes de type dépôt chimique par phase vapeur devront être développées conjointement au développement de méthodes de fabrication de fibres en continu pour éviter des pertes trop fortes aux jonctions. Il est clair que ces guides d'onde exceptionnels ne trouveraient qu'un intérêt limité sans la mise au point de sources, de modulateurs, et de récepteurs fiables dans la bande 2-4 microns.

Un autre type d'applications lié aux propriétés d'ultra transparence concerne aussi le transport sur de courtes ou moyennes distances de fortes énergies émanant de lasers de puissance émettant dans la région 2-4 μm .

Même si l'objectif ultime d'ultra transparence n'est pas atteint, le développement de fibres optiques en verre fluoré de quelques dB/km doit conduire à beaucoup d'applications que l'on peut schématiquement diviser en deux parties :

- l'une à vocation analytique dont la finalité est le captage et l'analyse d'un signal I.R. : c'est le domaine des capteurs optiques
- l'autre où la fibre sert de guide pour le transport d'énergie.

Le développement des fibres I.R. pour capteurs est fondamental pour les technologies suivantes :

a) pyrométrie à distance : une fibre optique transparente jusqu'à 5 μm doit permettre de recueillir des informations significatives jusqu'à des températures voisines de l'ambiante et évidemment vers les hautes températures. Les applications potentielles sont les suivantes : mesure de température dans des endroits reculés, difficiles d'accès, détecteurs d'incendie, thermographie, imagerie thermique, endoscopie médicale.

b) spectroscopie I.R. à distance : la mise au point de fibres I.R. à large bande doit permettre la réalisation de cellule de mesure spectrophotométrique à distance permettant des analyses de gaz, liquide, etc..., le contrôle in situ de réacteurs industriels, de gaz polluants, du métabolisme CO_2 dans les poumons, etc...

Le transport guidé d'énergie sur de courtes, moyennes ou longues distances constitue également un domaine d'application prometteur. Le couplage laser-fibre a jusqu'à présent été réalisé entre les lasers néodyme émettant à 1,06 μm et les fibres de silice très transparentes à cette longueur d'onde. Il faut toutefois remarquer que beaucoup de matériaux, dont le tissu humain, sont peu absorbants à cette longueur d'onde. Les matériaux organiques, on inclut ici les tissus humains, les polymères naturels ou artificiels bois, papier, tissus, plastiques, etc..., absorbent fortement le rayonnement I.R. entre 2 et 5 μm , région qui correspond aux vibrateurs les plus connus OH, CH, CO, etc...

Ce type d'applications, découpage, usinage, imprimante thermique, chirurgie laser, soudure, etc... est évidemment tributaire des sources lasers de puissance moyenne dans cette région I.R. du spectre. Le laser CO_2 émettant à 10,6 μm est évidemment inutilisable avec des fibres verres fluorés ; par contre, la région d'émission 5 μm du laser CO semble être plus réaliste et plus compatible avec des guides d'onde dont la limite de transparence se situe dans cette région du spectre.

BIBLIOGRAPHIE

- 1) M. Poulain et J. Lucas, Verres Réfract., 32, 505 (1978)
- 2) D.C. Tran, C.F. Fisher et G.H. Sigel, Electron. Letters, 18, 657 (1982)
- 3) S. Mitachi, S. Shibata et T. Manabe, Japan J. Appl. Phys., 20, L337 (1981)
- 4) G. Mazé, V. Cardin and M. Poulain, Proc. SPIE 400, 63 (1983)
- 5) J. Lucas, Proc. SPIE 320, 22 (1982)
- 6) D.C. Tran, G.H. Sigel, K.H. Levin and R.J. Ginther, Electron. Letters, 18, 1046 (1982)
- 7) D. Trégoat, G. Fonteneau et J. Lucas, Mat. Res. Bull., en cours de publication (1985)
- 8) M. Robinson, R.C. Pastor, R.R. Turk, D.P. Devor, M. Braunstein et R. Braunstein, Mat. Res. Bull., 15, 735 (1980)
- 9) D. Trégoat, G. Fonteneau et J. Lucas, Mat. Res. Bull.,

SUMMARY OF SESSION IV
COMMUNICATIONS

by

B. Hendrickson, Chairman

Seven papers were presented in this technical session covering a wide range of communication system applications of optical fiber. These papers are summarized below.

"Wide-Bandwidth, Long Distance Fiber Optic Communication Systems"

This paper discussed an advanced single mode fixed plant communication system with experimental demonstration at 140 MBPS at an unrepeated distance of 250 Km and experimental results up to 2 GBPS at distances of 90 Km.

"Performance of RF Fiber Optic Links"

This paper discussed a new application of single mode fiber as an RF waveguide alternative. Both direct laser modulated and externally modulated systems were discussed. This paper emphasized practical engineering considerations in implementing a single mode analog system as an alternative to waveguide.

"Fiber Optics - A Survivable and Cost Effective Transmission Medium for Terrestrial Networks"

This paper discussed a study aimed at trading off a fiber optic based communications system versus a line-of-sight microwave or coaxial cable based system. Results show a marked advantage of optical fiber versus these alternative systems from life cycle cost and operation and support cost point of view.

"Single Mode Fibers for Fiber Optic Guided Missiles - A Comparison with Graded Index Multimode Fibers"

This paper discussed a novel application of optical fiber to missile payout. Discussions centered on tradeoffs between single and multimode fiber. Multimode fiber was shown to outperform single mode fiber as a function of bend radius on the payout winding.

"Lightwave Technology in Future Radar Equipment Design"

This paper discussed tradeoff designs for the implementation of a fiber optic based radar system design. Practical results were reported in the area of system noise and performance. Additionally preliminary results were reported on a Frana-Kaldysh absorption modulator design.

"Tactical Fiber Optic Cable Assembly Requirements"

This paper reported on design requirements for a ruggedized, environmentally qualified multimode optical fiber cable and connector for the battlefield. Tradeoff analyses of fiber construction versus environment (emphasizing temperature) were presented.

"A Hybrid Transmission Scheme on Single - Mode Fibers for Tactical Communications"

This paper discussed a novel approach to the use of light emitting diode (LED's) on single mode optical fiber as well as proposing the use of laser power sharing at tactical command centers. This paper examined cost, reliability and flexibility of the proposed hybrid transmission scheme to battlefield operation.

WIDE BANDWIDTH, LONG DISTANCE FIBRE-OPTIC COMMUNICATION SYSTEMS

S D WALKER, L C BLANK and L BICKERS

BRITISH TELECOM RESEARCH LABORATORIES
MARTLESHAM HEATH
IPSWICH
SUFFOLK
IP5 7RE
UK

ABSTRACT

Recent advances in laser, fibre and receiver technology have allowed a series of unrepeatable optical transmission system experiments to be carried out at BTRL. These spans ranged from 90 km to 250 km at line-rates from 34 Mbit/s to 2 Gbit/s.

At data-rates of 34 Mbit/s and 140 Mbit/s, a single-line 1.525 μm distributed feedback laser was used in conjunction with step-index monomode fibre spans up to 251.6 km. In a second set of experiments, a 1.55 μm multi-longitudinal-mode laser gave error-free transmission over lengths of dispersion-shifted fibre up to 233 km. For gigabit transmission experiments, a 1.535 μm single-line laser and dispersion-shifted fibre provided a further system option which resulted in a recent fully-regenerated 2 Gbit/s, 90 km trial featuring commercially-available GaAs logic components.

This paper describes the various system configurations implemented and reviews the technical options for further long-span, unrepeatable optical transmission experiments using current and developmental direct-detection technology in the 1.5 μm wavelength region.

INTRODUCTION

At the present time, a number of laboratories are actively engaged in the design and development of long-span, high-capacity optical transmission systems. Significant increases have recently been made in system capability (expressed as a span/bit-rate product) [1,2] and in unrepeatable span [3,4]. The realisation of such high-performance optical transmission demonstrations requires careful consideration of laser spectral characteristics, fibre attenuation, fibre dispersion and the construction of low-noise receiver circuitry. The use of commercially-available lasers, fibre and receiver electronics in recent laboratory trials at BTRL will permit the rapid transfer of this technology into the development and production stages, and thus allow system planners to take advantage of the increased flexibility and reduced cost that such systems will offer.

This paper will review some recent unrepeatable system experiments and provide an assessment of the technical options available for future long-span direct-detection systems.

FIBRE ATTENUATION AND DISPERSION CHARACTERISTICS

Typically, the best step-index monomode fibre designs [5,6] have attenuation and dispersion properties shown in Figure 1. The principal attenuation minima occur at wavelengths of approximately 1.3 μm and 1.55 μm . Fibre loss in the second window can be below 0.2 dB/km whilst at 1.3 μm , better than 0.35 dB/km has been achieved. Waveguide and material dispersive effects introduce dispersion of approximately 17 ps/nm.km in the second window region and less than 4 ps/nm.km at 1.3 μm . Much research has been carried out to minimise dispersive effects at 1.55 μm whilst retaining the low attenuation; good results being reported from a number of laboratories [7,8]. Recently, fibre of this dispersion-shifted type has become commercially available.

A second approach to the dispersion problem which has aroused considerable interest is the use of single-longitudinal-mode lasers. These devices exhibit narrow linewidths under modulation and therefore allow high-speed transmission over conventional step-index monomode fibre. The lasers used in the long-span experiments reported here are described in the next section.

LASER TRANSMITTERS

To obtain wide-bandwidth, long-span optical transmission the optical source should have a high mean launch power and suitable spectral characteristics for the transmission medium. Two device types are described in this paper: the multi-longitudinal mode, double-channel planar buried heterostructure (DCPBH) and ridge waveguide, distributed feedback (DFB) laser. Both of these devices have featured in the long-span transmission experiments reported here.

Figure 2 shows the time-averaged spectral characteristics of a DCPBH laser under high drive level conditions. The mean wavelength is 1.55 μm with an rms spectral width of 3.5 nm. This spectrum corresponds to the second low-loss window in silica fibre but

would introduce significant dispersion in the conventional step-index type. Typically this would limit the span of a 140 Mbit/s, 1.55 μm optical transmission system to approximately 23 km.

In contrast, the time-averaged spectrum of a DFB laser produced at BTRL [9] is shown in Figure 3. The single-longitudinal-mode behaviour is maintained under high-speed modulation with a spectral width of approximately 0.2 nm at 1.8 Gbit/s. A gradual broadening occurs with high-speed drive in comparison to the (monochromator resolution-limited) spectrum observed under dc conditions. The transient spectral behaviour of a BTRL DFB laser is shown in more detail in Figure 4. Both instantaneous wavelength and intensity are subject to a damped oscillation or "chirping" effect which has received considerable attention in the literature [eg 10]. Wavelength chirping constitutes a further dispersive limit to system capacity and can be the dominant system impairment when dispersive fibre is used [11]. Chirp reduction may be achieved by operating the laser above threshold or by providing external modulation. However, both these techniques introduce additional penalties. Recently, chirp-reduction has been demonstrated at BTRL [12,13] by modification of the laser pumping pulse to influence the junction carrier density variation after turn-on and hence reduce the laser wavelength perturbation described above. The required laser drive pulse modification can be introduced by exploiting the similarity between the chirp effect shown in Figure 4 and the impulse response of a second-order network. Figure 5 is a schematic diagram of the basic experimental technique. With appropriate choice of second-order network transfer function, a substantial reduction in laser chirp can be obtained. This technique is currently undergoing further experimental and theoretical analysis.

RECEIVERS

Long span optical transmission can only be achieved with high performance optical receivers. To obtain sensitivity levels approaching -50 dBm at 140 Mbit/s requires careful attention to the noise contribution of the post-detection circuitry. In principle, the lowest noise is achieved with the high-impedance, GaAs FET input stage shown in Figure 6 provided that the total input capacitance is minimised. However, accurate compensation for the low-pass filtering action at the input must be provided. An alternative configuration is the transimpedance circuit shown in Figure 7. This design typically has greater noise than its high-impedance counterpart, but offers other advantages such as high dynamic range and simplified equalisation. Germanium avalanche photodiodes (Ge APD's) have been used in all the optical receivers developed for experiments described here. In contrast to the alternative PIN photodiode receivers commonly used, Ge APD's introduce non-negligible leakage current and signal-dependent noise but this is offset by the substantial avalanche gain provided. The most sensitive direct-detection optical receivers in current system or research use now routinely employ Ge or III-V APD's or high-performance PIN diodes.

Commercially available, 30 μm diameter Ge APD's have been incorporated in a number of transimpedance optical receiver designs for bit-rates ranging from 34 Mbit/s to 2 Gbit/s. Their performance is summarised in Figure 8.

The experimental points lie close to a straight line with a slope of 13.8 dB/decade. This slope can be taken as an indication of receiver design performance. If only bit-rate independent noise contributions are important, the receiver sensitivity is proportional to $1/T$ (where T is the bit duration) giving a slope of 10 dB/decade. Alternatively, if the receiver noise is dominated by the input-stage contribution, the sensitivity is proportional to $1/T^{3/2}$, giving a slope of 15 dB/decade. It is clear from the lesser slope obtained practically that the use of an avalanche photodiode gives an improved receiver noise performance even in the gigabits region together with attendant dynamic range increases. Avalanche photodiodes fabricated from III-V materials offer significant performance advantages compared to the Ge APD's mentioned above with excellent receiver sensitivities being reported at 2 Gbit/s [1] and 4 Gbit/s [2]. Quaternary compound detectors also offer potentially good performance in the 2-3 μm wavelength region [14] where fluoride glass-based fibres exhibit minimum attenuation [15].

SYSTEM RESULTS

A range of experimental systems with spans in excess of 200 km have been evaluated as shown in Table 1. Both monomode step-index and dispersion-shifted fibre have been used together with multi-longitudinal mode DCPBH and single-line DFB lasers. Full regeneration was provided in all cases. Figure 9 is a schematic diagram of a recent 222.8 km, 140 Mbit/s optical transmission experiment [16] which used a 1.525 μm DFB laser and a high-performance Ge APD receiver. The laser threshold was 50 mA at 17°C with a peak-to-peak modulation signal (from threshold) of 60 mA provided by a GaAs MESFET drive circuit. Pseudo-random data (2¹⁰-1, NRZ) was used throughout the experiment. An optimised objective lens arrangement allowed 40% coupling efficiency (or loss of 4 dB) between laser and fibre. This resulted in a mean launch power of +1.5 dBm at 140 Mbit/s and 1.525 μm . The 222.8 km optical transmission path consisted of commercially-available monomode step-index fibre. Low-loss fusion splices were used throughout the fibre span which was comprised of 5.3 km and 6.4 km lengths. An overall span loss of 49.3 dB was measured at 1.525 μm with an average splice loss of less than 0.1 dB.

At the receiver end, the system fibre was butted directly against a developmental chip-carrier 30 μm diameter Ge APD. Low-noise receiver performance was obtained from a GaAs FET input stage transimpedance circuit. After subsequent amplification, the detected

signal was passed to a 140 Mbit/s regenerator of conventional design employing SAW filter timing extraction. The regenerated signal was then available for BER measurements using a standard data test-set. Figure 10 shows the observed mean BER as a function of mean received optical power. No dispersive system power penalty was incurred since at a bit-rate-span product of 30 Gbit.km DFB laser chirp effects are negligible. Theoretical performance modelling is based on a standard Gaussian noise model and assumes no penalty due to laser pulse shape. The equivalent-time received "eye" is shown in Figure 11. An overall system margin of 1.2 dB was obtained. Further experiments at 34 Mbit/s with attendant improvements in laser launch power and receiver sensitivity (as described in Table 1) allowed a span of 251.6 km to be achieved.

An experimental set up similar to that of Figure 9 was used for the long-span dispersion-shifted experiments. The optical source was a 1.55 μm DCPBH laser providing a mean launch power of +5 dBm at bit-rates of both 34 Mbit/s and 140 Mbit/s. Avalanche photodiode receivers allowed margins of 3.7 dB after 233.5 km of fibre at 34 Mbit/s and 0.9 dB after 220.6 km at 140 Mbit/s respectively.

Recently, at BTRL, fully-regenerated system results have been obtained with a packaged GaAs master-slave D-type flip-flop operating at 2 Gbit/s with a 2^{15} -1, prb, NRZ, data sequence [17]. The optical source was a ridge-waveguide, DFB laser of similar construction to that described previously whilst the receiver consisted of a 30 μm diameter, Ge APD in conjunction with packaged monolithic microwave integrated circuits (MMIC's). Surface-mounting microwave printed circuit board construction techniques gave good broadband performance. Attenuation-limited transmission was achieved over a 90 km span of dispersion-shifted fibre.

A schematic diagram of the experimental system is shown in Figure 12. The transmitter was a stud-mounted, ridge-waveguide, DFB laser emitting at 1.535 μm . Light was coupled into the fibre by means of an objective lens arrangement with 40% coupling efficiency allowing a mean launch power of -1.0 dBm with the laser biased at threshold and a 2 Gbit/s, 60 mA peak-to-peak modulation current provided by a GaAs MEFFET pulse amplifier. The dispersion-shifted fibre span was on 14 reels joined by low-loss fusion splices with an average splice loss of 0.1 dB. Total path attenuation at 1.535 μm was 22 dB (0.234 dB/km), while at 1.55 μm , the nominal fibre loss is 0.213 dB/km [8]. The fibre dispersion zero was at 1.551 μm with approximately 1 ps/(nm.km) negative dispersion at 1.335 μm wavelength.

At the receive end of the transmission path, the detected and amplified signal was split and fed directly to the GaAs flip-flop 'D' input and timing extraction circuitry. As shown in Figure 12, the recovered clock signal was passed to the flip-flop and data test receiver clock inputs. The GaAs flip-flop provided both regeneration and retiming functions in a single stage. The output of the flip-flop was connected directly to the data test set for error-rate measurements.

Signals present in the receiver/regenerator circuitry are reproduced (attenuated by 20 dB) in Figures 13a, 13b and 13c. The received pulses are shown in Figure 13a. Figure 13b is the regenerated data obtained whilst Figure 13c shows the fully-regenerated equivalent-time "eye" diagram with approximate signal rise and fall times of 200 ps.

Subsequently, a series of error-rate measurements were performed over dispersion-shifted fibre spans of 4 km and 90 km; regeneration penalties being assessed over the complete system. The results obtained are given in Figure 14. No measurable system error-rate degradation was introduced by the GaAs D-type flip-flop as was expected from measurements of the device threshold ambiguity level and phase margin.

REVIEW AND CONCLUSIONS

Transmission distances in excess of 220 km at 140 Mbit/s can now be achieved using DFB lasers with commercially available monomode fibre and receiver components. At 34 Mbit/s, unrepeated transmission over a span of 251.6 km has been demonstrated. This believed to be the longest reported span up to the present time. Further system demonstrations with commercially available, low-loss dispersion-shifted fibre have shown that spans up to 233 km at 34 Mbit/s are technically feasible with current 1.55 μm , multi-mode lasers and high-sensitivity, direct-detection optical receivers. Recent work has centred on the fully-regenerated gigabit transmission system capability now available with commercial GaAs logic circuitry. The combination of single-line laser and dispersion-shifted fibre offers a new system option which will allow attenuation-limited transmission systems to be implemented at multi-gigabit line-rates. Apart from further advances in laser launch power and receiver sensitivity, it is expected that future systems will depend increasingly on the projected low attenuation of non-silica fibre for substantial increases in transmission distance.

REFERENCES

- 1 KASPER B L, LINKE R A et al: 'A 130 km Transmission Experiment at 2 Gbit/s Using Silica-Core Fibre and a Vapour Phase Transported DFB Laser', Post Deadline Paper PD-6, 10th European Conference on Optical Communication, Stuttgart, 3-6 Sept 1984.
- 2 KOROTKY B K et al: '4 Gbit/s Transmission Experiment Over 117 km of Optical Fibre Using a Ti:LiNbO₃ External Modulator', Post Deadline Paper PD01, OFC 85, San Diego, 11-13 Feb 1985.

- 3 BLANK L C, BICKERS L and WALKER S D: '220 km and 233 km Transmission Experiments Over Low-Loss Dispersion-Shifted Fibre at 140 Mbit/s and 34 Mbit/s', Post Deadline Paper PD07, OFC 85, San Diego, 11-13 Feb 1985.
- 4 BICKERS L, BLANK L C and WALKER S D: 'Long-Span Optical Transmission Experiment Over 222.8 km of Commercial Monomode Fibre at 140 Mbit/s and 1.525 μ m', Elect Lett, Vol 21, 1985, pp 267-268.
- 5 AINSLIE B J et al: 'The Design and Fabrication of Monomode Fibre', IEEE Jnl, Quant Elect, QE-18, 1982, pp 514-523.
- 6 CIEMIECKI NELSON K et al: 'Fabrication and Performance of Long Lengths of Silica Core Fiber', OFC 85, Technical Session Paper WH1, 11-13 Feb 1985.
- 7 COOPER D M et al: 'Multiple Index Monomode Fibres for Dispersion Modification', Proc 10th European Conference on Optical Communication, 3-6 Sept 1984, pp 280-281.
- 8 CROFT T D et al: 'Low-Loss Dispersion-Shifted Single-Mode Fiber Manufactured by the OVD Process', OFC 85, Technical Session Paper WD2, 11-13 Feb 1985.
- 9 WESTBROOK L D et al: 'Continuous-Wave Operation of 1.5 μ m Distributed-Feedback Ridge-Waveguide Lasers', Elect Lett, Vol 20, 1984, pp 225-226.
- 10 FRISCH D A and HENNING I D: 'Effect of Laser Chirp on Optical Systems - Initial Tests Using a 1480 nm DFB Laser', ibid, Vol 20, 1984, pp 631-633.
- 11 LINKS R A: 'Transient Chirping in Single-Frequency Lasers: Lightwave System Consequences', ibid, Vol 20, 1984, pp 472-474.
- 12 BICKERS L and WESTBROOK L D: 'Reduction of Laser Chirp in 1.5 μ m DFB Lasers by Modulation Pulse Shaping', ibid, Vol 21, 1985, pp 103-104.
- 13 BICKERS L and WESTBROOK L D: 'Chirp Reduction in 1.5 μ m Distributed Feedback Lasers by Modulation Pulse Shaping', Post Deadline Paper PD12, OFC 85, 11-13 Feb 1985.
- 14 OLSEN G H: 'Long-Wavelength Components by Vapour Phase Epitaxy', Laser Focus, Jan 1985, pp 124-132.
- 15 FRANCE P W et al: 'OH-Absorption in Fluoride Glass Infra-Red Fibres', Elect Lett, Vol 20, 1984, pp 607-608.
- 16 WALKER S D, BLANK L C and BICKERS L: 'Long-Span Optical Transmission Experiment Over 222.8 km of Commercial Monomode Fibre at 140 Mbit/s and 1.525 μ m', Elect Lett, Vol 21, 1984, pp 267-268.
- 17 BICKERS L, WALKER S D and BLANK L C: 'Fully-Regenerated 2 Gbit/s, 90 km Optical Transmission System Using a Commercial GaAs Master-Slave D-Type Flip-Flop', submitted to 11th ECOC 1985, Venice.

ACKNOWLEDGEMENT

The authors wish to thank the Direct of British Telecom Research Laboratories for permission to publish this paper.

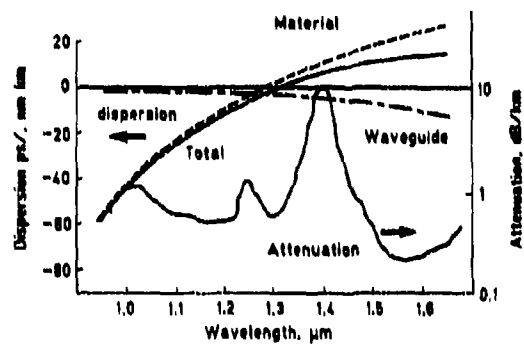


FIG. 1 TYPICAL MONOMODE ATTENUATION AND DISPERSION CHARACTERISTICS

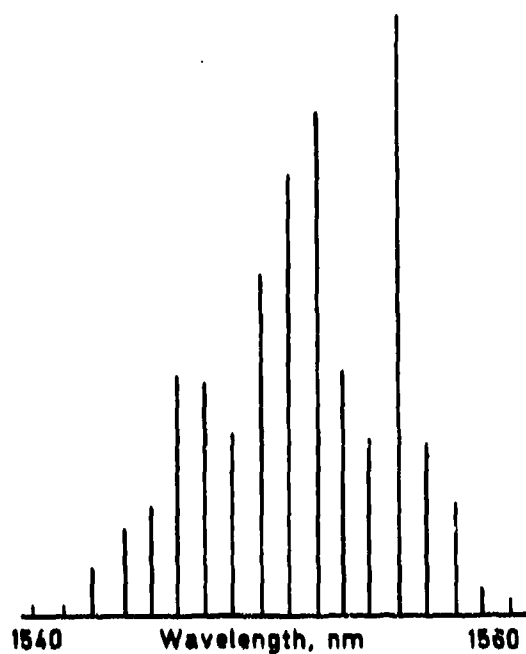


FIG. 2 1.55 μ m DCPBH LASER MODULATED SPECTRUM

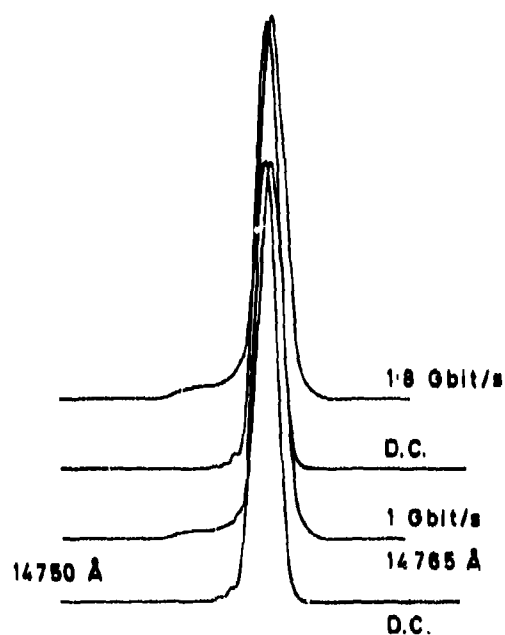


FIG. 3 1.470 μ m DFB LASER-MODULATED SPECTRAL CHARACTERISTICS

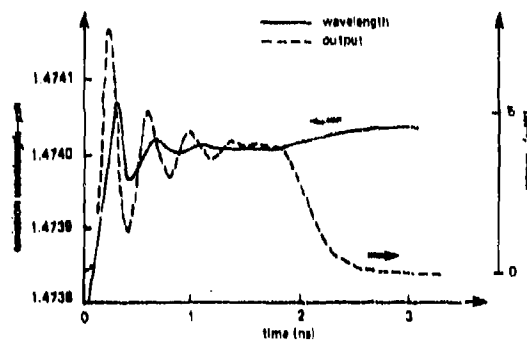


FIG. 4 1.470 μ m DFB LASER CHIRP EFFECTS

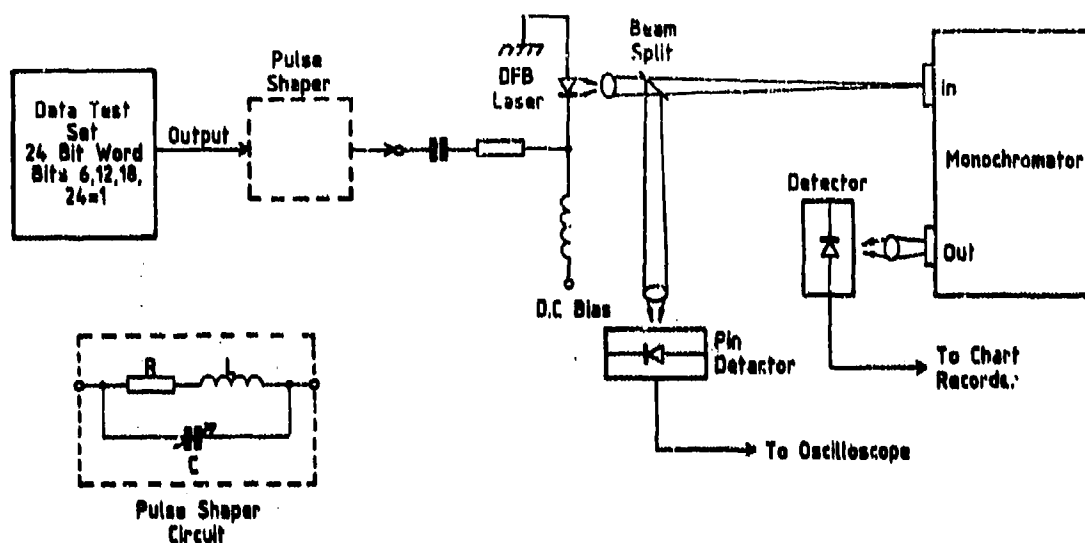
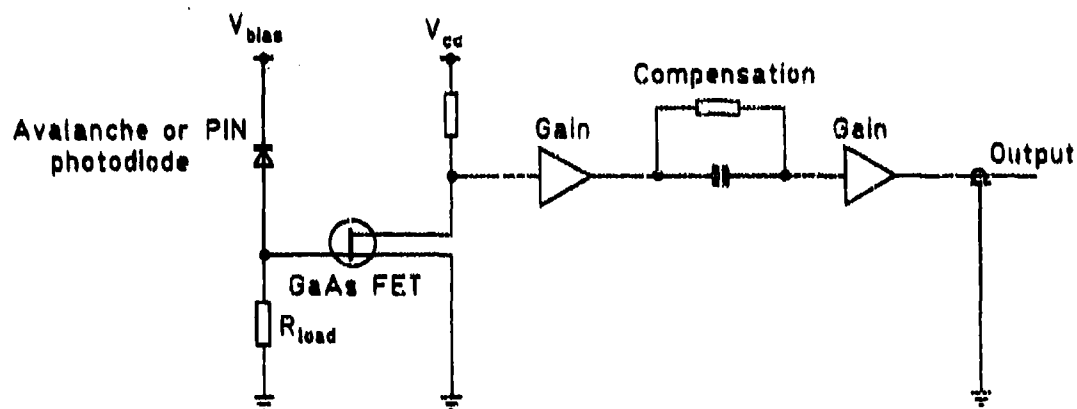
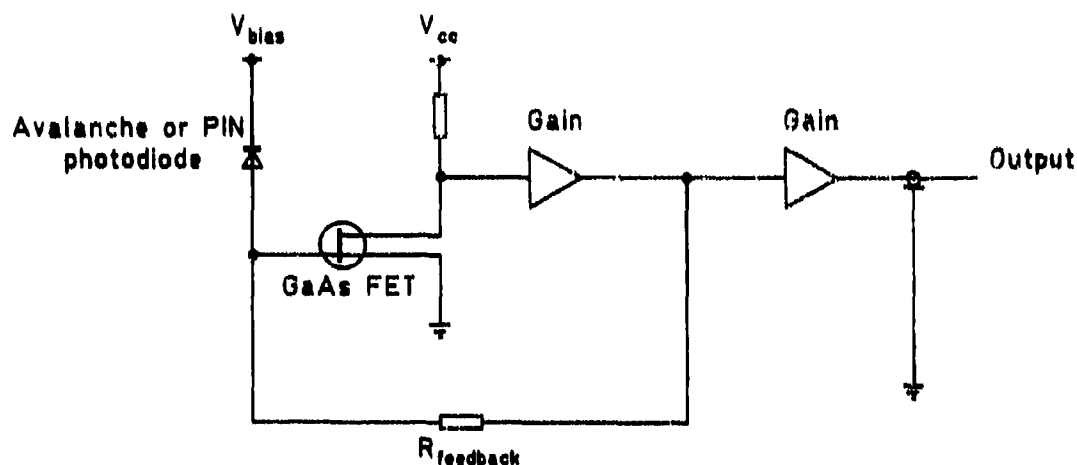


FIG. 5 LASER CHIRP REDUCTION TECHNIQUE



High impedance

FIG. 6 HIGH IMPEDANCE RECEIVER CIRCUIT



Transimpedance

FIG. 7 TRANSIMPEDANCE RECEIVER CIRCUIT

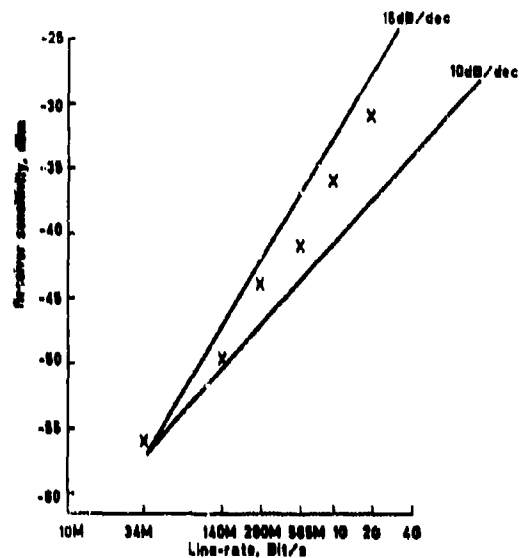


FIG. 9 OBSERVED RECEIVER PERFORMANCE AS A FUNCTION OF BIT-RATE

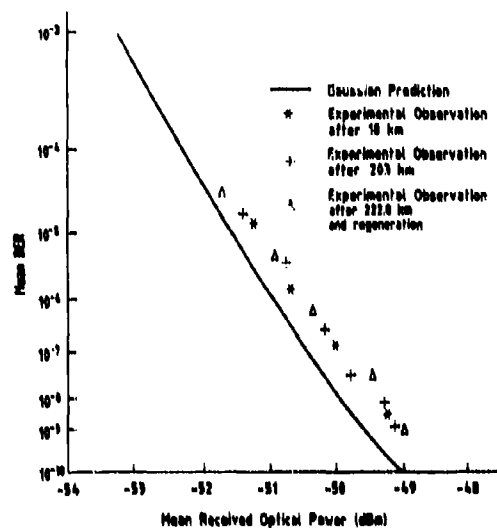


FIG. 10 R.R. CHARACTERISTIC OF 222.0km OPTICAL TRANSMISSION SYSTEM

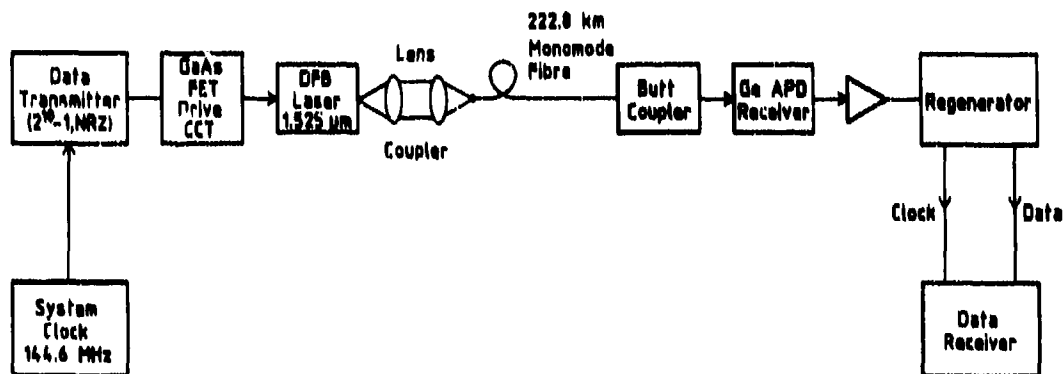


FIG. 9 TYPICAL LONG-SPAN SYSTEM BLOCK DIAGRAM



FIG. 11 EQUIVALENT-TIME RECEIVED "EYE" AT 140 Mbit/s

System detail	Fibre type			
	Step-index monomode		Dispersion-shifted monomode	
Bit rate Mbit/s	34	140	34	140
Launch power dBm	+4	+1.8	+8	+6
Fibre length km	251.6	222.0	299.9	220.6
Fibre loss dB/km	0.22	0.22	0.23	0.23
Total loss dB	55.3	48.8	64	50.6
Receiver sensitivity dBm	-55.3	-48	-52.7	-48.6
System margin dB	3	1.2	3.7	0.9

TABLE 1

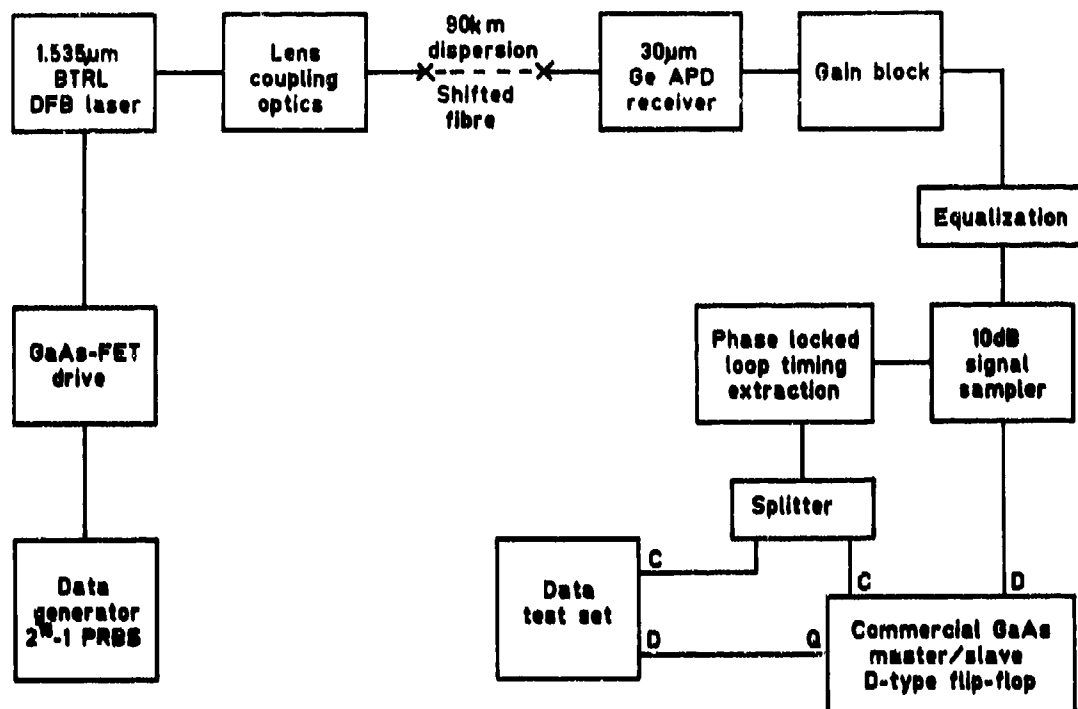


FIG. 12 SCHEMATIC DIAGRAM OF OPTICAL TRANSMISSION SYSTEM

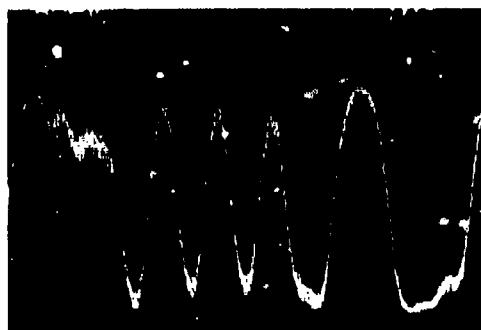


FIG. 13a RECEIVED PULSES AFTER 90km

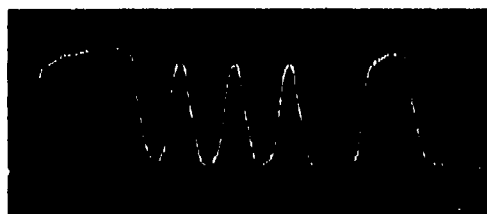


FIG. 13b REGENERATED DATA AFTER 90km



FIG. 13c REGENERATED "EYE" DIAGRAM AFTER 90km

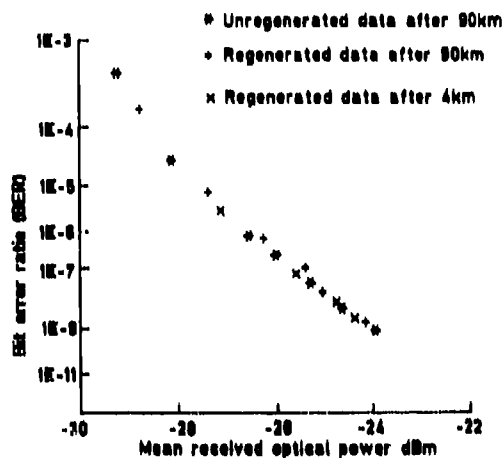


FIG. 14 SYSTEM BER MEASUREMENTS after 4km and 90km

DISCUSSION

J.Fridman, US

In your system at your receiver you use a Ge APD coupled to a FET, rather than a GaInAs PINFET. With a typical gain of 10 available at the Ge APD and a higher noise floor than a typical GaInAs PINFET why did you take this approach and what are its advantages? Disadvantages are the high bias voltages of the photodetector and its cooling requirements.

Author's Reply

This is an alternative approach, we decided to perform experiments at many different bit rates to explore the various system options.

B.Schwaderer, Ge

One of the main problems in high speed logical circuit design is the sensitivity to bias supply variation. Can you comment on the bias supply variation sensitivity of your GaAs/FF?

Author's Reply

The GaAs flip-flop used is from a commercial supplier. The bias voltages are critical but we used voltage regulators to obtain stable and reproducible performances.

PERFORMANCE OF RF FIBER OPTIC LINKS*

by

Dr. Thomas R. Joseph
Manager, Fiber Optic Communications
and

Dr. William E. Stephens
Head, Advanced Technology Section
TRW Electro Optics Research Center
One Space Park
Redondo Beach, California 90278

SUMMARY

RF fiber optic links have numerous applications to microwave systems. To fully exploit their usefulness, the RF system designer must understand their properties in terms of the performance parameters that are used to describe the terminal properties of other RF components such as loss, signal to noise, linearity, and dynamics. This paper details the performance of direct and external modulation fiber optic links in terms of those parameters. Specific examples of a 4.1-4.7 GHz direct modulation link and a 2.0-12.0 GHz external modulation link are used.

INTRODUCTION

Fiber optic links provide a unique capability to the RF system designer. They are light weight, low loss over large distances, and have demonstrated operation at RF frequencies almost into the millimeter wave range. Because the fiber is a dielectric, they are free from the effects of electromagnetic interference, EMI, unaffected by large electromagnetic pulses and can be closely confined with negligible crosstalk. Thus where distance, volume, weight, or EMI are concerns, the fiber optic RF link can present an attractive alternative. Application areas include a variety of platforms including shipboard, avionic, submarine, terrestrial and space. Any environment where a coaxial cable is currently used could be considered and indeed many new applications for distributed systems can be examined.

Fiber optic systems are particularly attractive because coaxial transmission systems exhibit excessive losses when operated over any appreciable distance. As an example, RG-400 coaxial cable has losses of 1115 dB/km, and 0.141 semirigid coaxial cable has losses of 790 dB/km at 5.0 GHz[1]. These losses contrast sharply with silica-based single-mode optical fiber losses at 1.3 μm of 0.47 dB/km[2], a reduction of three orders of magnitude. Even with the inclusion of loss due to electro-optical conversion and intercomponent optical coupling, the optical transmission system will provide lower losses for link lengths as short as 150 ft. As the frequency is increased above 5 GHz, the crossover point between coaxial cable systems and optical fiber-based systems will be reduced.

Before the RF designer can use a fiber optic link, he has to consider performance for many parameters and not just loss and bandwidth. Indeed, the loss of a link includes, in addition to the propagation loss term quoted above, losses due to the electrical to optical conversion in the transmitter and the optical to electrical conversion in the receiver. These additional terms can result in a link loss of 20 - 30 dB or more. While this loss can be offset by including gain, it is important to examine where in the link that gain is implemented.

It is the purpose of this paper to discuss the performance of RF fiber optic links in terms of several of the critical performance parameters that must be specified when one of these links is used in a realistic application. The parameters to be discussed include, bandwidth, loss, signal-to-noise ratio, linearity and link dynamic range. A large number of RF analog fiber optic links have been demonstrated. They include a 700-MHz broad-band analog link at 0.85 μm over a 1.1 km graded-index fiber [3], a link at 0.85 μm in the 2.0-4.0 GHz band over a 1.1-km single-mode fiber demonstrated by Bechtel and Siegel [4], a narrow-band analog fiber-optic link at 0.85 μm in the 4.4-5.0 GHz band over a 1.1-km single-mode fiber by Pan[5], a 4.4-5.1 GHz link by Stephens and Joseph[6], a 10.3 GHz link was demonstrated by Lau et al.[7], and a 12.5 GHz bandwidth was shown by Su et al.[8]. Each of the above results used direct laser modulation. Using external modulators, higher frequency links have been realized. Examples include, a 0-17 GHz .85 μm link by Gee et al [9], and 7.2 GHz bandwidth modulator at 1.32 μm developed by Alferness et al[10].

Figure 1 shows a schematic of the two principal RF fiber optic link types. Each fiber optic link consists of a transmitter module, a length of fiber and a receiver. By using single mode fiber at or near the zero dispersion wavelength, the effective bandwidth of the fiber is typically not a limiting factor in link performance. That performance is dictated primarily by the characteristic of the transmitter and the receiver. The two principal types of transmitters that have been investigated are direct modulation and external modulation.

*This work partially supported by the U.S. Air Force Electronic Systems Command, Rome Air Development Center under Contracts F30602-84-C-0020 and F30602-83-C-0166.

In direct laser modulation, the signal is imposed onto the laser bias current yielding an intensity modulation of the optical beam. Typical transmitters include a matching circuit to match the laser to the 50 Ω coaxial input. An amplifier may be used to amplify low level signals. The performance of this transmitter is determined by the modulation characteristic of the laser. For example, the frequency is normally limited by the relaxation oscillation of the laser. This occurs at a frequency determined by the bias conditions and the specific laser geometry. The relaxation oscillation frequency, f_R , is

$$f_R = \frac{1}{2\pi} \left[\frac{r N_{om} A_g + 1}{\tau_s \tau_p} \left(\frac{I}{I_{th}} - 1 \right) \right]^{1/2}$$

where r is the optical confinement factor, A is the differential optical gain, N_{om} is the carrier density for optical transparency, τ_s is the spontaneous emission lifetime of injected carriers, τ_p is the photo lifetime and I and I_{th} are the bias and threshold currents respectively. Typically, f_R is 2-5 GHz depending on the specific laser and the bias. However, some special geometries have achieved frequencies of up to 12 GHz [8].

External modulation based transmitters, shown in Figure 1b use a laser operated cw to drive a modulator which imposes the RF signal. Typically, the modulator is an electrooptic travelling wave device fabricated on LiNbO₃. These consist as shown in Figure 2, of an optical waveguide structure over which a microstrip electrode pattern is deposited. The waveguide pattern shown is a Mach-Zehnder interferometer. The fields generated by the microstrip cause a phase modulation of the optical beam which is converted by the interferometer into an intensity modulation. The modulator has low-pass frequency characteristic and 3 dB frequency and hence the bandwidth is determined by the cumulative phase shift between the RF and optical signals due to the mismatch in their velocities.

A bandwidth interaction length product results from the calculation of the effect of the velocity mismatch. In LiNbO₃, this product is 64.7 GHz-mm. Thus for maximum bandwidth, a short interaction length is required. However, the shorter the interaction length, the more voltage that is required to drive the modulator.

The output of each transmitter is an intensity modulated optical beam (Phase modulated beams and coherent links will not be considered in this paper). This is guided to the receiver by the optical fiber. The receiver converts the light back into an RF signal and usually contains some amplification and indeed may include a matching circuit between the photodiode and the amplifier. Primarily PIN, Schottky, and Avalanche photodiodes (APD), have been used for RF links. The Schottky diode on GaAlAs has been used to achieve operation at frequencies of up to 100 GHz.[11]. For long wavelength operation, the PIN diode has predominated because of the difficulty of forming a Schottky barrier in the InGaAsP material system. The APD typically does not have the bandwidth needed for operation at frequencies above several GHz and has not been available for use in the 1.3 μ m range.

The performance of RF fiber optic links has been characterized in the literature primarily in terms of frequency of operation, bandwidth, optical intensity levels and quantum efficiency. In specifying the performance of such a link, the RF system designer needs adequate bandwidth and operation at the proper center frequency. However, the parameters he is principally concerned with are, insertion loss, spur free dynamic range, signal to noise, linearity and the ability to provide the specified performance while exposed to a military operating environment. Much of the effort at TRW both under contract and previously on internal funding has been to characterize these links in terms of these parameters.

The following sections describe the performance of RF links in terms of these parameters. Two examples will be used for illustrative purposes. They are a 4.1 to 4.7 GHz direct modulation link developed and characterized at TRW and a 2-12 GHz external modulation link which is being developed under contract with the U.S. Air Force, Rome Air Development Center. Figure 3 shows a diagram of the 4.1-4.7 GHz link while Table 1 gives its measured performance. Figure 4 shows a diagram of the external modulation link and Table 2 gives the design performance data.

Insertion Loss

The insertion loss of a fiber optic link is the loss incurred in convention to and from the optical signal added to the optical propagation loss. Typical links have 0 dB loss due to the gain which is included in the amplifiers. Since the specific placement of the amplifiers can affect the noise characteristics, it can be assumed that the amplifiers are not present in the following discussion.

For direct-modulated direct-detection fiber-optic links, the RF insertion loss is given by

$$\rho = \frac{P_{out}}{P_{IN}} = \rho_m (n R_d \alpha_o \alpha_s \alpha_d)^2 \frac{R_L}{R_S} G_1 G_2$$

Table 1: Measured Performance of the Microwave
Fiber-Optic Link

Parameter	Performance Achieved
Optical Wavelength	1.3 μm
Frequency Center	4.4 GHz
Bandwidth	600 MHz
Length	1.1 km
Signal to Noise Ratio in 500 KHz band	60 dB
Frequency Response Flatness	± 1 dB
Harmonic Suppression	52 dBc
Two-Tone Intermodulation Product Suppression (-10 dBm signals, 1 MHz Separation)	36 dBc
Non-Harmonic Spurious Response	None Observed
Link Insertion Loss	-1 dB

Table 2: Performance Requirements for the External
Modulation Fiber Optic Link

Parameter	Design Performance
Optical Wavelength	1.3 μm
Frequency	2 - 12 GHz
Length	1 km
Signal to Noise Ratio (10 GHz bandwidth)	13 dB
Frequency Response Flatness	± 2 dB
Harmonic Suppression	35 dBc
Two-tone Intermod Suppression	43 dBc
Non-Harmonic Spurs	-40 dBc
Link Insertion Loss	0 dB

where ρ_m is the matching circuit loss, η is the laser external differential efficiency for one facet, R_d is the photodetector responsivity, α_f is the fiber losses, α_s is the fusion splice losses, α_c is the laser-fiber coupling loss and, α_p is the fiber-detector coupling loss, R_L and R_s are the load and source impedances, respectively, and G_1 and G_2 are the gains of the input and output amplifiers. The optical loss terms are all squared in this equation due to the square law detector which converts the incident optical signal into a current. As a consequence, optical losses have a greater impact on the link insertion loss. The values for calculating the insertion loss of the 4.1 - 4.7 GHz fiber-optic link are listed in Table 3. With the laser impedance matched, the insertion loss is dominated by η and α_c . In this link η was measured to be 0.19 W/A and α_c was measured to be 0.196 (-7.1 dB). The result is a total insertion loss of 36.4 dB. This was offset by using an amplifier with $G_2 = 39$ dB.

The insertion loss can be reduced by improved coupling between the laser and the single-mode fiber. Coupling losses of less than 2 dB have been reported in the literature [29]. Assuming a 2-dB coupling loss, the insertion loss for the RF link would be reduced to 26.3 dB. With other improvements in device efficiency, it is possible to reduce the RF insertion loss to around 15 dB.

The insertion loss of the external modulation link is given by

$$P_{\text{ext}} = \frac{P_{\text{out}}}{P_{\text{IN}}} = G_1 G_2 R_s R_L \left(\frac{1}{2V} P_0 \alpha_m \alpha_L R_D \right)^2$$

where P_{out} , P_{IN} are the output and input RF power levels, G_1 , G_2 , the amplifier gains, R_s , R_L , the source and load resistance, V is the voltage for 100% modulation, P_0 the optical power out of the laser, α_m , the optical loss through the modulator, α_L the optical losses in the link including connectors and fiber losses, and R_D is the detector responsivity. Again, the optical terms are squared and thus their impact on performance is increased.

Table 4 gives the parameter values obtainable for the 2 - 12 GHz modulator. The effective loss of the link is 67 dB. This is substantially greater than the loss of the direct modulated link. However, it has a much wider bandwidth. This shows up in the value of V which is proportional to bandwidth. Reduction of the loss can be achieved most directly by increasing P_0 , the optical intensity. Also, the input amplifier could have more gain before the modulator saturates (~ 1 W) than is possible with the direct modulated link where the laser saturates at a level of 1 to 5 mW depending on the laser. Thus, the loss of the link is an area that should be examined carefully. Note, it is true that link length is not a strong factor in the loss. Doubling from 1 km to 2 km yields only a 1 dB increase. This loss can be compensated by gain as shown in Figure 1, but the noise figure of the total link will depend upon where that gain is located.

Table 3. Measured Loss Data For The
4.1 - 4.7 GHz Link

Parameter	Symbol	Value
Matching Circuit Losses	ρ_m	0.71
Source and Load Impedance	R_s, R_L	50
Laser Ext. Differential Eff.	η	0.19 W/A
Detector Responsivity	R_D	78 A/W
Fiber Link	α_o	0.750
Fusion Splice	α_s	0.955
Laser-Fiber Coupling	α_c	0.196
Fiber-Detector Coupling	α_D	0.830
Amplifier Gains	G_1, G_2	1.0
Total Insertion Loss	ρ	36.4 dB

Table 4: Insertion Loss Parameters for the
2-12 GHz External Modulation Link

Parameter	Symbol	Value
Amplifier Gains	G_1, G_2	1
Source and Load Resistance	R_s, R_L	50 Ω
Voltage for 100% Modulation	V_m	7.5 V
Laser Output Power	P_o	1.5 mW
Optical Loss through Modulator	α_m	.4
Link Optical Loss	α_L	.37
Detector Responsivity	R_D	.6 A/W
Resulting Insertion Loss	ρ_{ext}	67 dB

Signal to Noise Ratio

Many noise sources contribute to the overall signal-to-noise ratio. They include thermal noise, shot noise, mode partition noise, reflection-induced noise and relative intensity noise. For the microwave fiber-optic link, an optical wavelength of 1.3 μm and single-mode fiber is used to achieve adequate RF bandwidth. If this is the case, then mode partition noise is minimal compared to other noise sources. The coupling between the laser and the single-mode optical fiber is low, and reflection-induced noise is nonexistent. This was verified by observing the noise floor at the output of the 4.1-4.7 GHz link. Reflection-induced noise manifests as periodic resonant peaks in the noise floor which were not observed. The noise-to-signal ratio due to the other three terms can be written as

$$\frac{\langle i_n^2 \rangle}{\langle i \rangle^2} = \frac{\langle i_{RIN}^2 \rangle}{\langle i \rangle^2} + \frac{\langle i_{shot}^2 \rangle}{\langle i \rangle^2} + \frac{\langle i_{TH}^2 \rangle}{\langle i \rangle^2}$$

where $\langle i \rangle$ is the average dc output current of the photodetector and $\langle i_{RIN}^2 \rangle$ is the Relative Intensity Noise current variance, $\langle i_{shot}^2 \rangle$ is the Shot Noise current variance and $\langle i_{TH}^2 \rangle$ is the Thermal Noise current variance. The thermal noise current variance and the shot noise variance are defined by the well-known formulas

$$\langle i_{TH}^2 \rangle = \frac{4 KTB NF}{R_L}$$

$$\langle i_{shot}^2 \rangle = \frac{q^2 n_D \alpha_D B P_{dc}}{h \nu}$$

where R_L is the load resistance, B is bandwidth, K is Boltzman's constant, NF is the post detection amplifier noise figure T is temperature, q is electronic charge; n_D is detector quantum efficiency, α_D is optical link loss, h is Planck's constant, ν is the optical frequency, and P_{dc} is the dc optical power radiating from the laser diode.

The RIN of the laser can be the dominant noise source. As shown by Yamamoto [12],[13], RIN is dependent upon a number of material, structural, and modulation parameters including the ratio of laser dc bias current or threshold current and modulation frequency. For highly biased lasers, typical values of RIN for BH semiconductor laser modulated well away from the resonance frequency is -150 dB/Hz. As the resonance frequency is approached, the RIN increases. For the 4.1-4.7 GHz link, the RIN increased to approximately -135 dB/Hz (since it was operated quite near resonance.)

Table 5 shows the magnitude of the noise terms for the two links discussed here. For the direct modulation link, the dominant term is the RIN at -59.7 dBm for a 1 MHz signal bandwidth. The overall SNR is 59.3 dB and the SNR over the 600 MHz wide passband is 32 dB. The RIN noise could be reduced if the link was operated at a frequency range farther from the laser resonance, resulting in a thermal noise limited link with an SNR of 70 dB for a 1 MHz bandwidth. For the external modulation link, the SNR is 53 dB for a 1 MHz bandwidth signal. Here the dominant term is the thermal noise of the receiver. This is because the increased optical throughput loss results in a lower light level received by the detector driving the shot noise down. The RIN noise is lower because the laser is operating CW and the value used for the noise level assumes that the operation is at frequencies well away from the laser resonance. This level will increase for the portion of the link bandwidth that corresponds to the resonance frequency of the laser. Notice that for the full bandwidth of the link (2-12 GHz) the SNR is 12 dB. However, no known system processes 10 GHz bandwidths without reduction of the bandwidth somewhere in the signal processing. Thus the actual SNR would depend upon the actual processor bandwidth.

Linearity

Non-Linearities and distortion are two performance parameters that are crucial in determining the utility of an analog link for most military applications. These non-linearities result in the generation of harmonics and intermodulation products. The nonlinearities of a fiber optic link are generated in the source module and potentially in any amplifiers. Thus the performance of the laser or the external modulator must be examined to determine harmonic and intermodulation signal levels.

For direct modulation sources, measurements at TRW [15] and Stubbair et al. [16] indicate that the primary cause of these nonlinearities is the laser photon-electron interaction. The values at the harmonics and intermodulation products are similar to those observed in microwave links even though they were measured for modulating fundamental frequencies of below 1 GHz. These measurements indicate that the laser diode acts to a first approximation like a simple nonlinearity without memory.

To model the nonlinearity, the modulation response of the laser is characterized by a set of rate equations. However, these are solved usually by a linearization process that gives the small signal response but does not result in any data on non-linear response. Analysis of the large signal response (required to yield the nonlinearities) in generality is beyond the scope of this paper. However, such an analysis for a 1.3 μm BH laser was performed on a minicomputer. Numerical methods must be applied because there are no explicit solutions to the rate equations and numerical methods must be applied. Preliminary results show that harmonic distortion is comparable to experimental observations. A typical large signal harmonic response is shown in Figure 5. As expected the second and third harmonics increase with increasing modulation index, with the second harmonic increasing quadratically and the third harmonic as a cube of the modulation index.

Many direct modulation links are passband links with bandwidths of one octave or less as a consequence the harmonics can be filtered since they fall out of band. The 4.1 to 4.7 GHz link has a 2nd harmonic suppression of 52 dB which resulted primarily from the roll off of the amplifier in the receiver. In narrow-band communication links, the two-tone third-order intermodulation products IMP are the primary measure of the link linearity. This is because these products are within the link passband while the harmonics are typically out-of-band. The IMP level is typically measured by adding two equal power RF signals at closely spaced frequencies f_1 , f_2 the IMP level by a power combiner and injecting the composite signal into the optical link. As the laser diode is a nonlinear device, intermodulation overtones will appear at $f_1 + f_2$, $2f_1 - f_2$, and $2f_2 - f_1$ along with the harmonics generated by each of the fundamentals.

Calculation of the intermodulation products is carried out in the same manner as for the harmonics. The specific values of the parameters depends upon the type of laser used. Figure 6 shows experimental data for the 4.1 - 4.7 GHz link. The two-tones were separated by .5 MHz at 4.700 GHz. From this plot the third order intercept which is 8 dBm can be obtained.

In an externally modulated fiber optic link, the largest source of nonlinearities will be the power preamplifier and the Mach-Zehnder LiNbO_3 modulator. The power preamplifier to get any substantial modulation index in the external modulator typically has to be driven so that the output signal is near the 1 dB compression point. Amplifiers operating in this mode have rather high harmonics and third intermodulation products. These result in a limitation on linearity. The nonlinearities in the Mach-Zehnder modulator are caused by the large signal optic intensity-voltage response relationship. This relationship is independent of optical wavelength.

It has been shown that an intensity modulated traveling wave modulator has a voltage optical intensity relationship that can be expressed as

$$I = I_0 \cos^2 \left[\frac{\pi V}{2 V_\pi} - \frac{\phi}{2} \right]$$

Table 5: Magnitude of the Noise Factor
in SNR Performance

	<u>Direct Modulation</u>	<u>External Modulation</u> (1.5 mW Source)
Noise Bandwidth	1 MHz	1 MHz
Output Level	0 dBm	0 dBm
Thermal Noise	-70.8 dBm	-53.6 dBm
Shot Noise	-75.8 dBm	-64.9 dBm
Laser RIN	-59.7 dBm	-66.0 dBm
SNR at output	59.3 dB	53.0 dB
SNR over link Bandwidth	32 dB (600 MHz)	13.0 dB (10 GHz)

In this expression, I_0 is the input optical power intensity, V is the input voltage to the modulator, V_{π} is the voltage required to achieve a π optical phase shift, ϕ is the static bias phase shift and I is the modulated optical power.

If we assume V is the result of two tones and given by $V = V_0(\cos \omega_1 t + \cos \omega_2 t)$ then this relation can be expanded. By collecting terms at the same frequencies, expressions are obtained for the principal non-linear terms. In this expression there are no second order terms so the first terms are the third harmonic and the third order intermodulation products.

The distortion at the output of the detector due to harmonic generation can be expressed as

$$D_{3rd,Harmonic} = 20 \log \left[\frac{m^2 \pi^2}{96 - 9 m^2 \pi^2} \right]$$

and the distortion due to third intermodulation products can be expressed as

$$D_{3rd,IMP} = 20 \log \left[\frac{m^2 \pi^2}{32 - 3 m^2 \pi^2} \right]$$

A graph of these expressions for varying modulation depth is shown in Figure 7. As can be seen in this figure, the third intermodulation product distortion is 10 dB higher than the harmonic distortion.

Spurious Response of Externally Modulated Links

Spurious signals in the passband of the fiber optic link can lead to a degradation of system performance. By definition, these signals cannot be attributed to signals caused by harmonic or intermodulation distortion. The primary sources for spurious signals and for an externally modulated link will be the relative intensity noise of an injection laser diode. It can be assumed that the other components do not cause spurious signals as they have a transfer function that can be closely approximated by a simple polynomial and therefore only generate harmonics and intermodulation products. For example, the external modulator and the RF amplifiers have third order nonlinearities and therefore can be approximated by a third order polynomial.

The injection laser diode has a non-uniform AM noise spectrum as originally shown by Jacket et.al.[17]. This noise floor is optical power dependent and has a shape that follows the laser modulated optical frequency response and peaks at the laser resonant frequency after which it declines rapidly. This peak is as much as 10 dB above the laser low frequency RIN component. Therefore, in the wideband externally modulated link, there should be a 10 dB rise in the noise floor in the frequency region of 3- to 5- GHz for a laser noise limited system. This artifact could contribute to a decline in the SNR in this region if RIN is the dominant noise source.

The other source of spurious signals are optical reflections back into the laser diode. These reflections generally originate from optical discontinuities such as optical connectors and external modulator interfaces. These discontinuities create extra Fabry-Perot laser cavity with the ILD resulting in large noise spikes in the laser noise floor. Depending on the strength of the optical feedback, spikes as large as 15 dB can appear in the shot noise floor of the photodetector at regular intervals independent of the modulated signal. Because of the low laser to fiber coupling efficiency this effect was not seen in the 4.1-4.7 GHz link.

6.0 Dynamic Range

The dynamic range of the fiber optic link is a measure of the variation of signal levels that can be carried by the link. Typically it is defined as the ratio of the fundamental output to the third order intermodulation product (IMP). But since the IMP level decreases faster than the fundamental, reduction of the input level yields any value of dynamic range required. However, as the input signal is decreased the signal

to noise ratio also decreases. Because the noise out of the link is constant for a specific noise bandwidth, there is an input signal level at which the IMP level matches the noise floor and at that input level the dynamic range is maximized. Hence, the definition used here is the dynamic range is the level of IMP suppression achieved when that level equals the link signal to noise ratio.

For example, Figure 6 plotted the IMP suppression. Also shown is a line indicating the noise level for a 1 MHz noise bandwidth. As indicated, the dynamic range obtained is 44 dB where the IMP line intersects the noise floor.

An alternative definition of dynamic range is the range of power levels between the noise floor and the point at which the link gain exhibits 1 dB of compression. This definition applies to systems when only 1 signal is present. The resulting value is typically higher, but if more than one signal is expected it does not indicate whether the output signals can be distinguished from harmonic and IMP spurs. Consequently this definition is not generally useful.

Summary and Conclusion

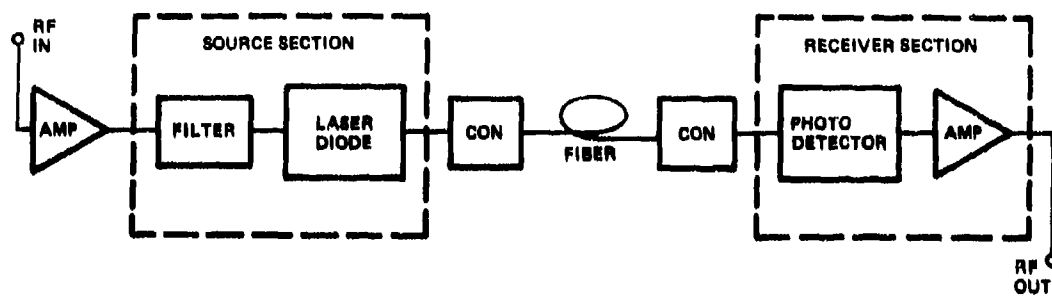
RF Analog Fiber Optic Link technology is reaching the level of maturity that application to new systems and retrofit into existing systems is becoming a reality. In order for this to occur, the fiber optic engineer has to provide data to the systems engineer that can be used to carry out the system design. This paper has discussed several of those parameters and described the functional relationships between the elements of the link and its performance. The parameters considered were insertion loss, signal to noise ratio, linearity and dynamic range. As examples, measured data for a 4.1 - 4.7 GHz direct modulation link and the design data for a 2 - 12 GHz externally modulated link was presented.

These links show performance that can be readily applied to numerous applications. New research is resulting in higher frequency sources and wider bandwidth links. Moving these devices from the laboratory to system applications requires complete characterization and a thorough understanding of the requirements and of link performance.

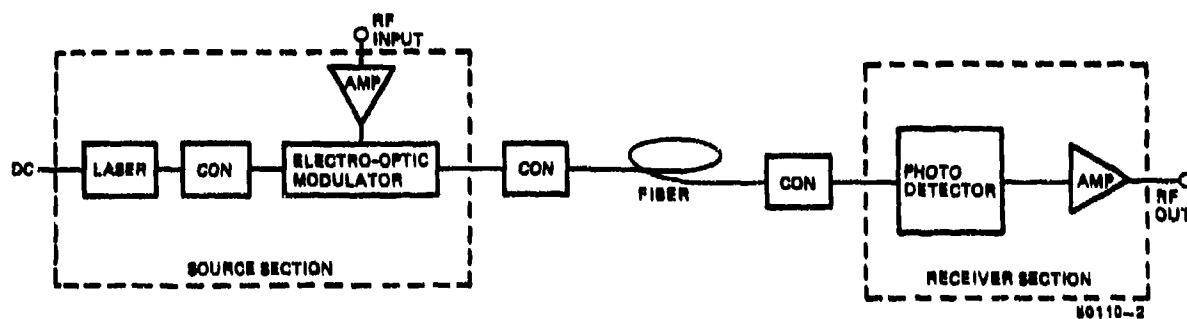
REFERENCES

- [1] United Microwave Products Catalog, 1982.
- [2] M. Horiguchi and H. Osani, "Spectral Losses of Low-OH-content Optical Fibers," *Electron. Lett.*, vol. 12, pp. 310-311, June 1976.
- [3] C.W. Slayman and K. Lang "GHz Bandwidth Analog Fiber Optic System," Los Alamos Scientific Laboratory, Los Alamos, NM, Contract X69-2908F-1, Final Rep., 1981.
- [4] D.W. Bechtle and S.A. Siegel, "An Optical Communications Link in the 2.0-6.0 GHz Band," *RCA Review*, vol. 43, pp. 277-309, 1982.
- [5] J.J. Pan, "5 GHz Wideband Fiber-Optic Link," in *IEEE/OSA Optical Fiber Communication Conf.*, New Orleans, Feb. 1983, paper TUK2.
- [6] W.E. Stephens, T.R. Joseph, "4.75 GHz, 1.3 μ m Fiber Optic Communications Link", *IEEE/OSA, Sixth Topical Meeting on Optical Fiber Communications #PD-7*, Feb. 1983.
- [7] K.Y. Lau, N. Bar-Chaim, I. Ury, A. Yariv, *Appl. Physics Letters* Vol. 45, 316 (1984).
- [8] C.B. Su, V. Lanzisera, W. Po Wazinski, E. Meland, R. Olshansky, R.B. Lauer. "12.6 GHz Direct Modulation Bandwidth of Vapor Phase regrown 1.3 μ m InGaAsP Buried Heterostructure Laser." *Appl. Phys. Lett.* Vol 46, (4) 344-346, Feb. 1985.
- [9] C.M. Gee, G.D. Thurmond, "Mack-Zehnder 17 GHz Bandwidth Modulator," *IEEE/OSA Conference on Optical Fiber Communication, #WQS*, New Orleans, 1984.
- [10] R.C. Alferness, C.H. Joyner, L.L. Buhl, and S.K. Korotky, "High Speed Traveling Wave Directional Coupler Switch/Modulator for $\lambda = 1.3 \mu$ m." *IEEE J. Quant. Electron.*, Vol. QE-19, p. 1339-1341 (1983).
- [11] S.Y. Wang, "Ultra-High Speed Photodiode", *Laser Focus*, p. 99, Dec. 1983.
- [12] G. Khoe, H. Kock, D. Kuppers, J.H.F.M. Poulissen, and H.M. DeVrieze, "Progress in monomode optical-fiber interconnection devices," *IEEE J. Lightwave Technol.*, vol. LT-2, no. 3, pp. 217-227, 1984.
- [13] Y. Yamamoto, "AM and FM Quantum Noise in Semiconductor Lasers-Part 1: Theoretical Analysis," *IEEE J. Quantum Electron.*, vol. QE-19, no. 1, pp. 34-46 1984.

- [14] Y. Yamamoto, S. Saiko, and T. Mukai, "AM and FM Quantum Noise in Semiconductor Lasers-Part II: Comparison of Theoretical and Experimental Results for AlGaAs Lasers," IEEE J. Quantum Electron., vol. QE-19, no. 1, pp. 47-58, 1984.
- [15] W.E. Stephens and A. Woo, "RF characteristics of opto-electronics semiconductor devices" in IEEE Nat. Telesystems Conf. (NTC '82), Galveston, TX, Nov. 7-10, 1982, Pap. F4.3-1.
- [16] K. Stuhkjaer and M. Danielsen, "Nonlinearities of GaAlAs lasers-harmonic distortion," IEEE J. Quantum Electron. vol QE-16, no. 5. pp 531-537, 1983.
- [17] H. Jackel and H. Melchior, "Fundamental limit of light intensity fluctuations of semiconductor lasers with dielectric transverse mode confinement," European Conference on Optical Communications, Amsterdam, The Netherlands, 1979.



(A)



(B)

FIGURE 1. RF FIBER OPTIC LINKS. A) DIRECT MODULATION
B) EXTERNAL MODULATION

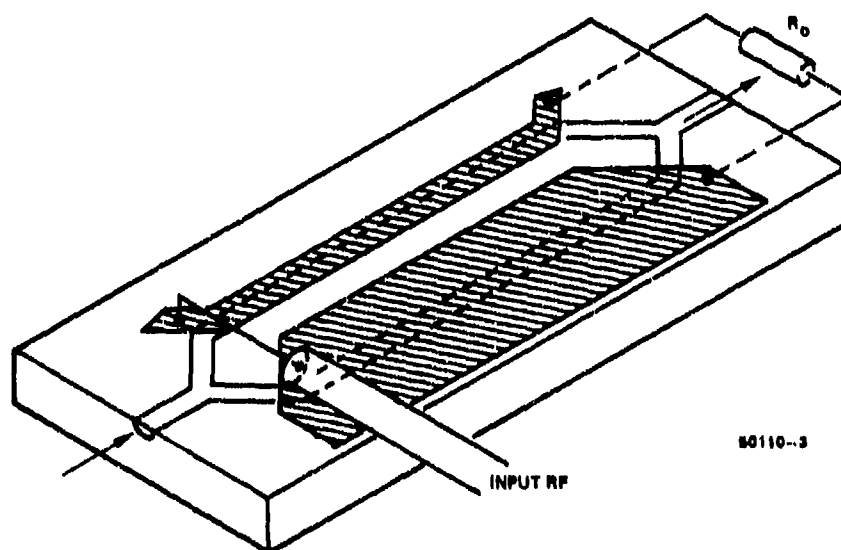


FIGURE 2. TRAVELING WAVE MODULATOR

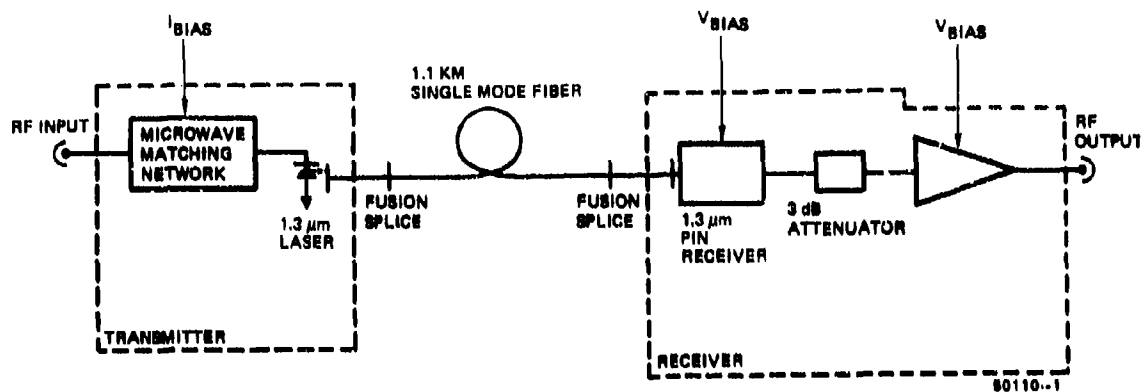


Figure 3. Principal Components of the 4.1- to 4.7- GHz Fiber-Optic Link

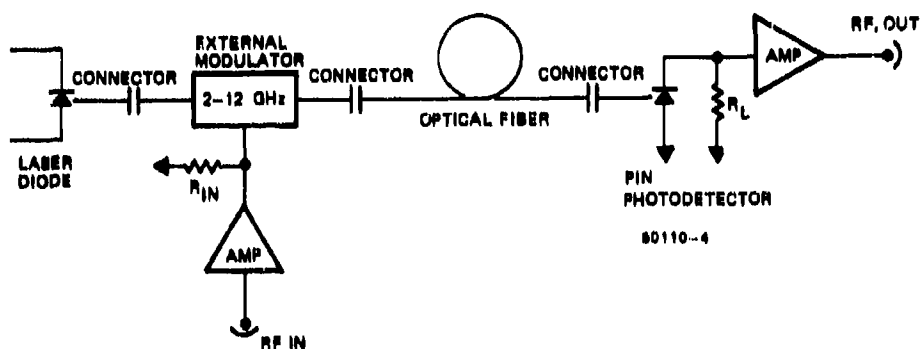


Figure 4. Schematic of External Modulation Fiber Optic Link

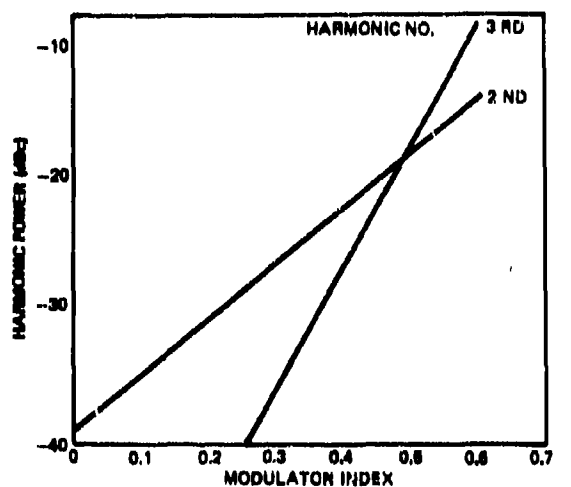


Figure 5. Calculated Harmonic Response using Large Signal Laser Model. As expected, the third harmonic response increased more quickly with increasing modulation index than the second harmonic.

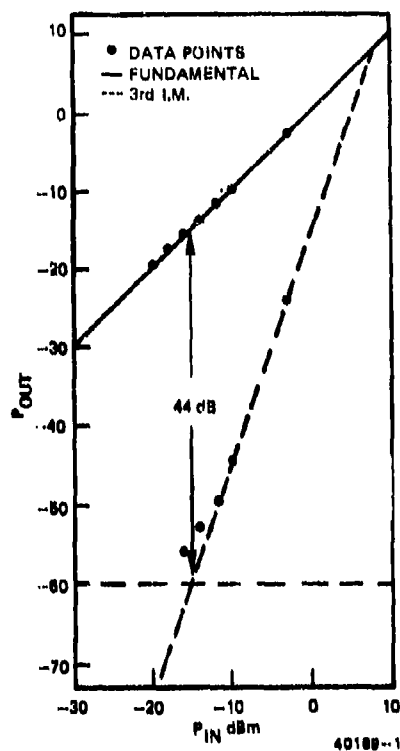


FIGURE 6: MEASURED THIRD ORDER INTERMODULATION PRODUCT LEVEL FOR THE 4.1 - 4.7 GHz LINK.

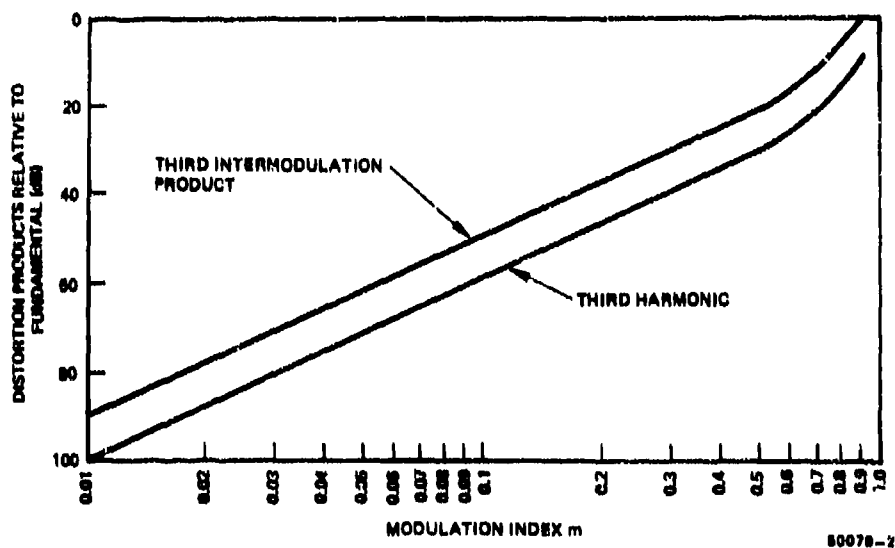


FIGURE 7: MODULATION INDEX VERSUS THIRD HARMONIC DISTORTION AND THIRD INTERMODULATION PRODUCT DISTORTION FOR MARCH-ZEHNDER EXTERNAL MODULATORS.

DISCUSSION

C.Gee, US

What laser did you use? Did you observe optical feedback?

Author's Reply

The laser was an Itachi laser operating at 1.3 μm . We didn't see any significant effects of optical feedback in the noise performance.

B.Schwaderer, Ge

The RF-performance, especially the harmonic suppression depends mainly on the laser diode used; did you measure several different lasers to this respect?

Author's Reply

We have looked at a couple of other lasers and have seen similar results.

J.Dakin, UK

(1) Can you account for the reason why the optical feedback from the fibre did not affect the harmonic distortion and noise figure? (2) What was the noise equivalent power of the optical receivers used?

Author's Reply

(1) The coupling of the laser light into the fibre is low and hence in all likelihood very little reflected light getting back to the laser. (2) We measure a noise level in dBm/unit bandwidth and without a calculator I can't quickly convert to a noise equivalent power.

FIBER OPTICS: A SURVIVABLE AND COST-EFFECTIVE TRANSMISSION MEDIUM FOR TERRESTRIAL NETWORKS

by
M. Aslam
SHAPE TECHNICAL CENTRE
P.O. Box 174
2301 GD The Hague
The Netherlands

SUMMARY

The performance of a fiber-optic transmission system is affected by nuclear radiation. This paper discusses the nuclear scenario vis a vis the terrestrial network, identifies the essential characteristics, and on this basis derives the principles for the design of a strategic communication fiber-optic cable system. The details of a cost analysis applicable to various scenarios are also given; the costs of each scenario are compared with those of a microwave line-of-sight system of approximately the same capacity.

1. INTRODUCTION

The acceptance of fiber optic cables by the world telephone and telegraph authorities as the new medium for all forms of modern communication is as significant today as was the introduction of coaxial cable and microwave radio relay transmission in the early 1950s. This development will obviously affect military communication networks, not least as a consequence of the superior survivability and cost-effective characteristics of optical fibers.

This report is a by-product of an STC study of fiber optics which reviewed

- .the technology,
- .the cost,
- .the suitability and performance under various threat situations,
- .the survivability, availability and maintainability.

The study yielded favourable results with regard to the maturity of the technology, the cost, its suitability in conventional and nuclear threat situations and its reliability, availability and maintainability.

For this present symposium, the study findings in respect of suitability and cost are considered the most interesting and appropriate, and consequently the dominant emphasis of the paper is on the effects of nuclear radiation and on cost implications.

The data used to develop the radiation scenario were derived from the open literature (Ref. 1 - which details the results of nuclear tests conducted by the US Department of Defense), as were details of the effects of radiation on fiber optics (Ref. 2 to 9).

Although the technical data for the basis of the report are available in the open literature, the price data for the cost study were obtained from a number of manufacturers. The cost estimates are for a long-distance network with repeaters spaced at 50 to 100 km and a transmission capacity of 8 to 30 Mbit/s. The resultant cost model has yielded cost estimates for scenarios likely to be encountered in a network spread over a large geographical area. The results show that fiber-optic communication systems are more than competitive with microwave terrestrial systems.

2. THE EFFECT OF NUCLEAR RADIATION ON OPTICAL FIBERS

2.1 NUCLEAR SCENARIO

The explosion of a nuclear weapon gives rise to the emission of various nuclear radiations, consisting of neutrons, gamma rays and alpha and beta-particles. Most of the neutrons and part of the gamma rays are emitted as a result of the fission and fusion reactions; i.e. simultaneously with the explosion. Both types of reaction, although different in their characteristics, give rise to radiations that travel considerable distances. Of specific interest here are the gamma rays and neutrons which produce harmful effects in living organisms and also influence semiconductors and optical fibers. The remainder of the gamma rays are produced in the secondary nuclear process. The ranges of the alpha and beta particles are comparatively short and not considered to be a threat.

Because of the nature of the associated phenomena, nuclear radiations are divided into two categories: initial nuclear radiation and residual nuclear radiation.

Initial nuclear radiation consists of gamma rays and neutrons produced during a period of one minute after a nuclear explosion. They reach very high intensity near the zero point but attenuate rapidly with distance because of the inverse square law and the high atmospheric attenuation. Typically, a radiation intensity of about 10,000 rad at

2 km from zero point, produced by a 1 megaton explosion, will reduce to about 30 rad at 3.6 km, and therefore does not present a major threat to a long-distance network.

The residual nuclear radiation is that which is emitted later than 1 minute from the instant of explosion. The main contributions are provided by the fallout from the surface material sucked up as the fireball rises into the air, debris from the weapon, and the radioactivity induced by the interaction of neutrons with various elements in the explosion environment. These debris are carried by the wind and spread over a wide area and pose a major threat to any strategic communication network. In the 1954 BRAVO Test (Fig. 1), conducted at Bikini Atoll with a yield equivalent to 15 megatons of TNT, a radiation fallout of 100 rad was monitored at a distance of 500 km downwind from the explosion. The residual nuclear radiation is a maximum when the nuclear explosion happens on, or near, the land surface.

In general, nuclear radiation is rapidly attenuated by shielding material. Table 1 shows the transmission attenuation factor for objects buried 3 feet underground and, for comparison, those for various forms of building material for initial and residual nuclear radiation.

Table 1
Dose attenuation factors for various structures

Structure	Initial gamma rays	Neutrons	Residual gamma rays
Underground (depth: 3 ft)	230-500	100-250	5000
House	1-1.25	1.25-3.33	1.66-3.33
Basement	1.66-10	1.25-10	10-20
Concrete blockhouse shelter:			
9-in. walls	5-10	2-3.33	11.1-142
12-in. walls	10-20	2.5-5	33.3-1000
24-in. walls	50-142	5-10	500-10000
Shelter, partly above ground:			
with 2 ft earth cover	14.2-33.3	12.5-50	50-200
with 3 ft earth cover	50-142	20-100	200-100

2.2 THE IMPACT ON FIBER OPTIC CABLES

The primary effect of nuclear radiation is to produce a darkening centre within the structure of the optical fiber. The darkening effect is caused by the formation of charge traps that absorb and scatter the incident light. The charge traps are formed when electrons are raised to the conduction band by absorption of nuclear radiation. After the source of radiation is removed, some of the electron and hole pairs disappear by recombination or by returning to their original states; others are trapped by impurities and defects in the core material. The lifetime of the darkening centres depends on how readily the trapped charge can tunnel from the trap or be thermally or optically freed.

The darkening centres produce an induced attenuation in the fibers, which progressively reduces after the source of radiation is removed, but which may or may not return to the original state. The magnitude of the induced loss effect at a given time depends on the nature of the radiation, its total level and rate of application, the wavelength of observation, the composition of the glass, the temperature and, in some cases, the previous history of the material and the optical power fed to the fiber.

A compendium of the radiation induced loss in several types of fibers, irradiated with different cobalt 60 doses, is shown in Fig. 2 (Ref. 2). Included are: a compound glass fiber (Pb silicate), plastic-clad fiber with different core material (TOS i.e. quartz); suprasil W-1, spectroil A; suprasil 1 and suprasil 2 (i.e. high-purity synthetic fused silica); and germanium-doped silica core fiber. Many interesting observations can be made but two are of special importance. Firstly, there is a correlation between the level of radiation-induced loss and the intrinsic material loss. Fibers with higher loss have a higher radiation sensitivity, which is probably due to the higher impurity concentration. Secondly, polymercoated fused silica fibers show a saturating behaviour such that after a certain dose their response becomes extremely saturated; other fibers tend not to saturate and show a fairly linear behaviour.

After irradiation a certain amount of recovery is observed (Fig. 3). The extent of the recovery seems to depend upon the nature and concentration of impurities in the silica. It can be seen that TOS fiber has substantially greater recovery than synthetic silica, while little recovery is shown by (Ge)-doped silica. The recovery time should improve when the system is in operation and optical power is being propagated through the fiber (Ref. 3).

Boron (B) and phosphorous (P) doping are often used to improve the intrinsic properties of the waveguide, but they also affect the radiation sensitivity of the fiber (Ref. 3). (B)-doping results in increased transient damage, more induced absorption at long wavelengths and much higher loss at low temperature (Ref. 4). (P)-doping, while suppressing the transient indirect loss, drastically increases the permanent damage, especially at longer wavelengths (Ref. 6).

The radiation-induced loss is wavelength-dependent (Ref. 7). Figure 4 shows the result for fibers produced by three different manufacturers. The induced radiation for a given dose is 5 to 10 times lower at 1.3 μm than at 0.85 μm . The performance of the Philips fiber at 0.85 μm and 1.3 μm is considerably superior to that of the other two. It is very encouraging that the attenuation of the Philips fiber at 1.3 μm increased by only 1.55 dB (per km) for 3 krad and returned to within 0.2 dB of the original attenuation within an hour.

However, the radiation-induced loss is also temperature dependent, as is the recovery time (Ref. 8). The loss and the recovery time are greater at lower temperatures, but if the cables are buried underground there is very little temperature variation and so the effect is minimal.

Optical fibers with high immunity to nuclear radiation have been developed for tactical systems, but as they have very high intrinsic attenuation they are economically unacceptable in strategic communication networks.

At present, considerable research effort is being devoted to transmission in the infra-red region, where the attenuation will be of the order of 0.01 dB/km. It is a rather fortunate coincidence that fibers at these wavelengths are showing a high degree of insensitivity to radiation. Fibers based on the fluorohafnate or fluorosilicate glasses show particular promise (Ref. 9). Figure 5 shows the effect of radiation, and the measurement of incremental loss as a function of wavelength, for a bulk sample of a few millimeters path-length. Whilst it is not yet clear exactly which mechanisms are operative, there is an obvious potential for fiber operation in the 2.5 to 4 μm wave band, where incremental losses are zero for dose rates as high as 45 Mrad.

2.3 SUMMARY

1. The attenuation of optical fiber increases rapidly when it is exposed to neutron and gamma radiation, but it may or may not return to the original state after the radiation source is removed; generally it is somewhat worse.
2. Because of the large number of variables which affect the characteristics of the fiber, radiation characteristics of various manufacturers' fibers, even when using the same composition, vary considerably. Consequently, it is difficult to formulate or predict, with any reasonable level of certainty, the characteristics of the fiber when exposed to radiation.
3. The induced attenuation is wavelength-dependent and is a factor of 5 to 10 times lower at 1300 nm than 870 nm; the results at 1550 nm are somewhat worse than 1300 nm depending, on the composition.
4. Fibers with low intrinsic attenuation also tend to offer lower radiation sensitivity.
5. The gamma and neutron radiations attenuate rapidly when travelling through high density material i.e., soil, concrete, etc.
6. In strategic networks, fiber optic cables would require external protection against radiation, i.e., cables should be buried.

It is evident that a nuclear-hardened fiber-optic cable suitable for long-distance transmission is not available at present. Nevertheless, with a carefully selected cable, which would be buried underground, it is possible to design a strategic communications fiber-optic cable system such that when operating at 1300 nm or 1550 nm wavelength with a good attenuation margin it will be survivable in a nuclear scenario.

3. COST ANALYSIS

The objective of cost analysis studies is to make a proper evaluation of the cost impacts of various alternative actions. Generally, the planning period extends a long period of time into the future. Because many of the cost elements are influenced by assumptions and judgments, it is important that the nature of the cost and the basic rules governing the comparisons are well understood. The cost components to be considered in the initial investment cost should include the cost of the equipment, initial spares, freight, insurance, installation, commissioning, engineering, training, land, right-of-way, documentation, etc.

Caution should be observed in basing the choice on initial investment costs alone, because one of the design objectives of new plants is frequently the reduction of oper-

ation and support cost. Often this reduction is achieved through higher initial investment cost due to acquisition of more robust, high-quality equipment. Although such equipment may be more expensive in initial cost, it can prove to be more economical in the long term due to longer life, fewer operators, lower maintenance and less running costs.

3.1 COST MODULE

A block schematic of a typical optical-fiber system is shown in Fig. 6.

The cost considered here is the initial investment cost, and is calculated for a transmission link from baseband-to-baseband level at the terminal stations.

In order to facilitate the cost calculations for different scenarios, and to ensure that all constituent parts of the initial investment cost are included, the cost elements are broken down into small units.

The unit cost used in the calculation is the average of commercially furnished data supplied by a number of manufacturers in western Europe, and expressed in Dutch Guilders (DG) and International Accounting Units (IAU) at the current rate. Prices include all overhead costs (i.e., freight, storage, travel, insurance, etc.) unless shown as a separate cost item. The unit cost estimates are for a system length of about 100 km, but rates could be lower for a larger contract. However, rates would increase appreciably because of fixed overhead cost, if the contracted route length were to be very much smaller.

3.1.1. Assumptions

For the costing process, the conditions and assumptions were as follows:

- (1) System length: 100 km
- (2) Data bit rate: 8 Mbit/s
- (3) Number of fibers: 4
- (4) System configuration: 1+1 hot stand-by
- (5) Distance between repeaters: 50 km
- (6) Power feeding for intermediate repeater from one of the terminals on a pair of copper wires
- (7) Terminal equipment installed directly inside the communication centre.

3.1.2. Cost elements

Excavation for trenches (ploughing)	100 km
Fiber optic cable (4 pairs)	100 km
Power feed cable	50 km
Number of joints	45
Number of surge protectors (EMP)	45
Number of terminal joints	4
Assuming:	
water crossing (2 x 10 m)	20 m
main road crossing (4 x 10 m)	40 m
railway crossing (4 x 10 m)	40 m
culvert crossing	50 m
Line terminal equipment	2
Line terminal Rx and Tx (1300 nm)	2
Intermediate underground equipment repeater case	2
Both-way 8 Mbit/s (1300 nm) repeater unit	2
Centralized supervisory equipment	1
Remote line power supply equipment	1
Hot stand-by 1+1 switching unit	2
Installation (percentage of the equipment cost)	25%
Test and commission	10%
Test equipment	15%
Spare parts	15%
Codification	1%
Training	7.1%
Documentation	1.5%

3.2 COST ESTIMATE

The cost estimates for various, specific scenarios are given in Table 2.

Table 2
Cost estimates for specific scenarios

Characteristic feature	Estimate	
	DG	IAU
100% soft soil	2,713,500	335,300
50% soft, 48% hard, and 2 % rock	3,475,500	429,500
95% hard and 5% rock soil	4,923,500	530,600
75% hard and 25 rock soil	5,413,500	609,000
FD cable installed on HVO cables	3,490,000	431,300
Additional cost for 34 Mbit/s system	43,000	5,300

3.3 COMPARATIVE EVALUATION

Cost comparisons between fiber-optic and LOS microwave transmission systems for various scenarios are shown in Fig. 7, and should be seen in the light of the accepted "norm-of-error" in any cost estimation study. The cost estimates for the LOS microwave systems are based on the contracts awarded in the last few years. It is clearly evident that in a military environment optic fiber transmission systems are cheaper than LOS systems. This is contrary to the impression created by commercial literature which can be attributed to two factors. Firstly, the military microwave system, even with commercial equipments, are more expensive to procure due to survivability aspects i.e., EMP protection, more stringent standards for building, electrical etc., which are not applicable in the case of fiber-optic systems. Secondly, the prices of fiber-optic systems have been falling so rapidly, as shown in Fig. 8, that any cost study based on prevailing prices is outdated by the time it is published or released to outside sources.

The study has covered costs for a number of scenarios. However, the cost calculations are for a hypothetical route, involving various assumptions, while in a real situation the relative prices can change from one route to another.

In addition, factors such as right-of-way, land ownership, access roads, and the allocation of frequency spectrum may have their own implications in some countries and could influence the choice of system. The cost for bulk encryption, which can be considerable, has not been included in either of the two systems. In the case of fiber optic systems, bulk encryption may not be considered necessary, while it will be essential for LOS microwave systems.

To summarize, it can be said that survivability, lifecycle cost, and other implications as mentioned earlier will influence the choice of system, but from the initial investment-cost viewpoint, even with adverse errors, fiber-optic systems are cost-competitive with LOS microwave terrestrial transmission systems.

3.4 PAST AND FUTURE COST TRENDS

The last decade has seen remarkable developments in the scientific field and in production techniques for fiber optics, and these are rapidly making it the dominant medium for transfer of information in the communication world. These developments, in conjunction with large volume production, have caused an almost exponential drop in the prices of the components. This is illustrated in Fig. 8. Most of the decrease in prices has probably already occurred and prices are levelling out, but a reduction in component prices at the rate of 10 to 15% per annum should still continue for at least a few more years. Additional reductions in the system cost can be expected from improvements in the performance of components, which will lead to longer distances without repeaters, higher channel capacity, and greater reliability. However, it should be recognised that 50% of the system cost constitutes civil work which may increase with time.

4. CONCLUDING SUMMARY

An overview of the fiber-optic, microwave and coaxial cable transmission systems considered in the STC study is presented in Table 3. Originally the table was published in Ref. 10, but it has been updated to reflect military requirements and their effect on cost. The table also includes an assessment for a coaxial cable; this was not examined in the STC study because of its known susceptibility to EMP and high cost.

Table 3

Qualitative overview of competing systems

Symbology: ++, +, 0, - indicates best to worst.

Considerations	Microwave Coaxial		Fiber optic	
			Multi-mode	Single-mode
Repeater spacing	++	--	++	++
Information-carrying capacity	+	+	+	++
Upgradability	0	+	++	++
RAM*	0	+	+	+
Environmental stability	-	-	+	+
Susceptibility to interference	0	-	++	++
Security	-	0	+	+
Ease of installation	+	-	+	+
O&S* cost	0	-	+	+
Lifecycle cost	0	-	++	++
Cost (low traffic)	+	-	+	0
Survivability	-	0	+	+

*RAM: Reliability, availability and maintainability

O&S: Operation and support

Some additional factors, such as right-of-way, land procurement, provision of access roads, and the allocation of frequency spectrum will have some implications which could influence the choice of system. However these implications would presumably be resolved on a case-by-case basis.

In conclusion, fiber optics:

- have become an established transmission technology with further advances expected in future;
- are currently cost-competitive with other transmission media in initial investment, and considerably cheaper in O&S and lifecycle cost;
- installed underground offer greater survivability under conventional and nuclear threat than any other transmission medium;
- offer a high level of reliability, availability and maintainability.

REFERENCES

1. S. Glasstone and P.J. Dolan "The Effects of Nuclear Radiation" US Department of Defense and US Department of Energy, Chpt. VIII and IX, 1977.
2. E. Friebel et al, "Enhanced Low Dose Radiation Sensitivity of Fused Silica and High Silica Core Fiber Optic Waveguides", Third European Conference on Optical Communication, Munich, September 1977.
3. E.J. Friebel et al, "Composition Effects on the Radiation Response of Ge-Doped Silica-Core Optical Fiber Waveguides", Applied Optics, Vol. 19, No. 17, September 1980.
4. S. Share and J. Wasilik, IEEE Trans. Nucl. Sci. NS-20, 4802 (1979).
5. R.M. Gilbert, "Photobleaching of Radiation-Induced Colour Centers in a Germanium Doped Glass Fiber", IEEE Trans. Nucl. Sci. Vol. NS 29, NO6, pp 1484-1488,
6. E.J. Friebel et al, Proceedings Twelfth International Congress on Glass, Albuquerque, N. Mex., 1980.

7. Dr. C.W. Lamberts, unpublished paper, Organisatie Voor Toegepast Natuurwetenschappelijk Onderzoek, The Netherlands.
8. S. Shara et al, "The Effect of Temperature on The Response of Glass-Clad Optical Waveguide to Ionising Radiation", IEEE Trans. Nucl. Sci. Vol. NS-25, No. 6, pp. 1288-1293, December 1978.
9. A. Rosiewicz et al, "Effect of Radiation on Mid-IR Transmitting Glass" Electronic Letter Vol. 17, No. 5, pp. 184-185, March 1981.
10. S.A.L.B. Latia et al, "Fiber Optics Fare Well in the Contest with Alternative Transmission" Telephony, 11th April 1983.

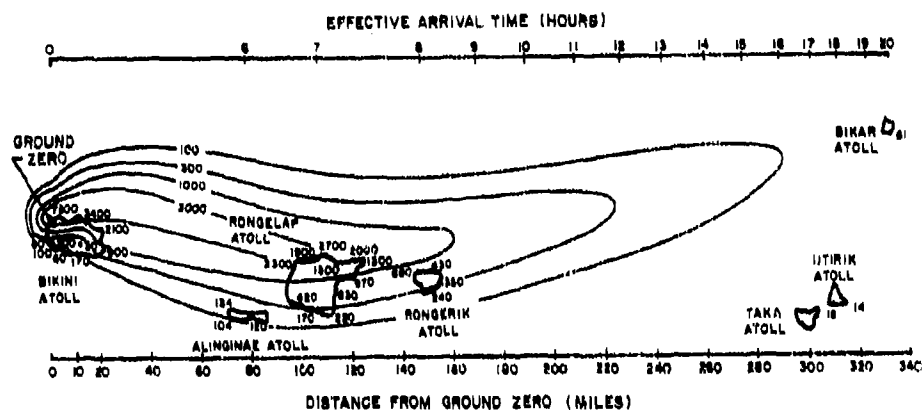


Fig. 1 Estimated total (accumulated) dose contours in rads at 96 hours after the BRAVO test explosion

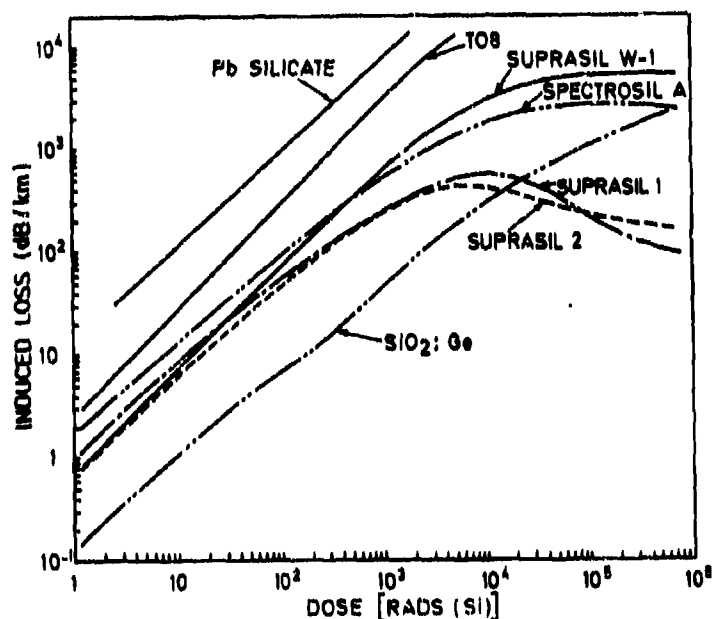


Fig. 2 Radiation-induced loss versus dose at 820 nm during ^{60}Co irradiation

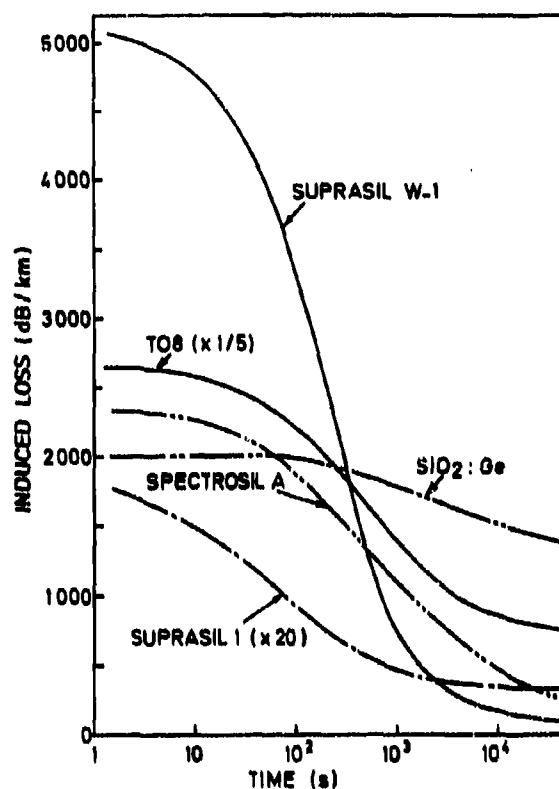


Fig. 3 Decay of radiation-induced loss at 820 nm following ^{60}Co irradiation

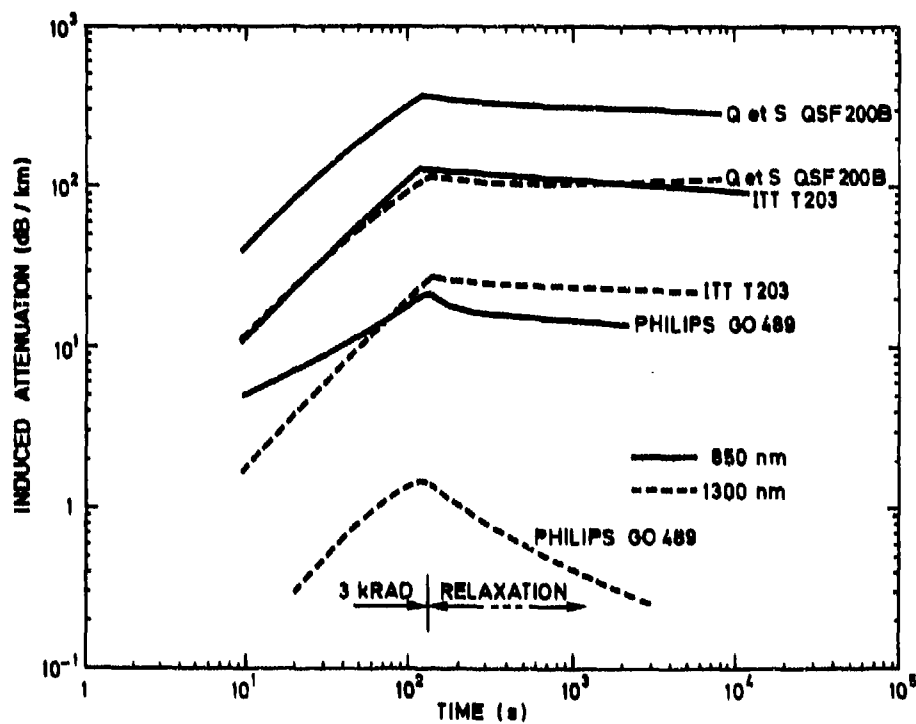


Fig. 4 Radiation induced attenuation and recovery at 850 nm and 1300 nm

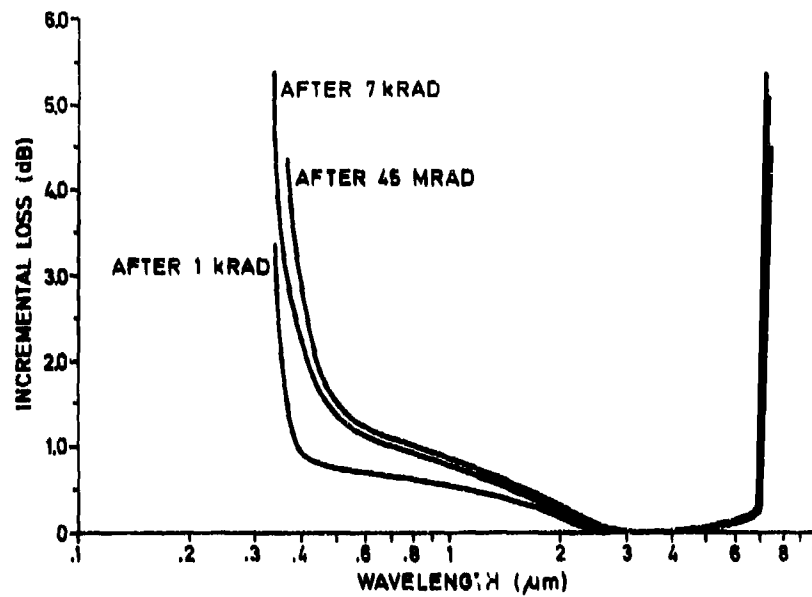


Fig. 5 Incremental loss of bulk fluorozirconate glass sample

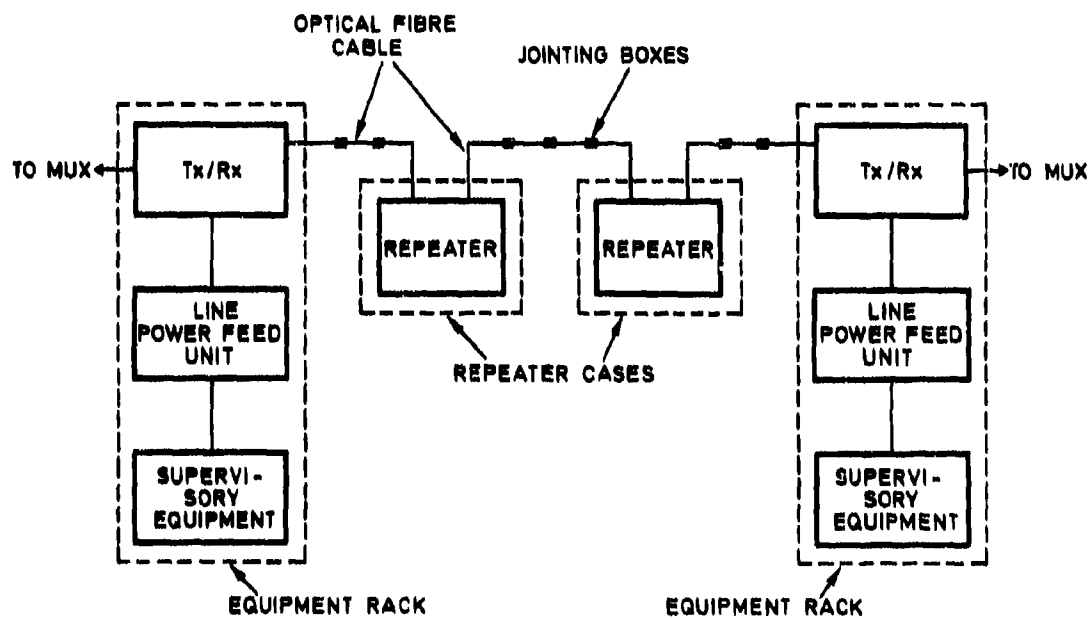


Fig. 6 System elements of an optical fiber transmission system

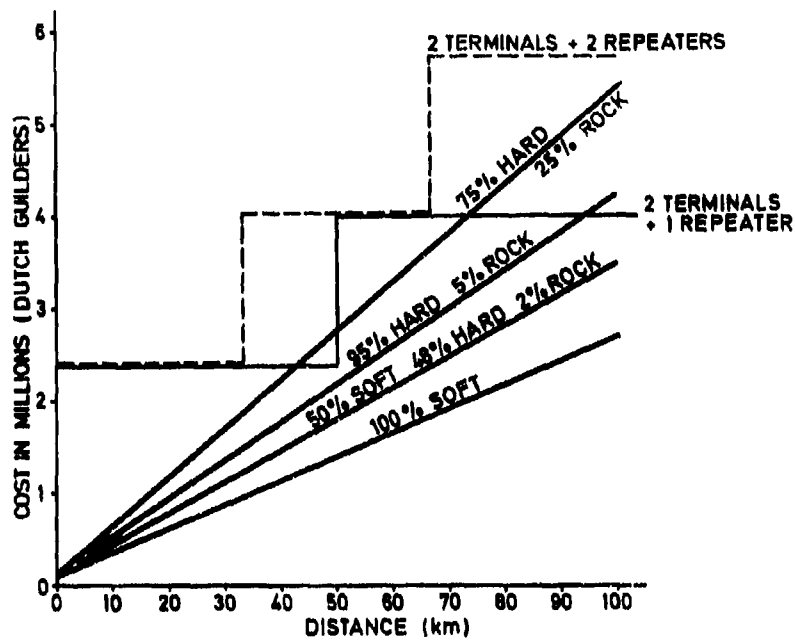


Fig. 7 Cost comparison of fiber optics and LOS microwave links

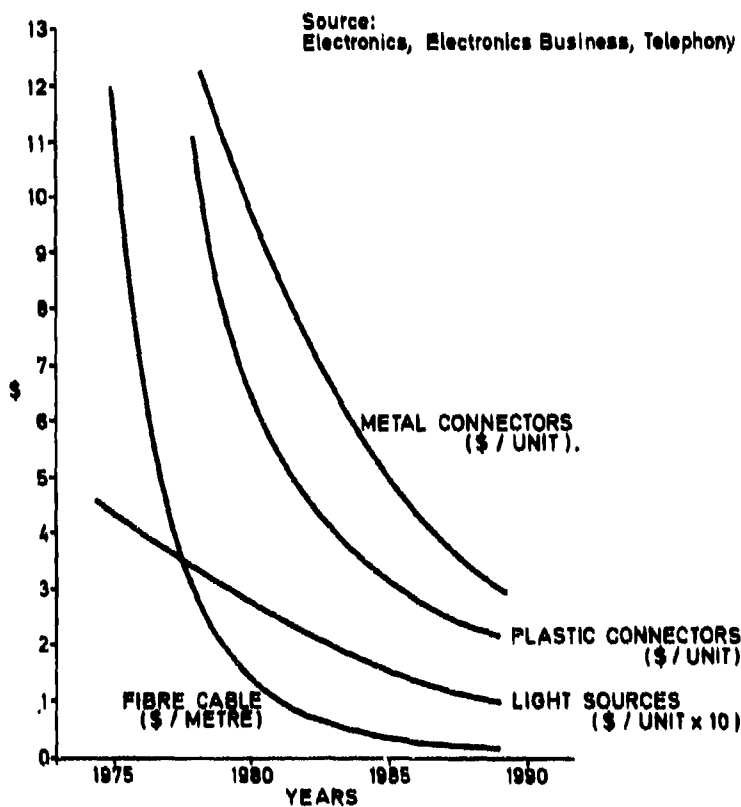


Fig. 8 Prices of optic components from 1975 through 1980 and forecast through 1985

SINGLE-MODE-FIBERS FOR FIBEROPTIC-GUIDED MISSILES - A COMPARISON
WITH GRADED - INDEX MULTIMODE FIBERS

by
K. H. Niederhofer
and
W. D. Schuck
Messerschmitt-Bölkow-Blohm GmbH
Dynamics Division
POB 80 11 49
8000 München 80
Federal Republic of Germany

ABSTRACT

Since a few years there are activities in the application of optical fibers as a broadband, secure transmission medium between a ground-station and tactical missiles for ranges of about 10 km. The idea is to put the "gunner's eye", i.e. a suitable imaging device, into the missile to provide a lock-on-after-launch capability together with a man-in-the-loop option.

A key problem is the rapid payout of the fiber from the missile during flight. Several successful flight test campaigns have been carried out by MBB, F. R. of Germany, where Kevlar-reinforced graded-index multimode fibers have been used for transmission of command- and TV-signals. The effects of additional attenuation resulting from the reinforcement, the bobbin-technology and payout process are well controlled.

For the first development of fiberoptic guidance systems single-mode transmission was not taken into account, since the suitable components were expensive, sensible and not readily available. Today the single-mode technology is quite advanced and offers some benefits compared with multimode transmission. The most important points are the higher bandwidth and the lower attenuation. As long as the missile range is below 10 km, this is no decisive advantage, but it encourages the extension of the missile range to much more than 10 km. The comparison of costs gives no clear-cut statement, but the production costs for single-mode fibers tend to be below that of multimode fibers. If the hardness against nuclear radiation is compared, single-mode fibers give the better results.

1 INTRODUCTION

Since the beginning of the seventies there are efforts to use optical fibers as a transmission medium between a missile and a ground station. The very first idea was to overcome some electrical problems of the wire-guided missiles, such as lightning stroke or the shot over high-voltage power lines, which does not affect the perfectly isolating optical fiber. But it is the capability to transmit broadband signals over long distance, that offers the possibility to realize missile systems with quite attractive features. It is now possible to put, simply spoken, the "gunner's eye" into the missile without the drawbacks of conventional RF-video-links. The main advantages of this fact are:

- * There is no line-of-sight between gunner and target, so you can shoot from cover to a target behind a cover.
- * It is possible to perform a dive-attack, thus hitting the target on the most vulnerable topside.
- * The vulnerability of the launcher is reduced by indirect firing, as the position of the gunner cannot be deduced from the direction of attack.
- * All the sophisticated image processing and target acquisition equipment is located on the ground and thus no expendable part.
- * Lock-on-after-launch and re-targeting during flight is possible.
- * If the video signal is recorded, it can be used for quasi-realtime reconnaissance.

In addition to all that, the fiber-optic link cannot be jammed by electromagnetic means. The only possibilities to interrupt transmission are mechanical damage and severe nuclear irradiation.

2 TRANSMISSION SYSTEM

2.1 Transmission capacity requirements

The transmission capacity needed for a fiber-optic guided missile with a high-resolution imaging device on-board can be defined quite accurately. It is determined by the signal bandwidth of the sensor or camera to be used. Commercially available cameras, that

are suited for this application, have a resolution of up to 1000 points per line. This gives a bandwidth of about 10 MHz in a CCIR-standard video signal. Sophisticated encoding in order to reduce redundancy has not been investigated more detailed, because it enlarges considerably the complexity of the missile electronics. But some sort of modulation is necessary to compensate fast changes of fiber attenuation during payout, to cancel reflexions within the transmission system and to provide good transmission-linearity. This can be achieved by using for example pulse-frequency-modulation (PFM), pulse-density-modulation (PDM) or pulse-code-modulation (PCM). The bandwidth of the modulated signal will then be larger than the baseband-signal bandwidth by a factor 2 to 8. As a result, the transmission bandwidth of the fiber should be at least 80 MHz over the whole length.

The part of operational telemetry channels from missile to ground is not calculated separately, since they can be easily integrated in the video frame without expense of further bandwidth. The requirements for the command link are about three orders of magnitude below that for the video transmission, as far as transmission capacity is concerned. A bandwidth of 10 to 100 kHz is sufficient to guarantee remote command and control of the missile functions.

2.2 Transmission length

The transmission length, that can be achieved without repeater, is a function of fiber attenuation, transmitter power and receiver sensitivity at a given bandwidth. These are the factors, that are defined by the transmission link. Other factors, like fiber volume and weight, time of exposure and break statistics can give an upper limit of the reasonable length, but the discussion of these points is beyond the scope of this paper. In a quite conservative calculation, one can assume, that a realistic transmitter power is about 0 dBm. Receiver sensitivity is about -45 dBm for 80 MHz and -60 dBm for 80 kHz, all values for 1300 nm wavelength. With a margin of 10 dB for splices, couplers and connectors, there remains a permissible attenuation of 35 dB for the video link and 50 dB for the command link, including the basic fiber loss and all attenuation components, that are induced by environmental conditions, radiation, spooling, cabling and payout.

2.3 System architecture

In the transmission system one single fiber is to be used for both transmission directions. Therefore multiplexing is necessary. Among several possibilities /1,2/ the wavelength division multiplexing technique has a lot of advantages. It offers full duplex capability, good isolation between the two channels and low attenuation of the multiplexing device. Figure 1 shows the block diagram of the transmission system, consisting of transmitters and receivers, multiplexers, optical connexions and the fiber bobbin. This transmission system was, with smaller modifications, used in our missile flight tests. The video signal is transmitted at 1300 nm because of the lower attenuation and the lower dispersion at this wavelength. The lower sensitivity of the 1300 nm receiver cancels out with the lower fiber loss after a certain length of transmission. The command link, which allows higher fiber attenuation, is designed to work at 850 to 900 nm. Connectors are avoided, if possible, and if really needed, they are placed in the receiver branch. The only important connector in the system plugs the missile to the ground station.

3. FIBER PROPERTIES AND PERFORMANCE

3.1 Specific fiber problems in payout applications

In missile applications the fiber has to work under conditions, that are not comparable with standard network applications. The fiber is wound up on bobbins with diameters less than 100 millimeters. To achieve a tight structure, the spooling is done under moderate but constant fiber strain. This is necessary to avoid strangling and tangling during payout. Because of the limited space in a missile, the fiber diameter is usually less than 0.5 mm. Therefore the protecting and buffering function of the coating is not very high, and spooling causes severe microbending and in consequence increased loss /3,4/. This additional attenuation can be kept at a minimum, if the fiber is properly designed. The loss increases somewhat, when the bobbin is cooled down to low temperatures. This is the result of slight structural changes of the bobbin and the fiber coating.

Another critical effect is the curvature radius at the peel-point (Fig. 2), which might be lower than 2 mm at the beginning of the payout process. This radius depends on payout force and velocity, on the stiffness of the fiber and the structure of the bobbin. The conditions of the unspooled fiber between missile and ground can cause additional loss. The fiber is under tension during the whole flight. The maximum force measured at the ground station was about 20 N. This produces microbending effects, if the structure of the reinforced fiber is not homogenous. The amount of attenuation, that arises, when the fiber touches trees or other obstacles, is not yet studied in detail.

3.2 Test procedures for guidance-fibers

The suitability of a potential fiber for payout applications is tested by several test procedures. In the first test, the fiber is simply bent while measuring the increase of attenuation (Fig. 3). The additional loss should be lower than 3 dB at a bending radius of 2 mm. Higher values can be tolerated, if fiber and bobbin properties guarantee a greater peel point radius.

The most important dynamic test in the laboratory is performed in the payout test facility (Fig. 4). In this facility the fiber is spooled off and wound up on a drum with velocities up to 200 m/s. Attenuation is constantly monitored by a 850 nm or 1300 nm level measuring setup. The resulting attenuation values are in a certain way worst case values, since the fiber stress is stored on the drum and therefore causes microbending effects, that cannot be observed during real flight. The payout behaviour of the bobbin is simulated sufficiently realistic in this facility.

The ultimate demonstration of suitability are flight tests. Therefore several flight campaigns have been carried out, using the first generation wire-guided anti-tank missile MAMBA as a test carrier. Because of the short range of the MAMBA-engine, the tests were limited to about 2.5 km. These flights proved the feasibility of rapid payout and the possibility of broadband digital video transmission from missile to ground.

3.3 Bending- and microbending sensitivity

In Figure 5 the bending sensitivity of standard 1300 nm singlemode fibers is compared with the bending sensitivity of standard multimode fibers and with fibers optimised for missile application. The fiber data are listed below.

No.	Manufacturer	Type	Core Size um	NA	Atten. dB/km	Jacket	Outer Dia. um
1	Amfox	GI	50	0.2	1.5	Acrylate	250
2	BOPD	GI	38	0.25	1.3	DeSoTo	280
3	Fujikura	GI	39	0.28	0.7	Acrylate + Kevlar	480
4	Philips	SM	9.6	0.1	0.42	Acrylate	250
5	Fujikura	SM	8	0.1	0.48	Nylon	900

Table 1: Data of tested fibers

The fibers 1,4 and 5 are fibers for standard applications without extreme bending, where a low NA has the advantage of lower attenuation and higher bandwidth /5/. Cladding diameter of all the fibers is 125 um, fiber 3 is reinforced with Kevlar (Fig. 6). The test results confirm the fact, that bending sensitivity of multimode fibers decreases dramatically, if the NA respectively the core/cladding index difference increases and core size decreases. Though this is only demonstrated with multimode fibers, this statement is also valid for single-mode fibers /7,9/. Bending attenuations of less than 0,03 dB for a bending radius of 5 mm are reported for a NA of 0,2 /4,6/.

On the other hand, the high doping level that is necessary for the high NA design especially of the graded index multimode fibers slightly increases fiber loss (0.1 to 0.5 dB/km). Moreover, fiber coupling is more affected by geometry mismatch /8/, and it is more difficult to keep dispersion down. Mechanical strength may be reduced by the different mechanical properties of core and cladding in highly doped fibers. When a step index structure is used, which is possible in single mode fibers, pure-silica production technologies for high NA fibers are available, that avoid excessive doping /14/.

Microbending sensitivity can be calculated from fiber data /10,11/ or estimated, if the bending sensitivity is known. Several microbending test methods are known, but the most evident and affirmative method to evaluate the microbending effect on the bobbin is to make a bobbin sample. The loss differences are significant for different fiber types. The spooling loss of a standard graded-index multimode fiber, like No 1 in Table 1 for instance, is exceeding 10 dB/km, while the additional loss of a high-NA fiber (No 3) is below 0.5 dB/km.

3.4 Dynamic attenuation

Dynamic attenuation is that part of the transmission loss, that changes during payout. It originates from deformations of the unspooled fiber mainly at the peel-point and in the bobbin canister. It oscillates rapidly and randomly with frequencies up to several kilohertz. (This is one of the reasons, why simple baseband video transmission is not applicable). The amplitude of oscillation is determined by the bending sensitivity, as shown above, and by the coating material. Hard coatings, that don't allow constant deformation, are preferable. Other coatings, like Nylon, tend to store deformation, and it lasts a considerable amount of time, seconds to minutes, until they have fully recovered. The oscillation amplitude of special guidance fibers is kept below 3 dB.

There is one significant difference in the dynamic behaviour of single-mode and multimode fibers; the relation of attenuation versus bending radius is more abrupt in single mode fibers. This makes the fades in single-mode fibers "harder" than multimode fading.

Another part of dynamic attenuation is caused by fiber stress. It is usually below 0.1 dB/km/N. It is primarily observed in reinforced fibers, where microbending is produced by inhomogenities. Stress-induced changes of the fiber refractive index are not significant.

3.5 Effects of nuclear radiation

Nuclear irradiation is generating transient ionisation in optical fibers. This produces two effects. The one is luminescence, which occurs only during irradiation. The other is the attenuation during and after irradiation. This is the more serious effect. The deterioration of transmission efficiency is affected in a complicated way by various factors, such as glass composition, nature and energy level of radiation source, temperature, wavelength and signal power /13/. It is primarily the doping material, that is responsible for the darkening of the fiber glass. In graded-index fibers, core glass must be doped to achieve the refractive index profile. These fibers degrade with up to approximately 1 dB/km/rad. Due to the high residual loss, graded-index fibers are not suited for nuclear environment, even at fairly low irradiation levels /12/.

Radiation resistant fibers are produced as well. They all have a step index profile. In most cases, the core is made of pure silica, and only the cladding is doped. Irradiation induced attenuation is two to three orders of magnitude lower than in graded-index fibers. In addition they need less time to recover. Residual attenuation values of about 1 dB/km one hour after irradiation with a total dose of 10000 rad are reported /13, 14/.

4. CONCLUSION

The comparison of the two fiber types shows, that the single-mode fiber can be designed and optimized for payout applications as well as the multimode fiber. In neither case, the standard telecommunication fiber can be used; thus it is risky to speculate on low prices.

The advantages of multimode fibers are:

- * simple connector and multiplexer technology can be used
- * coupling efficiency to light sources is quite good, even if "cheap" LEDs are used
- * variation of bending-induced loss is "soft" owing to mode conversion mechanisms.

So multimode fibers are the best solution for low cost missiles with ranges up to 10 km in a non-nuclear environment.

Single mode fibers offer the following benefits:

- * very long transmission links are feasible (e.g. distances up to 100 km are reported in telecommunication systems),
- * nuclear resistant design is possible.

These properties make single-mode fiber to a favourite for missile ranges of more than 10 km, or for medium distance links in nuclear environment.

REFERENCES

- | | | |
|-----|--|---|
| /1/ | Niederhofer, K. H.;
Rieger, R. M.;
Schuck, W.-D. | A Bidirectional Fiber Optic Link for Guided Missiles,
Proc. of the IDIE '82, Hannover 1982, pp. 235-243 |
| /2/ | Ferris, K.;
Wichansky, H. | Fiber optic communication link for missile payout
applications,
Proceedings of the SPIE, vol. 239, 1980, pp. 286-292 |
| /3/ | Fox, D. S.;
Eisentraut, R. A. | High Strength Rapid Payout Fiber Optic Cable Assembly,
CORADCOM Report No 78-2964-1, 1979 |
| /4/ | Akers, P. I.;
Mahurin, S. L. | Study of the Effects of Bending and Microbending on
Glass Fibers,
Office of Naval Research,
Contract No N 00014-78-C-0852,
Final technical report, 1979 |

- /5/ Lilly, C. J.; The state of the art and application of optical fibre systems operating at the longer wavelength of 1300-1600 nm
8th ECOC, Cannes, 1982, pp. 17-24
- /6/ Moriyama, T.; Miyamoto, M.; Akiyama, M.; Sanada, K.; Fukuda, O.; Fabrication of low loss and long length VAD fibres for 1.55 μ m wavelength region,
8th ECOC, Cannes 1982, pp. 31-35
- /7/ Gloge, D.; Weakly Guiding Fibers, Appl. Opt.
vol. 10, Oct. 1971, pp. 2252-2258
- /8/ Bickhoff, W.; Huber H.-P.; Krumpholtz, O.; Petermann, K.; Lichtleitfasern für die optische Nachrichtentechnik,
Wiss. Ber. AEG-Telefunken 52, 1979 pp. 111-122
- /9/ Inada, K.; Single Mode Fiber Measurements,
Fujikura Tech. Review, No. 12, 1982
- /10/ Furuya, K.; Suematsu, Y.; Random-bend loss in single-mode and parabolic-index multimode optical fiber cables,
Appl. Opt. vol. 19, no 9, May 1980, pp. 1493-1500
- /11/ Sharma, A. B.; Al-Ani, A.-H.; Halme, S. J.; Experimental Modification of the Bend-Loss Formula of Monomode Fibers,
10th ECOC, Stuttgart 1984, pp. 210-211
- /12/ Schneider, W.; Babst, U.; Induced attenuation in optical fibers during steady state and pulsed irradiation,
Photon 83, paper A 2.4, Paris 1983
- /13/ Tanaka, H.; Hirashima, T.; Shintani, T.; Pure-Silica Core Optical Fiber and Fiber Cable for Radiation Fields,
Proc. of the 31st Int. Wire and Cable Symposium New Jersey 1982, pp. 452-457
- /14/ Kakuta, T.; et al.; Radiation Resistance of Cl-free, OD Exchanged Pure Silica Core Optical Fibers,
Proc. of the ECOC 84, Stuttgart 1984, pp. 198-199

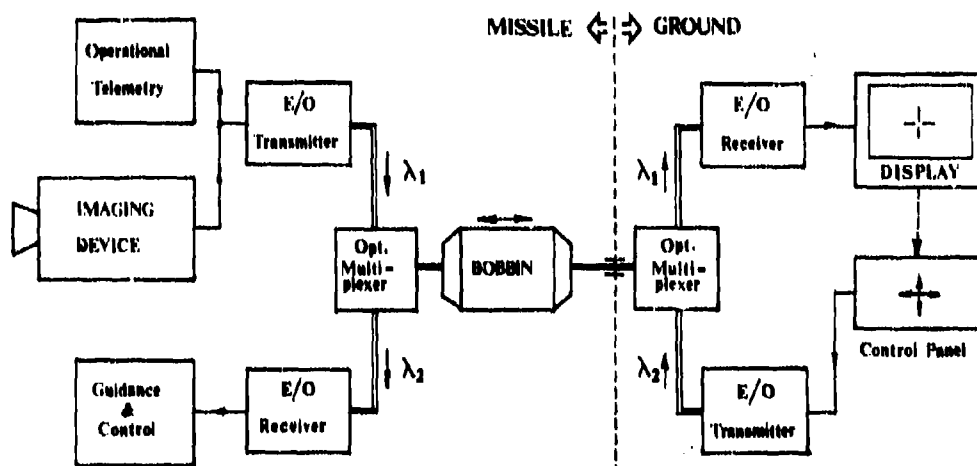


Fig. 1: Transmission system for a fiber-optic guided missile
(block diagram)

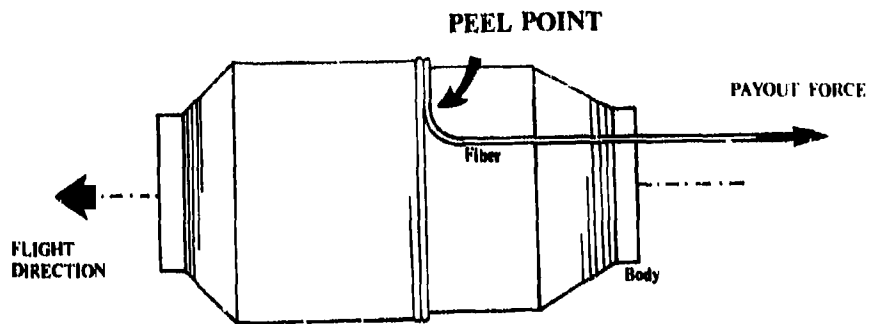


Fig. 2: Bobbin layout (schematic)

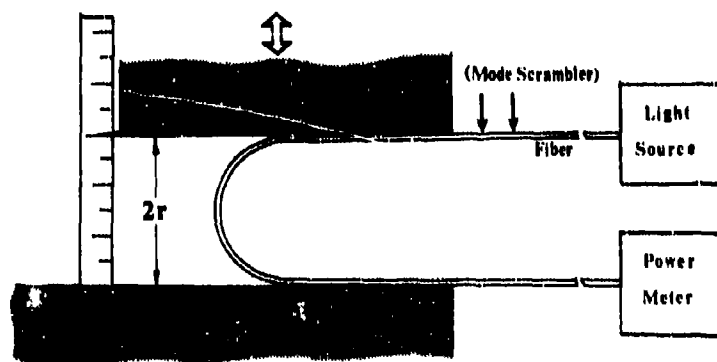


Fig. 3: Bend test arrangement

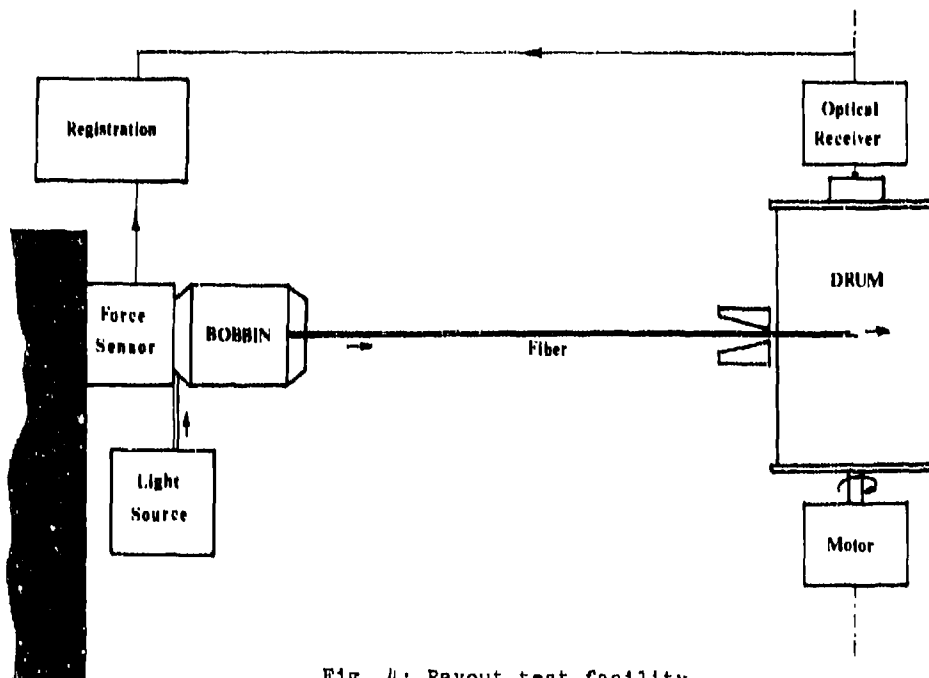


Fig. 4: Payout test facility

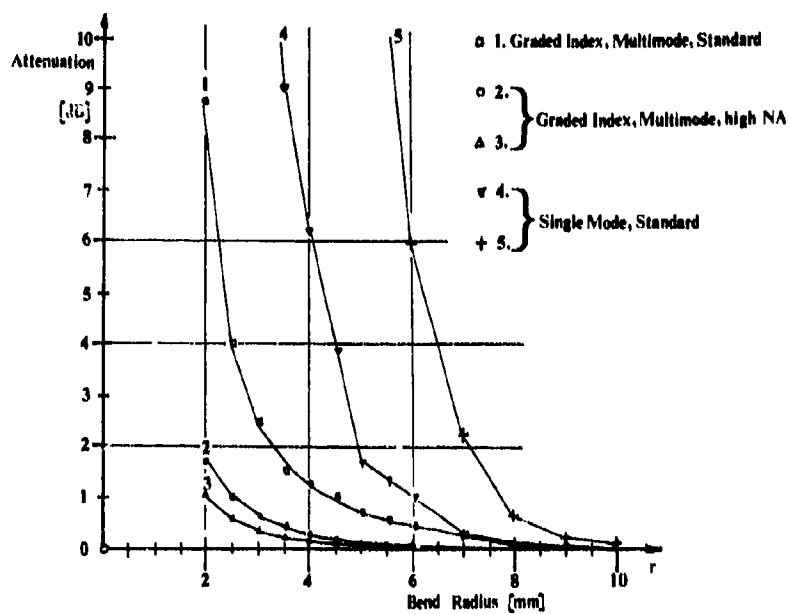


Fig. 5: Bend test results (Fiber data see table 1)

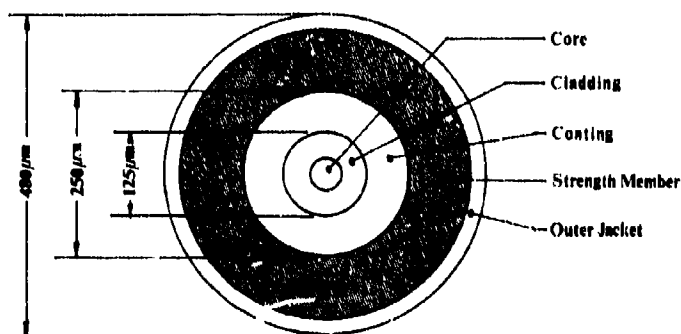


Fig. 6: Structure of reinforced fiber

DISCUSSION

J.Fridman, US

How did you handle the practical problem of splices in a 10 km, when you had a tightly packed bobbin on the payoff end?

Author's Reply

It is a good question; we didn't have any question splicing but it is a problem. See next comment.

J.Pan, US

Comment: A 17 km continuous fibre is available in US; therefore fibre splice may not be a problem.

Question: What was the inner diameter of your fibre bobbin in your flight test?

Author's Reply

80 mm and 100 mm.

Lightwave Technology in Future Radar Equipment Designs

C.M. Gee, A.E. Popa and H.W. Yen

Hughes Research Laboratories
3011 Malibu Canyon Road, Malibu, Ca. USA 90265

Abstract

Lightwave device technology can be implemented in future active aperture radar arrays. Transmitter and receiver components for a fiber optic antenna feed manifold in which the transceiver modules are connected to a central computer will be reviewed. Present link signal to noise limitations imposed by the performance of these components will be analyzed, and promising trends in component development will be discussed.

Introduction

The radar environment will become increasingly complex. The tactical radar of the future will be required to work in a severe air defense suppression environment while providing high-performance search, track and target-identification functions. Electronic counter-measures (ECM) and anti-radiation missiles (ARM) will force the radar to use a highly versatile architecture with adaptive signal processing coupled with low probability of intercept (LPI) transmitter waveforms and antenna characteristics. New radar systems will achieve processing gains while minimizing the spectral power density of the radar energy. Emphasis will be placed on encoding and decoding broadband signals, adaptive beam forming and filtering, jammer nulling and electronic agility in beam steering.

Signal processing techniques to counter the ECM and ARM threats in the radar environment are fairly well developed. Due to the complexity, size and cost of implementing these techniques, however, they are rarely used in mobile land-based and airborne radar systems. Guided-wave optical subsystems and components offer exciting new possibilities in meeting future radar systems processing requirements.

A future radar design

To achieve the physical and functional survivability required for a future mobile radar system, combined analog and digital signal processing will be required to implement a broad range of countermeasures. The typical radar system will consist of 2000 to 4000 transceiver modules, one for each element of an antenna array. For weather penetration, the radars will continue to operate at frequencies between 3 and 12 GHz. To achieve LPI, each solid-state transceiver module will transmit energy in pulses from 1 to 200 μ sec using waveforms occupying bandwidths up to 10% of the operating frequency. Received pulse compression ratios on the order of 200 will be used and the phase of each element in the antenna array will be quantized to an accuracy of 4 or 5 bits in order to maintain antenna side-lobes at least 40 dB below the main beam. A central processor based on Very High Speed Integrated Circuit (VHSIC) technology will communicate with each element of the array to provide the appropriate control signals and computations required for beam steering, clutter suppression, Doppler filtering, pulse compression, multiple target tracking and jammer suppression. Figure 1 shows a futuristic implementation of a radar with the array of modules connected to the array processor by a fiber-optic waveguide manifold. By using optical wavelength multiplexing and multiple

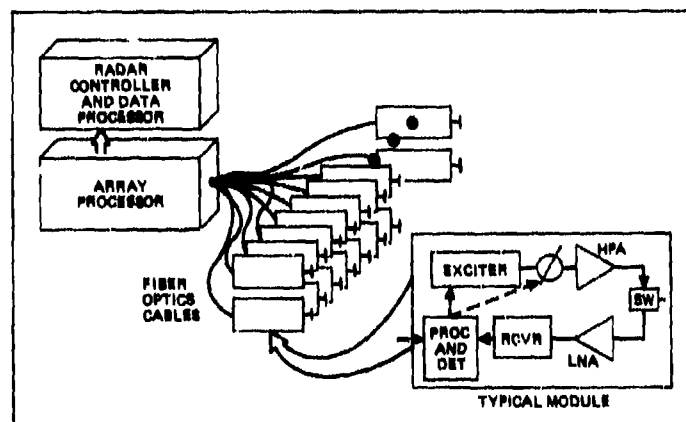


Figure 1. Implementation of an array radar with each transceiver module being a hybrid optical microwave circuit that provides signal generation, detection and processing functions. The modules are connected to the array processor by a manifold of fiber-optic cables.

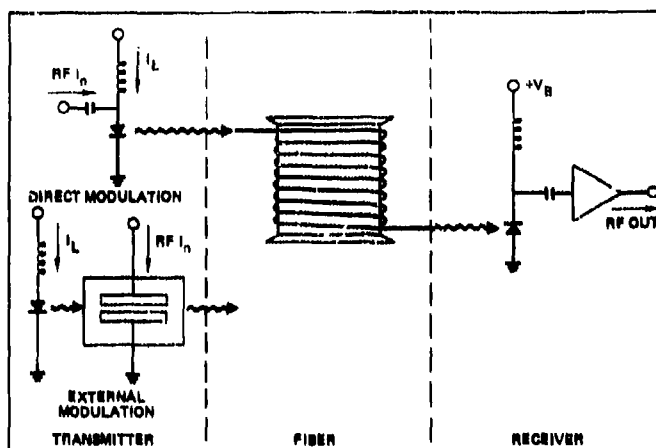


Figure 2. Schematic of an amplitude-modulated fiber-optic delay line. Either direct laser current modulation or an external electro-optic modulator can be used in the transmitter.

rf subcarriers, each fiber-guide could provide a wide variety of bi-directional signals between the array modules and the central processor. These signals would include transmitter waveform, transmit beam steering, transmit-receive switch position, polarization selection, receiver beam steering, received signal waveform and diagnostics. Besides being used as a wide-band data manifold, guided-wave optics will also contribute to the implementation of a variety of radar functions.

Radar functions using guided-wave optics

The large bandwidth, low loss, lightweight and electromagnetic immunity characteristics of optical waveguides offer promising capabilities in the implementation of microwave delay lines, phase shifters and signal processors. The amplitude-modulated fiber-optic delay line shown in Figure 2 consists of a modulated optical transmitter, optical fiber to provide the required delay and a photodetector.

The propagation delay in a conventional silica optical fiber is 4.8 nsec/km. For light in the 800 to 900 nm wavelength range, fiber loss is below 3 dB/km and material dispersion is 100 psec-nm/km. The spectral width of semiconductor laser sources can be less than 0.1 nm. Hence, fiber bandwidths are well in excess of 10 GHz even for a few kilometers of fiber. At 1.3 μ m wavelength, fiber loss can be less than 1 dB/km and dispersion less than 3 psec-nm/km.

Selection of transmitter components

The rf signal can be up-converted to an optical frequency by directly modulating the laser diode current or by using an external optical modulator. The performance of microwave fiber optic links will vary greatly depending upon which type of laser is used. For links using direct current modulation, the two most relevant laser diode operating characteristics are the modulation response and the intrinsic laser noise spectrum.

The frequency response of a laser diode under direct current modulation is influenced by both the intrinsic response of the laser and parasitic circuit elements associated with the laser packaging. The intrinsic small signal modulation response of a semiconductor laser is of the form:

$$S_{21} = \frac{1}{(f_r^2 - f^2)^2 + \gamma^2 f^2} \quad (1)$$

where f_r is the relaxation resonance frequency, a convenient measure of the useful bandwidth of a semiconductor laser. For most AlGaAs laser diodes, f_r is in the range 3-4 GHz at the maximum laser output power. However, by designing lasers to operate at higher output power densities or by decreasing the cavity lifetime, the resonance frequency can be increased. If laser diodes are designed in such a way as to minimize the effects of parasitic circuit elements then their frequency response is nearly the same as their intrinsic frequency response.

The second important operating characteristic of laser diodes for use in microwave fiber optic links is the intrinsic intensity noise spectrum of the laser. The intensity fluctuations of laser diodes arise from the shot noise processes associated with carrier injection and recombination inside the laser active layer. These noise generating processes result in an intensity noise spectrum which is characterized by a broad and pronounced resonance at f_r . The laser fluctuations are expressed in terms of the relative intensity noise, RIN, defined as:

$$\text{RIN}(f) = \frac{\langle \Delta P^2(f) \rangle}{P_L^2} \quad (2)$$

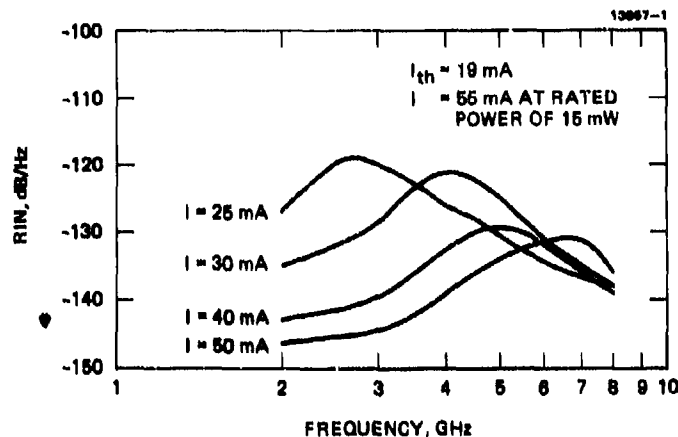


Figure 3. Relative intensity noise (RIN) of a Mitsubishi ML5101 laser.

where P_L is the DC laser power and $\langle \Delta P^2(f) \rangle$ is the spectral density of the square of the laser optical power fluctuation.

The noise spectra of a Mitsubishi ML5101A "crank" TJS laser for various bias currents are shown in Figure 3. The most relevant feature of these curves is that the RIN below the resonance frequency f_r of 3-4 GHz decreases significantly as the bias current is increased. The noise spectra shown in Figure 3 represent the laser RIN under conditions of low optical feedback. In the presence of optical feedback levels as small as -60 dB, the intensity noise is increased. Low noise direct modulation fiber optic links must therefore either incorporate optical isolation, or new laser structures must be developed which are less sensitive to optical feedback.

Although external modulators have problems as well, external modulation links are not limited in frequency by the laser relaxation resonance. Perhaps even more important is the ability to use stable, low noise laser sources with external modulators. In this paper we will restrict our discussion to LiNbO₃ traveling wave Mach Zehnder modulators which have been demonstrated to have a 3 dB bandwidth of 17 GHz.²

The modulation transfer function for an interference type modulator, such as the Mach Zehnder modulator, is given by:

$$P = P_{pk} \sin^2\left(\frac{\pi V}{2V_\pi} + \phi\right) \quad (3)$$

where V_π is the "half-wave voltage", a parameter that takes into account the dimensions and material of the modulator. For linear modulation, the modulator is typically biased to $\phi = \pm\pi/4$. The modulation characteristic is linear only for small signals around $V=J$, so distortion and the resulting intermodulation products will become an issue at high percentage modulation.

The capability of these modulators to operate at frequencies well above 10 GHz is a significant advantage of external modulation. The most serious disadvantage of using LiNbO₃ modulators in links operating at 0.83 μm is the limited optical power handling capability of the modulator. Due to photorefractive effects, less than 30 μW is typically launched into an optical fiber after taking into account propagation losses through the modulator and modulator-fiber coupling losses. Even for short links using efficient photodetectors, the DC photocurrent will be only of the order of 10 μA . As will be shown in the link analysis section of this paper, the receiver amplifier noise will be the dominant noise source in this case and the maximum S/N will be substantially less than that possible for links using direct current modulation at 0.8 μm wavelength.

Selection of Receiver Components

A receiver for a microwave fiber optic link consists of a high speed photodetector and a low noise amplifier. The detector should have a flat response over the frequency range of interest and as high an efficiency as possible. The amplifier should also have a flat response over the frequency range and as low a noise figure as possible.

At the Hughes Research Laboratories, GaAs Schottky photodiodes with bandwidths of 20 GHz and quantum efficiencies as high as 70% have been fabricated and characterized.³ Based upon a 1.5 μm depletion layer width, the frequency limitation due to transit time effects is approximately 30 GHz. In normal operation with low input impedance amplifiers (eg. 50 Ω), the bandwidth is actually determined by the RC time constant of the device plus parasitic C and the amplifier input impedance, R.

Most links for transmitting analog microwave signals require bandwidths of a few GHz or less centered at the microwave carrier frequency. Detectors for microwave fiber optic links need to be designed so that the frequency response limited by transit time

exceeds the carrier frequency, but the bandwidth limited by RC time constant need only exceed the link bandwidth. For most applications, the Schottky photodiodes described above will have bandwidths greatly in excess of that required when the detectors are operated into 50 Ω impedance amplifiers. The S/N of a receiver-amplifier-noise-limited link can be improved by increasing the amplifier input impedance, providing there is no corresponding increase in the amplifier noise figure. For links that are amplifier noise limited, it is therefore desirable to design amplifiers which have as large input impedances as possible, while still maintaining the (RC) bandwidth greater than the required link bandwidth. Tuned RLC circuits can be used to center the receiver bandwidth at the appropriate microwave carrier frequency.

Microwave Fiber Optic Link Analysis

In this subsection, we illustrate how the various parameters of a simple fiber optic link affect its signal-to-noise performance. Both direct laser current and external modulation techniques will be analyzed. The laser is characterized by a threshold current, I_{TH} ; a maximum operating current I_{PK} (determined by signal distortion, or ultimately, by laser burnout); a slope efficiency, η_L [optical power/electrical current, $^{\circ}W/A$]; and an incremental drive impedance about its point of bias of R_L ohms.

The optical fiber is characterized by its power attenuation, K_L [$^{\circ}W/^{\circ}W$], which includes the optical coupling losses to both the laser and photodiode. The photodetector is characterized by a slope efficiency of η_D [$A/^{\circ}W$]. Photodiodes are usually characterized electrically as a current generator in parallel with a capacitance, C_D (the capacitance of the PN junction plus the lead and package parasitic capacitance). The proper terminating load should be chosen so that $(R_D C_D)$ is large enough to pass the bandwidth, B.

We could define a current transfer function from laser to photodiode, $H_L' = \eta_L K_L \eta_D$. In terms of power rather than current, we introduce laser and detector transfer functions,

$$K_L = \eta_L / \sqrt{R_L} \quad (4)$$

$$K_D = \eta_D \sqrt{R_D} \quad (5)$$

We can now define an overall link transfer function,

$$H_L = K_L K_F K_D \quad (6)$$

which is dimensionless. The quantity H_L^2 is simply the electrical power transfer [W/W] between input and output of the link. It will generally be less than unity and therefore a loss rather than a gain.

We wish to find expressions for the signal-to-noise ratio of this link, and ultimately its noise figure in terms of the component parameters and system requirements. The equivalent electrical noise power generated in the laser is

$$N_L(f) = N_L'(f) - kTB = RIN_{DM}(f)(I_{BIAS} - I_{TH})^2 R_L B - kTB \quad (7)$$

where kTB is the thermal noise from the signal sources impedance. RIN as defined in Eq (2) represents the total output noise from a laser as determined by measurement, including the thermal noise from the signal sources, the shot noise associated with the DC laser current, and all other noise processes in the laser. The photodetector output noise power, N_D , is the shot noise associated with the average photocurrent, I_D :

$$N_D = 2e I_D F_D B R_D \quad (8)$$

where a factor $F_D \geq 1$ has been added to accommodate excess noise in the case of avalanche photodiodes. In terms of the laser current,

$$N_D = 2e(I_{BIAS} - I_{TH}) H_L F_D B \sqrt{R_L R_D} \quad (9)$$

The total noise power at the output of the link will then be the sum of the internal noise sources and the input noise, $N_{in} = kTB$, all referred to the output terminals.

$$\begin{aligned} N_{out} &= H_L^2 N_{in} + H_L^2 N_L + N_D \\ &= H_L^2 kTB + H_L^2 [RIN_{DM}(I_{BIAS} - I_{TH})^2 R_L B - kTB] + 2e(I_{BIAS} - I_{TH}) H_L F_D B \sqrt{R_L R_D} \end{aligned} \quad (10)$$

so that the noise figure of this directly modulated link is :

$$F_{DM} = \frac{(S/N)_{in}}{(S/N)_{out}} = \frac{RIN_{DM}(I_{BIAS} - I_{TH})^2 R_L + 2e(I_{BIAS} - I_{TH}) F_D \sqrt{R_L R_D}}{H_L kT} \quad (11)$$

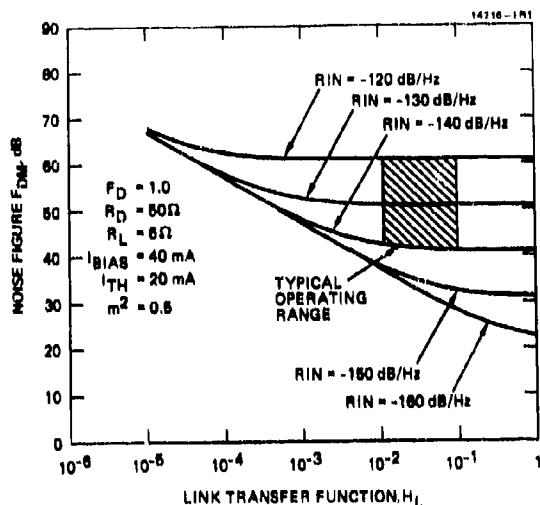


Figure 4. Noise figure attributable to the optoelectronic (laser, fiber, photo-detector) components of a direct modulation microwave link.

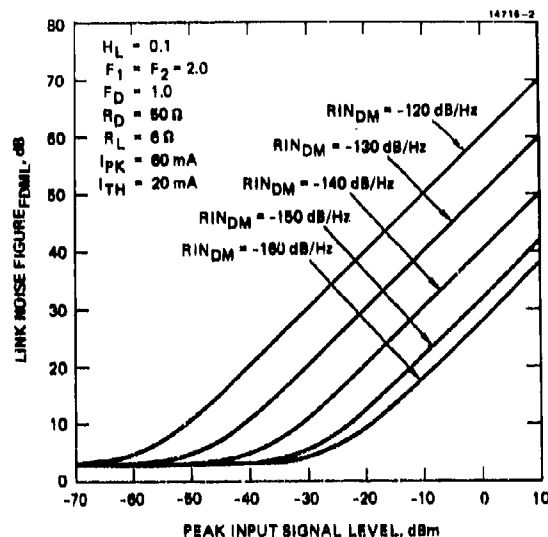


Figure 5. Overall link noise figure of a direct modulation microwave link.

F_{DM} is the noise figure that can be attributed to the optoelectronic components in the link (laser, fiber, photodetector). This noise figure is plotted in Figure 4 versus link transfer function H_L for different values of laser RIN. The values of the other relevant parameters are typical for direct modulation links using Mitsubishi ML5101 lasers. One of the most relevant features of this figure is that the noise figure attributable to the optoelectronic components is very large. The shaded portion of Figure 4 represents the range in which direct modulation links commonly operate. The dominant noise source in such links is laser noise. The noise figure is directly proportional to laser RIN and relatively insensitive to the link transfer function.

If we use amplifiers with noise figures $F_1, F_2 < F_{DM}$ before and after the link, respectively, we can generally improve the overall link noise figure. The overall link noise figure, F_{DML} , including the electronic amplifiers, may be determined from the noise figure cascade formula of Friis:

$$F_{DML} = 1 + (F_1 - 1) + \frac{(F_{DM} - 1)}{G_{1DM}} + \frac{(F_2 - 1)}{G_{1DM} H_L^2} \quad (12)$$

We see that to minimize the overall noise figure, we should maximize H_L . We would also like to choose the bias current so that the amplifier gain G_{1DM} is maximized (subject to the constraints of laser burnout and negative peak clipping) and RIN_{DM} is minimized. Taking $I_{BIAS} = (I_{TH} + I_{pk})/2$ then we would select:

$$G_{1DM} = (m^2 / 8 S_{inpk}) (I_{pk} - I_{TH})^2 R_L \quad (13)$$

where m is the modulation depth and S_{inpk} is the peak rf power from the signal source (before the amplifiers). Then, we have the following expression for F_{DML} :

$$F_{DML} = F_1 - \frac{8 S_{inpk}}{m^2 (I_{pk} - I_{TH})^2 R_L} + \frac{2 S_{inpk} RIN_{DM}}{m^2 kT} + \frac{8 e \sqrt{R_D / R_L} S_{inpk} F_D}{m^2 H_L kT (I_{pk} - I_{TH})} + \frac{8 S_{inpk} (F_2 - 1)}{m^2 H_L^2 (I_{pk} - I_{TH})^2 R_L} \quad (14)$$

The direct modulation link noise figure is shown in Figure 5. These curves show that when large input signal levels must be accommodated, the fiber optic link will seriously degrade the S/N. However, for low input signal levels the link noise figure is given by the preamplifier noise figure, F_1 . The importance of using lasers with low RIN is also clearly indicated by Figure 5.

There are important differences between direct and external optical modulation which influence the performance of microwave fiber optic links. We will now derive expressions which describe the performance of a link incorporating a Mach-Zehnder interferometer modulator. The extension of these results to other types of external modulators follows accordingly.

The optical power out of the modulator is

$$P = P_{pk} \sin^2 \left[\frac{\pi V}{2V_{\pi}} + \frac{\pi}{4} \right] [^{\circ}W] \quad (15)$$

where we now are able to bias the laser to its peak power P_{pk} . We define the modulator transfer function analogous to Eq (4):

$$K_M = \frac{1}{\sqrt{R_M}} \frac{\partial P}{\partial I} = \sqrt{R_M} \frac{\partial P}{\partial V} \Big|_{V=0} = \frac{\pi P_{pk} \sqrt{R_M}}{2V_{\pi}} [^{\circ}W/^{\circ}W] \quad (16)$$

The fiber link transfer function then becomes

$$H_M = K_M K_F K_D \quad (17)$$

As before, H_M^2 is the overall electrical transfer function from modulator to detector. The optical path transfer factor K_F will generally be smaller when an external modulator is used because of the propagation loss (a few dB) and coupling losses in the modulator.

Although the electro-optic modulator is, itself, a noiseless device, it passes along the thermal noise from the input amplifier via the transfer function, K_M . The laser, though now unmodulated, still contributes noise, which, as before, may be expressed in terms of the laser RIN. Thus, analogous to Eq (10) we may write the total noise out of an external modulator link as

$$N_{out} = H_M^2 N_{in} + H_C^2 N_L' + N_D = H_M^2 KTB + H_C^2 RIN_{EOM} (I_{BIAS} - I_{TH})^2 R_L B + 2e(I_{BIAS} - I_{TH}) H_C F_D B \sqrt{R_L R_D} \quad (18)$$

where H_C is the electrical transmission ratio from the laser terminals to the detector terminals [$^{\circ}W/^{\circ}W$]. H_C will generally have a smaller value than H_M because of additional optical losses, α , in K_F , and the laser power must be attenuated by some factor $y < 1$ from its peak value to prevent optical damage of the modulator. Thus $H_C = \alpha y H_M$. RIN_{EOM} reflects the fact that a generally lower noise laser may be employed than in the case of direct modulation, RIN_{DM} .

We may then write the noise figure for the electro-optic modulated link, F_{EOM} , analogously to Eq (11) for F_{DM} as

$$F_{EOM} = 1 + \frac{RIN_{EOM} (I_{BIAS} - I_{TH})^2 R_L}{kT} \left[\frac{H_C^2}{H_M^2} \right] + \frac{2e(I_{BIAS} - I_{TH}) F_D \sqrt{R_L R_D}}{H_L kT} \left[\frac{H_C^2}{H_M^2} \right] \left[\frac{H_L}{H_C} \right] \quad (19)$$

Just as in the case of direct modulation, an E-O modulated link will be preceded and followed by amplifiers of gains G_{1EOM} , G_{2EOM} , respectively. In the case of an E-O modulated link, the constraint on G_{1EOM} is due to the modulator distortion at large modulation depths, m . The optical modulation depth for an E-O modulator for small modulation depths is given by

$$m = \frac{\pi V_{max}}{V_{\pi}} \quad (20)$$

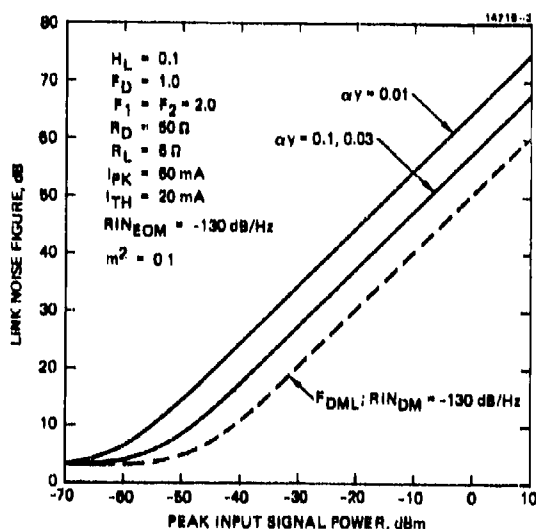


Figure 6. Overall link noise figure of an external modulation link incorporating a large RIN laser diode.

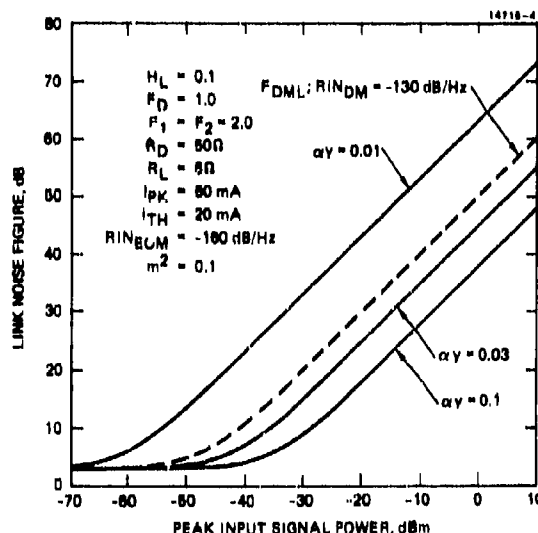


Figure 7. Overall link noise figure of an external modulation link incorporating a low RIN laser diode.

The constraint on G_{1EOM} can then be expressed as

$$G_{1EOM} S_{inpk} \leq \left[\frac{\pi^2}{2} \frac{V^2}{R_M} - m^2 (I_{pk} - I_{TH})^2 R_L \left[\frac{H_C}{H_M} \right]^2 \right] \quad (21)$$

The overall link noise figure is then:

$$F_{EOML} = F_1 + \frac{2R_{IN} S_{inpk}}{m^2 kT} + \frac{4e S_{inpk} \sqrt{R_D/R_L} F_D}{\alpha y^2 m^2 H_L^2 (I_{pk} - I_{TH}) kT} + \frac{2(F_2 - 1) S_{inpk}}{\alpha^2 y^2 m^2 H_L^2 (I_{pk} - I_{TH})^2 R_L} \quad (22)$$

The comparison between F_{DML} and F_{EOML} is illustrated in Figures 6 and 7. In both figures we assume $R_{INDM} = -130$ dB/Hz and $M = 0.3$. In Figure 6, we also take R_{INEOM} to be -130 dB/Hz and plot F_{DML} and F_{EOML} for various values of αy . This corresponds to the situation where we are using the same laser for both the direct and external modulation links. Direct modulation is clearly superior. In Figure 7, we take R_{INEOM} to be -160 dB/Hz. This corresponds to the case where a low noise, low bandwidth laser is used in the external modulation link. For small αy , direct modulation is still superior, but for $\alpha y \gg 1$, F_{EOML} can be significantly smaller than F_{DML} .

To summarize the most significant properties of direct and external modulation links:

- o The contribution to the link noise figure from the post amplifier and detector shot noise are always larger in an external modulation link. This is due to the lower linear modulation depth, m , and the additional optical losses, α and y . With presently available LiNbO₃ guided wave modulators, these are the dominant noise sources of the external modulation links.
- o If identical lasers and bias currents are used in direct modulation and external modulation links, then the laser noise contribution to the link noise figure will be larger in the external modulation link, due to the lower linear modulation depth.
- o Direct modulation links operate at $f \leq f_r$ where laser RIN is large. Laser noise is the dominant noise source in low optical loss direct modulation links.
- o External modulation links can use lasers with $f_r \ll f$. In this case the laser noise contribution to the link noise figure can be negligibly small. If the optical losses in the external modulation link are also small, then the external modulation link noise figure can be lower than that of a direct modulation link.

Microwave Fiber Optic Link Performance

In the preceding sections, the characteristics of the transmitter and receiver components of a microwave fiber optic link and the impact of these characteristics on link performance have been discussed. In this section, the actual performance of a short link will be described.

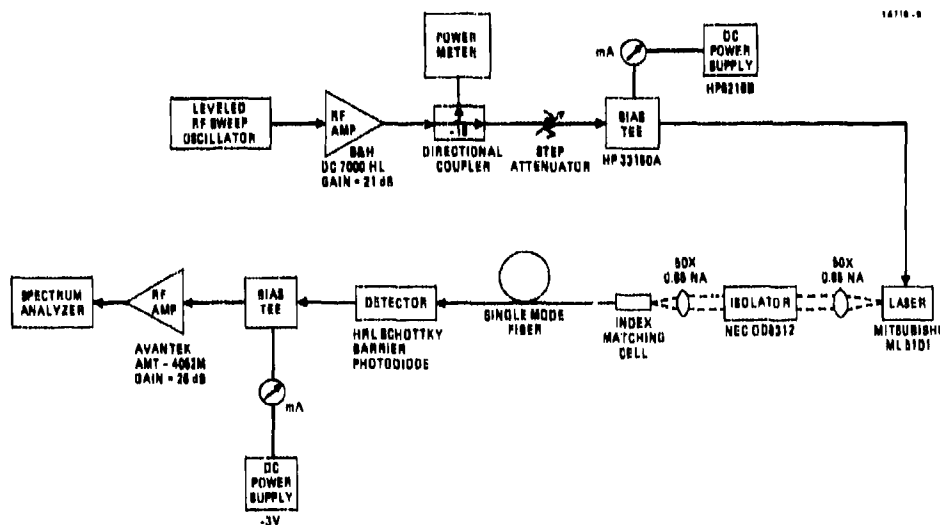


Figure 8. Experimental arrangement for evaluating the performance of microwave fiber-optic links.

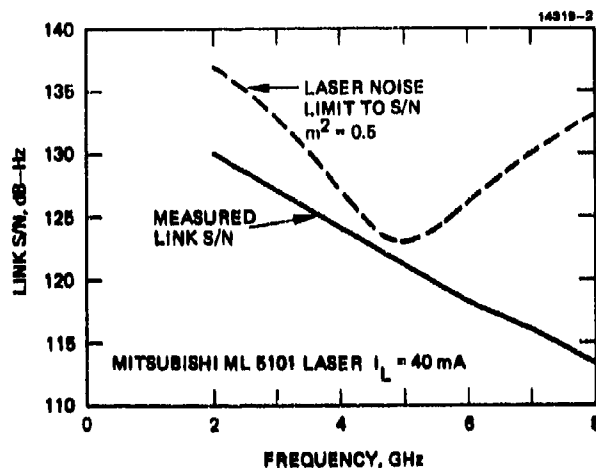


Figure 9. Experimentally observed link S/N for a direct modulation link.

The components used in an actual link are shown in Figure 8. This link has been characterized over the frequency range of 2-8 GHz. We found that the Mitsubishi ML 5101A laser resulted in the best link performance due to its low RIN and relatively flat frequency response in the 2-8 GHz frequency range. The optical isolator was included to minimize optical feedback into the laser diode. Optical feedback from the near end of the single mode fiber was found to greatly increase the laser noise when the isolator was omitted. The receiver for this link consisted of Schottky photodiodes fabricated at Hughes Research Labs and commercially available GaAs amplifiers. The dominant noise source of this link was the laser diode noise. The fiber optic link had an rf power loss, H_L^2 , of 33 dB at 3 GHz. The rf transfer function is given by:

$$H_L^2 = n_L^2 K_F^2 n_L^2 (R_D/R_L) \quad (23)$$

Of this loss, 11 dB was attributable to the laser DC differential quantum efficiency of 28% per facet, 10 dB was due to the laser parasitic and packaging, which reduced the laser efficiency below the DC level, 12 dB was due to the optical coupling losses and fiber attenuation, and 9 dB was due to the detector quantum efficiency of 35%. 9 dB of signal gain could be attributed to the ratio of the detector to laser impedances ($R_D = 50 \Omega$, $R_L = 6 \Omega$). Although we do not believe that the rf link loss of 33 dB resulted in any significant degradation of the link performance (see Figure 4), the link loss can probably be reduced to less than 15 dB by eliminating the laser packaging rolloff, improving the laser-fiber coupling, and improving the detector quantum efficiency.

We have measured the link S/N of a link consisting of a directly modulated Mitsubishi ML5101A laser, a 250 m single mode fiber, a Hughes Schottky photodiode, and commercial GaAs amplifiers. The signal to noise per unit bandwidth that we were able to achieve is shown in Figure 9. Also shown in this figure is the expected link S/N assuming 70% depth of modulation. The discrepancy between the two curves is partially due to a lower depth of modulation in the actual links, particularly at the higher frequencies. We limited the rf input power in the link S/N measurements to 5 mW, because of concerns about the effect of large rf drive powers on the laser reliability. We also observed that the presence of the rf signal made the laser more sensitive to optical feedback. Particularly noticeable was an increase in the laser noise at frequencies near the modulation frequency, which degraded the link S/N by 2-5 dB. Eliminating the fiber did not significantly change the link S/N. However, care had to be taken to minimize optical feedback from the fiber ends.

This work has been funded in part by Solid State Sciences Division of the Rome Air Development Center.

References

Present address: Ortel Corporation 2015 W. Chestnut

1. G. Harder, J. Katz, S. Margalit, J. Shocham, and A. Yariv "Noise Equivalent Circuit of a Semiconductor Laser Diode" IEEE J. Quant. Electron. QE-18 pp. 333-337 (1982).
2. C. Gee, G. Thurmond, and H. Yen "17 GHz Bandwidth Electro-optic Modulator Appl. Phys. Lett. 43 pp. 998-1000 (1983).
3. H. Blauvelt, G. Thurmond, J. Parsons, D. Lewis, and H. Yen "Fabrication and Characterization of GaAs Schottky Barrier Photodetectors for Microwave Fiber Optic Links" Appl. Phys. Lett. 45 pp. 195-196 (1984).
4. H.F. Friis, Proc. IRE, 32 p. 419 (1944).

DISCUSSION**J. Pan, US**

Have you measured the capacitance of your GaAs EOM?

Author's Reply

Yes, 1 to 2 pF.

TACTICAL FIBER OPTIC ASSEMBLY REQUIREMENTS

By

Vasilios E. Kalomiris
U.S. Army Communications-Electronics Command
Fort Monmouth, New Jersey 07703-5202

ABSTRACT

The advantages offered by fiber optic technology have surpassed the expectations of even the most optimistic scientists and continue to unfold. Within about eighteen years the progress on the silica doped fiber designs, including step index and graded index multimode and step index single mode, has led to extending the system operating wavelength from 0.85 μ m to 1.3 μ m and beyond with a significant reduction in attenuation with levels approaching 0.25 dB/km. Additional experimental work on other exotic fiber compositions is in progress with anticipated reduction in attenuation to levels of 10^{-3} dB/km.

The Army, recognizing the advantages of fiber optic technology, has been involved in the development of fiber optic components and systems with the main objective of replacing the twin metallic coaxial cable. The introduction of fiber optics in a tactical environment can be a success only if the components comprising the system can satisfy the unique requirements of the military environment and also can be shown to have service life not less than comparable equipments used in the commercial fixed plant communication systems.

This paper will outline the unique features of militarized fiber optic assemblies. The stringent requirements that make tactical deployment a challenge to the fiber optic industry are summarized. The requirements are broken down to the component level, fiber, cable and connector. These demands on components are necessary to assure successful system operation. The compilation of specifications is presented in tabular form to serve as a reference for those interested in satisfying a host of ground system needs.

INTRODUCTION

An optical fiber cable assembly, for use in tactical environment, consists of one kilometer, all dielectric, two-fiber cable terminated onto hermaphroditic tactical connectors. The main components of the optical cable assembly must be individually qualified before they are accepted and used in the assembly. The most stringent performance requirements that must be met by the optical cable and connector before acceptance for use in the cable assembly are reported in the following sections. The significance of the performance of the cable assembly in the performance of the optical subsystem is also described. In addition, the requirements that the transceivers have to meet are reported and a comparison of the tactical and fixed plant is presented.

FIBER

The optical fiber, Figure 1, in order to be accepted and packaged in the cable has

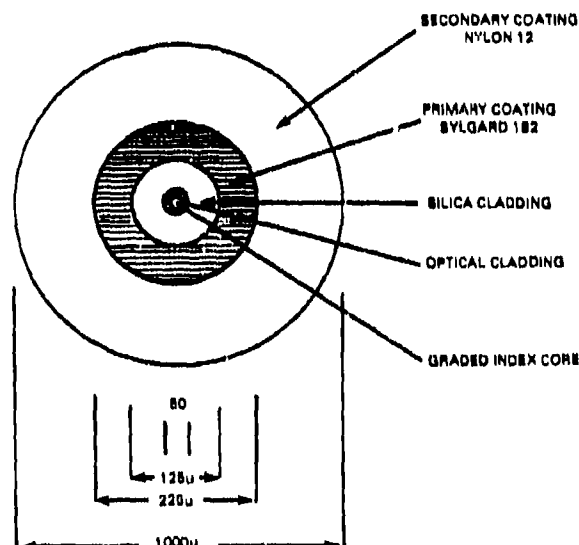
TIGHTLY BUFFERED FIBER CROSSSECTION

Figure 1. Tight Buffer Fiber Construction

to meet a number of stringent requirements derived from the environment in which the fiber optic system is to be deployed. In general the operating temperature of the fiber is defined between -46°C to $+71^{\circ}\text{C}$. Within this range the attenuation of the optical signal must remain within some predefined levels in order to maintain the optical link at constant lengths or within predictable limits. The allowable increase in attenuation due to temperature cycling is defined as 0.5dB/km maximum. In addition, the optical fiber has to meet the ruggedness requirement simultaneously with low temperature attenuation. It has been determined that the impact test can easily be met if the appropriate buffers have been selected and applied on the fiber bringing the fiber outer diameter to approximately 1.0 mm. Currently buffer materials have been selected, applied and tested showing attenuation increase within the acceptable limits. The requirement of a tight buffer is of the utmost importance since it provides the necessary degree of ruggedness. The optical fiber coatings and buffers have to be selected so that they can be mechanically strippable without the use of chemicals. The optical characteristics of the fiber are mainly dual wavelength operation 0.850 and 1,300 μm with a minimum bandwidth of 400 MHz-km. The dual wavelength requirement is desirable for possible use of the same cable assembly in other systems emphasizing short link lengths up to 4 km. Since the fiber optic cable assemblies are used in a mobile setup, demountable connections are utilized. The quality of the fiber as far as consistency in dimensions and numerical aperture directly affect the connector performance. It has been found that by maintaining the fiber core, cladding tolerances below 3 μm and core ellipticity below 4%, a fractional dB connector can be easily designed. The optical fiber in order to meet the rough handling has to be proof tested to 100 kpsi. The following, Table 1, summarizes the requirements before qualification.

TABLE 1
OPTICAL FIBER REQUIREMENTS

Fiber	Dual Wavelength 0.85 & 1.3 μm
Attenuation	2.5 dB/km and 1.25 dB/km respectively
Core	50 \pm 3 μm
Cladding	125 \pm 3 μm
Ellipticity	4%
Maximum Outer Diameter	1 mm
Numerical Aperture	0.22 \pm 0.02
Bandwidth	400 MHz-km
Proof Test Level	100 kpsi
Temperature Performance	-46°C to $+71^{\circ}\text{C}$
Construction	Tight Buffer

CABLE

The optical fibers are used in cabling once qualified. Currently significant emphasis has been placed on replacing the twin coaxial cable OX-11230 with fiber optics. The optical cable which will replace this coaxial metallic cable consists of two optical fibers terminated onto hermaphroditic connectors. The fiber optic cable,

CABLE DESIGN

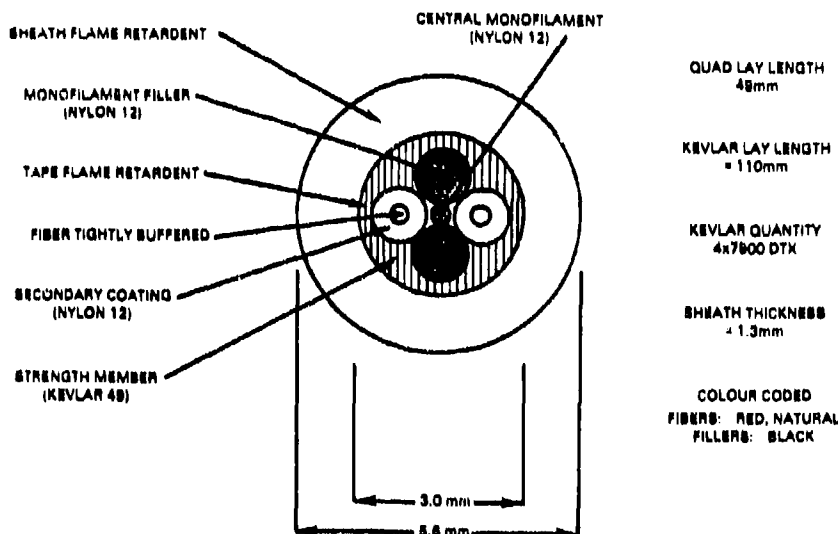


Figure 2. Two Fiber Tactical Cable Crosssection

Figure 2, is designed to meet a number of challenging requirements of which some are of a conflicting nature, i.e. low temperature performance and ruggedness. More ruggedness is obtained by increasing the cable jacket thickness but an extra increase in attenuation results due to unequal expansion and contraction coefficients among buffer material, Kevlar and cable jacket materials. In order to succeed in introducing this new technology into the field, extra care must be applied so that the minimum disturbance is introduced on the present way of doing business, i.e., minimize the impact and utilize as much as possible the presently available equipment. To meet these constraints, the cable reels used with CX-11230 and all the ancillary equipment are also utilized for fiber optics. The present reels RC-453 which are used to carry 300 m of twin coaxial cable are now utilized and easily carry 1,000 m of two fiber cable. The above constraint together with the two men lift requirement has defined that the optical cable diameter shall not exceed 6 mm. Based on the cable diameter DoD-STD-1678 the impact load, ruggedness, has been determined to be between 1.5 and 2.5 kg, see figure 3.

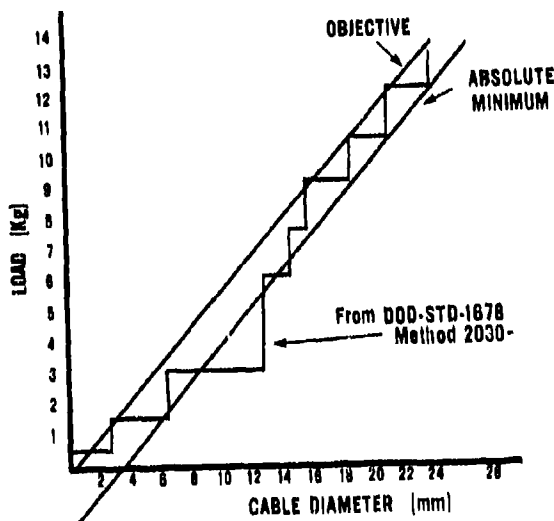


Figure 3. Linear Regression for Fiber Optic Cable Impact Testing Based on DoD-STD-1678

The minimum tensile strength of the cable is 1,780 Newtons, and the operating tensile loading is 300 Newtons. The optical fibers and strength members have to be stranded and jacketed with the appropriate materials in order for the cable performance during temperature cycling between -46°C to $+71^{\circ}\text{C}$ not to exceed 0.5 dB/km. The cable jacketing material must be selected so that the cable can withstand storage at environments -70°C to $+85^{\circ}\text{C}$.

The optical cable shall withstand a compressive load of 2,000 Newtons and the jacketing material shall exhibit no cracks or defects and no increase in attenuation. The cable shall be also designed to meet a knot test without increase in attenuation when it is wrapped around a mandrel of five times the cable diameter. The cable jacketing material has to also be selected to meet the flammability requirement which calls for burning less than 30 seconds and distance traveled by flame less than four times the outer circumference of the cable. The cable jacketing material which is considered the key of the successful cable design has to support the cable structure and meet the cyclic flexing requirements versus temperature, the freezing water immersion test and the long term aging test which verifies that the cable can provide service for 30 years. The following, Table 2, summarizes the key requirements that a tactical cable should meet.

TABLE 2
TACTICAL FIBER OPTIC CABLE REQUIREMENTS

		METHOD
Cable Construction	All dielectric	
Outer Diameter max	6 mm	
Tensile Strength	1780 Newtons (400 lbs)	
Temperature Cycling	-46°C to $+71^{\circ}\text{C}$	4020
Storage	MIL-STD-810D	
Altitude Cycling	MIL-STD-810D	520
Freezing Water Immersion		
Ice Crush	DoD-STD-1678	4050
Cyclic Flexing	DoD-STD-1678	2010
Cold Bend	DoD-STD-1678	2020
Impact Damage		
1. Room Temperature	DoD-STD-1678	2030

TABLE 2 (Cont)

2. -46°C	DoD-STD-1678	2030
3. +71°C	DoD-STD-1678	2030
Radial Compressive Strength	DoD-STD-1678	2040
Cable Twist-Bend	DoD-STD-1678	2060
Tensile Loading	DoD-STD-1678	3010
Flammability	DoD-STD-1678	5010
Fungus	MIL-STD-810D	508.3
Reasonably Priced		

CONNECTOR

In order to provide demountable connections the proven fiber optic cables shall be terminated onto hermaphroditic two fiber connectors. The connectors have to be designed and meet the requirements of the operating environment.

Based on the tolerances imposed on the core, cladding and concentricity it is easy to produce connectors with insertion loss below 1 dB. The connectors have to be installed on the cable so as to provide a cable retention strength of 1780 Newtons minimum, equivalent to cable breaking strength. For the tactical environment, the connector design shall provide for field termination and a strain relief shall be attached in order to protect the optical fibers for excessive bonding at the connector's end. To assure multiyear performance the connector interface shall be designed to withstand as a minimum 2,500 matings/unmatings without increase in insertion loss or need for cleaning.

The connector shall meet the low temperature, high temperature and temperature cycling and temperature shock requirement as required for the optical cable. The optical connector has to be water tight and meet the water immersion requirement which call for immersion in 6 foot head of water for 24 hours. The performance of the optical connector shall not be affected by exposure to high temperature and high humidity. One of the key requirements that a tactical connector has to meet is field cleanability without the use of special kits. The following Table 3 lists the test procedures and the requirements that an optical connector has to meet before it qualifies.

TABLE 3

TACTICAL FIBER OPTIC CONNECTOR REQUIREMENTS

Hermaphroditic	Two Fiber Connector
Insertion Loss	< 2 dB Loss, < 1 dB Butt Joint
Mating Durability	2,500 cycles
Ease of Interconnection	Minimum Force, Positive Locking
Connector Tensile Strength	DoD-STD-1678, Method 3010, Procedure 1I
Adequacy of Dust Cap	MIL-STD-810D, Procedure I, Method 512.1
Field Cleanability	No Special Kits Allowed
Impact	MIL-STD-1344, Method 2015
Vibration	MIL-STD-1344, Method 2005.1
Salt Fog	MIL-STD-1344, Method 1001.1
Fungus	MIL-STD-810D, Method 508.3
Leakage (Immersion)	MIL-STD-810D, Method 512.2
Sand and Dust	MIL-STD-810D, Method 510.2
Temperature Cycling	MIL-STD-1344, Method 1003.1
Temperature Storage	DoD-STD-1678, Method 4010
Altitude Cycling	MIL-STD-810D, Method 520
Freezing Water Immersion	DoD-STD-1678, Method 4050
Humidity	MIL-STD-810D, Method 507.2
Shock	MIL-STD-810D, Method 516.3
Weight	0.36 kg Plug/ 0.3 kg Receptacle
Flammability	MIL-STD-1344, Method 1012
Reasonably Priced	

TRANSMITTERS/RECEIVERS

The fiber optic transmitters and receivers operate at 1.3 um wavelength and are comprised of LED transmitters and PIN/FET receivers. The physical characteristics of an LED transmitter for a tactical communications system are listed in Table 4.

TABLE 4

LED PHYSICAL CHARACTERISTICS

Packaging	14 Pin Dual Inline Package
Fiber Retention	10 N (2.25 lbs)
Fiber Optic Pigtail	1 m (39.3 inches)
(Fiber identical with the one used in cable)	
Heat Transfer	Provided by the area between pins
Fully Hermetic	No epoxies internal to seal

The optical transmitters are designed to meet the environmental requirements listed in Table 5.

TABLE 5

LED ENVIRONMENTAL REQUIREMENTS

Operating Temperature	-55°C to +85°C
Storage Temperature	-55°C to +125°C
(Humidity performed when exposed to 95% RH for continuous and intermittent periods.)	
Barometric Pressure	
1. Storage and Transit	Sea level to 12200 m
2. Operating	sea level to 3050 m
Vibration and Shock	Induced during transportation
Radiation Hardness	
Safety	

The characteristics of the optical transmitter are listed in Table 6.

TABLE 6

LED OPTICAL CHARACTERISTICS

Peak Output Power @ 150 mA (Function of heat sink temperature)	See Figure 4
Emission Spectra	
Drive Current	150 milliamperes
Absmax Drive Current	200 milliamperes
Nominal Forward Voltage	1.8 volts @ 150 mA
Drop (Less than)	
Bias Conditions	
(No performance degradation after subjection to)	1V rev bias dir
Center Wavelength @ 25°C	1250 + 15 nm
Temperature Dependence (Over entire operating temperature range)	0.700 nm/°C
Linewidth @ FWHM (Over entire operating range)	< 100 nm
Optical Rise/Fall Time (10% to 90%) and Drive Current Change From 25% to 100% of	< 8 nanoseconds
Linearity Sufficient To Maintain (Total harmonic distortion)	150 milliamperes < 15% of AC.P
Contrast Ratio for 4 Milliamperes Drive Current	< 1.5% of output P Defined at 150 milliamperes

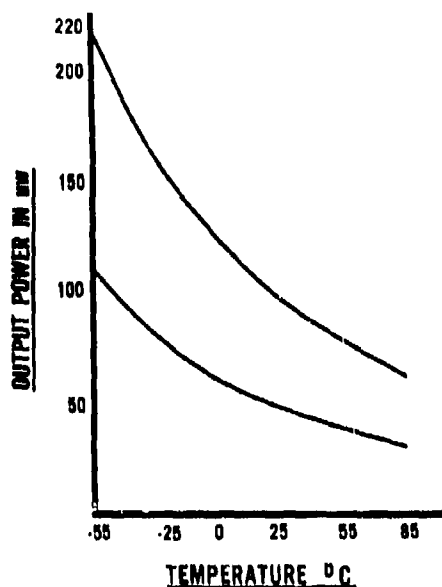


Figure 4. LED P_{out} in mW v Temperature in °C

The transmitters in order to qualify have to meet the requirements listed in Table 7. The screening tests are performed in accordance with MIL-STD-750.

TABLE 7
LED SCREENING TESTS

MIL-STD-750, Method

Fiber Retention	10 N
Internal Visual	2073
Stabilization Bake (At max temp)	1032
Temperature Cycling	1051 Test Cond. B
Constant Acceleration (Y, orientation 10,000 G-min)	2006
Seal	1071
1. Fine Leak	Test Cond. H
2. Gross Leak	Test Cond. C
Radiography	2076
Burn-in (168 hrs)	1038 Test Cond. B
External Visual	2071
Mechanical Shock (Half-size pulse @ 100 G's)	MIL-STD-750, Method 213

PIN/FET transimpedance optical receivers have been selected for use in the first tactical communications system. They are qualified to hybrid level of MIL-M-38510, including radiographic inspection.

The physical characteristics of PIN/FET receiver modules are listed in Table 8.

TABLE 8
PIN/FET PHYSICAL CHARACTERISTICS

Packaging	14 Pin Dual Inline Package
Lead Material	Type A or B per MIL-M-38510
Finish	Type C
Heat Transfer	Provided by the area between the pins
Fiber Optic Pigtail	Fiber identical to fiber in cable
Fully Hermetic	No epoxies internal to seal

The PIN/FET receivers are designed to meet the environmental requirements listed in Table 9.

TABLE 9
PIN/FET RECEIVER ENVIRONMENTAL CHARACTERISTICS

Operating Temperature	-46°C to +85°C
Storage Temperature	-55°C to +125°C
Humidity (Hermetically Sealed)	95% RH
Barometric Pressure	
1. Storage & Transit	Sea level upto 12200 m
2. Operating	Sea level upto 3050 m
Vibration and Shock	Transportation, rough handling
Radiation Hardness	With the exception of
	1. Module Responsivity
	2. Frequency Response
	3. Output Noise Voltage
Post Radiation Exposure	94%
Responsivity	
Post Radiation Frequency	94%
Response (From DC to 15 MHz)	
Post Noise Voltage (RMS)	
	285 to 420 mv for (-46 + 80°C)
	or -46 to 22°C 285 mv
	23 to 35°C 317 mv
	36 to 80°C 420 mv

The characteristics of an optical receiver for a tactical communication system are listed in Table 10.

TABLE 10

PIN/FET RECEIVER OPTICAL CHARACTERISTICS

Spectral Sensitivity	1100 - 1400 nm
Optical Damage - Withstanding	5 mwatts
Input Optical Power	-44.5 dBm to -4.5 dBm
Level (pp) for 5×10^{-11} BER	35.5 uW to 355 uW
Responsivity (No AGC)	5.3×10^4 to 5.9×10^4 $\frac{V}{W}$
(Full AGC)	5.3×10^3 to 5.9×10^3 $\frac{V}{W}$
Frequency Response	100 Hz to 20 MHz min
Group Delay	4 nansecs for 4 KHz to 15 MHz
Linearity	1 dB compression/decompression max
Output Noise Voltage	180-265 microvolts max
(Temperature Dependent)	

Receiver sensitivity versus temperature is shown in Figure 5.

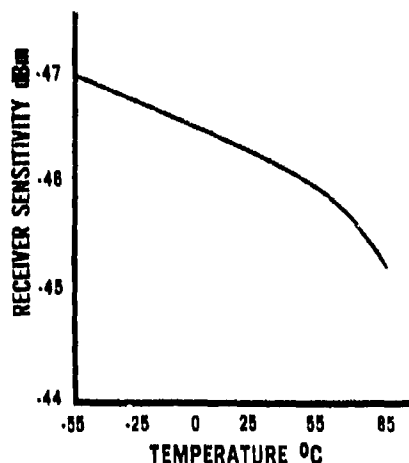


Figure 5. Receiver Sensitivity v Temperature

The receivers are evaluated in accordance with MIL-STD-883 for qualification. The screening tests are listed in Table 11.

TABLE 11

PIN/FET RECEIVER SCREENING TESTS

		Per MIL-STD-883 Method
Fiber Retention	10 N min	
Internal Visual		2017
Stabilization Bake	24 hrs min	1008 Cond B
Temperature Cycling		1010 Cond A
Constant Acceleration		2011 Cond B
in 11 orientation		
Visual Inspection	Defective parts	
Interim (Pre-burn-in)	Electrical parameters	
Burn-In-Test	160 hrs @ 100°C	1015
	160 hrs @ 125°C	
Seal		1014
	1. Fine	
	2. Gross	
Radiography Inspection		2012
Resistance to Solvents		2015
Bond Strength		2011
Moisture Analysis	5000 ppm max	1018
	at 100°C and 1 atm Pressure	

The stringent requirements³ that a tactical fiber optic system must meet to qualify for fielding are listed and compared with the requirements of a fixed plant communications system, see Table 12.

TABLE 12

FIXED PLANT VERSUS TACTICAL FIBER OPTIC COMMUNICATIONS SYSTEM

<u>ITEM</u>	<u>FIXED PLANT</u>	<u>TACTICAL SYSTEM</u>
Mobility	Permanent and Protected	Rapid Mobility 50% of Systems in Place for < 10 hrs
Installation	Underground or Aerial	On Ground, Underground or Aerial
Climate	Stable Environment Equipment Easily Qualifies	Severe Climatic Conditions Materials and Equipment Specifically Designed
Radiation Hardness	Metallic Strength Members Commonly Used	Severe Problems, All Dielectric Cables Required, Terminals and Equipment EMP/EMI Resistive
Cable Length	No Significant Constraints	Significant Constraints, No Splices, Use of Connectors and Existing Deploying & Retrieving Equipment
Durability	No Significant Problems	Handling and Environmental Factors Necessitate Highly Durable Cable
Flexibility	One Time Installation	Handling and Low Temperature Performance Require Highly Flexible Cable
Weight/Bulkiness	No Significant Problems	Need to Reduce Installation Time, Logistical Requirements and Improve Cost Effectiveness
Repeaters	Repeaters Might Not Be Required. Repeaters May Be Remotely Powered	Repeaters Required Must Be Fully Mil-Qualified and Uses Battery Power
Ancillary Equipment	Industrial Grade	Most of Equipments Used for Repair or Monitoring Must Be Mil-Qualified
Installation Machinery	Continuously Improving Upgraded Techniques	Same Equipment as the One Used for Twin-Coax Cable Same Techniques

CONCLUSION

When the physical, environmental and optical characteristics of a tactical fiber optic system are examined, it becomes apparent that significant differences between fixed plant telecommunications systems and tactical communications systems exist. The components and system, as a whole, for a fixed plant installation will not meet the requirements of a tactical environment. These differences in requirements necessitate additional research and development work to obtain acceptable components. This is a direct cause for delays in fielding and increases in cost of the militarized fiber optic systems.

REFERENCES

1. A.G. Mondrick, G. Chiu Chan, V. Mordowitz and M. Weinberg, "FOTS(LH): The Army's Long Haul Fiber Optic Transmission System," Signal Magazine, November 1983.
2. USA OECOM, Development Specification, "Fiber Optic Transmission System Long Haul, 27 May 1981.
3. H. Wichansky, L.U. Dworkin, S. DiVita and A. Mondrick, "Survivability of Army Fiber Optic Systems" SPIE, August 1981.

BIOGRAPHY

Vasilios E. Kalomiris, a project leader with the Center for Communications Systems of the U.S. Army Communications and Electronics Command, is responsible for fiber optic component and system development. He is a member of the Tri-Service Group, Chairman of the Working Group on Fibers, Cables, and Connectors. He is also a member of The Technical Cooperative Program JTP-12 on Fiber Optics and a member of the P6.7 Committee on Fiber Optic Standards. Previously, he worked for ITT-EOPD as a project engineer where he designed an air-layable fiber optic cable. Prior to joining ITT-EOPD, Vasilios was associated with General Cable Corp. R&D as a research engineer. Projects included electronic equipment calibration, communications cable design and evaluation, material evaluation and work on the first flexible superconductive power cable for Brookhaven National Laboratory. A graduate of New York University (B.A., B.S.E.E. and M.S.E.E.) he is a member of I.E.E.E. and The Technical Chamber of Greece (Society of Professional Engineers).

DISCUSSION**R. Keil, Gc**

(1) What kind of lenses do you use in your fibre connectors? (2) Is the coupling efficiency of your connectors stable over the whole temperature range you mentioned?

Author's Reply

(1) Cylindrical lens. (2) There is an approximately 0.4 dB maximum variation allowed.

A Hybrid Transmission Scheme on Single Mode Fibers for Tactical Communications

Steven S. Cheng
Division Manager, Exchange Network Research Division
Bell Communications Research, Inc.
Morristown, New Jersey USA 07960

SUMMARY

Tactical deployment of fiber optics communication links has many attributes similar to that of wideband subscriber loops. The availability of single-mode fibers and long wavelength devices enables the system designers to consider new link design with much improved performance not presently available in either the multimode fiber or the traditional metallic conductor systems. In this paper, we propose a hybrid transmission scheme on single-mode fibers in a star configuration. At the command post, a primary laser and its standby laser running at the cw mode are followed by an optical power splitter. Each output port is then externally modulated for downstream transmission. At each remote site, a dedicated LED is used for upstream transmission where the bandwidth requirement and therefore the dispersion penalty is generally lower. The cost, reliability and flexibility of this hybrid transmission scheme are examined. The use of bidirectional WDM devices and remote external modulators with polarization control is described as two potential variations to enhance this basic hybrid scheme. The deployment of such a system will provide cost-effective transmission links in a tactical environment suitable for high bandwidth analog and digital transmission.

1. Introduction

The use of fiber optics for tactical communications has many advantages over conventional metallic conductors. Most applications, to date, have been using short wavelength multimode fibers to replace the existing metallic conductor links. LED source is preferred in these systems because of its reliability, simpler transmitter design and cost.⁽¹⁾

The availability of rapidly maturing single-mode fibers and long wavelength devices enables the system designers to consider new tactical link design with much improved performance not presently available in either multimode fiber or metallic conductor systems.

Many of the considerations derived in this paper are first studied in conjunction with the deployment strategy of single-mode fibers in the subscriber loops for wideband service.⁽²⁾ The synergy between these two classes of applications will enable the advances in one to benefit the other in the years to come.

The paper will try to match the attributes of long wavelength fiber technology with the unique requirements of tactical environment. A basic hybrid transmission scheme and two variations for enhancement are proposed for closer examination.

2. Issues on Single-Mode Fibers and Sources

In the first generation commercial single-mode systems (Table 1), the links are designed for point-to-point transmission with direct modulation of laser current. For the intercity transmission where long repeater spacing (up to 40 km) and high bit rate (up to 680 Mb/s) transmission are of primary concern, this is an effective way of using single-mode long wavelength technology. However, for tactical communication, the typical distance between the command post and its remote sites is much shorter than the maximum achievable repeater spacing, therefore the laser based single-mode fiber link may prove to be an overkill from the cost and reliability point-of-view. However, the use of single-mode fibers running at zero-dispersion wavelength of 1.3 μm region does present a significant improvement in bandwidth/bit rate handling capability over the multimode fibers. For a laser based single-mode system, the limitation in speed comes primarily from the electronic circuitry such as transmitter, receiver, parallel to serial converter, encryptic device, and digital multiplexer. However, the state-of-the-art silicon integrated microwave circuits can operate up to 1 Gb/s which is several orders of magnitude higher than the achievable speed in the copper based system and is expected to be more than adequate for a broad range of new high speed services including transmission of high definition television pictures. The availability of very high speed logic and VLSI will push the design of the next generation tactical links to handle high speed serial data streams instead of low speed parallel data carried today in most of the metallic links.

Another advantage of using single-mode fibers over multimode fibers is in the reduction of several noise sources. When laser diodes are used as sources in multimode fiber systems, the mode partition noise⁽³⁾, modal noise⁽⁴⁾ and optical feedback to laser cavity can cause severe performance degradation. These noise processes are usually present simultaneously in a laser based multimode system, but are essentially absent when an LED is used. This is also the main reason why LEDs are preferred over laser diodes in the first generation tactical fiber optic systems.

Having established that single-mode fiber is the preferred transmission medium for high speed, high performance link in the tactical environment, let us now examine two optical source strategies for such applications.

3. Principle of Laser Power Sharing

A laser power sharing scheme is proposed to share the cw laser power among many users. In Figure 1, we place a single transverse mode laser running in cw mode at a command post (denoted as central node) to be followed by an optical power splitter, in the form of a single stage 1 by N star coupler or a cascade of optical star couplers, to evenly divide its output power. A second cw laser is used as a standby to enhance the optical source reliability and serviceability. The external modulation is done immediately following the power splitting. The number of output ports in the power splitting can be estimated based on the link loss budget calculation. Table 2 shows that up to 41 and 371 ports can be served by one laser for links with a distance/bit rate of 10 km/140 Mb/s and 4 km/50 Mb/s respectively. In the tactical deployment, by properly cascading power splitters with different numbers of output ports according to the distance/bit rate requirement of each link and subject to the overall laser power constraint, one can custom implement the laser power sharing scheme to a very high degree of flexibility. Since various optical components are interconnected by connectors, with the aid of a simple computer program, one can engineer and assemble a field system in a very short time (Figure 2). The key to this flexibility lies in the availability of an assortment of power splitters with N as small as two and as large as, perhaps, eight. Since the two lasers and all the power splitters are located centrally, it provides easy access for performance monitoring and maintenance activities. The vulnerable part of this scheme is limited to the very short optical path between lasers and the first star coupler (usually several inches). Failure of an output port of any power splitter will affect at most one subgroup of customers. The use of an external modulator has the added advantage of eliminating the degradation caused by the optical feedback to the laser cavity.

4. LED On Single-Mode Fiber

For cost effective short distance wideband transmission (i.e., subscriber loop), LED has recently been investigated as an optical source. This radical approach suffers two major penalties making it unacceptable for consideration in intercity long distance transmission, namely, the large LED single-mode fiber coupling loss (typically 30 dB) and the chromatic dispersion due to broad LED linewidth. However, recent studies⁽⁹⁾ indicated that by using off-the-shelf edge emitting diodes with some minor improvements, a distance of 15 km at 140 Mb/s can be achieved in actual installation. Further improvement can be expected when the edge emitters are designed for maximum power coupling into single-mode fibers. The cost and reliability advantages of LED over lasers could be realized in these single-mode fiber installations for tactical applications.

5. A Hybrid Transmission Scheme

By combining the best of these two novel schemes, we propose a hybrid transmission scheme on single-mode fibers by using two shared lasers at the command post in a radiating star configuration for downstream transmission to a multitude of remote sites. In each remote site a dedicated LED is used for upstream transmission where the bandwidth requirement and therefore the dispersion is generally lower. External modulation is done at the command post at each output port of the optical power splitter.

PIN-FET detectors are used at the command post and throughout all remote sites. In this hybrid scheme, the use of lasers is reduced to a minimum. The laser power can be flexibly distributed and quickly rearranged according to the needs in the tactical situation. Since LEDs are used in all remote sites, they require virtually no control circuit and the performance would be fairly stable under large temperature variations. Thus, the scheme provides an optimum solution with simplicity, reduced cost, enhanced capability and reliability.

6. Two Variations

By properly utilizing wavelength division multiplexer (WDM) devices, the number of fibers deployed can be reduced by half or even further. In the first variation, bidirectional two-wavelength WDM devices are used at both ends of each link⁽⁶⁾. In this scheme, additional power should be allocated to account for the loss in the WDM pair, typically two to three dBs.

The second variation involves the use of unidirectional WDM devices⁽⁷⁾. In Figure 3 two primary cw lasers (λ_1, λ_2) are operating at the command post. After the power splitting, the modulated signal on λ_1 (1.3 μm) is combined with an unmodulated light at λ_2 (1.5 μm) in a WDM device for downstream transmission. Upon WDM demultiplexing at the remote site, the signal on λ_1 is detected and λ_2 is modulated, then looped back to the central node via a returning fiber. In this sourceless scheme higher losses are encountered in the round trip path (λ_2), including WDMs (2-3 dB) and a polarization controller (2 dB). The latter is needed in front of the external modulator at the remote site because by the time cw light λ_2 arrives there, the originally linearly polarized laser beam from the laser source would have changed its state-of-polarization. The controller acts to restore the state-of-polarization to be linearly polarized again before entering the optical modulator. This transmission scheme will remove the dispersion constraint imposed by the LEDs in the hybrid scheme. In order for this scheme to be successful, however, one generally needs a more powerful laser source and more importantly the availability of polarization controller and external modulator.

7. Device and Engineering Issues

To increase the number of output ports in the optical power sharing scheme, one would like to increase the available system gain (power coupled into fiber subtracted by the receiver sensitivity). The first logical step is to increase the coupled cw laser power beyond the typical 1 mw achievable in today's semiconductor lasers. Since these lasers will be located at the command post and their cost shared by many users, the cost and size issues become less critical.

One might consider high power semiconductor lasers⁽⁷⁾ as well as other solid state lasers as sources with a power level up to 100 mw, but not to exceed the power threshold of generating nonlinear Raman signals at longer wavelength region if WDM devices are to be used.

At this power level, care must be taken to safeguard the operation personnel by devising proper operational and maintenance procedures and installing interlocking mechanisms for safe operation of lasers. The danger at outside plant or remote sites is much reduced because the power is quickly divided near the laser sources. By the time it reaches remote site it is on the order of several dBs above the receiver sensitivity which is quite safe.

While the cost and reliability of integrated optical modulator is not yet well established, intrinsically it is a passive device with a manufacturing process similar to that of silicon VLSI. Likewise, the *LiNbO₃* or glass waveguide technology may lend itself for cost-effective mass production of optical splitters and WDM. If we are to pursue the sourceless scheme at the remote sites, the polarization controller is required. It is also needed in the receiving part of any coherent communication link. Today it exists in the form of a manually adjustable mechanical device. It is desirable that a miniaturized version incorporating feedback circuitry to compensate for the slow variation due to temperature and aging effect be developed⁽⁸⁾.

8. Conclusion

In adapting the first generation long wavelength single-mode technology into the tactical military communication, we propose to take advantage of the excess power of laser by power sharing at a central location and to use dedicated LEDs at remote sites. This hybrid transmission scheme has many desirable attributes in cost, compactness, maintainability, flexibility and reliability. The critical element that needs further work is the external modulator. With the deployment of such a tactical communication system, each link is considered as a virtual universal information pipe for analog and digital transmission for low bit rate voice, data at any speed, images up to high definition television picture and even multiplexed video signals.

REFERENCES

1. D. H. Rice and G. E. Keiser, "Application of Fiber Optics to Tactical Communication Systems," IEEE Communications Magazine, Vol. 23, No. 5, May 1985, pp. 46-57.
2. S. S. Cheng, "Novel Systems Architecture for Broadband Distribution in the Local Access and Transport Areas," OFC'85 Digest, Feb. 1985, pp. 8-9.
3. K. Ogawa and R. W. Vodhanel, "Measurement of Mode Partition Noise of Laser Diodes," IEEE Quantum Electronics Vol. 18, July 1982, pp. 1090-1093.
4. R. E. Epworth, "Modal Noise, Causes and Cures," Laser Focus, September 1981, pp. 109-115.
5. P. W. Shumate, Jr., et al., "Transmission of 140 Mb/s Signals over Single-Mode Fiber Using Surface and Edge-Emitting 1.3 μm LEDs," Electronics Letters, Vol. 21, No. 12, June 1985, pp. 522-524.
6. J. D. Spalink et al., "Bi-directional 1.3 μm /1.5 μm WDM Fiber-Optic 144 Mb/s Transmission System Experiment," OFC'83 Digest, March 1983, pd. 1.
7. Y. Sakakibaro et al. "High Power 1.3 μm InGaAsP P-Substrate Buried Crescent Laser Diode," OFC'85 Digest, Feb. 1985, pp. 12-13.
8. P. Granestrang et al., "Active Stabilization of Polarization on a Single Mode Fiber," Electronics Letter, Vol. 20, No. 9, April 1984, p. 365.

TABLE 1

CHARACTERISTICS OF FIRST GENERATION SINGLE-MODE LIGHTWAVE SYSTEMS

- Multiple DS3 (9-12) Intercity Transports, Using Bit Stuffing Multiplexers
- Line Rates: 417-880 Mb/s, Usually Without Crossconnect At Intermediate Or Final Rate
- High Performance 1.3 μm Laser With Direct Current Modulation For Point-to-Point Link
- Engineered Repeater Spacing: 20-40 km, Loss Limited
- Some Upgradable To Handle An Aggregate Of 1.8-2.2 Gb/s Input Signal

TABLE 2
LOSS BUDGET OF TWO SHARED-LASER LINKS
IN TACTICAL SITUATION

Link Parameters	140 Mb/s at 10 Km	50 Mb/s at 4 Km
Laser power into fiber (dBm)	0	0
Receiver sensitivity (dBm) at 10^{-9} BER	-42	-46
System gain (dB)	42	46
Excess Loss in splitters	2 (cascade of 2 splitters)	3 (cascade of 3 splitters)
Installed* fiber loss	12	4.8
Insertion loss of modulator	3	3
Connector loss at both ends	2.8 (4 connectors)	3.5 (5 connectors)
System margin	6	6
Available power for splitting (dB)	16.2	25.7
Equivalent number of output ports in splitting	41	371

*Connectors are generally used in tactical links in lieu of permanent splices. 0.7 dB/connection per kilometer is assumed here and the unconnectorized cable loss is assumed to be 0.5 dB/km at $1.3 \mu\text{m}$

FIGURE 1
A HYBRID WIDEBAND TRANSMISSION SCHEME
FOR TACTICAL COMMUNICATIONS

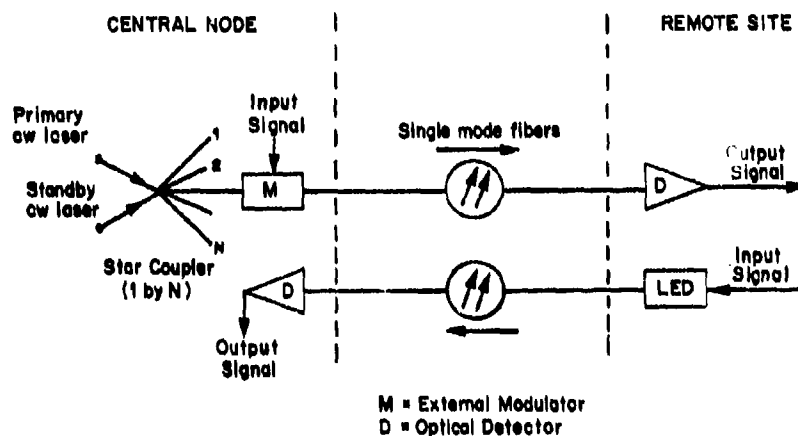


FIGURE 2
FLEXIBILITY IN LASER POWER SHARING

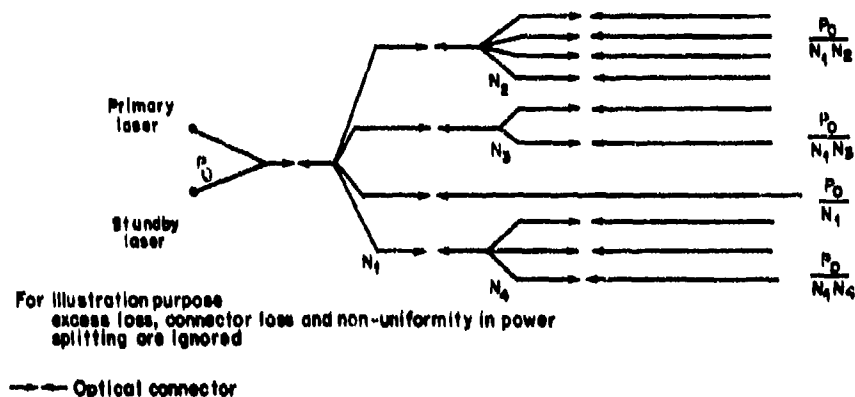
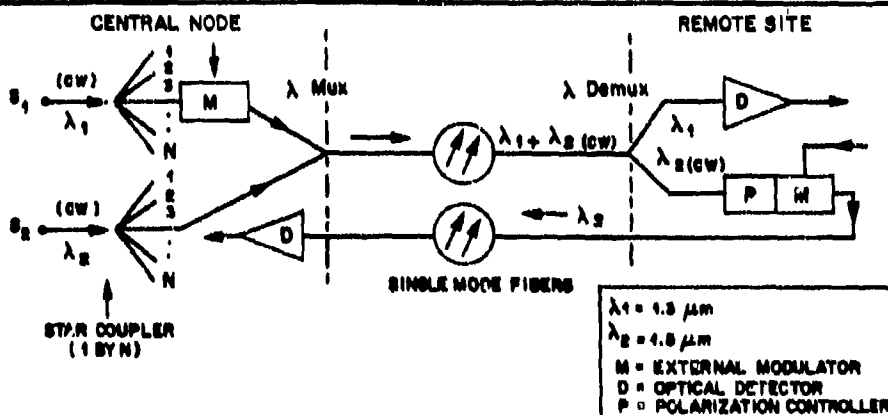


FIGURE 3
A SOURCELESS WIDEBAND
LOOP ARCHITECTURE



Laser sources shared and located at central node only

DISCUSSION**G. Winzer, Ge**

You have shown a star coupler in combination with an array of modulators. You said that it is intended to monolithically integrate the LD source in the same substrate. So, the substrate must be GaAs or InP. When do you believe such a device will be available at least as a laboratory prototype?

Author's Reply

For GaAs in the 0.8—0.9 μm region it is possible to do such integration now. For long wavelength region it may take several years before laboratory prototype devices become available.

B. Schwaderer, Ge

If I have picked-up the right figures from your slides, the fibre from the central node down to the remote node has 1.2 dB/Km, but in the reverse direction you have shown 0.45 dB/Km to use the ELED. Can you comment on this?

Author's Reply

The 0.45 dB/Km loss was the actual loss measured.

LIST OF PARTICIPANTS

AKKAYA, I. Prof.	Suadiye, Plaj Volu Sok 12/13, Istanbul, Turkey
ALBRECHT, H.J. Dr*	FGAN/FHP, Neuenahrer Strasse 20, 5307 Wachtberg-Werthhoven, Federal Republic of Germany
ARIKAN, H. First Lt.	MSB ARGE Daire Baskanligi, Bakanliklar, Ankara, Turkey.
ASLAM, M. Mr†	SHAPE Technical Centre, P.O. Box 174, 2501 CD The Hague, Netherlands
ATAMAN, A. Prof.†	Elektrik Fakultesi, Teknik Universitesi, Istanbul, Turkey
BAKKER, T. Ir.	Physics and Electronics Lab., P.O. Box 96864, 2509 JG The Hague, Netherlands
BAYKAL, Y. Dr	57. Sok 1/8 Emek, Ankara, Turkey
BERTOLOTTI, M. Mr†	Sezione Fisica, Dipartimento di Energetica, Universita di Roma, Via Scarpa 16, 00161 Roma, Italy
BLYTHE, J.H. Dr* (Panel Chairman)	Communications Research Laboratory, GEC Research Ltd., West Hanningfield Road, Chelmsford CM2 8HN, United Kingdom
BOGENBERGER, R. Dipl. Ing.	MBB GmbH, Dep. LKE 326, Postfach 80 11 60, D-8000 München 80, Federal Republic of Germany
CASSARA, A. Lt. Col.	Ricercaereo, Aeroporto Pratica di Mare, Pratica di Mare (RM), Italy
CHANEY, R.J. Dr	Q131 Rad. Nav. Dept, RAE (F), Farnborough, Hants GU14 6TD, United Kingdom
CHENG, S. Dr†	Division Manager, Exchange Network, Bell Communications Research, 435 South St. Room 26-287, Morristown, NJ 07960, United States
COYNE, V.J. Mr*	RADC/OCS, Griffiss Air Force Base, NY 13441-5700 United States
CROSIGNANI, B. Prof.*	Fondazione "Ugo Bordoni"/ISPT, Viale Europa 160, Roma, Italy
CULSHAW, B. Prof.†	Dept of Electronic and Electrical Engineering, University of Strathclyde, Royal College Bld., 204 George Street, Glasgow, United Kingdom
DAKIN, J.P. Dr†	Plessey Electronic Systems Research Ltd., Roke Manor, Romsey, Hants, United Kingdom
DAY, G.W. Dr†	National Bureau of Standards 724-02, 325 Broadway Boulder, CO 80303, United States
DEIMEL, P. Dr	MBB GmbH, P.O. Box 80 11 49, D-8000 München 80, Federal Republic of Germany
ELLIALTIOGLU, R.M. Dr	P.O. Box 21, Gebze-Kocaeli, Turkey
FALCIAI, R. Dr	Istituto Ricerca Onde Elettromagnetiche del CNR, Via Panciatichi, 50127 Firenze, Italy
FEIGELSON, R.S. Prof.†	Director, Crystal Growth Div., McCullough Building, Rm 105, Stanford University, Stanford CA 94305-2176, United States
FITZSIMONS, T. Dr*	ARFA, CCCS Division, IMS, NATO, 1110 Evere, Belgium
FORBES, N. Mr	Ferranti plc, Optical Components Group, Dunsinane Avenue, Dundee DD2 3PN, United Kingdom
FRIDMAN, J.D. Prof. Dr	Mitre Corporation, MSEOSO, Burlington Road, Bedford, MA 01730, United States
GEE, C. Dr†	Hughes Research Laboratories, 3011 Malibu Cyn. Rd RL67, Malibu, CA 90265, United States

* Member of Electromagnetic Wave Propagation Panel

† Author of paper presented at the meeting.

GIALLORENZI, T.G. Mr*	Optical Sciences Division, Department of the Navy, Naval Research Laboratory, Washington D.C. 20375, United States
GOUTELARD, C. Prof.*	Directeur du LETTI, 9 Avenue de la Division Leclerc, 94230 Cachan, France
HEGARTY, J. Dr†	AT & T Bell Laboratories, 600 Mountain Avenue, Murray Hill, NJ 07974, United States
HENDRICKSON, B. Mr	RADC/DCLW, Griffiss AFB, NY 13441, United States
HENNEN, N.M. Dr rer. nat.	MBB GmbH, Space Division RR28, Postfach 80 11 69, D-8000 München 80, Federal Republic of Germany
HODARA, H. Dr*	President, Tetra Tech, Inc. 630 North Rosemead Bld, Pasadena, CA 99107, United States
INCE, A. Prof. Dr.*	Science & Engineering Research Council, TUBITAK, Ataturk Bulvari 221, Ankara, Turkey
JOSEPH, T.R. Dr†	TRW Electro-Optics Research Center, 1 Space Park, Bldg 135—1831, Redondo Beach, CA 90278, United States
KALOMIRIS, V.E. Mr†	US Army Communications, AMSEL-COM-RM-1, Fort Monmouth, N.J. 07703-5202, United States
KAYA, D. Colonel	Ministry of National Defence, Dept. of Research & Development (ARGE), Ankara, Turkey
KEIL, R. Dr Ing.†	Research Laboratories of Siemens AG Abt.ZRT ZFE FKE 31, Otto-Hahn-Ring, 8, München 83, Federal Republic of Germany
KOHNLE, A. Dr	Schloss Kressbach, D-7400 Tübingen, Federal Republic of Germany
KUMCU, K. Mr	P.O. Box 21, Gebze-Kocaeli 1, Turkey
LEFEVRE, H. Dr†	Thomson CSF, B.P. 10, Domaine de Corbeville 91401 Orsay, France
LEWIS, D.H. Mr†	Advanced Optical Systems, Litton Systems (Canada) Limited, 25 Cityview Drive, Rexdale, Ontario M9W 5A7, Canada
LIZOT, M.J. Mr	Chef de la Division Optique, D.R.E.T., 26 Bld Victor, 75996 Paris Armées, France
LUCAS, J. Prof.†	Université de Rennes, Campus de Beaulieu, Laboratoire de Chimie Minérale, 35042 Rennes, France
MACDONALD, R.I. Dr†	C.R.C., P.O. Box 11490 Station H, Ottawa, K1H 8S2, Canada
MALFAGIA, R. Dr	Elettronica San Giorgio — ELSAG s.p. Via Puccini, 2 16154 Genoa, Italy
MCDONACH, A. Dr†	R & D Project Leader, Barr and Stroud Ltd, Caxton St., Anniesland, Glasgow, United Kingdom
NEAT, R.C. Ms.	STC Telecommunications Ltd., Defence Systems Division, Christchurch, Greenwich, London SE10 0AG, United Kingdom
NEWBERY, G.W. Mr	Thorn EMI Electronics Ltd, Wookey Hole Road, Wells, Somerset, BA5 1AA, United Kingdom
NIEDERHOFER, K. Dipl. Ing.†	Messerschmitt-Bölkow-Blohm GmbH, Dynamics Division, AE 322, P.O. Box 801149, Ottobrunn, Federal Republic of Germany
PAN, J.J. Mr†	E-TEK Dynamics, Inc., 250 East Drive, Melbourne, FL 32901, United States
PATRICIO, J.F. Eng.*	CTT-Director dos Serviços de Radiocomunicações, Rua Conde de Redondo, 79—10, 1189 Lisboa Codex, Portugal
PITT, N.J. Dr†	STC-Standard Telecommunication Lab., London Road, Harlow, Essex CM17 9NA, United Kingdom
ROMAN, P. Prof. Dr	Liaison Scientist, ONR, Branch, 223 Old Marylebone Rd, London NW1 5TH, United Kingdom
ROTHER, D. Dr*	Ostendstrasse 3, D-7530 Pforzheim, Federal Republic of Germany

* Member of Electromagnetic Wave Propagation Panel

† Author of paper presented at the meeting.

SCHWADERER, B. Mr†	ANT Nachrichtentechnik, Gerberstrasse 33, 7150 Backnang, Federal Republic of Germany
SCOTT, M.G. Dr†	STC-Standard Telecommunication Lab., London Road, Harlow, Essex CM17 9NA, United Kingdom
SEATON, C.T. Dr†	Optical Sciences Center, University of Arizona, Tucson, AZ 85721, United States
SEPP, G. Dr	MBB GmbH, Dept. AE 343, P.O. Box 801149, D-8000 München, Federal Republic of Germany
SEPP, H. Dr*	SHAPE Technical Centre, P.O. Box 174, 25501 CD The Hague, Netherlands
SIBILIA, C. Dr†	Dipartimento di Energetica, Via Scarpa N.16, 00161 Roma, Italy
SMITH, G.P. Dr	Corning Glass Works, Sullivan Park, FR-21, Corning, N.Y. 14831, United States
SOICHER, H. Dr* (Panel Deputy Chairman)	US Army Communication-Electronic Cmd Center for Communications Systems, Attn: AMSEL-COM:RN-1, Fort Monmouth, N.J. 07703, United States
SOTTINI, S. Dr†	Istituto di Ricerca sulle Onde Electromagnetiche, Via Panciatichi 64, 50123 Firenze, Italy
SPITZ, E. Dr*	Thomson CSF, B.P. 10, Domaine de Corbeville, 91401 Orsay, France
SPRENKELS, C.R.C. Colonel*	Etat-Major de la Force Aérienne, Section Communications & Electronique, Quartier Reine Elisabeth, B-1140 Bruxelles, Belgium
STEGEMAN, G.I. Dr†	Optical Sciences Center, University of Arizona, Tucson, AZ 85721, United States
STOCKMANN, M. Mr†	Research Laboratories of Siemens AG, Otto-Hahn-Ring 6, 8, München 83, Abt. ZFE FKE 32, Federal Republic of Germany
TRAN, D.C. Dr†	Code 6570, Naval Research Laboratory, Washington D.C. 20375-5000, United States
TRILLO, S. Dr	Fondazione "Ugo Bordonini", Viale de Trastevere 108, 00153 Roma, Italy
TULUNAY, Y. Prof.*	ITU Ucak ve Uzah Bilimleri Fakultesi, Ayazaga, Istanbul, Turkey
VISSINGA, H. Mr*	Physics and Electronics lab., P.O. Box 96864, 2509 JG The Hague, Netherlands
WALKER, S.D. Dr†	British Telecom Research Lab., Martlesham Heath, Ipswich IP5 7RE, United Kingdom
WATANABE, S. Dr†	McDonnell Douglas Astronautics Company, 5301 Bolsa Avenue, Huntington Beach, CA 92647, United States
WHITE, M.B. Dr*	Office of Naval Research, EC Region, Bldg 114, Section D, 425 Summer St., Boston, MA 02210, United States
WILLSON, J.P. Dr	S.T.C. Ltd, London Road, Harlow, Essex CM17 9NA, United Kingdom
WINZER, G. Dr	Siemens AG Zentrals Forschung und Entwicklung, Forschungs Laboratorien, Otto-Hahn-Ring 6, D-8000 München 83, Federal Republic of Germany
YARGICOGLU, O. Mr	TUBITAK-BAE, Ataturk Bulvari 221, Kavaklıdere, Ankara, Turkey
YAZGAN, B. Prof.	ITU Elektrik Elektronik Fakultesi, Ayazaga Istanbul, Turkey
YEH, K.C. Prof.*	Dept. ECE, University of Illinois, 1406 W. Green Street, Urbana, IL 61801, United States

* Member of Electromagnetic Wave Propagation Panel
† Author of paper presented at the meeting.

REPORT DOCUMENTATION PAGE											
1. Recipient's Reference	2. Originator's Reference	3. Further Reference	4. Security Classification of Document								
	AGARD-CP-383	ISBN 92-835-0391-0	UNCLASSIFIED								
5. Originator	Advisory Group for Aerospace Research and Development North Atlantic Treaty Organization 7 rue Ancelle, 92200 Neuilly sur Seine, France										
6. Title	GUIDED OPTICAL STRUCTURES IN THE MILITARY ENVIRONMENT										
7. Presented at	the Electromagnetic Wave Propagation Panel Specialists' Meeting held in Istanbul, Turkey, 23--27 September 1985.										
8. Author(s)/Editor(s)	edited by Dr H.Hodara and Prof. B.Crosignani		9. Date May 1986								
10. Author's/Editor's Address	Various		11. Pages 310								
12. Distribution Statement	This document is distributed in accordance with AGARD policies and regulations, which are outlined on the Outside Back Covers of all AGARD publications.										
13. Keywords/Descriptors	<table border="0"> <tr> <td>Optical structures</td> <td>Strategic/tactical communications</td> </tr> <tr> <td>Waveguide</td> <td>Optical fibres</td> </tr> <tr> <td>Wavelength</td> <td>Planar waveguides</td> </tr> <tr> <td>Attenuation</td> <td>Dispersion</td> </tr> </table>			Optical structures	Strategic/tactical communications	Waveguide	Optical fibres	Wavelength	Planar waveguides	Attenuation	Dispersion
Optical structures	Strategic/tactical communications										
Waveguide	Optical fibres										
Wavelength	Planar waveguides										
Attenuation	Dispersion										
14. Abstract	<p>A new technology has arisen and is expanding quickly: single-mode structures in the form of optical fibres and planar waveguides operating at long wavelength, 1.3 μm and beyond, with minimum attenuation and dispersion. Fibres with attenuation below 0.5 dB/km, and bandwidths in the hundreds of GHz-Km have opened up long distance, repeaterless transmission on land and underwater. In addition, the single-mode structure has bred a new class of passive devices: sensors capable of detecting sound, magnetic field, motion, temperature, humidity and many other characteristics, all of them approaching the theoretical detection limit. New active components are developing: single mode, high efficiency, long-life laser chips operating at room temperature, electro-optic switches and components capable of generating new frequencies through Raman scattering and other nonlinear phenomena.</p> <p>This symposium brought together experts in optical structures and theory from military, industry and academia who discussed current advances in optical technology.</p>										

<p>addition, the single-mode structure has bred a new class of passive devices: sensors capable of detecting sound, magnetic field, motion, temperature, humidity and many other characteristics, all of them approaching the theoretical detection limit. New active components are developing: single mode, high efficiency, long-life laser chips operating at room temperature, electro-optic switches and components capable of generating new frequencies through Raman scattering and other nonlinear phenomena.</p> <p>This symposium brought together experts in optical structures and theory from military, industry and academia who discussed current advances in optical technology.</p> <p>Papers presented at the Electromagnetic Wave Propagation Panel Specialists' Meeting held in Istanbul, Turkey, 23-27 September 1985.</p> <p>ISBN 92-835-0391-0</p>	<p>addition, the single-mode structure has bred a new class of passive devices: sensors capable of detecting sound, magnetic field, motion, temperature, humidity and many other characteristics, all of them approaching the theoretical detection limit. New active components are developing: single mode, high efficiency, long-life laser chips operating at room temperature, electro-optic switches and components capable of generating new frequencies through Raman scattering and other nonlinear phenomena.</p> <p>This symposium brought together experts in optical structures and theory from military, industry and academia who discussed current advances in optical technology.</p> <p>Papers presented at the Electromagnetic Wave Propagation Panel Specialists' Meeting held in Istanbul, Turkey, 23-27 September 1985.</p> <p>ISBN 92-835-0391-0</p>
<p>addition, the single-mode structure has bred a new class of passive devices: sensors capable of detecting sound, magnetic field, motion, temperature, humidity and many other characteristics, all of them approaching the theoretical detection limit. New active components are developing: single mode, high efficiency, long-life laser chips operating at room temperature, electro-optic switches and components capable of generating new frequencies through Raman scattering and other nonlinear phenomena.</p> <p>This symposium brought together experts in optical structures and theory from military, industry and academia who discussed current advances in optical technology.</p> <p>Papers presented at the Electromagnetic Wave Propagation Panel Specialists' Meeting held in Istanbul, Turkey, 23-27 September 1985.</p> <p>ISBN 92-835-0391-0</p>	<p>addition, the single-mode structure has bred a new class of passive devices: sensors capable of detecting sound, magnetic field, motion, temperature, humidity and many other characteristics, all of them approaching the theoretical detection limit. New active components are developing: single mode, high efficiency, long-life laser chips operating at room temperature, electro-optic switches and components capable of generating new frequencies through Raman scattering and other nonlinear phenomena.</p> <p>This symposium brought together experts in optical structures and theory from military, industry and academia who discussed current advances in optical technology.</p> <p>Papers presented at the Electromagnetic Wave Propagation Panel Specialists' Meeting held in Istanbul, Turkey, 23-27 September 1985.</p> <p>ISBN 92-835-0391-0</p>

AGARD

NATO OTAN

7 RUE ANCELLE · 92200 NEUILLY-SUR-SEINE

FRANCE

Telephone (1) 47.45.08.10 · Telex 610176

**DISTRIBUTION OF UNCLASSIFIED
AGARD PUBLICATIONS**

AGARD does NOT hold stocks of AGARD publications at the above address for general distribution. Initial distribution of AGARD publications is made to AGARD Member Nations through the following National Distribution Centres. Further copies are sometimes available from these Centres, but if not may be purchased in Microfiche or Photocopy form from the Purchase Agencies listed below.

NATIONAL DISTRIBUTION CENTRES

BELGIUM

Coordonnateur AGARD — VSL
Etat-Major de la Force Aérienne
Quartier Reine Elisabeth
Rue d'Evere, 1140 Bruxelles

CANADA

Defence Scientific Information Services
Dept of National Defence
Ottawa, Ontario K1A 0K2

DENMARK

Danish Defence Research Board
Ved Idraetsparken 4
2100 Copenhagen Ø

FRANCE

O.N.E.R.A. (Direction)
29 Avenue de la Division Leclerc
92320 Châtillon

GERMANY

Fachinformationszentrum Energie,
Physik, Mathematik GmbH
Kernforschungszentrum
D-7514 Eggenstein-Leopoldshafen

GREECE

Hellenic Air Force General Staff
Research and Development Directorate
Holargos, Athens

ICELAND

Director of Aviation
c/o Flugrad
Reykjavik

ITALY

Aeronautica Militare
Ufficio del Delegato Nazionale all'AGARD
3 PIAZZALE Adenauer
00144 Roma/EUR

LUXEMBOURG

See Belgium

NETHERLANDS

Netherlands Delegation to AGARD
National Aerospace Laboratory, NLR
P.O. Box 126
2600 AC Delft

NORWAY

Norwegian Defence Research Establishment
Attn: Biblioteket
P.O. Box 25
N-2007 Kjeller

PORTUGAL

Portuguese National Coordinator to AGARD
Gabinete de Estudos e Programas
CLAFIA
Base de Alfragide
Alfragide
2700 Amadora

TURKEY

Department of Research and Development (ARGE)
Ministry of National Defence, Ankara

UNITED KINGDOM

Defence Research Information Centre
Kentigern House
65 Brown Street
Glasgow G2 8EX

UNITED STATES

National Aeronautics and Space Administration (NASA)
Langley Research Center
M/S 180
Hampton, Virginia 23665

**THE UNITED STATES NATIONAL DISTRIBUTION CENTRE (NASA) DOES NOT HOLD
STOCKS OF AGARD PUBLICATIONS, AND APPLICATIONS FOR COPIES SHOULD BE MADE
DIRECT TO THE NATIONAL TECHNICAL INFORMATION SERVICE (NTIS) AT THE ADDRESS BELOW.**

PURCHASE AGENCIES

Microfiche or Photocopy

National Technical
Information Service (NTIS)
5285 Port Royal Road
Springfield
Virginia 22161, USA

Microfiche

ESA/Information Retrieval Service
European Space Agency
10, rue Mario Nikis
75015 Paris, France

Microfiche or Photocopy

British Library Lending
Division
Boston Spa, Wetherby
West Yorkshire LS23 7BQ
England

Requests for microfiche or photocopies of AGARD documents should include the AGARD serial number, title, author or editor, and publication date. Requests to NTIS should include the NASA accession report number. Full bibliographical references and abstracts of AGARD publications are given in the following journals:

Scientific and Technical Aerospace Reports (STAR)
published by NASA Scientific and Technical
Information Branch
NASA Headquarters (NIT-40)
Washington D.C. 20546, USA

Government Reports Announcements (GRA)
published by the National Technical
Information Service, Springfield
Virginia 22161, USA



*Printed by Specialised Printing Services Limited
40 Chigwell Lane, Loughton, Essex IG10 3TZ*

ISBN 92-835-0391-0